Pathology & Oncology Research – Editors' Picks from 2022

Issue Editors

József Tímár
Semmelweis University,
Hungary

László Kopper
Semmelweis University,
Hungary

Andrea Ladányi
National Institute of
Oncology (NIO),
Hungary

Anna Sebestyén
Semmelweis University,
Hungary

*P*athology &
*O*ncology *R*esearch

Pathology & Oncology Research – Editors' Picks from 2022

On behalf of the Arányi Lajos Foundation for Modern Pathology, we are pleased to introduce our second annual collection Pathology & Oncology Research Editors' Picks from 2022. This collection showcases the most well-received and innovative stand-alone articles published in 2022, evaluated carefully by our Editors-in-Chief and Associate Editors.

The work presented here highlights strong contributions to the literature, representing compelling advancement of the fields of pathology and oncology, as well as work effectively bridging the gap between basic research and clinical medicine. This collection aims to further support the journal's strong community of researchers by recognizing highly deserving authors, as well as extending our thanks to the contributing efforts of the journal's dedicated editors and reviewers.

Last year's collection, the Editors' Picks from 2021, is available to view **here**.

Articles authored by the Special Issue Editors were selected by our Associate Editors.
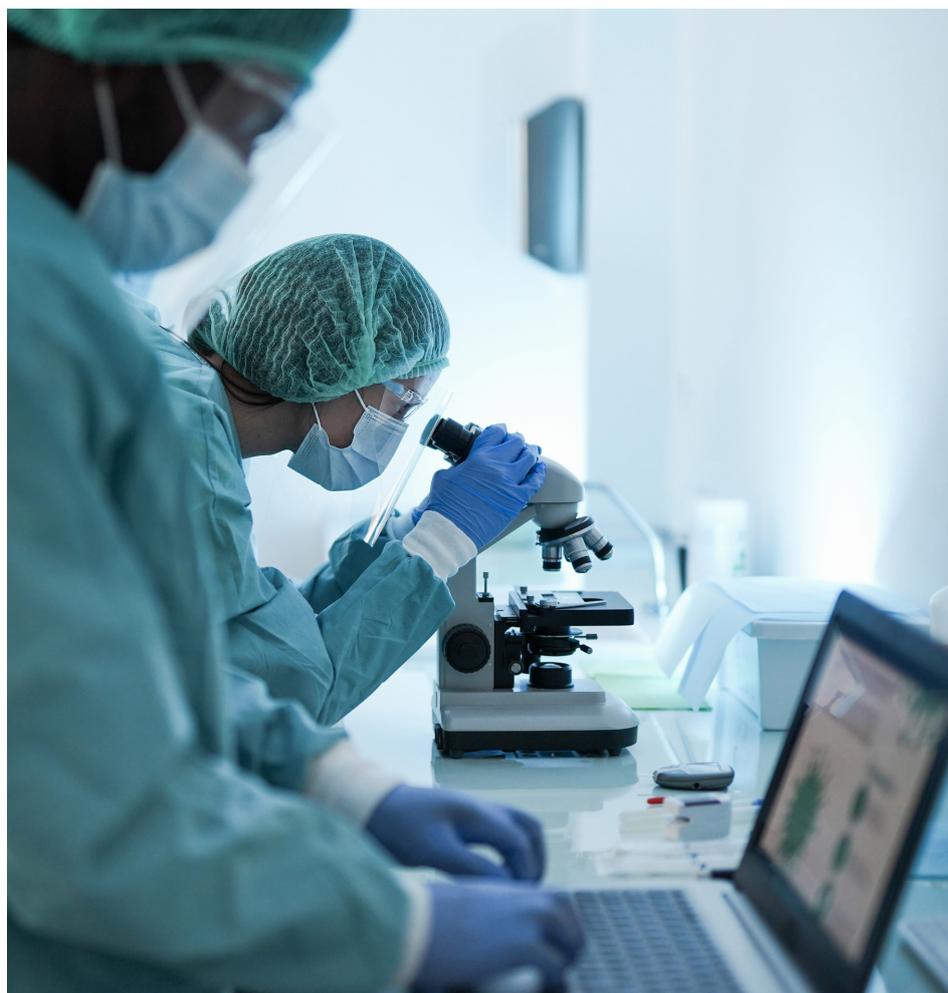
*P*athology &
*O*ncology *R*esearch

Table of contents

NTRK Fusions Detection in Paediatric Sarcomas to Expand the Morphological Spectrum and Clinical Relevance of Selected Entities

Filippo Nozzoli[1]*, Alexander J. Lazar[2], Francesca Castiglione[1], Domenico Andrea Campanacci[3], Giovanni Beltrami[4], Francesco De Logu[5], Chiara Caporalini[6], Daniela Massi[1] and Giandomenico Roviello[7]

[1]Section of Anatomic Pathology, Department of Health Sciences, University of Florence, Florence, Italy, [2]Departments of Pathology and Genomic Medicine, The University of Texas M.D. Anderson Cancer Center, Houston, TX, United States, [3]Department of Orthopaedic Oncology and Reconstructive Surgery, Careggi University Hospital, Florence, Italy, [4]Department of Paediatric Orthopaedic Oncology, Meyer Children's Hospital, Florence, Italy, [5]Clinical Pharmacology and Oncology Unit, Department of Health Sciences, University of Florence, Florence, Italy, [6]Pathology Unit, Meyer Children's Hospital, University of Florence, Florence, Italy, [7]Medical Oncology, Department of Health Sciences, University of Florence, Florence, Italy

Undifferentiated round cell sarcomas (URCS) of soft tissue and bone and tumours of uncertain differentiation (TUD) are commonly ascribed to a subset of neoplasms with low frequency of NTRK gene fusions. However, more recently NTRK-rearranged round and spindle cell tumours have been noted in case reports and in limited or heterogeneous cohorts. The aim of our study was to investigate the presence of NTRK gene fusions in a large retrospective cohort of paediatric URCS and TUD after a systematic review of the diagnosis, according to the recently updated WHO classification scheme. One-hundred and five patients with diagnosis of URCS or TUD, involving the bone or soft tissue, were retrospectively evaluated. After the case selection and the histopathological review of the case cohort, pan-Trk immunohistochemistry (IHC) testing was performed on formalin-fixed paraffin-embedded (FFPE) tissues. Tumour RNA was extracted from FFPE tissue and subjected to next-generation sequencing (NGS) library preparation, using a 10-gene NGS fusion panel, sequenced on an Illumina MiSeq. The NGS-positive cases were further confirmed by real-time PCR. On immunohistochemical screening, 12/105 (11.4%) cases were positive using the pan-Trk antibody, showing three different staining patterns with the cytoplasmic distribution being most common. Molecular analysis using NGS and confirmed by the real-rime PCR detected two positive cases for the ETV6-NTRK3 fusion. The histological pattern of the two positive cases, together with the demonstration of the NTRK rearrangement, leaded to re-classify these previously not otherwise specified sarcomas with uncertain differentiation into the emerging category of NTRK-rearranged neoplasms. In addition, we found the two NTRK fused neoplasms showing a clinical indolent course, in contrast with literature.

Keywords: Pan-Trk, NTRK, ETV6-NTRK3, NTRK-rearranged tumors, paediatric sarcomas

Abbreviations: NTRK, neurotrophic tyrosine kinase receptor; URCS, undifferentiated round cell sarcomas; USTS, undifferentiated soft tissue sarcomas; IHC, immunohistochemistry; FFPE, formalin-fixed paraffin-embedded; NGS, next-generation sequencing; PCR, polymerase chain reaction; FISH, fluorescence *in-situ* hybridization; ESMO, European Society for Medical Oncology; WHO, World Health Organization; AJCC, American Joint Committee on Cancer.

INTRODUCTION

According to the 2020 WHO Classification of Soft Tissue and Bone Tumours (1), the category of undifferentiated round cell sarcomas (URCS) includes a new section containing not only the paradigmatic round cell sarcoma, well known as Ewing sarcoma, but also three distinct entities with different clinical, pathological, and molecular features: round cell sarcomas with EWSR1 gene fusion to non-ETS family members, CIC-rearranged sarcomas, and BCOR-rearranged sarcomas. When no identifiable line of differentiation is shown when analysed by presently available technology, the classification scheme allows to include these entities within the heterogeneous group of undifferentiated soft tissue sarcomas (USTS). The detection of gene rearrangements in URCS and USTS represents a crucial challenging field of diagnostic pathology, as the tumour molecular profiling turned out to have a crucial role in establishing accurate classification schemes and correspondingly in improving the quality of diagnosis and therapeutic options. URCS and USTS are commonly ascribed to a category of neoplasms with low frequency of NTRK gene fusions (2). The inclusion of NTRK-rearranged spindle cell neoplasms (excluding infantile fibrosarcoma that represent a distinct clinicopathologic entity molecularly characterized by the presence of NTRK3-ETV6 fusion gene), within the category of tumours of uncertain differentiation represents one of the most relevant innovations. Most recently, NTRK-rearranged round cell sarcomas have been noted in heterogeneous case studies (3–5). In the largest study conducted on NTRK fusions by Solomon et al. (6), including multiple detection assays across more than 33,000 cases of a wide range of tumour types, immunohistochemistry for pan-Trk staining demonstrated positivity for 1 of 5 Ewing sarcomas and 3 of 5 sarcomas with BCOR translocations, but no positivity for NTRK gene fusions was found by RNA sequencing. Specifically, all immunohistochemically positive cases demonstrated cytoplasmic or membranous expression only, and no nuclear staining was observed. In a cohort of 30 paediatric NTRK-rearranged mesenchymal tumours, Davis et al. (7) characterized the clinicopathologic features of 12 classic ETV6-NTRK3 fused infantile fibrosarcoma and 18 variant paediatric NTRK-rearranged mesenchymal tumours. This series included a TPM3-NTRK1 rearranged inflammatory spindle and round cell sarcoma and an ETV6-NTRK3 rearranged spindle and round cell sarcoma. The aim of our retrospective study was to detect NTRK fusions in a cohort of more than 100 paediatric cases of undifferentiated round cell sarcoma and tumours with uncertain differentiation, following the published ESMO guidelines on methods and diagnostic algorithm to target NTRK fusion (8). In our scenario, NTRK fusions needed to be screened in a population where prevalence of such gene fusions was not expected at high frequency, and a targeted sequencing assay was available, therefore we followed the recommendation to adopt a two-step approach: IHC followed by targeted RNA sequencing, with the latter representing the gold standard for molecular detection. We also aimed to demonstrate the utility of the detection methods used in this family of neoplasms. Prior to the immunohistochemical and molecular testing, we re-examined the entire case collection to assess the diagnosis in the light of the diagnostic criteria of the 2020 WHO Classification of Soft Tissue and Bone Tumours.

MATERIALS AND METHODS

Ethics Approval

The use of FFPE samples of human tissue was approved by the Regional Ethics Committee for Clinical Trials of Tuscany (15248_bio). This study was performed in accordance with the Declaration of Helsinki. Written informed consent has been obtained from the patients to publish this paper.

Case Selection and Tumour Specimen Collection

A total of 105 paediatric patients, aged between 1 and 21 years old, diagnosed with first diagnosis of round cell sarcoma of soft tissue or bone or tumour of uncertain differentiation, observed and treated at Careggi University Hospital (Florence, Italy) and Meyer Children University Hospital (Florence, Italy) between 2000 and 2020, were included. The haematoxylin and eosin (HE) stained slides and formalin-fixed paraffin-embedded (FFPE) tissue specimens were selected in the archive of the Pathology Unit, Careggi University Hospital (Florence, Italy). The histologic diagnosis was based on the results of open biopsy and/or surgical excision. Prior to NTRK immunohistochemistry and molecular testing, all cases were re-reviewed to confirm the diagnosis, to exclude those re-qualified as doubts, those related to post-chemotherapy treatment or exposed to decalcifying agents. If needed, additional immunohistochemical and/or FISH analyses were performed to support the final diagnosis. Eligibility criteria to enter this study also included a tumor content of >50% per slide and the lowest possible rate of fibrosis and necrosis.

Clinical Data Collection

Clinical features were considered for age, sex, presentation, treatment, and outcome. Staging was reported with both the main systems currently proposed: the Enneking (9) classification and the UICC/AJCC classification (10), with the latter more informative as it considers the skips metastases and the different metastases pattern. The tumour size was determined by CT scan measurement of the three diameters of the and the tumour volume was calculated with the following formula: AxBxC, where dimensions are expressed as width (A) by length (B) by depth (C) in three-dimensional space. The response to neoadjuvant chemotherapy was determined by histologic examination, according to the Picci method (11) and consequently classified as grade 1, for evidence of macroscopic foci of viable tumour cells; grade 2, when only isolated microscopic nodules of viable tumour cells can be observed; grade 3 to

indicate absence of nodules of viable cells. This staging method was simplified labelling the histological response as "good" in the case of grade 2 or 3, "poor" in case of grade 1. Other clinical features taken into account included the presence of metastases at diagnosis, local and distant recurrences, and oncologic outcomes (CDF, continuous disease free; NED, no evidence of disease; AWD, alive with disease; DOC, dead other cause; DOD, dead of disease). The follow up data were considered for 95 of the 105 total cases, as 10 cases had too recent diagnosis for follow up data to be collected.

Morphology, Immunoprofile and Molecular Review

The entire specimen collection was reviewed for the morphology features and immunoprofile to re-examine the diagnosis, according to the 2020 WHO Classification of Soft Tissue and Bone Tumours. HE stained sections and immunohistochemical stains, including those from the pathologic evaluation made at time of diagnosis, were revised by two independent pathologists and cases of difficult interpretation were discussed under the microscope until full consensus was achieved. A small round cell morphology and the CD99 membranous expression by immunohistochemistry were therefore considered necessary to validate the diagnosis of Ewing sarcoma, with the EWSR1-ETS family group fusion detection as desirable criterion in selected cases. A spindled to rounded cytomorphology and the EWSR1 break-apart FISH showing amplification of the 5′ probe in EWSR-non-ETS rearrangement (EWSR1-NFATC2) were considered essential for the diagnosis of round cell sarcoma with EWSR1-non-ETS fusions (1). CIC-rearranged sarcoma needed predominant round cell phenotype, an immunoprofile showing variable CD99 staining, with WT1, ETV4 positivity and CIC gene rearrangement demonstration. The diagnosis of BCOR-rearranged sarcoma was assessed with primitive round to spindle cells arranged in nests, sheets, or fascicular growth; immunohistochemical positivity for BCOR, SATB2, cyclin D1 and a molecular confirmation of BCOR genetic abnormality as desirable criterion. The definition of undifferentiated sarcoma was applied with the following elements: spindle, pleomorphic, epithelioid, or round cell morphology; absence of any morphological or immunohistochemical feature of specific differentiation; demonstrated absence of distinctive molecular aberration.

Immunohistochemistry

Immunohistochemistry was performed on 4 μm paraffin-embedded whole tissue sections using standard techniques. IHC staining for Trk A, B, and C expression was performed with pan-Trk antibody, a rabbit recombinant monoclonal antibody (mAb) clone EPR17341 (#790-7026, ready to use, Ventana Medical Systems, Tucson, AZ, United States). All assays were performed on Ventana Discovery XT immunostainer (Ventana Medical Systems, Tucson, AZ, United States), a fully automated method for staining and designed for the immunohistochemical detection of the

TABLE 1 | Summary of additional IHC antibodies performed to support the final diagnosis.

Antibody	Technology	Clone	Dilution
CD99	Rabbit Monoclonal	SP119	1:200
CD34	Mouse Monoclonal	QBEND/10	1:100
S-100	Rabbit Polyclonal	-	1:500
Desmin	Rabbit Monoclonal	SP138	1:100
Vimentin	Rabbit Monoclonal	SP20	1:200
SMA	Mouse Monoclonal	1A4	1:100
Pan Cytokeratin	Mouse Monoclonal	AE1/AE3	1:100
Ki-67	Rabbit Monoclonal	SP6	1:250
SOX10	Rabbit Monoclonal	EPR4007-104	1:250
Chromogranin A	Rabbit Polyclonal	-	1:200
Synaptophysin	Rabbit Monoclonal	SP11	1:200
BCOR	Rabbit Polyclonal	-	1:100
Pan Trk	Rabbit Monoclonal	EPR17341	1:500

C-terminal region of proteins A, B and C of tropomyosin receptor kinase (Trk), known to be preserved in fusion proteins both chimeric and "wild-type". The staining protocol included pre-treatment with cell conditioner followed by incubation with antibody. The signal for antibody was then developed with Discovery anti-Rabbit HQ, Discovery Anti-HQ HRP and CromoMap DAB. After the staining run was complete, the tissue sections were counterstained with haematoxylin. The laboratory practice included a control tissue sample of infantile fibrosarcoma containing elements with positive and negative staining to use it as both positive and negative control. Pan-Trk IHC staining was assessed in both tumour nuclei and cytoplasm and recorded as weak, moderate, or strong, as previously described (12). Specifically, in the case of staining distributed only to the cytoplasm, the involvement of at least 50% of the neoplastic cells was required; in the case of nuclear involvement, any reactivity, even if minimal, was considered acceptable to assess the case as positive. Other patterns, such as perinuclear and membranous, were also assessed, as previously reported (12). Further IHC antibodies performed to support the final diagnosis are listed in **Table 1**.

RNA Extraction and Quantification

The haematoxylin and eosin-stained tumor slides were examined to identify representative areas of tumor suitable for molecular testing. RNA extraction from 12 FFPE tumor specimens, previously characterized for IHC pan-Trk positivity, was carried out according to the manufacturers' protocols, utilizing the MagCore® Total RNA FFPE One-Step Kit (RBC Bioscience Corp., New Taipei City, Taiwan) on the automated extraction system MagCore® Super (RBC Bioscience Corp., New Taipei City, Taiwan), based on magnetic beads extraction technology. RNA input quantification was measured by real-time PCR on EasyPGX® qPCR instrument 96 (Diatech Pharmacogenetics, Jesi, Italy), ensuring an accurate and precise measurement of the amplifiable RNA in the following amplification reaction of the target library regions. The assay allows the detection of two RNA regions highly conserved of 105 and 175 bp; the detection was performed using probes labelled with FAM and HEX,

respectively. The RNA concentration was assessed by quantification with a standard curve in the HEX channel; the ratio between the quantification (ng/μl) obtained in FAM and that obtained in the HEX allows to evaluate the DNA fragmentation. The analysis of the assay was done by the dedicated EasyPGX® Analysis Software (Diatech Pharmacogenetics, Jesi, Italy), that calculates the concentration and degree of fragmentation of the samples. After the quantification step, of the original 12 cases selected for sequencing, two cases were respectively excluded due to insufficient quantity and quality of nucleic acids. Therefore, 10 tumor samples with adequate quantity and quality of nucleic acids for sequencing were utilized for NGS library preparation.

RNA Libraries Preparation and NGS Sequencing

RNA libraries were generated using the Myriapod® NGS Cancer panel RNA (Diatech Pharmacogenetics, Jesi, Italy), according to the manufacturers' instructions. The kit consists in a commercially available CE-IVD workflow from extraction to bioinformatics and it allows the detection of fusions regarding ten recurrently rearranged cancer genes: ALK, ROS1, RET, NTRK1, NTRK2, NTRK3, FGFR2, FGFR3, PPARG and the skipping of exon 14 of MET in total RNA, isolated from tumour tissue. The RNA was retro-transcribed into cDNA using random hexamers. Subsequently, cDNA was amplified by multiplex-PCR using two primer mixtures to obtain fragments between 47 and 184 bases, including fusions of interest and endogenous control genes (PCR1). The amplification products were purified with magnetic beads to remove residual primers. An amplification-based indexing reaction (PCR2) follows which allows a unique pair of two sample-specific barcodes (indexes) and an Illumina® platform-specific adapter to be attached to each fragment. The libraries thus constituted were normalized in quantity by magnetic beads to guarantee a homogeneous coverage of the samples during sequencing. Finally, the normalized libraries were mixed (library pool) and sequenced in parallel on the Illumina® MiSeq™ platform (Illumina Inc., San Diego, CA, United States) with MiSeq™ Reagent Kit v2 Micro (300 cycles) flow cell (Illumina Inc., San Diego, CA, United States).

Sequencing Data Analysis

The data generated by the sequencer were then analyzed locally with the dedicated Myriapod® NGS Data Analysis Software (Diatech Pharmacogenetics, Jesi, Italy).

Real-Time-PCR

Following a two-step approach, data obtained with NGS were confirmed by real-time PCR. The kit used was the "EasyPGX® ready NTRK fusion" (Diatech Pharmacogenetics, Jesi, Italy), a commercially available CE-IVD test for the detection of NTRK1, NTRK2 and NTRK3 gene fusions in the total RNA selected from FFPE tumour sample and amplified by One Step Real-Time RT-PCR. The control group comprised a control assay: an expressed

TABLE 2 | Clinical and pathologic features of all the 105 patients included in the cohort.

Age	
<2	5
2–5	9
6–14	59
15–21	32
Sex	
Male	58
Female	47
Site	
Soft Tissue	23
Bone	82
Volume	
<100 cm^3	72
>100 cm^3	33
Enneking Staging	
I–II	71
III–IV	34
UICC/AJCC Staging	
I–II	59
III–IV	46
Metastasis at diagnosis	
Yes	23
No	82
Treatment	
Surgery	105
Neoadjuvant chemotherapy	105
Response to chemotherapy	
Poor (Picci grade 1)	32
Good (Picci grade 2-3)	63
Not Available	10
DOD (dead of disease)	
Yes	26
No	79
CD99 expression	
Yes	99
No	6
t(11;22)(q24;q12) translocation	
Yes	96
No	6
Not available	3

gene amplified in the channel stably and independently from the original tumour tissue to verify the correct execution of the amplification process, the RNA quantity used and the possible presence of inhibitors that can cause false negative results. A positive and a negative control were also used. The detection took place via fluorescent probe marked with FAM and HEX; it is also composed of eight assays for the detection of gene alterations. Each of them provides the simultaneous detection of the target, through a probe marked with FAM, and an endogenous control gene, through a probe marked with HEX. Data were analyzed by
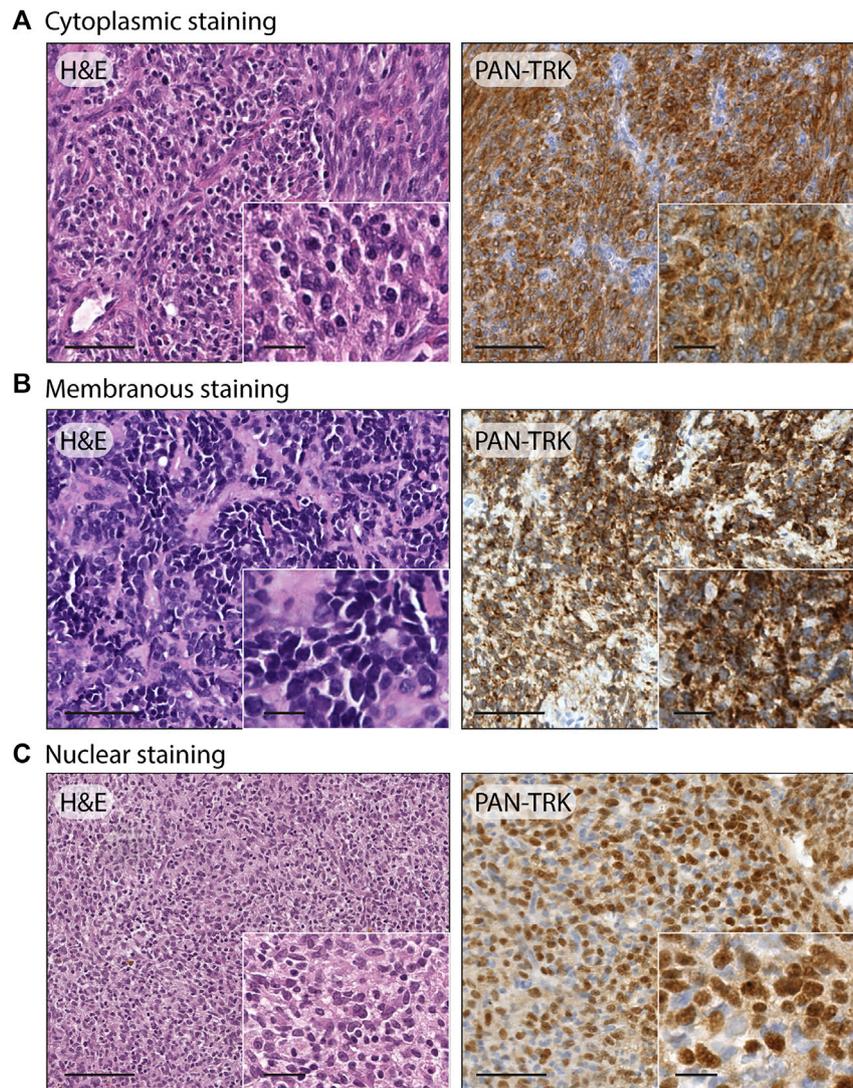
FIGURE 1 | Examples of different staining patterns found in the case series. **(A)** Ewing sarcoma: H&E, 20x (scale bar = 100 μm) and 40× (scale bar = 25 μm); pan-TRK IHC with cytoplasmic staining, 20× (scale bar = 100 μm) and 40× (scale bar = 25 μm). **(B)** Ewing sarcoma: H&E, 20× (scale bar = 100 μm) and 40× (scale bar = 25 μm); pan-TRK IHC with membranous staining, 20× (scale bar = 100 μm) and 40× (scale bar = 25 μm). **(C)** Undifferentiated soft tissue sarcoma: H&E 20× (scale bar = 100 μm) and 40× (scale bar = 25 μm); pan-TRK IHC with nuclear staining, 20× (scale bar = 100 μm) and 40× (scale bar = 25 μm).

EasyPGX® Analysis Software (Diatech Pharmacogenetics, Jesi, Italy).

RESULTS

Morphology, Immunoprofile, Molecular Review

Our cohort consisted of 105 paediatric patients with suspected diagnosis of undifferentiated round cell sarcoma of soft tissue or bone. Of those, 96 cases were assessed as Ewing sarcoma, 3 as EWSR1-non-ETS round cells sarcoma, 1 as sarcoma with BCOR genetic alteration and 5 cases showed no identifiable line of differentiation and were labelled as USTS. The main

clinical and pathologic features of the cohort are summarized in **Table 2**.

Immunohistochemistry

After the immunohistochemistry screening, 12/105 cases emerged for the Trk protein expression, including 8/96 Ewing sarcomas, 3/5 USTS and 1/1 sarcoma with BCOR genetic alteration, with a comprehensive percentage of positive immunoreactivity of 11.4%. The pan-Trk staining showed three different cellular distribution patterns, specifically: isolated cytoplasmic staining was the predominate pattern found, as it occurred in 9/12 cases (7 Ewing sarcoma, 1 USTS and 1 sarcoma with BCOR genetic alteration) while a nuclear staining in 2/12 cases (2 USTS) and a membranous staining in 1/

TABLE 3 | Summary of clinical, immunohistochemical, and molecular data of the twelve IHC pan-Trk positive cases.

Pts	Age (years)	Sex	Diagnosis	Location	Mass volume (cm^3)	AJCC staging	Oncologic outcome	IHC Pan-Trk pattern	NTRK fusion
1	14	M	ES	Lower Leg	12.6	IIB	DOD	Cytoplasmic	-
2	10	F	ES	Sacrum	0.6	IIA	CDFS	Cytoplasmic	-
3	13	M	USTS	Lower Leg	45	IIIA	CDFS	Nuclear	ETV6-NTRK3
4	10	F	ES	Iliac Crest	56	IIB	DOD	Membranous	-
5	11	M	USTS	Thigh	10.8	IIA	CDFS	Nuclear	ETV6-NTRK3
6	2	F	USTS	Lower Leg	3	IIA	NED	Cytoplasmic	-
7	13	M	ES	Lower Leg	28.2	IIIA	CDFS	Cytoplasmic	-
8	12	F	ES	Scapula	241.3	IVB	DOD	Cytoplasmic	-
9	11	F	ES	Sacrum	105.6	IVB	CDFS	Cytoplasmic	-
10	10	M	BCOR	Lower Leg	35	IIA	CDFS	Cytoplasmic	-
11	13	F	ES	Pelvis	12	IIA	CDFS	Cytoplasmic	*
12	16	M	ES	Upper Leg	52.5	IIB	CDFS	Cytoplasmic	*

RNA, not suitable for testing.2.

ES, ewing sarcoma; USTS, undifferentiated soft tissue sarcoma; BCOR, sarcoma with BCOR, genetic alterations; DOD, dead of disease; CDFS, continuous disease-free survival; NED, no evidence of disease.

FIGURE 2 | NTRK fusion tumours. **(A)** Undifferentiated soft tissue sarcoma: diffuse nuclear IHC pan-Trk staining with ETV6-NTRK3 fusion detected by next-generation sequencing and confirmed by real-time PCR. **(B)** Undifferentiated soft tissue sarcoma: strong nuclear IHC pan-Trk staining with ETV6-NTRK3 fusion detected by next-generation sequencing and confirmed by real-time PCR.

12 cases (1 Ewing sarcoma). Examples of the three different cellular staining distribution patterns found are shown in **Figure 1**. Demographic, clinical, immunohistochemical, and molecular data of the twelve IHC pan-Trk positive cases are summarized in **Table 3**.

Molecular Testing

NGS RNA fusion panel testing was successfully completed for 10 cases, revealing ETV6-NTRK3 fusion in 2 tumor samples, confirmed by real-time PCR. Both cases harbouring NTRK fusion, showed a nuclear staining distribution pattern when the pan-Trk antibody was performed (**Figure 2**). Other 8 cases resulted negative for NTRK fusions, while the remaining 2 cases were not assessable because the RNA was not suitable for testing after the quantification process. The first NTRK fusion positive case (**Figure 2A**) is a 13-year-old male with an initial diagnosis of Ewing-like sarcoma involving the extraosseous soft tissue component along the left tibia, then re-diagnosed as undifferentiated soft tissue sarcoma. The tumour mass, calculated by the product of all the three diameters of the

lesion, had a volume of 45 cm^3 and presented itself as a IIB grade, according to the Enneking staging system and as a IIIA, according to the AJCC staging. Histopathologically, the neoplasm showed a polymorphic small round and spindle cell phenotype and a weak CD99 immunoexpression, lacking the canonical EWSR1-ETS family rearrangement demonstration; immunohistochemical findings also showed positivity for S-100 and pan-Trk with a nuclear distribution pattern. The pan-Trk IHC positivity was not known at the time of treatment. Neoadjuvant chemotherapy was given [ISG/SSG III protocol, using 6 drugs active in Ewing's family tumours: Ifosfamide (Ifo), Etoposide (Eto), Vincristine (V), Actinomycin-D (Act), Adriamycin (Adm), Cyclophosphamide (C)]. The patient showed a Picci grade 3 response, meaning no evidence of viable tumour cells. After surgery, maintenance chemotherapy was adopted with VAdmC regimen as first cycle, then continued with the same 6 drugs and modalities as in the induction treatment. Without local relapse or distant metastases after surgery, the oncologic result is a continuous disease-free survival during the last 4 years. The second NTRK-fused tumour in our cohort (**Figure 2B**) belongs to a 11-year-old male with an expansive mass of 10.8 cm^3 of volume, observed on the left thigh and diagnosed as undifferentiated soft tissue sarcoma. The open biopsy revealed a predominately spindle cells morphology with isolated round elements. The immunohistochemical profile included weak S-100, CD99, vimentin and desmin; pan-Trk testing showed a strong nuclear distribution pattern. Surgery for the tumour resection was performed as local treatment, and adjuvant multiagent chemotherapy (VAC/IE protocol: Vincristine + Doxorubicin + Cyclophosphamide, alternating with Ifosfamide + Etoposide) was then adopted, resulting in no further relapse with a continuous disease-free survival, persisting for the last 6 years.

DISCUSSION

The focus on NTRK rearrangements detection has increased recently due to some specific molecular targeted agents that demonstrated a marked and durable antitumour activity in patients with NTRK gene fusions positive cancers, regardless of tumour histology [13,14]. This study evaluated the presence of NTRK gene fusions in a large paediatric cohort entirely composed of URCS and USTS of soft tissue and bone, where the cases were categorized, according to the 2020 WHO classification. The immunohistochemistry performed with pan-Trk antibody showed reactivity in 12/105 (11.4%) analyzed samples, but the molecular analysis showed positivity for ETV6-NTRK3 fusion in 2 cases only; therefore, we can confirm that NTRK gene fusions emerge in a only a small fraction (approximately 2%) in contradistinction to other rare paediatric neoplasms, including secretory carcinoma of the breast [15], congenital mesoblastic nephroma [16] and infantile fibrosarcoma [17] where NTRK fusion is characteristic and often disease defining. Suurmeijer et al. [18] reported a series of seven NTRK3-rearranged soft tissue sarcomas as a morphologically diverse group of tumors with variable histological and immunohistochemical findings.

Similarly, the morphological features of the two positive cases of our study, together with the demonstration of the NTRK rearrangement, lead to re-classify these previously not otherwise specified undifferentiated soft tissue sarcoma into the emerging category of NTRK-rearranged neoplasms. Therefore, the histological phenotype seems to play an essential role in the identification of sarcomas that are worthy candidates for immunohistochemical and/or molecular testing. As in other tumor types, URCS of soft tissue and bone and TUD represent a challenging field in NTRK fusion detection due to the rarity of fusion events [19]. Several factors can explain the low positive predictive value of the IHC screening in our series. First, the pan-Trk antibody is not optimized to distinguish between wild-type protein expression and expression of chimeric fusion Trk proteins. Hechtman et al. [20] defined the pan-Trk immunohistochemistry as an efficient and reliable screen method to detect NTRK fusions. Our present series suggests that TRK can be used to direct further molecular investigation, but detection of expression is not specific to a fusion event. Thus, specificity is 20% (2 of 10 fully evaluable cases). Various factors can influence the reliability of the IHC results and correlation with molecular characterization. Certainly, histological type of tissue analyzed is increasingly evident. This study illustrates that specificity is lower in sarcomas compared to other tumour types, perhaps due differentiation in tumours of mesenchymal origin, such as neuronal (or less likely in this case, myogenic). In these and tissue types, pan-Trk antibody is known to be limited in terms of detection accuracy [21]. This suboptimal specificity of IHC for fusion identification, with the antibody marking expression of wild-type Trk protein as emerged in this study, had already been noted in previous work experiences for other cancers with variable myogenic differentiation, including uterine leiomyosarcoma [22], rhabdomyosarcoma [23], and desmoplastic small round cell tumour [3]. Therefore, sarcomas likely due to its tissue differentiation characteristics, can reasonably be considered a tumour type where Trk IHC lack specificity. Thus, the use and the interpretation of the IHC must be carried out with some caution, reserving primary role to the molecular testing, preferably RNA-based methods to detect NTRK gene fusions in sarcomas. This appears to be particularly important when cytoplasmic staining is present in the absence of nuclear, peri-nuclear, or membranous staining. Both NTRK fusion positive cases in our study showed a pan-Trk staining with a nuclear pattern, strengthening the IHC reliability for NTRK fusion in sarcomas, when a nuclear distribution pattern is observed. Distinct staining patterns seem to relate to the subcellular localization of fusion partner; equivalent staining patterns have been reported as well as for several of the same NTRK partner genes when they are fused to other kinases [20]. The main reason of the specific staining pattern emerged in our case series may be reasonably tracked in the subcellular localization of the fusion partner; ETV6 gene encodes a transcription factor, which localizes to the nucleus. However, despite the high rate of specificity and sensitivity [24] of the molecular methods used to detect NTRK fusion in both clinical practice and research, RNA-based techniques are

not free of obstacles. The main limiting factor emerged in our study was the quality or quantity of RNA available for testing, specifically in older specimens, due to degradation in formalin-fixed, paraffin-embedded tissue whilst having a larger molecular dataset would offer further insight about the sensitivity of the IHC screening. This limit predominately affects retrospective studies, when old samples are included by necessity but may be less of a barrier in daily diagnostic practice. In our study we did not detect Ewing sarcoma with distinct NTRK and EWSR1 fusions. By the clinical point of view, ETV6-NTRK3 fused sarcomas were reported as aggressive tumours, regardless of the grade of cytological atypia (18,25); we described two neoplasms with ETV6-NTRK3 fusion showing an indolent course, chemosensitive and without any signs of recurrence or metastatic spread, in contrast with what previously reported, so that the fusion partner does not seem a potential marker to predict prognosis. Further studies are needed to explore the significance of NTRK in this setting.

DATA AVAILABILITY STATEMENT

The datasets presented in this study can be found in online repositories. The names of the repository/repositories and accession number(s) can be found in the article/supplementary material.

ETHICS STATEMENT

The studies involving human participants were reviewed and approved by Regional Ethics Committee for Clinical Trials of Tuscany (15248_bio). Written informed consent to participate in this study was provided by the participants' legal guardian/next of kin.

AUTHOR CONTRIBUTIONS

FUNDING

CONFLICT OF INTEREST

AL reports to be in a consulting role for Hoxo/Bayer and Ignyta/Genentech. DM has received honoraria for professional services and consultancy for Novartis, Bayer HealthCare Pharmaceuticals Inc., Pierre-Fabre, Sanofi Genzyme, MSD Italia S.r.l., Roche, Skyline Dx B.V. FD is founding scientist of FloNext Srl.

The remaining authors declare that the research was conducted in the absence of any commercial or financial relationships that could be construed as a potential conflict of interest.

REFERENCES

1. Sbaraglia M, Bellan E, Dei Tos AP. The 2020 WHO Classification of Soft Tissue Tumours: News and Perspectives. *Pathologica* (2020) 113:70–84. doi:10.32074/1591-951X-213

2. Albert CM, Davis JL, Federman N, Casanova M, Laetsch TW. TRK Fusion Cancers in Children: A Clinical Review and Recommendations for Screening. *Jco* (2019) 37(6):513–24. doi:10.1200/JCO.18.00573

3. Wong DD, Vargas AC, Bonar F, Maclean F, Kattampallil J, Stewart C, et al. NTRK-rearranged Mesenchymal Tumours: Diagnostic Challenges, Morphological Patterns and Proposed Testing Algorithm. *Pathology* (2020) 52(4):401–9. doi:10.1016/j.pathol.2020.02.004

4. Vargas AC, Ardakani NM, Wong DD, Maclean FM, Kattampallil J, Boyle R, et al. Chromosomal Imbalances Detected in NTRK -rearranged Sarcomas by the Use of Comparative Genomic Hybridisation. *Histopathology* (2020) 78(7):932–42. doi:10.1111/his.14295

5. Kao Y-C, Sung Y-S, Argani P, Swanson D, Alaggio R, Tap W, et al. NTRK3 Overexpression in Undifferentiated Sarcomas with YWHAE and BCOR Genetic Alterations. *Mod Pathol* (2020) 33(7):1341–9. doi:10.1038/s41379-020-0495-2

6. Solomon JP, Linkov I, Rosado A, Mullaney K, Rosen EY, Frosina D, et al. NTRK Fusion Detection across Multiple Assays and 33,997 Cases: Diagnostic Implications and Pitfalls. *Mod Pathol* (2020) 33(1):38–46. doi:10.1038/s41379-019-0324-7

7. Davis JL, Lockwood CM, Stohr B, Boecking C, Al-Ibraheemi A, DuBois SG, et al. Expanding the Spectrum of Pediatric NTRK-Rearranged Mesenchymal Tumors. *Am J Surg Pathol* (2019) 43(4):435–45. doi:10.1097/PAS.0000000000001203

8. Marchiò C, Scaltriti M, Ladanyi M, Iafrate AJ, Bibeau F, Dietel M, et al. ESMO Recommendations on the Standard Methods to Detect NTRK Fusions in Daily Practice and Clinical Research. *Ann Oncol* (2019) 30(9):1417–27. doi:10.1093/annonc/mdz204

9. Enneking WF, Spanier SS, Goodman MA. A System for the Surgical Staging of Musculoskeletal Sarcoma. *Clin Orthop Relat Res* (1980) 153(153):106–120. PMID: 7449206. doi:10.1097/00003086-198011000-00013

10. Tanaka K, Ozaki T. New TNM Classification (AJCC Eighth Edition) of Bone and Soft Tissue Sarcomas: JCOG Bone and Soft Tissue Tumor Study Group. *Jpn J Clin Oncol* (2019) 49(2):103–7. PMID: 30423153. doi:10.1093/jjco/hyy157

11. Picci P, Rougraff BT, Bacci G, Neff JR, Sangiorgi L, Cazzola A, et al. Prognostic Significance of Histopathologic Response to Chemotherapy in Nonmetastatic Ewing's Sarcoma of the Extremities. *Jco* (1993) 11(9):1763–9. PMID: 8355043. doi:10.1200/JCO.1993.11.9.1763

12. Rudzinski ER, Lockwood CM, Stohr BA, Vargas SO, Sheridan R, Black JO, et al. Pan-Trk Immunohistochemistry Identifies NTRK Rearrangements in Pediatric Mesenchymal Tumors. *Am J Surg Pathol* (2018) 42(7):927–35. doi:10.1097/PAS.0000000000001062

13. Drilon A, Laetsch TW, Kummar S, DuBois SG, Lassen UN, Demetri GD, et al. Efficacy of Larotrectinib inTRKFusion-Positive Cancers in Adults and Children. *N Engl J Med* (2018) 378(8):731–9. doi:10.1056/NEJMoa1714448

14. Kheder ES, Hong DS. Emerging Targeted Therapy for Tumors with *NTRK* Fusion Proteins. *Clin Cancer Res* (2018) 24(23):5807–14. doi:10.1158/1078-0432.CCR-18-1156

15. Tognon C, Knezevich SR, Huntsman D, Roskelley CD, Melnyk N, Mathers JA, et al. Expression of the ETV6-NTRK3 Gene Fusion as a Primary Event in Human Secretory Breast Carcinoma. *Cancer Cell* (2002) 2:367–76. doi:10.1016/s1535-6108(02)00180-0

16. Rubin BP, Chen C-J, Morgan TW, Xiao S, Grier HE, Kozakewich HP, et al. Congenital Mesoblastic Nephroma T(12;15) Is Associated withETV6-NTRK3 Gene Fusion. *Am J Pathol* (1998) 153:1451–8. doi:10.1016/S0002-9440(10)65732-X

17. Knezevich SR, McFadden DE, Tao W, Lim JF, Sorensen PHB. A Novel ETV6-NTRK3 Gene Fusion in Congenital Fibrosarcoma. *Nat Genet* (1998) 18:184–7. doi:10.1038/ng0298-184

18. Suurmeijer AJ, Dickson BC, Swanson D, Zhang L, Sung YS, Huang HY, et al. The Histologic Spectrum of Soft Tissue Spindle Cell Tumors with NTRK3 Gene Rearrangements. *Genes Chromosomes Cancer* (2019) 58(11):739–46. doi:10.1002/gcc.22767

19. Solomon JP, Hechtman JF. Detection of *NTRK* Fusions: Merits and Limitations of Current Diagnostic Platforms. *Cancer Res* (2019) 79(13):3163–8. doi:10.1158/0008-5472.CAN-19-0372

20. Hechtman JF, Benayed R, Hyman DM, Drilon A, Zehir A, Frosina D, et al. Pan-Trk Immunohistochemistry Is an Efficient and Reliable Screen for the Detection of NTRK Fusions. *Am J Surg Pathol* (2017) 41(11):1547–51. doi:10.1097/PAS.0000000000000911

21. Murphy DA, Ely HA, Shoemaker R, Boomer A, Culver BP, Hoskins I, et al. Detecting Gene Rearrangements in Patient Populations through a 2-Step Diagnostic Test Comprised of Rapid IHC Enrichment Followed by Sensitive Next-Generation Sequencing. *Appl Immunohistochem Mol Morphol* (2017) 25(7):513–23. doi:10.1097/PAI.0000000000000360

22. Chiang S, Cotzia P, Hyman DM, Drilon A, Tap WD, Zhang L, et al. NTRK Fusions Define a Novel Uterine Sarcoma Subtype with Features of Fibrosarcoma. *Am J Surg Pathol* (2018) 42(6):791–8. doi:10.1097/PAS.0000000000001055

23. Hung YP, Fletcher CDM, Hornick JL. Evaluation of Pan-TRK Immunohistochemistry in Infantile Fibrosarcoma, Lipofibromatosis-like Neural Tumour and Histological Mimics. *Histopathology* (2018) 73(4):634–44. doi:10.1111/his.13666

24. Penault-Llorca F, Rudzinski ER, Sepulveda AR. Testing Algorithm for Identification of Patients with TRK Fusion Cancer. *J Clin Pathol* (2019) 72(7):460–7. doi:10.1136/jclinpath-2018-205679

25. Siozopoulou V, Smits E, De Winne K, Marcq E, Pauwels P. *NTRK* Fusions in Sarcomas: Diagnostic Challenges and Clinical Aspects. *Diagnostics* (2021) 11(3):478. doi:10.3390/diagnostics11030478

Check for
updates

Correlations Between the Expression of Stromal Cell Activation Related Biomarkers, L-NGFR, Phospho-ERK1-2 and CXCL12, and Primary Myelofibrosis Progression

Tamas Szekely[1], Tibor Krenacs[1]*, Mate Elod Maros[1,2,3], Csaba Bodor[1,4], Viktoria Daubner[1], Annamaria Csizmadia[1,5], Brigitta Vrabely[6] and Botond Timar[1]

[1]First Department of Pathology and Experimental Cancer Research, Semmelweis University, Budapest, Hungary, [2]Department of Biomedical Informatics, Center for Preventive Medicine and Digital Health, Mannheim, Germany, [3]Department of Neuroradiology, Medical Faculty Mannheim, University of Heidelberg, Mannheim, Germany, [4]HCEMM-SE Molecular Oncohematology Research Group, Budapest, Hungary, [5]3DHISTECH Ltd., Budapest, Hungary, [6]Department of Pathology, Sandor Peterfy Street Hospital and Clinic, Budapest, Hungary

In myelofibrosis, pathologically enhanced extracellular matrix production due to aberrant cytokine signalling and *clonal megakaryocyte functions* result(s) in impaired hemopoiesis. Disease progression is still determined by detecting reticulin and collagen fibrosis with Gomori's silver impregnation. Here, we tested whether the expression growth related biomarkers L-NGFR/CD271, phospho-ERK1-2 and CXCL12 can be linked to the functional activation of bone marrow stromal cells during primary myelofibrosis progression. Immunoscores for all tested biomarkers showed varying strength of positive statistical correlation with the silver impregnation based myelofibrosis grades. The intimate relationship between spindle shaped stromal cells positive for all three markers and aberrant megakaryocytes was likely to reflect their functional cooperation. L-NGFR reaction was restricted to bone marrow stromal cells and revealed the whole length of their processes. Also, L-NGFR positive cells showed the most intersections, the best statistical correlations with myelofibrosis grades and the strongest interrater agreements. CXCL12 reaction highlighted stromal cell bodies and a weak extracellular staining in line with its constitutive release. Phospho-ERK1-2 reaction showed a similar pattern to CXCL12 in stromal cells with an additional nuclear staining in agreement with its role as a transcription factor. Both *p*-ERK1-2 and CXCL12 were also expressed at a moderate level in sinus endothelial cells. Connexin 43 gap junction communication channels, known to be required for CXCL12 release to maintain stem cell niche, were also expressed progressively in the myelofibrotic stromal network as a support of compartment functions. Our results suggest that, diverse growth related pathways are activated in the functionally coupled bone marrow stromal cells during myelofibrosis progression. L-NGFR expression can be a useful biological marker of stromal cell activation which deserves diagnostic consideration for complementing Gomori's silver impregnation.

Keywords: primary myelofibrosis progression, -stromal cell activation, -L-NGFR/CD271, -CXCL12, -phospho-ERK1-2, -connexin 43 channels

INTRODUCTION

Primary myelofibrosis (PMF) belongs to a group of Philadelphia chromosome (BCR-ABL1)-negative myeloproliferative neoplasms (MPN) of the multipotent hematopoietic stem cells, also including polycythaemia vera (PV) and essential thrombocythemia (ET) [1]. These malignancies are characterised by clonal proliferation of the myeloid lineages accompanied by progressive stromal cell activation, extracellular matrix production and impeded hemopoesis [2]. Myelofibrosis is an adverse prognostic factor in MPNs, which is mainly driven by impaired megakaryocyte functions resulting in the elevated expression of inflammatory cytokines, transforming growth factor-β (TGF-β), platelet derived growth factor (PDGF), as well as the aberrant JAK-STAT signaling as a result of JAK2V617F, MPL515 L/K or CALR mutations [3]. Myelofibrosis grading is still based on Gomori's silver staining, which reveals reticular and collagen fibers proportional with disease progression [4]. However, standardisation of the selective silver impregnation of these matrix components is challenging due to preanalytical and staining variables [5]. Here we studied, the growth related biomarkers L-NGFR, phospho-ERK1-2 and CXCL12 in primary myelofibrosis, which were predominantly expressed in bone marrow stromal cells and potentially involved in the promotion of fibroblast activation, responsible for accelerated and pathognomic matrix production during myelofibrosis. Correlations between the expression of these makers and myelofibrosis grades were tested to see if they could support reticulin silver impregnation based prognostic decisions on a biological basis.

Low affinity nerve growth factor receptor (L-NGFR; CD271, or p75 neurotrophin receptor - p75NTR), an unusual member of the tumor necrosis factor family of receptors, has long been detected in the bone marrow (reticular) stromal cell network [6]. L-NGFR has been involved in the regulation of neuronal survival and apoptosis but it can also act as a tyrosine kinase co-receptor for the anti-apoptotic tropomyosin receptor kinase A (TrkA) to enhance MAPK pathway activation, culminating in ERK1-2 phosphorylation and nuclear translocation [7, 8]. Both L-NGFR expression and NGF-TrkA signaling can support bone and bone marrow mesenchymal stem cell (MSc) development [9, 10]. In addition, TrkA upregulation can enhance the survival and regenerative capacity of bone marrow stromal stem cells through upregulation of the Erk/Bcl-2 pathway [11]. In myelofibrotic bone marrow MAPK activation can also be induced through receptor tyrosine kinase signaling i.e. PGDFR by PDGF overproduced by pathological megakaryocytes, as one of the major driving forces of fibroblast activation [12]. In line with this, PDGFR-β expression in the stromal network showed close correlation with the silver impregnation based myelofibrosis grades [13-15].

The chemokine CXCL12 (stromal cell-derived factor 1 - SDF1, or C-X-C motif chemokine 12) produced by stromal and endothelial cells and osteoblasts, plays an important role in maintaining stem cell quiescence by safeguarding both the perivascular or endosteal bone marrow niches [16]. Its receptor CXCR4 is known to be expressed in CD34+/c-kit +

hemopoetic progenitors and leukemic blasts. Mesenchymal stromal cells can resist in radiation-induced cell death and the CXCL12 (SDF1)-CXCR4 signaling in the stromal microenvironment promotes niche regeneration during stem cell transplantation [17]. Bone marrow stromal cells, as a dynamic syncytium, communicate via Cx43 (and Cx45) gap junctions, which are required for proper CXC12 secretion and hematopoietic stem cell homeostasis [18]. Accordingly, inhibition of gap junctions impaired CXCL12 secretion and the homing of CD34 [+] bone marrow progenitors. We have earlier demonstrated the upregulation of Cx43 gap junctions in leukemic tumor samples, characterized by an increased stromal/hematopoietic cell ratio [19].

The CXCL12/CXCR4 pathway can be induced by oncogenic JAK2, which frequently suffers activating mutations in primary myelofibrosis, and JAK2 inhibition can reduce the chemotaxis of hematopoietic cells isolated from primary myelofibrosis [20]. A subpopulation of leukemic cells with stem cell-like features can maintain tumor growth by escaping antitumor therapies and repopulating the tumor [21]. Myelofibrosis, featured by increased stromal cell activation, may also involve CXCL12 upregulation, which can contribute to protecting leukemic stem cells [22].

In this study, using immunohistochemistry, we tested the expression of L-NGFR, pER1-2 and CXCL12 proteins, which were primarily expressed in stromal cells in bone marrow biopsies of primary myelofibrosis. We also studied Cx43 communication channel protein expression in the myelofibrotic stroma. All these markers are potentially involved in the promotion of growth and activation of bone marrow stromal network to produce excess matrix proteins including reticular and collagen fibers, which determine myelofibrosis progression. Therefore, we examined for their correlations with stromal fibrosis in myelofibrosis in association with Gomori's-silver impregnation based tumor grades.

MATERIALS AND METHODS

Bone Marrow Biopsy Samples Tested

Our cohort included Jamshidi biopsies of patients diagnosed with primary myelofibrosis at the first Department of Pathology, Semmelweis University between 2016 and 2021. Samples were fixed for 10–16 h in Schaefer's fixative (4% neutral buffered formaldehyde containing methanol and glucose), then decalcified overnight in 10% EDTA-Na$_2$ (ethylenediaminetetraacetic acid disodium salt) and embedded routinely into paraffin wax. Having excluded some fragmented, or non-representative samples, overall 60 were selected. All cases were reevaluated and the grades confirmed by an expert hematopathologist based on the WHO 2016 criteria. Thirty six cases were considered as grade 3 (MF-3) (22 males, 14 females; median age 66.3 years; range 45–86), 18 cases as grade 2 (MF-2) (5 males, 13 females; median age 56.2 years; range 31–76) and 6 cases were diagnosed as prefibrotic myelofibrosis with grade 1 (MF-1) fibrosis (3 males, three females; median age 54.1 years; range 29–86). Forty eight patients (80%) carried either the JAK2 V617F mutation (43 out of 60; 4 MF-1, 13 MF-2 and 26 MF-3

cases; 71,7%) or CALR mutations (5 out of 60; 2 MF-2 and 3 MF-3 cases; 8.3%). Four out of five patients harboured type 1 and 1 patient had a type 2 CALR mutation. Twelve patients (20%) were double negative for the JAK2 and CALR analysis. The study was conducted in accordance with the Helsinki Declaration, and the application for ethical approval has been submitted.

Myelofibrosis grading was based on routine Gomori's reticular fiber staining, which can also reveal excess of collagen fibers (collagen fibrosis). Briefly, rehydrated slides were oxidized using 1% potassium permanganate for 2 min followed by decoloration in 2% potassium metabisulfite for 1 min, then curing was done in 2% ferric ammonium sulphate solution for 1 min and silver impregnation in 10% silver nitrate containing 2% potassium hydroxide also for 1 min. Staining was finished with sequential treatments in 10% formalin for 5 min, then in 0.02% gold chloride for 10 s, 2% potassium metabisulfite for 1 min and finally in 1% sodium thiosulphate also for 1 min. The sections were washed in distilled water between incubation steps and mounted after dehydration.

Our diagnostic reticulin grading followed the European Consensus set up for bone marrow fibrosis [23]: MF-0, only perivascular reticulin fragments with no intersections; MF-1, focal, loose reticulin network with mainly perivascular intersections; MF-2, paratrabecular or central deposition of dense reticulin with regular intersections and occasional collagen bundles; MF-3: diffuse and dense intersecting reticulin network and collagen bundles with osteosclerosis.

Immunohistochemistry

For immunohistochemistry 3 μm think sections mounted on adhesive glass slides were heat activated for >2 h at 62 °C and dewaxed after reaching room temperature. Immunostaining, except for CXCL12, was done using the Ventana Benchmark Ultra automated system (Roche Diagnostics, Tucson, AR) including antigen retrieval for 40 min in the high pH CC1 buffer, incubation with the primary antibodies for 60 min and then with the Ultraview detection system for 40 min, and visualization using DAB/hydrogen peroxide development. CXCL12 was detected with manual immunostaining after TRIS-EDTA retrieval (pH 9) for 40 min, using the same incubation times as in the automated system with peroxidase conjugated Histols micropolymer (Histopathology Kft, Pécs) and revealed with DAB Quanto (TA-060-PHDX, Thermo Sci. Runcon, United Kingdom) kit. All immunoreactions were completed with nuclear counterstaining using hematoxylin.

Primary antibodies used in this study were monoclonal mouse anti-human p75 low affinity nerve growth factor receptor (L-NGFR, 1:100, clone: 7F10, Leica-NovoCastra, Newcastle, United Kingdom), CXCL12/SDF-1⟨ (1:50, clone:#79018, R&D, Minneapolis, MN, United States), rabbit anti-phospho-ERK1-2 (p44/42; Thr202/Tyr204; 1:100, clone:20G11, Cell Signaling, Danvers, MA, United States), as well as rabbit polyclonal connexin43 (Cx43, 1:100, #3512, Cell Signaling).

In addition, the rabbit anti-Cx43 (1:100) and the mouse anti-L-NGFR (1:100) primary antibodies were simultaneously combined in 10 cases of myelofibrosis for double immunofluorescence, and detected using a mixture of Alexa

Fluor 488 (green, 1:200) or Alexa Fluor 546 (red, 1:200) conjugated goat anti-mouse/or -rabbit (IgG H + L) antibodies (both Invitrogen/-Life Technologies, Eugene, OR, United States), for 90 min incubations at each sequence. Cell nuclei were revealed in blue using the DNA staining Hoechst (bisbenzimide,1:500; Sigma-Aldrich, St. Louis, MO, United States) fluorescing dye for 1 min, and finally the sections were coverslipped with fluorescent mounting medium (Dako).

Scoring and Image Analysis on Digital Slides

All immunostained sections were digitalized using the Pannoramic Scan system (3DHistech Ltd, Budapest) and scored either by visual analysis in the Pannoramic Viewer software or by using the HistoQuant semi-automated scoring program of the QuantCenter software package (all 3DHistech) for L-NGFR and Cx43 double stained fluorescence samples. At visual scoring we considered DAB reactions in elongated cells and their processes positive for the tested marker immunoreactions. The whole sections were taken into account but the final scores were determined by the areas of the highest density and intensity of positive immunreactions. Each marker reaction was assessed only within its own class to reveal potential correlations between its relative expression scores and Gomori's silver impregnation based grading. Three categories, similar to silver grading, were used; score 1: scarce and weak positive; score 2: moderate/medium density and/or positive; and score 3: high density and intensity of the defined positive structures representing elongated cells and cell processes.

Double immunofluorescence (NGFR plus Cx43) reactions of 10 cases of myelofibrosis were studied using semi-automated image analysis as described before [24]. Immunostained slides were digitalized at separated color channels (R, G and B for cell nuclei) through five layers at each field of views (FOVs) and analyzed at extended focus using the HistoQuant program (3DHistech). Five to eight digital annotations representing the given samples were made in each slide, making up 67 areas (20 x MF-3, 20 x MF-2 and 20 x MF-1) to be tested. The automated semiquantitative image analysis was based on the measurement of immunopositive area fractions within the selected annotations. Saturated immunofluorescent signals at each relevant channel (red or green) were highlighted by image segmentation and considered to be positive. The segmented areas were measures in μm^2 and the results were extrapolated and standardized to $1 mm^2$, and the correlations between the expression of the two markers were determined.

Statistical Analyses

All analyses were performed with the R statistics program (v.4.1.0, R Core Team 2021, Vienna Austria; RStudio IDE v. April 1, Boston, MA, United States). Non-normally distributed variables were displayed as median, range and interquartile range (IQR). Categorical variables were reported as proportions. The Cohen's kappa statistic was used to assess inter-rater agreement pairwise between the visual scoring assessment of the three readers (K.T, Sz.T. and K.B, indicated as assessor 1, two and
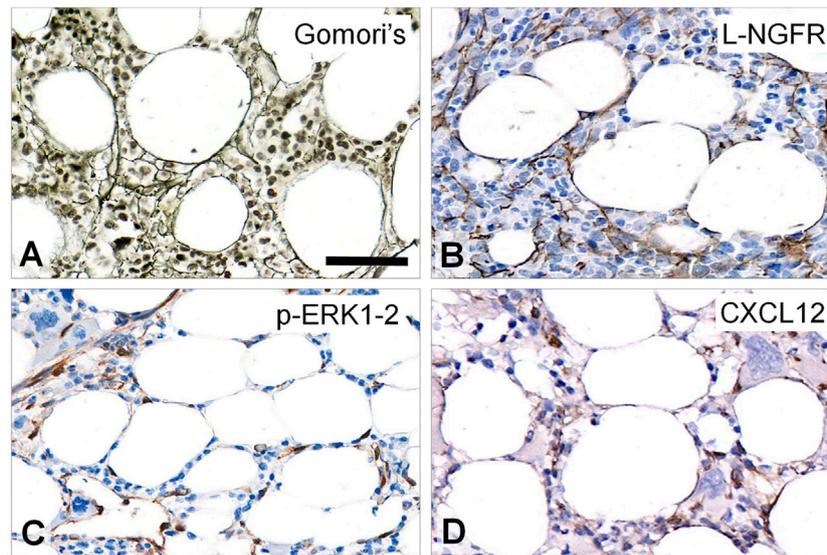
FIGURE 1 | Staining pattern of the tested immunoreactions in intact areas of MF-1 bone marrow samples compared to Gomori's silver impregnation **(A)**. L-NGFR highlights random stromal cells with their thin processes **(B)**. Phosphorylated ERK1-2 (*p*-ERK1-2) is detected mainly in oval nuclei of stromal and endothelial cells **(C)**, while CXCL12 reaction stains cell bodies of these elements **(D)** with both revealing only few cell processes. DAB immunoperoxidase reactions (brown) counterstained using hematoxylin **(B–D)**. Scale bar: 50 μm.

three respectively throughout) for each of the investigated markers [25]. Spearman's rank correlation was used to evaluate the association between the scoring values of experts (on the Likert scale 0–3) or the semiquantitatively segmented HistoQuant estimates (NGFR and Cx43) for each marker and grade respectively. Linear regression lines were fitted as orientation. The Kruskal-Wallis rank sum test was used as a global trend test to investigate the difference between L-NGFR, CXCL12, pERK12, Cx43 positivity and MF grades (MF-1, MF-2 and MF-3). As post hoc tests, Wilcoxon-Mann-Whitney U tests for two samples comparing their mean rank for each pair of grade levels were applied [25]. Figures were generated with the ggplot2 library using colorblind-friendly palettes. *p*-values were adjusted for multiple testing to counteract type 1 error inflation using the conservative Bonferroni correction (*p*⋆) [25]. Adjusted *p*-values <0.05 were considered significant.

RESULTS

Expression of the Tested Markers in Non-fibrotic Bone Marrow

In normal-looking, intact areas of MF-1 bone marrow samples L-NGFR was detected in the bodies and processes of elongated, unevenly arranged stromal cells both in peri-trabecular and peri-sinusoidal regions with sporadic interconnections similar to Gomori's silver impregnation (**Figure 1A,B**). Phosphorylated ERK1-2 was primarily seen in oval cell nuclei and rarely in their processes (**Figure 1C**), while CXCL12 positivity was linked to randomly dispersed, elongated cell bodies and scarce processes, along with a weak extracellular reaction (**Figure 1D**).

Expression of the Tested Markers in Myelofibrosis

All tested immunoreactions showed elevated number of marker positive cells in line with the increasing fibrosis. L-NGFR staining in perisinusoidal fibroblasts (pericytes) was obvious around arteri (oles)es, and high power view also confirmed this around capillary sinuses, but without any staining of the inner lining endothelial cells (**Figure 2A**). This was the only marker restricted to stromal cells, while both *p*-ERK1-2 and CXCL12 reactions were also seen in endothelial cells (**Figure 2B,C**). Immunopositive cell processes were frequently detected in close association with aberrant megakaryocytes with all three marker reactions (**Figure 2D–F**), suggesting a close interaction and functional cooperation with them.

Correlations Between Growth Related Marker Expression and Myelofibrosis Grade
L-NGFR Scores as the Best Discriminators Among Myelofibrosis Grades
The incidence and density of stromal cell bodies and processes positive for the tested markers at the "hot spots" (where marker reactions were seen at the highest density), were compared to the Gomori's-reticulin silver staining based grading using a similar 3-tier scale 1-2-3.

Immunoreactions were scored independently by three expert assessors and correlated with myelofibrosis grades both separately for each assessor and after consolidating the scores finally agreed on by all assessors.

By using the Kruskal-Wallis rank sum test and the Wilcoxon-Mann-Whitney post-hoc test the scoring results of all three
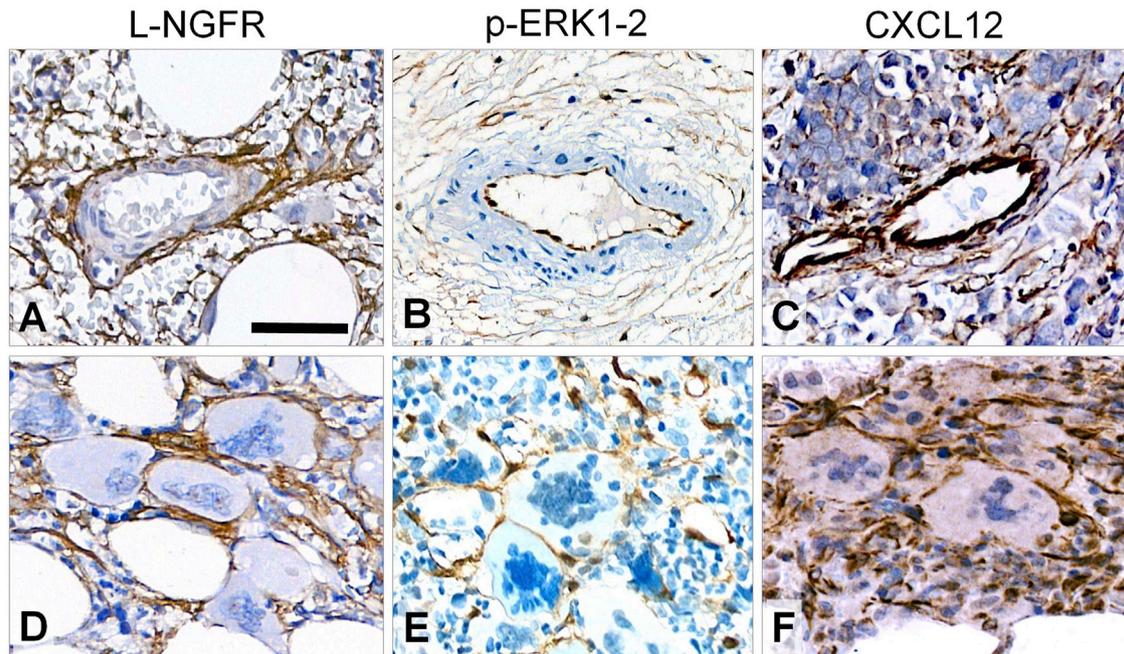
FIGURE 2 | Immunoreaction patterns of the tested markers in arteries, periarterial stroma and abnormal megakaryocytes in myelofibrosis. L-NGFR positive stromal network spread from adventitial pericytes without endothelial reaction **(A)**; while both *p*-ERK1-2 **(B)** and CXCL12 **(C)** reactions occur in endothelial and inter-arteriolar stromal cells with rare interconnections (upper row). Immunopositive elongated cell processes are intimately associated with aberrant megakaryocytes with all three markers **(D, E** and **F**; lower panel). DAB immunoperoxidase reactions (brown) counterstained using hematoxylin. Scale bar is 100 μm on A and B; and 50 μm on C-F.

biomarker reactions proved to be suitable for differentiating myelofibrosis grades. L-NGFR positive stromal cell density and the related scores showed the highest statistical correlations with the Gormori' silver staining based fibrosis grades at all three assessors (**Figure 3A–C**). Also, Spearman-rank analysis of L-NGFR scores showed high statistical link between assessors' results when they were tested in pairs (**Figure 3D–F**). The progressively increasing density of L-NGFR positive stromal cell processes (**Figure 4A–C**) were matched with that of the reticular and collagen fibers of silver impregnation when demonstrated in parallel sections (**Figure 4D–F**). However, the less interconnections among L-NGFR positive projections compared to silver stained fibers was obvious. The consolidated immunoscores agreed on by all assessors resulted in Kuskall-Wallis $p = 4.4e-07$, along with $p = 0.0045$ between grade 1 and grade 2; $p = 1.3e-05$ between grade 1 and grade 3; and $p = 2.3e-05$ between grade 2 and grade 3 cases when using the Wilcoxon post-hoc test (**Figure 4G**). Cohen's kappa values reflecting the inter-rater agreement between assessors scores on 60 cases also showed moderate to strong agreement. The association was moderate between assessors one and 2 (kappa = 0.682; z = 7.92; $p = 1.41e-11$); and between assessors two and 3 (kappa = 0.664; z = 7.41; $p = 1.27e-13$) and strong between assessors one and 3 (kappa = 0.916; z = 9.7; $p = 0$).

Correlations of pERK or CXCL12 Scores With Myelofibrosis Grades

Both *p*-ERK1-2 and CXCL12 scores showed less prominent significance concerning their grade discrimination values

compared to that of L-NGFR. These markers occurred mainly in stromal cell nuclei (*p*-ERK1-2) and bodies (both *p*-ERK1-2 and CXCL12) projecting only thin processes, with almost no interconnections (**Figure 5A–D**). The consolidated immunoscores for *p*-ERK1-2 resulted in Kuskall-Wallis $p = 0.00039$, besides $p = 0.015$ between grade 1 and grade 2; $p = 0.0063$ between grade 1 and grade 3; and $p = 0.014$ between grade 2 and grade 3 cases when using the Wilcoxon post-hoc test. For CXCL12 the consolidated immunoscores led to Kruskal-Wallis $p = 3.3e-05$, followed by $p = 0.0098$ between grade 1 and grade 2; $p = 0.00016$ between grade 1 and grade 3; and $p = 0.0021$ between grade 2 and grade 3 cases when using the Wilcoxon post-hoc test. Both *p*-ERK1-2 and CXCL12 immunoreactions were less evident for straight assessment, which was also reflected by their weaker Spearman-rank correlations (*p*-ERK1-2, R = 0.76–0.81; CXCL12 R = 0.82–0.89) and Cohen's kappa interrater values only weak correlations (*p*-ERK-1-2, kappa = 0.415–0.526; CXCL12, kappa = 0.512–0.578) than those of NGFR.

Colocalization of L-NGFR Positive Stromal Network With Connexin 43 Gap Junction Plaques

Earlier we observed that Cx43 direct cell-cell communication channels were upregulated in pathological bone marrow samples where stromal/hemopoetic cell ratio was increased [19]. Therefore, L-NGFR as the best marker to highlight stromal network in this study and Cx43 protein were detected

FIGURE 3 | Statistical correlations between L-NGFR immunoreaction scores and Gomori's silver staining based myelofibrosis grades as recognized by the individual assessors after using both the Kruskal-Wallis test and the Wilcoxon post-hoc test **(A–C)**. Pearson's correlation values among scores of L-NGFR immunoreactions revealed between pairs of assessors in relation to Gomori's silver staining based myelofibrosis grades **(D–F)**.

simultaneously using immunofluorescence in samples representing all grades of myelofibrosis to see their potential link (**Figure 6A–C**). Multilayer scanning revealed Cx43 positive particles of <1 micrometer throughout the ~4 micrometer section thickness and their significant co-localization with L-NGFR positive stromal cell processes. The HistoQuant software was used for quantifying both reactions in representative areas (67 areas of 10 cases) after image segmentation highlighting the specific reactions in each channel (**Figure 6D,E**). The massive coexpression of the two biomarker reactions was obvious after merging the segmented immune signals (**Figure 6D**). Spearman's rank test was used to evaluate the association between the expression of the two makers, which showed strong statistical correlations (**Figure 6E**).

DISCUSSION

Despite the novel prognostic models considering driver and passenger mutations, karyotype and sex-adjusted hemoglobin levels, bone marrow fibrosis reflecting the abnormal activation of the fibrotic stromal microenvironment is still a major predictor of the outcome in primary myelofibrosis [2, 5]. Here we tested growth related markers which were primarily expressed by stromal cells including L-NGFR/CD271, p-ERK1-2 and CXCL-12, and found that the density of positive cells for each marker was progressively increased in line with the Gomori's silver

staining-based tumor grades. NGFR reactions restricted to and revealed the whole length of stromal cells (the others also showed some endothelial positivity) with most intersections of the 3 markers, showed the best statistical correlation and the most reproducible agreement among assessors' judgements with myelofibrosis grades. L-NGFR positive stromal cells co-expressed Cx43 protein, particularly in advanced myelofibrosis, suggesting an enhanced communication and functional coupling within the overgrown stromal network. Therefore, our findings revealed some biomarkers of stromal cell activation of which L-NGFR expression proved to be the most promising to complement Gomori's silver staining for myelofibrosis grading.

Myelofibrosis is driven by augmented and pathological extracellular matrix production resulted from the increasing number and activation of bone marrow stromal cells as a result of aberrant cytokine signaling and clonal megakaryocyte functions [3]. The extent of matrix overproduction, still assessed using Gomori's silver impregnation, determines grades in primary myelofibrosis and predicts disease progression and outcome [2]. However, selective silver deposition on reticular and collagen fibers can be highly dependent on preanalytical (fixation, decalcification) and staining (components, timing, ambient temperature and light conditions) variables [5]. Furthermore, it can't directly reveal the functional activation of stromal cells and differentiate between "prefibrotic" and "overtly fibrotic" phase of primary myelofibrosis [1]. Though none of our selected markers highlighted the reticular or collagen matrix in the bone marrow, they were primarily expressed
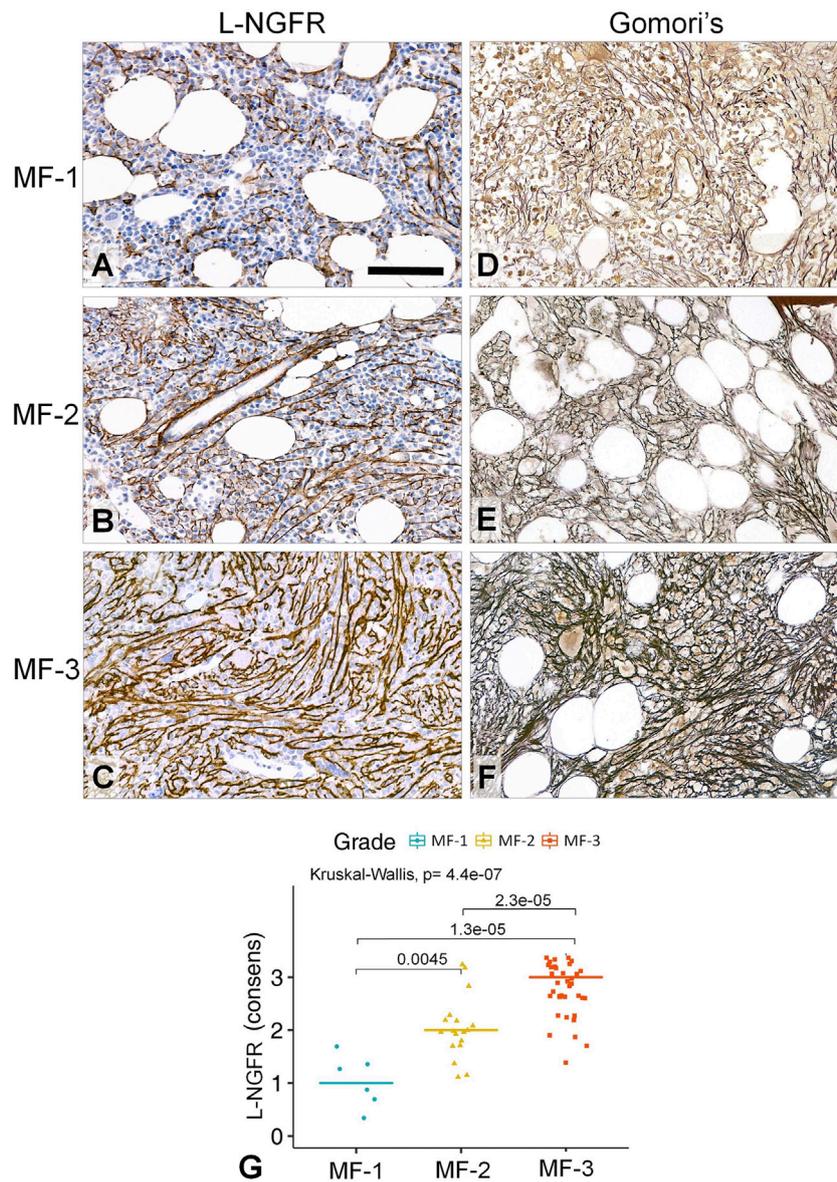
FIGURE 4 | Correlations between the L-NGFR immunopositive stromal network **(A–C)** and the reticulin (and collagen) scaffolding **(D–F)** in myelofibrotic bone marrow samples. The gradually increasing density with some interconnections among L-NGFR positive cell processes show good correlation with reticular (and collagen) fibrosis determining myelofibrosis grade as revealed by Gomori's silver impregnation. DAB immunoperoxidase reactions (brown) counterstained using hematoxylin **(A–C)**. Scale bar: 50 μm. High statistical correlation was detected between the consensus scores of the three assessors and the sliver impregnation based fibrosis grades both with the Kruskal-Wallis global trend test and the pairwise Wilcoxon post-hoc test **(G)**.

in stromal cells and were linked to growth related pathways as potential indicators of their activation. Since MF-0, "normal-looking bone marrow" showed only few spindle shaped positive stromal cells in random localization when the immunoreactions were set up, very similar to the intact looking areas in MF-1 cases (see **Figure 1**), we considered these to represent the basic MF-0 situation. Intimate association of spindle shaped stromal cells, which were positive for each marker, with aberrant megakaryocytes was likely to reflect their functional co-operation and the potential impact of cytokines and growth factors released by megakaryocytes on pathological stromal cell activation.

L-NGFR (CD271) is a low affinity receptor for neurotrophins including NGF, which by cooperating with tropomyosin receptor kinase A (TrkA) can catalyze its receptor tyrosine kinase (RTK) mediated signaling in neurons [26, 27]. Alternatively, L-NGFR may prevent this growth signaling by interacting with non-preferred neurotrophins, which may lead to programmed cell death response (apoptosis) e.g. in oligodendrocytes [28]. In our study, L-NGFR was progressively expressed in the growing stromal cell network along with disease progression in myelofibrosis, which suggests its involvement in growth promotion rather than in apoptosis. TrkA may assist L-NGFR
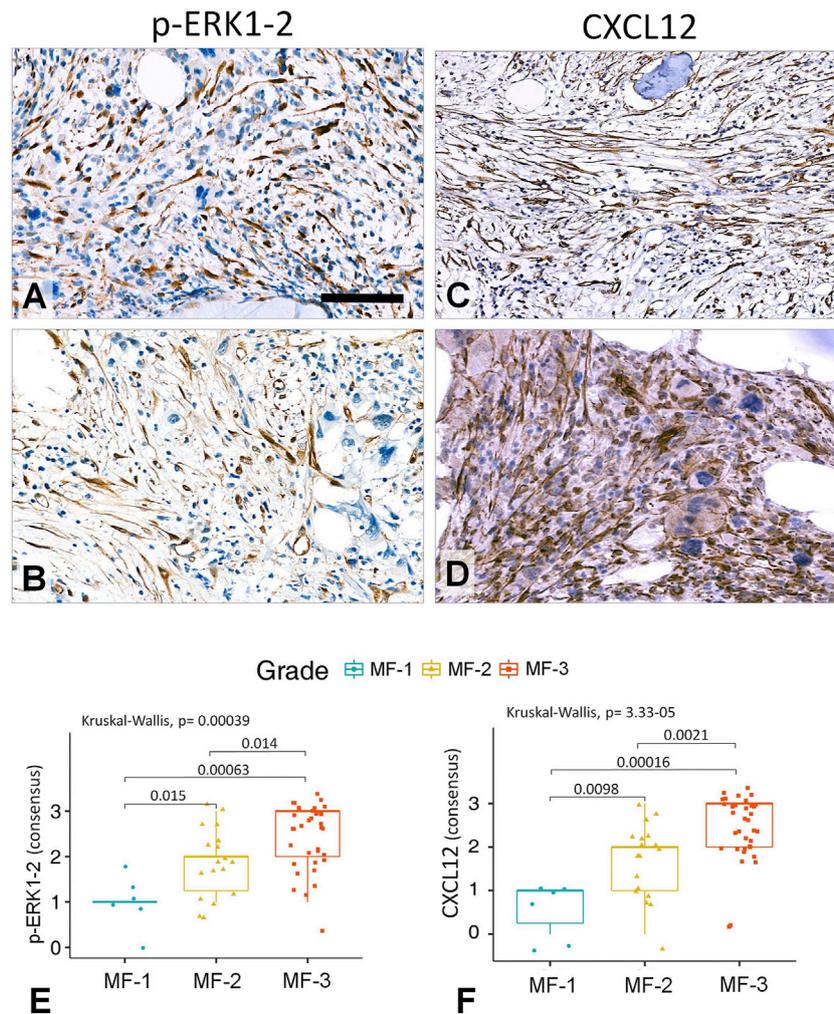
FIGURE 5 | Representative examples of grade 3 myelofibrotic bone marrow samples where either *p*-ERK1-2 **(A,B)** or CXCL12 **(C,D)** immunoreactions reveal elongated stromal cells, which however, are rarely interconnected by their processes into contiguous meshworks. DAB immunoperoxidase reactions (brown) counterstained using hematoxylin. Scale bar is 50 μm on A, B and D; and 100 μm on **C**. Both the *p*-ERK1-2 **(E)** and CXCL12 **(F)** immunoreaction consensus scores showed statistical correlations with reticulin-silver staining based myelofibrosis grades either when using Kruskal-Wallis trend test or the pairwise Wilcoxon test. However, their discrimination power was weaker than that of L-NGFR.

in this, since both of them are thought to be involved in mesenchymal stromal cell functions [29], despite that Trk neurotrophin receptors have been only rarely detected in bone marrow stromal network [30]. Nevertheless, the finding that upregulated TrkA in bone marrow stromal stem cells can augment their survival and regenerative capacity in nerve grafts through the MAPK pathway, can also support this view [11]. Bone marrow stromal cells may also produce nerve growth factor which raises a potential autocrine regulation of stromal proliferation too [31].

L-NGFR expression was first observed in bone marrow stromal cells nearly 30 years ago, when its correlation with reticulin silver staining in myelofibrosis was already mentioned, but it was based on only 2 cases [6]. Immuno-electron microscopy of L-NFGR confirmed labeling all along stellate or spindle-shaped filamentous stromal processes,

primarily in bone marrow adventitial reticular cells [32]. This supports our finding of L-NGFR immunoreaction through the whole length of stromal cell processes in the myelofibrotic bone marrow. L-NGFR/CD271 has been considered as a selective marker for mesenchymal stromal (stem) cell isolation, since positive cell fraction were rich in clonogenic precursors, which showed increased proliferation [33] and trilineage differentiation into fibroblastic, adipocytic and osteoblastic cells, significantly more than CD271 negative stromal cells [9, 34]. These findings also suggest that L-NGFR/CD271 is involved in the functional activation of bone marrow stromal network. Though L-NGFR immunoreaction was recommended for differential diagnosis within myeloproliferative neoplasms by showing that positive stromal cells were more frequent in primary myelofibrosis that in essential thrombocythemia (ET) or in polycythaemia vera (PV) [35], its correlations with myelofibrosis grades had not been

FIGURE 6 | Double immunofluorescence for L-NGFR (green, **A**) and Cx43 (red, **B**) along with Hoechst nuclear counterstain (blue) in a grade 3 myelofibrosis. Merged images proved massive colocalization of the biomarkers **(C)**, which became apparent after highlighting the green (in turquoise) and red signals (merged in yellow) with the image segmentation algorithm of the HistoQuant software **(D)**. Semiautomated image analysis of the area fractions of fluorescent signals with this program in 67 standard areas of 10 myelofibrotic marrow samples **(E)** revealed strong overlap and correlation between L-NGFR and Cx43 signals suggesting that most particulate Cx43 belong to L-NGFR positive stromal cells **(F)**. Scale bar on A is 25 μm on A-D and 500 μm on E.

studied systematically before. In our work, L-NGFR reaction showed the strongest discriminating power of the tested biomarkers among myelofibrosis grades as shown both by the Kruskal-Wallis global trend-tests and the Wilcoxon post-hoc test. This was the only marker to be detected exclusively in stromal cells and throughout their processes. Furthermore, L-NGFR scores demonstrated the best interrater agreement between pairs of assessors and thus L-NGFR immunoreaction can be a biological indicator of stromal cell activation and overproduction of reticular and collagen fibers revealed by silver impregnation.

Receptor tyrosine kinase (RTK) signaling is the major promoter of profibrogenic responses [36]. RTKs (TrkA may be too) have been strongly involved in the regulation of mesenchymal stromal cell activation, growth and proliferation, including the bone marrow stromal microenvironment, mainly through PDGFR, EGFR [37] and FGF2/bFGF receptors [38]. PDGFR-β (but not PDGFR-⟨) expression was found to indicate the functional activation of bone stromal cells in the myelofibrotic marrow and to statistically correlate with the Gomori's silver

impregnation based fibrosis grades [13-15]. RTK signaling converges to ERK1-2 phosphorylation as a sign of its activation, resulting in its translocation into cell nuclei to promote growth and proliferation related adaptation responses in stromal fibroblasts as a transcription factor [39, 40]. In agreement with this, our p-ERK1-2 immunoreactions occurred both in the nuclei and the cytoplasm of spindle shaped cells. However, the reaction did not highlight the whole length of stromal cell processes, thus rarely showed interconnections, and also occurred in some sinus endothelial cells of similar morphology. Despite these limitations, p-ERK1-2 protein positive cell density statistically correlated with myelofibrosis progression in line with Gomori's silver impregnation. Though p-ERK1-2 immunoreaction proved to be another biomarker of bone marrow stromal cell activation and myelofibrosis evolution it showed less potential than NGFR reaction for diagnostic use.

The CXCL12 chemokine is constitutively released from bone marrow stromal cells and contributes to maintaining stem cells in bone marrow niches by binding to CXCR4 on CD34+/CD117 +

hemopoietic progenitors and leukemic blasts too [16]. Therefore, CXCL12 may also be involved in protecting the leukemic stem cells and contributing to myelofibrosis progression [22], though CXCR4 is downregulated in the malignant progenitors, which may explain extramedullary clonal hematopoiesis in myelofibrosis [41]. Endothelial cells may also express CXCL12, although at a lower level [16]. CXCL12 plays an essential role in stem cell homing at transplantation and the CXCL12/CXCR4 interaction supports stromal cell resistance and restoration of the stromal network after myeloablative irradiation [17]. CXCL12/CXCR4 pathway is activated by oncogenic JAK2, which frequently suffers activating mutations in primary myelofibrosis [20]. In line with this, we detected CXCL12 positive perivascular and peri-osteoblastic stromal cells at increasing density with the Gomori's silver staining based myelofibrosis grades. However, similar to that of *p*-ERK1-2, CXCL12 immunoreactions might not reveal all stromal cells and highlight only part of stromal cell bodies. The mild extracellular staining was in line with CXCL12 functions, which, however, is another reason preventing it to be a useful diagnostic biomarker of myelofibrosis progression.

Connexins form direct cell-cell communication channels that allow the controlled passage of small (<1.8 kDa) regulatory molecules between coupled cells and thus, support the formation of functional cell compartments within tissues including the bone marrow [19]. CXCL12 release requires close cooperation of stromal cells, which need to function as a network coupled by Cx43 (and less by CX45) gap junctions [18]. In line with our earlier study [19], we confirmed this close association in the form of protein colocalization between the stromal L-NGFR immunoreaction and Cx43 gap junction plaques. Their parallel and progressively elevated expression suggests an increasing functional activation and potential communication within the stromal network in myelofibrosis in line with disease advancement.

In conclusion, all of our tested growth related biomarkers including L-NGFR, *p*-ERK1-2 and CXCL12 were likely to be expressed in activated bone marrow stromal cells and their immunoscores were statistically correlated with Gomori's silver impregnation based myelofibrosis grades at varying strength. L-NGFR reaction was restricted to and revealed the whole length of stromal cells, and showed the best correlations with myelofibrosis grades and the strongest interrater agreements. The progressive expression of Cx43 gap junctions in the stromal cells may support compartmental co-ordination within the myelofibrotic stroma. Our results suggest that L-NGFR expression can be a useful biological marker of stromal cell activation which deserves diagnostic consideration for complementing Gomori's silver impregnation. Further, direct biological evidence of stromal activation will be gained by detecting the expression of different matrix proteins in myelofibrosis, which is under way in our laboratory.

DATA AVAILABILITY STATEMENT

The raw data supporting the conclusions of this article will be made available by the authors, without undue reservation.

ETHICS STATEMENT

This work was approved by the Scientific and Research Board of The Health Ethical Council (ETT TUKEB) in Hungary (IV/129/2022/EKU).

AUTHOR CONTRIBUTIONS

TK designed the project assisted by TS and BT who selected the biopsy samples helped by VD and BV. TK, BT and TS performed the final scoring separately based on common criteria. MEM performed the statistics, AC performed the image analysis and photo documentation helped by VD and BV, who also assisted in digitalizing the stained samples. The manuscript was written by TK, BT and TS.

FUNDING

CONFLICT OF INTEREST

The authors declare that this study received shared facilities from 3DHISTEC Ltd. AC has been both the employee of 3DHISTECH Ltd. and a PhD student at Semmelweis University under the Co-operative PhD Program funded by the Hungarian Ministry of Innovation. TK is Member of the Editorial Board regularly reviewing manuscripts for POR. TS is a PhD student at Semmelweis University which supports PhD students publications in POR.

The remaining authors declare that the research was conducted in the absence of any commercial or financial relationships that could be construed as a potential conflict of interest.

ACKNOWLEDGMENTS

REFERENCES

1. Barbui T, Thiele J, Gisslinger H, Kvasnicka HM, Vannucchi AM, Guglielmelli P, et al. The 2016 WHO Classification and Diagnostic Criteria for Myeloproliferative Neoplasms: Document Summary and In-Depth Discussion. *Blood Cancer J* (2018) 8:15. doi:10.1038/s41408-018-0054-y

2. Tefferi A. Primary Myelofibrosis: 2019 Update on Diagnosis, Risk-Stratification and Management. *Am J Hematol* (2018) 93:1551–60. doi:10.1002/ajh.25230

3. Schieber M, Crispino JD, Stein B. Myelofibrosis in 2019: Moving beyond JAK2 Inhibition. *Blood Cancer J* (2019) 9:74. doi:10.1038/s41408-019-0236-2

4. Gömöri G. Silver Impregnation of Reticulum in Paraffin Sections. *Am J Pathol* (1937) 13:993–5.

5. Kvasnicka HM, Beham-Schmid C, Bob R, Dirnhofer S, Hussein K, Kreipe H, et al. Problems and Pitfalls in Grading of Bone Marrow Fibrosis, Collagen Deposition and Osteosclerosis - a Consensus-based Study. *Histopathology* (2016) 68:905–15. doi:10.1111/his.12871

6. Cattoretti G, Schiró R, Orazi A, Soligo D, Colombo M. Bone Marrow Stroma in Humans: Anti-nerve Growth Factor Receptor Antibodies Selectively Stain Reticular Cells *In Vivo* and *In Vitro*. *Blood* (1993) 81:1726–38. doi:10.1182/blood.v81.7.1726.bloodjournal8171726

7. Covaceuszach S, Konarev PV, Cassetta A, Paoletti F, Svergun DI, Lamba D, et al. The Conundrum of the High-Affinity NGF Binding Site Formation Unveiled? *Biophysical J* (2015) 108:687–97. doi:10.1016/j.bpj.2014.11.3485

8. Micera A, Lambiase A, Stampachiacchiere B, Bonini S, Bonini S, Levischaffer F. Nerve Growth Factor and Tissue Repair Remodeling: trkANGFR and p75NTR, Two Receptors One Fate. *Cytokine Growth Factor Rev* (2007) 18:245–56. doi:10.1016/j.cytogfr.2007.04.004

9. Barilani M, Banfi F, Sironi S, Ragni E, Guillaumin S, Polveraccio F, et al. Low-affinity Nerve Growth Factor Receptor (CD271) Heterogeneous Expression in Adult and Fetal Mesenchymal Stromal Cells. *Sci Rep* (2018) 8:9321. doi:10.1038/s41598-018-27587-8

10. Tomlinson RE, Li Z, Zhang Q, Goh BC, Li Z, Thorek DLJ, et al. NGF-TrkA Signaling by Sensory Nerves Coordinates the Vascularization and Ossification of Developing Endochondral Bone. *Cel Rep* (2016) 16:2723–35. doi:10.1016/j.celrep.2016.08.002

11. Zheng MG, Sui WY, He ZD, Liu Y, Huang YL, Mu SH, et al. TrkA Regulates the Regenerative Capacity of Bone Marrow Stromal Stem Cells in Nerve Grafts. *Neural Regen Res* (2019) 14:1765–71. doi:10.4103/1673-5374.257540

12. Bock O, Loch G, Büsche G, von Wasielewski R, Schlué J, Kreipe H. Aberrant Expression of Platelet-Derived Growth Factor (PDGF) and PDGF Receptor-Alpha Is Associated with Advanced Bone Marrow Fibrosis in Idiopathic Myelofibrosis. *Haematologica* (2005) 90:133–4.

13. Bedekovics J, Kiss A, Beke L, Károlyi K, Méhes G. Platelet Derived Growth Factor Receptor-Beta (PDGFRβ) Expression Is Limited to Activated Stromal Cells in the Bone Marrow and Shows a strong Correlation with the Grade of Myelofibrosis. *Virchows Arch* (2013) 463:57–65. doi:10.1007/s00428-013-1434-0

14. Bedekovics J, Szeghalmy S, Beke L, Fazekas A, Méhes G. Image Analysis of Platelet Derived Growth Factor Receptor-Beta (PDGFRβ) Expression to Determine the Grade and Dynamics of Myelofibrosis in Bone Marrow Biopsy Samples. *Cytometry* (2014) 86:319–28. doi:10.1002/cyto.b.21167

15. Méhes G, Tzankov A, Hebeda K, Anagnostopoulos I, Krenács L, Bedekovics J. Platelet-derived Growth Factor Receptor β (PDGFRβ) Immunohistochemistry Highlights Activated Bone Marrow Stroma and Is Potentially Predictive for Fibrosis Progression in Prefibrotic Myeloproliferative Neoplasia. *Histopathology* (2015) 67:617–24. doi:10.1111/his.12704

16. Kitagawa M, Kurata M, Onishi I, Yamamoto K. Bone Marrow Niches in Myeloid Neoplasms. *Pathol Int* (2020) 70:63–71. doi:10.1111/pin.12870

17. Singh P, Mohammad KS, Pelus LM. CXCR4 Expression in the Bone Marrow Microenvironment Is Required for Hematopoietic Stem and Progenitor Cell Maintenance and Early Hematopoietic Regeneration after Myeloablation. *Stem cells (Dayton, Ohio)* (2020) 38:849–59. doi:10.1002/stem.3174

18. Schajnovitz A, Itkin T, D'Uva G, Kalinkovich A, Golan K, Ludin A, et al. CXCL12 Secretion by Bone Marrow Stromal Cells Is Dependent on Cell Contact and Mediated by Connexin-43 and Connexin-45 gap Junctions. *Nat Immunol* (2011) 12:391–8. doi:10.1038/ni.2017

19. Krenacs T, Rosendaal M. Connexin43 gap Junctions in normal, Regenerating, and Cultured Mouse Bone Marrow and in Human Leukemias: Their Possible Involvement in Blood Formation. *Am J Pathol* (1998) 152:993–1004.

20. Abdelouahab H, Zhang Y, Wittner M, Oishi S, Fujii N, Besancenot R, et al. CXCL12/CXCR4 Pathway Is Activated by Oncogenic JAK2 in a PI3K-dependent Manner. *Oncotarget* (2017) 8:54082–95. doi:10.18632/oncotarget.10789

21. López-Gil JC, Martin-Hijano L, Hermann PC, Sainz B, Jr. The CXCL12 Crossroads in Cancer Stem Cells and Their Niche. *Cancers (Basel)* (2021) 13. doi:10.3390/cancers13030469

22. Schepers K, Pietras EM, Reynaud D, Flach J, Binnewies M, Garg T, et al. Myeloproliferative Neoplasia Remodels the Endosteal Bone Marrow Niche into a Self-Reinforcing Leukemic Niche. *Cell stem cell* (2013) 13:285–99. doi:10.1016/j.stem.2013.06.009

23. Thiele J, Kvasnicka HM, Facchetti F, Franco V, van der Walt J, Orazi A. European Consensus on Grading Bone Marrow Fibrosis and Assessment of Cellularity. *Haematologica* (2005) 90:1128–32.

24. Balla P, Maros ME, Barna G, Antal I, Papp G, Sapi Z, et al. Prognostic Impact of Reduced Connexin43 Expression and gap junction Coupling of Neoplastic Stromal Cells in Giant Cell Tumor of Bone. *PLoS one* (2015) 10:e0125316. doi:10.1371/journal.pone.0125316

25. Maros ME, Wenz R, Förster A, Froelich MF, Groden C, Sommer WH, et al. Objective Comparison Using Guideline-Based Query of Conventional Radiological Reports and Structured Reports. *In Vivo* (2018) 32:843–9. doi:10.21873/invivo.11318

26. Canossa M, Twiss JL, Verity AN, Shooter EM. p75(NGFR) and TrkA Receptors Collaborate to Rapidly Activate a p75(NGFR)-associated Protein Kinase. *EMBO J* (1996) 15:3369–76. doi:10.1002/j.1460-2075.1996.tb00702.x

27. Barker PA. p75NTR: A Study in Contrasts. *Cell Death Differ* (1998) 5:346–56. doi:10.1038/sj.cdd.4400375

28. Casaccia-Bonnefil P, Kong H, Chao MV. Neurotrophins: the Biological Paradox of Survival Factors Eliciting Apoptosis. *Cel Death Differ* (1998) 5:357–64. doi:10.1038/sj.cdd.4400377

29. Zha K, Yang Y, Tian G, Sun Z, Yang Z, Li X, et al. Nerve Growth Factor (NGF) and NGF Receptors in Mesenchymal Stem/stromal Cells: Impact on Potential Therapies. *Stem Cell translational Med* (2021) 10:1008–20. doi:10.1002/sctm.20-0290

30. Labouyrie E, Dubus P, Groppi A, Mahon FX, Ferrer J, Parrens M, et al. Expression of Neurotrophins and Their Receptors in Human Bone Marrow. *Am J Pathol* (1999) 154:405–15. doi:10.1016/s0002-9440(10)65287-x

31. García R, Aguiar J, Alberti E, de la Cuétara K, Pavón N. Bone Marrow Stromal Cells Produce Nerve Growth Factor and Glial Cell Line-Derived Neurotrophic Factors. *Biochem Biophys Res Commun* (2004) 316:753–4. doi:10.1016/j.bbrc.2004.02.111

32. Caneva L, Soligo D, Cattoretti G, De Harven E, Lambertenghi Deliliers G. Immuno-electron Microscopy Characterization of Human Bone Marrow Stromal Cells with Anti-NGFR Antibodies. *Blood Cell Mol Dis* (1995) 21:73–85. doi:10.1006/bcmd.1995.0011

33. Calabrese G, Giuffrida R, Lo Furno D, Parrinello N, Forte S, Gulino R, et al. Potential Effect of CD271 on Human Mesenchymal Stromal Cell Proliferation and Differentiation. *Ijms* (2015) 16:15609–24. doi:10.3390/ijms160715609

34. Quirici N, Soligo D, Bossolasco P, Servida F, Lumini C, Deliliers GL. Isolation of Bone Marrow Mesenchymal Stem Cells by Anti-nerve Growth Factor Receptor Antibodies. *Exp Hematol* (2002) 30:783–91. doi:10.1016/s0301-472x(02)00812-3

35. Yigit N, Covey S, Barouk-Fox S, Turker T, Geyer JT, Orazi A. Nuclear Factor-Erythroid 2, Nerve Growth Factor Receptor, and CD34-Microvessel Density Are Differentially Expressed in Primary Myelofibrosis, Polycythemia Vera, and Essential Thrombocythemia. *Hum Pathol* (2015) 46:1217–25. doi:10.1016/j.humpath.2015.05.004

36. Beyer C, Distler JHW. Tyrosine Kinase Signaling in Fibrotic Disorders. *Biochim Biophys Acta (Bba) - Mol Basis Dis* (2013) 1832:897–904. doi:10.1016/j.bbadis.2012.06.008

37. Satomura K, Derubeis AR, Fedarko NS, Ibaraki-O'Connor K, Kuznetsov SA, Rowe DW, et al. Receptor Tyrosine Kinase Expression in Human Bone Marrow Stromal Cells. *J Cel Physiol.* (1998) 177:426–38. doi:10.1002/(sici)1097-4652(199812)177:3<426::aid-jcp6>3.0.co;2-f

38. Dupree MA, Pollack SR, Levine EM, Laurencin CT. Fibroblast Growth Factor 2 Induced Proliferation in Osteoblasts and Bone Marrow Stromal Cells: a Whole Cell Model. *Biophysical J* (2006) 91:3097–112. doi:10.1529/biophysj.106.087098

39. Pagès G, Lenormand P, L'Allemain G, Chambard JC, Meloche S, Pouysségur J. Mitogen-activated Protein Kinases P42mapk and P44mapk Are Required for Fibroblast Proliferation. *Proc Natl Acad Sci* (1993) 90:8319–23. doi:10.1073/pnas.90.18.8319

40. Plotnikov A, Zehorai E, Procaccia S, Seger R. The MAPK Cascades: Signaling Components, Nuclear Roles and Mechanisms of Nuclear Translocation. *Biochim Biophys Acta (Bba) - Mol Cel Res* (2011) 1813:1619–33. doi:10.1016/j.bbamcr.2010.12.012

41. Song M-K, Park B-B, Uhm J-E. Understanding Splenomegaly in Myelofibrosis: Association with Molecular Pathogenesis. *Ijms* (2018) 19:898. doi:10.3390/ijms19030898

Check for
updates

PD-L1 Testing in Urothelial Carcinoma: Analysis of a Series of 1401 Cases Using Both the 22C3 and SP142 Assays

Harriet Evans *, Brendan O'Sullivan, Frances Hughes, Kathryn Charles, Lee Robertson, Philippe Taniere and Salvador Diaz-Cano

Molecular Pathology Diagnostic Service, Queen Elizabeth Hospital Birmingham, Birmingham, United Kingdom

Immune checkpoint blockade (ICB) drugs are a novel, effective treatment for advanced urothelial carcinoma. Worldwide, several different ICB drugs are approved, each developed and clinically validated with a specific PD-L1 compound diagnostic assay. As a result, PD-L1 testing workflows in routine practice are complex: requiring multiple assays across two platforms, with each assay having a different method of interpretation. Our service tested 1,401 urothelial carcinoma cases for PD-L1 expression, using both the 22C3 PharmDx assay (required prior to Pembrolizumab therapy) and SP142 assay (required prior to Atezolizumab therapy). Of the 1,401 cases tested, 621 cases (44%) were tested with both the 22C3 PharmDx and SP142 assays, 492 cases (35%) with 22C3 PharmDx only, and 288 cases (21%) with SP142 only. Each assay was used and interpreted according to the manufacturer's guidelines. The rate of positivity we observed was 26% with the 22C3 assay and 31% with the SP142 assay, similar to the pre-licensing studies for both drugs. The discrepancy observed between the assays was 11%, which reinforces the requirement for utilisation of the correct assay for each agent, and limits potential cross-utility of assays. This aspect must be considered when setting up a PD-L1 testing strategy in laboratories where both Pembrolizumab and Atezolizumab are available for the treatment of urothelial carcinoma but also has broader implications for testing of other cancers where multiple ICB drugs and their respective assays are approved.

Keywords: PD-L1, urothelial bladder carcinoma, predictive marker, Pembrolizumab, Atezolizumab

INTRODUCTION

Immune checkpoint blockade (ICB) drugs have emerged as an effective treatment for many cancers and their use is approved across cancer types. Each ICB drug has been developed alongside a specific PD-L1 companion diagnostic assay. These PD-L1 assays have been designed and validated by clinical trials for specific use in different disease-drug combinations. They use different PD-L1 primary antibody clones, immunohistochemistry (IHC) platforms and protocols, and have different scoring algorithms [1,2].

As a result, when testing laboratories decide which PD-L1 tests to implement in routine practice; they must consider data on both clinical and technical validation. There is little evidence in the literature on the clinical equivalence between the various compound diagnostics. Therefore, it would

be hard to justify using a compound diagnostic test other than the one shown to be clinically validated in trials (whether an alternative compound diagnostic test or a laboratory-developed PD-L1 IHC protocol). Furthermore, ICB drugs can be both toxic to patients and expensive for healthcare providers which necessitates accuracy in selecting patients suitable for ICB therapy.

In order to deliver an exhaustive PD-L1 testing service in solid tumours, laboratories have to implement PD-L1 assays on both the Dakolink48 and the Ultra platforms and validate the four companion diagnostics assays, each on the relevant platform (22C3 PharmDx and 28.8 PharmDx on Dakolink 48; SP142 and SP263 assays on Ultra platform). Furthermore, as the readout and the scoring algorithm varies both between and within tumour types, there must be appropriate training for reporting pathologists and scientists.

Worldwide, five ICB drugs are currently approved by the Food and Drug Authority (Atezolizumab, Avelumab, Durvalumab, Nivolumab and Pembrolizumab), and three by the European Medicines Agency (EMA) Atezolizumab, Nivolumab and Pembrolizumab) for the treatment of advanced urothelial cancer following chemotherapy. Furthermore both Atezolizumab and Pembrolizumab are EMA approved for the first line treatment of in advanced urothelial cancer where patients are ineligible for cisplatin containing chemotherapy [3,4]. Currently, only Atezolizumab is NICE approved in urothelial cancer, for use in both cisplatin-ineligible patients and for treatment following platinum-containing chemotherapy [5,6]. When being used as a first line drug, both NICE and the EMA specify that the use of Atezolizumab or Pembrolizumab is based on specific PD-L1 cut off values being met and so PD-L1 assessment is mandatory before prescription in these scenarios [5,7,8].

Based on clinical trial data, when using the 22C3 PharmDx assay (the assay approved for PD-L1 testing prior to Pembrolizumab prescription), a positive PD-L1 test result is defined as a combined positive score (CPS) including tumour and immune cells above 10 (CPS >10) [9,10]. However, when using the Ventana SP142 assay (the approved assay for use prior to Atezolizumab prescription), a positive PD-L1 result is defined as PD-L1 positive immune cells (IC) staining covering more than 5% of the tumour area (>5% IC) [11,12]. This highlights that there are numerous differences between interpretation of these assays: including what cell types are included in the assessment (immune cells or immune cells and tumours cells), the type of inflammatory cells that are included (22C3 allows only lymphocytes and macrophages, whereas SP142 also includes dendritic cells and granulocytes), whether the assessment is of the total number of cells or of the area involved, and finally, the positive cut off values [4,13].

Data from clinical studies found that prior to Atezolizumab, the percentage of tumours with PD-L1 expression of >5% IC varied from 27% (previously untreated tumours in Cisplatin ineligible patients) to either 28% or 33% in those who had prior chemotherapy treatment (28% in metastatic tumour samples, 33% in primary tumour samples) [11,12]. For Pembrolizumab, trials found that 33% (Keynote-052 trial) or 30.3% (Keynote-045 trial) of urothelial carcinoma patients had PD-L1 expressing tumours with a CPS >10 [9,10]. Additionally, a study from Eckstein et al. assessed 251 urothelial carcinomas with four different PD-L1 assays. Their results found that when using the PharmDx assay with the designated cut off of CPS >10, 35.1% of cases were positive. however, when using the SP142 assay with the cut off value of IC >5%, only 16.3% of cases were positive [14].

The existence of multiple different ICB drugs, each with their different compound diagnostic is challenging and inflexible for laboratories in terms of cost, achieving turn around times and preserving patient tissue. This had leads to the drive to assess the interchangeability between different assays. This is a valid consideration that could allow reduce cost, easier testing strategies and preservation of patient tissue [4,13,15].

Several studies have looked at the concordance between multiple different ICB drug assays in urothelial carcinoma. Some compared the concordance between assays using a common criteria, for example, immune cell (IC) value or tumour cell (TC) value rather than each test according to the manufacture guidelines [4,16,17]. Although having a unified assessment method would come with several benefits in terms of ease of assessment and training, and although several studies did find concordance using this method, this is not how the assays were designed and remains unvalidated. As mentioned by Schwamborn et al., the assays are designed to stain for different things; they use different epitopes that are present in different PD-L1 isoforms so a direct comparison is not valid [16]. This is highlighted by the work by Zajac et al., who assessed urothelial carcinoma samples using four available PD-L1 assays. They found that although there was good correlation between SP263, 22C3 and 28-8 assays for both TC and IC PD-L1 staining, when the assays were used with their specific clinical scoring systems, there were substantial differences in scoring, resulting in the conclusion that the appropriately clinically validated algorithm must be used for each drug [4].

A study by Hodgson et al. tested urothelial carcinomas with three commercial kits (SP263, SP142 and 22C3) and assessed each according to the manufacturers algorithm and recommended cut-off value. This study found that the percentages of UC deemed positive in each cancer were 21% using the SP263 clone, 18% using the SP142 clone and 20% using the 22C3 clone. This was deemed a high rate of concordance, however, this was a smaller study of 197 cases of urothelial cancer and it was performed on tissue microarrays, rather than clinical samples [14]. In contrast, as discussed, when Zajac et al. compared the SP263 assay specifically against each of the other three assays (SP142, 22C3 and 28-8), each according to their assay-specific clinically relevant algorithm, their criteria for concordance was not met for any of the assays [4].

In this study we report on the rate of PD-L1 positivity of urothelial carcinomas with the 22C3 and SP142 assay and the clinical correlation between assays. Our aim was to assess whether each assay, if reported according to the relevant manufacturer guidance for urothelial carcinomas, provided reliable information for the alternate drug. For example, in practice, would a 22C3 assay assessment with CPS >10 be reliable to determine if patients would be eligible for Atezolizumab therapy, and would the SP142

assessment with >5% IC be reliable to determine if patients would be eligible for Pembrolizumab therapy?

This data is relevant across cancers with multiple approved ICB drugs because the current inflexibility of the testing strategies is challenging for laboratories. The example provided in this series builds on previous studies comparing concordance between ICB assays in urothelial cancer, when used according to guidelines. Additionally, it sheds light on the tests clinical cross-utility, which may help testing laboratories adjust their strategies to meet oncology requirements more efficiently, while still following the clinically validated manufacturer guidelines.

MATERIALS AND METHODS

Our department has been offering PD-L1 testing across various tumour type since 2016, with over 40,000 PD-L1 tests done between 2016 and March 2021. All four compound diagnostics have been validated according to tumour type on the appropriate platforms. Between July 2018 and March 2020, we tested 1,490 advanced urothelial carcinomas for PD-L1 expression.

PD-L1 expression was assessed on formalin-fixed paraffin-embedded (FFPE) tumour samples. Cytology samples, including FFPE clots, were excluded from testing since the preserved architecture of the tissue is required to identify intra-tumoral inflammatory cells to be included in both CPS and IC assessments. In addition, non-invasive carcinomas were not assessed with SP142 assay due to the absence of intra-tumoral inflammatory cells.

Samples were prepared using 4 µm thick sections on Dako slides for the 22C3 assay or on Tomo slides for the Ventana SP142 assay. PD-L1 testing was undertaken using the PD-L1 22C3 PharmDx assay (Agilent Technologies, Santa Clara, CA) on an Autostainer Link 48 and/or the SP142 test (Ventana Medical Systems) on a Benchmark Ultra system. Both assays were validated according the department's policy for compliance with ISO:15198(2012) standards.

The interpretation of assays was performed by Consultant Histopathologists and one scientist. Reporting members of staff had participated in formal training provided by either Roche Ventana/Dako Agilent, subcontracted specialist training providers or been part of a formal in-house training scheme led by a provider-trained Consultant. The department regularly participates in EQA schemes which assess both the technical staining quality and interpretation of both PD-L1 stains.

22C3 pharmDX assay stained sections were assessed to determine a CPS, with a positive value being CPS >10 as per Pembrolizumab licensing; the maximum CPS was 100. SP142 assay stained sections were assessed to determine an IC score, with a cut-off of 5% of tumour surface positivity as per Atezolizumab licensing.

RESULTS

There were 1,490 urothelial carcinoma cases submitted to our department for PD-L1 testing between June 2018 and March 2020. Test failure occurred in 89 cases (6%), most of which were due to insufficient material in the sample submitted. Other reasons for failure included submission of cytology samples that are not suitable for PD-L1 assessment (as described previously), samples that lacked an invasive component, or uninterpretable cases due to marked diathermy artifact or necrosis (mostly TURB chippings).

Of the 1,401 samples that had a successful PD-L1 assessment, 621 cases (44%) were tested with both the 22C3 PharmDx and SP142 assays, 492 cases (35%) with 22C3 PharmDx only, and 288 cases (21%) with SP142 only. Therefore, a total of 2022 PD-L1 assays were untaken across these 1,401 samples (1,113 cases were tested with the 22C3 PharmDx assay and 909 cases with the SP142 assay).

Of the cases tested with the 22C3 PharmDx assay, 289/1,113 (26%) cases showed CPS >10 and so were eligible for Pembrolizumab therapy. This figure is a slightly lower rate than shown in the Keynote trials of 30.3% or 33%, and lower than the 35.1% seen by Eckstein et al [9,10,14]. In the cases tested with the SP142 assay, 284/909 (31%) showed IC >5% with the SP142 assay and were eligible for Atezolizumab therapy; this is similar to the range of positivity found in phase 2 trials, and is higher than the 16.3% recorded by Eckstein et al [11,12,14].

The immunoexpression revealed concordant results (both tests being either positive or negative) in 553/621 cases (89%) and discordant results in 68 cases (11%). Of the concordant results, 403/621 were negative on both assays and 150/553 were positive on both assays (**Figure 1A**). Of the discordant cases, 49 cases (8%) showed positivity with the SP142 assay (Atezolizumab eligibility) exclusively, and 19 cases (3%) showed positivity with the 22C3 PharmDx assay (Pembrolizumab eligibility) exclusively.

DISCUSSION

Worldwide, PD-L1 testing workflows for urothelial carcinomas in routine practice are complex; they potentially require two platforms, multiple assays and appropriately trained pathologists and scientists. Our data provides some insight on how to rationalise PD-L1 testing before ICB therapy in order to improve efficiency.

We have obtained data on the clinical discrepancy between both PD-L1 assays, rather than merely comparing the pattern of PD-L1 expression between the assays. This point is vital because the assays have been designed in specific conditions and have different staining characteristics. Indeed, in practice, we see significant differences in the intensity and the proportion of both tumour and inflammatory cell staining depending on which assay has been used. Therefore, it would not be appropriate to apply a cut-off of CPS >10 on sections stained with SP142 assay or a cut-off of >5% IC on sections stained with the 22C3 PharmDx assay. Instead, it is essential to adhere to the guidance provided by the companion diagnostics to ensure accurate results and to maintain the comparability of results among different laboratories.

Our data shows that PD-L1 testing is feasible in routine practice with a low rate of failure. Our positivity rate for each

FIGURE 1 | (A) Number of positive results across both assays. **(B)** Number of negative results across both assays.
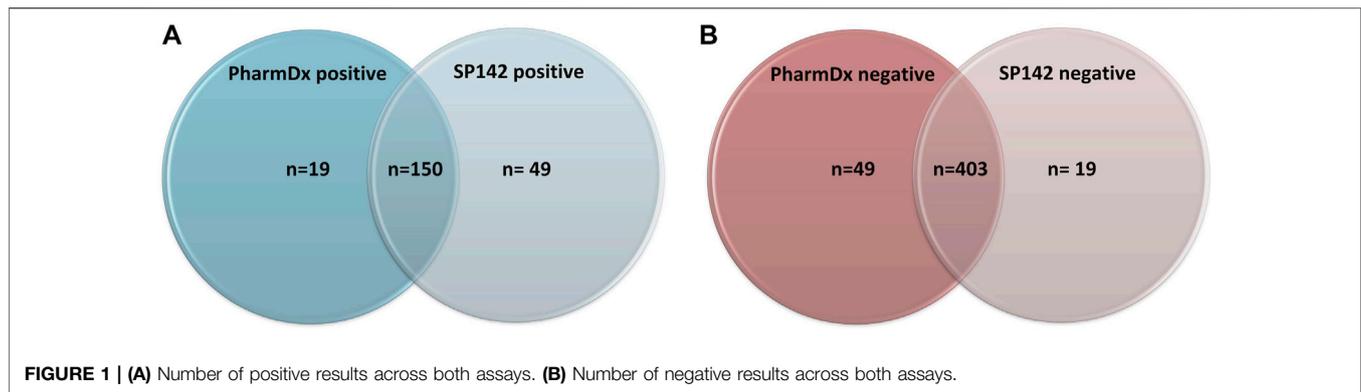
assay is very similar to that in Keynote trials for 22C3PharmDx and pre-licensing studies for SP142 assay. Furthermore, the positivity seen with the SP142 assay in our study was significantly higher than seen by Eckstein et al and so does not support their conclusion that using the SP142 assay would detect fewer patients eligible for PD-L1 therapy [14]. Additionally, PD-L1 testing with both assays on 621 tumours found that the clinical discrepancy was 11%. Unfortunately, no statistical analysis could be performed because of the low number of discrepant cases; however, a discrepancy of 11% is too high to be ignored and limits the clinical cross-utility between tests.

Interestingly, when two ICB drugs were licensed for use in urothelial cancer, dual 22C3 SP142 PD-L1 expression testing was only requested in 44% of cases. This value is lower than would be expected and may be because as PD-L1 testing was the first molecular test to be mandatory before targeted therapy for urothelial carcinomas, so the teams of clinicians and pathologists may not have been familiar with the pathway, workflow and logistics for requesting and collecting results of molecular tests. This is important to address to avoid introducing bias into the test selection.

Moving forward, since we have demonstrated limited cross-utility between assays, laboratories must find other approaches in scenarios where multiple ICB drugs are available. One approach laboratories could employ to avoid testing all tumours with multiple assays is to implement sequential testing. This approach would require a case-by-case assessment, with the first assay used guided by the oncologists' preferences between the available drugs. This could represent an acceptable and sensible option despite requiring complex logistics.

To facilitate logistics in our lab, when multiple ICB drugs were approved for urothelial cancer we used a detailed request form, which described both PD-L1 testing assays and which drug corresponds to each assay. This clarity is essential as the choice of drug and, by extension, the selection of the PD-L1 assay is driven by oncologists, not the testing laboratory (as this choice is based on clinical criteria including modalities of prescription and expected potential side effects).

In conclusion, it is paramount to utilise PD-L1 assays according to the manufacturer guidelines to allow result accuracy and standardisation. Furthermore, due to limited cross utility the appropriate assay must be used for each different ICB drug. The factors contributing to the discrepancy between assays remain undefined and further research into this is warranted, particularly to meet the continued drive to improve the testing strategies for ICB drugs. Finally, further research into whether discordant assay results lead to any clinical differences in patient response to different ICB would be valuable to the field. Together, this would increase our understanding of how best to test and treat patients with different ICB drugs, ensuring maximum patient benefit is achieved.

DATA AVAILABILITY STATEMENT

The raw data supporting the conclusion of this article will be made available by the authors, without undue reservation.

ETHICS STATEMENT

Due to the retrospective nature of this study, ethical review and approval was not required in accordance with the local legislation and institutional requirements.

AUTHOR CONTRIBUTIONS

HE and PT: writing and editing. SD-C and BO'S: Analysis of tumours with both 22c3 and sp142 scoring, editing. FH, KC, and LR: technical assistance: set up and validation of both 22c3 and SP142 PD-L1 tests.

CONFLICT OF INTEREST

The authors declare that the research was conducted in the absence of any commercial or financial relationships that could be construed as a potential conflict of interest.

REFERENCES

1. Cheung CC, Barnes P, Bigras G, Boerner S, Butany J, Calabrese F, et al. Fit-for-purpose PD-L1 Biomarker Testing for Patient Selection in Immuno-Oncology: Guidelines for Clinical Laboratories from the Canadian Association of Pathologists-Association Canadienne Des Pathologistes (CAP-ACP). *Appl Immunohistochem Mol Morphol* (2019) 27(10):699–714. doi:10.1097/pai.0000000000000800

2. Eckstein M, Cimadamore A, Hartmann A, Lopez-Beltran A, Cheng L, Scarpelli M, et al. PD-L1 Assessment in Urothelial Carcinoma: a Practical Approach. *Ann Transl Med* (2019) 7:690–22. doi:10.21037/atm.2019.10.24

3. Powles T, Walker J, Andrew Williams J, Bellmunt J. The Evolving Role of PD-L1 Testing in Patients with Metastatic Urothelial Carcinoma. *Cancer Treat Rev* (2020) 82:101925. doi:10.1016/j.ctrv.2019.101925

4. Zajac M, Scott M, Ratcliffe M, Scorer P, Barker C, Al-Masri H, et al. Concordance Among Four Commercially Available, Validated Programmed Cell Death Ligand-1 Assays in Urothelial Carcinoma. *Diagn Pathol* (2019) 14(1):99–10. doi:10.1186/s13000-019-0873-6

5. National Institute for Health and Care Excellence. Atezolizumab for Untreated PD-L1-Positive Advanced Urothelial Cancer when Cisplatin Is Unsuitable. last update (2021). Available at https://www.nice.org.uk/guidance/ta739/chapter/1-Recommendations Oct 27 (Accessed February 28, 2022)

6. National Institute for Health and Care Excellence. Atezolizumab for Treating Locally Advanced or Metastatic Urothelial Carcinoma after Platinum-Containing Chemotherapy. last update (2018). Available at https://www.nice.org.uk/guidance/ta525/chapter/1-Recommendations June 13 (Accessed February 28, 2022)

7. European Medicines Agency, -last Update, Tecentriq/Atezolizumab. Summary of Product Characteristics. last update (2021). Available at: https://www.ema.europa.eu/en/documents/product-information/tecentriq-epar-product-information_en.pdf Nov 10 (Accessed February 28, 2022)

8. European Medicines Agency. Keytruda/Pembrolizumab. Summary of Product Characteristics. last update (2022). Available at https://www.ema.europa.eu/en/documents/product-information/keytruda-epar-product-information_en.pdf Jan 11 (Accessed February 28, 2022)

9. Balar AV, Castellano D, O'Donnell PH, Grivas P, Vuky J, Powles T, et al. First-line Pembrolizumab in Cisplatin-Ineligible Patients with Locally Advanced and Unresectable or Metastatic Urothelial Cancer (KEYNOTE-052): a Multicentre, Single-Arm, Phase 2 Study. *Lancet Oncol* (2017) 18(11):1483–92. doi:10.1016/s1470-2045(17)30616-2

10. Fradet Y, Bellmunt J, Vaughn DJ, Lee JL, Fong L, Vogelzang NJ, et al. Randomized Phase III KEYNOTE-045 Trial of Pembrolizumab versus Paclitaxel, Docetaxel, or Vinflunine in Recurrent Advanced Urothelial Cancer: Results of >2 Years of Follow-Up. *Ann Oncol* (2019) 30(6):970–6. doi:10.1093/annonc/mdz127

11. Balar AV, Galsky MD, Rosenberg JE, Powles T, Petrylak DP, Bellmunt J, et al. Atezolizumab as First-Line Treatment in Cisplatin-Ineligible Patients with Locally Advanced and Metastatic Urothelial Carcinoma: a Single-Arm, Multicentre, Phase 2 Trial. *The Lancet* (2017) 389(10064):67–76. doi:10.1016/s0140-6736(16)32455-2

12. Rosenberg JE, Hoffman-Censits J, Powles T, Van Der Heijden MS, Balar AV, Necchi A, et al. Atezolizumab in Patients with Locally Advanced and Metastatic Urothelial Carcinoma Who Have Progressed Following Treatment with Platinum-Based Chemotherapy: a Single-Arm, Multicentre, Phase 2 Trial. *The Lancet* (2016) 387(10031):1909–20. doi:10.1016/s0140-6736(16)00561-4

13. Lee KS, Choe G. Programmed Cell Death-Ligand 1 Assessment in Urothelial Carcinoma: Prospect and Limitation. *J Pathol Transl Med* (2021) 55(3):163–70. doi:10.4132/jptm.2021.02.22

14. Eckstein M, Erben P, Kriegmair MC, Worst TS, Weiss C-A, Wirtz RM, et al. Performance of the Food and Drug Administration/EMA-Approved Programmed Cell Death Ligand-1 Assays in Urothelial Carcinoma with Emphasis on Therapy Stratification for First-Line Use of Atezolizumab and Pembrolizumab. *Eur J Cancer* (2019) 106:234–43. doi:10.1016/j.ejca.2018.11.007

15. Hodgson A, Slodkowska E, Jungbluth A, Liu SK, Vesprini D, Enepekides D, et al. PD-L1 Immunohistochemistry Assay Concordance in Urothelial Carcinoma of the Bladder and Hypopharyngeal Squamous Cell Carcinoma. *Am J Surg Pathol* (2018) 42(8):1059–66. doi:10.1097/pas.0000000000001084

16. Schwamborn K, Ammann JU, Knüchel R, Hartmann A, Baretton G, Lasitschka F, et al. Multicentric Analytical Comparability Study of Programmed Death-Ligand 1 Expression on Tumor-Infiltrating Immune Cells and Tumor Cells in Urothelial Bladder Cancer Using Four Clinically Developed Immunohistochemistry Assays. *Virchows Arch* (2019) 475(5):599–608. doi:10.1007/s00428-019-02610-z

17. Tretiakova M, Fulton R, Kocherginsky M, Long T, Ussakli C, Antic T, et al. Concordance Study of PD-L1 Expression in Primary and Metastatic Bladder Carcinomas: Comparison of Four Commonly Used Antibodies and RNA Expression. *Mod Pathol* (2018) 31(4):623–32. doi:10.1038/modpathol.2017.188

HLA Class I Downregulation in Progressing Metastases of Melanoma Patients Treated With Ipilimumab

Andrea Ladányi[1]*[†], Barbara Hegyi[2,3†], Tímea Balatoni[4], Gabriella Liszkay[4], Raphael Rohregger[5], Christoph Waldnig[5], József Dudás[5] and Soldano Ferrone[6]

[1]Department of Surgical and Molecular Pathology, National Institute of Oncology, Budapest, Hungary, [2]Department of Thoracic and Abdominal Tumors and Clinical Pharmacology, National Institute of Oncology, Budapest, Hungary, [3]Doctoral School of Pathological Sciences, Semmelweis University, Budapest, Hungary, [4]Department of Oncodermatology, National Institute of Oncology, Budapest, Hungary, [5]Department of Otorhinolaryngology and Head and Neck Surgery, Medical University of Innsbruck, Innsbruck, Austria, [6]Department of Surgery, Massachusetts General Hospital and Harvard Medical School, Boston, MA, United States

Characterization of the molecular mechanisms underlying antitumor immune responses and immune escape mechanisms has resulted in the development of more effective immunotherapeutic strategies, including immune checkpoint inhibitor (ICI) therapy. ICIs can induce durable responses in patients with advanced cancer in a wide range of cancer types, however, the majority of the patients fail to respond to this therapy or develop resistance in the course of the treatment. Information about the molecular mechanisms underlying primary and acquired resistance is limited. Although HLA class I molecules are crucial in the recognition of tumor antigens by cytotoxic T lymphocytes, only a few studies have investigated the role of their expression level on malignant cells in ICI resistance. To address this topic, utilizing immunohistochemical staining with monoclonal antibodies (mAbs) we analyzed HLA class I expression level in pre-treatment and post-treatment tumor samples from melanoma patients treated with ipilimumab. Twenty-nine metastases removed from six patients were available for the study, including 18 pre-treatment and 11 post-treatment lesions. Compared to metastases excised before ipilimumab therapy, post-treatment lesions displayed a significantly lower HLA class I expression level on melanoma cells; HLA class I downregulation was most marked in progressing metastases from nonresponding patients. We also evaluated the level of infiltration by CD8^{+} T cells and NK cells but did not find consistent changes between pre- and post-treatment samples. Our results indicate the potential role of HLA class I downregulation as a mechanism of ICI resistance.

Keywords: immunotherapy, melanoma, ipilimumab, HLA class I expression, longitudinal study

INTRODUCTION

Immune checkpoint inhibitor (ICI)-based therapy has brought major breakthrough in cancer treatment, becoming the mainstream of treatment for many cancer types. The first such agent was the anti-CTLA-4 (cytotoxic T lymphocyte-associated antigen 4) monoclonal antibody ipilimumab, which was approved for treatment of patients with advanced melanoma in 2011 [1, 2], later followed by antibodies blocking PD-1 (programmed death receptor 1) or its ligand, PD-L1

(programmed death ligand 1). These monoclonal antibodies have induced impressive clinical responses in a small proportion of patients in a broad spectrum of cancer types. However, the majority of patients do not respond or develop resistance to these immunotherapeutic agents. The mechanisms of primary and acquired resistance are poorly understood. Many potential biomarkers have been proposed that could predict the efficacy of ICI therapies. They include, among others, PD-L1 expression by tumors when PD-1- or PD-L1-specific mAbs are used, tumor mutational burden (TMB), neoantigen load, microsatellite instability, tumor infiltration by immune cells and immune-related gene expression in tumors [3, 4]. Moreover, many potential mechanisms underlying acquired resistance to ICI-based therapy have been identified [3–5]. They include neoantigen loss [6], loss of PTEN expression and activation of β-catenin [7], mutations in JAK1/2 leading to defects in the IFN signaling pathway, mutations in beta-2 microglobulin (B2M), the light chain of HLA class I antigens, resulting in defective HLA class I antigen presentation [8–10], or upregulation of other immune checkpoints such as TIM-3, LAG-3 or VISTA [7, 9]. The same mechanisms have also been implicated in primary resistance to ICI-based therapy [3, 4, 8, 10, 11].

The efficacy of ICI-based therapy depends on the recognition of tumor antigens by cognate cytotoxic T lymphocytes in the context of human leukocyte antigen (HLA) class I molecules. The key role played by HLA class I molecules may account for the described associations of some of their characteristics with response to checkpoint blockade-based therapy. They include the association of maximal heterozygosity of HLA-I loci as well as high evolutionary divergence of HLA class I genotype with improved survival following ICI-based therapy [12, 13], and the association of high degree of HLA-I promiscuity with reduced survival and lower response rate in patients receiving ICIs [14], in addition to the mentioned primary or acquired resistance to anti-PD-1 mAb-based therapy in patients with structural mutations or loss of heterozygosity (LOH) of B2M [8–10]. The frequency of defects in HLA class I antigen processing machinery (APM) component expression and/or function caused by structural mutations is low [15, 16] and therefore has limited clinical relevance. In contrast, the frequency of defects in HLA class I APM component expression and/or function caused by epigenetic mechanisms and/or transcription dysregulation is high in most, if not all cancer types analyzed [15–17]. Nevertheless only a few studies have assessed the value of HLA class I expression level as a biomarker to predict the clinical responses to ICI-based therapy and have found an association between these two parameters [18, 19]. Furthermore, low gene or protein expression of the HLA class I APM components has been described in progressing lesions in some patients with melanoma, lung cancer, or Merkel cell carcinoma treated with ICI-based therapy [7, 9, 10, 20]. These results have been mainly obtained in patients treated with anti-PD-1 mAb; to the best of our knowledge, no information is available about melanoma patients treated with ipilimumab. In a recent study we have shown that tumor cell HLA class I expression level in pre-treatment samples of melanoma patients is a biomarker of clinical response to ipilimumab therapy

and of patients' survival [19]. To explore potential changes in HLA-I expression level in ipilimumab-treated patients, in the present investigation we have assessed HLA class I expression level on melanoma cells in pre- and post-treatment metastases removed from patients treated with ipilimumab. Since effective tumor antigen recognition relies on the interaction between CD8^{+} cytotoxic T lymphocytes and HLA class I molecules while HLA-I negative tumors may be sensitive to killing by natural killer (NK) cells, we also examined infiltration of pre- and post-treatment tumor samples by CD8^{+} T cells and NK cells.

MATERIALS AND METHODS

Tumor Samples
We obtained archived paraffin blocks of sequential (pre- and post-treatment) tissue samples of patients with metastatic melanoma treated with ipilimumab between 2010 and 2015. Sample collection was restricted to metastases surgically removed within a 2 years range before or after ipilimumab treatment; 29 metastases of six patients were available for the study. The clinical characteristics of the patients are shown in **Table 1**. TNM classifications and stage grouping criteria were based on the 7th Edition of AJCC Staging System. Five of the six patients received systemic treatment before ipilimumab therapy; all of them had chemotherapy while two also received radiotherapy, and one patient (Pt3) had already received ipilimumab therapy 32 months before the ipilimumab reinduction treatment evaluated in the present study. Responses to therapy were evaluated based on immune-related response criteria (irRC) [21]. One patient (Pt1) was scored as complete response (CR) with a few residual cutaneous papules, which showed minimal progression 11 months following initiation of ipilimumab therapy and were excised. Pt2 achieved stable disease (SD) lasting for 10 months, while Pt 3 showed short-term SD lasting for 4 months; the other three patients exhibited progressive disease (PD). Pt1 and Pt2 were classified as responders while the other four patients as nonresponders in the analysis. Progression-free survival (PFS) and overall survival (OS) were calculated from the commencement of ipilimumab treatment till the last follow-up, tumor progression or death, respectively. Altogether 29 metastases were studied, 18 pre-treatment and 11 post-treatment surgical samples (**Table 1**). Of the post-treatment samples, three were residual metastases from Pt1 while the other eight were progressing lesions.

Monoclonal Antibodies
The mouse monoclonal antibody (mAb) HCA2, recognizing B2M-free HLA-A (excluding -A24), -B7301, and -G heavy chains, the mAb HC10, which recognizes B2M-free HLA-A3, -A10, -A28, -A29, -A30, -A31, -A32, -A33, HLA-B (excluding -B5702, -B5804, and -B73), and HLA-C heavy chains and the B2M-specific NAMB-1 were developed and characterized as described [22, 23]. The mouse anti-human CD8 mAb and the mouse anti-human NKp46 mAb were purchased from Dako

TABLE 1 | Patient and sample characteristics.

	Age (years)	Gender	Stage	ECOG Status	BRAF Status	BOR	PFS (months)	OS (months)	Pre samples analyzed	Post samples analyzed
Pt1	52	Female	III N3c	0	mut	CR	11	67+	2 (cut.)	3 (cut./sc.—residual)
Pt2	51	Female	IV M1c	0	mut	SD	10	43	1 (sc.)	1 (sc.—progression)
Pt3	73	Male	IV M1a	0	wt	SD	4	42	4 (LN, cut./sc.)	2 (LN, sc.—progression)
Pt4	53	Female	IV M1b	0	mut	PD	4	29	3 (LN, sc.)	3 (sc.—progression)
Pt5	59	Male	IV M1c	1	wt	PD	3	9	1 (sc.)	1 (cut.—progression)
Pt6	57	Female	IV M1c	0	mut	PD	3	8	7 (LN, breast)	1 (LN—progression)

ECOG, Eastern Cooperative Oncology Group; mut, mutant; wt, wild type; BOR, best overall response; CR, complete response; SD, stable disease; PD, progressive disease; PFS, progression-free survival; OS, overall survival; Pre, pre-treatment; Post, post-treatment; cut., cutaneous; sc., subcutaneous; LN, lymph node.

(Glostrup, Denmark) and from R&D Systems (Abingdon, United Kingdom), respectively.

Immunohistochemical Staining of Tumor Tissue Sections

Immunohistochemical staining of tissue sections of formalin-fixed, paraffin-embedded tumor samples was performed as described earlier [19, 24]. Briefly, deparaffinated sections were treated with 3% H_2O_2 in methanol to block endogenous peroxidases, then antigen retrieval was performed by heating at 98°C for 40 min in citrate buffer (pH 6.0), followed by incubation with protein blocking solution (Protein Block, Serum-Free, Dako) for 10 min at room temperature, and incubation with the primary antibodies overnight at 4°C. For staining detection the SS™ One-Step Polymer-HRP IHC Detection System (BioGenex, Fremont, CA) and 3-amino-9-ethylcarbazole (AEC; Vector Laboratories, Inc., Burlingame, CA) were used followed by counterstaining with hematoxylin. In the case of labeling with anti-HLA class I mAbs, the percentage of the area displaying stained melanoma cells was determined in the metastases. Intratumoral density of $CD8^+$ and $NKp46^+$ lymphocytes was assessed as described earlier [24]; briefly, the number of labeled cells was counted within the metastases in at least 10 (median: 35, range: 10–120) randomly chosen fields per sample, using a graticule of 10×10 squares designating an area of $0.0625 \, mm^2$ at ×400 magnification. For patients with more than one metastasis available the average values were also calculated for each marker, separately for pre- and post-treatment samples. The statistical significance of the differences between pre- and post-treatment samples was determined using the Mann-Whitney U test.

Computerized Analysis of the Staining Intensity by Anti-HLA Class I Antibodies

The immunohistochemistry slides were acquired in TissueFaxs brightfield (Tissuegnostics, Vienna, Austria) system with a ×40 magnification dry lens coupled onto a Zeiss Axio Imager Z2 Microscope (Jena, Germany) and an eight slide automatic stage (Märzenhäuser, Wetzlar, Germany) using a Pixelink camera (Pixelink, Rochester, NY, United States). Regions of interest

containing metastases without obvious artifacts were selected (**Supplementary Figure S1**) and analyzed using the HistoQuest (TissueGnostics) image cytometry software. "Cells" were identified on the basis of the hematoxylin stained nuclei and the immunohistochemical reaction was identified by ring mask (**Supplementary Figure S2**) [25]. The cell nuclei area was used to distinguish among cell populations (**Supplementary Figure S3**). The staining signal was quantified using a single-reference-shade color deconvolution algorithm [26]. Quantifications were confirmed visually by the backward connection function of the HistoQuest program (**Supplementary Figures S3, S4**).

RESULTS

Utilizing IHC staining with mAbs we analyzed the expression of HLA class I subunits in sequential metastasis samples from six melanoma patients treated with ipilimumab; the samples analyzed included 18 pre- and 11 post-treatment surgically excised metastases (**Table 1**). Comparing pre-treatment and post-treatment samples of all patients evaluated together, the expression of HLA class I subunits, as measured by the % of stained melanoma cells, was significantly lower in post-treatment metastases compared to pre-treatment ones (**Figures 1**, **2**). The medians and ranges of the percentage values of melanoma cells stained by HLA-A heavy chain-specific mAb HCA-2, by HLA-B,C heavy chain-specific mAb HC10 and by anti-B2M mAb NAMB-1 were 94.0 (5.1–100), 91.0 (4.5–100) and 90.5 (62.2–100) in the pre-treatment metastases, and 63.5 (0–83.6), 25.0 (0–84.2) and 57.6 (0–93.1) in the post-treatment metastases, respectively. The percentage of melanoma cells stained by all three mAbs tested was higher than 80 in the majority of the 18 pre-treatment metastases analyzed, compared to only 1 of the 11 post-treatment metastases. In agreement with our previous results [19], metastases with a heterogenous staining pattern displayed higher labeling at the margin of the tumors in the proximity of inflammatory cells, consistent with locally induced expression. Percentages of staining with the three antibodies were fairly consistent in the majority of cases, with discrepancies larger than 30% in only 7 of the 29 metastases. Furthermore, comparing tumor cell staining of different lesions with the same antibody, we detected a moderate level of intrapatient heterogeneity in most patients in the case of pre-treatment
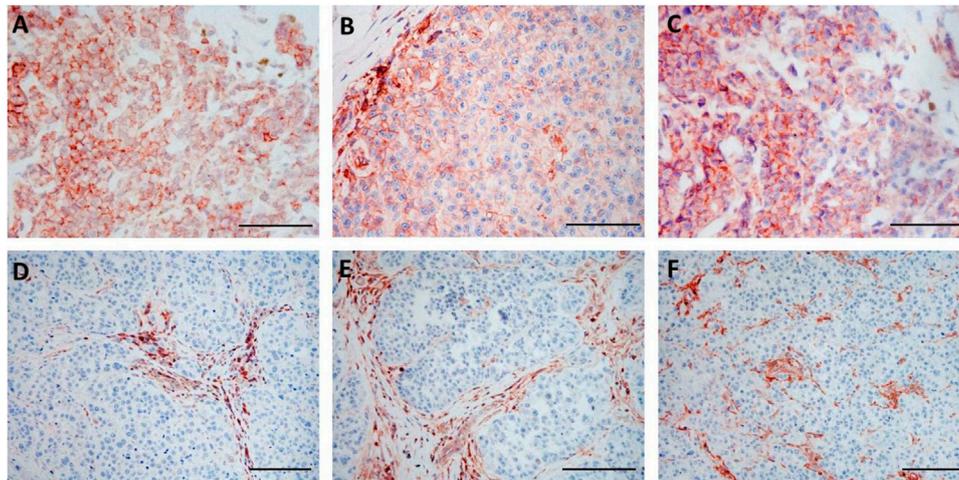
FIGURE 1 | Immunohistochemical staining of pre-treatment **(A–C)** and post-treatment **(D–F)** samples from the same patient (Pt3) with HLA-A heavy chain-specific mAb HCA2 **(A,D)**, HLA-B,C heavy chain-specific mAb HC10 **(B,E)** and B2M-specific mAb NAMB-1 **(C,F)** (3-amino-ethylcarbazole, red). Scale bars: 100 μm.
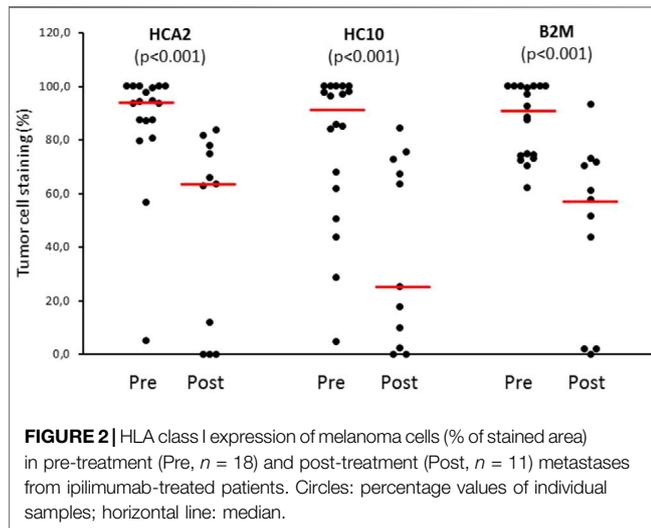
FIGURE 2 | HLA class I expression of melanoma cells (% of stained area) in pre-treatment (Pre, $n = 18$) and post-treatment (Post, $n = 11$) metastases from ipilimumab-treated patients. Circles: percentage values of individual samples; horizontal line: median.

metastases and in two of the three patients with more than one post-treatment lesions (**Supplementary Table S1**).

Comparison of the HLA class I subunit expression levels in pre- and post-treatment metastases removed from each individual patient revealed HLA-I downregulation mainly in the case of progressing lesions of nonresponding patients; in contrast, minimal or no change was found in responding patients (Pt1 and Pt2). Interestingly, in Pt1 exhibiting the best overall response and long-term survival, the baseline HLA class I subunit expression was high in the pre-treatment metastases and remained high in the post-treatment (residual) metastases (**Figures 3A–C**, **Supplementary Table S1**). In contrast, HLA class I subunit downregulation was maximal in the metastases from Pt5 and Pt6 exhibiting the shortest PFS and OS (**Figure 3D**, **Supplementary Table S1**). Results of quantitative evaluation of staining intensity in representative pre- and post-treatment

samples of nonresponding patients with progressing lesions are in agreement with this finding (**Figure 3E**).

Since the efficacy of immune checkpoint inhibitors depends on the recognition of tumor antigen derived peptides by cytotoxic T lymphocytes in the context of HLA class I proteins, we also examined the extent of infiltration of CD8+ T cells in pre-treatment vs. post-treatment tumors. The infiltration showed considerable intertumor variability and did not exhibit any consistent change between pre- and post-treatment time points (**Supplementary Figure S5**). Furthermore, the extent of NK cell infiltration was also tested because these cells are known to recognize HLA class I negative cells so their activity could possibly complement that of CD8+ T lymphocytes. Using NKp46 as a NK cell marker, we detected a very low number of NK cells infiltrating both pre-treatment and post-treatment tumors; furthermore, no significant difference could be found between the two sample sets (**Supplementary Figure S5**).

DISCUSSION

Many currently used antitumor immunotherapeutic modalities rely on T cell recognition of tumor antigens, in which presentation by HLA class I antigens has a crucial role. It is also an important factor in spontaneous (not therapy-induced) immunity against tumors, which is reflected by the reported association of defects of HLA class I APM component expression with immune escape, disease progression and poor prognosis in several tumor types [16, 17, 27]. Moreover, B2M aberrations have been implicated as resistance mechanisms in patients treated with different T-cell based immunotherapies [28–30] or with immune checkpoint inhibitors [8–10]. However, genomic loss of B2M occurs infrequently, and there is little information about the role of other possible causes of decreased B2M and HLA class I expression in unresponsiveness or acquired resistance to ICIs.

FIGURE 3 | (A–C) Average HLA class I expression of melanoma cells (% of stained area) in pre-treatment (Pre) and post-treatment (Post) metastases from ipilimumab-treated patients, labeled by HLA class I subunit-specific mAbs HCA2 **(A)**, HC10 **(B)** and NAMB-1 **(C)**. **(D,E)** Decrease of mean expression (% of stained area) **(D)** and of staining intensity **(E)** in post-treatment metastases as compared to autologous pre-treatment metastases from ipilimumab-treated patients, stained by HLA class I subunit-specific mAbs.

Results of studies on associations of gene alterations or loss of HLA class I APM components with response to ICIs are equivocal. While mutations or LOH of B2M were described in some patients exhibiting primary or acquired resistance to PD-1 inhibitors [8–10], other recent studies did not find an association between LOH in B2M or HLA class I loci and response to anti-PD-1/PD-L1 agents [31, 32]. Moreover, pre-treatment HLA class I gene expression or mutational status did not differ in responders vs. nonresponders to ipilimumab [33]. On the other hand, an APM score composed of eight APM-associated genes (including B2M) predicted response to anti-PD-1/PD-L1 agents [34]. Furthermore, HLA genes were found to be upregulated in on-therapy samples of responders, but downregulated in nonresponders in melanoma patients treated with anti-PD-1 therapy [35].

Few studies have examined protein expression of HLA class I molecules in patients receiving ICI therapy. A study on metastatic melanoma patients treated with ICI therapies [10] found decreased B2M and/or HLA class I expression in some patients harboring B2M gene alterations and showing primary or acquired ICI resistance. Another report on metastatic melanoma [7] described downregulation of HLA-A expression in biopsies of progressing lesions compared to pre-treatment ones in 4 of 18 melanoma patients receiving ICI therapy [7]. However, no significant alterations in gene or protein expression of HLA class I were found in progressing tumors in six patients with different types of carcinomas [36]. A recent study [37] demonstrated low HLA class I expression in 40% of pre-treatment and 31% of progression melanoma tumors, and no association with response to PD-1 inhibition. Similarly, no association between HLA class I expression and response to anti-PD-1 therapy was found in

melanoma patients in another study, although it proved predictive of response to anti-CTLA-4 treatment [18]. The results of our previous study corroborated the role of HLA class I expression in influencing the efficacy of ipilimumab [19].

In the present work, we analyzed HLA class I tumor cell expression as well as CD8^{+} T cell and NK cell infiltration in longitudinal tumor samples from a subset of patients with available pre-treatment and post-treatment surgically removed metastases. Analyses of longitudinal tumor samples from different stages of treatment are necessary for better understanding of the mechanisms of response or resistance to this type of therapy [3]. Most such studies performed so far have focused mainly on characterization of early on-treatment tumor biopsies, yielding important information regarding the biological effects of ICI therapies as well as predictive biomarkers [35, 38–42] while few studies aimed at investigating tumors progressing after or on ICI therapy, especially in case of CTLA-4 inhibitors [43]. To the best of our knowledge, ours is the first study interrogating HLA class I expression longitudinally in tumor samples of patients treated with ipilimumab. We found decreased tumor cell expression in the majority of progressing metastases of all nonresponding patients; this decrease was most marked in the case of patients with the worst prognosis, although a statistical analysis of the correlation with survival could not be performed because of the limited number of patients tested. Nevertheless, these results support the hypothesis of immunoediting in patients receiving ipilimumab treatment, resulting in HLA class I loss and in tumor progression. This process has been described in the case of acquired resistance to immunotherapy, but a low level of antitumor immune activity may be present even in clinically nonresponding patients, which could

shape the immunogenicity of the progressing tumors. Unfortunately, we had only one responding patient with residual (minimally progressing) metastases: therefore solid conclusions could not be drawn from our study. Nonetheless, it is worth mentioning that HLA class I expression in both pre-treatment and post-treatment tumors was consistently high in this patient, implicating lack of immunoediting, at least regarding HLA class I expression.

We also examined potential changes in infiltration level of two types of immune effector cells, CD8^{+} T lymphocytes and NK cells, both of which were found associated with clinical response to ipilimumab in our previous study on pre-treatment metastatic samples [24]. The density of CD8^{+} T cells showed considerable variability among metastases, even in the same patient, and no consistent difference could be observed between pre-treatment and post-treatment samples. Similarly, no significant pre-treatment/post-treatment change could be found in the case of NK cells; the latter were not detectable or present in only a low number in most of the metastases examined, in agreement with the information in the literature [24, 44, 45]. Investigations on longitudinal samples from melanoma patients receiving anti-PD-1 mAbs found elevated infiltration level of CD8^{+} T cells in on-treatment samples of responding patients [35, 40, 41, 46], while few and uncertain data are available on progressing cases [41]. In a recent study higher density of NK cells was observed in pre-treatment and early during treatment tumor samples of responders compared to nonresponders [45]. Few reports have been published on longitudinal studies in melanoma patients treated with ipilimumab. A study on advanced melanoma patients demonstrated increase in tumor-infiltrating lymphocytes in early on-treatment biopsies of patients benefiting from the therapy, but no significant change in the number of CD8^{+} T cells [38].

We recognize the inherent limitations of our study caused by its retrospective nature and also by the limited number of cases with available pre-treatment and post-treatment surgical samples. However, there are few reports of longitudinal studies on local immunological features of patients receiving immune checkpoint inhibitor therapy, especially in the case of ipilimumab, and most of them encompass a relatively small sample size. The findings of our pilot study will require validation in future prospective studies involving larger patient cohorts enabling more complex statistical analysis. A strength of our analysis, on the other hand, is that it was performed on whole sections from surgical samples; therefore the results we have presented are expected to be more reliable than those generated by the analysis of biopsies, given the known heterogeneous distribution within tumors of both HLA antigens and immune cells [47, 48].

In conclusion, we found a decreased HLA class I expression level by malignant cells in post-treatment progressing metastases of melanoma patients receiving ipilimumab therapy compared to pre-treatment metastatic samples. This finding was a consistent feature in our cohort of patients with progressing tumors, but was not observed in the residual metastases of a responding patient. Further work is warranted to validate these findings in larger patient cohorts, as well as to explore whether HLA class I loss represents a common mechanism of primary and acquired resistance to immune checkpoint inhibitors as well as other T-cell based immunotherapeutic modalities in melanoma and other cancer types. Accumulating evidence on immunologic changes observed in longitudinal studies of patients receiving immunotherapy will contribute to an improved understanding of the molecular mechanisms underlying resistance to such therapies and may help to find appropriate strategies to overcome them [3–5].

ETHICS STATEMENT

The study followed the Declaration of Helsinki and was approved by the Scientific and Ethical Committee of Medical Research Council, Hungary (2506-3/2017/EKU, 12120-1/2019/EKU). Informed consents from patients were not required by the board in case of retrospective studies where it is not possible to obtain consents from the majority of patients as in this case where most patients were deceased at the time of the study.

AUTHOR CONTRIBUTIONS

Study conception and design: AL. Sample acquisition and patient data management: TB and GL. Immunohistochemistry evaluation: AL, BH, and TB. Computerized image analysis: RR, CW, and JD. Supervision: SF. Manuscript writing and reviewing: AL, JD, and SF.

FUNDING

CONFLICT OF INTEREST

AL is an assistant chief editor for Pathology and Oncology Research.

The remaining authors declare that the research was conducted in the absence of any commercial or financial relationships that could be construed as a potential conflict of interest.

ACKNOWLEDGMENTS

SUPPLEMENTARY MATERIAL

The Supplementary Material for this article can be found online at: https://www.por-journal.com/articles/10.3389/pore.2022.1610297/full#supplementary-material

REFERENCES

1. Hodi FS, O'Day SJ, McDermott DF, Weber RW, Sosman JA, Haanen JB, et al. Improved Survival with Ipilimumab in Patients with Metastatic Melanoma. *N Engl J Med* (2010) 363:711–23. doi:10.1056/NEJMoa1003466

2. Robert C, Thomas L, Bondarenko I, O'Day S, Weber J, Garbe C, et al. Ipilimumab Plus Dacarbazine for Previously Untreated Metastatic Melanoma. *N Engl J Med* (2011) 364:2517–26. doi:10.1056/NEJMoa11046210.1056/nejmoa1104621

3. Sharma P, Hu-Lieskovan S, Wargo JA, Ribas A. Primary, Adaptive, and Acquired Resistance to Cancer Immunotherapy. *Cell* (2017) 168:707–23. doi:10.1016/j.cell.2017.01.017

4. Gide TN, Wilmott JS, Scolyer RA, Long GV. Primary and Acquired Resistance to Immune Checkpoint Inhibitors in Metastatic Melanoma. *Clin Cancer Res* (2018) 24:1260–70. doi:10.1158/1078-0432.CCR-17-2267

5. Zhou B, Gao Y, Zhang P, Chu Q. Acquired Resistance to Immune Checkpoint Blockades: the Underlying Mechanisms and Potential Strategies. *Front Immunol* (2021) 12:693609. doi:10.3389/fimmu.2021.693609

6. Anagnostou V, Smith KN, Forde PM, Niknafs N, Bhattacharya R, White J, et al. Evolution of Neoantigen Landscape during Immune Checkpoint Blockade in Non-small Cell Lung Cancer. *Cancer Discov* (2017) 7:264–76. doi:10.1158/2159-8290.CD-16-0828

7. Kakavand H, Jackett LA, Menzies AM, Gide TN, Carlino MS, Saw RPM, et al. Negative Immune Checkpoint Regulation by VISTA: a Mechanism of Acquired Resistance to Anti-PD-1 Therapy in Metastatic Melanoma Patients. *Mod Pathol* (2017) 30:1666–76. doi:10.1038/modpathol.2017.8

8. Zaretsky JM, Garcia-Diaz A, Shin DS, Escuin-Ordinas H, Hugo W, Hu-Lieskovan S, et al. Mutations Associated with Acquired Resistance to PD-1 Blockade in Melanoma. *N Engl J Med* (2016) 375:819–29. doi:10.1056/NEJMoa1604958

9. Gettinger S, Choi J, Hastings K, Truini A, Datar I, Sowell R, et al. Impaired HLA Class I Antigen Processing and Presentation as a Mechanism of Acquired Resistance to Immune Checkpoint Inhibitors in Lung Cancer. *Cancer Discov* (2017) 7:1420–35. doi:10.1158/2159-8290.CD-17-0593

10. Sade-Feldman M, Jiao YJ, Chen JH, Rooney MS, Barzily-Rokni M, Eliane J-P, et al. Resistance to Checkpoint Blockade Therapy through Inactivation of Antigen Presentation. *Nat Commun* (2017) 8:1136. doi:10.1038/s41467-017-01062-w

11. Shin DS, Zaretsky JM, Escuin-Ordinas H, Garcia-Diaz A, Hu-Lieskovan S, Kalbasi A, et al. Primary Resistance to PD-1 Blockade Mediated by JAK1/2 Mutations. *Cancer Discov* (2017) 7:188–201. doi:10.1158/2159-8290.CD-16-1223

12. Chowell D, Morris LGT, Grigg CM, Weber JK, Samstein RM, Makarov V, et al. Patient HLA Class I Genotype Influences Cancer Response to Checkpoint Blockade Immunotherapy. *Science* (2018) 359:582–7. doi:10.1126/science.aao4572

13. Chowell D, Krishna C, Pierini F, Makarov V, Rizvi NA, Kuo F, et al. Evolutionary Divergence of HLA Class I Genotype Impacts Efficacy of Cancer Immunotherapy. *Nat Med* (2019) 25:1715–20. doi:10.1038/s41591-019-0639-4

14. Manczinger M, Koncz B, Balogh GM, Papp BT, Asztalos L, Kemény L, et al. Negative Trade-Off between Neoantigen Repertoire Breadth and the Specificity of HLA-I Molecules Shapes Antitumor Immunity. *Nat Cancer* (2021) 2:950–61. doi:10.1038/s43018-021-00226-4

15. Cai L, Michelakos T, Yamada T, Fan S, Wang X, Schwab JH, et al. Defective HLA Class I Antigen Processing Machinery in Cancer. *Cancer Immunol Immunother* (2018) 67:999–1009. doi:10.1007/s00262-018-2131-2

16. Maggs L, Sadagopan A, Moghaddam AS, Ferrone S. HLA Class I Antigen Processing Machinery Defects in Antitumor Immunity and Immunotherapy. *Trends Cancer* (2021) 7:1089–101. doi:10.1016/j.trecan.2021.07.006

17. Campoli M, Ferrone S. HLA Antigen Changes in Malignant Cells: Epigenetic Mechanisms and Biologic Significance. *Oncogene* (2008) 27:5869–85. doi:10.1038/onc.2008.273

18. Rodig SJ, Gusenleitner D, Jackson DG, Gjini E, Giobbie-Hurder A, Jin C, et al. MHC Proteins Confer Differential Sensitivity to CTLA-4 and PD-1 Blockade in Untreated Metastatic Melanoma. *Sci Transl Med* (2018) 10:eaar3342. doi:10.1126/scitranslmed.aar3342

19. Ladányi A, Papp E, Mohos A, Balatoni T, Liszkay G, Oláh J, et al. Role of the Anatomic Site in the Association of HLA Class I Antigen Expression Level in Metastases with Clinical Response to Ipilimumab Therapy in Patients with Melanoma. *J Immunother Cancer* (2020) 8:e000209. doi:10.1136/jitc-2019-000209

20. Ugurel S, Spassova I, Wohlfarth J, Drusio C, Cherouny A, Melior A, et al. MHC Class-I Downregulation in PD-1/PD-L1 Inhibitor Refractory Merkel Cell Carcinoma and its Potential Reversal by Histone Deacetylase Inhibition: a Case Series. *Cancer Immunol Immunother* (2019) 68:983–90. doi:10.1007/s00262-019-02341-9

21. Wolchok JD, Hoos A, O'Day S, Weber JS, Hamid O, Lebbé C, et al. Guidelines for the Evaluation of Immune Therapy Activity in Solid Tumors: Immune-Related Response Criteria. *Clin Cancer Res* (2009) 15:7412–20. doi:10.1158/1078-0432.CCR-09-1624

22. Pellegrino MA, Ng A-K, Russo C, Ferrone S. Heterogeneous Distribution of the Determinants Defined by Monoclonal Antibodies on HLA-A and B Antigens Bearing Molecules. *Transplantation* (1982) 34:18–23. doi:10.1097/00007890-198207000-00004

23. Stam NJ, Vroom TM, Peters PJ, Pastoors EB, Ploegh HL. HLA-A- and HLA-B-specific Monoclonal Antibodies Reactive with Free Heavy Chains in Western Blots, in Formalin-Fixed, Paraffin-Embedded Tissue Sections and in Cryo-Immuno-Electron Microscopy. *Int Immunol* (1990) 2:113–25. doi:10.1093/intimm/2.2.113

24. Balatoni T, Mohos A, Papp E, Sebestyén T, Liszkay G, Oláh J, et al. Tumor-infiltrating Immune Cells as Potential Biomarkers Predicting Response to Treatment and Survival in Patients with Metastatic Melanoma Receiving Ipilimumab Therapy. *Cancer Immunol Immunother* (2018) 67:141–51. doi:10.1007/s00262-017-2072-1

25. Ingruber J, Savic D, Steinbichler TB, Sprung S, Fleischer F, Glueckert R, et al. KLF4, Slug and EMT in Head and Neck Squamous Cell Carcinoma. *Cells* (2021) 10:539. doi:10.3390/cells10030539

26. Steinbichler TB, Dudas J, Ingruber J, Glueckert R, Sprung S, Fleischer F, et al. Slug Is a Surrogate Marker of Epithelial to Mesenchymal Transition (EMT) in Head and Neck Cancer. *J Clin Med* (2020) 9:2061. doi:10.3390/jcm9072061

27. Marincola FM, Jaffee EM, Hicklin DJ, Ferrone S. Escape of Human Solid Tumors from T-Cell Recognition: Molecular Mechanisms and Functional Significance. *Adv Immunol* (2000) 74:181–273. doi:10.1016/s0065-2776(08)60911-6

28. Restifo NP, Marincola FM, Kawakami Y, Taubenberger J, Yannelli JR, Rosenberg SA. Loss of Functional Beta2-Microglobulin in Metastatic Melanomas from Five Patients Receiving Immunotherapy. *JNCI J Natl Cancer Inst* (1996) 88:100–8. doi:10.1093/jnci/88.2.100

29. Benitez R, Godelaine D, Lopez-Nevot MA, Brasseur F, Jimenez P, Marchand M, et al. Mutations of the β2-Microglobulin Gene Result in a Lack of HLA Class I Molecules on Melanoma Cells of Two Patients Immunized with MAGE Peptides. *Tissue Antigens* (1998) 52:520–9. doi:10.1111/j.1399-0039.1998.tb03082.x

30. Tran E, Robbins PF, Lu Y-C, Prickett TD, Gartner JJ, Jia L, et al. T-cell Transfer Therapy Targeting Mutant KRAS in Cancer. *N Engl J Med* (2016) 375:2255–62. doi:10.1056/NEJMoa1609279

31. Liu D, Schilling B, Liu D, Sucker A, Livingstone E, Jerby-Arnon L, et al. Integrative Molecular and Clinical Modeling of Clinical Outcomes to PD1 Blockade in Patients with Metastatic Melanoma. *Nat Med* (2019) 25:1916–27. doi:10.1038/s41591-019-0654-5

32. Shim JH, Kim HS, Cha H, Kim S, Kim TM, Anagnostou V, et al. HLA-corrected Tumor Mutation burden and Homologous Recombination Deficiency for the Prediction of Response to PD-(L)1 Blockade in Advanced Non-small-cell Lung Cancer Patients. *Ann Oncol* (2020) 31:902–11. doi:10.1016/j.annonc.2020.04.004

33. Van Allen EM, Miao D, Schilling B, Shukla SA, Blank C, Zimmer L, et al. Genomic Correlates of Response to CTLA-4 Blockade in Metastatic Melanoma. *Science* (2015) 350:207–11. doi:10.1016/j.annonc.2020.04.004

34. Thompson JC, Davis C, Deshpande C, Hwang WT, Jeffries S, Huang A, et al. Gene Signature of Antigen Processing and Presentation Machinery Predicts Response to Checkpoint Blockade in Non-small Cell Lung Cancer (NSCLC)

and Melanoma. *J Immunother Cancer* (2020) 8:e000974. doi:10.1136/jitc-2020-000974

35. Chen PL, Roh W, Reuben A, Cooper ZA, Spencer CN, Prietov PA, et al. Analysis of Immune Signatures in Longitudinal Tumor Samples Yields Insight into Biomarkers of Response and Mechanisms of Resistance to Immune Checkpoint Blockade. *Cancer Discov* (2016) 6:827–37. doi:10.1158/2159-8290.CD-15-154

36. Yoo SH, Yun J, Keam B, Hong S-P, Ock C-Y, Koh J, et al. Discovery of Acquired Molecular Signature on Immune Checkpoint Inhibitors in Paired Tumor Tissues. *Cancer Immunol Immunother* (2021) 70:1755–69. doi:10.1007/s00262-020-02799-y

37. Lee JH, Shklovskaya E, Lim SY, Carlino MS, Menzies AM, Stewart A, et al. Transcriptional Downregulation of MHC Class I and Melanoma De-Differentiation in Resistance to PD-1 Inhibition. *Nat Commun* (2020) 11:1897. doi:10.1038/s41467-020-15726-7

38. Hamid O, Schmidt H, Nissan A, Ridolfi L, Aamdal S, Hansson J, et al. A Prospective Phase II Trial Exploring the Association between Tumor Microenvironment Biomarkers and Clinical Activity of Ipilimumab in Advanced Melanoma. *J Transl Med* (2011) 9:204. doi:10.1186/1479-5876-9-204

39. Ji R-R, Chasalow SD, Wang L, Hamid O, Schmidt H, Cogswell J, et al. An Immune-Active Tumor Microenvironment Favors Clinical Response to Ipilimumab. *Cancer Immunol Immunother* (2012) 61:1019–31. doi:10.1007/s00262-011-1172-6

40. Tumeh PC, Harview CL, Yearley JH, Shintaku IP, Taylor EJM, Robert L, et al. PD-1 Blockade Induces Responses by Inhibiting Adaptive Immune Resistance. *Nature* (2014) 515:568–71. doi:10.1038/nature13954

41. Vilain RE, Menzies AM, Wilmott JS, Kakavand H, Madore J, Guminski A, et al. Dynamic Changes in PD-L1 Expression and Immune Infiltrates Early during Treatment Predict Response to PD-1 Blockade in Melanoma. *Clin Cancer Res* (2017) 23:5024–33. doi:10.1158/1078-0432.CCR-16-0698

42. Sharma A, Subudhi SK, Blando J, Scutti J, Vence L, Wargo J, et al. Anti-CTLA-4 Immunotherapy Does Not Deplete FOXP3+ Regulatory T Cells (Tregs) in Human Cancers. *Clin Cancer Res* (2019) 25:1233–8. doi:10.1158/1078-0432.CCR-18-0762

43. Huang RR, Jalil J, Economou JS, Chmielowski B, Koya RC, Mok S, et al. CTLA4 Blockade Induces Frequent Tumor Infiltration by Activated Lymphocytes Regardless of Clinical Responses in Humans. *Clin Cancer Res* (2011) 17:4101–9. doi:10.1158/1078-0432.CCR-11-040

44. Erdag G, Schaefer JT, Schaefer ME, Deacon DH, Shea SM, Dengel LT, et al. Immunotype and Immunohistologic Characteristics of Tumor-Infiltrating Immune Cells Are Associated with Clinical Outcome in Metastatic Melanoma. *Cancer Res* (2012) 72:1070–80. doi:10.1158/0008-5472.CAN-11-3218

45. Lee H, Quek C, Silva I, Tasker A, Batten M, Rizos H, et al. Integrated Molecular and Immunophenotypic Analysis of NK Cells in Anti-PD-1 Treated Metastatic Melanoma Patients. *Oncoimmunology* (2018) 8:e1537581. doi:10.1080/2162402X.2018.1537581

46. Edwards J, Wilmott JS, Madore J, Gide TN, Quek C, Tasker A, et al. CD103+ Tumor-Resident CD8+ T Cells Are Associated with Improved Survival in Immunotherapy-Naive Melanoma Patients and Expand Significantly during Anti-PD-1 Treatment. *Clin Cancer Res* (2018) 24:3036–45. doi:10.1158/1078-0432.CCR-17-2257

47. Ladányi A, Tímár J. Immunologic and Immunogenomic Aspects of Tumor Progression. *Semin Cancer Biol* (2020) 60:249–61. doi:10.1016/j.semcancer.2019.08.011

48. Wu Y, Biswas D, Swanton C. Impact of Cancer Evolution on Immune Surveillance and Checkpoint Inhibitor Response. *Semin Cancer Biol* (2021). doi:10.1016/j.semcancer.2021.02.013

Pretreatment Systemic Immune-Inflammation Index Can Predict Response to Neoadjuvant Chemotherapy in Cervical Cancer at Stages IB2-IIB

Pingping Liu[†], Yinan Jiang, Xiaojing Zheng, Baoyue Pan, Huiling Xiang and Min Zheng *

Department of Gynecology, State Key Laboratory of Oncology in South China, Collaborative Innovation Center for Cancer Medicine, Sun Yat-Sen University Cancer Center, Guangzhou, China

Background: The systemic immune-inflammation index (SII) has been identified as a predictor of chemotherapy efficacy for a variety of cancers, and we aimed to determine its ability to predict the response to chemotherapy and its long-term prognosis for patients with cervical squamous cell carcinoma (CSCC) who have underwent platinum-based neoadjuvant chemotherapy (NACT).

Methods: The date from 210 patients (133 in the training cohort and 77 in the validation cohort) with CSCC who received NACT were analyzed retrospectively. The association between SII and the pathological complete response (pCR) was determined using Pearson's chi-square test, receiver operating characteristic (ROC) curve, and Logistic regression analysis. The Kaplan-Meier method and Cox proportional regression model were used to assess the relationship between SII and progression-free survival (PFS) or overall survival (OS).

Results: The calculated optimal SII cutoff values for pCR and survival were 568.7051 and 600.5683, respectively, and patients were divided into two groups: a low SII group (≤568.7051 or ≤600.5683) and a high SII group (>568.7051 or >600.5683). A high SII was associated significantly with a lower pCR. Further analysis determined that SII was a more efficient predictor of pCR than the prognostic nutritional index, platelet-to-lymphocyte ratio, and lymphocyte-to-monocyte ratio. Upon multivariate logistic analysis, SII proved to be an independent risk factor to predict the pCR of patients with CSCC. Kaplan-Meier analysis demonstrated that PFS and OS rates were significantly higher in the low-SII group

Abbreviations: AUC, area under curve; CI, confidence interval; CSCC, cervical squamous cell carcinoma; CTC, circulating tumor cells; ECOG, Eastern Cooperative Oncology Group; HR, hazard ratio; IL-6, interleukin 6; LMR, lymphocyte-to-monocyte ratio; MDSCs, myeloid-derived suppressor cells; MMP9, matrix metalloproteinase-9; NACRT, Neoadjuvant Chemoradiotherapy; NACT, neoadjuvant chemotherapy; NLR, neutrophil-to-lymphocyte ratio; Nnets, neutrophil extracellular traps; OR, odds ratio; OS, overall survival; pCR, pathological complete response; PDAC, pancreatic ductal adenocarcinoma; PDGF, platelet-derived growth factor; PFS, progression-free survival; PLR, platelet-to-lymphocyte ratio; PNI, prognostic nutritional index; ROC, receiver operating characteristic; SII, systemic immune-inflammation index; TGF-β, transforming growth factor-β; TILs, tumor-infiltrating lymphocytes; TNF-β, tumor necrosis factor-β; VEGF, vascular endothelial growth factor.

compared with those in the high-SII group. Additional multivariate analysis indicated that the SII is an independent prognostic factor for patients with CSCC treated with NACT.

Conclusion: The results confirmed that the pre-treatment SII is not only an independent predictor of pCR but also an independent prognostic factor of CSCC patients treated with platinum based NACT.

Keywords: cervical cancer, prognosis, neoadjuvant chemotherapy, pathological complete response, systemic immune-inflammation index

INTRODUCTION

Cervical cancer is the most common malignancy of the female reproductive system and has the highest morbidity and mortality rate among all gynecological tumors in China [1, 2]. In recent years, the occurrence of cervical cancer has increased, while the median age of patients has decreased, highlighting cervical cancer as a serious threat to women's health. Early diagnosis and appropriate treatment are the best ways to optimize patient outcome. For patients with early stage (IB-IIB) cervical cancer, radical surgery is commonly the first choice. However, in cases, namely those with patients with large tumors, where radical surgery cannot achieve satisfactory results, neoadjuvant chemotherapy (NACT) might serve as an alternate and more effective treatment method.

NACT is commonly defined as chemotherapy that is administered to a patient before their operation or radiotherapy with the aim of shrinking the tumor, thus improving its resection rate, reducing the scope of the operation and the injury caused by surgery, and suppressing or eliminating possible micrometastatic foci. NACT can improve patient prognosis, so it is especially preferable for young patients who wish to maintain their fertility. Furthermore, the use of NACT can help to understand a patient's sensitivity to chemotherapy and provide guidance for postoperative treatment [3]. However, if NACT treatment fails, patients might lose their optimal surgical opportunity. Therefore, it is imperative to find effective and feasible indicators to predict the efficacy of chemotherapy and to ultimately guide the individualized treatment of patients.

Recent research has demonstrated that a patient's pre-treatment inflammatory and immunological status plays a crucial role in the development of solid malignant tumors [4–6], the relevant indicators of which include the platelet-to-lymphocyte ratio (PLR), the lymphocyte-to-monocyte ratio (LMR), the prognostic nutritional index (PNI), and the systemic immune-inflammation index (SII). Among them, the SII, an integrated indicator based on peripheral lymphocyte, neutrophil, and platelet counts, has been considered to best reflect the balance of host inflammatory and immune status. The SII can also be used to predict the treatment response and survival for a variety of malignant cancers, including breast cancer, rectal cancer, gastric cancer, and pancreatic adenocarcinoma [7–11]. However, the potential utility of the SII on predicted response to NACT for patients with cervical cancer has not been determined.

In this study, the SII in patients with cervical cancer who underwent NACT was evaluated as an indicator for treatment response, and the association between the SII and patient survival was also explored. We found that the SII was a promising, independent, predictive factor for the pathological complete response (pCR) of cervical cancer treated with NACT and might be an independent factor for survival.

MATERIALS AND METHODS

Patient Selection

A total of 210 patients with cervical squamous cell carcinoma (CSCC) who received NACT in our hospital from November 2005 to November 2014 and met the following criteria were included in this study: 1) the patient had been histologically confirmed with CSCC; 2) their Eastern Cooperative Oncology Group (ECOG) performance status was ≤2; 3) their FIGO stage (2009) was IB2-IIB; 4) the patient received preoperative NACT and did not receive antitumor therapy before chemotherapy; 5) blood biochemical examination data was available 7 days before NACT; 6) clinicopathological data was complete; 7) the patient had no history of malignant disease; 8) no factors were present that could affect the results of blood tests, including acute or chronic infection, blood disease, or special drugs taken before treatment.

Our analysis involved two independent patient cohorts: the training cohort, which consisted of 133 patients diagnosed from November 2005 to November 2012, and the validation cohort, which consisted of 77 patients diagnosed from January 2013 to November 2014.

The present study was performed according to the ethical standards of the World Medical Association Declaration of Helsinki and was approved by the Institutional Review Board and Independent Ethics Committee of the Sun Yat-sen University Cancer Center (B2021-417-01).

Data Collection and Analysis

Demographic, laboratory value, tumor stage, tumor size, and postoperative pathological features including tumor differentiation, lymph node metastasis, and pCR, were retrieved retrospectively from patients' electronic medical records. Pretreatment laboratory values within 7 days before neoadjuvant therapy were analyzed. The clinical outcomes evaluated included pCR, overall survival (OS) and progression-free survival (PFS) rates. pCR was defined as the absence of viable

tumor cells in the evaluated pathological specimen. OS was defined as the interval from the date of chemotherapy until death from any cause or the last follow-up, and PFS was defined as the interval from surgery to disease recurrence, death, or the last follow-up.

From the blood sample laboratory values, the absolute platelet (P), neutrophil (N), and lymphocyte (L) counts were used to calculate the SII (SII = P*[N/L]). The PNI was based on albumin and absolute lymphocyte count; briefly, PNI = serum albumin level (g/L) + 5 × total lymphocyte count (10^9/L). PLR was defined as the total platelet count divided by the absolute lymphocyte count. LMR was calculated using the following formula: LMR = total lymphocyte count (109/L)/absolute monocyte count (109/L). Optimal cutoff values for SII, PNI, PLR, LMR, platelet, neutrophil, and lymphocyte were calculated individually using a receiver operating characteristic (ROC) curve.

Surveillance and Statistical Analysis

The follow-up schedule for patients was as follows: Evaluation at 3-month intervals during the first 2 years, 6-month intervals over the next 3 years, and then annually. All patient outcomes were evaluated in March 2021, with the primary endpoint being pCR and secondary endpoints being OS and PFS.

Data were analyzed using IBM SPSS version 22.0 (IBM Corp., Armonk, NY, United States). The ROC analysis was performed to determine the best cutoff values for predicting pCR, and the area under curve (AUC) was used to assess these predictive values (including SII, PNI, PLR, LMR, platelet, neutrophil, and lymphocyte). Logistic regression analysis was performed to determine which independent factors were predictive of pCR. Pearson's chi-square test was used to assess the association between the SII and other clinicopathological factors. For survival analysis (both OS and PFS), the optimal cutoff values for relative indexes were also calculated by ROC curves according to the OS of patients. All survival curves were plotted using the Kaplan-Meier method and compared using the log-rank test. Cox proportional hazards regression analysis was performed to identify independent factors. $p \leq 0.05$ indicated statistical significance, and all p-values were based on two-sided testing.

RESULTS

Patient Characteristics

Data from a total of 210 patients with CSCC, who fit enrollment criteria, were collected for analysis. Among them, 133 patients were placed in the training cohort, while 77 were placed in the validation cohort. The basic characteristics of the patients from these two independent cohorts were listed in **Tables 1**, **2**. All patients underwent platinum-based NACT followed by radical surgery, with a median of two courses of NACT (range, 2–3 courses). In the training cohort, only 18 patients (13.5%) achieved pCR. The median age of the training cohort was 51 years (range, 29–69 years). According to FIGO staging criteria (2009 revision), 64 patients (48.1%) classified as stage IB2, 46 patients (34.6%) as stage IIA2, and 23 patients (17.3%) as stage IIB. The number of cases with high, medium and low differentiation were 4 (3%), 50

(37.6%) and 79 (59.4%), respectively. Additionally, 100 patient cases classified as exogenous tumors (75.2%) and 33 cases as endogenous tumors (24.8%). As for the validation cohort, there were 13 patients (16.9%) achieved pCR. The median age of the training cohort was 48 years (range, 30–64 years). There were 17 patients (22.1%) classified as stage IB2, 50 patients (64.9%) as stage IIA2, and 10 patients (13.0%) as stage IIB. The number of cases with high, medium and low differentiation were 0 (0%), 34 (44.2%) and 43 (55.8%), respectively. Additionally, 72 patient cases classified as exogenous tumors (93.5%) and 5 cases as endogenous tumors (6.5%). Other clinicopathological parameters of these two cohorts are listed in **Tables 1**, **2**.

As determined by the ROC curve, the optimal cutoff value of SII for pCR was 568.7051, with an AUC of 0.638, a sensitivity of 66%, and a specificity of 66.7% (**Supplementary Figure S1**). In the training cohort, the number of cases belonging to the SII≤568.7052 group and SII>568.7051 group were 51 and 82, respectively. As for validation cohort, the cases number of the low SII group and the high SII group were 43 and 34, respectively. The optimal cutoff values for other indexes were as follows: PNI (PNI ≤58.4, PNI >58.4), PLR (PLR ≤129.7001, PNI >129.7001), LMR (LMR ≤6.2917, LMR >6.2917), platelet (platelet ≤226.5, platelet >226.5), neutrophil (neutrophil ≤6.15, neutrophil >6.15), and lymphocyte (lymphocyte ≤2.65, lymphocyte >2.65).

As for survival analysis, we also use the ROC curve to determine the optimal cutoff values for relative indexes. The optimal cutoff value of SII was 600.5683, with an AUC of 0.699, a sensitivity of 88.2%, and a specificity of 47.4% (**Supplementary Figure S2**). The optimal cutoff values for other indexes were as follows: PNI (PNI ≤49.5, PNI >49.5), PLR (PLR ≤153.4314, PNI >153.4314), LMR (LMR ≤12.25, LMR >12.25), platelet (platelet ≤216, platelet >216), neutrophil (neutrophil ≤5.35, neutrophil >5.35), and lymphocyte (lymphocyte ≤0.87, lymphocyte >0.87).

Relationship Between Pre-treatment SII and pCR in CSCC

The associations between the SII and patients' clinicopathological characteristics are presented in **Tables 1**, **2**. In the training cohort, a negative association was found between SII and pCR: a high SII was significantly associated with a lower pCR rate (SII ≤568.7051 vs. SII >568.7051, 23.5% vs. 7.3%, $p = 0.008$; **Figure 1A**; **Table 1**). In the validation cohort, a SII of ≤568.7051 was associated with high pCR rate (SII ≤568.7051 vs. SII >568.7051, 27.9% vs. 2.9%, $p = 0.005$; **Figure 1B**; **Table 2**). Further analysis determined that the SII was a more reliable predictor of pCR than PNI, PLR, LMR, platelet, neutrophil, and lymphocyte. When the relationship between various inflammatory indicators and pCR was plotted using a ROC curve, the SII occupied the largest AUC compared with that of PNI, PLR, LMR, platelet, neutrophil, and lymphocyte ($p = 0.026$; **Figure 2A** and $p = 0.013$; **Figure 2B**).

Univariate and Multivariate Analysis of pCR

For the univariate logistic analysis, we included the patients' age, FIGO stage, histological grade, tumor size, tumor growth pattern, NACT cycles, SII, PNI, PLR, LMR, platelet, neutrophil, and lymphocyte. The results showed that the SII was associated

TABLE 1 | Clinical characteristics of 133 patients with CSCC divided by pre-treatment SII in the traning cohort.

Characteristics	Patients, n (%)	SII ≤568.7051 (n = 51)	SII >568.7051 (n = 82)	P
Age (years)				
≤45	41 (30.8%)	13 (25.5%)	28 (34.1%)	0.293
>45	92 (69.2%)	38 (74.5%)	54 (65.9%)	
FIGO stage				
IB2	64 (48.1%)	21 (41.2%)	43 (52.4%)	0.392
IIA2	46 (34.6%)	21 (41.2%)	25 (30.5%)	
IIB	23 (17.3%)	9 (17.6%)	14 (17.1%)	
Histological grade				
G1	4 (3%)	2 (3.9%)	2 (2.4%)	0.830
G2	50 (37.6%)	18 (35.3%)	32 (39%)	
G3	79 (59.4%)	31 (60.8%)	48 (58.5%)	
Tumor size (cm)				
≤5	98 (73.7%)	41 (80.4%)	57 (69.5%)	0.166
>5	35 (26.3%)	10 (19.6%)	25 (30.5%)	
Tumor growth pattern				
Exogenous	100 (75.2%)	38 (74.5%)	62 (75.6%)	0.886
Endogenous	33 (24.8%)	13 (25.5%)	20 (24.4%)	
Lymph node metastasis				
Negative	110 (82.7%)	46 (90.2%)	64 (78%)	0.072
Positive	23 (17.3%)	5 (9.8%)	18 (22%)	
Response to NACT				
pCR	18 (13.5%)	12 (23.5%)	6 (7.3%)	0.008
Non-pCR	115 (86.5%)	39 (76.5%)	76 (92.7%)	
NACT cycles				
≤2	108 (81.2%)	42 (82.4%)	66 (80.5%)	0.789
>2	25 (18.8%)	9 (17.6%)	16 (19.5%)	
Adjuvant treatment				
Yes	123 (92.5%)	46 (90.2%)	77 (93.9%)	0.506
No	10 (7.5%)	5 (9.8%)	5 (6.1%)	
PNI				
≤58.4	118 (88.7%)	41 (80.4%)		
>58.4	15 (11.3%)	10 (19.6%)		
PLR				
≤129.7001	56 (42.1%)	41 (80.4%)		
>129.7001	77 (57.9%)	10 (19.6%)		
LMR				
≤6.2917	107 (80.5%)	36 (70.6%)		
>6.2917	26 (19.5%)	15 (29.4%)		

CSCC, cervical squamous cell carcinoma; SII, systemic immune-inflammation index; NACT, neoadjuvant chemotherapy; pCR, pathological complete response; PLR, platelet-to-lymphocyte ratio; PNI, prognostic nutritional index; LMR, lymphocyte-to-monocyte ratio.

significantly with pCR (odds ratio (OR): 3.897, 95% confidence interval (CI): 1.359–11.174, p = 0.011, **Table 3** and OR: 12.774, 95% CI: 1.567–104.115, p = 0.017, **Table 4**). We then performed further multivariate logistic analyses of the patients' FIGO stage, histological grade, tumor size, NACT cycles, SII, and platelet. The results demonstrated that the SII was an independent risk factor to predict the pCR rate for patients with CSCC who were treated with NACT (OR: 3.897, 95% CI: 1.359–11.174, p = 0.011, **Table 3** and OR: 30.903, 95% CI: 2.152–443.833, p = 0.012, **Table 4**).

Association Between Pre-Treatment SII and Survival Outcome

The last follow-up for all patients was March 2021, and the median follow-up time for the training cohort and validation cohort was 98 months (range 4–156 months) and 84.6 months (range 13–106 months), respectively. During follow-up for the training cohort, 23 (17.3%) patients experienced tumor

recurrence or metastasis, and 21 (15.8%) patients ultimately died from tumor progression. In the validation cohort, tumor progression and death occurred in 11 (14.3%) and 9 (11.7%) patients, respectively.

Overall, the 5-year PFS and OS rates, in the training cohort, were 84.2% and 87.2%. The patients with a SII ≤600.5683 displayed 5-year PFS and OS rates of 93.0% and 96.5%, respectively, while patients with a SII >600.5683 displayed 5-year PFS and OS rates of 77.6% and 80.3%, respectively. Kaplan-Meier analysis demonstrated that the PFS and OS rates of the low-SII group were significantly higher than those of the high-SII group (p = 0.0202 and p = 0.0008, respectively; **Figures 3A,B**).

In the validation cohort, the patients with a SII ≤600.5683 displayed 5-year PFS and OS rates of 95.7% and 95.7%, respectively, while patients with a SII >600.5683 displayed 5-year PFS and OS rates of 80.6% and 83.9%, respectively. Moreover, patients with a low SII had higher PFS and OS

TABLE 2 | Clinical characteristics of 77 patients with CSCC divided by pre-treatment SII in the validation cohort.

Characteristics	Patients, n (%)	SII ≤568.7051 (n = 43)	SII >568.7051 (n = 34)	p
Age (years)				
≤45	25 (32.5%)	12 (27.9%)	13 (38.2%)	0.336
>45	52 (67.5%)	31 (72.1%)	21 (61.8%)	
FIGO stage				
IB2	17 (22.1%)	12 (27.9%)	5 (14.7%)	0.274
IIA2	50 (64.9%)	27 (62.8%)	23 (67.6%)	
IIB	10 (13%)	4 (9.3%)	6 (17.6%)	
Histological grade				
G1	0 (0%)	0 (0%)	0 (0%)	0.167
G2	34 (44.2%)	16 (37.2%)	18 (52.9%)	
G3	43 (55.8%)	27 (62.8%)	16 (47.1)	
Tumor size (cm)				
≤5	55 (71.4%)	32 (74.4%)	23 (67.6%)	0.514
>5	22 (28.6%)	11 (25.6%)	11 (32.4%)	
Tumor growth pattern				
Exogenous	72 (93.5%)	39 (90.7%)	33 (97.1%)	0.376
Endogenous	5 (6.5%)	4 (9.3%)	1 (2.9%)	
Lymph node metastasis				
Negative	76 (98.7%)	43 (100%)	33 (97.1%)	0.442
Positive	1 (1.3%)	0 (0%)	1 (2.9%)	
Response to NACT				
pCR	13 (16.9%)	12 (27.9%)	1 (2.9%)	0.005
Non-pCR	64 (83.1%)	31 (72.1%)	33 (97.1)	
NACT cycles				
≤2	48 (62.3%)	27 (62.8%)	21 (61.8%)	0.926
>2	29 (37.7%)	16 (37.2%)	13 (38.2%)	
Adjuvant treatment				
Yes	10 (13%)	6 (14%)	4 (11.8%)	0.777
No	67 (87%)	37 (86%)	30 (88.2%)	
PNI				
≤58.4	75 (97.4%)	42 (97.7%)	33 (97.1%)	
>58.4	2 (2.6%)	1 (2.3%)	1 (2.9%)	
PLR				
≤129.7001	26 (33.8%)	21 (48.8%)	5 (14.7%)	
>129.7001	51 (66.2%)	22 (51.2%)	29 (85.3%)	
LMR				
≤6.2917	63 (81.8%)	32 (74.4%)	31 (91.2%)	
>6.2917	14 (18.2%)	11 (25.6%)	3 (8.8%)	

CSCC, cervical squamous cell carcinoma; SII, systemic immune-inflammation index; NACT, neoadjuvant chemotherapy; pCR, pathological complete response; PLR, platelet to lymphocyte ratio; PNI, prognostic nutritional index; LMR, lymphocyte-to-monocyte ratio.

FIGURE 1 | Distribution of pCR and non-pCR in high-SII and low-SII expression groups in the training cohort **(A)** and the validation cohort **(B)**. Abbreviations: SII, systemic immune-inflammation index; pCR, pathological complete response.

FIGURE 2 | ROC curves evaluating the accuracy of different inflammatory markers for pCR prediction in the training cohort **(A)** and the validation cohort **(B)**. Abbreviations: SII, systemic immune-inflammation index; PNI, prognostic nutritional index; PLR, platelet-to-lymphocyte ratio; LMR, lymphocyte-to-monocyte ratio; AUC, area under curve; ROC, receiver operating characteristic; pCR, pathological complete response.

TABLE 3 | Evaluation of the relationship between patient characteristics and pCR using univariate and multivariate analysis in the training cohort.

Variable	Univariate		Multivariate	
	p	OR (95% CI)	*p*	OR (95% CI)
Age (≤45 vs. >45 years)	0.399	0.602 (0.185–1.956)		
FIGO stage (IB2-IIA2 vs. IIB)	0.461	1.787 (0.382–8.3721)	0.367	2.086 (0.422–10.324)
Histological grade (G1-G2 vs. G3)	0.501	0.698 (0.245–1.990)	0.340	0.579 (0.189–1.777)
Tumor size (≤5 vs. >5 cm)	0.672	1.292 (0.395–4.225)	0.947	1.044 (0.290–3.754)
Tumor growth pattern (exogenous vs. endogenous)	0.165	2.952 (0.641–13.588)		
NACT cycles (≤2 vs. >2)	0.377	2.000 (0.429–9.323)	0.384	2.044 (0.408–10.233)
SII (≤568.7051 vs. >568.7051)	0.011	3.897 (1.359–11.174)	0.011	3.897 (1.359–11.174)
PNI (≤58.4 vs. >58.4)	0.422	2.356 (0.291–19.105)		
PLR (≤129.7001 vs. >129.7001)	0.086	2.444 (0.882–6.772)		
LMR (≤6.2917 vs. >6.2917)	0.341	2.110 (0.454–9.815)		
Neutrophil (≤6.15 vs. >6.15)	0.107	3.500 (0.763–16.046)		
Lymphocyte (≤2.65 vs. >2.65)	0.342	2.747 (0.342–22.098)		
Platelet (≤226.5 vs. >226.5)	0.018	3.423 (1.232–9.512)	0.219	2.069 (0.649–6.599)

pCR, pathological complete response; NACT, neoadjuvant chemotherapy; SII, systemic immune-inflammation index; PNI, prognostic nutritional index; PLR, platelet-to-lymphocyte ratio; LMR, lymphocyte-to-monocyte ratio; OR, odds ratio; CI, confidence interval.

relative those with a high SII (Kaplan–Meier analysis, *p* = 0.0183 and *p* = 0.0167, respectively; **Figures 3C,D**).

Prognostic Analysis of Clinical Factors
In the training cohort, univariate analysis revealed that SII (HR 3.049, 95% CI: 1.131–8.219, *p* = 0.028), PLR (HR 3.230, 95% CI:

1.396–7.475, *p* = 0.006), FIGO stage (HR 2.808, 95% CI: 1.189–6.631, *p* = 0.018), tumor growth pattern (HR 2.807, 95% CI: 1.238–6.362, *p* = 0.013), and lymph node metastasis (HR 5.601, 95% CI: 2.464–12.734, P < 0.001) were prognostic factors for PFS (**Table 5**); while a high SII (HR 8.060, 95% CI: 1.876–34.628, *p* = 0.005), high PLR (HR 4.171, 95% CI:

TABLE 4 | Evaluation of the relationship between patient characteristics and pCR using univariate and multivariate analysis in the validation cohort.

Variable	Univariate		Multivariate	
	p	OR (95% CI)	*p*	OR (95% CI)
Age (≤45 vs. > 45 years)	0.886	0.910 (0.251–3.300)		
FIGO stage (IB2-IIA2 vs. IIB)	0.048	0.233 (0.055–0.989)	0.020	0.059 (0.005–0.641)
Histological grade (G1-G2 vs. G3)	0.651	0.754 (0.222–2.557)	0.795	1.211 (0.285–5.143)
Tumor size (≤5 vs. > 5 cm)	0.261	2.500 (0.506–12.341)	0.545	1.704 (0.303–9.574)
Tumor growth pattern (exogenous vs. endogenous)	0.178	0.270 (0.040–1.810)		
NACT cycles (≤2 vs. >2)	0.575	1.442 (0.401–5.189)	0.339	2.137 (0.451–10.122)
SII (≤568.7051 vs. >568.7051)	0.017	12.774 (1.567–104.115)	0.012	30.903 (2.152–443.833)
PNI (≤58.4 vs. >58.4)	0.999	>1 (0- >1)		
PLR (≤129.7001 vs. >129.7001)	0.305	1.886 (0.561–6.335)		
LMR (≤6.2917 vs. >6.2917)	0.206	0.417 (0.107–1.619)		
Neutrophil (≤6.15 vs. >6.15)	0.466	2.222 (0.259–19.052)		
Lymphocyte (≤2.65 vs. >2.65)	0.651	0.675 (0.124–3.693)		
Platelet (≤226.5 vs. >226.5)	0.601	0.649 (0.129–3.278)		

pCR, pathological complete response; NACT, neoadjuvant chemotherapy; SII, systemic immune-inflammation index; PNI, prognostic nutritional index; PLR, platelet-to-lymphocyte ratio; LMR, lymphocyte-to-monocyte ratio; OR, odds ratio; CI, confidence interval.
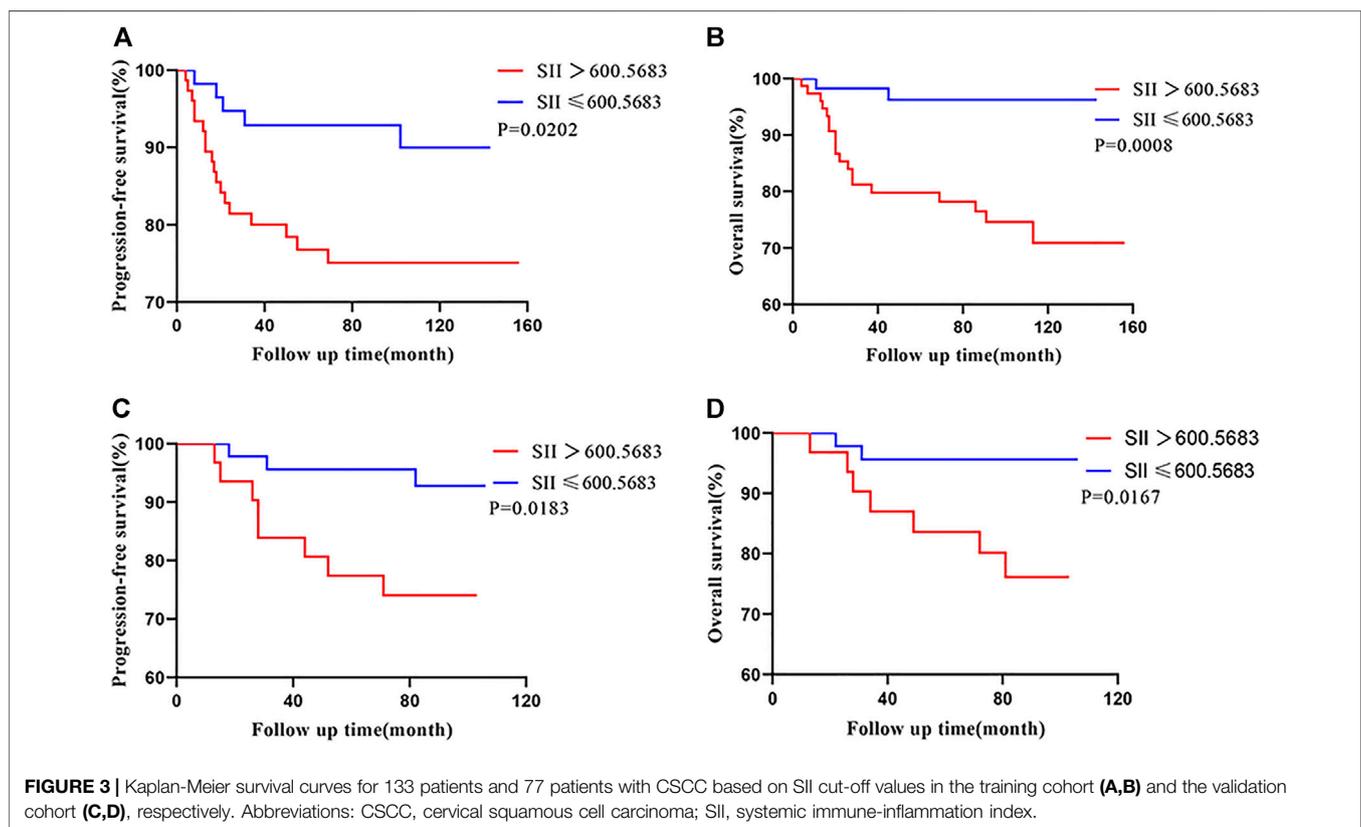
FIGURE 3 | Kaplan-Meier survival curves for 133 patients and 77 patients with CSCC based on SII cut-off values in the training cohort **(A,B)** and the validation cohort **(C,D)**, respectively. Abbreviations: CSCC, cervical squamous cell carcinoma; SII, systemic immune-inflammation index.

1.679–10.365, $p = 0.002$), and positive lymph node metastasis (HR 9.471, 95% CI: 3.922–22.87, $p < 0.001$) were significant negative predictors of OS (**Table 7**). In the validation cohort, univariate analysis revealed that SII (HR 4.331, 95% CI: 1.148–16.334, $p = 0.030$) was significantly associated with patient PFS (**Table 6**), similar findings were observed when OS was used as primary treatment outcome (**Table 8**).

In the training cohort, multivariate analysis further indicated that the SII (HR 2.962, 95% CI: 1.057–8.301, $p = 0.039$), FIGO stage (HR 3.729, 95% CI: 1516–9.175, $p = 0.004$), and lymph node metastasis (HR 5.092, 95% CI: 2.217–11.694, $p < 0.001$) were independent predictors of PFS (**Table 5**); as for OS, the SII (HR 5.171, 95% CI: 1.176–22.733, $p = 0.030$) and lymph node metastasis (HR 6.961, 95% CI: 2.843–17.043, $p < 0.001$) were its independent prognostic factors (**Table 7**). In the validation

TABLE 5 | Univariate and multivariate analysis of prognostic factors for PFS in patients with CSCC in the training cohort.

Variable	Univariate		Multivariate	
	p	HR (95% CI)	p	HR (95% CI)
Age (≤45 vs. >45 years)	0.555	1.324 (0.522–3.359)		
FIGO stage (IB2-IIA2 vs. IIB)	0.018	2.808 (1.189–6.631)	0.004	3.729 (1.516–9.175)
Histological grade (G1-G2 vs. G3)	0.822	1.101 (0.476–2.545)		
Tumor size (≤5 vs. >5 cm)	0.656	0.798 (0.296–2.150)		
Tumor growth pattern (exogenous vs. endogenous)	0.013	2.807 (1.238–6.362)	0.187	1.752 (0.761–4.031)
Lymph node metastasis (negative vs. positive)	<0.001	5.601 (2.464–12.734)	<0.001	5.092 (2.217–11.694)
NACT cycles (≤2 vs. >2)	0.133	1.978 (0.813–4.811)		
Adjuvant treatment (yes vs. no)	0.227	0.473 (0.141–1.593)		
SII (≤600.5683 vs. >600.5683)	0.028	3.049 (1.131–8.219)	0.039	2.962 (1.057–8.301)
PNI (≤49.5 vs. >49.5)	0.914	0.943 (0.321–2.772)		
PLR (≤153.4314 vs. >153.4314)	0.006	3.230 (1.396–7.475)	0.279	1.761 (0.633–4.901)
LMR (≤12.25 vs. >12.25)	0.146	4.445 (0.596–33.160)		
Neutrophil (≤5.35 vs. >5.35)	0.289	1.557 (0.687–3.530)		
Lymphocyte (≤0.87 vs. >0.87)	0.674	20.622 (0- >1)		
Platelet (≤216 vs. >216)	0.320	1.851 (0.550–6.229)		

CSCC, cervical squamous cell carcinoma; PFS, progression free survival; HR, hazard ratio; CI, confidence interval; NACT, neoadjuvant chemotherapy; SII, systemic immune-inflammation index; PNI, prognostic nutritional index; PLR, platelet-to-lymphocyte ratio; LMR, lymphocyte-to-monocyte ratio.

TABLE 6 | Univariate and multivariate analysis of prognostic factors for PFS in patients with CSCC in the validation cohort.

Variable	Univariate		Multivariate	
	p	HR (95% CI)	p	HR (95% CI)
Age (≤45 vs. >45 years)	0.090	0.358 (0.109–1.175)		
FIGO stage (IB2-IIA2 vs. IIB)	0.203	2.370 (0.629–8.937)	0.201	2.623 (0.598–11.495)
Histological grade (G1-G2 vs. G3)	0.562	0.704 (0.215–2.306)	0.847	0.884 (0.251–3.790)
Tumor size (≤5 vs. >5 cm)	0.197	2.184 (0.666–7.160)	0.227	2.120 (0.627–7.164)
Tumor growth pattern (exogenous vs. endogenous)	0.616	1.693 (0.216–13.254)		
NACT cycles (≤2 vs. >2)	0.560	1.424 (0.434–4.667)	0.985	1.013 (0.271–3.790)
Adjuvant treatment (yes vs. no)	0.643	0.615 (0.079–4.803)		
SII (≤600.5683 vs. >600.5683)	0.030	4.331 (1.148–16.334)	0.038	4.090 (1.077–15.526)
PNI (≤49.5 vs. >49.5)	0.673	1.331 (0.353–5.020)		
PLR (≤153.4314 vs. >153.4314)	0.674	1.291 (0.394–4.231)		
LMR (≤12.25 vs. >12.25)	0.787	0.049 (0- >1)		
Neutrophil (≤5.35 vs. >5.35)	0.154	2.443 (0.715–8.351)		
Lymphocyte (≤0.87 vs. >0.87)	—	—		
Platelet (≤216 vs. >216)	0.649	1.612 (0.206–12.604)		

CSCC, cervical squamous cell carcinoma; PFS, progression free survival; HR, hazard ratio; CI, confidence interval; NACT, neoadjuvant chemotherapy; SII, systemic immune-inflammation index; PNI, prognostic nutritional index; PLR, platelet-to-lymphocyte ratio; LMR, lymphocyte-to-monocyte ratio.

cohort, we further performed multivariate analyses of the patients' FIGO stage, histological grade, tumor size, NACT cycles, and SII, the results indicated that the SII was an independent prognostic predictor for PFS (**Table 6**). A similar trend was also identified for OS in the validation cohort (**Table 8**).

DISCUSSION

Recent studies have described pre-treatment SII as having a role in predicting the prognosis of solid malignant tumors. However, to the best of our knowledge, no studies have investigated the predictive ability of pre-treatment SII with regard to response to treatment of cervical cancer. In the present study, we demonstrated the significant predictive ability of pre-treatment SII in patients with cervical cancer who were treated with NACT.

Our results concluded that a high SII (≤568.7051 vs. > 568.7051) was associated significantly with a decreased pCR to NACT. Logistic regression analysis showed that a SII of ≤568.7051 was an independent predictor for pCR. Moreover, a high pre-treatment SII (>600.5683) was associated significantly with reduced OS and PFS in patients with cervical cancer treated with NACT. Multivariate analysis confirmed the SII as an independent prognostic factor.

The SII was first constructed as a novel index in 2014 and is based on host lymphocyte, neutrophil, and platelet counts [7]; its predictive ability with regard to solid cancers can be explained by the function of these three kinds of cells.

Lymphocytes play an important role in tumor defense by inducing apoptosis of tumor cells through immune surveillance, thereby inhibiting cancer cell invasion, proliferation, and metastasis. Denkert et al. [12] reported that an increased

TABLE 7 | Univariate and multivariate analysis of prognostic factors for OS in patients with CSCC in the training cohort.

Variable	Univariate		Multivariate	
	p	HR (95% CI)	*p*	HR (95% CI)
Age (≤45 vs. >45 years)	0.206	2.020 (0.680–6.006)		
FIGO stage (IB2-IIA2 vs. IIB)	0.119	2.123 (0.823–5.478)		
Histological grade (G1-G2 vs. G3)	0.111	2.262 (0.828–6.176)		
Tumor size (≤5 vs. >5 cm)	0.411	1.464 (0.590–3.628)		
Tumor growth pattern (exogenous *vs.* endogenous)	0.181	1.825 (0.756–4.406)		
Lymph node metastasis (negative vs. positive)	<0.001	9.471 (3.922–22.87)	<0.001	6.961 (2.843–17.043)
NACT cycles (≤2 vs.>2)	0.232	1.784 (0.691–4.608)		
Adjuvant treatment (yes vs. no)	0.6	0.677 (0.158–2.909)		
SII (≤600.5683 vs. >600.5683)	0.005	8.060 (1.876–34.628)	0.030	5.171 (1.176–22.733)
PNI (≤49.5 vs. >49.5)	0.800	1.171 (0.344–3.980)		
PLR (≤153.4314 vs. >153.4314)	0.002	4.171 (1.679–10.365)	0.650	1.275 (0.447–3.632)
LMR (≤12.25 vs. >12.25)	0.114	5.077 (0.677–38.063)		
Neutrophil (≤5.35 vs. >5.35)	0.064	2.263 (0.953–5.374)		
Lymphocyte (≤0.87 vs. >0.87)	0.681	20.652 (0- >1)		
Platelet (≤216 vs. >216)	0.091	5.655 (0.759–42.151)		

CSCC, cervical squamous cell carcinoma; OS, overall survival; HR, hazard ratio; CI, confidence interval; NACT, neoadjuvant chemotherapy; SII, systemic immune-inflammation index; PNI, prognostic nutritional index; PLR, platelet-to-lymphocyte ratio; LMR, lymphocyte-to-monocyte ratio.

TABLE 8 | Univariate and multivariate analysis of prognostic factors for OS in patients with CSCC in the validation cohort.

Variable	Univariate		Multivariate	
	p	HR (95% CI)	*p*	HR (95% CI)
Age (≤45 vs. >45 years)	0.120	0.352 (0.014–1.312)		
FIGO stage (IB2-IIA2 vs. IIB)	0.483	1.755 (0.356–8.454)	0.528	1.744 (0.311–9.788)
Histological grade (G1-G2 vs. G3)	0.555	0.673 (0.181–2.507)	0.751	0.799 (0.200–3.195)
Tumor size (≤5 vs. >5 cm)	0.282	2.059 (0.552–7.680)	0.372	1.844 (0.480–7.081)
Tumor growth pattern (exogenous *vs.* endogenous)	0.475	2.137 (0.267–17.128)		
NACT cycles (≤2 vs. >2)	0.628	1.384 (0.372–5.158)	0.897	1.100 (0.260–4.654)
Adjuvant treatment (yes vs. no)	0.803	0.768 (0.096–6.140)		
SII (≤600.5683 vs. >600.5683)	0.032	5.560 (1.155–26.776)	0.042	5.143 (1.061–24.927)
PNI (≤49.5 vs. >49.5)	0.500	1.717 (0.356–8.267)		
PLR (≤153.4314 vs. >153.4314)	0.651	1.354 (0.363–5.045)		
LMR (≤12.25 vs. >12.25)	0.729	1.320 (0.274–6.355)		
Neutrophil (≤5.35 vs. >5.35)	0.076	3.295 (0.884–12.277)		
Lymphocyte (≤0.87 vs. >0.87)	—	—		
Platelet (≤216 vs. >216)	0.824	1.266 (0.158–10.125)		

CSCC, cervical squamous cell carcinoma; OS, overall survival; HR, hazard ratio; CI, confidence interval; NACT, neoadjuvant chemotherapy; SII, systemic immune-inflammation index; PNI, prognostic nutritional index; PLR, platelet-to-lymphocyte ratio; LMR, lymphocyte-to-monocyte ratio.

concentration of tumor-infiltrating lymphocytes (TIL) could be used to predict the response to NACT in patients with breast cancer across all molecular subtypes. Furthermore, TILs were associated with survival benefit in both HER2-positive and triple-negative breast cancers. D'Alessandris et al. [13] also found that higher TIL infiltration correlated with a higher pCR rate in patients with cervical cancer treated with NACT. Meanwhile, decreased proportions of tumor-infiltrating CD4+T cells were found to be closely related to tumor progression and lymph node metastasis in cervical carcinoma [14]. The cell numbers of lymphocyte subsets, including CD4^{+}, CD8^{+}, CD3^{+}, and CD56 + T cells, are decreased in patients with advanced cancer, leading to weakened lymphocyte-mediated anti-tumor immune responses [15]. Therefore, lymphopenia is deemed to be an independent prognostic factor for patient survival in several cancers.

In contrast to lymphocytes, neutrophils have a significant tumor-promoting effect. In the tumor microenvironment, neutrophils can derive subsets of myeloid-derived suppressor cells (MDSCs), which, in circulation, can produce reactive oxygen species and arginase, suppressor of T lymphocytes, thereby causing a strong immunosuppressive effect. In addition, the lysis of the neutrophils' nuclear membrane and the release of their nuclear DNA forms neutrophil extracellular traps (Nnets), which transport circulating tumor cells (CTC) to the metastatic site for further growth [16–18]. Neutrophils can also release matrix metalloproteinase-9 (MMP9), vascular endothelial growth factor (VEGF), and inflammatory mediators, such as interleukin 6(IL-6) and tumor necrosis factor-β (TNF-β), which promote the invasion, proliferation and distant metastasis of tumor cells [19]. Gentles et al. [20] analyzed

immune cells in 14 types of solid tumors and found that neutrophils were the cell group with the most unfavorable prognosis in patients with tumors. Murakami et al. [21] found that patients with gastric cancer with higher levels of peripheral blood neutrophils had a poor response to chemotherapy, and that their OS was shorter by an average of 8 months compared with patients with lower neutrophil counts. In cervical cancer, a high degree of neutrophil infiltration within the tumor is associated with resistance to radiotherapy and is a factor for poor prognosis [22, 23].

Increased platelets due to thrombosis, which is common in patients with tumors, can promote tumor angiogenesis and assist the immune escape of tumor cells [24]. Meanwhile, platelets can also induce the production of CTCs, and their secretion of transforming growth factor-β (TGF-β) and platelet-derived growth factor (PDGF) can promote the epithelial-mesenchymal transformation of CTCs [25]. Therefore, platelets also play an important role in promoting tumor progression.

As a comprehensive indicator, the SII can reflect host immune and inflammatory status in a more extensive manner than other indicators. A growing body of data point to the SII being a predictor of chemotherapy efficacy for a variety of cancers. Jiang et al. [8] retrospectively analyzed 387 female patients with breast cancer who were treated with NACT followed by surgery and determined that the SII was an independent predictor of pCR for patients with breast cancer, with the low-SII group showing the highest pCR rate. Eraslan et al. [9] studied 188 patients diagnosed with locally advanced rectal cancer who received neoadjuvant chemoradiotherapy (NACRT) and found that among several inflammatory indices, including neutrophil-to-lymphocyte ratio (NLR), PLR, and SII, only the SII, at a value of <748, was an independent predictive factor of pCR after NACRT (OR: 0.471, 95% CI: 0.224–0.991, $p = 0.047$). Murthy et al. [11] found that the SII could reflect treatment response and outcome following NACT for patients with pancreatic adenocarcinoma. However, no relevant research has yet been reported regarding the predictive value of the SII for response to chemotherapy for patients with cervical cancer.

The results of the present study showed that patients with cervical cancer with an SII of ≤568.7051 before NACT exhibited a higher pCR rate. Additionally, we found that the SII was a better predictor of pCR than PNI, PLR, LMR, platelet, neutrophil, and lymphocyte. In the logistic regression analysis, the SII was an independent predictor of pCR for patients with cervical cancer treated with NACT.

Recently, the pre-treatment SII was demonstrated to predict the prognosis of solid malignant tumors. Dong et al. [26] analyzed a total of 12 studies published between 2016 and 2019 and showed that a high SII was associated significantly with poorer OS and PFS ($p = 0.001$) for colorectal cancer. Jomrich et al. [27] studied 320 consecutive patients undergoing esophagectomy and found that in patients with gastroesophageal junction adenocarcinoma, a high SII was associated significantly with lower survival in patients undergoing neoadjuvant treatment. Zeng et al. [28] revealed that the SII is an important independent prognostic index for pulmonary sarcomatoid carcinoma. Aziz et al. [29] assessed 590 patients with resectable pancreatic ductal adenocarcinoma (PDAC) retrospectively and identified an SII >900 as an independent predictor of cancer-specific survival and recurrence. Hu et al. [7] studied 133 patients with hepatocellular carcinoma who underwent resection and concluded that a high SII (cut-off > $330*10^9$/L) was a potent prognostic indicator of poor outcome. The results were further validated in a prospective study involving 123 patients. In the present study, the optimal cutoff value for SII, calculated using the ROC curve, was 600.5683, and we also determined that a low pretreatment SII was associated significantly with increased OS and PFS in patients with cervical cancer treated with NACT. Moreover, the patients' pre-treatment SII was an independent prognostic factor in multivariable analysis.

Despite this study's successful demonstration that pre-treatment SII is an independent predictor of patients' response to NACT, as well as an independent prognostic factor for cervical cancer, it still had some limitations. First, the hematological data for each patient was collected within 1 week before receiving NACT; however, the value of inflammatory indexes might be affected by various pathological conditions and might vary with time. Second, our study was a retrospective, single center study with a limited number of patients ($n = 133$) and thus might contain selection bias; therefore, a multicenter study with a larger sample size is warranted.

CONCLUSION

The present study demonstrated the predictive ability of the pre-treatment SII for patients with cervical cancer after NACT. Our results confirmed that the SII qualifies as an independent predictor of pCR and as an independent prognostic factor for cervical cancer. The low pCR rate and short survival time of patients with high SII scores might be caused by poor chemotherapy sensitivity and, as such, should be managed with other treatments, such as concomitant chemotherapy and radiotherapy. In conclusion, SII measurement will aid patients in their clinical treatment selection, which is bolstered by the fact that measurement of pre-treatment SII is available, inexpensive, and reliable for cervical cancer in clinical practice. Further investigations are warranted to validate these results.

DATA AVAILABILITY STATEMENT

The datasets presented in this article are not readily available due to patient privacy requirements. Requests to access the datasets should be directed to the corresponding author.

ETHICS STATEMENT

AUTHOR CONTRIBUTIONS

All authors listed have made a substantial, direct, and intellectual contribution to the work and approved it for publication.

FUNDING

CONFLICT OF INTEREST

SUPPLEMENTARY MATERIAL

The Supplementary Material for this article can be found online at: https://www.por-journal.com/articles/10.3389/pore.2022.1610294/full#supplementary-material

Supplementary Figure S1 | ROC curve analyzing the predictive value of SII for the pCR of patients with CSCC. Notes: AUC, area under the ROC curve; * indicates the cutoff value. Abbreviations: ROC, receiver operating characteristic; pCR, pathological complete response; CSCC, cervical squamous cell carcinoma; SII, systemic immune-inflammation index.

Supplementary Figure S2 | ROC curve analyzing the predictive value of SII for the OS of patients with CSCC. Notes: AUC, area under the ROC curve; * indicates the cutoff value. Abbreviations: ROC, receiver operating characteristic; OS, overall survival; CSCC, cervical squamous cell carcinoma; SII, systemic immune-inflammation index.

REFERENCES

1. Bray F, Ferlay J, Soerjomataram I, Siegel RL, Torre LA, Jemal A Global Cancer Statistics 2018: GLOBOCAN Estimates of Incidence and Mortality Worldwide for 36 Cancers in 185 Countries. *CA Cancer J Clin* (2018) 68(6):394–424. doi:10.3322/caac.21492

2. Chen W, Zheng R, Baade PD, Zhang S, Zeng H, Bray F, et al. Cancer Statistics in China, 2015. *CA Cancer J Clin* (2016) 66(2):115–32. doi:10.3322/caac.21338

3. Licitra L, Vermorken JB Is There Still a Role for Neoadjuvant Chemotherapy in Head and Neck Cancer? *Ann Oncol* (2004) 15(1):7–11. doi:10.1093/annonc/mdh001

4. Shi L, Qin X, Wang H, Xia Y, Li Y, Chen X, et al. Elevated Neutrophil-To-Lymphocyte Ratio and Monocyte-To-Lymphocyte Ratio and Decreased Platelet-To-Lymphocyte Ratio Are Associated with Poor Prognosis in Multiple Myeloma. *Oncotarget* (2017) 8:18792–801. doi:10.18632/oncotarget.13320

5. Templeton AJ, Ace O, McNamara MG, Al-Mubarak M, Vera-Badillo FE, Hermanns T, et al. Prognostic Role of Platelet to Lymphocyte Ratio in Solid Tumors: a Systematic Review and Meta-Analysis. *Cancer Epidemiol Biomarkers Prev* (2014) 23(7):1204–12. doi:10.1158/1055-9965.EPI-14-0146

6. Mellman I, Coukos G, Dranoff G Cancer Immunotherapy Comes of Age. *Nature* (2011) 480(7378):480–9. doi:10.1038/nature10673

7. Hu B, Yang X-R, Xu Y, Sun Y-F, Sun C, Guo W, et al. Systemic Immune-Inflammation index Predicts Prognosis of Patients after Curative Resection for Hepatocellular Carcinoma. *Clin Cancer Res* (2014) 20(23):6212–22. doi:10.1158/1078-0432.CCR-14-0442

8. Jiang C, Huang Y Predictive Effect of Systemic Immune-Inflammation Index on Pathological Complete Response of Breast Cancer to Neoadjuvant Chemotherapy and its Relation with P53. *Cancer Prev Treat Res* (2020) 47(10):756–60. doi:10.3971/j.issn.1000-8578.2020.20.0273

9. Eraslan E, Adas YG, Yildiz F, Gulesen AI, Karacin C, Arslan UY Systemic Immune-Inflammation Index (SII) Predicts Pathological Complete Response to Neoadjuvant Chemoradiotherapy in Locally Advanced Rectal Cancer. *J Coll Phys Surg Pak* (2021) 31(4):399–404. doi:10.29271/jcpsp.2021.04.399

10. Chen L, Yan Y, Zhu L, Cong X, Li S, Song S, et al. Systemic Immune-Inflammation index as a Useful Prognostic Indicator Predicts Survival in Patients with Advanced Gastric Cancer Treated with Neoadjuvant Chemotherapy. *Cancer Manag Res* (2017) 9:849–67. doi:10.2147/CMAR.S151026

11. Murthy P, Boone BA ASO Author Reflections: Systemic Immune-Inflammation Index (SII) as a Biomarker of Response to Neoadjuvant Therapy in Patients with Pancreatic Adenocarcinoma. *Ann Surg Oncol* (2020) 27(3):907–8. doi:10.1245/s10434-019-08136-7

12. Denkert C, von Minckwitz G, Darb-Esfahani S, Lederer B, Heppner BI, Weber KE, et al. Tumour-infiltrating Lymphocytes and Prognosis in Different Subtypes of Breast Cancer: a Pooled Analysis of 3771 Patients Treated with Neoadjuvant Therapy. *Lancet Oncol* (2018) 19(1):40–50. doi:10.1016/S1470-2045(17)30904-X

13. D'Alessandris N, Palaia I, Pernazza A, Tomao F, Di Pinto A, Musacchio L, et al. PD-L1 Expression Is Associated with Tumor Infiltrating Lymphocytes that Predict Response to NACT in Squamous Cell Cervical Cancer. *Virchows Arch* (2021) 478(3):517–25. doi:10.1007/s00428-020-02922-5

14. Sheu B-C, Hsu S-M, Ho H-N, Lin R-H, Torng P-L, Huang S-C Reversed CD4/CD8 Ratios of Tumor-Infiltrating Lymphocytes are Correlated with the Progression of Human Cervical Carcinoma. *Cancer* (1999) 86(8):1537–43. doi:10.1002/(sici)1097-0142(19991015)86:8<1537:aid-cncr21>3.0.co;2-d

15. Ray-Coquard I, Cropet C, Van Glabbeke M, Sebban C, Le Cesne A, Judson I, et al. Lymphopenia as a Prognostic Factor for Overall Survival in Advanced Carcinomas, Sarcomas, and Lymphomas. *Cancer Res* (2009) 69(13):5383–91. doi:10.1158/0008-5472.CAN-08-3845

16. Cools-Lartigue J, Spicer J, McDonald B, Gowing S, Chow S, Giannias B, et al. Neutrophil Extracellular Traps Sequester Circulating Tumor Cells and Promote Metastasis. *J Clin Invest* (2013) 123:3446–58. doi:10.1172/JCI67484

17. Martinez PJ, Farhan A, Mustafa M, Javaid N, Darkoh C, Garrido-Sanabria E, et al. PspA Facilitates Evasion of Pneumococci from Bactericidal Activity of Neutrophil Extracellular Traps (NETs). *Microb Pathogenesis* (2019) 136:103653. doi:10.1016/j.micpath.2019.103653

18. Groth C, Hu X, Weber R, Fleming V, Altevogt P, Utikal J, et al. Immunosuppression Mediated by Myeloid-Derived Suppressor Cells (MDSCs) during Tumour Progression. *Br J Cancer* (2019) 120(1):16–25. doi:10.1038/s41416-018-0333-1

19. Jaillon S, Galdiero MR, Del Prete D, Cassatella MA, Garlanda C, Mantovani A Neutrophils in Innate and Adaptive Immunity. *Semin Immunopathol* (2013) 35(4):377–94. doi:10.1007/s00281-013-0374-8

20. Gentles AJ, Newman AM, Liu CL, Bratman SV, Feng W, Kim D, et al. The Prognostic Landscape of Genes and Infiltrating Immune Cells across Human Cancers. *Nat Med* (2015) 21(8):938–45. doi:10.1038/nm.3909

21. Murakami Y, Saito H, Shimizu S, Kono Y, Shishido Y, Miyatani K, et al. Neutrophil-to-Lymphocyte Ratio as a Prognostic Indicator in Patients with

Unresectable Gastric Cancer. *Anticancer Res* (2019) 39(5):2583–9. doi:10.21873/anticanres.13381

22. Wisdom AJ, Hong CS, Lin AJ, Xiang Y, Cooper DE, Zhang J, et al. Neutrophils Promote Tumor Resistance to Radiation Therapy. *Proc Natl Acad Sci U.S.A* (2019) 116(37):18584–9. doi:10.1073/pnas.1901562116

23. Matsumoto Y, Mabuchi S, Kozasa K, Kuroda H, Sasano T, Yokoi E, et al. The Significance of Tumor-Associated Neutrophil Density in Uterine Cervical Cancer Treated with Definitive Radiotherapy. *Gynecol Oncol* (2017) 145(3): 469–75. doi:10.1016/j.ygyno.2017.02.009

24. Franco AT, Corken A, Ware J Platelets at the Interface of Thrombosis, Inflammation, and Cancer. *Blood* (2015) 126(5):582–8. doi:10.1182/blood-2014-08-531582

25. Lou XL, Sun J, Gong SQ, Yu XF, Gong R, Deng H Interaction between Circulating Cancer Cells and Platelets: Clinical Implication. *Chin J Cancer Res* (2015) 27(5):450–60. doi:10.3978/j.issn.1000-9604.2015.04.10

26. Dong M, Shi Y, Yang J, Zhou Q, Lian Y, Wang D, et al. Prognostic and Clinicopathological Significance of Systemic Immune-Inflammation index in Colorectal Cancer: a Meta-Analysis. *Ther Adv Med Oncol* (2020) 12: 175883592093742. doi:10.1177/1758835920937425

27. Jomrich G, Paireder M, Kristo I, Baierl A, Ilhan-Mutlu A, Preusser M, et al. High Systemic Immune-Inflammation Index is an Adverse Prognostic Factor for Patients with Gastroesophageal Adenocarcinoma. *Ann Surg* (2021) 273(3): 532–41. doi:10.1097/SLA.0000000000003370

28. Zeng Q, Li J, Sun N, Xue Q, Gao Y, Zhao J, et al. Preoperative Systemic Immune-Inflammation index Predicts Survival and Recurrence in Patients with Resected Primary Pulmonary Sarcomatoid Carcinoma. *Transl Lung Cancer Res* (2021) 10(1):18–31. doi:10.21037/tlcr-20-960

29. Aziz MH, Sideras K, Aziz NA, Mauff K, Haen R, Roos D, et al. The Systemic-Immune-Inflammation Index Independently Predicts Survival and Recurrence in Resectable Pancreatic Cancer and its Prognostic Value Depends on Bilirubin Levels. *Ann Surg* (2019) 270(1):139–46. doi:10.1097/SLA.0000000000002660

Check for
updates

High Neutrophil-To-Lymphocyte Ratio (NLR) and Systemic Immune-Inflammation Index (SII) Are Markers of Longer Survival After Metastasectomy of Patients With Liver-Only Metastasis of Rectal Cancer

Nándor Polk[2], Barna Budai[3]*, Erika Hitre[4], Attila Patócs[1,3,5]* and Tamás Mersich[2]

[1]Department of Laboratory Medicine, Semmelweis University, Budapest, Hungary, [2]Departmet of Visceral Surgery, National Institute of Oncology, Budapest, Hungary, [3]Department of Molecular Genetics, National Institute of Oncology, Budapest, Hungary, [4]Medical Oncology and Clinical Pharmacology "B" Department, National Institute of Oncology, Budapest, Hungary, [5]Clinical Central Laboratory, National Institute of Oncology, Budapest, Hungary

Background: The literature data regarding colon cancer patients with liver-only metastases (CLM) show that NLR determined before metastasectomy is a prognostic marker of shorter relapse-free survival (RFS), but no results has been reported to date for rectal cancer patients with liver-only metastases (RLM). This study aimed to investigate the NLR and SII in CLM and RLM.

Methods: Relapse-free (RFS) and overall survival (OS) were evaluated in 67 CLM and 103 RLM patients with a median follow-up of 46.5 and 59.8 months, respectively. Pre- and/or postoperative chemotherapy ± targeted treatment was applied in 96% and 87% of CLM and RLM patients, respectively. The cut-off level for hematologic parameters were determined by receiver operating characteristic (ROC) analysis. Univariate analysis was performed by Kaplan-Meier method and log rank test. For multivariate analysis Cox regression was applied.

Results: In univariate analysis low NLR (cut-off 2) and SII (535) were predictors of longer RFS in case of CLM ($p < 0.01$). In contrast, for RLM high NLR (2.42) and SII (792) were predictors of longer RFS ($p < 0.001$). For RLM both NLR and SII proved to be independent markers of RFS (HR 0.66 (95% CI 0.52–0.84) and 0.73 (0.57–0.91), respectively) and OS (0.76 (0.58–0.99) and 0.66 (0.5–0.87), respectively). Only NLR (1.44 (1.04–1.99)) was independent marker of RFS for CLM. The preoperative treatment has not influenced the role of NLR or SII.

Conclusion: In contrast to CLM, in RLM the high NLR or SII determined before metastasectomy proved to be independent prognostic factors of longer RFS and OS.

Keywords: neutrophil-to-lymphocyte ratio, liver-only metastases of rectal cancer, metastasectomy, relapse-free survival, systemic immune-inflammation index, liver-only metastases of colon cancer, preoperative treatment

BACKGROUND

In Hungary the incidence and mortality of colorectal cancer (CRC) is currently the second most common among malignancies [1]. Liver metastases develop in nearly half of CRC patients, and the best treatment for patients with colorectal liver-only metastases (CRLM) is the surgical resection, however, 60–80% of them experience recurrence after resection [2]. Knowledge of derived preoperative hematologic parameters, which are readily available data, may be important in assessing the risk of recurrence. The best known prognostic parameter is the neutrophil-to-

TABLE 1 | Clinicopathological characteristics and preoperative laboratory parameters of patients with colon cancer liver-only metastases.

Parameters		N (%)	Median (range)	Cut-off value RFS/OS
Age (yrs)			65 (38–80)	62/66
	<62	23 (34)		
	≥62	44 (66)		
	<66	35 (52)		
	≥66	32 (48)		
Gender				
	male	36 (54)		
	female	31 (46)		
Type of surgery used for metastasectomy				
	laparoscopy	11 (16)		
	open	56 (84)		
Resection margin				
	R0	46 (69)		
	R1	21 (31)		
Synchronicity of primary surgery and metastasectomy				
	synchronous	7 (10)		
	metachronous	60 (90)		
Preoperative (metastasectomy) chemotherapy ± targeted therapy				
	none	16 (24)		
	yes	51 (76)		
	targeted	43 (84)		
Postoperative (metastasectomy) chemotherapy ± targeted therapy				
	none	18 (27)		
	yes	49 (73)		
	targeted	27 (55)		
Pre- or postoperative chemotherapy ± targeted therapy				
	none	3 (4)		
	yes	64 (96)		
	targeted	48 (75)		
WBC (G/l)			6.8 (3.5–12.5)	6.8/7.1
	<6.8	32 (48)		
	≥6.8	35 (52)		
	<7.1	35 (52)		
	≥7.1	32 (48)		
neutrophil (G/l)			4.3 (1.2–9.2)	4/4.8
	<4	27 (40)		
	≥4	40 (60)		
	<4.8	41 (61)		
	≥4.8	26 (39)		

(Continued on following page)

TABLE 1 | (*Continued*) Clinicopathological characteristics and preoperative laboratory parameters of patients with colon cancer liver-only metastases.

Parameters		N (%)	Median (range)	Cut-off value RFS/OS
lymphocyte (G/l)			2 (0.8–3.7)	1.94/2
	<1.94	32 (48)		
	≥1.94	35 (52)		
	<2	36 (54)		
	≥2	31 (46)		
platelet (G/l)			244 (105–446)	210/184
	<210	20 (30)		
	≥210	47 (70)		
	<184	10 (15)		
	≥184	57 (85)		
NLR			2 (0.7–8.8)	2/1.7
	<2	30 (45)		
	≥2	37 (55)		
	<1.7	18 (27)		
	>1.7	49 (73)		
SII (G/l)			502 (125–1952)	535/290
	<535	39 (58)		
	≥535	28 (42)		
	<290	9 (16)		
	≥290	58 (84)		
GOT (U/l)			25 (13–343)	24/24
	<24	22 (37)		
	≥24	37 (63)		
	NA	8		
GPT (U/l)			22 (9–296)	31/17
	<31	48 (80)		
	≥31	12 (20)		
	<17	14 (23)		
	≥17	46 (77)		
	NA	7		
Site of progression				
	liver	33 (63)		
	lung	5 (10)		
	liver+lung	7 (13)		
	other	7 (13)		
Extent of progression				
	single	41 (61)		
	multiple	11 (16)		
	none	15 (22)		

lymphocyte ratio (NLR), which has also been studied in several studies evaluating patients with CRLM [3, 4, 5]. In these studies, patients were dichotomized based on a calculated or from the literature taken cut-off value, and based on this, significantly different relapse-free survival (RFS) curves were found. In general, the lower NLR has been identified as a marker of longer RFS, but at the same cut-off value (e.g., Ref. 5), strongly significant [6, 7] or non-significant [8, 9] differences of RFS curves were demonstrated.

All these data together reflect the incoherent association. The systemic immune-inflammation index (SII = platelet count x NLR), which has been shown to be the best prognostic marker for occurrence of liver metastasis in CRC [10], was investigated in only two studies for the recurrence in CRLM [11, 12].

In previous studies, the presence of pre- and postoperative chemo- and targeted therapies was not an exclusion criterion, although in some studies all patients received

TABLE 2 | Clinicopathological characteristics and preoperative laboratory parameters of patients with rectal cancer liver-only metastases.

Parameters	N (%)	Median (range)	Cut-off value RFS/OS
Age (yrs)		62 (31–81)	68/64
<68	68 (66)		
≥68	35 (34)		
<64	58 (56)		
≥64	45 (44)		
Gender			
male	69 (67)		
female	34 (33)		
Type of surgery used for metastasectomy			
laparoscopy	19 (18)		
open	84 (82)		
Resection margin			
R0	65 (63)		
R1	38 (37)		
Synchronicity of primary surgery and metastasectomy			
synchronous	10 (10)		
metachronous	93 (90)		
"liver first"	10 (11)		
Preoperative (metastasectomy) chemotherapy ± targeted therapy			
none	37 (36)		
yes	66 (64)		
targeted	41 (62)		
Postoperative (metastasectomy) chemotherapy ± targeted therapy			
none	29 (28)		
yes	74 (72)		
targeted	23 (31)		
Pre- or postoperative chemotherapy ± targeted therapy			
none	13 (13)		
yes	90 (87)		
targeted	49 (54)		
WBC (G/l)		5.9 (3.4–18.6)	7.3/4.2
<7.3	79 (77)		
≥7.3	24 (23)		
<4.2	14 (14)		
≥4.2	89 (86)		
neutrophil (G/l)		3.8 (2–13.5)	5.5/3.5
<5.5	85 (83)		
≥5.5	18 (17)		
<3.5	37 (36)		
≥3.5	66 (64)		
lymphocyte (G/l)		1.4 (0.4–3.6)	0.97/1.7
<0.97	32 (31)		
≥0.97	71 (69)		
<1.7	77 (75)		
≥1.7	26 (25)		

(Continued on following page)

TABLE 2 | (*Continued*) Clinicopathological characteristics and preoperative laboratory parameters of patients with rectal cancer liver-only metastases.

Parameters		N (%)	Median (range)	Cut-off value RFS/OS
platelet (G/l)			210 (111–396)	161/314
	<161	18 (17)		
	≥161	85 (83)		
	<314	90 (87)		
	≥314	13 (13)		
NLR			2.9 (0.9–11.3)	2.42/2.56
	<2.42	31 (30)		
	≥2.42	72 (70)		
	<2.56	39 (38)		
	>2.56	64 (62)		
SII (G/l)			616 (189–3,500)	792/742
	<792	65 (63)		
	≥792	38 (37)		
	<742	63 (61)		
	≥742	40 (39)		
GOT (U/l)			23 (9–72)	25/20
	<25	50 (58)		
	≥25	36 (42)		
	<20	20 (23)		
	≥20	66 (77)		
	NA	17		
GPT (U/l)			19 (5–77)	22/13
	<22	52 (60)		
	≥22	34 (40)		
	<13	13 (15)		
	≥13	73 (85)		
	NA	17		
Site of progression				
	liver	43 (42)		
	lung	21 (20)		
	liver+lung	8 (8)		
	other	13 (13)		
Extent of progression				
	single	69 (67)		
	multiple	16 (16)		
	none	18 (17)		

GOT, aspartate aminotransferase; GPT, alanine aminotransferase; NA, not available; NLR, neutrophil-to lymphocyte ratio; OS, overall survival; RFS, relapse-free survival; SII, systemic immune-inflammation index; WBC, white blood cells.

pseudoneoadjuvant (hereafter preoperative) [13, 14, 15] or pseudoadjuvant (hereafter postoperative) treatment [16, 17]. The difference in rate of pre- and postoperative treatments reflects data from everyday practice. The localization of the primary tumor has not been detailed in many studies, and the calculation method of cut-off values is also not uniform; the most common is based on ROC analysis. Several studies exclusively investigated the overall survival (OS), but their results are also non convergent [18, 19, 20].

Based on our previous experience [21] and moreover on the histologic, genetic, behavioral, etc. differences between colon and rectum tumors detailed by Paschke et al. [22] and [23, 24], we hypothesized that the role of NLR may depend on the site of primary tumor of CRLM patients. For colon cancer Chang et al. [25] proved that low NLR is a significant marker of RFS, but no report was found for rectal cancer. The aim of the present study was to separately investigate the colon and rectal cancer patients with liver-only metastases wether

TABLE 3 | Uni- and multivariate analysis of RFS and OS for CLM.

Parameters	mRFS (95%CI)	p	HR$_{Cox1}$ (95%CI)	p$_{Cox1}$	HR$_{Cox2}$ (95%CI)	p$_{Cox2}$
Age						
<62	6.6 (4.4–8.9)	7×10^{-4}	-		-	
≥62	14.6 (10.2–16.8)					
Resection margin						
R0	13.8 (8.3–17.8)	0.001	1 (ref)	0.048	1 (ref)	0.182
R1	6.6 (5.2–10)		1.42 (1.003–2.1)		1.3 (0.89–1.9)	
Synchronous						
yes	8.2 (2–8.2)	0.012	-		-	
no	12.9 (7–14.6)					
Postoperative chemotherapy ± targeted therapy						
none	5.5 (2–5.8)	3×10^{-4}	-		1 (ref)	0.012
yes	13.4 (9.9–16.3)				0.61 (0.42–0.9)	
Pre- or postoperative chemotherapy ± targeted therapy						
none	2.5 (2–2.5)	0.006	-		-	
yes	10.8 (8.2–13.9)					
WBC						
<6.8	14.6 (10.8–19.3)	0.011	-		-	
≥6.8	8.3 (5.5–10.2)					
Neutrophil						
<4	19.3 (10.8–24.9)	0.002	-		-	
≥4	8.3 (5.8–10.5)					
NLR						
<2	14.6 (6.8–24.2)	0.004	1 (ref)	0.03	-	
≥2	9.9 (6–12.7)		1.44 (1.04–1.99)			
SII						
<535	14.4 (10.5–19.3)	0.005	-		1 (ref)	0.229
≥535	8.2 (5–9.9)				1.24 (0.87–1.78)	
GOT						
<24	12.9 (8.3–17.8)	0.043	1 (ref)	0.043	1 (ref)	0.013
≥24	6.8 (5.5–10.5)		1.43 (1.01–2.02)		1.6 (1.1–2.33)	
GPT						
<31	12.7 (7–14.4)	0.03	-		-	
≥31	5 (3.2–8.9)					
	mOS (95% CI)					
WBC						
<7.1	NR (40.5–46.6)	0.004	-		-	
≥7.1	30.1 (23.2–37.5)					
Neutrophil						
<4.8	NR (34.4–46.6)	0.004	-		1 (ref)	0.114
≥4.8	30.1 (23.2–37.5)				1.45 (0.91–2.31)	
Lymphocyte						

(Continued on following page)

TABLE 3 | (*Continued*) Uni- and multivariate analysis of RFS and OS for CLM.

Parameters	mRFS (95%CI)	p	HR_Cox1 (95%CI)	p_Cox1	HR_Cox2 (95%CI)	p_Cox2
<2	68.3 (42.1–68.3)	0.005	-		1 (ref)	0.053
≥2	31.3 (24.2–34.4)				1.63 (0.99–2.67)	
Platelet						
<184	24.2 (17.9–33.1)	0.045	1 (ref)	0.853	-	
≥184	42.1 (31.3–68.3)		1.06 (0.59–1.9)			
GOT						
<24	NR (39.7–42.1)	0.021	1 (ref)	0.073	1 (ref)	0.233
≥24	31.3 (24.6–40.8)		1.64 (0.96–2.81)		1.4 (0.81–2.41)	
GPT						
<17	NR (–33.1)	0.011	-		-	
≥17	34.4 (25–40.8)					
Extent of progression						
single	37.5 (31.1–46.6)	0.016	1 (ref)	0.043	1 (ref)	0.011
multiple	20.3 (16.3–24.2)		1.71 (1.02–2.88)		1.98 (1.17–3.34)	

CI, confidence interval; Cox(1 or 2), multivariate Cox regression analysis (model 1 or 2); GOT, aspartate aminotransferase; GPT, alanine aminotransferase; HR, hazard ratio; mOS, median overall survival; mRFS, median relapse-free survival; NLR, neutrophil-to lymphocyte ratio; NR, not reached; ns, not significant; ref, reference; SII, systemic immune-inflammation index; WBC, white blood cells.

NLR and SII determined before metastasectomy are possible markers of RFS and OS.

MATERIALS AND METHODS

Patients

All patients underwent curative resection of primary cancer. Those patients whom liver metastases were surgically treated between 2001 and 2018 were reviewed ($n = 205$). The exclusion criteria were: 1) Radio-frequency thermal ablation (RFTA) or radiofrequency ablation (RFA) of liver metastases ($n = 16$); 2) unavailable laboratory parameters ($n = 16$); 3) presence of other synchronous malignancies ($n = 3$). A total of 170 patients were included in the study, 67 of whom had a primary tumor in the colon (CLM) and 103 in the rectum (RLM). Besides the clinicopathologic parameters the presence of chemotherapy (±targeted treatment) before and/or after metastasectomy was recorded. The 5-FU-based chemotherapy was administered alone or combined with oxaliplatin or irinotecan. Targeted therapy (cetuximab, bevacizumab or panitumumab) was also applied in several cases. All hematological parameters were determined from the blood samples taken before metastasectomy.

Metastasectomy was laparoscopic (16 and 18%, for CLM and RLM, respectively) or classic, including synchronous surgery of primary tumor and liver metastasis (10%, both CLM and RLM). In case of 10 RLM patients the "liver first" strategy was chosen. Hepatic magnetic resonance imaging (MRI) to assess the local disease extension and to evaluate chemotherapy response, thoraco-abdominal computed tomography (CT) and positron emission tomography (PET-CT) were systematically performed to evaluate the presence of disease. Follow-up of all patients was performed every 3 months (physical examination, abdominal ultrasonography, CT, MRI or PET-CT, and routine laboratory).

Statistics

The primary objective was the prognostic value of NLR and SII for RFS; secondary objectives included OS and the effect of preoperative treatment on the role of NLR and SII. RFS was calculated from date of metastasectomy to date of progression or end of follow-up. OS was calculated from date of metastasectomy to date of cancer-related death or end of follow-up. The cut-off values for dichotomization of continuous variables were determined by ROC analysis of relapse or death for RFS and OS, respectively. The ratio of relapse was not underestimated because of enough follow-up duration. Survival curves were constructed by Kaplan-Meier method and compared by log rank test. Multivariate Cox regression analysis was used to find independent markers of survival. To avoid multicollinearity only uncorrelated variables were used in the Cox regression analysis. The NCSS program (NCSS 2019 Statistical Software (2019). NCSS, LLC. Kaysville, Utah, United States, ncss.com/software/ncss.) was used for statistical analyses.

RESULTS

The clinical and laboratory parameters of patients are presented in **Table 1** and **Table 2**.

The median follow-up was 46.5 (95% CI 43.5–50.1) and 59.8 (48.8–73.9) months for CLM and RLM patients, respectively. For CLM the median RFS and OS was 10.2 (95% CI 5.8–14.4) and 34.4 (30.1–42.1) months, respectively. In case of RLM the median

TABLE 4 | Uni- and multivariate analysis of RFS and OS for RLM.

Parameters	mRFS (95%CI)	p	HR$_{Cox1}$ (95%CI)	p$_{Cox1}$	HR$_{Cox2}$ (95%CI)	p$_{Cox2}$
Resection margin						
R0	11.7 (7.1–17.3)	0.005	1 (ref)	0.001	-	
R1	6.5 (4.8–11.1)		1.58 (1.2–2.07)			
Postoperative chemo ± targeted therapy						
none	6.6 (4.1–8.6)	0.084	1 (ref)	0.014	1 (ref)	0.114
yes	11.1 (7–15.4)		0.69 (0.52–0.93)		0.79 (0.6–1.06)	
WBC						
<7.3	10.9 (6.5–15.6)	0.06	1 (ref)	0.568	1 (ref)	0.416
≥7.3	6.9 (4.8–11.5)		1.09 (0.81–1.48)		1.13 (0.84–1.52)	
Neutrophil						
<5.5	11.1 (7.1–15.6)	0.014	-		-	
≥5.5	6.6 (4.2–8.3)					
Lymphocyte						
<0.97	13.6 (6.6–23.7)	0.025	-		-	
≥0.97	7.1 (6.2–11.2)					
NLR						
<2.42	6.3 (4.8–7.6)	1.6×10^{-4}	1 (ref)	0.021	-	
≥2.42	14.9 (7.8–19.2)		0.71 (0.54–0.95)			
SII						
<792	6.5 (5.7–7.6)	1.8×10^{-4}	-		1 (ref)	0.002
≥792	19.2 (11.9–23.7)				0.65 (0.5–0.85)	
GPT						
<22	8.6 (5.9–14.2)	0.085	1 (ref)	0.151	1 (ref)	0.139
≥22	11.2 (6.2–24.2)		0.82 (0.63–1.07)		0.82 (0.63–1.07)	
	mOS (95% CI)					
Age						
<64	47.3 (40.2–62.4)	0.054	1 (ref)	0.004	1 (ref)	0.012
≥64	33.1 (26.1–39.2)		1.57 (1.15–2.14)		1.47 (1.09–1.99)	
Resection margin						
R0	52.5 (37.8–71.4)	0.002	1 (ref)	0.025	-	
R1	31 (20.9–41.1)		1.4 (1.04–1.88)			
Postoperative targeted therapy						
none	46.5 (36.8–62)	0.059	-		-	
yes	31.7 (20.3–40.5)					
WBC						
<4.2	31.2 (20.3–35.2)	0.036	1 (ref)	0.031	1 (ref)	0.005
≥4.2	46 (39.2–62.4)		0.67 (0.47–0.96)		0.58 (0.40–0.85)	
Lymphocyte						
<1.7	39.3 (31.7–46)	0.059	-		-	
≥1.7	101 (39.2–101)					
Platelet						

TABLE 4 | (*Continued*) Uni- and multivariate analysis of RFS and OS for RLM.

Parameters	mRFS (95%CI)	p	HR$_{Cox1}$ (95%CI)	p$_{Cox1}$	HR$_{Cox2}$ (95%CI)	p$_{Cox2}$
<314	39.2 (31.7–46)	0.032	1 (ref)	0.044	-	
≥314	NR (52.5–62.4)		0.47 (0.22–0.98)			
NLR						
<2.56	39.2 (26.7–41.1)	0.084	1 (ref)	0.038	-	
>2.56	47.3 (35.2–63.1)		0.72 (0.53–0.98)			
SII						
<742	36.8 (26.7–41.1)	0.011	-		1 (ref)	0.001
≥742	62 (41.2–138)				0.57 (0.41–0.79)	
GPT						
<13	26.5 (16.6–41.2)	0.237	1 (ref)	0.002	1 (ref)	0.006
≥13	40.2 (33.8–50.3)		0.54 (0.34–0.8)		0.58 (0.39–0.86)	

CI, confidence interval; Cox(1 or 2), multivariate Cox regression analysis (model 1 or 2); GPT, alanine aminotransferase; HR, hazard ratio; mOS, median overall survival; mRFS, median relapse-free survival; NLR, neutrophil-to lymphocyte ratio; NR, not reached; ns, not significant; ref, reference; SII, systemic immune-inflammation index; WBC, white blood cells.

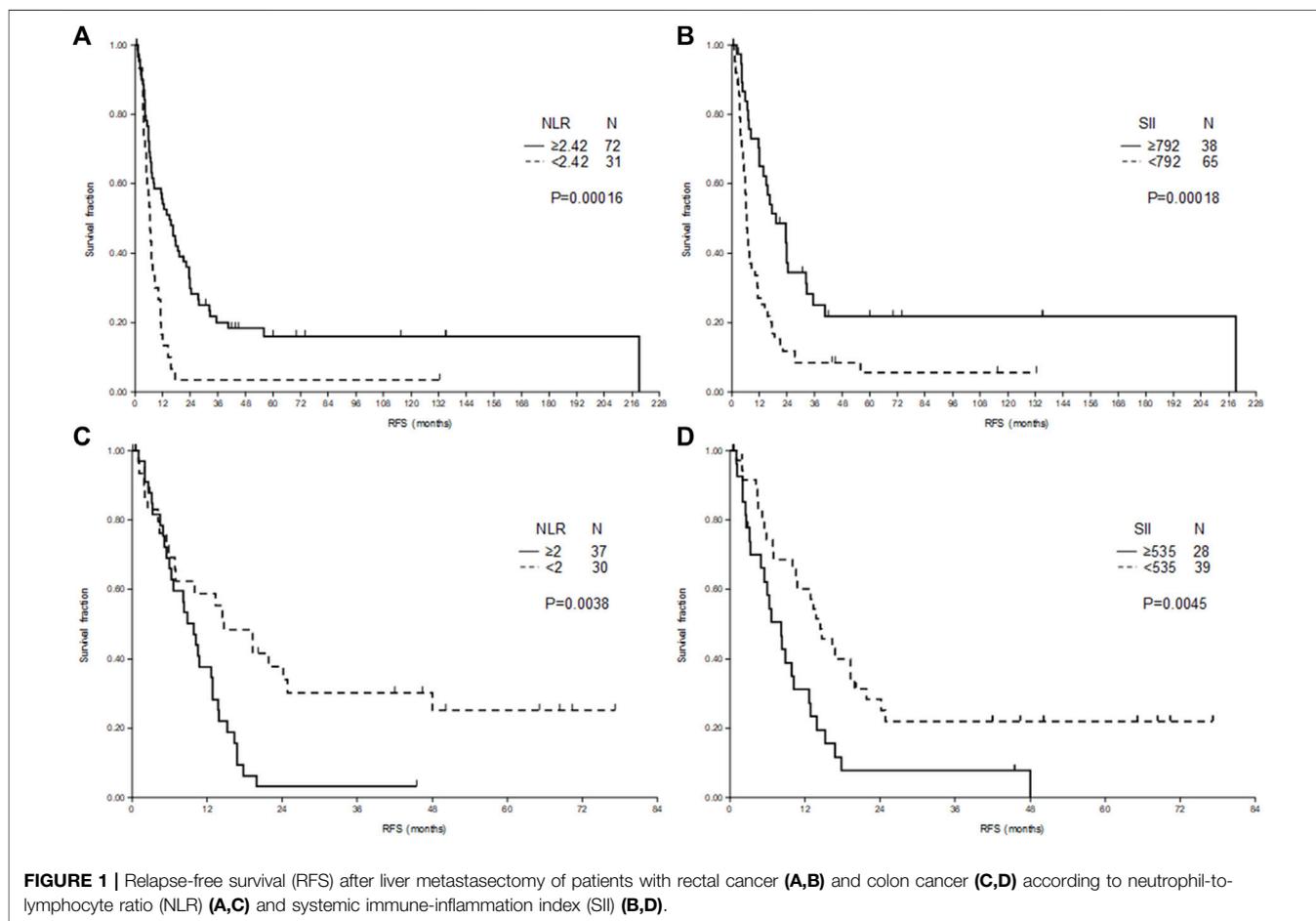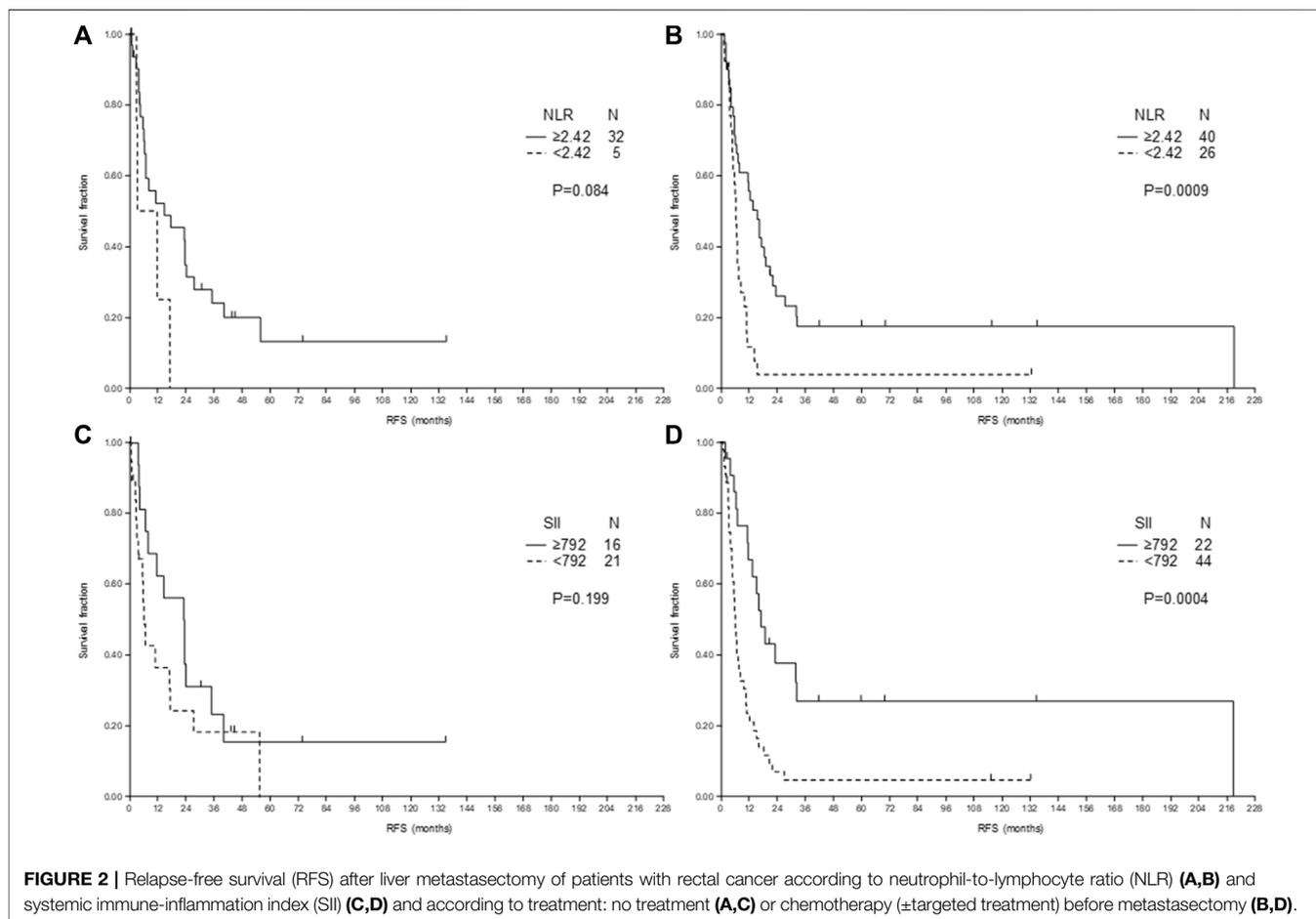**FIGURE 1 |** Relapse-free survival (RFS) after liver metastasectomy of patients with rectal cancer **(A,B)** and colon cancer **(C,D)** according to neutrophil-to-lymphocyte ratio (NLR) **(A,C)** and systemic immune-inflammation index (SII) **(B,D)**.

FIGURE 2 | Relapse-free survival (RFS) after liver metastasectomy of patients with rectal cancer according to neutrophil-to-lymphocyte ratio (NLR) **(A,B)** and systemic immune-inflammation index (SII) **(C,D)** and according to treatment: no treatment **(A,C)** or chemotherapy (±targeted treatment) before metastasectomy **(B,D)**.

RFS and OS were 8.6 (6.6–12.4) and 41.1 (35.2–48.6) months, respectively.

Primarily, the prognostic role of different parameters for RFS was tested. The parameters with significant effect ($p < 0.05$) or close to the significance level ($p < 0.1$) in univariate analysis or significant ($p < 0.05$) in multivariate analysis were included in **Tables 3** and **4**. To avoid multicollinearity some parameters had to be omitted, therefore NLR and SII were tested in two different multivariate model (Cox1 and Cox2). Both, NLR and SII proved to be independent markers of RFS in case of RLM, while only NLR was independent marker of RFS of CLM (**Tables 3**, **4**).

At 18 months only one patient (3%) remained free of relapse in the low NLR group of RLM, while in the high NLR group 28 patients (39%) were free of progression (**Figure 1A**). In contrast, at 18 months in low NLR group of CLM 50% of patients were free of relapse, while in the high NLR group all, but three patients progressed (**Figure 1C**). The number of patients free from relapse at 18 months for low and high SII of RLM was 10 (15%) and 19 (50%), respectively (**Figure 1B**) and for CLM was 15 (38%) and 3 (11%), respectively (**Figure 1D**).

Survival analysis of OS was conducted with the recalculated cut-off values for continuous variables. Besides, age, resection margin, GPT, platelet and WBC count, both NLR or SII proved to be significant predictors of OS in RLM (**Table 4**). In univariate

analysis for CLM nor NLR neither SII was statistically significant predictor of OS (**Table 3**).

As Hand et al. [17] reported that preoperative chemotherapy influenced the role of NLR in CRLM, we analyzed the RFS stratified according to treatment before metastasectomy. In case of RLM the longer RFS of high NLR (**Figures 2A,B**) or SII (**Figures 2C,D**) was present both for treated and untreated patients, however, in case of untreated patients the significance level was not reached because of relatively low number of cases (**Figure 2**).

Preoperative treatment also did not influence the effect of NLR and SII in case of CLM (data not shown).

Moreover, if the preoperative treatment was included as covariate in multivariate tests of PFS and OS its effect was non-significant. A very similar result was found for SII, and the presence or not of targeted treatment prior metastasectomy also did not influence the results for NLR or SII (data not shown).

DISCUSSION

There are some articles which analyzed the role of NLR in prediction of RFS after resection of liver metastases of CRC patients. In some of them the localization of primary tumor

TABLE 5 | Literature data about RFS according to primary colorectal cancer (CRC) localization after metastasectomy of liver-only metastases.

Primary tumor localization	Ref no	N	Colon %	Longer RFS NLR (SII) cut-off	p Univ	p Multiv	Preop %	Sync %	Postop %	Follow-up[a] months
CRC										
	3, 26	586	NA	>5	0.272	-	23	38	27	>6
	6	440	NA	<5	<0.001	<0.001	11	33	>33	24
	8	247	NA	<5	0.77	-	-	-	-	20
	13	169	NA	<2.5	0.09	0.347	100	72	76	34.6
	14	140	NA	<2.4	0.033	0.609	100	71	74	33
	16	92	NA	<5	0.047	0.022	76	0	100	27.1[b]
COLON cancer										
	25	98	100	<2.5	0.044	0.029	-	0	-	35.2[b]
	Our study	67	100	<2 (<535)	0.004 0.005	0.03 0.229	76	10	73	46.5
>50% of patients with COLON cancer										
	9	575	78	≤5	0.104	-	86	66	90	37
	11	452	56	<2.6 (≤517)	0.163 0.068	- -	63	53	74	28
	4	343	58	<2.5	0.017	-	58	49	-	49
	5	295	60	<2	<0.001?	0.001	19	78	37	63.2
	12	283	66	(≤0.0135)	0.003	0.005	51	58	77	35.4
	31	231	67	≤3	0.049	0.06	76	35	72	73.2
	30	197	62	<3	0.284	0.617	26	57	-	-
	15	183	57	<2.3	ns	-	100	85	78	36.3
	29	150	58	<4.63	0.017	0.452	39	63	73	36
	28	182	70	>3	0.939	-	19	65	91	32.5[b]
	27	128	79[c]	<1.71	ns	-	74	63	-	45
	32	130	54	≤5	0.044	0.03	16	38	26	44[b]
>50% of patients with RECTAL cancer										
	17	83	24	<1.94	0.026	0.006	29	100	100	-
	7, 33	174	46	<5	0.008	ns	42	0	39	36
RECTAL cancer										
	Our study	103	0	≥ 2.42 (≥ 792)	<0.001 <0.001	<0.001 0.002	64	10	72	59.8

CRC, colorectal cancer; multiv, multivariate; NA, not available; ns, non-significant; Postop, postoperative treatment; Preop, preoperative treatment; Ref, reference; RFS, relapse-free survival; SII, systemic immune-inflammation index; Sync, synchronous; univ, univariate.
[a]*Median.*
[b]*Average.*
[c]*Personal communication.*

was not reported or rectal tumors were studied together with the left sided colon tumors (**Table 5**).

In the few articles where the colon and rectum appears among patients' characteristics, no stratified test was performed based on localization. There is only one article where exclusively colon tumors were analyzed. To the best of our knowledge, the present study is the first investigation, which performed a separate analysis of rectal tumors. All relevant studies have been summarized in **Table 5**.

Since no study has been found where the high NLR would be a significant marker of longer RFS, in case of CLM the association between high NLR and shorter RFS is obvious. For RLM there are very few articles where patients with primary rectal cancer were in

the majority. [7, 33] examined the role of NLR in two articles (88% overlap with patient data), and found longer RFS and OS for low NLR, however their result was in correlation with the high frequency of postoperative infectious complications (77% of all postoperative complications) [33], which was lower in our study (29%, data not shown). Kim et al. [17] reported similar result, however, their study investigated only patients with synchronous surgery of primary and metastases and all patients received adjuvant chemotherapy. Moreover, there were far fewer preoperatively-treated patients in Kim's article (29%) than in ours (64%) or in Neal's reports (42%). Can the preoperative treatment alter the results? Interestingly, in **Table 3** of the six reports where colon cancer patients were in the majority, in five

where preoperative treatment was common (>60%), NLR was not significant for RFS. On the other hand, in four out of six reports with lower preoperative treatment frequency (<60%) the NLR was significant marker of RFS. Hand et al. [18] reported NLR as a non-significant or significant marker of OS (RFS was not studied) after liver metastasectomy of CRC patients (the location of primary tumor was not reported) depending whether the patients received or not preoperative chemotherapy, respectively. In our study, in contrast to the results of [18] in patients who received preoperative treatment the high NLR proved to be a very significant predictor of longer RFS. The discrepancy can be explained by different preoperative treatment (chemotherapy only in Hand's study vs chemotherapy+targeted therapy in >50% of patients in our study) and different location of the primary tumor, as we have seen that in case of rectum and colon, the role of NLR is completely different. In spite that the influence of chemo- and targeted therapies on NLR of patients with advanced CRC [34] and on immunologic characteristics of liver metastases of CRC tumors [35] was already reported, further studies should clarify the effect of preoperative treatment on NLR in case of liver metastases of colon and separately rectal cancer.

A publication studying SII in CRLM patients was reported by [11], but neither NLR (**Table 3**), nor SII was significant for RFS after metastasectomy. Another recent study by [12] found significantly longer survival for low SII, which proved to be independent predictor of RFS. Their results may differ from that ours because they investigated colon (56–66%) and rectal cancer patients together (**Table 3**).

Our results can also be an explanation why [4] concluded that an integrated cut-off value can't be determined for the preoperatively measured NLR in CRLM patients. The various colon/rectum ratio and different frequencies of preoperative treatment in reviewed studies made the results inconsistent. Therefore, it is important to primarily shed light on the difference between colon and rectum, and not to find a cut-off that could be used in the clinic.

The histologic, genetic, behavioral, etc. differences between colon and rectum tumors detailed by [22] and moreover the inflammation pattern (IL-6, CRP), which differs in colon and rectum tumors described by [23, 24] may explain our results.

McCoy et al. [36] studied the relation between the presence of stromal Foxp3 and RFS in rectal cancer patients after preoperative treatment and reported a significantly longer RFS ($p = 0.025$) for low Foxp3+ cell density. In another study, [37] demonstrated a strong negative correlation ($p = 0.006$) between stromal Foxp3+ infiltration and preoperative serum CRP levels in CRC patients. A study by [38] showed that high preoperative CRP levels were associated ($p < 0.001$) with high NLR in CRC patients. According to the above data it can be hypothesized that RLM patients with high NLR, which is associated with high CRP and subsequently with low Foxp3 levels may have longer RFS, as a consequence of a specific tumor immune microenvironment (TIME).

The longer RFS for colon in cases of low NLR may be explained by the presence of tumor-infiltrating lymphocytes (TILs). According to the results of [39] the low NLR in CRC patients (73% colon cancer) was significantly associated with higher TILs ($p = 0.005$) at the invasive margin of the tumor and a significantly longer DFS. CD8$^+$ TILs may account for antitumoral effect, resulting in an unfavorable tumor immune microenvironment (TIME) and longer RFS. [40] studied 94 liver metastases of CRCs (65% colon cancer) and the level of CD8$^+$ TILs. The distribution of high and low CD8$^+$ density was significantly different for rectal and colon origin. A high CD8$^+$ was more frequently observed for colon (54%) than for rectal origin (30%, $p = 0.027$). There was no difference between left and right sided colon. The RFS was significantly better ($p = 0.018$) for cases with high CD8$^+$. Similarly, [41] reported a similar result, that high CD8/CD3 ratio was significantly more frequent in intra- and peritumoral tissue of liver metastases of colon tumors (60% and 54%) than that of rectal tumors (37% and 35%, $p = 0.011$ and 0.035, respectively). The RFS for high CD8/CD3 was significantly longer ($p = 0.035$). Other results of studies investigating NLR on recurrence of primary colon or rectal tumors can be used for comparison only with reservations, because the CRLM differ from primary lesions in terms of immune cell infiltration [42, 43, 44].

In accordance with [45] the location of primary tumor did not influence the RFS after hepatic resection. Instead, NLR, which reflects TIME, can influence the survival in different manner depending on primary localization.

The limitation of this study consist in its retrospective character. The treatments administered after relapse (surgery, chemotherapy, etc) were not considered for OS analysis. The prognostic factor (RAS mutation) [2, 8] and other tumor markers (e.g. fibrinogen/albumin index [11] or prognostic nutrition index [5], etc.) were also not available. In spite of limitations, this study has the power to clarify the controversies, which still exists between NLR and RFS after liver resection of patients with CRLM.

Conclusion

The NLR and SII determined before surgery of liver metastases of patients with RLM proved to be an independent prognostic factor of RFS and OS in an opposite manner as for CLM where low NLR predicts longer RFS, namely NLR and SII above the cut-off level predicts longer RFS. Further prospective studies stratified according to primary tumor location and TIME may strengthen our findings.

DATA AVAILABILITY STATEMENT

The datasets presented in this article are not readily available due to patient privacy. Requests to access the datasets should be directed to the corresponding author.

ETHICS STATEMENT

The studies involving human participants were reviewed and approved by Ethical Committee of the institute and by the

Medical Research Council (21679-2/2016/EKU). The patients/participants provided their written informed consent to participate in this study.

AUTHOR CONTRIBUTIONS

Study concepts and design: NP, BB, EH, AP, TM. Data acquisition: NP, BB, EH, TM. Quality control of data and algorithms: NP, BB, EH, TM. Data analysis and interpretation: NP, BB, EH, AP, TM. Statistical analysis: BB. Manuscript preparation: NP, BB. Manuscript editing: NP, BB, EH, AP, TM. Manuscript revising critically for important intellectual content: AP, TM. Final approval of the manuscript: NP, BB, EH, AP, TM.

FUNDING

CONFLICT OF INTEREST

The authors declare that the research was conducted in the absence of any commercial or financial relationships that could be construed as a potential conflict of interest.

REFERENCES

1. Sung H, Ferlay J, Siegel RL, Laversanne M, Soerjomataram I, Jemal A, et al. Global Cancer Statistics 2020: GLOBOCAN Estimates of Incidence and Mortality Worldwide for 36 Cancers in 185 Countries. *CA A Cancer J Clin* (2021) 71:209–49. doi:10.3322/caac.21660

2. Liu W, Zhang W, Xu Y, Li Y-H, Xing B-C. A Prognostic Scoring System to Predict Survival Outcome of Resectable Colorectal Liver Metastases in This Modern Era. *Ann Surg Oncol* (2021) 28:7709–18. doi:10.1245/s10434-021-10143-6

3. Alabraba E, Ibrahim H, Olaru A, Cameron I, Gomez D, Group NHS. Retrospective Cohort Study of Statin Therapy Effect on Resected Colorectal Liver Metastases. *Wjgs* (2020) 12:34–44. doi:10.4240/wjgs.v12.i2.34

4. Dupré A, Jones RP, Diaz-Nieto R, Fenwick SW, Poston GJ, Malik HZ. Preoperative Leucocyte-Based Inflammatory Scores in Patients with Colorectal Liver Metastases: Can We Count on Them? *World J Surg* (2019) 43:1351–9. doi:10.1007/s00268-019-04914-2

5. Kim W-J, Lim T-W, Kang S-H, Park P-J, Choi S-B, Lee S-i., et al. Development and Validation of Novel Scoring System for the Prediction of Disease Recurrence Following Resection of Colorectal Liver Metastasis. *Asian J Surg* (2020) 43(2):438–46. doi:10.1016/j.asjsur.2019.06.001

6. Halazun KJ, Aldoori A, Malik HZ, Al-Mukhtar A, Prasad KR, Toogood GJ, et al. Elevated Preoperative Neutrophil to Lymphocyte Ratio Predicts Survival Following Hepatic Resection for Colorectal Liver Metastases. *Eur J Surg Oncol (Ejso)* (2008) 34:55–60. doi:10.1016/j.ejso.2007.02.014

7. Neal CP, Mann CD, Sutton CD, Garcea G, Ong SL, Steward WP, et al. Evaluation of the Prognostic Value of Systemic Inflammation and Socioeconomic Deprivation in Patients with Resectable Colorectal Liver Metastases. *Eur J Cancer* (2009) 45:56–64. doi:10.1016/j.ejca.2008.08.019

8. Western CE, Wiggans M, Aroori S, Bowles M, Stell D. PMO-089 Preoperative Neutrophil: Lymphocyte Ratio Is Not a Predictor of Outcome Following Hepatic Resection for Colorectal Metastases. *Gut* (2012) 61:2–A109. doi:10.1136/gutjnl-2012-302514b.89

9. Yamashita S, Sheth RA, Niekamp AS, Aloia TA, Chun YS, Lee JE, et al. Comprehensive Complication index Predicts Cancer-specific Survival after Resection of Colorectal Metastases Independent of RAS Mutational Status. *Ann Surg* (2017) 266:1045–54. doi:10.1097/SLA.0000000000002018

10. Lu Y, Xin D, Wang F. Predictive Significance of Preoperative Systemic Immune-Inflammation index Determination in Postoperative Liver Metastasis of Colorectal Cancer. *Ott* (2019) Vol. 12:7791–9. doi:10.2147/OTT.S223419

11. Wang Y-Y, Liu Z-Z, Xu D, Liu M, Wang K, Xing B-C. Fibrinogen-albumin Ratio index (FARI): a More Promising Inflammation-Based Prognostic Marker for Patients Undergoing Hepatectomy for Colorectal Liver Metastases. *Ann Surg Oncol* (2019) 26:3682–92. doi:10.1245/s10434-019-07586-3

12. Deng Y, Zhao Y, Qin J, Huang X, Wu R, Zhou C, et al. Prognostic Value of the C-Reactive Protein/Albumin Ratio and Systemic Immune-Inflammation Index for Patients with Colorectal Liver Metastasis Undergoing Curative Resection. *Pathol Oncol Res* (2021) 27:633480. doi:10.3389/pore.2021.633480

13. Giakoustidis A, Neofytou K, Khan AZ, Mudan S. Neutrophil to Lymphocyte Ratio Predicts Pattern of Recurrence in Patients Undergoing Liver Resection for Colorectal Liver Metastasis and Thus the Overall Survival. *J Surg Oncol* (2015) 111:445–50. doi:10.1002/jso.23845

14. Neofytou K, Smyth EC, Giakoustidis A, Khan AZ, Cunningham D, Mudan S. Elevated Platelet to Lymphocyte Ratio Predicts Poor Prognosis after Hepatectomy for Liver-Only Colorectal Metastases, and it Is superior to Neutrophil to Lymphocyte Ratio as an Adverse Prognostic Factor. *Med Oncol* (2014) 31:239. doi:10.1007/s12032-014-0239-6

15. Mao R, Zhao J-J, Bi X-Y, Zhang Y-F, Li Z-Y, Huang Z, et al. A Low Neutrophil to Lymphocyte Ratio before Preoperative Chemotherapy Predicts Good Outcomes after the Resection of Colorectal Liver Metastases. *J Gastrointest Surg* (2019) 23:563–70. doi:10.1007/s11605-018-3796-8

16. Zhang Y, Peng Z, Chen M, Liu F, Huang J, Xu L, et al. Elevated Neutrophil to Lymphocyte Ratio Might Predict Poor Prognosis for Colorectal Liver Metastasis after Percutaneous Radiofrequency Ablation. *Int J Hyperthermia* (2012) 28:132–40. doi:10.3109/02656736.2011.654374

17. Kim H, Jung HI, Kwon SH, Bae SH, Kim HC, Baek M-J, et al. Preoperative Neutrophil-Lymphocyte Ratio and CEA Is Associated with Poor Prognosis in Patients with Synchronous Colorectal Cancer Liver Metastasis. *Ann Surg Treat Res* (2019) 96:191–200. doi:10.4174/astr.2019.96.4.191

18. Hand F, Ryan EJ, Harrington C, Durand M, Maguire D, O'Farrelly C, et al. Chemotherapy and Repeat Resection Abrogate the Prognostic Value of Neutrophil Lymphocyte Ratio in Colorectal Liver Metastases. *Hpb* (2020) 22:670–6. doi:10.1016/j.hpb.2019.09.003

19. Hamada T, Ishizaki H, Haruyama Y, Hamada R, Yano K, Kondo K, et al. Neutrophil-to-lymphocyte Ratio and Intratumoral CD45RO-Positive T Cells as Predictive Factors for Longer Survival of Patients with Colorectal Liver Metastasis after Hepatectomy. *Tohoku J Exp Med* (2020) 251:303–11. doi:10.1620/tjem.251.303

20. Kishi Y, Kopetz S, Chun YS, Palavecino M, Abdalla EK, Vauthey J-N. Blood Neutrophil-To-Lymphocyte Ratio Predicts Survival in Patients with Colorectal Liver Metastases Treated with Systemic Chemotherapy. *Ann Surg Oncol* (2009) 16:614–22. doi:10.1245/s10434-008-0267-6

21. Komlósi V, Hitre E, Pap É, Adleff V, Réti A, Székely É, et al. SHMT1 1420 and MTHFR 677 Variants Are Associated with Rectal but Not colon Cancer. *BMC Cancer* (2010) 10:525. doi:10.1186/1471-2407-10-525

22. Paschke S, Jafarov S, Staib L, Kreuser E-D, Maulbecker-Armstrong C, Roitman M, et al. Are colon and Rectal Cancer Two Different Tumor Entities? A Proposal to Abandon the Term Colorectal Cancer. *Ijms* (2018) 19:2577. doi:10.3390/ijms19092577

23. Slattery ML, Wolff RK, Herrick JS, Caan BJ, Potter JD. IL6 Genotypes and colon and Rectal Cancer. *Cancer Causes Control* (2007) 18:1095–105. doi:10.1007/s10552-007-9049-x

24. Slattery ML, Curtin K, Poole EM, Duggan DJ, Samowitz WS, Peters U, et al. Genetic Variation in C-Reactive Protein in Relation to colon and Rectal Cancer Risk and Survival. *Int J Cancer* (2011) 128:2726–34. doi:10.1002/ijc.25721

25. Chang Z, Zheng J, Ma Y, Zhao J, Wang C, Liu Z. The Neutrophil-To-Lymphocyte Ratio as a Predictor for Recurrence of Colorectal Liver Metastases Following Radiofrequency Ablation. *Med Oncol* (2014) 31:855. doi:10.1007/s12032-014-0855-1

26. Sanyal S, Alabraba E, Ibrahim H, Olaru A, Cameron I, Gomez D. ACE Inhibitor Therapy Does Not Influence the Survival Outcomes of Patients with Colorectal Liver Metastases Following Liver Resection. *J Gastrointest Canc* (2021) 52:106–12. doi:10.1007/s12029-019-00350-6

27. Cimino MM, Donadon M, Giudici S, Sacerdote C, Di Tommaso L, Roncalli M, et al. Peri-tumoural CD3+ Inflammation and Neutrophil-To-Lymphocyte Ratio Predict Overall Survival in Patients Affected by Colorectal Liver Metastases Treated with Surgery. *J Gastrointest Surg* (2020) 24:1061–70. doi:10.1007/s11605-019-04458-9

28. Liu Y-W, Lu C-C, Chang C-D, Lee K-C, Chen HH, Yeh WS, et al. Prognostic Value of Sarcopenia in Patients with Colorectal Liver Metastases Undergoing Hepatic Resection. *Sci Rep* (2020) 10:6459. doi:10.1038/s41598-020-63644-x

29. Peng J, Li H, Ou Q, Lin J, Wu X, Lu Z, et al. Preoperative Lymphocyte-To-Monocyte Ratio Represents a superior Predictor Compared with Neutrophil-To-Lymphocyte and Platelet-To-Lymphocyte Ratios for Colorectal Liver-Only Metastases Survival. *Ott* (2017) Vol. 10:3789–99. doi:10.2147/OTT.S140872

30. Taniai T, Haruki K, Hamura R, Fujiwara Y, Furukawa K, Gocho T, et al. The Prognostic Significance of C-Reactive Protein-To-Lymphocyte Ratio in Colorectal Liver Metastases. *J Surg Res* (2021) 258:414–21. doi:10.1016/j.jss.2020.08.059

31. Verter E, Berger Y, Perl G, Peretz I, Tovar A, Morgenstern S, et al. Neutrophil-to-lymphocyte Ratio Predicts Recurrence Pattern in Patients with Resectable Colorectal Liver Metastases. *Ann Surg Oncol* (2021) 28:4320–9. doi:10.1245/s10434-021-10000-6

32. Zeman M, Maciejewski A, Półtorak S, Kryj M. Evaluation of Outcomes and Treatment Safety of Patients with Metastatic Colorectal Cancer to the Liver with Estimation of Prognostic Factors. *Pol Przegl Chir* (2013) 85:333–9. doi:10.2478/pjs-2013-0050

33. Neal CP, Mann CD, Garcea G, Briggs CD, Dennison AR, Berry DP. Preoperative Systemic Inflammation and Infectious Complications after Resection of Colorectal Liver Metastases. *Arch Surg* (2011) 146:471–8. doi:10.1001/archsurg.2011.50

34. Nemoto T, Endo S, Isohata N, Takayanagi D, Nemoto D, Aizawa M, et al. Change in the Neutrophil-To-Lymphocyte Ratio during Chemotherapy May Predict Prognosis in Patients with Advanced or Metastatic Colorectal Cancer. *Mol Clin Oncol* (2021) 14:107. doi:10.3892/mco.2021.2269

35. Eefsen RL, Engelholm L, Alpizar-Alpizar W, Van den Eynden GGE, Vermeulen PB, Christensen IJ, et al. Inflammation and uPAR-Expression in Colorectal Liver Metastases in Relation to Growth Pattern and Neo-Adjuvant Therapy. *Cancer Microenvironment* (2015) 8:93–100. doi:10.1007/s12307-015-0172-z

36. McCoy MJ, Hemmings C, Miller TJ, Austin SJ, Bulsara MK, Zeps N, et al. Low Stromal Foxp3+ Regulatory T-Cell Density Is Associated with Complete Response to Neoadjuvant Chemoradiotherapy in Rectal Cancer. *Br J Cancer* (2015) 113:1677–86. doi:10.1038/bjc.2015.427

37. Gunnarsson U, Strigård K, Edin S, Gkekas I, Mustonen H, Kaprio T, et al. Association between Local Immune Cell Infiltration, Mismatch Repair Status and Systemic Inflammatory Response in Colorectal Cancer. *J Transl Med* (2020) 18:178. doi:10.1186/s12967-020-02336-6

38. Kubo H, Murayama Y, Arita T, Kuriu Y, Nakanishi M, Otsuji E. The Prognostic Value of Preoperative Neutrophil-To-Lymphocyte Ratio in Colorectal Cancer. *World J Surg* (2016) 40:2796–802. doi:10.1007/s00268-016-3595-x

39. Pine JK, Morris E, Hutchins GG, West NP, Jayne DG, Quirke P, et al. Systemic Neutrophil-To-Lymphocyte Ratio in Colorectal Cancer: the Relationship to Patient Survival, Tumour Biology and Local Lymphocytic Response to Tumour. *Br J Cancer* (2015) 113:204–11. doi:10.1038/bjc.2015.87

40. Xiao B, Peng J, Wang Y, Deng Y, Ou Q, Wu X, et al. Prognostic Value of Tumor Infiltrating Lymphocytes Combined with PD-L1 Expression for Patients with Solitary Colorectal Cancer Liver Metastasis. *Ann Transl Med* (2020) 8:1221. doi:10.21037/atm-20-2762a

41. Peng J, Wang Y, Zhang R, Deng Y, Xiao B, Ou Q, et al. Immune Cell Infiltration in the Microenvironment of Liver Oligometastasis from Colorectal Cancer: Intratumoural CD8/CD3 Ratio Is a Valuable Prognostic index for Patients Undergoing Liver Metastasectomy. *Cancers* (2019) 11:1922. doi:10.3390/cancers11121922

42. Halama N, Spille A, Lerchl T, Brand K, Herpel E, Welte S, et al. Hepatic Metastases of Colorectal Cancer Are rather Homogeneous but Differ from Primary Lesions in Terms of Immune Cell Infiltration. *Oncoimmunology* (2013) 2:e24116. doi:10.4161/onci.24116

43. Lin H-C, Shao Q, Liang J-Y, Wang Y, Zhang H-Z, Yuan Y-F, et al. Primary Tumor Immune Score Fails to Predict the Prognosis of Colorectal Cancer Liver Metastases after Hepatectomy in Chinese Populations. *Ann Transl Med* (2021) 9:310. doi:10.21037/atm-20-4932

44. Ahtiainen M, Elomaa H, Väyrynen JP, Wirta E-V, Kuopio T, Helminen O, et al. Immune Contexture of MMR-Proficient Primary Colorectal Cancer and Matched Liver and Lung Metastases. *Cancers* (2021) 13:1530. doi:10.3390/cancers13071530

45. Wang K, Xu D, Yan X-L, Poston G, Xing B-C. The Impact of Primary Tumour Location in Patients Undergoing Hepatic Resection for Colorectal Liver Metastasis. *Eur J Surg Oncol* (2018) 44:771–7. doi:10.1016/j.ejso.2018.02.210

NTRK Fusions in a Sarcomas Series: Pathology, Molecular and Clinical Aspects

Vasiliki Siozopoulou[1,2]*, Elly Marcq[2], Koen De Winne[1], Koen Norga[3], Gertjan Schmitz[4], Valerie Duwel[5], Philippe Delvenne[6], Evelien Smits[2,7] and Patrick Pauwels[1,2]

[1]Department of Pathology, Antwerp University Hospital, Edegem, Belgium, [2]Center for Oncological Research (CORE), Integrated Personalized and Precision Oncology Network (IPPON), University of Antwerp, Wilrijk, Belgium, [3]Department of Pediatrics, Antwerp University Hospital, Edegem, Belgium, [4]Department of Orthopaedics, Hospital of Klina, Antwerp, Belgium, [5]Department of Pathology, Hospital of Klina, Antwerp, Belgium, [6]Department of Anatomopathology, CHU Sart Tilman, Liège, Belgium, [7]Center for Cell Therapy and Regenerative Medicine, Antwerp University Hospital, Edegem, Belgium

Targeting molecular alterations has been proven to be an inflecting point in tumor treatment. Especially in recent years, inhibitors that target the tyrosine receptor kinase show excellent response rates and durable effects in all kind of tumors that harbor fusions of one of the three neurotrophic tyrosine receptor kinase genes (*NTRK1*, *NTRK2* and *NTRK3*). Today, the therapeutic options in most metastatic sarcomas are rather limited. Therefore, identifying which sarcoma types are more likely to harbor these targetable *NTRK* fusions is of paramount importance. At the moment, identification of these fusions is solely based on immunohistochemistry and confirmed by molecular techniques. However, a first attempt has been made to describe the histomorphology of *NTRK*-fusion positive sarcomas, in order to pinpoint which of these tumors are the best candidates for testing. In this study, we investigate the immunohistochemical expression of pan-TRK in 70 soft tissue and bone sarcomas. The pan-TRK positive cases were further investigated with molecular techniques for the presence of a *NTRK* fusion. Seven out of the 70 cases showed positivity for pan-TRK, whereas two of these seven cases presented an *NTRK3* fusion. Further analysis of the fused sarcomas revealed some unique histological, molecular and clinical findings. The goal of this study is to expand the histomorphological spectrum of the *NTRK*-fused sarcomas, to identify their fusion partners and to correlate these parameters with the clinical outcome of the disease. In addition, we evaluated the immunohistochemical expression pattern of the pan-TRK and its correlation with the involved *NTRK* gene.

Keywords: sarcoma, prognosis, NTRK fusion, TRK immunohistochemistry, NTRK fusion partner, histology

INTRODUCTION

Soft tissue and bone tumors are a very heterogenous group of neoplasms which makes prognosis difficult to assess. Moreover, given their rarity of occurrence, standardization of diagnostic criteria and precise treatment protocols is challenging. The majority of localized sarcomas are treated with excision mostly followed by adjuvant radiotherapy to control local recurrence [1, 2]. Few sarcoma types are chemo-sensitive, such as rhabdomyosarcoma, osteosarcoma and Ewing sarcoma [2, 3]. In the metastatic setting, the 5-year overall survival rates do not exceed 20%, highlighting that effective

treatment of advanced disease remains a challenge. There is clear need for new therapeutic options in advanced sarcomas [4].

Some of the molecular alterations that are found in tumors are druggable and this has been a significant turning point in cancer treatment. One of the most important representatives are tyrosine kinase inhibitors (TKI) that are used for the treatment of diverse tumor types, such as imatinib for gastrointestinal stromal tumors (GIST) [5]. Unfortunately, today most of the oncogenic driver alterations remain undruggable.

Very recently, it has been proven that tumors with fusions of one of the three neurotrophic tyrosine receptor kinase genes (*NTRK1*, *NTRK2* and *NTRK3*) can be treated with tyrosine receptor kinase (TRK) -inhibitors. The first generation TRK-inhibitors, larotrectinib and entrectinib [6], show excellent response rates and durable effects in tumors that harbor fusion of one of the *NTRK* genes, regardless of tumor type or site of origin. The adverse events are well tolerated. Still, a major obstacle for those inhibitors is the development of resistance. Therefore, new generation TRK-inhibitors are developed, such as LOXO-195 and repotrectinib [7, 8].

Despite the promising results of TRK-inhibition, *NTRK* fusions are rare genetic events. Among sarcomas, infantile fibrosarcomas show fusions of the *NTRK3* gene in more than 90% of the cases [9]. The rates of *NTRK* fusions in the remaining sarcoma types are unfortunately very low. Moreover, no clear morphologic criteria are established for the recognition of the *NTRK*-fused sarcomas. A NTRK fusion has to be demonstrated by means of molecular analysis. Immunohistochemistry can be performed as an enrichment strategy to select tumors for subsequent molecular analysis In a previous publication, we suggested an algorithm for determining which sarcomas are more likely to carry this fusion [10].

In this study, we investigated the expression of the pan-TRK antibody in different types of soft tissue and bone tumors by immunohistochemistry and we correlated the expression of the positive cases with the presence of *NTRK* fusions. Furthermore, we summarized the clinicopathological characteristics, in an attempt to give more information about the identification of these tumors, in conjunction with the cases that are described in the literature.

MATERIALS AND METHODS

Tissue Samples

Archival formalin-fixed paraffin embedded (FFPE) tissue samples from 70 patients with soft tissue and bone tumors were retrieved from the Department of Pathology at the Antwerp University Hospital. The tissue samples were collected from biopsy material as well as excision specimens. The material was not older than 5 years, to avoid loss of immunoreactivity and to obtain quality material for the additional molecular analysis. The biopsies were fixed in 4% formaldehyde for up to 12 h while the excision samples were fixed for up to 32 h.

Inclusion criteria where all locally aggressive and malignant soft tissue tumors, except infantile fibrosarcoma, given their know molecular status with *NTRK3* fusions [9]. This was the only

TABLE 1 | Tumor characteristics.

Characteristics	Number (n)
Gender	
Male	46
Female	24
Tumor location	
Bone	19
Deep soft tissue extremities	17
Deep soft tissue trunk and back	5
Deep soft tissue head and neck	4
Skin and subcutaneous fat tissue	12
Abdomen	6
Mediastinum	5
Retroperitoneum	2
Histological type	
Chondrosarcoma	10
Ewing sarcoma	3
Osteosarcoma	5
Angiosarcoma	7
Kaposi sarcoma	8
Leiomyosarcoma	5
Liposarcoma	9
Myxofibrosarcoma	5
Rhabdomyosarcoma	3
Synovial sarcoma	3
Sarcoma NOS	12
Grade	
High grade	48
Low grade	18
Not known	4
Local or metastatic disease	
Local aggressive	15
Monometastatic disease	11
Multimetastatic disease	13
No local recurrence or metastatic disease reported	31
Oncogenic mechanism	
Oncogenic mechanism known	14
Not known oncogenic mechanism	48
Oncogenic virus (HIV)	8
Survival	
Alive	42
Death from disease	22
Death from other cause	6
Medical history	
No medical history	56
HIV	5
Lymphoma and HIV	1
Lymphoma and other tumors	1
Epithelial tumor	5
Melanoma	1
Syndrome	1
Therapy	
Excision only	28
Excision + adjuvant therapy[a]	28
Neoadjuvant CHMT	12
Not known	2

Abbreviations: n, number; NOS, not otherwise specified.
[a]*Adjuvant therapy was either chemotherapy or radiotherapy or immunotherapy or targeted therapy or protontherapy or their combinations.*

exclusion criterion, while all age groups and ethnicities were incorporated.

All methods were carried out in accordance with relevant guidelines and regulations.

TABLE 2 | Evaluation of immunohistochemical positivity for pan-TRK according to H-score.

Tumor Type	Intensity of Staining	Percentage of positive tumor cells (%)	H-score	Subcellular Staining patterns
Epithelioid angiosarcoma	3+	10	30	Cytoplasmic
Alveolar rhabdomyosarcoma	3+	20	60	Cytoplasmic
Osteosarcoma	3+	40	120	Cytoplasmic
MPNST	2+	15	30	Cytoplasmic
Alveolar rhabdomyosarcoma	3+	85	255	Cytoplasmic
Sarcoma, NOS	1+	90	90	Nuclear
Sarcoma NOS	3+	100	300	Cytoplasmic

Abbreviations: H-score, Histoscore; MPNST, malignant peripheral nerve seath tumor; NOS, not otherwise specified.

TABLE 3 | Summary of clinical, immunohistochemical, and molecular data.

Pt	Age	Sex	Diagnosis	Location	Fusion	IHC	
						Pattern	Intensity
1	10	M	Low grade spindle cell tumor	Skin, finger	*ETV6-NTRK3*	Nuclear	Weak
2	19	M	High grade spindle cell tumor	Deep soft tissue of the lower leg	*TFG-NTRK3*	Cytoplasmic	Strong

Abbreviations: IHC, immunohistochemistry; Pt, patient; M, male.

As it was a retrospective study on archival material, no informed consent of the patients could be obtained.

We received approval by the Ethics Committee of the Antwerp University Hospital/University of Antwerp (EC 18/45/517) to use historical samples without additional informed consent from the patients.

Immunohistochemistry

As a reference method we used the VENTANA pan-TRK assay (clone EPR17341) performed according to the instructions of the vendor on a Benchmark Ultra (Ventana Medical Systems, Tucson, AZ, United States). This widely used EPR17341 clone is reactive with a conserved proprietary peptide sequence from the C-terminus of TRKA, TRKB and TRKC, and is therefore reactive with any of the oncogenic TRK proteins, although a lesser sensitivity for *NTRK3* fusions is described.

We looked at the expression of TRK in the tumor cells. All stained slides were assessed and scored independently by two pathologist (VS. and PP). Tumors were considered positive if ≥1% of tumor cells exhibit staining at any intensity above background [11, 12]. In addition, the different subcellular staining patterns (cytoplasmic, membranous, nuclear and peri-nuclear) were all considered to be positive. Moreover, for the evaluation of the immunohistochemical staining we also used the modified Histoscore (H-score) [13]. This is a semiquantitative assessment of both intensity and staining and the percentage of positive cells.

Evaluation of the slides was based on scanned slides at a Philips platform.

Molecular Techniques

The *NTRK* fusion status and possible fusion partner of the samples was confirmed by next generation sequencing (NGS). Targeted RNA-based NGS was conducted with the Oncomine Focus Assay (OFA) panel (Thermo Fisher Scientific, San Francisco, CA, United States) on an S5 instrument, according to the manufacturer's recommendations.

RESULTS

Pan-TRK Immunohistochemical Expression in Diverse Tumor Types and Correlation With *NTRK* Fusions

We investigated the immunohistochemical expression of TRK in diverse types of soft tissue and bone tumors. Tumor characteristics are summarized in **Table 1**.

Among the different tumor types, seven tumors (10%) displayed immunohistochemical positivity for pan-TRK in the tumor cells. The remaining 63 tumors showed no pan-TRK expression. The immunohistochemical expression of these seven cases according to the H-score is illustrated in **Table 2**.

Among the positive tumors there were two alveolar rhabdomyosarcomas, one epithelioid angiosarcoma, one malignant peripheral nerve sheath tumor (MPNST), one osteosarcoma and two spindle cell sarcomas, not otherwise specified (NOS). All but one were reported as high grade tumors. The low-grade tumor was a spindle cell sarcoma NOS.

NGS RNA analysis was performed in all positive cases. Two out of these (nearly 28,6% among the pan-TRK positive cases and 2,86% among all tumors included in this study) showed an *NTRK* fusion, while the rest did not. The characteristics of the tumors with the fusion are summarized in **Table 3**.

A Low-Grade Spindle Cell Tumor With an *ETV6-NTRK3* Fusion

The first case concerned a 10 year-old male with a cutaneous tumor on his finger. The duration of the lesion could not be
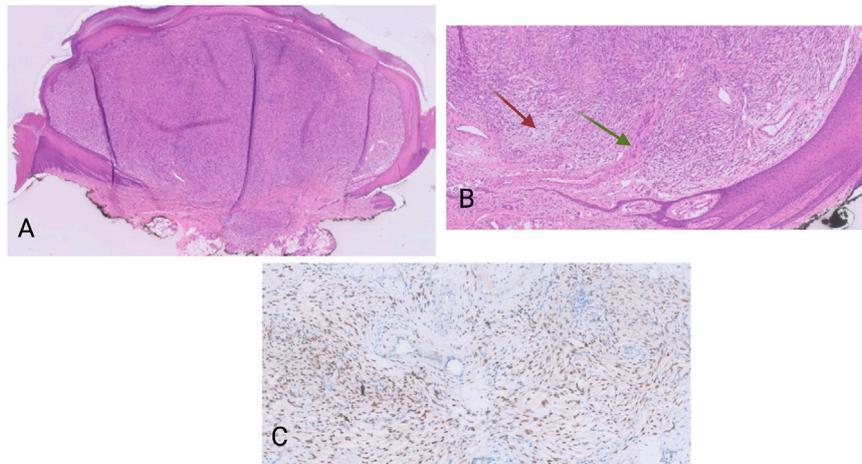
FIGURE 1 | (A) HE, 20×. Polypoid dermal spindle cell proliferation. (B) HE, 100×. The tumors display a fascicular growth pattern. There are myxoid areas (red arrow), as well as vessel walls with presence of multinucleated cells (green arrow). (C) Pan-TRK nuclear positivity in the tumor cells. Pan-TRK assay (clone EPR17341), DAB, magnification ×200.

determined accurately but was estimated by the parents to be six to seven years. No previous operations or other therapies were mentioned.

Macroscopically, there was a polypoid lesion that measured approximately 5 mm (Figure 1A). Microscopy revealed a dermal spindle cell proliferation. The cells were arranged in a fascicular pattern. There was some variation in size and shape but there was no striking pleiomorphism. Mitotic activity was present (up to 5 mitosis/10 high power fields), but no necrosis was perceived. There was local mucin deposition between tumor cells. Finally, some blood vessels within the tumor showed hyalinization and presence of multinucleated cells in the vessel wall (Figure 1B). A wide range of immunohistochemical stainings were performed, such as CD68, SMA, desmin, EMA, mucin 4, SOX10, S100 and CD34, from which we could not deduce a specific differentiation line of the tumor cells. More specifically, CD68 and SMA stained focally, while the rest was negative. Moreover, immunohistochemical examination for Anaplastic Lymphoma Kinase (ALK) proved to be negative.

The tumor was located in the dermis with focal extension in to the subcutis. The lesion was completely removed but with narrow margins.

Nuclear positivity of the tumor cells for pan-TRK was noticed on immunohistochemistry (Figure 1C). The NGS analysis revealed an *ETV6-NTRK3* fusion (1,328 reads out of a total of 52,464 mapped fusion panel reads). The patient underwent positron emission tomography–computed tomography (PET-CT) but no metastatic lesions could be detected. No signs of local recurrence or disseminations were noticed almost a year after the excision.

A High-Grade Spindle Cell Tumor With a *TFG-NTRK3* Fusion

The second case concerned a 19 years-old man. The patient presented with a tumor on the antero-external side of the right tibia dating for several months. The tumor was located intramuscularly with extension to the subcutaneous fat tissue. Three months after the first examination, the tumor was excised. Macroscopically, an almost 14 cm large mass was seen. Microscopy revealed a multinodular lesion that was partially surrounded by a thin capsule. Spindle-shaped tumor cells with a fascicular growth pattern were noticed. Thickened collagen bundles were seen in between tumor cells, as well as areas with calcification and ossification (Figure 2A). There was high mitotic activity and also necrosis. After extensive immunohistochemical analysis, including antibodies against pan-cytokeratin, S100, CD34, beta-catenin, SMA, desmin, CD10 and MDM2, the tumor was classified as high-grade spindle cell sarcoma NOS. Again here, immunohistochemistry for S100 and CD34 was negative. Despite the fact that the tumor was completely excised, given its high-grade, the patient received adjuvant radiotherapy. Four months after the excision the patient developed multiple lung metastases, which were treated with radiotherapy. Immunohistochemistry on the material from the first excision revealed a cytoplasmatic positivity for pan-TRK in the majority of the tumor cells (Figure 2B). NGS analysis showed the presence of a *TFG-NTRK3* fusion (424 reads out of a total of 2,668 mapped fusion panel reads). The patient started with larotrectinib at a dose of 100 mg twice daily. The patient was still alive a month after the initiation of treatment and was then lost from follow-up.

DISCUSSION

TRK is a member of the tyrosine kinase family, predominantly known for its role in neuronal cell differentiation. There are three receptors (TRK A, B, and C) encoded by the three *NTRK* genes, *NTRK 1*, *2*, and *3*, respectively [9]. TRK is a transmembrane receptor, that upon its binding with a ligand, undergoes
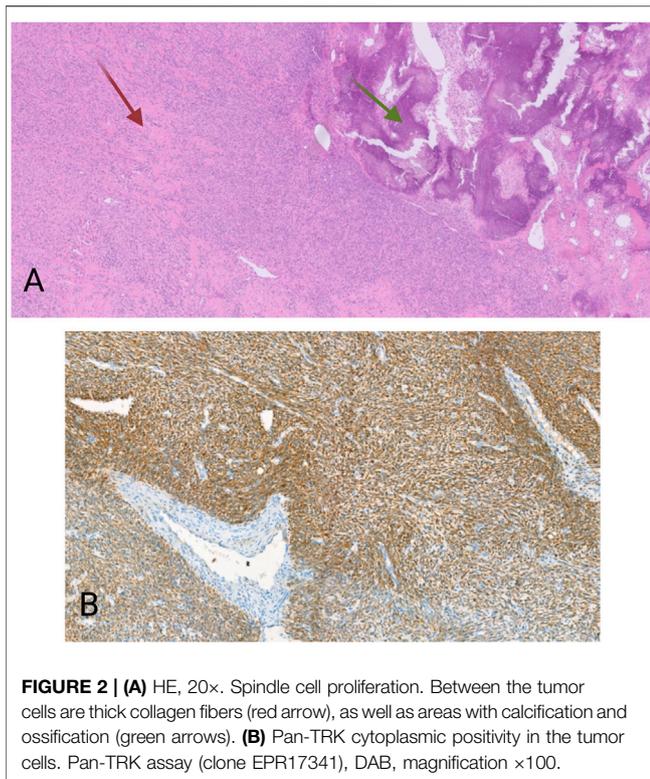
FIGURE 2 | (A) HE, 20×. Spindle cell proliferation. Between the tumor cells are thick collagen fibers (red arrow), as well as areas with calcification and ossification (green arrows). (B) Pan-TRK cytoplasmic positivity in the tumor cells. Pan-TRK assay (clone EPR17341), DAB, magnification ×100.

dimerization. TRK dimerization leads to activation of three signaling pathways: the PI3K/AKT, the MAPK and the PLCγ pathway, all of which impact cell proliferation, cell growth, and cell survival [14] (**Figure 3**). Fusion of one of the three *NTRK* genes leads to ligand independent constitutive activation of the TRK signaling pathway that can induce uncontrolled cell growth and proliferation, neo-angiogenesis and cell migration [15].

NTRK fusions are highly actionable driver alterations that are found across many different tumor types. TRK inhibitors are very active against tumors that harbor one of the *NTRK* fusions. These drugs have a high response rate and durable responses [14, 15]. Hence, detection of *NTRK*-fused tumors can have important therapeutic consequences for the patient.

With regard to sarcomas, Infantile Fibrosarcoma (IF) shows the *ETV6-NTRK3* fusion in more than 90% of the cases [9]. No other specific sarcoma types are corelated with the presence of fusions of one of the *NTRK* genes. Moreover, sarcomas with an *NTRK* fusion show no other actionable alterations within the same tumor [16]. Thus, sarcomas with a known driver oncogenic alteration, as for instance alveolar rhabdomyosarcoma or synovial sarcoma, are less likely to harbor fusions of one of the three *NTRK* genes. This is in line with our results, where the two *NTRK*-fused tumors where not of a histologic type that carries a specific genetic alteration. Consequently, testing for *NTRK* fusions should be prioritized in sarcomas with high *NTRK* fusion frequency, while testing in sarcomas with a canonical oncogenic alteration might not have any diagnostic or therapeutic value [17].

Currently, correct identification of *NTRK*-fused sarcomas is only possible by means of molecular techniques. However,

recently there have been attempts to describe the morphological features of tumors carrying this molecular alteration. To date, various morphological features have been described in *NTRK*-fused sarcomas, the most consistent being spindle cell morphology [10]. Growth patterns attributed to these tumors are summarized in our previous review[10] and include lipofibromatosis-like [18, 19], hemangiopericytoma-like [20], fibrosarcoma-like [21–23], neoplasms resembling inflammatory myofibroblastic tumors [24, 25] and dermatofibrosarcoma protuberans-like [26]. Moreover, spindle cell tumors with myxoid features [27] as well as characteristic blood vessels with perivascular thick collagen deposition [28] are also reported.
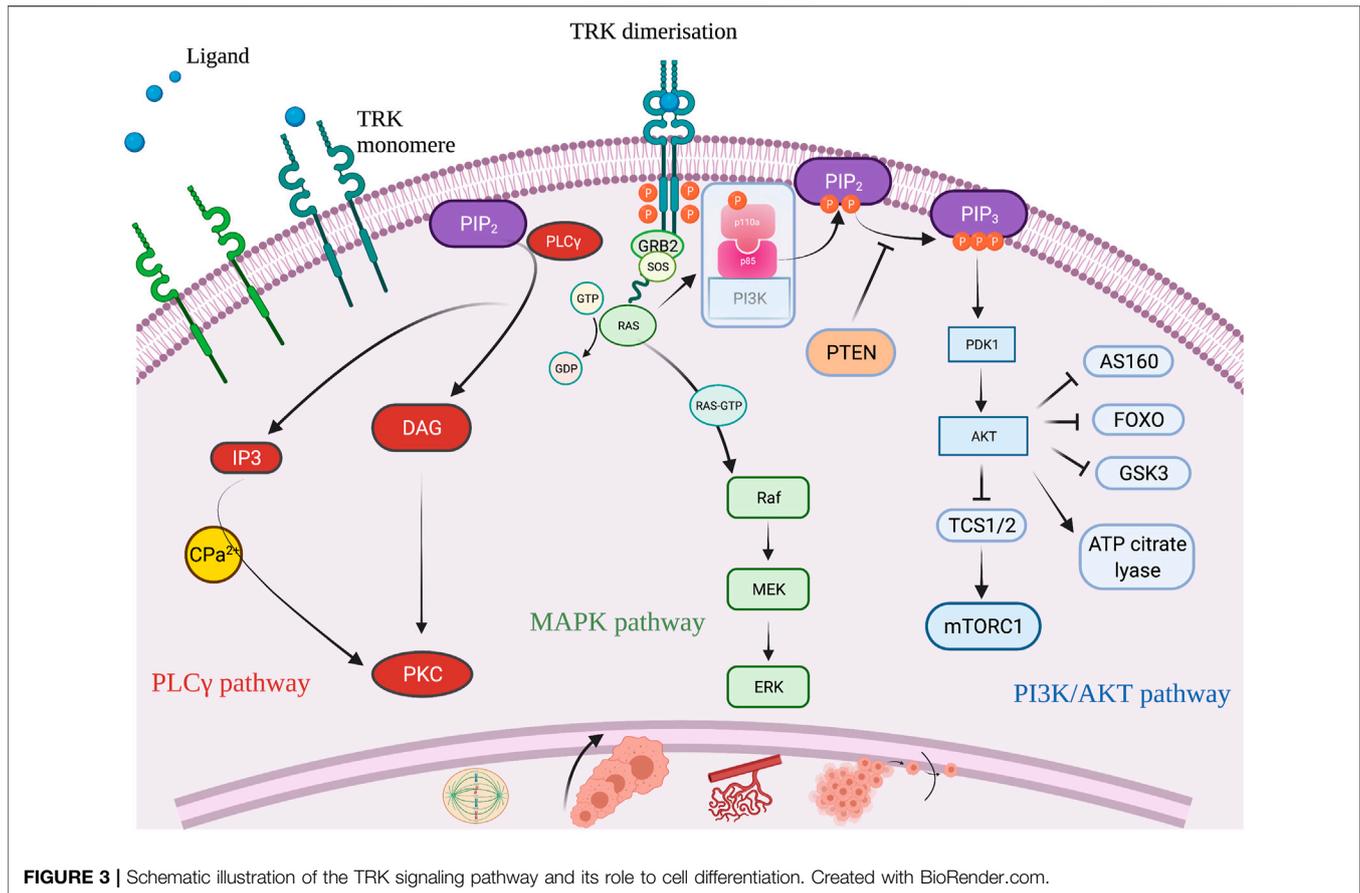
On a molecular basis, *NTRK* fusions are the driving oncogenic mechanisms, with fusions of the *NTRK3* gene being the most frequent, followed by fusions of the *NTRK1* gene, while only a few show *NTRK2* fusions [10].

In our case, both tumors with *NTRK* fusion presented with a spindle cell morphology. None of the tumors showed a characteristic growth pattern like those previously mentioned. It is suggested that the majority of the *NTRK*-rearranged mesenchymal neoplasms display a combination of morphological patterns, which could be a helpful clue in tumor recognition [29]. Indeed, one of the tumors that we present also showed hyalinization of the blood vessels while the other displayed thickened collagen bundles between the tumor cells.

In many cases in literature, the tumors expressed CD34 and/or S100-protein on immunohistochemistry [18–23, 26, 28, 30]. None of the *NTRK*-fused cases in our series were positive for these immunohistochemical markers. However, this could be a useful diagnostic tool in cases of a spindle cell tumor without a specific growth pattern, in order to pinpoint those neoplasms that need further investigation for the presence of the fusion.

Pan-TRK immunohistochemistry is a reliable screening method for the detection of *NTRK* fusions with sensitivity and specificity exceeding 95% [12, 31]. Careful interpretation of the immunohistochemical staining is though recommended, since its specificity is low in sarcomas with neural or myogenic differentiation, as wild-type TRK protein is physiologically expressed in neural and smooth muscle tissue [32].

In our samples, two out of the seven immunohistochemical positive cases (nearly 28,6%) correlated with the presence of a *NTRK* fusion. This is in line with a very recently published study of Nozzoli et.al., where two of the eight immunohistochemical positive cases that had available RNA material for NGS, proven to harbor an *NTRK* fusion [33]. The ratio of sarcomas with a fusion in relation to the total population of the 70 cases examined in our series is approximately 2,8%. False-negative cases, with negative pan-TRK immunohistochemistry while the tumor was proven to harbor a *NTRK* fusion, are rarely described [29, 31, 34]. The staining pattern of the antibody also varies in intensity and localization. Different subcellular staining patterns have been documented such as cytoplasmic, cell membranous, nuclear with or without peri-nuclear accentuation, all of which are considered as positive [22, 31, 35, 36]. All these staining patterns suggest the presence of the fusion, and molecular testing is needed for confirmation. Subsequently, there has

FIGURE 3 | Schematic illustration of the TRK signaling pathway and its role to cell differentiation. Created with BioRender.com.

been an attempt to demonstrate a correlation between the staining pattern and the *NTRK* gene fusion. Hence, it has been shown that fusions of the *NTRK1* gene mostly correlate with a diffuse cytoplasmic staining, while nuclear and rather weak pan-TRK staining is frequently mentioned with *NTRK3* gene fusions [29]. Furthermore, nuclear positivity is correlated with *ETV6-NTRK3* fusion in different tumor types [31, 37]. This is consistent with our findings, where one of the tumors showed pan-TRK weak nuclear positivity, and this tumor harbored an *ETV6-NTRK3* rearrangement.

The prognosis of *NTRK1-* and *NTRK3-* fused sarcomas in correlation with histomorphology, has also been a subject of investigation. Sarcomas with *NTRK1* gene fusions can present a low- or a high-grade histomorphology. While morphologically high-grade *NTRK1*-fused tumors display an aggressive course in the majority of the cases, morphologically low-grade *NTRK1*-fused sarcomas can have a favorable clinical course [10, 38]. On the other hand, sarcomas with fusions of the *NTRK3* gene and especially those with *ETV6* fusion partner, are mainly aggressive neoplasms, even those with intermediate cytological atypia [10, 39]. Low-grade cytomorphology is usually not a feature of these fusions. This is in contrast with our findings. We describe a tumor with *ETV6-NTRK3* fusion with a rather indolent course. The tumor was present for almost six to seven years prior to the diagnosis and showed no signs of recurrence or metastatic spread almost a year after the excision. Morphologically, the tumor

showed a cellular spindle cell proliferation without pronounced cytological atypia; mitotic activity was apparent but rather limited, while no necrosis was seen. An interesting feature was the hyalinization and presence of multinucleated cells in the blood vessel wall.

In addition, we describe a *TFG-NTRK3* fused sarcoma with an aggressive course. From a histological point of view, the tumor was a high-grade neoplasm with marked cytological atypia, increased mitotic activity as well as areas of necrosis. No CD34 or S100-protein expression was observed. The patient also developed disseminated disease. These findings are again in contrast with the features of the limited *TFG-NTRK3* fused mesenchymal tumors documented in the literature [18, 39]. *TFG-NTRK3* sarcomas are amongst the rare *NTRK3*-fused sarcoma cases with a rather favorable histological and clinical picture. Opposite to our case, the tumors are known to display mostly an intermediate cytological grade or a lipofibromatosis-like morphology. Immunohistochemical positivity of the neoplastic cells with CD34 and S100-protein were documented, in contrast to our case. The prognosis of these tumors is reported favorable with no evidence of recurrence or metastasis in the (rather limited) follow up period.

Among these two tumors, the one with the best prognosis was a superficial lesion on the acral skin, while the one with the worst clinical course was located in the deep soft tissues. It therefore seems that in addition to the presence of an *NTRK* fusion, tumor location might also has a prognostic value.

Conclusion

NTRK fusions are rare genetic events that can appear in a wide range of tumor types, including mesenchymal tumors. Identification of rearrangement of one of the three *NTRK* genes can lead to right treatment choices, as they show great benefit from TRK-inhibitory therapy. Nowadays, we start to recognize the histomorphology that in most cases correlates with the presence of the *NTRK* fusion in sarcomas. With our research, we aimed to broaden the diagnostic spectrum of this category and its correlation with the clinical and prognostic aspects. We described two soft tissue tumors with *NTRK3* fusions among 70 soft tissue and bone sarcomas. Both are spindle cell neoplasm from the soft tissues with variable growth patterns, in accordance with prior publications. Pan-TRK immunohistochemistry was positive, and one of the cases displayed weak nuclear staining which correlated with the *ETV6* fusion partner. In contrast to what has been described in literature, none of the tumors we present showed CD34 or S100-protein expression on immunohistochemistry. Moreover, we investigated the correlation of morphology and clinical behavior of these tumors. Namely, the neoplasm with the *ETV6-NTRK3* fusion was superficial located and displayed an indolent course, in contrast to the published cases that display an aggressive behavior. Finally, we described an exceedingly rare *TFG-NTRK3* – fused sarcoma with location in deep soft tissue that developed metastatic disease.

To conclude, *NTRK*-fused sarcomas are spindle cell tumors with variable growth patterns. Pan-TRK immunohistochemistry can pinpoint the cases that need further investigation by means of molecular testing. Nuclear positivity correlates with *ETV6-NTRK3* fusion. According to our results, the presence of specific fusion partners do not seem to be a good surrogate marker to predict prognosis. Location of the tumor (superficial versus deep) may be an additional prognostic factor.

DATA AVAILABILITY STATEMENT

The original contributions presented in the study are included in the article/supplementary material, further inquiries can be directed to the corresponding author.

ETHICS STATEMENT

The studies involving human participants were reviewed and approved by Ethics Committee of the Antwerp University Hospital/University of Antwerp. Written informed consent for participation was not provided by the participants' legal guardians/next of kin because: the study is retrospective and we used only historical samples for which additional informed consent from the patients was not needed.

AUTHOR CONTRIBUTIONS

Conceptualization, VS, PP; Formal analysis, VS; Funding acquisition, PP and ES; Investigation, VS, KW; Methodology, VS; Supervision, ES, PP and EM; Visualization, V.S.; Writing—original draft, VS; Writing—review andamp; editing, VS, KW, KN, GS, VD, PD, ES, EM. All authors have read and agreed to the published version of the manuscript.

CONFLICT OF INTEREST

The authors declare that the research was conducted in the absence of any commercial or financial relationships that could be construed as a potential conflict of interest.

REFERENCES

1. Gamboa AC, Gronchi A, Cardona K. Soft-tissue Sarcoma in Adults: An Update on the Current State of Histiotype-specific Management in an Era of Personalized Medicine. *CA A Cancer J Clin* (2020) 70(3):200–29. doi:10.3322/caac.21605

2. Dangoor A, Seddon B, Gerrand C, Grimer R, Whelan J, Judson I. UK Guidelines for the Management of Soft Tissue Sarcomas. *Clin Sarcoma Res* (2016) 6:20. doi:10.1186/s13569-016-0060-4

3. Gerrand C, Athanasou N, Athanasou N, Brennan B, Grimer R, Judson I, et al. UK Guidelines for the Management of Bone Sarcomas. *Clin Sarcoma Res* (2016) 6:7. doi:10.1186/s13569-016-0047-1

4. Bessen T, Caughey GE, Shakib S, Potter JA, Reid J, Farshid G, et al. A Population-Based Study of Soft Tissue Sarcoma Incidence and Survival in Australia: An Analysis of 26,970 Cases. *Cancer Epidemiol* (2019) 63:101590. doi:10.1016/j.canep.2019.101590

5. Reichardt P. The Story of Imatinib in GIST - a Journey through the Development of a Targeted Therapy. *Oncol Res Treat* (2018) 41(7-8):472–7. doi:10.1159/000487511

6. Drilon A. TRK Inhibitors in TRK Fusion-Positive Cancers. *Ann Oncol* (2019) 30(Suppl. 8):viii23–viii30. doi:10.1093/annonc/mdz282

7. Drilon A, Nagasubramanian R, Blake JF, Ku N, Tuch BB, Ebata K, et al. A Next-Generation TRK Kinase Inhibitor Overcomes Acquired Resistance to Prior TRK Kinase Inhibition in Patients with TRK Fusion-Positive Solid Tumors. *Cancer Discov* (2017) 7(9):963–72. doi:10.1158/2159-8290.CD-17-0507

8. Drilon A, Ou S-HI, Cho BC, Kim D-W, Lee J, Lin JJ, et al. Repotrectinib (TPX-0005) Is a Next-Generation ROS1/TRK/ALK Inhibitor that Potently Inhibits ROS1/TRK/ALK Solvent- Front Mutations. *Cancer Discov* (2018) 8(10):1227–36. doi:10.1158/2159-8290.CD-18-0484

9. Cocco E, Scaltriti M, Drilon A. NTRK Fusion-Positive Cancers and TRK Inhibitor Therapy. *Nat Rev Clin Oncol* (2018) 15(12):731–47. doi:10.1038/s41571-018-0113-0

10. Siozopoulou V, Smits E, De Winne K, Marcq E, Pauwels P. NTRK Fusions in Sarcomas: Diagnostic Challenges and Clinical Aspects. *Diagnostics* (2021) 11(3):478. doi:10.3390/diagnostics11030478

11. Gatalica Z, Xiu J, Swensen J, Vranic S. Molecular Characterization of Cancers with NTRK Gene Fusions. *Mod Pathol* (2019) 32(1):147–53. doi:10.1038/s41379-018-0118-3

12. De Winne K, Sorber L, Lambin S, Siozopoulou V, Beniuga G, Dedeurwaerdere F, et al. Immunohistochemistry as a Screening Tool for NTRK Gene Fusions: Results of a First Belgian Ring Trial. *Virchows Arch* (2021) 478(2):283–91. doi:10.1007/s00428-020-02921-6

13. Detre S, Saclani Jotti G, Dowsett M. A "quickscore" Method for Immunohistochemical Semiquantitation: Validation for Oestrogen Receptor in Breast Carcinomas. *J Clin Pathol* (1995) 48(9):876–8. doi:10.1136/jcp.48.9.876

14. Kummar S, Lassen UN. TRK Inhibition: A New Tumor-Agnostic Treatment Strategy. *Targ Oncol* (2018) 13(5):545–56. doi:10.1007/s11523-018-0590-1

15. Vaishnavi A, Le AT, Doebele RC. TRKing Down an Old Oncogene in a new era of Targeted Therapy. *Cancer Discov* (2015) 5(1):25–34. doi:10.1158/2159-8290.CD-14-0765

16. Hong DS, Bauer TM, Lee JJ, Dowlati A, Brose MS, Farago AF, et al. Larotrectinib in Adult Patients with Solid Tumours: a multi-centre, Open-Label, Phase I Dose-Escalation Study. *Ann Oncol* (2019) 30(2):325–31. doi:10.1093/annonc/mdy539

17. Demetri GD, Antonescu CR, Bjerkehagen B, Bovée JVMG, Boye K, Chacón M, et al. Diagnosis and Management of Tropomyosin Receptor Kinase (TRK) Fusion Sarcomas: Expert Recommendations from the World Sarcoma Network. *Ann Oncol* (2020) 31(11):1506–17. doi:10.1016/j.annonc.2020.08.2232

18. Kao YC, Suurmeijer AJH, Argani P, Dickson BC, Zhang L, Sung YS, et al. Soft Tissue Tumors Characterized by a Wide Spectrum of Kinase Fusions Share a Lipofibromatosis-like Neural Tumor Pattern. *Genes Chromosomes Cancer* (2020) 59(10):575–83. doi:10.1002/gcc.22877

19. Agaram NP, Zhang L, Sung Y-S, Chen C-L, Chung CT, Antonescu CR, et al. Recurrent NTRK1 Gene Fusions Define a Novel Subset of Locally Aggressive Lipofibromatosis-like Neural Tumors. *Am J Surg Pathol* (2016) 40(10):1407–16. doi:10.1097/PAS.0000000000000675

20. Haller F, Knopf J, Ackermann A, Bieg M, Kleinheinz K, Schlesner M, et al. Paediatric and Adult Soft Tissue Sarcomas withNTRK1gene Fusions: a Subset of Spindle Cell Sarcomas Unified by a Prominent Myopericytic/haemangiopericytic Pattern. *J Pathol* (2016) 238(5):700–10. doi:10.1002/path.4701

21. Croce S, Hostein I, Longacre TA, Mills AM, Pérot G, Devouassoux-Shisheboran M, et al. Uterine and Vaginal Sarcomas Resembling Fibrosarcoma: a Clinicopathological and Molecular Analysis of 13 Cases Showing Common NTRK-Rearrangements and the Description of a COL1A1-PDGFB Fusion Novel to Uterine Neoplasms. *Mod Pathol* (2019) 32(7):1008–22. doi:10.1038/s41379-018-0184-6

22. Chiang S, Cotzia P, Hyman DM, Drilon A, Tap WD, Zhang L, et al. NTRK Fusions Define a Novel Uterine Sarcoma Subtype with Features of Fibrosarcoma. *Am J Surg Pathol* (2018) 42(6):791–8. doi:10.1097/PAS.0000000000001055

23. Rabban JT, Devine WP, Sangoi AR, Poder L, Alvarez E, Davis JL, et al. NTRK Fusion Cervical Sarcoma: a Report of Three Cases, Emphasising Morphological and Immunohistochemical Distinction from Other Uterine Sarcomas, Including Adenosarcoma. *Histopathology* (2020) 77(1):100–11. doi:10.1111/his.14069

24. Alassiri AH, Ali RH, Shen Y, Lum A, Strahlendorf C, Deyell R, et al. ETV6-NTRK3 Is Expressed in a Subset of ALK-Negative Inflammatory Myofibroblastic Tumors. *Am J Surg Pathol* (2016) 40(8):1051–61. doi:10.1097/PAS.0000000000000677

25. Yamamoto H, Yoshida A, Taguchi K, Kohashi K, Hatanaka Y, Yamashita A, et al. ALK,ROS1andNTRK3gene Rearrangements in Inflammatory Myofibroblastic Tumours. *Histopathology* (2016) 69(1):72–83. doi:10.1111/his.12910

26. Olson N, Rouhi O, Zhang L, Angeles C, Bridge J, Lopez-Terrada D, et al. A Novel Case of an Aggressive Superficial Spindle Cell Sarcoma in an Adult Resembling Fibrosarcomatous Dermatofibrosarcoma Protuberans and Harboring anEML4-NTRK3fusion. *J Cutan Pathol* (2018) 45(12):933–9. doi:10.1111/cup.13348

27. So YK, Chow C, To KF, Chan JKC, Cheuk W. Myxoid Spindle Cell Sarcoma with LMNA-NTRK Fusion: Expanding the Morphologic Spectrum of NTRK-Rearranged Tumors. *Int J Surg Pathol* (2020) 28(5):574–8. doi:10.1177/1066896920905888

28. Kao Y-C, Flucke U, Eijkelenboom A, Zhang L, Sung Y-S, Suurmeijer AJH, et al. Novel EWSR1-SMAD3 Gene Fusions in a Group of Acral Fibroblastic Spindle Cell Neoplasms. *Am J Surg Pathol* (2018) 42(4):522–8. doi:10.1097/PAS.0000000000001002

29. Brčić I, Godschachner TM, Bergovec M, Igrec J, Till H, Lackner H, et al. Broadening the Spectrum of NTRK Rearranged Mesenchymal Tumors and Usefulness of Pan-TRK Immunohistochemistry for Identification of NTRK Fusions. *Mod Pathol* (2021) 34(2):396–407. doi:10.1038/s41379-020-00657-x

30. Davis JL, Lockwood CM, Stohr B, Boecking C, Al-Ibraheemi A, DuBois SG, et al. Expanding the Spectrum of Pediatric NTRK-Rearranged Mesenchymal Tumors. *Am J Surg Pathol* (2019) 43(4):435–45. doi:10.1097/PAS.0000000000001203

31. Hechtman JF, Benayed R, Hyman DM, Drilon A, Zehir A, Frosina D, et al. Pan-Trk Immunohistochemistry Is an Efficient and Reliable Screen for the Detection of NTRK Fusions. *Am J Surg Pathol* (2017) 41(11):1547–51. doi:10.1097/PAS.0000000000000911

32. Solomon JP, Benayed R, Hechtman JF, Ladanyi M. Identifying Patients with NTRK Fusion Cancer. *Ann Oncol* (2019) 30(Suppl. l_8):viii16–viii22. doi:10.1093/annonc/mdz384

33. Nozzoli F, Lazar AJ, Castiglione F, Campanacci DA, Beltrami G, De Logu F, et al. NTRK Fusions Detection in Paediatric Sarcomas to Expand the Morphological Spectrum and Clinical Relevance of Selected Entities. *Pathol Oncol Res.* 2022;28. doi:10.3389/pore.2022.1610237

34. Rudzinski ER, Lockwood CM, Stohr BA, Vargas SO, Sheridan R, Black JO, et al. Pan-Trk Immunohistochemistry Identifies NTRK Rearrangements in Pediatric Mesenchymal Tumors. *Am J Surg Pathol* (2018) 42(7):927–35. doi:10.1097/PAS.0000000000001062

35. Solomon JP, Linkov I, Rosado A, Mullaney K, Rosen EY, Frosina D, et al. NTRK Fusion Detection across Multiple Assays and 33,997 Cases: Diagnostic Implications and Pitfalls. *Mod Pathol* (2020) 33(1):38–46. doi:10.1038/s41379-019-0324-7

36. Hung YP, Fletcher CDM, Hornick JL. Evaluation of Pan-TRK Immunohistochemistry in Infantile Fibrosarcoma, Lipofibromatosis-like Neural Tumour and Histological Mimics. *Histopathology* (2018) 73(4):634–44. doi:10.1111/his.13666

37. Csanyi-Bastien M, Lanic M-D, Beaussire L, Ferric S, François A, Meseure D, et al. Pan-TRK Immunohistochemistry Is Highly Correlated with NTRK3 Gene Rearrangements in Salivary Gland Tumors. *Am J Surg Pathol* (2021) 45:1487–98. doi:10.1097/PAS.0000000000001718

38. Suurmeijer AJH, Dickson BC, Swanson D, Zhang L, Sung Y-S, Cotzia P, et al. A Novel Group of Spindle Cell Tumors Defined by S100 and CD34 Co-expression Shows Recurrent Fusions Involving RAF1, BRAF, and NTRK1/2 Genes. *Genes Chromosomes Cancer* (2018) 57(12):611–21. doi:10.1002/gcc.22671

39. Suurmeijer AJ, Dickson BC, Swanson D, Zhang L, Sung YS, Huang HY, et al. The Histologic Spectrum of Soft Tissue Spindle Cell Tumors with NTRK3 Gene Rearrangements. *Genes Chromosomes Cancer* (2019) 58(11):739–46. doi:10.1002/gcc.22767

Survival of HT29 Cancer Cells Is Affected by IGF1R Inhibition *via* Modulation of Self-DNA-Triggered TLR9 Signaling and the Autophagy Response

Ferenc Sipos[1]*[†], Bettina Bohusné Barta[1†], Ágnes Simon[1], Lőrinc Nagy[1], Titanilla Dankó[2], Regina Eszter Raffay[2], Gábor Petővári[2], Viktória Zsiros[3], Barnabás Wichmann[4], Anna Sebestyén[2] and Györgyi Műzes[1]

[1]Department of Internal Medicine and Hematology, Semmelweis University, Budapest, Hungary, [2]Department of Pathology and Experimental Cancer Research, Semmelweis University, Budapest, Hungary, [3]Department of Anatomy, Histology and Embryology, Semmelweis University, Budapest, Hungary, [4]Lufthansa Systems Hungária, Budapest, Hungary

Purpose: In HT29 colon cancer cells, a close interplay between self-DNA-induced TLR9 signaling and autophagy response was found, with remarkable effects on cell survival and differentiation. IGF1R activation drives the development and malignant progression of colorectal cancer. IGF1R inhibition displays a controversial effect on autophagy. The interrelated roles of IGF1R inhibition and TLR9/autophagy signaling in HT29 cancer cells have not yet been clarified. In our study, we aimed to investigate the complex interplay of IGF1R inhibition and TLR9/autophagy signaling in HT29 cells.

Methods: HT29 cells were incubated with tumor-originated self-DNA with or without inhibitors of IGF1R (picropodophyllin), autophagy (chloroquine), and TLR9 (ODN2088), respectively. Cell proliferation and metabolic activity measurements, direct cell counting, NanoString and Taqman gene expression analyses, immunocytochemistry, WES Simple Western blot, and transmission electron microscopy investigations were performed.

Results: The concomitant use of tumor-derived self-DNA and IGF1R inhibitors displays anti-proliferative potential, which can be reversed by parallel TLR9 signaling inhibition. The distinct effects of picropodophyllin, ODN2088, and chloroquine *per se* or in combination on HT29 cell proliferation and autophagy suggest that either the IGF1R-associated or non-associated autophagy machinery is "Janus-faced" regarding its actions on cell proliferation. Autophagy, induced by different combinations of self-DNA and inhibitors is not sufficient to rescue HT29 cells from death but results in the survival of some CD133-positive stem-like HT29 cells.

Conclusion: The creation of new types of combined IGF1R, autophagy, and/or TLR9 signaling inhibitors would play a significant role in the development of more personalized anti-tumor therapies for colorectal cancer.

Keywords: autophagy, CD133, IGF1R, TLR9, HT29 cancer cell, self-DNA

INTRODUCTION

Insulin-like growth factor 1 receptor (IGF1R), a transmembrane protein belonging to the receptor tyrosine kinase family, consists of two subunits (i.e., IGF1R-α and IGF1R-β). IGF1R ligands include insulin and insulin-like growth factors (IGF)-1 and -2. Upon ligand stimulation, the auto-phosphorylated IGF1R-β phosphorylates adaptor proteins (e.g., IRS1/2, SHC, 14-3-3); afterwards, it activates downstream signaling pathways, like PI3K/AKT, JAK/STAT, Src, FAK and RAS/MAPK, finally modulating gene expressions related to apoptosis or cell proliferation [1, 2]. Within physiological circumstances, IGF1R is frequently expressed in various tissues, serving multiple functions in growth, development, and feeding [3].

IGF1R activation in tumors can promote tumorigenesis, maintain the transformed phenotype, promote cancer progression, stimulate cell migration, epithelial-mesenchymal transformation, and chemotherapy resistance [4, 5]. In colorectal cancer (CRC), IGF1R gene and protein expression levels are usually elevated in cancerous tissues as compared to adjacent normal tissues [6]. Elevated IGF1R expression is associated with poor prognosis in CRC [7]. Given the significant roles of IGF1R in tumor development and progression, inhibition of IGF1R activity has been suggested as a therapeutic strategy for many malignancies [8]. Although several anti-IGF1R monoclonal antibodies and small-molecule inhibitors have been produced, and these inhibitors display potent anti-tumor effects in preclinical models [8], clinical trials of these agents are mostly disappointing in unselected cancer patients, suggesting the existence of mechanisms to antagonize IGF1R inhibition in tumor cells.

Autophagy is an evolutionarily conserved proteolytic process including lysosomal degradation and recycling of impaired cellular components and energy to maintain homeostasis [9]. In preclinical studies, protective autophagy blockade has been applied simultaneously with either chemotherapies or targeted therapies to optimize their efficacy in different cancers [10]. The connection of the IGF1R signaling pathway to the autophagy machinery is rather complicated [11]. Furthermore, IGF1R inhibition has been shown to have different effects (i.e., inhibitory or stimulatory) on autophagy in cancer cells [12–14]. Recently, it has been found that the combined use of autophagy-disrupting agents can enhance the therapeutic efficacy of IGF1R inhibitors in triple-negative breast cancers and may therefore provide a valuable treatment strategy for IGF1R inhibitor-based therapies for IGF1 signaling-associated tumors [15].

The existence of cell-free nucleic acids (including cell-free DNA/cfDNA/sequences) in human blood, as well as in urine, saliva, or feces, is a known fact [16]. The methylation status or fragmentation of cfDNAs may carry information about their source [17]. In terms of their origin, cfDNAs fall into several categories. Endogenous cfDNA sequences are derived from tissues and cells, whereas exogenous sequences are primarily derived from the host microbiome, infectious agents, the fetus, and food [18–20]. Toll-like receptors (TLRs) are innate immune receptors [21]. TLR9 is capable of detecting DNA from both endogenous and exogenous sources [21]. We have previously demonstrated that the structural modifications of self-DNA (e.g., methylation status and fragment length) play a significant role in activation of the TLR9-mediated signaling pathways [22]. However, little data is available on the relationship between Toll-like receptor signaling and the IGF1R-associated pathway. It was demonstrated that exposure to CpG-oligodeoxynucleotide (CpG-ODN), a ligand of TLR9, can increase the expression of IGF1 in intestinal epithelial cells [23]. IGF1 further contributes to the intestinal homeostasis by inducing macrophages with immune suppressive properties [23]. These data are in line with the finding that the physiologic TLR9/CpG-ODN-DNA interaction is essential for the homeostasis of the intestinal immune system [24].

In HT29 colon cancer cells, a close interplay between self-DNA-induced TLR9 signaling and autophagy response was found, with notable effects on cell survival and differentiation [25]. However, the interrelated role of IGF1R inhibition and TLR9/autophagy signaling in HT29 colon cancer cells has not yet been clarified. Therefore, we aimed to assess this complex interaction in HT29 cells.

We decided to use HT29 cells because of several aspects. There is basal TLR9 expression in HT29 cells, which is essential for induction with self-DNA [23]. Since DNA treatment via TLR9 can exert its effects in both MyD88-dependent and MyD88-independent ways, it is also important that the MyD88-dependent and MyD88-independent TLR signaling pathways are intact in HT29 cells [26]. IGF1R expression in HT29 cells is moderate as compared to other CRC cell lines (e.g., SW480 or DLD-1) [27]. Also, in HT29 cells, elevated IGF2 expression can be detected, which is essential for both autocrine activation of IGF1R signaling and studying the effect of IGF1R inhibition [28]. The HT29 cells adequately represent sporadic colon cancers [29]. Not all colorectal cancer cell lines meet these criteria.

Here, we found that the concomitant use of tumorous self-DNA and IGF1R inhibitor displays anti-proliferative potential, which can be inhibited by parallel TLR9 signaling inhibition. The different effects of IGF1R, TLR9, and autophagy inhibitors alone or in combination on HT29 cell proliferation and autophagy suggest that the IGF1R-associated and non-IGF1R-associated autophagy machinery is "Janus-faced" regarding its effect on cell proliferation. Autophagy induced by different combinations of self-DNA and inhibitors may result in the survival of some CD133-positive stem-like HT29 cancer cells, which may play an important future role in the recurrence of CRC.

MATERIALS AND METHODS

Maintenance of HT29 Cell Culture and Self-DNA Isolation

The HT29 undifferentiated colon adenocarcinoma cell line was purchased from the 1st Department of Pathology and Experimental Cancer Research (Semmelweis University, Budapest, Hungary). The cells were maintained in RPMI 1640 medium (Sigma-Aldrich, United States) supplemented with 10%

TABLE 1 | Treatment plan for HT29 cancer cells. gDNA, genomic deoxyribonucleic acid; ODN, O, CpG oligonucleotide; K, non-treated, control; P, picropodophyllin; C, chloroquine; Kg, gDNA control; gO, gDNA + ODN2088; gP, gDNA + picropodophyllin; gC, gDNA + chloroquine; gOP, gDNA + ODN2088 + picropodophyllin; gPC, gDNA + picropodophyllin + chloroquine.

Sample groups	GDNA	ODN2088	Picropodophyllin	Chloroquine
K	–	–	–	–
O	–	+	–	–
P	–	–	+	-
C	–	–	–	+
Kg	+	–	–	–
gO	+	+	-	–
gP	+	–	+	–
gC	+	–	–	+
gOP	+	+	+	–
gPC	+	–	+	+

(v/v) fetal bovine serum (FBS; Standard Quality; PAA Laboratories GmbH, Austria), 125 µg/ml amphotericin B (Sigma-Aldrich, United States), and 160 µg/ml gentamycin (Sandoz, Sandoz GmbH, Austria). The medium was replaced every second day.

Genomic DNA (gDNA; g) was isolated from 5×10^7 steady state, proliferating HT29 cells. DNA isolation was performed by using a High Pure PCR template preparation kit containing proteinase K (Roche GmbH, Germany). The DNA samples were treated with 5 µl RNase A/T1 Mix (Thermo Scientific, Germany). The DNA concentration was determined by Nanodrop (Thermo Scientific, Germany). Gel electrophoresis determined that the fragment length of gDNA was approximately 10,000 base pairs [22].

According to the bisulfite sequencing analysis of Ogoshi et al. [30], the basal methylation status of HT29 cells' CpG sites is as follows: 31.6% in the low range; 11.6 percent in the middle; and 56.7 percent in the high range. Based on MALDI-TOF mass spectrometry measurements, the DNA samples were free of RNA, protein, or lipopolysaccharide contamination (data not shown).

HT29 Cell Treatments

For incubation with the DNA samples, 0.5×10^6 HT29 cells were placed into a 12-well-plate in RPMI 1640, supplemented with amphotericin B, gentamycin, and FBS, as described above. After 24 h, the starting medium was changed to RPMI 1640 with gentamycin but without FBS. Aliquots of 15 µg of self-DNA were separately dissolved in 200 µl sterile phosphate buffered saline (PBS).

HT29 cells were incubated with the self-DNA samples at 37°C in a humidified atmosphere of 5% CO_2 and 95% O_2. For the control cells, only 200 µl sterile PBS was added. After 72 h, cells were washed twice with 5 ml of sterile PBS and resuspended in a final volume of 5 ml of PBS.

Inhibition of TLR9 and IGF1R Signaling

To inhibit TLR9 or IGF1R signaling, HT29 cells were pretreated for 1 h with TLR9 antagonist (O) (5 µM ODN2088; Invivogen, CA, United States) or picropodophyllin (P) (0.05 µM; BML-EI372-0001; EnzoLifeSciences, BioMarker Kft., Gödöllő,

Hungary; diluted in dimethyl sulfoxide/DMSO; Sigma-Aldrich Budapest, Hungary/) for 1 h before treatments with DNA. All treatments were performed in triplicate. Between plates, two samples received the same treatment to avoid possible manual errors in the treatments between plates.

Inhibition of Autophagy

Chloroquine (C), an anti-inflammatory substance, is the most commonly used autophagy completion inhibitory drug to ascertain autophagic flux because of its suitability *in vivo* [31]. HT29 cells were treated with chloroquine (10 µM; C6628 Sigma-Aldrich, Budapest, Hungary; diluted in DMSO) for 1 h before treatments with DNA. All treatments were performed in triplicate. Between plates, two samples received the same treatment to avoid possible manual errors in the treatments between plates.

The treatment plan for HT29 cells is shown in **Table 1**.

Measuring Cell Viability and Proliferation

The use of the Alamar Blue assay served a dual purpose: partly to examine cell viability (metabolic activity) and partly to study cell proliferation [32].

The anti-proliferative effects of the treatments were measured after a 4 h incubation period using Alamar Blue (Thermo Fisher Scientific, Budapest, Hungary). The fluorescence was measured at 570–590 nm (Fluoroskan Ascent FL fluorometer; Labsystems International Ltd., Budapest, Hungary) and the results were analyzed by the Ascent Software.

As metabolic activity is not necessarily proportional to proliferative activity, direct cell counts (average cell numbers determined by using Bürker-Türk counting chambers) were also performed in the examined cell groups to determine the proliferative activity compared to the control sample. We used Trypan Blue dye (302643 Sigma-Aldrich, Budapest, Hungary) to exclude dead cells.

Semithin Sections

From the HT29 cell blocks fixed for TEM semithin sections were cut for viewing by a digital microscope. The sections were stained with toluidine blue (toluidine blue O 4 g, pyronin 1 g, borax 5 g in distilled water). Semithin sections were then digitalized using a high-resolution PANNORAMIC 1000 FLASH DX instrument (3DHISTECH Ltd., Budapest, Hungary), and analyzed with CaseViewer software (3DHISTECH Ltd., Budapest, Hungary). The average number of proliferative cells was counted in five fields of view per sample (mean ± SD/sample).

Total mRNA Isolation and NanoString Analysis

Total mRNA from HT29 cells was extracted with the RNeasy Mini Kit (Qiagen, United States) according to the manufacturer's instructions. Quantitative (Nanodrop) and qualitative analysis (Bioanalyzer Pico 600 chip kit RNA program; RIN > 8 in all cases) were performed.

mRNA samples required for gene expression assays of HT29 cells were prepared by tripling the treated groups. In HT29

samples, cell numbers ranged from 100,000 to 11,135,000 per well, and the recovered mRNA concentration ranged from 8 to 256 ng/µl/sample. mRNAs recovered from triplicates were pooled and used in the NanoString assay.

The custom mRNA Assay Evaluation panel (NA-SPRINT-CAR-1.0, nCounter SPRINT Cartridge) containing our custom gene code set (NA-XT-GXA-P1CS-04 nCounter GX Custom CodeSet) was designed by NanoString (the order was placed through Biomedica Hungaria Ltd., Budapest, Hungary). The NanoString experiments were carried out by RT-Europe Research Center Ltd. (Mosonmagyaróvár, Hungary; website: http://rt-europe.org/) as part of a contract work.

In brief, as input material, a total of 50 ng (10 ng/µl) RNA samples were denatured at 85°C for 5 min and cooled on ice. 5 µl samples were added to 8 µl mix containing the Reporter code set in Hybridization buffer. 2 µl Capture ProbeSet was added to each tube and incubated at 65°C for 18 h. The resulting reaction vials were supplemented with 17 µl molecular biology grade dH2O. 30 µl of the resulting sample mixes were loaded into the microfluidic sample chambers of the nCounter SPRINT Cartridge (SPRINT-CAR-1.0, Nanostring) directly before initiating the run on the nCounter Sprint Profiler. Primary data analysis was performed using the nSolver 4.0 Analysis software.

The criterion for selecting the genes to be examined was to establish an association between IGF1R and TLR9 signaling, apoptosis, cell proliferation, autophagy, and cancer cell stemness.

The Gene Set Contained the Following Genes (With Probe NSIDs)

IGF1R signaling pathway: IGF1R (Insulin-like growth factor 1 receptor; NM_000875); MAPK (Mitogen-activated protein kinase; NM_002755.2:970); PI3K (Phosphoinositide 3-kinase; NM_006218.2:2445); Akt (Ak strain transforming; NM_001014432.1:1275).

TLR9 signaling pathway: TLR9 (Toll-like receptor 9; NM_017442); MyD88 (Myeloid differentiation factor 88; NM_002468), NF-kB (nuclear factor-kappa B; NM_003998).

Extrinsic and intrinsic apoptosis-related genes: Caspase-3 (NM_004346.3:2156), Caspase-8 (NM_033355), Caspase-9 (NM_032996).

Anti-apoptotic and autophagy suppressor genes: PI3K (Phosphoinositide 3-kinase; NM_006218.2:2445), Akt (Ak strain transforming; NM_001014432.1:1275), mTOR (Mechanistic/mammalian target of rapamycin; NM_004958.3: 1865), Bcl-2 (B-cell lymphoma 2; NM_000657.2:5).

Pro-apoptotic and autophagy activator genes: MAPK (Mitogen-activated protein kinase; NM_002755.2:970), AMPK (AMP-activated protein kinase; NM_006251.5:366), Bax (BCL2 associated X; NM_138761.3:342).

Autophagy genes: Beclin1 (NM_003766.2:810), ATG16L1 (Autophagy related 16 like 1; NM_017974.3:2405), MAP1LC3B (Microtubule-associated proteins 1A/1B light chain 3B; NM_022818.4:1685), ULK1 (Unc-51 like autophagy activating kinase; NM_003565.1:465), Ambra-1 (activating molecule in beclin-1-regulated autophagy; NM_017749).

HT29 cancer cell stemness-related gene: CD133 (NM_006017).

Housekeeping genes: C1orf43 (NM_015449.2:477), CHMP2A (NM_014453.3:241), PSMB2 (NM_002794.3:639), RAB7A (NM_ 004637.5:277), REEP5 (NM_005669.4:280), SNRPD3 (NM_ 004175.3:309), VCP (NM_007126.2:615), VPS29 (NM_016226. 4:565).

Taqman Real-Time Polymerase Chain Reaction Analysis

For validating the NanoString gene expression analysis method, mTOR (ID: Hs00234508_m1), ATG16L1 (ID: Hs01003142_m1), LC3B (ID: Hs00797944_s1), BCN1 (ID: Hs01007018_m1), IGF1R (ID: Hs00609566_m1) and TLR9 (ID: Hs00370913_s1) triplicated Taqman real-time polymerase chain reactions were used in an Applied Biosystems Micro Fluidic Card System. The measurements were performed using an ABI PRISM 7900HT Sequence Detection System as described in the product's User Guide (http://www.appliedbiosystems.com, CA, United States). Gene expression levels for each individual sample were normalized to GAPDH (ID: Hs02786624_g1) expression. Mean relative gene expression was determined and differences were calculated using the $2-\Delta C(t)$ method. The whole cycle number was 45.

IGF1R, CD133, and Autophagy Immunocytochemistry

To detect IGF1R, CD133, and autophagy-associated ATG16L2, Beclin1, and LC3 protein expression, HT29 cell smears were incubated for 1 h at 37°C with optimally diluted anti-IGF1R monoclonal antibody (Chemicon International; Clone: 24-31; 1:50 dilution in PBS), anti-CD133/1-biotin antibody (1:100, Miltenyi), and anti-ATG16L1-, anti-BECN1-, and anti-MAP1LC3B antibodies (1:200, Antibody Verify, LA, USA). After rinsing 3 times with PBS, cell smears were finally treated with an anti-rabbit EnVision polymerHRP conjugate kit (K4003, DAKO) for 40 min. Secondary immunodetection was performed with EnVision System Labelled Polymer–HRP K4001 (Anti-Mouse 1/1; DAKO), as described in the manual. Signal conversion was carried out with the Liquid DAB + Substrate Chromogen System (DAKO). After rinsing in PBS, hematoxylin co-staining was performed. Cell smears were then digitalized using a high-resolution PANNORAMIC 1000 FLASH DX instrument (3DHISTECH Ltd., Budapest, Hungary), and analyzed with CaseViewer software (3DHISTECH Ltd., Budapest, Hungary). The immunocytochemistry analyses were carried out as part of contract work (Pathology Laboratory, Heim Pál National Institute of Pediatrics, Budapest, Hungary).

WES Simple Western Blot

WES Simple (ProteinSimple 004-600, Minneapolis, MN, USA) analysis was also performed. A 12–230 kDa Separation Module (ProteinSimple SM-W004) was used for all the proteins (Phospho-mTOR (Ser2448) Rabbit Antibody/Cell Signaling; #2971; 1:50 dilution; 199 kDa/; mTOR (7C10) Rabbit mAb/ Cell Signaling; #2983; 1:50 dilution; 200 kDa/; Atg16L1 (D6D5) Rabbit mAb/Cell Signaling; #8089; 1:50 dilution;

66.68 kDa/; Beclin-1 (D40C5) Rabbit mAb/Cell Signaling; #3495; 1:50 dilution; 60 kDa/; LC3B (D11) XP Rabbit mAb/ CellSignaling; #3868; 1:50 dilution; 14.16 kDa/; Anti-β-Actin (AC-74) Mouse mAb/SigmaAldrich; A2228; 1:50 dilution; 48 kDa/), and either the Anti-Rabbit Detection Kit (ProteinSimple DM-001) or Anti-Mouse Detection Kit (ProteinSimple DM-002) were used, depending on the primary antibodies. Briefly, based on the used primary antibodies, 0.2 or 1 µg/µl cell lysates were diluted in 0.1× WES Sample Buffer (ProteinSimple 042-195), and Fluorescent Master Mix (1:4, ProteinSimple PS-FL01-8) was also added. Following a 5-min incubation at 95°C, the Antibody Diluent (ProteinSimple 042-203), primary and secondary antibodies, and chemiluminescent substrate were applied to the WES capillary plate. The WES system settings were (a) stacking and separation (395 V, 30 min), (b) blocking (5 min), (c) incubations with primary and secondary antibodies (30 min) and (d) luminol/peroxide chemiluminescence detection (15 min) (the exposure time was 2 s). The electropherograms were manually corrected if required for the evaluations.

Cell Counting and Interpretation of Immunoreactions

At ×200 magnification, 10 fields of view and at least 100 cells (mainly 110 cells) per field of view were examined in a semiquantitative manner in each digitalized sample. The percentage of immunopositivity and non-immunoreactive HT29 cells was determined.

In the case of the IGF1R immune response, weak, moderate, and strong membrane staining and perinuclear cytoplasm staining were examined. As for autophagy, weak, moderate, and strong ATG16L1 and Beclin1 homogenous or spotted immunoreactions were detected in the cytoplasm. In the case of LC3, weak, moderate, and strong punctuated or spotted cytoplasmic immunoreactions were observed. The notation "−/+" indicates non-immunoreactive and weakly immunopositive cells. The designation "++/+++" indicates moderately or strongly immunopositive cells.

Transmission Electron Microscopy for Evaluation of Autophagy

HT29 cells in the wells were fixed in 2% glutaraldehyde (0.1 M Millonig buffer, pH 7.4) for 60 min. After washing with both 0.1 M of phosphate buffer (3 times for 5 min) and 0.1 M pH 7.2 sodium cacodylate buffer (3 times for 5 min), the samples were post-fixed with 1% osmium tetroxide in 0.1 M sodium-cacodylate buffer for 60 min at 4°C in the dark. After washing 3 times for 5 min with sodium-cacodylate buffer (pH 7.4), the cells were pelleted by centrifugation and embedded in 10% gelatin in phosphate buffer (pH 7.4). After dehydration in a graded series of alcohol, the samples were embedded into Poly/Bed epoxy resin. Ultrathin sections (70–80 nm) were contrast stained with uranyl acetate and lead citrate, respectively. Ultrastructural analyses were performed by using a JEM-1200EXII Transmission Electron Microscope (JEOL, Akishima, Tokyo, Japan).

The average number of autophagic vacuoles was counted in five HT29 cells per sample (mean ± SD/cell).

Statistical Analysis

At least three independent experiments were conducted. Data of cell viability, cell number, and proliferation were presented as means ± SD. The Chi2-test and Student's t-test were used for statistical analyses. $p < 0.05$ was considered statistically significant. In the case of immunocytochemistry, statistical analysis with one-way ANOVA and Tukey HSD test was performed by using R Core Team [33].

Regarding NanoString gene expression analysis, after importing RCC files to the nSolver Analysis Software, quality checking was performed. Then agglomerative cluster heat maps were created. The Euclidean distance metric was used to calculate the distance between two samples (or genes) as the square root of the sum of squared differences in their log count values. The average linkage method was used to calculate the distance between two clusters.

RESULTS

Cell Viability and Proliferation Measurements

The metabolic activity of the HT29 cells was significantly ($p < 0.05$) increased in all treatment groups except the gOP combination as compared to K (control, non-treated cells). The highest metabolic activity was found for P treatment.

The significantly lowest ($p < 0.05$) cell proliferation was found in the Kg treatment group of cells, as compared to K.

When gDNA, ODN2088, picropodophyllin, and chloroquine treatments were co-administered (i.e., gO, gP, gC), effective inhibition of HT29 cell proliferation with high metabolic activity was observed. The combination of gDNA, ODN2088, and picropodophyllin (i.e., gOP) raised proliferative activity back to levels close to non-treated control group.

Viability, cell number, and proliferation data are illustrated in **Table 2** and **Figure 1**.

Semithin Sections

To investigate whether the changes in cell numbers after treatments with genomic DNA and/or TLR9, IGF1R, or autophagy inhibitors were due to low proliferation activity or increased cell death, semithin sections were also examined in selected cases.

In the case of incubation with gDNA, the incidence of proliferation was proportional to the cell numbers obtained. When gDNA was co-administered with picropodophyllin and/or chloroquine, remarkably reduced proliferative activity was observed. In contrast, after combining gDNA with ODN2088 and picropodophyllin, higher proliferative activity was detected (**Figures 2A–D**).

NanoString and Taqman Gene Expression Analyses

Regarding TLR9 mRNA expression, gDNA treatment resulted in TLR9 upregulation as compared to untreated control cells. As for

TABLE 2 | Numerical data of viability, cell number, and proliferation.

Sample	Alamar blue (mean% ± SD)	Average cell number/350 μl (±SD)	Proliferation% (±SD)
K	100 ± 1.1	800000 ± 8800	100 ± 1.1
O	120.17 ± 4.5[a]	760000 ± 32680	95 ± 4.3
P	142.15 ± 4.7[a]	810000 ± 25920	101.25 ± 1.8
C	116.23 ± 2.9[a]	775000 ± 31775	96.87 ± 4.1
Kg	127.51 ± 3.1[a]	220000 ± 9900	27.5 ± 4.5*
gO	139 ± 3.1[a]	270000 ± 3780	33.75 ± 1.4*
gP	119.57 ± 3.2[a]	270000 ± 7020	33.75 ± 2.6*
gC	123.55 ± 3.1[a]	230000 ± 4370	28.75 ± 1.9*
gOP	91.3 ± 2.4[a]	660000 ± 16500	82.5 ± 2.5*
gPC	127.38 ± 2.8[a]	250000 ± 9250	31.25 ± 3.7*

[a]Represents significant alteration as compared to K (control, non-treated sample) (p < 0.05).

g, genomic deoxyribonucleic acid; O, ODN2088 CpG oligonucleotide; P, picropodophyllin; C, chloroquine; SD, standard deviation.
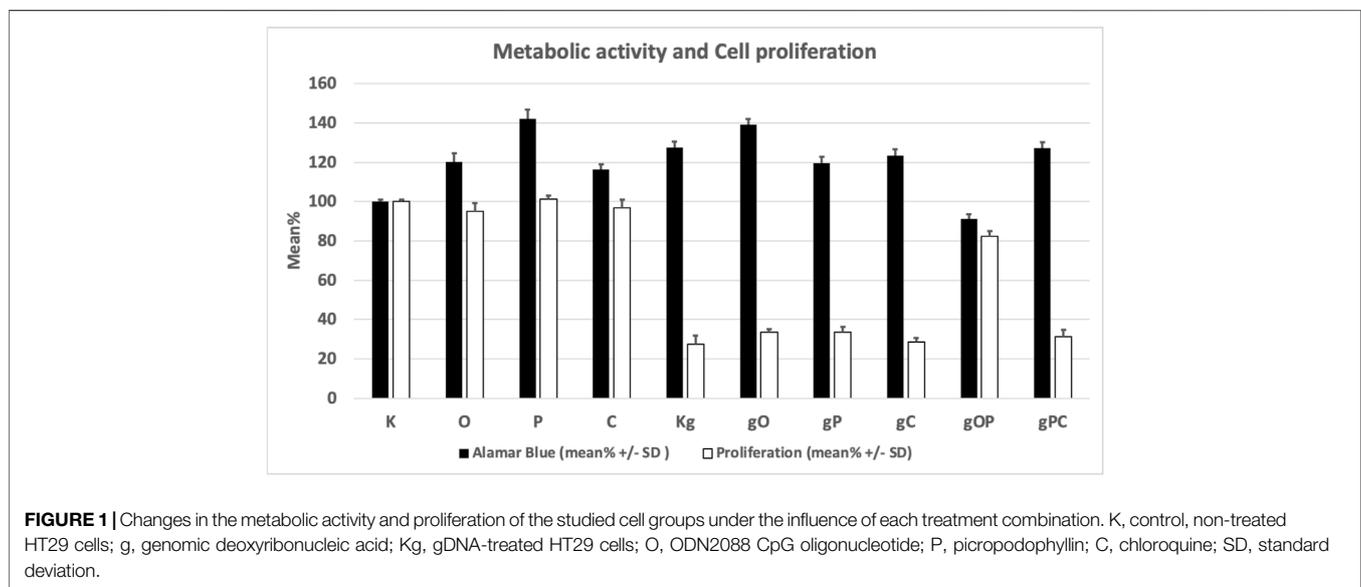

FIGURE 1 | Changes in the metabolic activity and proliferation of the studied cell groups under the influence of each treatment combination. K, control, non-treated HT29 cells; g, genomic deoxyribonucleic acid; Kg, gDNA-treated HT29 cells; O, ODN2088 CpG oligonucleotide; P, picropodophyllin; C, chloroquine; SD, standard deviation.

IGF1R gene expression, gDNA treatment did not increase the expression as compared to untreated control. Otherwise, incubation with gDNA displayed a similar gene expression profile as seen in control samples.

Concerning the effect of combined IGF1R inhibition and gDNA treatment on the expression of IGF1R signaling elements, slight IGF1R overexpression was found without any substantive difference in MAPK, PI3K, and Akt expressions. Except for TLR9 in gC and Bcl2 in gO, gDNA combined with ODN2088 or chloroquine resulted in remarkable overexpression of all examined genes.

Because cell-free DNA treatment affects both TLR9 signaling and the autophagy machinery, we also examined how the effect of concomitant IGF1R inhibition and gDNA treatment is altered by the inhibition of TLR9 signaling or autophagy.

gDNA in combination with picropodophyllin and chloroquine caused the most pronounced increase in TLR9 signaling related (i.e., MyD88, NF-kB), autophagy-related (i.e., ATG16L1, Beclin1, MAP1LC3B, ULK1, Ambra-1), autophagy suppressor/anti-apoptotic (i.e., PI3K, Akt, mTOR), and autophagy activator/pro-apoptotic (i.e., MAPK, AMPK, Bax) gene expressions, except that of TLR9 and Bcl2. On the contrary, gDNA combined with ODN2088 and picropodophyllin resulted in general down-regulation of the assayed genes, with the exception of TLR9 and Bcl2.

The cancer stemness-related gene, CD133, was overexpressed in the case of gP, gC, gO, and gPC treatment combinations. Alterations in gene expression are visualized in **Figure 3**.

The results of Taqman RT-PCR validated the gene expression alterations detected by NanoString/nCounter analysis. Fold changes of the analyzed gene expressions are summarized in **Figure 4**.

Immunocytochemistry Analysis and WES Simple Western Blot

Regarding IGF1R and autophagy-related genes (i.e., ATG16L1, Beclin1, and MAP1LC3B), we performed immunocytochemistry to validate gene expression results at the protein level.
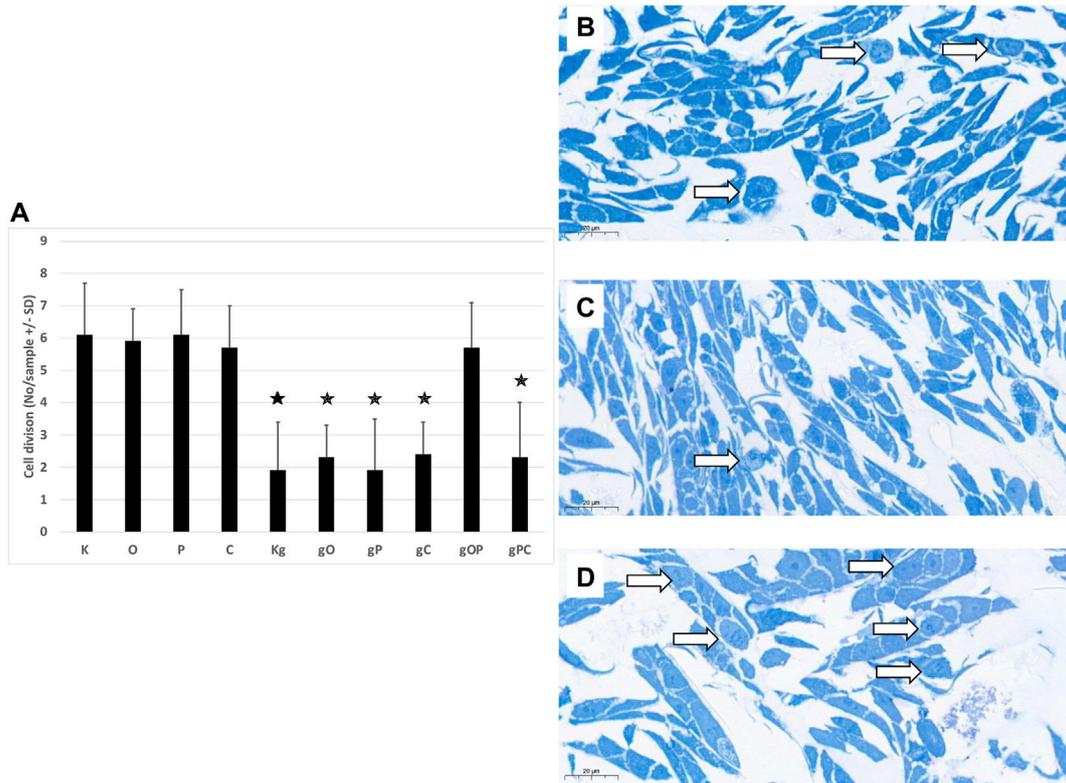
FIGURE 2 | Cell divisions in HT29 cells. **(A)** The graph indicates the average number of cell divisions per sample in the different treatment groups. The representative image inserts highlight the signs of cell division in HT29 cells. **(B)** Control, non-treated cells; **(C)** gDNA-treated control cells; **(D)**: larger number of cell divisions in gOP sample. K, control, non-treated HT29 cells; O, ODN2088; P, picropodophyllin; C, chloroquine; Kg, genomic DNA control; g, genomic DNA; arrows indicate cell divisions; scale bar represents 20 µm; the presence of stars indicates significant differences from K ($p < 0.05$).

FIGURE 3 | Heatmap visualization of the NanoString gene expression analysis. Gene expression alterations in HT29 cells after incubation with genomic self-DNA. g, genomic deoxyribonucleic acid (gDNA); O, ODN2088—TLR9 inhibitor; P, picropodophyllin; C, chloroquine; K, control, non-treated HT29 cells; Kg, gDNA treated control HT29 cells; red, overexpression, green, downregulation.
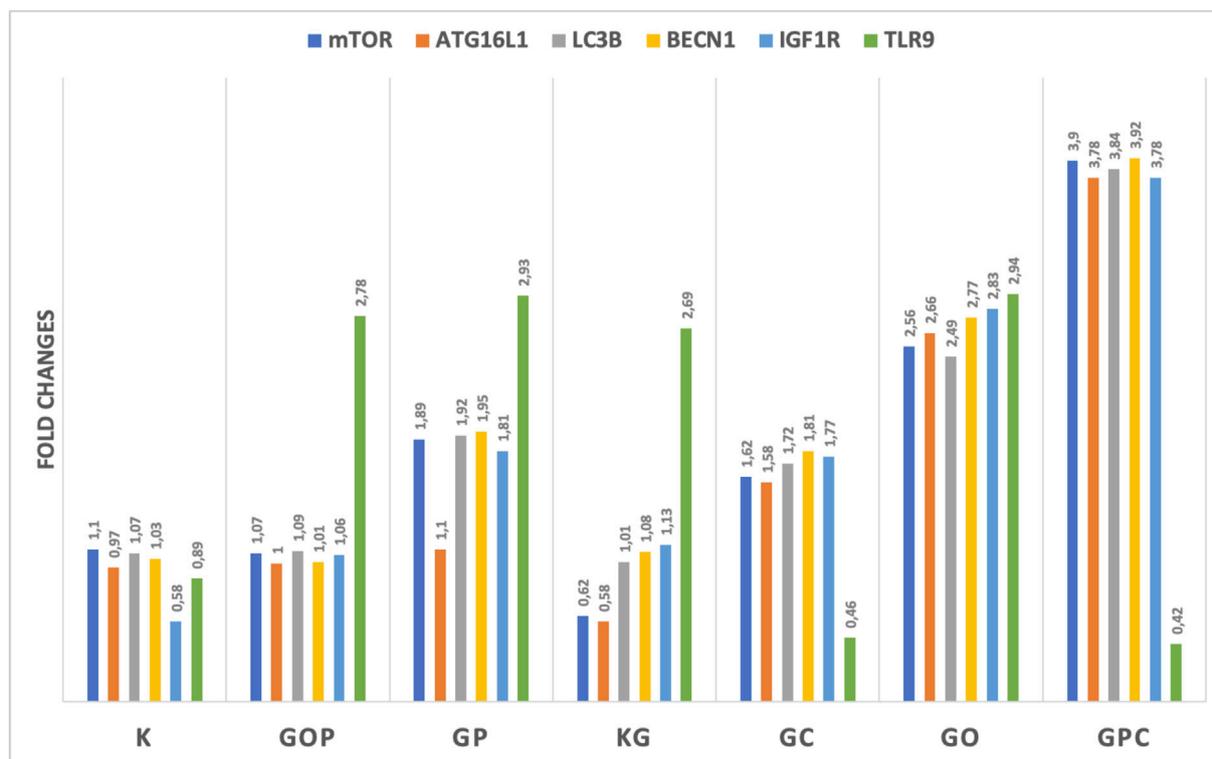
FIGURE 4 | Fold changes in the assayed genes. The gene expression fold changes were in correlation with the NanoString gene expression results. The table indicates the SD values in each case. G/g: genomic deoxyribonucleic acid (gDNA); O, ODN2088—TLR9 inhibitor; P, picropodophyllin; C, chloroquine; K, control, non-treated HT29 cells; Kg, gDNA treated control HT29 cells.

First, we observed that the distribution of non-immunoreactive and weak immunopositive ("−/+"), as well as moderately and strongly immunoreactive ("++/+++") HT29 cells was in correlation with the gene expression results. In the case of IGF1R, moderate to strong immunopositivity was detected to a greater extent after incubation with gO, gC, and gPC. As for autophagy, strong upregulation of ATG16L1 protein expression was found in the gO and pPC groups, followed by the Kg, gP, and gOP treatments. The highest proportion of strong Beclin1 and LC3 immunoreactivity was detected in the gO and gPC groups, followed by the gP and gC treatments.
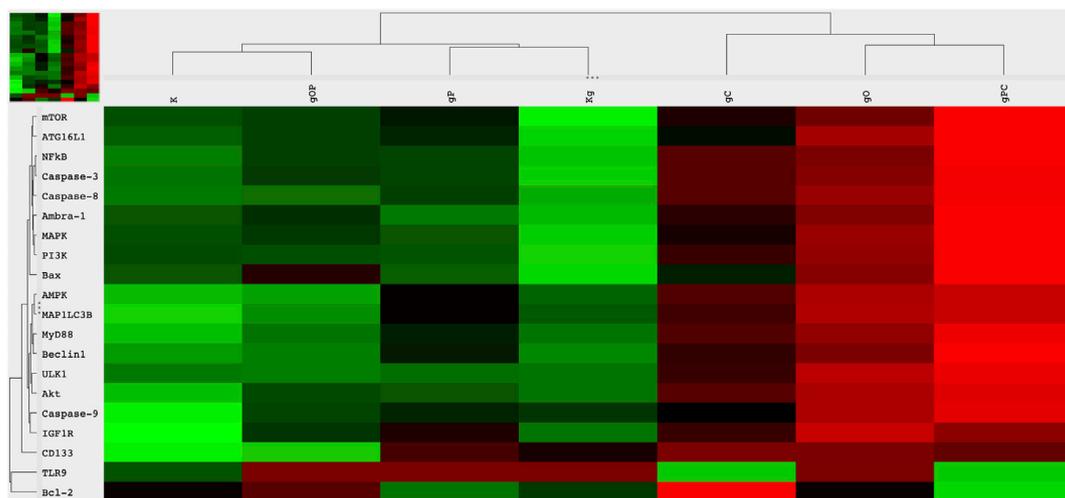
Based on the NanoString gene expression results, we examined whether there was an HT29 cell expressing CD133 protein in each

treatment group. CD133-positive cells were found only scattered in the gO, gP, gC, and gPC treatment groups. The results of the one-way ANOVA test and the representative immunocytochemistry images are visualized in **Figure 5**. The results of the Tukey HSD test can be seen in **Supplementary Figure S1**.

In our experiment, by adding picropodophyllin to gDNA-treated cells, the relatively smaller decrease in PI3K, Akt, AMPK, and mTOR gene expressions resulted in a potential inhibitory effect on autophagy initiation. If autophagy is inhibited, mTOR must be active, so a WES Simple Western blot was also performed. In the cases of K, Kg, and gP groups, the mTOR, phospho-mTOR, and autophagy-related protein expressions,

FIGURE 5 | One-way ANOVA results of IGF1R, ATG16L1, Beclin1, and LC3 immunocytochemistry analyses. The percentages of non-immunoreactive and weakly immunopositive ("–/+"), as well as moderately and strongly immunopositive ("++/+++") HT29 cells within the treatment groups were plotted on box and whisker plots. **(A)** The boxplots for IGF1R. The right upper inserts represent the moderate to strong IGF1R immunopositivity (at ×200 magnification; the scale bar indicates 10 μm). The boxplots and representative immunostainings for ATG16L1 **(B)**, Beclin1 **(C)**, and LC3B **(D)** are also visualized. **(E)** Right lower insert represents CD133 positive HT29 cells (×200 magnification; the scale bar indicates 10 μm). K, control, non-treated HT29 cells; Kg, genomic DNA (gDNA) treated control; gO, gDNA + ODN2088; gP, gDNA + picropodophyllin; gC, gDNA + chloroquine; gOP, gDNA + ODN2088 + picropodophyllin; gPC, gDNA + picropodophyllin + chloroquine.

together with phospho-mTOR activity, were in relation to the gene expression results (**Figure 6**).

Transmission Electron Microscopy

Control, non-treated, metabolically active HT29 cells (3 ± 1 pieces/cell), similarly to chloroquine-treated controls (4 ± 1.5 pieces/cell), displayed autophagic vacuoles (AVs) in the cytoplasm, indicating macroautophagy. The frequency of AVs in ODN2088 (7 ± 1.4 pieces/cell) control cells was higher as compared to control. However, in picropodophyllin-treated control cells AVs were only scattered (0.5 ± 0.5 piece/cell). Incubation with gDNA resulted in the appearance of a more intense macroautophagy (6 ± 2 pieces/cell), and co-administration of ODN2088 (10 ± 2.2 pieces/cell) or chloroquine (5 ± 1.5 pieces/cell) also favored the presence of intense autophagy, represented by disorganized cell structure along with chromatin condensation and blebbing. The combination of gDNA with picpropodophyllin and/or ODN2088, similarly to non-treated control cells, resulted in low number of AVs (2 ± 1.5 pieces/cell in gP; 3 ± 1 pieces/cell in gOP). On the contrary, gDNA, picropodophyllin and chloroquine co-administration caused an intense macroautophagy (11 ± 2.6 pieces/cell).

In the case of the gDNA + picropodophyllin combination, multivesicular bodies (MVBs) were also detected.

Thus, the presence of autophagy was observed in each group of HT29 cells, but to a varying degree. The representative microstructural changes together with the numerical data can be seen in **Figure 7**.

DISCUSSION

In our study, we attempted to answer how IGF1R inhibition modulates the effect of tumor-derived self-DNA on TLR9 signaling and autophagy response by examining the metabolic activity and proliferation of HT29 colon cancer cells.

First, we determined the effect of self-DNA-induced TLR9 signaling modulation on HT29 cell survival. The term "cell-free DNA" refers to all non-encapsulated DNA sequences in the blood stream. A portion of cfDNA is produced by tumor cells through apoptosis, necrosis, or active secretion [34, 35]. In addition to its role in the field of cancer diagnostics, cfDNA could influence the immune response, or promote tumorigenesis and "genometastasis" [36]. These biological effects can be triggered by signaling pathways activated by the interplay of cfDNA with certain cell receptors (including TLRs) or by increasing the
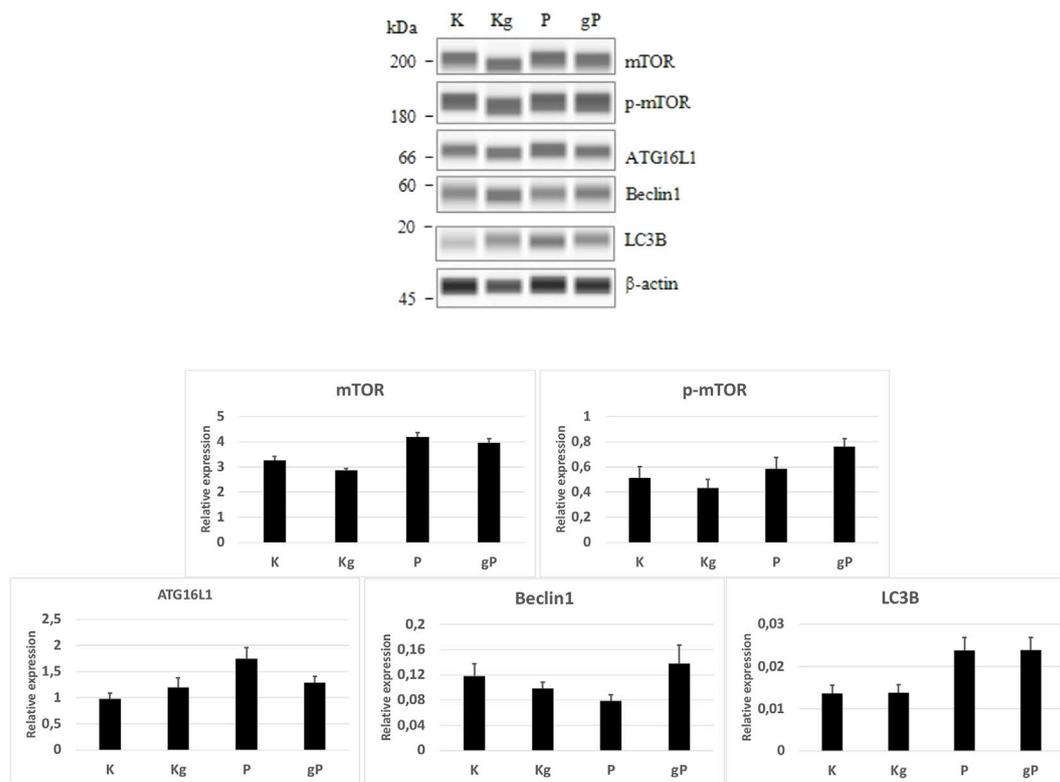
FIGURE 6 | WES Simple Western blot analyses of selected proteins. According to protein expression values normalized to β-actin (bar graphs), the mTOR and phospho-mTOR (p-mTOR) protein activities, as well as the autophagy-related protein (ATG16L1, Beclin1, LC3B) expressions were in relation to the gene expression results. K, control, non-treated HT29 cells; P, picropodophyllin; Kg, genomic DNA control; g, genomic DNA.

transcriptional levels of several genes in an interaction similar to that observed with DNA aptamers [37].

HT29 cells constitutively express TLR9 mRNA [22]. The basal TLR9 gene expression in these cells is low, whereas TLR9 expression is increased by incubation with CpG-ODN or tumorous self-DNA [22, 38]. To support this, in our current experiment, we also detected increased TLR9 gene expression in HT29 cells treated with gDNA as compared to the control, non-treated HT29 group.

Regarding cell survival, we found that gDNA treatment with or without ODN2088, picropodophyllin, or chloroquine altered the metabolic activity and proliferation of HT29 cells to varying degrees. Interestingly, in the case of incubation with only gDNA, this was due to a decrease in the expression level of all examined genes (except for TLR9), while in the case of a combination of gDNA with inhibitors (i.e., O, C, and PC), an increase in gene expression was observed. Partly, this could be explained by the fact that the gDNA-triggered TLR9 signaling pathway may exhibit both survival-promoting and inhibitory effects [25, 39–43]. Blocking TLR9 signaling with ODN2088 increased cellular metabolic activity but did not significantly alter cell proliferation. gDNA treatment alone resulted in a notable decrease in cell proliferation. When ODN2088 was added to cells treated with gDNA, it had a tendency to counteract gDNA's antiproliferative effect. This could be due to the differences in

gene expression levels of central TLR signaling molecules, such as MAPK, PI3K, or NF-κB, which could play key roles [44].

In the following steps, the effect of changes in the interaction of IGF1R and TLR9 signaling pathways on HT29 cell survival was investigated. We observed that IGF1R inhibition *per se* increased the metabolic activity of HT29 cells, but did not significantly affect proliferation. gDNA treatment (and its combination with O, P, C, and PC treatments) significantly reduced cell division. However, gDNA with the combined inhibition of IGF1R and TLR9 signaling (i.e., gOP) abolished suppression of cell proliferation. In the background of this, a notable discrepancy is that the down-regulation of autophagy and apoptosis-related genes was observed, but Bcl2 was overexpressed. The anti-apoptotic and autophagy suppressor effects of Bcl2 overexpression are also reflected in the low level of AVs and increased number of cell divisions found in the gOP treatment group. Bcl-2 regulates programmed cell death during development and tissue repair, and it can have oncogenic abilities by inhibiting cell death rather than promoting cell proliferation [45]. TLR9 activation by CpG-ODN can increase the expression of IGF1 in intestinal epithelial cells [23], and intracellular IGF1 induces Bcl2 expression via IGF1R and epidermal growth factor receptor (EGFR) pathways [45]. According to these results, gDNA together with picropodophyllin could prevent Bcl2 overexpression. However,
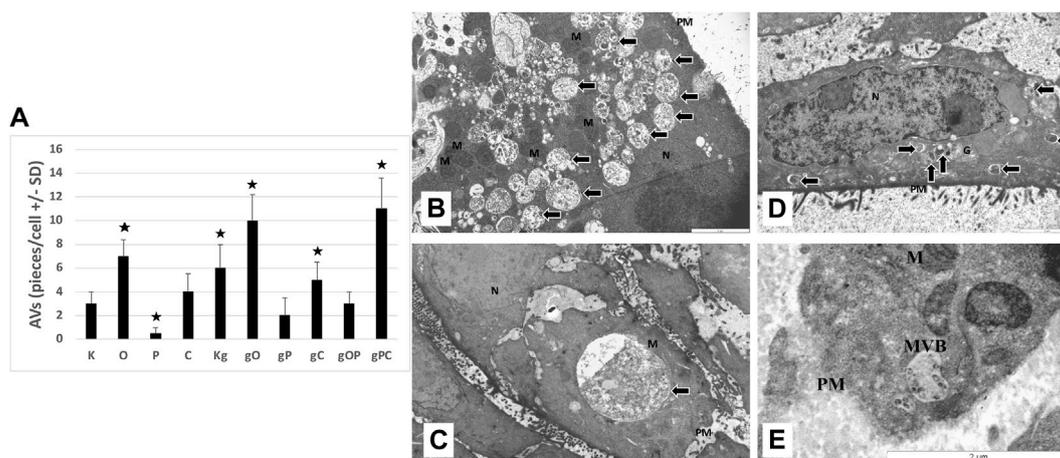
FIGURE 7 | Transmission electron microscopy results. **(A)** The graph indicates the average number of autophagic vacuoles (AVs; pieces/cell) in the different treatment groups. The representative image inserts highlight the autophagy-related structural changes in HT29 cells; **(B)** large number of AVs in gPC (scale bar: 2 µm); **(C)** large late-stage AV in gO (scale bar: 5 µm); **(D)** disorganized nucleus with chromatin condensation (scale bar: 2 µm); **(E)** multivesicular body in gP (scale bar: 2 µm). K, control, non-treated HT29 cells; O, ODN2088; P, picropodophyllin; C, chloroquine; Kg, genomic DNA control; g, genomic DNA; arrows, autophagic vacuoles; MVB, multivesicular body; PM, plasma membrane; N, nucleus; M, mitochondrion; the presence of stars indicates significant differences from K ($p < 0.05$).

by adding ODN2088, Bcl2 became overexpressed, presumably via the IGF1R/EGFR or the TLR9/EGFR signaling cross-talk [45, 46]. Hence, the combined use of tumorous self-DNA and IGF1R inhibitors may display therapeutic (i.e., anti-proliferative) potential. Nevertheless, concomitant TLR9 inhibition may counteract this beneficial effect (**Figure 8**).

We also examined how the interaction of TLR9 and IGF1R signaling affects autophagy and HT29 cell proliferation. Autophagy can be triggered by CpG-ODNs in tumor cell lines (e.g., colon, breast, and prostate cancers) in a TLR9-dependent manner [47]. TLRs and autophagy may be linked by altered glyceraldehyde-3-phosphate dehydrogenase gene expression as well as the generation of reactive oxygen species [48, 49]. There are several shared features between TLR9 and autophagy pathways, such as their effects on cell survival and death, their interactions in endosomes, the positive effect of class III PI3K on their signaling, or their common inhibitors (e.g., chloroquine, 3-methyladenine, bafilomycin A1) [47]. We recently demonstrated a close relationship between TLR9 signaling and autophagy response, with remarkable effects on survival in HT29 cells treated with modified (i.e., hypermethylated or fragmented) self-DNA [25].

In this study, the use of IGF1R inhibition reduced autophagy and also mitigated the pro-autophagic effects of gDNA treatment and TLR9 signaling inhibition. However, concomitant use of chloroquine acted against picropodophyllin, i.e., increased autophagy.

Previous studies have shown that cellular autophagy can be mediated by PI3K/Akt inactivation and consequent AMPK/mTOR downregulation [50, 51]. We found that gDNA treatment caused the downregulation of these genes, which finally resulted in a reduction in the inhibition of autophagy initiation.

IGF1R activation can activate the PI3K/Akt and MAPK pathways, which are mediated by IRS1 and IRS2

phosphorylation after ligand binding [52, 53]. The PI3K/Akt pathway activates the mTOR pathway, which directs protein synthesis and cell growth via downstream effectors [53]. IGF1R can inhibit AMPK activity via Akt1, which phosphorylates an AMPK inhibitory site [54] (**Figure 8**). Picropodophyllin has been recently discovered as a potent inducer of autophagic flux that acts on-target [13].

In our experiment, by adding picropodophyllin to gDNA-treated cells, the relatively smaller decreases in PI3K, Akt, AMPK, and mTOR gene expressions resulted in an inhibitory effect on autophagy initiation, finally leading to a lower number of AVs. On the contrary, pharmacological inhibition of TLR9 resulted in the accumulation of AVs (as compared to gP), suggesting that ODN2088 decreased the anti-autophagic effect of gP combination. Since TLR9 sustains autophagic flux [55], this phenomenon is also understandable.

Chloroquine in itself has been found to inhibit cell growth by blocking autophagy in its late stage and inducing mitochondrion-mediated apoptosis [56]. While the gP combination had anti-autophagic effects, the addition of chloroquine (i.e., gPC) resulted in significantly increased autophagy as well as decreased cell proliferation. Based on these, we hypothesize that the complex balance of inhibitory and promoting factors of autophagy contributes greatly to the development of the ultimate intensity and final biological effect of the process. Regarding HT29 cell proliferation and autophagy, the different effects of P, O, and C individual and combined treatments also highlight that in addition to the TLR9-IGF1R-Bcl2 molecular link, the IGF1R-related and unrelated autophagy machinery is also "Janus-faced" in terms of its effect on cell proliferation.

In this study, we also investigated the impact of IGF1R and autophagy inhibition on the HT29 stem-like phenotype. The presence of CD133-positive cells accompanied by low cell proliferation activity and intense autophagy in the inhibitor-
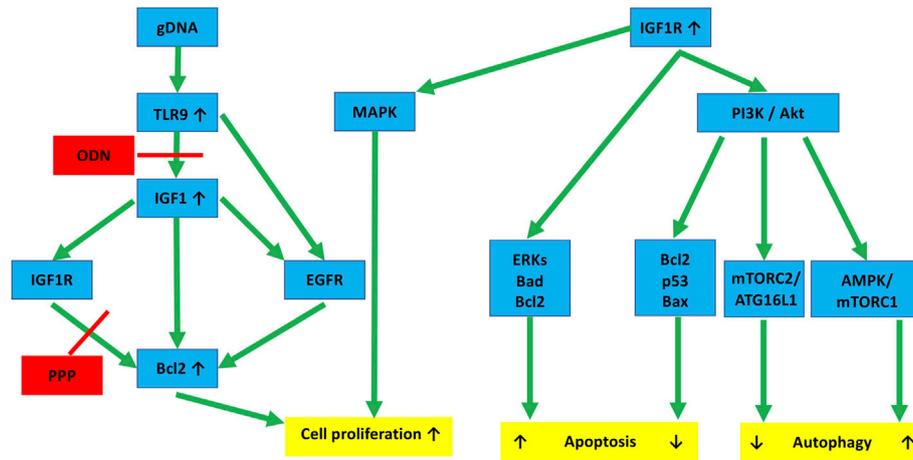
FIGURE 8 | Hypothesized molecular links connecting IGF1R and TLR9 signaling to autophagy and cell proliferation in HT29 cancer cells. TLR9 binding of gDNA through IGF1 and IGF1R activation promotes cell division by enhancing Bcl2. ODN and PPP may inhibit this, but the inhibitory effect can be counteracted by EGFR cross-activation. IGF1R activation via the PI3K/Akt pathway affects autophagy. If it is through the AMPK/mTORC1 pathway, it is a stimulant. If it is through the mTORC2/ATG16L1 pathway, it is primarily inhibitory. Similarly, IGF1R inhibits apoptosis via the Akt-Bcl2-p53-Bax proteins, whereas the Erk-Bad-Bcl2 pathway tends to stimulate it. The final effects are always context-dependent. Red lines, inhibitory effect; gDNA, genomic self-DNA; TLR9, Toll-like receptor 9; ODN, oligodeoxynucleic acid 2088; IGF1, insulin-like growth factor 1; IGF1R, insulin-like growth factor 1 receptor; EGFR, epidermal growth factor receptor; PPP, picropodophyllin; Bcl2, B-cell lymphoma 2; MAPK, Mitogen-activated protein kinase; PI3K, Phosphoinositide 3-kinase; Akt, Ak strain transforming; Bax, BCL2 associated X; AMPK, AMP-activated protein kinase; mTOR, Mechanistic/mammalian target of rapamycin; mTORC1/2, mTOR complex 1/2; ERKs, extracellular signal-regulated kinases; ATG16L1, Autophagy Related 16 Like 1; Bad, BCL2-associated agonist of cell death.

treated groups (i.e., gP, gC, gO, and gPC) calls attention to a potentially serious therapeutic consequence of IGF1R and/or autophagy-inhibition. In several tumor tissues, unbalanced IGF1R signaling can promote cancer cell proliferation and activate cancer reprogramming [2, 57]. Recently, IGF1R has been shown to facilitate epithelial-mesenchymal transition and cancer stem cell properties via Akt activation [58, 59]. In addition, autophagy is known to assist stem cell maintenance in several cell types [60]. In the case of IGF1R inhibition, the simultaneously induced protective autophagy could promote cell proliferation and suppress apoptosis. Thus, *via* autophagy, it antagonizes its own original biological effects on cells [11]. By combining IGF1R inhibition with autophagy disruptive agents, autophagy can be blocked, which can lead to suppressing cancer cell proliferation and enhancing apoptosis [11]. Because CD133-positive HT29 cells were only scattered in cell smears and could not be differentiated in TEM sections, we cannot tell how autophagy develops in CD133-positive HT29 stem-like cells. We only know that the overall autophagy flux in HT29 treatment groups is favorable for the appearance of the CD133 phenotype. However, the assessment of autophagic flux within CD133-positive HT29 stem-like cells would definitely be worth examining in the future.

From our experiment, it is possible that autophagy induced by different combinations of gDNA and the used inhibitors is unable to save HT29 cells from death. Furthermore, it could force some CD133-positive stem-like HT29 cells to promote survival. Supporting this hypothesis, it was found that curcumin promoted proliferation and autophagic survival of colon cancer stem cells [61]. This finding suggests the survival benefit from autophagy, permitting the long-term persistence of CRC stem cells [62].

By using TEM, we examined the relationship between IGF1R inhibition and autophagy to ultrastructural changes. In the case of gP-treated HT29 cells, multivesicular bodies (MVBs) were detected. There are at least three possible reasons for this phenomenon. The first is that receptors (such as the receptor tyrosine kinase IGF1R) can be quickly recycled back from early endosomes to the plasma membrane in a process called "back fusion." During the maturation of the early endosome, its biochemical composition changes with increasing luminal acidification. Finally intraluminal vesicles, or MVBs are formed [57]. At this level, IGF1R can be delivered for recycling. The second is that MVBs containing endocytosed IGF1R can fuse with the plasma membrane and then release their content as "exosomes." IGF1R has been reported to be released by cells in this way [2, 58, 59]. Thirdly, it has been recently demonstrated that in the absence of stromal cells, MVB-like small extracellular vesicle complexes can be released by HT29 cells [60].

In our study, the observed ultrastructural alterations call attention to the role of autophagy in cell protection or even in promoting cell death. In the gP cell group where the presence of MVBs was detected in addition to autophagic vacuoles, the expression of autophagy-related proteins (Beclin1, ATG16L1, LC3B) was increased as compared to control, non-treated cells. This result suggests that autolysosomal degradation is also likely to be present following the formation of amphisomes via the interconnection of autophagosome and multivesicular body pathways [61]. The amphisome functions as a prelysosomal compartment where the endocytic and autophagic pathways meet [62, 63]. The contents of amphisomes could have multiple fates, such as extracellular

release or lysosomal degradation. Both exosome biogenesis and autophagy display pivotal roles in maintaining cellular homeostasis and enhancing stress tolerance [64–68]. Influencing these functions for cancer cells may allow the identification of realistic therapeutic targets.

CONCLUSION

In summary, the combination of tumorous self-DNA treatment with ODN2088, picropodophyllin, or chloroquine alters the metabolic activity and proliferation of HT29 cells to varying degrees. Inhibition of TLR9 signaling adversely affects the influence of self-DNA treatment on cell proliferation. The concomitant use of tumor-derived self-DNA and IGF1R inhibitors displays anti-proliferative potential. However, parallel TLR9 signaling inhibition negatively changes this beneficial effect. We found that the complex balance of inhibitory and promotional factors in autophagy greatly contributes to the characteristics of its final intensity and biological outcomes. The different effects of picropodophyllin, ODN2088, and chloroquine alone or in combination on HT29 cell proliferation and autophagy suggest that in addition to the TLR9-IGF1R-Bcl2 molecular linkage, the IGF1R-associated and non-IGF1R-associated autophagy machinery is "Janus-faced" in terms of its effect on cell proliferation. Based on our results, it is also possible that autophagy, induced by different combinations of tumorous self-DNA and inhibitors is not sufficient to rescue HT29 cells from irreversible death, but may result in the survival of some CD133-positive stem-like cancer cells, which could promote CRC recurrence. The ultrastructural changes we observed also support the context-dependent role of IGF1R inhibition and autophagy on cell survival and proliferation.

The creation of new types of combined IGF1R, autophagy, and/or TLR9 signaling inhibitors would play a significant role in the development of more personalized anti-tumor therapies. However, our present experiments should be tested in additional TLR9-expressing cell lines. Further research is also mandatory to investigate the biological effects of modified self-DNA fragments, since methylation status or fragment length may also affect the experimental results.

DATA AVAILABILITY STATEMENT

The original contributions presented in the study are included in the article/**Supplementary Material**, further inquiries can be directed to the corresponding author.

REFERENCES

1. Girnita L, Worrall C, Takahashi S-I, Seregard S, Girnita A. Something Old, Something New and Something Borrowed: Emerging Paradigm of Insulin-like Growth Factor Type 1 Receptor (IGF-1R) Signaling Regulation. *Cell. Mol. Life Sci.* (2014) 71(13):2403–27. doi:10.1007/s00018-013-1514-y

AUTHOR CONTRIBUTIONS

FUNDING

CONFLICT OF INTEREST

Author BW was employed by the company Lufthansa Systems Hungária.

The remaining authors declare that the research was conducted in the absence of any commercial or financial relationships that could be construed as a potential conflict of interest.

ACKNOWLEDGMENTS

SUPPLEMENTARY MATERIAL

The Supplementary Material for this article can be found online at: https://www.por-journal.com/articles/10.3389/pore.2022.1610322/full#supplementary-material

Supplementary Figure S1 | Regarding immunocytochemistries, the results of the Tukey HSD test and the adjusted *p*-values of the comparisons of each treatment group can be seen (*p* < 0.05 represents statistical significance).

2. Chen P-C, Kuo Y-C, Chuong C-M, Huang Y-H. Niche Modulation of IGF-1R Signaling: Its Role in Stem Cell Pluripotency, Cancer Reprogramming, and Therapeutic Applications. *Front Cel Dev. Biol.* (2021) 8:625943. doi:10.3389/fcell.2020.625943
3. Wit JM, Walenkamp MJ. Role of Insulin-like Growth Factors in Growth, Development and Feeding. *World Rev Nutr Diet* (2013) 106:60–5. doi:10.1159/000342546

4. Sell C, Rubini M, Rubin R, Liu JP, Efstratiadis A, Baserga R. Simian Virus 40 Large Tumor Antigen Is Unable to Transform Mouse Embryonic Fibroblasts Lacking Type 1 Insulin-like Growth Factor Receptor. *Proc Natl Acad Sci U.S.A* (1993) 90(23):11217–21. doi:10.1073/pnas.90.23.11217

5. Sell C, Dumenil G, Deveaud C, Miura M, Coppola D, DeAngelis T, et al. Effect of a Null Mutation of the Insulin-like Growth Factor I Receptor Gene on Growth and Transformation of Mouse Embryo Fibroblasts. *Mol Cel Biol* (1994) 14(6):3604–12. doi:10.1128/mcb.14.6.3604-3612.1994

6. Weber MM, Fottner C, Liu SB, Jung MC, Engelhardt D, Baretton GB. Overexpression of the Insulin-like Growth Factor I Receptor in Human colon Carcinomas. *Cancer* (2002) 95(10):2086–95. doi:10.1002/cncr.10945

7. Hakam A, Yeatman TJ, Lu L, Mora L, Marcet G, Nicosia SV, et al. Expression of Insulin-like Growth Factor-1 Receptor in Human Colorectal Cancer. *Hum Pathol* (1999) 30(10):1128–33. doi:10.1016/s0046-8177(99)90027-8

8. Mitsiades CS, Mitsiades NS, McMullan CJ, Poulaki V, Shringarpure R, Akiyama M, et al. Inhibition of the Insulin-like Growth Factor Receptor-1 Tyrosine Kinase Activity as a Therapeutic Strategy for Multiple Myeloma, Other Hematologic Malignancies, and Solid Tumors. *Cancer Cell* (2004) 5(3): 221–30. doi:10.1016/s1535-6108(04)00050-9

9. White E. The Role for Autophagy in Cancer. *J Clin Invest* (2015) 125:42–6. doi:10.1172/JCI73941

10. Lin X, Peng Z, Wang X, Zou J, Chen D, Chen Z, et al. Targeting Autophagy Potentiates Antitumor Activity of Met-TKIs against Met-Amplified Gastric Cancer. *Cell Death Dis* (2019) 10:139. doi:10.1038/s41419-019-1314-x

11. Sipos F, Székely H, Kis ID, Tulassay Z, Műzes G. Relation of the IGF/IGF1R System to Autophagy in Colitis and Colorectal Cancer. *World J Gastroenterol* (2017) 23(46):8109–19. doi:10.3748/wjg.v23.i46.8109

12. Wu Q, Tian A-L, Kroemer G, Kepp O. Autophagy Induction by IGF1R Inhibition with Picropodophyllin and Linsitinib. *Autophagy* (2021) 17:2046–7. doi:10.1080/15548627.2021.1936934

13. Wu Q, Tian A-L, Li B, Leduc M, Forveille S, Hamley P, et al. IGF1 Receptor Inhibition Amplifies the Effects of Cancer Drugs by Autophagy and Immune-dependent Mechanisms. *J Immunother Cancer* (2021) 9(6):e002722. doi:10. 1136/jitc-2021-002722

14. Renna M, Bento CF, Fleming A, Menzies FM, Siddiqi FH, Ravikumar B, et al. IGF-1 Receptor Antagonism Inhibits Autophagy. *Hum Mol Genet* (2013) 22(22):4528–44. doi:10.1093/hmg/ddt300

15. Wu W, Ma J, Shao N, Shi Y, Liu R, Li W, et al. Co-Targeting IGF-1R and Autophagy Enhances the Effects of Cell Growth Suppression and Apoptosis Induced by the IGF-1R Inhibitor NVP-AEW541 in Triple-Negative Breast Cancer Cells. *PLoS One* (2017) 12(1):e0169229. doi:10.1371/journal.pone. 0169229

16. Mandel P, Metais P. Nuclear Acids in Human Blood Plasma. *C R Seances Soc Biol Fil* (1948) 142:241–3.

17. Mansour H. Cell-free Nucleic Acids as Noninvasive Biomarkers for Colorectal Cancer Detection. *Front Genet* (2014) 5:182. doi:10.3389/fgene.2014.00182

18. Butt AN, Swaminathan R. Overview of Circulating Nucleic Acids in Plasma/ serum. *Ann N Y Acad Sci* (2008) 1137:236–42. doi:10.1196/annals.1448.002

19. Gormally E, Caboux E, Vineis P, Hainaut P. Circulating Free DNA in Plasma or Serum as Biomarker of Carcinogenesis: Practical Aspects and Biological Significance. *Mutat Res Reviews Mutat Res* (2007) 635:105–17. doi:10.1016/j. mrrev.2006.11.002

20. Rauh P, Rickes S, Fleischhacker M. Microsatellite Alterations in Free-Circulating Serum DNA in Patients with Ulcerative Colitis. *Dig Dis* (2003) 21:363–6. doi:10.1159/000075361

21. Gosu V, Basith S, Kwon O-P, Choi S. Therapeutic Applications of Nucleic Acids and Their Analogues in Toll-like Receptor Signaling. *Molecules* (2012) 17:13503–29. doi:10.3390/molecules171113503

22. Fűri I, Sipos F, Spisák S, Kiszner G, Wichmann B, Schöller A, et al. Association of Self-DNA Mediated TLR9-Related Gene, DNA Methyltransferase, and Cytokeratin Protein Expression Alterations in HT29-Cells to DNA Fragment Length and Methylation Status. *Scientific World J* (2013) 2013: 1–8. doi:10.1155/2013/293296

23. Ge R-T, Mo L-H, Wu R, Liu J-Q, Zhang H-P, Liu Z, et al. Insulin-like Growth Factor-1 Endues Monocytes with Immune Suppressive Ability to Inhibit Inflammation in the Intestine. *Sci Rep* (2015) 5:7735. doi:10.1038/srep07735

24. Hofmann C, Dunger N, Doser K, Lippert E, Siller S, Edinger M, et al. Physiologic TLR9-CpG-DNA Interaction Is Essential for the Homeostasis

25. Sipos F, Kiss AL, Constantinovits M, Tulassay Z, Műzes G. Modified Genomic Self-DNA Influences *In Vitro* Survival of HT29 Tumor Cells via TLR9- and Autophagy Signaling. *Pathol Oncol Res* (2019) 25:1505–17. doi:10.1007/ s12253-018-0544-z

26. Wang C, Ji L, Yuan X, Jin Y, Cardona CJ, Xing Z. Differential Regulation of TLR Signaling on the Induction of Antiviral Interferons in Human Intestinal Epithelial Cells Infected with Enterovirus 71. *PLoS One* (2016) 11(3):e0152177. doi:10.1371/journal.pone.0152177

27. Li Y, Lu K, Zhao B, Zeng X, Xu S, Ma X, et al. Depletion of Insulin-like Growth Factor 1 Receptor Increases Radiosensitivity in Colorectal Cancer. *J Gastrointest Oncol* (2020) 11(6):1135–45. doi:10.21037/jgo-20-210

28. Buck E, Gokhale PC, Koujak S, Brown E, Eyzaguirre A, Tao N, et al. Compensatory Insulin Receptor (IR) Activation on Inhibition of Insulin-like Growth Factor-1 Receptor (IGF-1R): Rationale for Cotargeting IGF-1R and IR in Cancer. *Mol Cancer Ther* (2010) 9(10):2652–64. doi:10.1158/1535-7163.MCT-10-0318

29. Nowakowska M, Pospiech K, Lewandowska U, Piastowska-Ciesielska AW, Bednarek AK. Diverse Effect of WWOX Overexpression in HT29 and SW480 colon Cancer Cell Lines. *Tumor Biol* (2014) 35(9):9291–301. doi:10.1007/ s13277-014-2196-2

30. Ogoshi K, Hashimoto S-i., Nakatani Y, Qu W, Oshima K, Tokunaga K, et al. Genome-wide Profiling of DNA Methylation in Human Cancer Cells. *Genomics* (2011) 98(4):280–7. doi:10.1016/j.ygeno.2011.07.003

31. Moulis M, Vindis C. Methods for Measuring Autophagy in Mice. *Cells* (2017) 6(2):14. doi:10.3390/cells6020014

32. Rampersad SN. Multiple Applications of Alamar Blue as an Indicator of Metabolic Function and Cellular Health in Cell Viability Bioassays. *Sensors* (2012) 12(9):12347–60. doi:10.3390/s120912347

33. R Core Team. *R: A Language and Environment for Statistical Computing*. Vienna, Austria: R Foundation for Statistical Computing (2019). Available at: https://www.R-project.org/.

34. Bronkhorst AJ, Wentzel JF, Aucamp J, van Dyk E, du Plessis L, Pretorius PJ. Characterization of the Cell-free DNA Released by Cultured Cancer Cells. *Biochim Biophys Acta Mol Cel Res* (2016) 1863(1):157–65. doi:10.1016/j. bbamcr.2015.10.022

35. Ungerer V, Bronkhorst AJ, Van den Ackerveken P, Herzog M, Holdenrieder S. Serial Profiling of Cell-free DNA and Nucleosome Histone Modifications in Cell Cultures. *Sci Rep* (2021) 11(1):9460. doi:10.1038/s41598-021-88866-5

36. Souza AGD, Bastos VAF, Fujimura PT, Ferreira ICC, Leal LF, da Silva LS, et al. Cell-free DNA Promotes Malignant Transformation in Non-tumor Cells. *Sci Rep* (2020) 10(1):21674. doi:10.1038/s41598-020-78766-5

37. Zhou J, Rossi J. Aptamers as Targeted Therapeutics: Current Potential and Challenges. *Nat Rev Drug Discov* (2017) 16(3):181–202. doi:10.1038/nrd. 2016.199

38. Akhtar M, Watson JL, Nazli A, McKay DM. Bacterial DNA Evokes Epithelial IL-8 Production by a MAPK-dependent, NFκB-independent Pathway. *FASEB J.* (2003) 17:1319–21. doi:10.1096/fj.03-0950fje10.1096/fj.02-0950fje

39. Shahriari S, Rezaeifard S, Moghimi HR, Khorramizadeh MR, Faghih Z. Cell Membrane and Intracellular Expression of Toll-like Receptor 9 (TLR9) in Colorectal Cancer and Breast Cancer Cell-Lines. *Cancer Biomark* (2017) 18: 375–80. doi:10.3233/cbm-160260

40. Sun H, Li X, Fan L, Wu G, Li M, Fang J. TRAF6 is Upregulated in colon Cancer and Promotes Proliferation of colon Cancer Cells. *Int J Biochem Cel Biol* (2014) 53:195–201. doi:10.1016/j.biocel.2014.04.010

41. Marcuello M, Mayol X, Felipe-Fumero E, Costa J, López-Hierro L, Salvans S, et al. Modulation of the colon Cancer Cell Phenotype by Pro-inflammatory Macrophages: A Preclinical Model of Surgery-Associated Inflammation and Tumor Recurrence. *PLoS One* (2018) 13:e0192958. doi:10.1371/journal.pone. 0192958

42. Ning Y, Manegold PC, Hong YK, Zhang W, Pohl A, Lurje G, et al. Interleukin-8 is Associated with Proliferation, Migration, Angiogenesis and Chemosensitivity *In Vitro* and *In Vivo* in colon Cancer Cell Line Models. *Int J Cancer* (2011) 128:2038–49. doi:10.1002/ijc.25562

43. Liu H, Li G, Zhang B, Sun D, Wu J, Chen F, et al. Suppression of the NF-κB Signaling Pathway in colon Cancer Cells by the Natural Compound Riccardin

D from Dumortierahirsute. *Mol Med Rep* (2018) 17:5837–43. doi:10.3892/mmr.2018.8617

44. Li X, Jiang S, Tapping RI. Toll-like Receptor Signaling in Cell Proliferation and Survival. *Cytokine* (2010) 49(1):1–9. doi:10.1016/j.cyto.2009.08.010

45. Chand HS, Harris JF, Mebratu Y, Chen Y, Wright PS, Randell SH, et al. Intracellular Insulin-like Growth Factor-1 Induces Bcl-2 Expression in Airway Epithelial Cells. *J Immunol* (2012) 188(9):4581–9. doi:10.4049/jimmunol.1102673

46. Veleeparambil M, Poddar D, Abdulkhalek S, Kessler PM, Yamashita M, Chattopadhyay S, et al. Constitutively Bound EGFR-Mediated Tyrosine Phosphorylation of TLR9 is Required for its Ability to Signal. *J Immunol* (2018) 200(8):2809–18. doi:10.4049/jimmunol.1700691

47. Bertin S, Pierrefite-Carle V. Autophagy and Toll-like Receptors: A New Link in Cancer Cells. *Autophagy* (2008) 4:1086–9. doi:10.4161/auto.7138

48. Colell A, Ricci J-E, Tait S, Milasta S, Maurer U, Bouchier-Hayes L, et al. GAPDH and Autophagy Preserve Survival after Apoptotic Cytochrome C Release in the Absence of Caspase Activation. *Cell* (2007) 129:983–97. doi:10.1016/j.cell.2007.03.045

49. Lemasters JJ. Selective Mitochondrial Autophagy, or Mitophagy, as a Targeted Defense against Oxidative Stress, Mitochondrial Dysfunction, and Aging. *Rejuvenation Res* (2005) 8:3–5. doi:10.1089/rej.2005.8.3

50. Zhao Z-Q, Yu Z-Y, Li J, Ouyang X-N. Gefitinib Induces Lung Cancer Cell Autophagy and Apoptosis via Blockade of the PI3K/AKT/mTOR Pathway. *Oncol Lett* (2016) 12(1):63–8. doi:10.3892/ol.2016.4606

51. Wang H, Liu Y, Wang D, Xu Y, Dong R, Yang Y, et al. The Upstream Pathway of mTOR-Mediated Autophagy in Liver Diseases. *Cells* (2019) 8(12):1597. doi:10.3390/cells8121597

52. Le Roith D, Zick Y. Recent Advances in Our Understanding of Insulin Action and Insulin Resistance. *Diabetes Care* (2001) 24(3):588–97. doi:10.2337/diacare.24.3.588

53. Cheng Z, Tseng Y, White MF. Insulin Signaling Meets Mitochondria in Metabolism. *Trends Endocrinol Metab* (2010) 21(10):589–98. doi:10.1016/j.tem.2010.06.005

54. Ning J, Xi G, Clemmons DR. Suppression of AMPK Activation via S485 Phosphorylation by IGF-I during Hyperglycemia is Mediated by AKT Activation in Vascular Smooth Muscle Cells. *Endocrinology* (2011) 152(8):3143–54. doi:10.1210/en.2011-0155

55. De Leo MG, Staiano L, Vicinanza M, Luciani A, Carissimo A, Mutarelli M, et al. Autophagosome-lysosome Fusion Triggers a Lysosomal Response Mediated by TLR9 and Controlled by OCRL. *Nat Cel Biol* (2016) 18(8):839–50. doi:10.1038/ncb3386

56. Liu L, Han C, Yu H, Zhu W, Cui H, Zheng L, et al. Chloroquine Inhibits Cell Growth in Human A549 Lung Cancer Cells by Blocking Autophagy and Inducing Mitochondrial-Mediated Apoptosis. *Oncol Rep* (2018) 39(6):2807–16. doi:10.3892/or.2018.6363

57. Ngo M-HT, Jeng H-Y, Kuo Y-C, Diony Nanda J, Brahmadhi A, Ling T-Y, et al. The Role of IGF/IGF-1R Signaling in Hepatocellular Carcinomas: Stemness-Related Properties and Drug Resistance. *Int J Mol Sci* (2021) 22(4):1931. doi:10.3390/ijms22041931

58. Wang X-H, Wu H-Y, Gao J, Wang X-H, Gao T-H, Zhang S-F. IGF1R Facilitates Epithelial-Mesenchymal Transition and Cancer Stem Cell Properties in Neuroblastoma via the STAT3/AKT axis. *Cancer Manag Res* (2019) 11:5459–72. doi:10.2147/CMAR.S196862

59. Singh RK, Dhadve A, Sakpal A, De A, Ray P. An Active IGF-1r-AKT Signaling Imparts Functional Heterogeneity in Ovarian CSC Population. *Sci Rep* (2016) 6:36612. doi:10.1038/srep36612

60. Xue F, Hu L, Ge R, Yang L, Liu K, Li Y, et al. Autophagy-deficiency in Hepatic Progenitor Cells Leads to the Defects of Stemness and Enhances Susceptibility to Neoplastic Transformation. *Cancer Lett* (2016) 371(1):38–47. doi:10.1016/j.canlet.2015.11.022

61. Kantara C, O'Connell M, Sarkar S, Moya S, Ullrich R, Singh P. Curcumin Promotes Autophagic Survival of a Subset of colon Cancer Stem Cells, Which are Ablated by DCLK1-siRNA. *Cancer Res* (2014) 74(9):2487–98. doi:10.1158/0008-5472.CAN-13-3536

62. Nazio F, Bordi M, Cianfanelli V, Locatelli F, Cecconi F. Autophagy and Cancer Stem Cells: Molecular Mechanisms and Therapeutic Applications. *Cell Death Differ* (2019) 26(4):690–702. doi:10.1038/s41418-019-0292-y

63. Wollert T, Hurley JH. Molecular Mechanism of Multivesicular Body Biogenesis by ESCRT Complexes. *Nature* (2010) 464(7290):864–9. doi:10.1038/nature08849

64. DeRita RM, Zerlanko B, Singh A, Lu H, Iozzo RV, Benovic JL, et al. c-Src, Insulin-like Growth Factor I Receptor, G-Protein-Coupled Receptor Kinases and Focal Adhesion Kinase Are Enriched into Prostate Cancer Cell Exosomes. *J Cel Biochem.* (2017) 118(1):66–73. doi:10.1002/jcb.25611

65. Crudden C, Song D, Cismas S, Trocmé E, Pasca S, Calin GA, et al. Below the Surface: IGF-1R Therapeutic Targeting and its Endocytic Journey. *Cells* (2019) 8(10):1223. doi:10.3390/cells8101223

66. Valcz G, Buzás EI, Kittel Á, Krenács T, Visnovitz T, Spisák S, et al. *En Bloc* Release of MVB-like Small Extracellular Vesicle Clusters by Colorectal Carcinoma Cells. *J Extracellular Vesicles* (2019) 8(1):1596668. doi:10.1080/20013078.2019.1596668

67. Fader CM, Colombo MI. Autophagy and Multivesicular Bodies: Two Closely Related Partners. *Cel Death Differ* (2009) 16:70–8. doi:10.1038/cdd.2008.168

68. Berg TO, Fengsrud M, Strømhaug PE, Berg T, Seglen PO. Isolation and Characterization of Rat Liver Amphisomes. Evidence for Fusion of Autophagosomes with Both Early and Late Endosomes. *J Biol Chem* (1998) 273:21883–92. doi:10.1074/jbc.273.34.21883

The Prevalence of High-Risk Human Papillomavirus in Hungary—A Geographically Representative, Cross-Sectional Study

András István Fogarasi[1]*, Márta Benczik[1], Ágota Moravcsik-Kornyicki[2], Adrienn Kocsis[1], Anikó Gyulai[3] and Zsigmond Kósa[2]

[1]SYNLAB Genoid Molecular Diagnostic Laboratory, SYNLAB Hungary Ltd., Budapest, Hungary, [2]Department of Health Visitors Methodology and Prevention, University of Debrecen, Nyíregyháza, Hungary, [3]Department of Preventive Health Sciences, Institute of Applied Health Sciences, University of Miskolc, Miskolc, Hungary

Background: The estimated age-standardized incidence and mortality rates of cervical cancer in Hungary are substantially higher than the European average. In many countries, human papillomavirus (HPV) testing is the first-line method of cervical cancer screening in women >30 years. According to the European guidelines, evidence-based improvement of a national prevention strategy requires the monitoring of representative data.

Methods: ThinPrep cervical samples were collected over a period of 8 months at 84 sampling sites, including 4,000 eligible samples with valid laboratory results from the screening target population of females aged 25–65 years, with addresses in the representative geographic area (19 counties and four major settlement types). Genotyping of high-risk HPV (hrHPV) was performed using the Confidence HPV-X (Neumann Diagnostics) and Linear Array HPV Genotyping (Roche) tests. Demographic data were collected using a questionnaire, enabling the analysis of hrHPV genotype distribution by age, geography, education, and HPV vaccination.

Results: Overall, 446 samples were hrHPV-positive, showing a prevalence of 11.15% (9.73% age-representative), similar to the world average, higher than the European average, and lower than the Eastern-European average. After age standardization, no significant geographic differences were found, except for low hrHPV prevalence in villages ($p = 0.036$) and in those with elementary education ($p = 0.013$). Following genotypes 16 and 31, in order of frequency, certain non-vaccine hrHPV genotypes (HPV51, 66, 56) showed unexpectedly higher prevalence than international data.

Conclusion: Our study provides the first geographically representative genotype-specific hrHPV prevalence baseline database in Hungary to support policy-making efforts. Significant correlations with demographic data have transferable conclusions.

Keywords: cervical cancer, cancer screening, cross-sectional studies, genotype, human papillomavirus infection, human papillomavirus vaccines, prevalence studies, rural population

INTRODUCTION

The estimated age-standardized incidence and mortality rates of cervical cancer in Hungary (17.2 and 4.9 per 100,000 women, respectively) are substantially higher than the European averages (10.7 and 3.8 per 100,000 women, respectively). In regional comparisons, Central and Eastern Europe had notably higher incidence and mortality rates (14.5 and 6.1 per 100,000 women, respectively) than Western, Southern, and Northern Europe (7.0, 7.7, and 10.4 per 100,000 women and 2.0, 2.3, and 2.2 per 100,000 women, respectively). In addition, the age-standardized overall cancer mortality in Hungary was found to be the least favorable in the European Union, adding a burden to an ageing population, economy, and health care system (1).

Testing for high-risk genotypes of human papillomavirus (hrHPV) has already been widely considered a more effective first-line screening method for preventing cervical cancer than the conventional Papanicolaou Pap-smear. This also requires less frequent screening intervals, owing to its superior sensitivity and negative predictive value (2). The European Guideline has recommended the use of hrHPV screening alone for women aged >30 years (3). Therefore, many countries have implemented this in their public health policies and practices.

In addition to optimizing immunization, screening, triage, and therapy procedures, evidence-based improvement of national prevention policy requires the collection and evaluation of representative data to continuously monitor the efficacy of changes, better understand and respond to demographic differences, and focus efforts and resources accordingly. Our study aimed to provide the first geographically representative baseline hrHPV genotype database for Hungary to prepare an update in the guidelines for HPV-based screening, shortly after the introduction of the nonavalent vaccine, replacing the bivalent one, into the nationwide school vaccination program.

MATERIALS AND METHODS

Our objective was to collect and analyze 4,000 cervical samples from women aged 25–65 years who were inhabitants of settlements geographically representative of Hungary's such sub-population. A predetermined patient number matrix was prepared for each of Hungary's 19 counties and stratified according to the four major settlement type levels (capital, county-level city, town, and village). This reflected the previously published official demographic data on women aged 25–65 years (see grey part of **Table 1**).

A total of 4,731 cervical samples were collected using the Rovers Cervex-Brush Combi RT™ device (Rovers Medical Devices; Oss, Netherlands) into ThinPrep PreservCyt™ liquid-based cytology containers (Cytyc Corporation; MA, United States) over a period of 8 months (December 2018–July 2019) by 84 competent sampling sites that were appointed randomly. These included 4,000 eligible samples with valid laboratory results from the screening target population of females aged 25–65 years, with addresses in the representative geographic area (counties and settlement types). We excluded participants with histories of hysterectomies, immunosuppression, recent (within 2 months) childbirths, operations or samplings that affected the cervix, and current menstruation. In each county, there were an average of 2–3 health care institutions and 2–3 registered health visitors who collected samples from women after securing their informed consent, guided by the approved standard recruitment, sampling, and documentation protocol in compliance with the Declaration of Helsinki (ethical approval obtained from ETT TUKEB; approval no. 61407-2/2016/EKU).

The detection and genotyping of hrHPV were performed through nucleic acid testing (multiplex real-time PCR amplification) using the Confidence HPV-X™ (Neumann Diagnostics; Budapest, Hungary) and Linear Array™ HPV Genotyping (Roche; Basel, Switzerland), which are both clinically validated commercial CE-marked *in vitro* diagnostic tests (4). The laboratory that performed the tests was selected through a public procurement process. The procedure commenced with the primary HPV test, using the QuantStudio™ 6 Flex (LifeTechnologies; CA, United States) platform, to detect all 14 hrHPV genotypes. However, only seven hrHPV genotypes were detected individually (HPV 16, 18, 31, 33, 45, 52, 58, present in the 9-valent vaccine), while the rest were detected in a group (HPV 35, 39, 51, 56, 59, 66, 68—66 and 68 have been re-classified by the World Health Organization as "potentially hrHPV"). Non-template preparation and PCR control, human control, internal control, PCR positive control, and contamination cut-off were applied for technical validation, resulting in 2.2% invalid results in the first test. When an hrHPV genotype was detected in the group, a secondary HPV test using the Linear Array™ HPV Genotyping test was conducted for individual identification.

A logical decision-making algorithm was designed to settle possible inter-test inconsistencies through single repetition of one or each of the tests for consistency or exclusion. The rate of invalid results for the second test, including repeated inconsistencies, was 1.5%. We utilized two consecutive HPV tests for cost-effectiveness; the first test saved costs by group detection in negative samples and only nonavalent genotype positives, so the second genotyping test was needed for a smaller fraction (303/4,731, 6.4%) of the whole sample set.

An anonymous questionnaire collecting demographic (city of permanent address, birth date, and highest level of education) and HPV vaccination data was given to each patient, allowing us to understand hrHPV genotype distribution and perform further cross-analyses using subgroups according to geography, age, education, and vaccination.

A descriptive statistical analysis was used to compute the frequency rates of each variable. Differences between the counties and the national averages were analyzed and statistically (95% MT; $p \leq 0.05$) demonstrated using two-sample t-tests with STATA software (version 13.0; TX, United States). In addition, the relationship between variables was analyzed using analysis of variance and logistic regression models to estimate the odds ratios.

TABLE 1 | Number of samples (N°) from and hrHPV prevalence in the different counties and settlement types of Hungary.

7 Regions (EU)	19 Counties (village > 2SD)	4 Settlement types				4000 N° of sample	hrHPV prevalence (> 1 SD)	p-value age-st.
		Capital	C. City	Town	Village			
West-Trans-Danubia	Vas		32	32	41	105	11.43%	0.861
	Zala		44	20	49	113	9.73%	0.665
	Győr-Moson-S.		79	33	74	186	13.98%	0.306
South-Trans-Danubia	Baranya		59	38	52	149	11.41%	0.951
	Tolna		13	38	40	91	14.29%	0.508
	Somogy		26	39	60	125	6.40%	0.168
Central-Hungary	Pest*		26	320	153	499	9.80%*	0.309*
	Budapest Capital	753	-	-	-	753	13.70%	ref
North-Hungary	Borsod-Abaúj-Z.		62	90	107	259	11.97%	0.963
	Nógrád		14	18	45	77	15.58%	0.210
	Heves		22	35	62	119	9.24%	0.733
North-Great Plain	Szabolcs-Sz.-B.		47	75	103	225	11.11%	0.998
	Hajdú-Bihar		81	90	43	214	10.28%	0.615
	Jász-N.-Sz.		28	80	40	148	10.81%	0.528
South-Great Plain	Bács-Kiskun		45	94	65	204	11.27%	0.872
	Békés		24	82	32	138	7.97%	0.305
	Csongrád-Cs.		84	39	41	164	5.49%	0.051
Central-Trans-Danubia	Fejér		59	44	67	170	12.35%	0.716
	Veszprém		24	61	54	139	11.51%	0.613
	Komárom-E.		27	55	40	122	8.20%	0.647
N° (and %) of samples		753 (18.8%)	796* (19.9%)*	1283 (32.1%)	1168 (29.2%)	4000 (100%)	446	
hrHPV prevalence: *without Capital		13.7%	10.3%*	11.9%	9.2%		**11.15%**	
		11.9%						

Remarks: County with rate of rural village population outside two standard deviations from country average without capital is underlined. hrHPV prevalence values outside one standard deviation from the country average are underlined. hrHPV prevalence in Pest county including Capital was 12.14%. C. City, County-level city. age-st., age-standardized to the country.

RESULTS

The overall prevalence of hrHPV was 11.15% (446 high-risk HPV-positive samples out of 4,000; 95% confidence interval [CI]: 10.05–12.25%) before age standardization. After adjusting for age to better represent female Hungarians aged 25–65 years, it decreased to 9.73% (95% CI: 8.31–11.15).

Patients

The mean age of the 4,000 eligible women was 41.36 years (standard deviation [SD]: 9.972). Of the eligible samples,

TABLE 2 | hrHPV prevalence by groups with the highest education level.

Highest level of education	hrHPV prevalence	OR	p-value
High school or University degree	12.8 %	ref	ref
Middle (College, Matura, 12 years of education)	10.5 %	0.843	0.159
Higher than Elementary (without Matura)	12.1 %	1.058	0.720
Elementary (8 years of education)	7.2 %	0.550	0.013*
Less than Elementary	6.7 %	0.477	0.481

[a]Significant p ≤ 0.05.
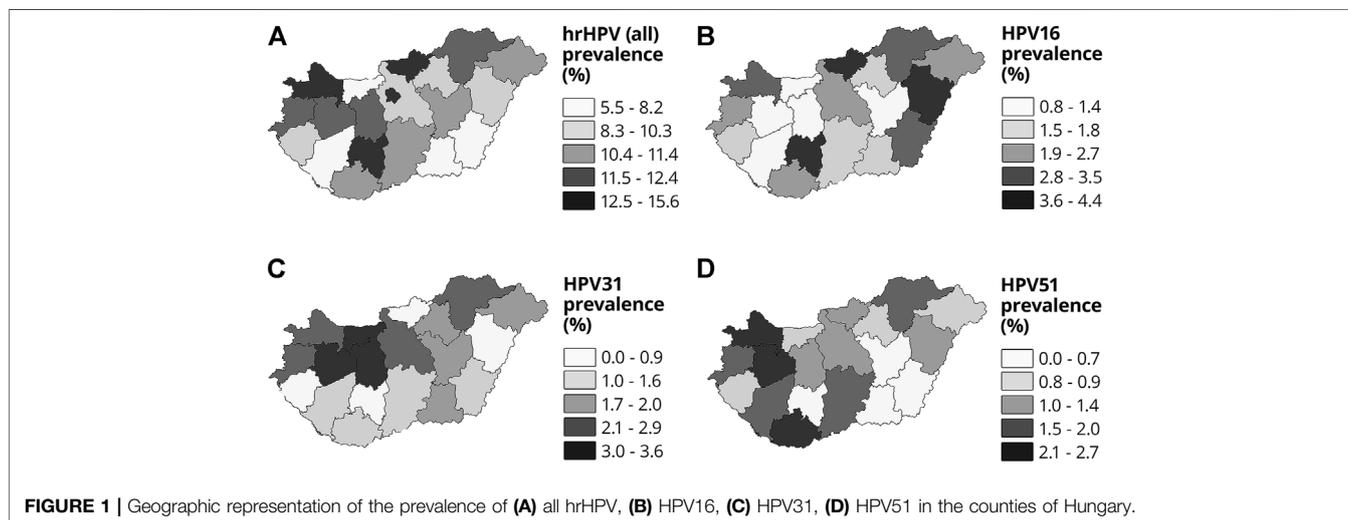
FIGURE 1 | Geographic representation of the prevalence of **(A)** all hrHPV, **(B)** HPV16, **(C)** HPV31, **(D)** HPV51 in the counties of Hungary.

31.3% were from the Capital and Central Region, 30.0% from the three western regions, and 38.7% from the three eastern regions, proportional to the population. In total, 29.2% of the population lived in villages. However, there was a wide variation in this proportion among counties (SD = 10.0). It was beyond 2 SD in one of the 19 counties, significantly above country average without capital (Nógrád county, $p = 0.028$, underlined in **Table 1**).

Geographic Distribution
Table 1 summarizes the total samples and the rate of hrHPV-positive samples in each county and by settlement type. **Figure 1A** presents graphical representation of hrHPV prevalence in each county (color depth-coded ranges). Without age standardization, hrHPV prevalence was beyond 1 SD higher in the Nógrád, Tolna and Győr-Moson-Sopron counties and in the Capital and beyond 1 SD lower in the Komárom-Esztergom, Békés, Somogy and Csongrád-Csanád counties than the country average.

Education
A higher level of education was associated with a higher (almost double) prevalence of hrHPV: hrHPV prevalence among women with "High school or University degrees" was 12.8% (p-value as

reference), while among those with "Less than Elementary" education 6.7%. hrHPV prevalences among women with "Middle education level (College, Matura, 12 years of education)," with "Higher than Elementary education (but without Matura)," and with just "Elementary level (8 years of education)" with OR and p-values are presented in **Table 2**.

A significant difference ($p ≤ 0.05$) was found only between "Elementary level (8 years of education)" versus "High school or University degrees" (OR = 0.550, $p = 0.013$), even without the effect of age. Meanwhile, the size of the "Less than Elementary" subgroup was too small ($n = 15$) to be significant.

Age Correspondence
The prevalence decreased by age, from 19.43% in the 25–29 years age group, through 14.63% in the 30–34 age group, 11.94% in the 35–39 age group, 9.16% in the 40–44 age group, 8.35% in the 45–49 age group, and 7.85% in the 50–54 age group, to 5.0% and 5.3% in the 55–59 and 60+ years age groups, respectively. **Figure 2** shows hrHPV positivity (%) in 5-year age groups from 25 to 65 years on a graph.

During our sample collection, the representativeness to the age distribution of the female population was not a requirement. However, we ensured the validity of the conclusions for the country through statistical adjustments. Analysis of the
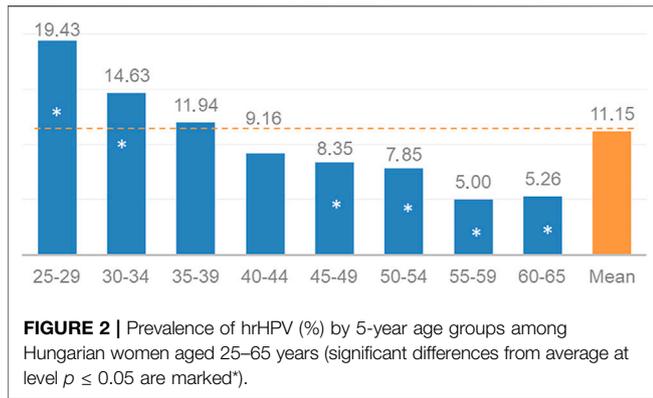
FIGURE 2 | Prevalence of hrHPV (%) by 5-year age groups among Hungarian women aged 25–65 years (significant differences from average at level $p \leq 0.05$ are marked*).

demographic data in the sample set showed that women under the age of 51 were overrepresented, while those aged 52 years and above were underrepresented (see **Figure 3**). After eliminating the effect of mean patient age differences by aligning the size of each age subset in our model (see *Discussion - Age Correspondence*), the hrHPV prevalence representative of the female Hungarian population aged 25–65 years was determined to be 9.73%.

Vaccination

Based on our data, 174 enrolled women (4.3%) had received vaccination against HPV; among them, 55 (32%) received the quadrivalent vaccine; 47 (27%), the bivalent; 16 (9%), the latest nonavalent vaccine; while 56 (32%) did not know the type. The average age at the time of the survey was 36 years and that at the time of vaccination was 27 years. Among the reported vaccinated women, 11 were hrHPV-positive, and four among them had a genotype matching her previous vaccine. The prevalence of HPV16 and/or HPV18 was 10% among the vaccinated vs.

29% among the unvaccinated hrHPV-positive women ($p = 0.211$).

Genotypes

Among the 446 positive samples, a single hrHPV was detected in 355 (79.6%) samples. Multiple infections were present in 91 cases (20.4%); with 76 (17.0%) having a double infection, 13 (2.9%) having a triple infection, and two (0.5%) having a quadruple infection with different hrHPV genotypes. The frequencies of the examined hrHPV genotypes are shown in **Figure 4**, divided if singular or as part of a multiple infection.

Immediately following genotypes 16 and 31 (together comprising 39% of positives) in order of frequency, certain non-vaccine high-risk HPV genotypes (HPV51, HPV66, HPV56) had the highest prevalence (together comprising 32% of positive cases).

The geographic distributions of HPV 16, 31, and 51 are shown in **Figures 1B–D**, respectively, for comparison. HPV66 was mainly present in the capital and Baranya county. **Figure 5** shows the rate of the three most prevalent genotypes per county.

Bivalent vaccine-types (HPV16 and/or HPV18) were present in 110 females (29%), while any or more of the nonavalent vaccine 7 hrHPV genotypes were found in 269 (73%) of the positive samples.

As shown in **Figure 6**, the prevalence of individual hrHPV genotypes decreased with age, though some had a minor second increase. The most pathogenic HPV16 had the highest prevalence at 4.9% in the 25–29 years age group, which remained above 3% in the 30–34 and 35–39 years age groups but decreased to approximately 1% in the 40+ years groups. In the 25–29 years age group, the following other genotypes had prevalence above 2%, in their order of frequency: HPV 31, 18, 52, 51. Approximately 2% of the patients tested positive for HPV31, 51, and 56 in the 30–34 years age group.
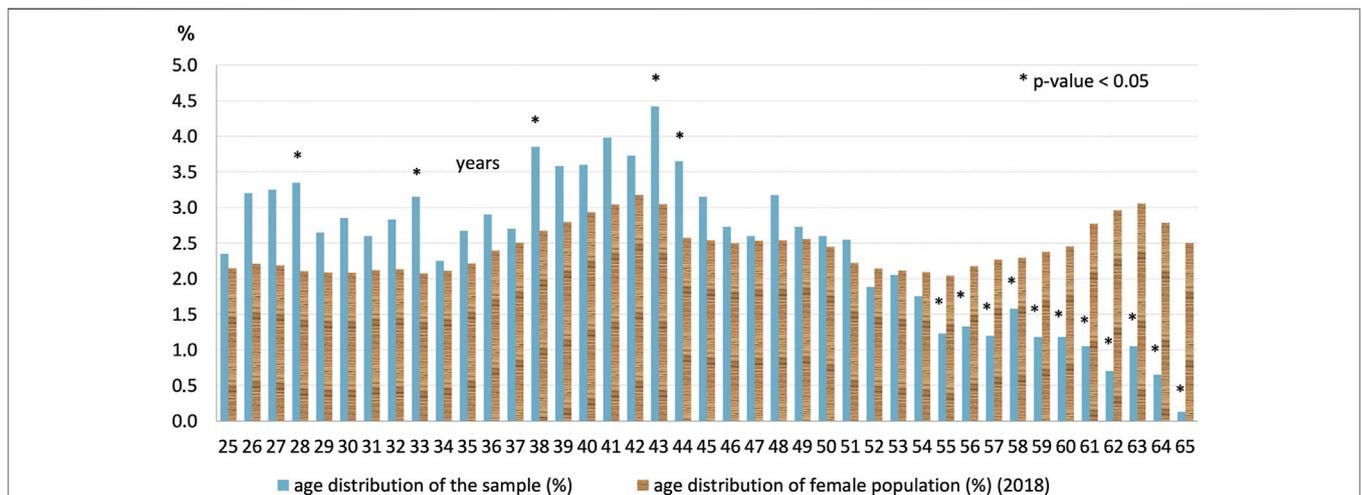

FIGURE 3 | Age distribution (%) of the sample set ($n = 4,000$) and the female population aged 25–65 years in Hungary (2018) (*significant differences at level $p \leq 0.05$). Age in completed years.
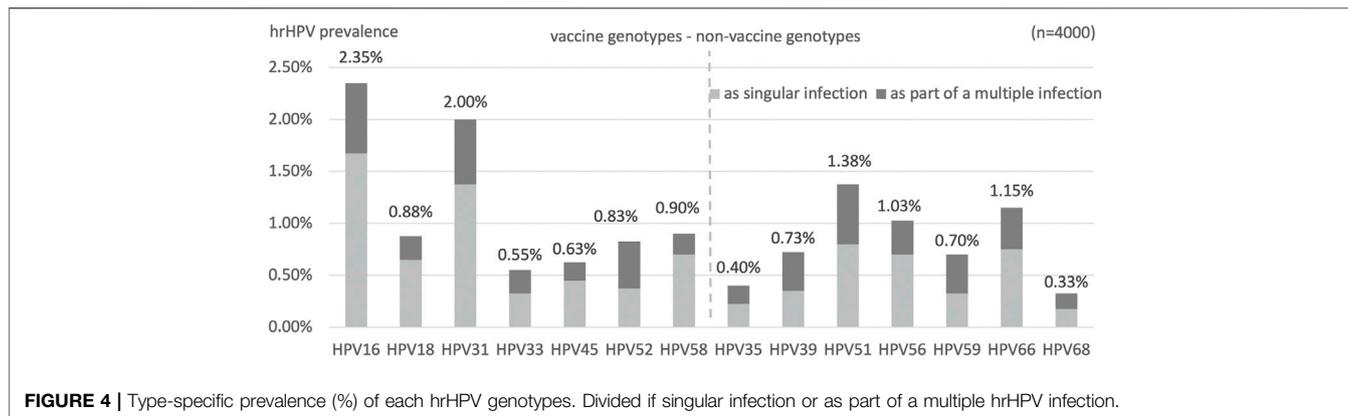
FIGURE 4 | Type-specific prevalence (%) of each hrHPV genotypes. Divided if singular infection or as part of a multiple hrHPV infection.

DISCUSSION

The nationwide prevalence of 11.15% was similar to the world average of 11.7%, based on normal cytology, lower than that of the Eastern-Europe average (21.4%) (5), but higher than that of most Western European countries, ranging from 1.7% to 12.5% (6). Some Western European countries have a higher hrHPV prevalence (presumably migration-related) but lower morbidity and mortality rates of cervical cancer than Hungary, providing a benchmark for improving the effectiveness of secondary and tertiary prevention.

Previous Studies

In Central and Eastern Europe, the mean prevalence of HPV infection was 12.6% among 8,610 women with normal cervical cytology, with HPV16 being the most common (7). Some countries in this subregion have already published more detailed population-based screening data on hrHPV prevalence with substantial variance (8, 9).

1. Budapest
2. Bács-Kiskun
3. Baranya
4. Békés
5. Borsod-Abaúj-Zemplén
6. Csongrád-Csanád
7. Fejér
8. Győr-Moson-Sopron
9. Hajdú-Bihar
10. Heves
11. Jász-Nagykun-Szolnok
12. Komárom-Esztergom
13. Nógrád
14. Pest
15. Somogy
16. Szabolcs-Szatmár-Bereg
17. Tolna
18. Vas
19. Veszprém
20. Zala

FIGURE 5 | Geographic representation of rate of the three most frequent genotypes per county among Hungarian women aged 25–65 years.

In Hungary, only a few studies have been previously conducted that covered HPV prevalence. One study in 2001 examined 728 women in more centers and estimated that the overall rate of HPV infection was 17% (10). Another study in 2002 collecting 1,121 samples from two major cities found a 17.5% HPV prevalence in a healthy population with broad regional (15%–27%) and age group (10%–32%) differences. At the Szeged center, the HPV-positivity was 27.6%, whereas at the three centers in Budapest, HPV prevalence did not exceed 15% (11). In 2006, one of the authors of this paper found a genotype frequency rank of 16, 31, 51, 66, 56, 58, 33, 39, and 18 in 75% monovalent, 20% bivalent, and 5% infections with three or more genotypes (12). A single HPV-center (University Clinic) examined 1,155 women (not screening population) and found that 55.5% of patients tested positive for HPV DNAs, with 38.5% having high-risk HPV DNA. The most common HPV type found was type 16 (19.5%), with high prevalence of type 51 and 31 among patients with cytological atypia (13). A study in 2016 examined the HPV genotypes from 2048 cytology results (not in a screening population) and found an hrHPV positivity of 12.7%, with the most prevalent (ranked in order) being 16-52-51-31-66-58 (14).

However, none of these earlier studies attempted to proportionally represent the urban and rural populations of the whole country, making our recent study the first and unique survey in this aspect.

Geographic Distribution

The distribution of local hrHPV prevalence can be compared to the strong geographic inhomogeneity in the morbidity and mortality of cervical cancer (15). In some counties, the relatively high hrHPV prevalence correlated with the higher morbidity and mortality rates (e.g., Nógrád, despite the high >2 SD rural population rate) or lower prevalence with lower morbidity and mortality (e.g., Komárom-Esztergom). However, in other counties, only the morbidity rate matched but mortality did not (high prevalence and high morbidity, e.g., Tolna; low prevalence and low morbidity, e.g., Somogy). In contrast, in some counties, these did not correlate at all (high prevalence with low morbidity and mortality, e.g., Győr-Moson-Sopron, and low prevalence with high morbidity and mortality, e.g., Békés, Csongrád-Csanád). This is explained by the indirect chain of
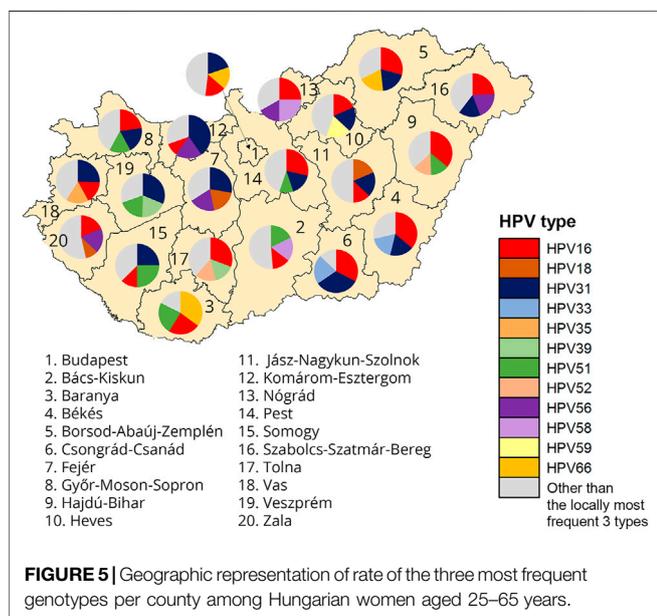
relation between prevalence and morbidity, highly influenced by the genotype pathogenicity and effectiveness of screening and therapy efforts.

It is important to consider the potentially significant effect of the different settlement types and age distribution among the counties to better understand the observed hrHPV prevalence differences. In urban areas (towns and county-level cities, with the highest prevalence in the capital), the prevalence was 11.9%, while in villages, it was significantly ($p = 0.036$) lower (by 23%) at 9.2%. This finding was not unprecedented as a similar difference was found in Romania (9), where hrHPV prevalence was 20.0% and 14.8% (lower by 26%) in urban and rural areas, respectively. However, in Romania, the logistic regression model did not show a significant association between hrHPV positivity and settlement type, while it did in Hungary.

Education

Although the results of our study suggest that hrHPV prevalence is higher in urban population groups with high school or university degrees, we know from other study results that this may be an effect of HPV screening compliance as well. Higher level of HPV knowledge was significantly associated with HPV testing behavior (odds ratio: 3.792, 95% CI: 3.400–4.230). The effect of residence and educational attainment on testing behavior only became significant if women had low levels of HPV knowledge (16).

Age Correspondence

Similar to previous findings (17), the hrHPV positivity rate had a strong negative correlation with age until a certain middle age group, when the graph plateaued or only increased slightly. The prevalence in females in their 20s was approximately 20%, falling to <10% among those in their 40s and approximately 5% among those around the age of 60, suggesting an exponential function. In our applied regression model (negative log), the change in the odds ratio of hrHPV positivity with each year of aging (additionally) did not differ significantly ($p = 0.726$) from 4% per year

(mathematically multiplied by 0.96^y) for the entire age range. The use of this simplified model can achieve the aim of filtering out the significant (regression analysis $R^2 = 0.0016$, $p < 0.05$) effect of age.

Based on the literature, the peak of HPV prevalence is in the early 20s, which presumably correlates with the initiation of sexual activity and the number of different partners over a certain period of time. Cervical pre-cancer findings cumulate approximately 10 years after this age, while the peak of cervical cancer appears even later. Only approximately 10% of HPV infections persist over 2 years, and persistence with the same hrHPV genotype indicates a higher risk for cervical neoplasia (18).

As mentioned before, analysis of the demographic data in our sample set showed that women under the age of 51 were overrepresented, while those aged 52 years and above were underrepresented (see **Figure 3**), which reflects also an important aspect of age differences in the attendance of and compliance with cervical screening programs. Adjustment to the 2000–2025 World Health Organization World Standard Population might permit better international comparison, with the limitation that standard age distribution data combine the data for males and females.

Among the different counties of Hungary, differences in the hrHPV prevalence from the country average (see **Table 1**) were not significant ($p = 0.243$) without the effect of age differences, suggesting that domestic screening programs should be targeted based on age groups instead of geographic regions. However, the hrHPV prevalence remained significantly lower in village settlement types than in the capital, even after adjusting for age.

Vaccination

The average age at the time of reported vaccination was 27 years in our study group, suggesting that most of the patients received vaccination after engaging in sexual activity. In their cases, there may be incomplete protection because of the potential presence of hrHPV genotypes that were already in the cervix. Indeed, among the reported vaccinated women, 11 were hrHPV-positive, and four of

FIGURE 6 | hrHPV genotype prevalence (%) according to each 5-year age group.
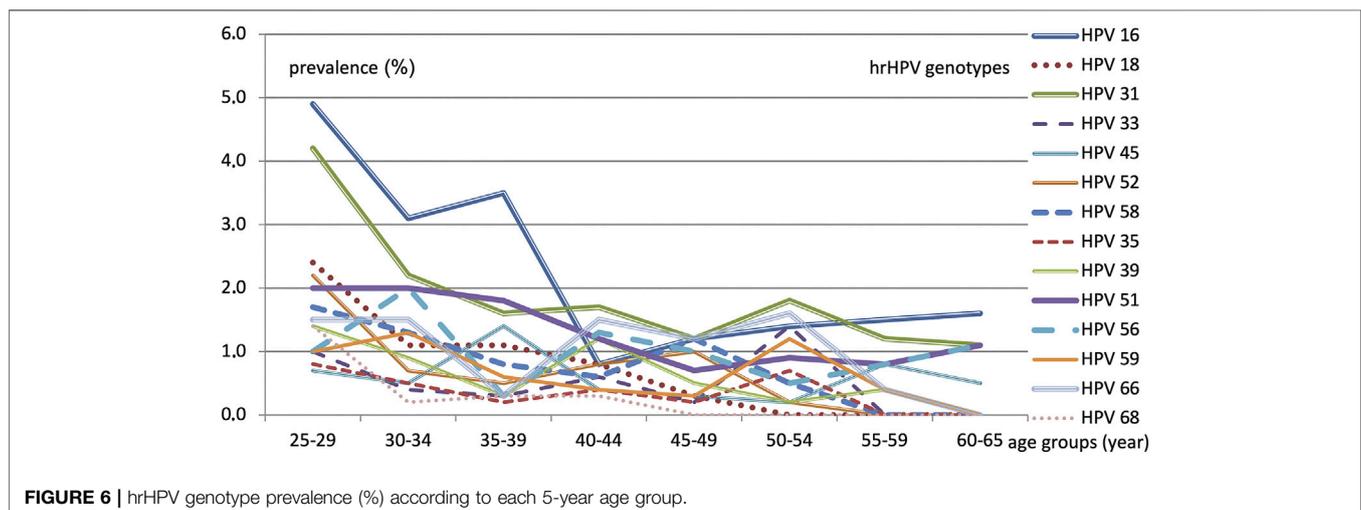
them had a genotype in her cervix against which she received lege artis vaccination in the previous years (HPV16 — vaccination age 34 — quadrivalent; HPV16,58 — vaccination age 45 — nonavalent; HPV18 — vaccination age 28 — nonavalent; HPV31 — vaccination age 36 — nonavalent).

Vaccination can be also an important aspect in achieving a higher level of knowledge, according to a previous research result, which found that vaccinated women were more likely to know that screening should be continued despite vaccination (60.0% vs. 25.6%, *p* = 0.06) (19).

Genotypes

Individual genotyping of each positive sample was included in our study design because the risk of HPV-related pre-cancer differs substantially among the individual hrHPV genotypes (20). Specifically, in a prospective study (*n* = 8,656, follow-up 12 years), when HPV16 was present in the cervix, the risk of CIN3+ (cervical intraepithelial neoplasm grade 3 or worse) was more than 25%, with HPV18 it was approximately 20%, with HPV31 and HPV33 approximately 15%, and with the rest of the hrHPV genotypes only <5% (18).

Immediately following genotypes 16 and 31, in order of frequency, certain non-vaccine high-risk HPV genotypes (HPV51, 66, 56) had unexpectedly high prevalence in Hungary compared with international data. The latter three were not listed in the five most frequent worldwide, a surprising result that necessitates further research to be understood.

Worldwide, the following genotypes were the most prevalent: HPV16 (3.2%), HPV18 (1.4%), HPV52 (0.9%), HPV31 (0.8%), HPV58 (0.7%), and the remaining hrHPV are 0.6% or less (21). Another high-population study found that HPV16 (1.6%) and HPV52 (1%) were the most prevalent in the United States (22). Meanwhile, HPV16 and HPV31 were the two most prevalent in Europe (21% and 9% among positives, respectively) in contrast with other continents where other genotypes came up earlier in the frequency rank list: Asia: HPV33 (6%), HPV56 (6%), South-America: HPV58 (7%), and Sub-Saharan Africa: HPV35 (8%) (23).

In our geographically-representative screening population, the most frequent genotypes were similar to those found in some of the earlier studies in Hungary. Genotype 16, 51 and 31 had the highest prevalence in 2011 among patients with cytological atypia (13). A study in 2016 examined the HPV genotypes from 2048 cytology results (not in a screening population) the most prevalent (ranked in order) being HPV16-52-51-31-66-58 (14). Five out of the six most frequent genotypes were similar to our findings, with less HPV56 and more HPV52. HPV51 deserves special attention according to all genotyping studies in Hungary.

Summary/Conclusion

Key Points: According to Our Results

- A hrHPV prevalence of 11.15% (9.73% age-representatively) was found in Hungary, similar to the world average, higher than the European average, and lower than the Eastern-European average;

- Domestic screening programs should focus on age group rather than geographic regions, with an attention to the involvement of women above 51;
- High education level and urban residence (even after age-standardization) was associated with statistically significantly higher hrHPV prevalence;
- Following genotypes 16 and 31, in order of frequency, certain non-vaccine hrHPV genotypes (HPV51, HPV66, HPV56) showed unexpectedly higher prevalence than previous international data, projecting a potential tendency of further growing relative prevalence of these non-vaccine genotypes.

Evidence supports the introduction of primary HPV screening in Hungary. Our study provided the first geographically representative genotype-specific hrHPV prevalence baseline database for supporting policy-making efforts. Further follow-ups should reveal probable genotype distribution shifts over time toward the growing prevalence of the non-vaccine genotypes, in conjunction with HPV vaccination and organized cervical screening programs.

DATA AVAILABILITY STATEMENT

The raw data supporting the conclusion of this article will be made available by the authors, without undue reservation.

ETHICS STATEMENT

The studies involving human participants were reviewed and approved by the ETT TUKEB. The patients/participants provided their written informed consent to participate in this study.

AUTHOR CONTRIBUTIONS

FUNDING

CONFLICT OF INTEREST

Authors AIF, MB, and AK were employed by or contracted to the company SYNLAB Hungary Ltd.

The remaining authors declare that the research was conducted in the absence of any commercial or financial relationships that could be construed as a potential conflict of interest.

ACKNOWLEDGMENTS

REFERENCES

1. Ferlay J, Ervik M, Lam F, Colombet M, Mery L, Piñeros M, et al. *Global Cancer Observatory: Cancer Today*. Lyon, France: International Agency for Research on Cancer (2020). Available from: https://gco.iarc.fr/today (Accessed March 2, 2022).

2. Ronco G, Dillner J, Elfström KM, Tunesi S, Snijders PJF, Arbyn M, et al. Efficacy of HPV-Based Screening for Prevention of Invasive Cervical Cancer: Follow-Up of Four European Randomised Controlled Trials. *Lancet* (2014) 383:524–32. doi:10.1016/S0140-6736(13)62218-7

3. von Karsa L, Arbyn M, De Vuyst H, Dillner J, Dillner L, Franceschi S, et al. European Guidelines for Quality Assurance in Cervical Cancer Screening. Summary of the Supplements on HPV Screening and Vaccination. *Papillomavirus Res* (2015) 1:22–31. doi:10.1016/j.pvr.2015.06.006

4. Kocsis A, Takács T, Jeney C, Schaff Z, Koiss R, Járay B, et al. Performance of a New HPV and Biomarker Assay in the Management of hrHPV Positive Women: Subanalysis of the Ongoing Multicenter TRACE Clinical Trial (N > 6,000) to Evaluate POU4F3 Methylation as a Potential Biomarker of Cervical Precancer and Cancer. *Int J Cancer* (2017) 140:1119–33. doi:10.1002/ijc.30534

5. Forman D, de Martel C, Lacey CJ, Soerjomataram I, Lortet-Tieulent J, Bruni L, et al. Global burden of Human Papillomavirus and Related Diseases. *Vaccine* (2012) 30(Suppl. 5):F12–F23. doi:10.1016/j.vaccine.2012.07.055

6. De Vuyst H, Clifford G, Li N, Franceschi S. HPV Infection in Europe. *Eur J Cancer* (2009) 45:2632–9. doi:10.1016/j.ejca.2009.07.019

7. Poljak M, Seme K, Maver PJ, Kocjan BJ, Cuschieri KS, Rogovskaya SI, et al. Human Papillomavirus Prevalence and Type-Distribution, Cervical Cancer Screening Practices and Current Status of Vaccination Implementation in Central and Eastern Europe. *Vaccine* (2013) 31:H59–H70. doi:10.1016/j.vaccine.2013.03.029

8. Tachezy R, Smahelova J, Kaspirkova J, Salakova M. Human Papillomavirus Type-specific Prevalence in the Cervical Cancer Screening Population of Czech Women. *PLOS ONE* (2013) 8:e79156. doi:10.1371/journal.pone.0079156

9. Ilisiu MB, Hashim D, Andreassen T, Støer NC, Nicula F, Weiderpass E. HPV Testing for Cervical Cancer in Romania: High-Risk HPV Prevalence Among Ethnic Subpopulations and Regions. *Ann Glob Health* (2019) 85(1):89. doi:10.5334/aogh.2502

10. Nya´ri T, Cseh I, Woodward M, Szöllösi J, Bak M, Dea´k J. Screening for Human Papillomavirus Infection in Asymptomatic Women in Hungary. *Hum Reprod* (2001) 16:2235–7. doi:10.1093/humrep/16.10.2235

11. Kornya L, Cseh I, Deak J, Bak M, Fulop V. The Diagnostics and Prevalence of Genital Human Papillomavirus (HPV) Infection in Hungary. *Eur J Obstet Gynecol Reprod Biol* (2002) 100:231–6. doi:10.1016/S0301-2115(01)00474-2

12. Benczik M. HPV Genotypes Detected by GenoID Laboratory in Hungary at 2005/2006. [article in Hu]. *STD és Genitális Infektol* (2008) 2:10–6.

13. Galamb Á, Pajor A, Langmár Z, Sobel G. Results of the First Human Papilloma Virus center in Hungary (2007-2011). *Orvosi Hetilap* (2011) 152:1804–7. doi:10.1556/OH.2011.29233

14. Szentirmay Z, Veleczki Z, Kásler M. Human Papillomavirus Associated Cervix Uteri Morbidity in Hungary: Epidemiology and Correlation with the HPV Types and the Simultaneous Cytological Diagnosis. [article in Hu]. *Orvosi Hetilap* (2017) 158:1213–21. doi:10.1556/650.2017.30807

15. Public Health Analysis Centre Information System (NEKIR). *Methodology Development of Health Service System Project No. EFOP 1.8.0-VEKOP-17-2017-00001*. National Public Health Centre (2019). Available from: https://efop180.antsz.hu/nepegeszsegugyi-elemzesi-kozpont/75-nepegeszsegugyi-elemzesi-kozpont/168-nekir-adatvalaszto.html (Accessed Apr 28, 2021).

16. Lin W, Chen B, Hu H, Yuan S, Wu B, Zhong C, et al. Joint Effects of HPV-Related Knowledge and Socio-Demographic Factors on HPV Testing Behaviour Among Females in Shenzhen. *Eur J Public Health* (2021) 31: 582–8. doi:10.1093/eurpub/ckab049

17. Wright TC, Stoler MH, Behrens CM, Apple R, Derion T, Wright TL. The ATHENA Human Papillomavirus Study: Design, Methods, and Baseline Results. *Am J Obstet Gynecol* (2012) 206:e1–e46. doi:10.1016/j.ajog.2011.07.024

18. Kjær SK, Frederiksen K, Munk C, Iftner T. Long-term Absolute Risk of Cervical Intraepithelial Neoplasia Grade 3 or Worse Following Human Papillomavirus Infection: Role of Persistence. *J Natl Cancer Inst* (2010) 102:1478–88. doi:10.1093/jnci/djq356

19. Lutringer-Magnin D, Kalecinski J, Cropet C, Barone G, Ronin V, Régnier V, et al. Prevention of Sexually Transmitted Infections Among Girls and Young Women in Relation to Their HPV Vaccination Status. *Eur J Public Health* (2013) 23(6):1046–53. doi:10.1093/eurpub/ckt018

20. Guan P, Howell-Jones R, Li N, Bruni L, de Sanjosé S, Franceschi S, et al. Human Papillomavirus Types in 115,789 HPV-Positive Women: a Meta-Analysis from Cervical Infection to Cancer. *Int J Cancer* (2012) 131:2349–59. doi:10.1002/ijc.27485

21. Bruni L, Diaz M, Castellsagué X, Ferrer E, Bosch FX, de Sanjosé S. Cervical Human Papillomavirus Prevalence in 5 Continents: Meta-Analysis of 1 Million Women with Normal Cytological Findings. *J Infect Dis* (2010) 202:1789–99. doi:10.1086/657321

22. Monsonego J, Cox JT, Behrens C, Sandri M, Franco EL, Yap P-S, et al. Prevalence of High-Risk Human Papilloma Virus Genotypes and Associated Risk of Cervical Precancerous Lesions in a Large U.S. Screening Population: Data from the ATHENA Trial. *Gynecol Oncol* (2015) 137:47–54. doi:10.1016/j.ygyno.2015.01.551

23. Clifford G, Gallus S, Herrero R, Muñoz N, Snijders P, Vaccarella S, et al. Worldwide Distribution of Human Papillomavirus Types in Cytologically normal Women in the International Agency for Research on Cancer HPV Prevalence Surveys: A Pooled Analysis. *Lancet* (2005) 366:991–8. doi:10.1016/S0140-6736(05)67069-9

A Detailed Overview About the Single-Cell Analyses of Solid Tumors Focusing on Colorectal Cancer

William J. Kothalawala[1]*, Barbara K. Barták[1], Zsófia B. Nagy[1], Sára Zsigrai[1], Krisztina A. Szigeti[1], Gábor Valcz[1,2], István Takács[1], Alexandra Kalmár[1,2] and Béla Molnár[1,2]

[1]Department of Internal Medicine and Oncology, Semmelweis University, Budapest, Hungary, [2]Molecular Medicine Research Group, Eötvös Loránd Research Network, Budapest, Hungary

In recent years, the evolution of the molecular biological technical background led to the widespread application of single-cell sequencing, a versatile tool particularly useful in the investigation of tumor heterogeneity. Even 10 years ago the comprehensive characterization of colorectal cancers by The Cancer Genome Atlas was based on measurements of bulk samples. Nowadays, with single-cell approaches, tumor heterogeneity, the tumor microenvironment, and the interplay between tumor cells and their surroundings can be described in unprecedented detail. In this review article we aimed to emphasize the importance of single-cell analyses by presenting tumor heterogeneity and the limitations of conventional investigational approaches, followed by an overview of the whole single-cell analytic workflow from sample isolation to amplification, sequencing and bioinformatic analysis and a review of recent literature regarding the single-cell analysis of colorectal cancers.

Keywords: bioinformatics, colorectal cancer, multi-omics, heterogeneity, single-cell sequencing

INTRODUCTION

In 2012, researchers at The Cancer Genome Atlas Network published their work on the comprehensive molecular biological characterization of human colorectal cancers (CRC) [1]. They analyzed the exomes, copy number alterations, promoter methylation levels, transcriptomes, and microRNA fraction of bulk samples acquired from 276 patients with colorectal cancer. Since then, with the evolution of the equipment and toolbox of molecular biology with methods such as single-cell next generation sequencing (NGS), the need for an even more detailed investigation of organisms at a single-cell level has emerged. In this review article, we aimed to present contemporary methods and techniques for the sampling, isolation, and analysis of single cells and to give an overview of the current scientific literature about CRC at the single-cell level.

MODELS FOR TUMOR HETEROGENEITY

Tumor heterogeneity means that neoplastic cells from the same tumor can genotypically, phenotypically, morphologically, or metabolically differ from each other. The concept of heterogeneity has been around for several decades and gained attention in the 1990s when cancer stem cells were identified in acute myeloid leukemia [2]. There are two not mutually exclusive models explaining tumor heterogeneity: the cancer stem cell and the clonal evolution

model. In the former model, tumor cells are hierarchically organized: a portion of cells, called the "stem cells" retain their ability to proliferate, while their offspring "differentiate" into nonproliferating cells [3]. The latter model describes cancer as a sequential process driven by somatic mutations following Darwinian mechanisms for subclonal selection [4]. Over the past decades, intratumoral heterogeneity has been intensively researched. Some cancer types (e.g., leukemias [2], breast cancer [5], brain tumors [6] and CRCs [7]) are thought to behave according to the cancer stem cell model, with evidence of a portion of cells being capable of inducing cancer in immunodeficient mice. Compelling evidence was found to the monoclonal origin and subclonal selection of several tumors including breast cancer [8], glioblastoma multiforme [9], and renal cell carcinoma [10].

TUMOR MICROENVIRONMENT AND COMPONENTS OF TUMORS

Heterogeneity in solid tumors is not limited to the differences between neoplastic cancer cells. Cancerous cells are embedded into diverse tissues consisting of cancer-associated fibroblasts, extracellular matrix, vascular and lymphatic networks, and immune cells, among others. Cancer-associated fibroblasts, which have a constantly activated phenotype are the main components of tumor stroma [11]. Their exact origin and functions are not fully understood, but it is hypothesized that they can enhance tumor growth and progression, invasion, and metastatic potential as well [12]. They are more heterogeneous than normal fibroblasts and express various surface receptors and cytokines that facilitate tumor progression, angiogenesis, etc. [13]. Many tumors have been described to have marked immune cell infiltration. Some of these cells have antitumoral behavior (NK cells, CD8$^+$ T cells, CD4$^+$ Th1 cells, and APCs), while others can promote tumor progression (CD4$^+$ Th2 cells, regulatory T cells, and tumor-associated macrophages) [13]. A meta-analysis published in 2020 found that high tumor-infiltrating lymphocyte (TIL) count with CD3$^+$, CD8$^+$ and FOXP3+ T-cells pose a prognostic benefit in CRC [14].

Another phenomenon that further expands heterogeneity of the tumor stroma is tumor budding and was described in several cancers including esophageal, pancreatic, endometrial, and breast cancer and was most extensively researched in CRCs. Tumor buds are isolated or small clusters of undifferentiated cancerous cells at the invasive front of the tumor tissue. The malignant cells in a tumor bud are morphologically different (loss of basal membrane, diverse shapes) from cells of the main tumor mass and express decreased epithelial and increased mesenchymal marker levels [15].

The extent of tumor heterogeneity has clinical implications as well. A recent study showed that sequencing of multiple tissue biopsy samples was able to detect more than twice as many mutations in solitary colorectal cancers compared to single tissue biopsy [16]. The genetic and epigenetic landscape of tumors influence tumor initiation, progression and drug response [17] thus the assessment of the degree of tumor heterogeneity may prove diagnostic and prognostic value and help treatment selection, monitoring of drug response and patient follow-up.

METHODS FOR EVALUATING TUMOR HETEROGENEITY

The above-mentioned characteristics of tumor heterogeneity explain the need for more sophisticated and sensitive methods for cancer cell biology research. Frequently used approaches for evaluating heterogeneity include various types of methods, such as immunohistochemistry, fluorescence *in situ* hybridization (FISH), comparative genome hybridization (CGH), microdissection combined with PCR, microarray techniques, etc. In 2005, Losi et al. confirmed the presence of intratumoral heterogeneity during the progression of CRC using microdissection and the above techniques, focusing on *p53* and *K-ras* mutations, and loss-of-heterozygosity on chromosomes 5q and 18q [18]. Their study concluded that prognostic and diagnostic genetic markers should be evaluated for heterogeneity as well.

The development and widespread use of NGS opened new paths towards understanding tumor heterogeneity more precisely. NGS is used for analyzing the genome, transcriptome, or accessible chromatin with techniques including DNA-seq, RNA-seq, or chromatin profiling methods, such as ChIP-seq. The sequence of a targeted gene panel, the exome (whole-exome sequencing, WES), or the whole genome (whole-genome sequencing, WGS) of multiple samples can be rapidly and relatively cost-effectively analyzed for single-nucleotide variations (SNVs) and copy-number variations (CNVs/SCNVs) with DNA-seq by fragmenting the genome into smaller pieces and sequencing them in parallel. Market leader companies in the genetic research industry, e.g., Illumina (San Diego, United States) offer several commercially available targeted gene panels for oncology including the field of both hematologic malignancies and solid tumors. Tumor samples can be sequenced in bulk or at a single cellular level with the evolving technical background. Bulk samples may contain several types of tissue including cancerous cells and their surrounding stroma, healthy surrounding tissue, smooth muscles, fat, and connective tissue. The sensitivity of bulk analysis is dependent on the coverage (average number of reads aligning to a known reference base) of the sequencing run and is typically between 5 and 10% [19]. This means that the detectability of a sought variant is highly dependent on its allele frequency, which in the field of oncology can be lower than the typical sensitivity of bulk sequencing. Thus, single-cell sequencing methods could be far more accurate and focused on characterizing intratumoral heterogeneity, however, the current isolation techniques are much more challenging and require designated equipment with relatively higher cost of reagents and subsequent analyses.

TECHNIQUES FOR THE ISOLATION OF SINGLE CELLS

Numerous approaches have been developed for the isolation of single cells which differ in throughput, speed, cost, and efficiency. The starting sample material can be cell cultures, cell suspensions, or histopathologic slides.

The simplest method is termed limiting dilution. This technique is based on the dilution of cell suspensions and then aliquoting them into such volumes that it is statistically probable that a well contains only one cell [20].

Micromanipulation systems typically work with an inverted microscope and a motorized stage combined with glass micropipettes. Live, individual cells can be observed under the microscope and transferred to different compartments using the micropipettes [21]. The process is labour intensive manually but can be automatized with the help of computer vision and motorized stages [22].

Several microfluidics techniques exist for the separation of single cells. Cell suspensions can be separated through microchannels based on physical properties, immunomagnetic labelling or cell surface protein binding antibodies on the microfluidics chip [21]. 10x Genomics' Chromium Controller (10x Genomics, Pleasanton, California, United States) solution offers a droplet-in-oil-based technique in which individual cells are encapsulated with uniquely barcoded beads thus enabling parallel sorting of cells and library preparation for NGS. The Bio-Rad ddSEQ Single-Cell Isolator (Bio-Rad Laboratories, Hercules, California, United States) offers a similar technique. Both platforms are capable of sorting and barcoding thousands of cells a day.

Fluorescence-activated cell sorting (FACS) is another high throughput method for separating individual cells. Cells bound with fluorescence-conjugated antibodies are passed through a flow cytometer and the antibodies are activated with laser beams. Detectors pick up scatter- and fluorescence signals from each cell which can then be individually diverted towards collecting compartments by an electromagnetic field based on their phenotype [23]. Penter et al. individually sorted cells applying this technique, and according to their results, the error rate was less than 1 out of 100 cells [24].

Magnetic-activated cell sorting (MACS) is an affinity-based cell sorting method. Antibodies conjugated with magnetic beads are bound to cells' surface antigens. Cells are then placed in an external magnetic field, and after washing away unlabeled cells, the labelled cells can also be eluted [21].

Optical tweezers offer a procedure for non-contact cell separation using highly focused laser beams. Single cells can be selected, trapped and moved from one compartment to another with the help of optical forces [25].

Laser capture microdissection is a popular technique for isolating homogeneous, uniform cell populations or even single cells from histopathological slides while simultaneously assessing tissue and cellular morphology. A typical instrument consists of an inverted microscope, a motorized stage, a laser unit, and a CCD camera [26]. The operator can manually adjust the power, speed, and focus of the laser, and can select preformed shapes or draw unique areas for dissection. Various methods exist for the subsequent isolation of dissected areas including gravitational forces pulling down the specimen to a collecting compartment, the use of adhesive-coated caps, or using a defocused laser beam to catapult the sample into the desired compartment [26]. These systems need to be manually supervised, moreover, working with single cells requires high operator skills due to the limited size of samples and lack of feedback systems. **Figure 1** summarizes the workflow of single cell isolation, sequencing, and analysis.

MOLECULAR BIOLOGICAL ANALYSIS OF SINGLE CELLS

A typical eukaryotic cell contains ~4 pg of genomic material while Illumina's sequencing solutions need at least 1 ng of DNA for sequencing according to the manufacturer. Therefore, in eukaryotic single-cell sequencing at least a ~1000-fold amplification is needed for subsequent analysis. This can be achieved by several methods including degenerate oligonucleotide-primed polymerase chain reaction (DOP-PCR), multiple displacement amplification (MDA), and multiple annealing and looping-based amplification cycles (MALBAC) among others. Some of these methods are PCR-based (e.g., MALBAC, DOP-PCR), while others use isothermal amplification (e.g., MDA).

Multiple displacement amplification utilizes the φ29 DNA polymerase, a high-fidelity enzyme with proofreading and strand displacement activity that works in an isothermal environment [27]. MDA uses random hexamer primers which offer great genome coverage and due to the enzyme's strand displacement activity, multibranched DNA structures are generated. Its amplification is exponential, meaning small differences are disproportionally amplified causing sequence-dependent bias, producing over- and underamplified regions. As a result, this method is less effective in copy number variation (CNV) analysis than linear amplification methods, however, owing to the φ29 polymerase's proofreading activity it is ideal for single nucleotide variation (SNV) detection [27].

Multiple annealing and looping-based amplification cycles is a PCR-based quasi-linear amplification technique. It utilizes the isothermal Bst DNA polymerase with strand displacement activity but does not have proofreading activity. The main advantage of MALBAC is that it only amplifies the original DNA template by using special primers that can form loops in full amplicons preventing them from serving as templates for another amplification cycle. After a few cycles of linear amplification, the product is further amplified with traditional PCR steps. The quasi-linear sense of this method makes it a great choice for CNV detection; however, it is less reliable for SNV detection due to the lack of the enzyme's proofreading activity [28].

Degenerate oligonucleotide-primed *PCR* is another PCR-based amplification procedure using primers with a random hexamer sequence at the 3′ end and a fixed sequence at the 5′ end. In the first step, the random hexamer binds the genome and primer extension begins. Next, another set of primers specific to the 5' end of the primers amplifies the products from the previous step. Thereby, DOP-PCR yields exponential amplification, yet, it is suitable for analyzing large CNVs [27].

Sequencing of RNA transcripts from single cells is also a possible approach. This requires the reverse transcription of RNA molecules to complementary DNA (cDNA) which can

FIGURE 1 | Summary of the workflow of single cell isolation and downstream analyses.
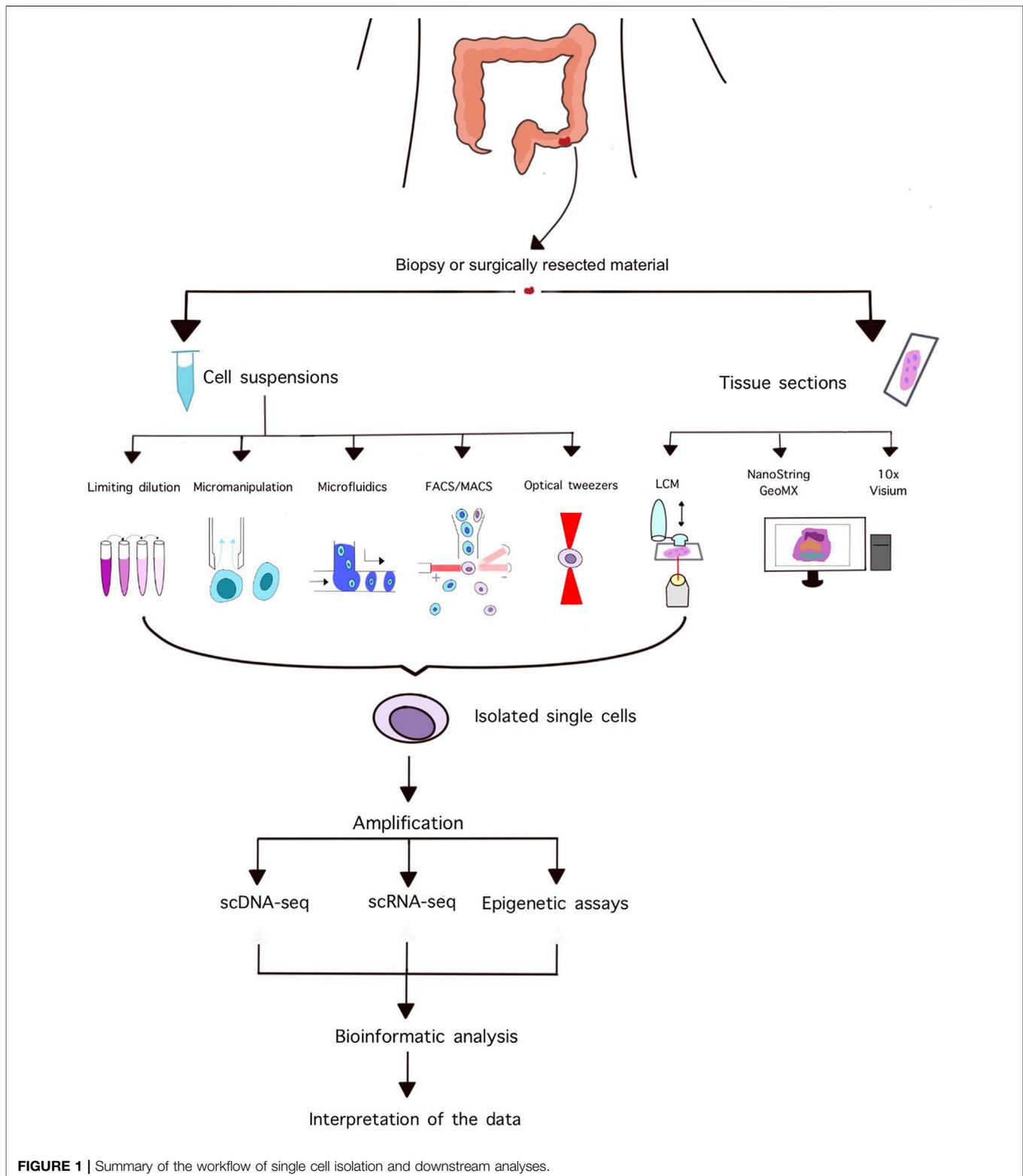
then be amplified and sequenced. To selectively target mRNA and exclude tRNA and rRNA, primers containing poly (dT) sequence binding the poly(A) tail of mRNA molecules are usually used for the reverse transcriptase enzyme generating cDNA [29]. After

reverse transcription, cDNA can be amplified using several methods including PCR-based amplification [30] and *in vitro* transcription (IVT) using T7 RNA polymerase [31]. Amplified cDNA can then be subjected to library preparation and

TABLE 1 | Summary of DNA/RNA amplification methods.

Method	Enzyme used	Advantages	Limitations	References
DOP-PCR	*Taq* DNA pol	suitable for CNV detection with large bin sizes	Often yields low coverage, expontential amplification	[71]
MALBAC	*Bst* DNA pol	suitable for CNV detection	No proofreading activity, less reliable in SNV detection	[28]
MDA	*φ29* pol	proofreading activity	expontential amplification, less reliable in CNV detection	[72]
Homopolymertailing, PCR	*M-MuLV RT, TdT, Taq pol*	Captures truncated cDNAs as well [73]	Reduced coverage towards 3′ ends of transcripts, loss of strand information, exponential amplification	[30]
Template switching, PCR	*M-MuLV RT, Taq* pol	Maintains strand information, homogeneous transcript coverage	Lower sensitivity compared to homopolymer tailing, exponential amplification	[74]
In vitro transcription	T7 RNA pol	Linear amplification	Each round shortens products [75], labor intensive	[37]

sequencing. Several protocols have been devised for single-cell RNA amplification and library preparation based on PCR amplification (Smart-Seq2 [32], SCRB-seq [33], DropSeq [34]) and IVT (MARS-Seq [35], inDrop [36], CEL-Seq [37]). **Table 1** shows the advantages and limitations of different DNA and RNA amplification methods.

Epigenetic assays providing information about accessible chromatin and histone modifications such as bisulfite sequencing (BS-seq), chromatin immunoprecipitation sequencing (ChIP-seq), and assay for transposase accessible chromatin sequencing (ATAC-seq) are also available at a single-cell resolution. These methods offer a way to assess parts of the genome on a functional level by measuring DNA methylation level, open chromatin sites or histone modifications.

Bisulfite sequencing is an important method for DNA methylation analysis. Treatment of DNA with bisulfite salts converts unmethylated cytosines to uracil while methylated cytosines are spared allowing the assessment of DNA methylation at a single nucleotide level after sequencing. Clark et al. presented a protocol for single-cell BS-seq with which the methylation status of ~50% of all CpG sites can be measured in single cells using post-bisulfite adaptor tagging, limiting the loss of adaptor-tagged sequences otherwise occurring during bisulfite treatment [38].

During ChIP-seq, protein-DNA complexes are cross-linked, followed by exonuclease-mediated DNA fragmentation. Fragmented DNA is then immunoprecipitated with antibodies specific to histone modifications or transcription factors allowing the sequencing of these target regions. Rotem et al. devised a way to perform single-cell ChIP-seq on multiple pooled cells to overcome the difficulties of the low input material from single cells [39]. They used a microfluidic system where fragmented chromatin from individual cells was uniquely barcoded by adapters and then pooled together for the immunoprecipitation step. After sequencing, the signal can be demultiplexed and fragments can be assigned to individual cells during the computational analysis.

Single-cell ATAC-seq was developed by Buenrostro et al. in 2015 using the Fluidigm C1 programmable microfluidic platform [40]. ATAC-seq uses a mutant hyperactive Tn5 transposase that identifies fragments and appends adaptors to nucleosome-free active regions. These tagged sequences are then purified and sequenced allowing the identification of active genomic regions [41].

Recently, two spatial transcriptomics platforms became commercially available: the 10X Visium Spatial Gene Expression and the NanoString Technologies' GeoMX Digital Spatial Profiler (Seattle, United States). Although these platforms cannot yet reach exact single-cell levels, they add valuable histological and spatial information to the high-resolution transcriptomic data. 10X's solution uses a special, oligo probe coated slide, where FFPE or fresh frozen tissue sections can be mounted. Staining and imaging are followed by tissue permeabilization, and the RNA molecules that have been released from cells bind to adjacent probes. The cDNA library constructed can then be sequenced and the probes are used to reconstruct spatial information of the sequenced transcriptome. NanoString's solution works with tissue mounted on any type of glass slide. Targeted mRNA probes with unique barcodes joined by a photocleavable linker are hybridized to mRNA released from the tissue section which is also stained with fluorescent antibodies. After fluorescent imaging ROIs are selected where UV light cleaves the unique barcodes. Finally, the barcodes are sequenced and linked to unique mRNA targets mapping them to specific locations of the slide [42].

However, it is important to emphasize that the link between mRNA expression and protein translation is not always guaranteed [43], and genomic and transcriptomic studies should be validated at a protein level. Single-cell resolution analysis of proteins, such as single-cell flow cytometry and single-cell mass cytometry is also possible, the description of which is beyond the scope of this article.

BIOINFORMATIC ANALYSIS OF SINGLE-CELL SEQUENCING DATA

Sequencing instruments can produce several gigabytes of raw sequencing data which need to be processed and analyzed by a bioinformatics expert with sophisticated software tools and bioinformatic pipelines. A typical DNA-seq pipeline consists of quality control of the sequencing data followed by the alignment of reads to a reference genome. After this, variant calling can be performed to identify SNVs, and their allele frequencies compared to the reference genome. In single-cell analysis SNV allele frequencies should be close to 0.5 or 1 theoretically suggesting whether the cell is either heterozygous or homozygous to the SNV. However, because of the widely used

Tool	Usage	Reference
SCAN-SNV	Measures amplification balance, SNV detection	[44]
HMMCopy	CNV detection	[46]
AneuFinder	CNV detection	[47]
Ginkgo	CNV detection	[48]
SCNV	CNV detection	[49]

non-linear amplification methods and the proportionally higher impact of artifacts occurring either before or during the early stages of the amplification step, the detected allele frequencies can deviate from the theoretically expected values [44]. To overcome this challenge, dedicated software tools such as SCAN-SNV measure amplification balance throughout the genome and calculate whether the detected allele frequencies are erroneous or not [44]. In bulk sequencing data, CNVs are called by measuring target read counts. Therefore, in single-cell analysis, the uniformity of genomic coverage needs to be taken into account during CNV calling [45]. Software tools for the analysis of CNVs in single-cell data include HMMCopy [46], AneuFinder [47], Ginkgo [48], and SCNV [49]. Mallory et al. conducted a performance assessment of popular single-cell CNV detection tools [45]. **Table 2** lists examples of the software tools used in single-cell DNA-seq data analysis.

An RNA-seq pipeline starts with quality control of the raw data and is followed by read alignment, transcriptome reconstruction, expression quantification, and downstream analyses. Particularities of single-cell isolation techniques, such as doublet formation (two cells in the same oil droplet) or the capture of dead cells with droplet-based approaches must be considered during quality control of the raw data for which the ratio of transcripts/unique molecular identifier is widely used [50]. Read aligners can be splice-aware (TopHat [51], STAR [52]) or non-splice aware (BWA [53], Bowtie2 [54]), the former enabling larger gaps like those occurring at exon boundaries, while the latter does not allow such gaps. Transcriptome reconstruction aims to uncover all transcripts and their splice variants expressed in a sample [55]. This can be performed in either a reference-based manner where overlapping reference-aligned reads are used (Cufflinks) [56] or by de novo assembly, where an algorithm builds transcripts from short reads (SPAdes) [57]. Normalization techniques (e.g., median and quantile normalization) and gene-length corrections are usually used to reduce technical variation between samples and facilitate their comparison. The most widespread gene-length corrections are TPM (transcripts per million) and RPKM/FPKM (reads/fragments per kilobase per million reads). Several software packages are available for the normalization and differential expression analysis of single-cell RNA-seq data, including scran [58], SCnorm [59], TASC [60], and SCDE [61] (the detailed description of which is beyond the scope of this article). A performance comparison of normalization and differential expression analysis methods are summarized in Cole et al.'s [62] and Wang et al.'s work [63], respectively. **Table 3** shows software tools for RNA-seq data analysis.

BULK VS. SINGLE-CELL EXPERIMENTS IN COLORECTAL ADENOMAS AND ADENOCARCINOMAS

The comprehensive molecular characterization of CRCs by The Cancer Genome Atlas project identified several recurrent mutations, somatic copy number variations (SCNAs), DNA methylation patterns, and gene expression profiles and the integration of these findings has uncovered some key altered pathways deregulated during CRC formation and progression. The recurrently mutated genes included *APC*, *TP53*, *KRAS*, *PIK3CA*, *FBXW7*, *SMAD4*, *TCF7L2*, *NRAS*, *CTNNB1*, *SMAD2*, *SOX9*, *ATM*, *ARID1A*, and *FAM123B* in the non-hypermutated, and *ACVR2A*, *APC*, *TGFBR2*, *MSH3*, *MSH6*, *SLC9A9*, *TCF7L2*, and *BRAF* in the hypermutated tumors. Among SCNVs, chromosomal changes found included the gains of 1q, 7p and q, 8p and q, 12q, 13q, 19q and 20p and q with losses of 1p, 4q, 5q, 8p, 14q, 15q, 17p, and q, 18p and q, 20p, and 22q. Recurrent subchromosomal deletion peaks including *FHIT*, *RBFOX1*, *WWOX*, *SMAD4*, *APC*, *PTEN*, *SMAD3*, and *TCF7L2* were also observed. Furthermore, subchromosomal focal amplifications were detected in the case of *USP12*, *KFL5*, *CDK8*, *WHSC1L1*, *MYC*, *ERBB2*, *IGF2*, *INS*, and *TH* [1].

Since their integrative analysis, investigations using single-cell techniques have also been conducted to further evaluate intratumoral heterogeneity and clonal expansion in CRC. **Table 4** presents a list of publications about single-cell analysis of colorectal cancers. Yu et al. performed scWES on cells isolated by micropipetting from a single-cell suspension of cancerous and normal adjacent tissues of colon cancer patient in 2014 [64]. Population genetics and potential driver events were investigated in 63 single tumor cells and compared to the results of the bulk sequencing data of 21 colon cancer patients. They identified two independent clones in the tumor cell population with the major clone containing *APC* and *TP53* mutations, which were absent in the minor clones harboring mutations in *CDC27* and *PABPC1* genes, indicating biclonality in CRC. They also identified a potential driver event, the frequent mutation of *SLC12A5* in single tumor cells, showing how single-cell sequencing can provide insight into rare genetic events otherwise masked by the whole population. In 2017 Wu et al. studied the heterogeneity and evolution of non-hereditary CRC in two patients by combining bulk WES with scWES [65]. Normal polyps, adenomatous polyps, CRC, and matched normal mucosa acquired via biopsy were in part sequenced in bulk, while the other part was digested into cell suspensions from which single cells were isolated by a micromanipulation system. By comparing the results of bulk WES with scWES, they found that bulk sequencing underestimated the level of heterogeneity of the tissues compared to single-cell analyses, and with scWES, they were also able to cluster the cells. Based on their results they proposed a monoclonal origin of CRC. In 2018 Roerink et al. used immortalized clonal organoids as proxies for the single cells obtained by flow-sorting normal and cancerous colorectal stem cells [66]. Their argument for choosing this method was that using true single cells with the contemporaneous amplification techniques would result in incomplete coverage and artefactual

TABLE 3 | Software tools for the bioinformatic analyses of RNA-seq data.

Tool	Usage	References
TopHat	Splice aware read aligner	[51]
STAR	Splice aware read aligner	[52]
BWA	Non-splice aware read aligner	[53]
Bowtie2	Non-splice aware read aligner	[54]
Cufflinks	Reference-based transcriptome reconstruction	[56]
SPAdes	de novo assembly	[57]
Scran	QC, normalization, complex analytic methods	[58]
SCnorm	Normalization	[59]
TASC	Differential expression analysis	[60]
SCDE	Differential expression, gene set overdispersion analysis	[61]

TABLE 4 | Overview of single-cell CRC publications and their findings.

Year	Method	Findings	References
2014	scWES	Observed biclonality in CRC, identified a rare driver mutation at single-cell level with low prevalence at the population level (SLC12A5)	Yu et al. [64]
2017	scWES	Proposed a monoclonal origin of CRCs	Wu et al. [65]
2018	Bulk sequencing of organoids derived from single cells	Assessment of intratumoral heterogeneity and phylogeny of cells	Roerink et al. [66]
2018	scTrio-seq2	Successful multi-omics characterization of ~1900 single cells of 12 CRC patients	Bian et al. [67]
2020	Parallel single-cell genome and transcriptome sequencing	Identification of SCNAs present in more than 10000 cells, DEGs in fibroblasts from tumor compared to fibroblasts from NAT	Zhou et al. [68]
2021	scRNA-seq	Found protumoral gene expression activity in tumor-derived cells in different cell types, proved insights into progression of UC to CAC	Wang et al. [69]
2022	Analysis of scRNA-seq, RNA-seq and microarray cohorts	Built a prognostic model based on immune cell type composition, analyzed the immune cell subgroups in the TME	Liu et al. [70]

SNV calling. By profiling the SNVs, mutational patterns, methylome, transcriptome, and drug response of clonal organoids derived from 4–6 tumor sites and matching normal tissue from 3 colorectal patients they were able to describe intratumoral heterogeneity and possible phylogeny of these tumors. In the same year, Bian et al. investigated FACS/MACS sorted single cells obtained from multiregional samples of surgically resected material of 10 CRC patients using scTrio-seq2 method. This technique can simultaneously assess SCNVs, methylation level, and also the transcriptome of cells [67]. After investigating cells from multiple sites including the primary tumor, lymph node metastases, liver metastases, and posttreatment liver metastases and identifying sublineages based on subclonal SCNAs within chromosome arms assessed intratumoral heterogeneity and the dynamics of DNA methylation and gene expression. Zhou et al. investigated single cells of CRC patients and elderly cancer-free individuals using parallel single-cell genome and transcriptome sequencing. They included 21 CRC patients with primary tumor and matched normal mucosal samples with peripheral blood, adjacent lymph nodes and mesenteric blood vessel samples also obtained from 12, 4, and 4 of those patients, respectively. Six elderly cancer-free individuals' peripheral blood samples were also obtained. After digesting the samples into cell suspensions and sorting them by FACS based on surface markers, they performed genome and transcriptome sequencing. Analyzing the SCNA profile of the cells they concluded that every cell type, even the immune cells isolated from cancer-free individuals' blood contained SCNAs,

mostly deletions of X chromosome in females and Y chromosome in males. Fibroblasts isolated from primary tumors had the highest percentage of SCNAs (as high as 48% of cells) with frequent gains of the whole chromosome 7. These cells, compared to fibroblasts isolated from normal adjacent tissues had 76 differentially expressed genes (DEG), 5 of which (BGN, RCN3, TAGLN, MYL9, and TPM2) were associated with poorer prognosis in the TCGA database [68]. Wang et al. performed droplet-based scRNA-seq on cancerous and adjacent non-malignant inflamed tissue from a patient with ulcerative colitis-associated colon cancer [69]. They analyzed 2250 cells from tumor tissues and 2527 cells from non-malignant tissues, and classified them into cell types (myeloid cells, T cells, B cells, fibroblasts, endothelial cells, and epithelial cells) based on their transcriptional activity and further clustered them using the t-SNE method. This enabled to compare gene expression activity between malignant and non-malignant derived cells among each cell types, characterizing the tumor microenvironment, and found that many malignant clusters presented protumoral activity. They also performed pseudotime analysis to evaluate the development of ulcerative colitis (UC) to colitis-associated colon cancer (CAC), and found that CD74, CLCA1 and DPEP1 may play a key role in disease progression. Recently, Liu et al. analyzed four cohorts containing gene expression data and developed a prognostic model based on immune cell type composition of colorectal cancers [70]. They were able to associate several immune cell subtypes with the prognosis of patients, such as a subgroup of dendritic cells with

better, and certain subgroups of macrophages, and B cells with poorer prognosis. One of the cohorts analyzed contained scRNA-seq data, and they evaluated the ratio of these subtypes in the tumor microenvironment of these samples, showing how single-cell analyses may prove prognostic value in oncologic patient care.

CONCLUSION

Single-cell genomic, transcriptomic, and epigenetic methods are powerful tools in cancer cell biology research. With these methods, intratumoral heterogeneity and cancer evolution can be investigated in unprecedented detail, unveiling otherwise averaged out cell populations, identifying driver events, and understanding cancer phylogenetics. In the forthcoming era of precision medicine, single-cell analyses will be essential for a more detailed understanding of cancer formation, progression, and metastatic spread. Moreover, by identifying therapy-resistant clones and potential sensitivity to treatments the above-mentioned techniques will provide a tool for clinicians to administer the best possible treatment regimen to patients.

AUTHOR CONTRIBUTIONS

BM and AK: conceptualization and revision; WK: literature research and drafting; ZN, KS, BBK, SZ, GV, and IT: critical revision of the manuscript. All authors read and approved the final manuscript.

FUNDING

CONFLICT OF INTEREST

The authors declare that the research was conducted in the absence of any commercial or financial relationships that could be construed as a potential conflict of interest.

REFERENCES

1. The Cancer Genome Atlas Network. Comprehensive Molecular Characterization of Human colon and Rectal Cancer. *Nature* (2012) 487: 330–7. doi:10.1038/nature11252

2. Bonnet D, Dick JE. Human Acute Myeloid Leukemia is Organized as a Hierarchy that Originates from a Primitive Hematopoietic Cell. *Nat Med* (1997) 3(7):730–7. doi:10.1038/nm0797-730

3. Shackleton M, Quintana E, Fearon ER, Morrison SJ. Heterogeneity in Cancer: Cancer Stem Cells versus Clonal Evolution. *Cell* (2009) 138(5):822–9. doi:10.1016/j.cell.2009.08.017

4. Nowell PC. The Clonal Evolution of Tumor Cell Populations. *Science* (1976) 194(4260):23–8. doi:10.1126/science.959840

5. Al-Hajj M, Wicha MS, Benito-Hernandez A, Morrison SJ, Clarke MF. Prospective Identification of Tumorigenic Breast Cancer Cells. *Proc Natl Acad Sci U.S.A* (2003) 100(7):3983–8. doi:10.1073/pnas.0530291100

6. Dirks PB. Brain Tumour Stem Cells: the Undercurrents of Human Brain Cancer and Their Relationship to Neural Stem Cells. *Phil Trans R Soc B* (2008) 363:139–52. doi:10.1098/rstb.2006.2017

7. Munro MJ, Wickremesekera SK, Peng L, Tan ST, Itinteang T. Cancer Stem Cells in Colorectal Cancer: A Review. *J Clin Pathol* (2018) 71(2):110–6. doi:10.1136/jclinpath-2017-204739

8. Navin N, Krasnitz A, Rodgers L, Cook K, Meth J, Kendall J, et al. Inferring Tumor Progression from Genomic Heterogeneity. *Genome Res* (2010) 20(1): 68–80. doi:10.1101/gr.099622.109

9. Snuderl M, Fazlollahi L, Le LP, Nitta M, Zhelyazkova BH, Davidson CJ, et al. Mosaic Amplification of Multiple Receptor Tyrosine Kinase Genes in Glioblastoma. *Cancer Cell* (2011) 20(6):810–7. doi:10.1016/j.ccr.2011.11.005

10. Gerlinger M, Rowan AJ, Horswell S, Larkin J, Endesfelder D, Gronroos E, et al. Intratumor Heterogeneity and Branched Evolution Revealed by Multiregion Sequencing. *N Engl J Med* (2012) 366(10):883–92. doi:10.1056/NEJMoa1113205

11. Li H, Fan X, Houghton J. Tumor Microenvironment: The Role of the Tumor Stroma in Cancer. *J Cel Biochem.* (2007) 101(4):805–15. doi:10.1002/jcb.21159

12. Valcz G, Sipos F, Tulassay Z, Molnar B, Yagi Y. Importance of Carcinoma-Associated Fibroblast-Derived Proteins in Clinical Oncology. *J Clin Pathol* (2014) 67(12):1026–31. doi:10.1136/jclinpath-2014-202561

13. Wei R, Liu S, Zhang S, Min L, Zhu S. Cellular and Extracellular Components in Tumor Microenvironment and Their Application in Early Diagnosis of Cancers. *Anal Cell Pathol* (2020) 2020:1–13. doi:10.1155/2020/6283796

14. Idos GE, Kwok J, Bonthala N, Kysh L, Gruber SB, Qu C. The Prognostic Implications of Tumor Infiltrating Lymphocytes in Colorectal Cancer: A Systematic Review and Meta-Analysis. *Sci Rep* (2020) 10(1):1–14. doi:10.1038/s41598-020-60255-4

15. Grigore A, Jolly M, Jia D, Farach-Carson M, Levine H. Tumor Budding: The Name Is EMT. Partial EMT. *J Clin Med* (2016) 5(5):51. doi:10.3390/jcm5050051

16. Guo S, Ye Y, Liu X, Gong Y, Xu M, Song L, et al. Intra-Tumor Heterogeneity of Colorectal Cancer Necessitates the Multi-Regional Sequencing for Comprehensive Mutational Profiling. *Cancer Manag Res* (2021) 13: 9209–23. doi:10.2147/CMAR.S327596

17. Alizadeh AA, Aranda V, Bardelli A, Blanpain C, Bock C, Borowski C, et al. Toward Understanding and Exploiting Tumor Heterogeneity. *Nat Med* (2015) 21(8):846–53. doi:10.1038/nm.3915

18. Losi L, Baisse B, Bouzourene H, Benhattar J. Evolution of Intratumoral Genetic Heterogeneity during Colorectal Cancer Progression. *Carcinogenesis* (2005) 26(5):916–22. doi:10.1093/carcin/bgi044

19. Yohe S, Thyagarajan B. Review of Clinical Next-Generation Sequencing. *Arch Pathol Lab Med* (2017) 141(11):1544–57. doi:10.5858/arpa.2016-0501-RA

20. Gross A, Schoendube J, Zimmermann S, Steeb M, Zengerle R, Koltay P. Technologies for Single-Cell Isolation. *Int J Mol Sci* (2015) 16(8):16897–919. doi:10.3390/ijms160816897

21. Hu P, Zhang W, Xin H, Deng G. Single Cell Isolation and Analysis. *Front Cel Dev. Biol.* (2016) 4(Oct). doi:10.3389/fcell.2016.00116

22. Lu Z, Moraes C, Zhao Y, You L, Simmons CA, Sun Y. A Micromanipulation System for Single Cell Deposition. In: 2010 IEEE International Conference on Robotics and Automation, Anchorage, AK, May 03–07, 2010. Anchorage, AK (2010). p. 494–9. doi:10.1109/ROBOT.2010.5509784

23. Liao X, Makris M, Luo XM. Fluorescence-activated Cell Sorting for Purification of Plasmacytoid Dendritic Cells from the Mouse Bone Marrow. *J Vis Exp* (2016) 117:54641. doi:10.3791/54641

24. Penter L, Dietze K, Bullinger L, Westermann J, Rahn HP, Hansmann L. FACS Single Cell index Sorting is Highly Reliable and Determines Immune Phenotypes of Clonally Expanded T Cells. *Eur J Immunol* (2018) 48(7): 1248–50. doi:10.1002/eji.201847507

25. Zhang H, Liu K-K. Optical Tweezers for Single Cells. *J R Soc Interf* (2008) 5(24):671–90. doi:10.1098/rsif.2008.0052

26. Ladanyi A, Sipos F, Szoke D, Galamb O, Molnar B, Tulassay Z. Laser Microdissection in Translational and Clinical Research. *Cytometry* (2006) 69A(9):947–60. doi:10.1002/cyto.a.20322

27. Huang L, Ma F, Chapman A, Lu S, Xie XS. Single-Cell Whole-Genome Amplification and Sequencing: Methodology and Applications. *Annu Rev Genom Hum Genet* (2015) 16(1):79–102. doi:10.1146/annurev-genom-090413-025352

28. Zong C. Multiple Annealing and Looping-Based Amplification Cycles (MALBAC) for the Analysis of DNA Copy Number Variation. In: JM Frade FH Gage, editors. *Genomic Mosaicism in Neurons and Other Cell Types*, 131. New York, NY: Springer New York (2017). p. 133–42. doi:10.1007/978-1-4939-7280-7_7

29. Saliba A-E, Westermann AJ, Gorski SA, Vogel J. Single-cell RNA-Seq: Advances and Future Challenges. *Nucleic Acids Res* (2014) 42(14):8845–60. doi:10.1093/nar/gku555

30. Tang F, Barbacioru C, Wang Y, Nordman E, Lee C, Xu N, et al. mRNA-Seq Whole-Transcriptome Analysis of a Single Cell. *Nat Methods* (2009) 6(5):377–82. doi:10.1038/nmeth.1315

31. Eberwine J, Yeh H, Miyashiro K, Cao Y, Nair S, Finnell R, et al. Analysis of Gene Expression in Single Live Neurons. *Proc Natl Acad Sci U.S.A* (1992) 89(7):3010–4. doi:10.1073/pnas.89.7.3010

32. Picelli S, Björklund ÅK, Faridani OR, Sagasser S, Winberg G, Sandberg R. Smart-seq2 for Sensitive Full-Length Transcriptome Profiling in Single Cells. *Nat Methods* (2013) 10(11):1096–8. doi:10.1038/nmeth.2639

33. Soumillon M, Cacchiarelli D, Semrau S, van Oudenaarden A, Mikkelsen TS. Characterization of Directed Differentiation by High-Throughput Single-Cell RNA-Seq. *bioRxiv* (2014). Preprint. doi:10.1101/003236

34. Macosko EZ, Basu A, Satija R, Nemesh J, Shekhar K, Goldman M, et al. Highly Parallel Genome-wide Expression Profiling of Individual Cells Using Nanoliter Droplets. *Cell* (2015) 161(5):1202–14. doi:10.1016/j.cell.2015.05.002

35. Jaitin DA, Kenigsberg E, Keren-Shaul H, Elefant N, Paul F, Zaretsky I, et al. Massively Parallel Single-Cell RNA-Seq for Marker-free Decomposition of Tissues into Cell Types. *Science* (2014) 343(6172):776–9. doi:10.1126/science.1247651

36. Klein AM, Mazutis L, Akartuna I, Tallapragada N, Veres A, Li V, et al. Droplet Barcoding for Single-Cell Transcriptomics Applied to Embryonic Stem Cells. *Cell* (2015) 161(5):1187–201. doi:10.1016/j.cell.2015.04.044

37. Hashimshony T, Wagner F, Sher N, Yanai I. CEL-seq: Single-Cell RNA-Seq by Multiplexed Linear Amplification. *Cel Rep* (2012) 2(3):666–73. doi:10.1016/j.celrep.2012.08.003

38. Clark SJ, Smallwood SA, Lee HJ, Krueger F, Reik W, Kelsey G. Genome-wide Base-Resolution Mapping of DNA Methylation in Single Cells Using Single-Cell Bisulfite Sequencing (scBS-Seq). *Nat Protoc* (2017) 12(3):534–47. doi:10.1038/nprot.2016.187

39. Rotem A, Ram O, Shoresh N, Sperling RA, Goren A, Weitz DA, et al. Single-cell ChIP-Seq Reveals Cell Subpopulations Defined by Chromatin State. *Nat Biotechnol* (2015) 33(11):1165–72. doi:10.1038/nbt.3383

40. Buenrostro JD, Wu B, Litzenburger UM, Ruff D, Gonzales ML, Snyder MP, et al. Single-cell Chromatin Accessibility Reveals Principles of Regulatory Variation. *Nature* (2015) 523(7561):486–90. doi:10.1038/nature14590

41. Schwartzman O, Tanay A. Single-cell Epigenomics: Techniques and Emerging Applications. *Nat Rev Genet* (2015) 16(12):716–26. doi:10.1038/nrg3980

42. Li X, Wang C-Y. From Bulk, Single-Cell to Spatial RNA Sequencing. *Int J Oral Sci* (2021) 13(1):36. doi:10.1038/s41368-021-00146-0

43. Vannay Á, Fekete A, Ádori C, Tóth T, Losonczy G, László L, et al. Divergence of Renal Vascular Endothelial Growth Factor mRNA Expression and Protein Level in post-ischaemic Rat Kidneys: Post-transcriptional Regulation of Renal VEGF Synthesis. *Exp Physiol* (2004) 89(4):435–44. doi:10.1113/expphysiol.2004.027516

44. Luquette LJ, Bohrson CL, Sherman MA, Park PJ. Identification of Somatic Mutations in Single Cell DNA-Seq Using a Spatial Model of Allelic Imbalance. *Nat Commun* (2019) 10(1):3908. doi:10.1038/s41467-019-11857-8

45. Mallory XF, Edrisi M, Navin N, Nakhleh L. Methods for Copy Number Aberration Detection from Single-Cell DNA-Sequencing Data. *Genome Biol* (2020) 21(1). doi:10.1186/s13059-020-02119-8

46. Daniel Lai GH. HMMcopy: Copy Number Prediction with Correction for GC and Mappability Bias for HTS Data. *Bioconductor* (2021). doi:10.18129/B9.BIOC.HMMCOPY

47. Bakker B, Taudt A, Belderbos ME, Porubsky D, Spierings DCJ, de Jong TV, et al. Single-cell Sequencing Reveals Karyotype Heterogeneity in Murine and Human Malignancies. *Genome Biol* (2016) 17(1):115. doi:10.1186/s13059-016-0971-7

48. Garvin T, Aboukhalil R, Kendall J, Baslan T, Atwal GS, Hicks J, et al. Interactive Analysis and Assessment of Single-Cell Copy-Number Variations. *Nat Methods* (2015) 12(11):1058–60. doi:10.1038/nmeth.3578

49. Wang X, Chen H, Zhang NR. DNA Copy Number Profiling Using Single-Cell Sequencing. *Brief Bioinform* (2018) 19(5):731–6. doi:10.1093/bib/bbx004

50. Yu X, Abbas-Aghababazadeh F, Chen YA, Fridley BL. Statistical and Bioinformatics Analysis of Data from Bulk and Single-Cell RNA Sequencing Experiments. *Methods Mol Biol* (2021) 2194:143–75. doi:10.1007/978-1-0716-0849-4_9

51. Trapnell C, Pachter L, Salzberg SL. TopHat: Discovering Splice Junctions with RNA-Seq. *Bioinformatics* (2009) 25(9):1105–11. doi:10.1093/bioinformatics/btp120

52. Dobin A, Davis CA, Schlesinger F, Drenkow J, Zaleski C, Jha S, et al. STAR: Ultrafast Universal RNA-Seq Aligner. *Bioinformatics* (2013) 29(1):15–21. doi:10.1093/bioinformatics/bts635

53. Li H, Durbin R. Fast and Accurate Short Read Alignment with Burrows-Wheeler Transform. *Bioinformatics* (2009) 25(14):1754–60. doi:10.1093/bioinformatics/btp324

54. Langmead B, Salzberg SL. Fast Gapped-Read Alignment with Bowtie 2. *Nat Methods* (2012) 9(4):357–9. doi:10.1038/nmeth.1923

55. Lu B, Zeng Z, Shi T. Comparative Study of De Novo Assembly and Genome-Guided Assembly Strategies for Transcriptome Reconstruction Based on RNA-Seq. *Sci China Life Sci* (2013) 56(2):143–55. doi:10.1007/s11427-013-4442-z

56. Trapnell C, Williams BA, Pertea G, Mortazavi A, Kwan G, van Baren MJ, et al. Transcript Assembly and Quantification by RNA-Seq Reveals Unannotated Transcripts and Isoform Switching during Cell Differentiation. *Nat Biotechnol* (2010) 28(5):511–5. doi:10.1038/nbt.1621

57. Bankevich A, Nurk S, Antipov D, Gurevich AA, Dvorkin M, Kulikov AS, et al. SPAdes: A New Genome Assembly Algorithm and its Applications to Single-Cell Sequencing. *J Comput Biol* (2012) 19(5):455–77. doi:10.1089/cmb.2012.0021

58. Lun ATL, McCarthy DJ, Marioni JC. A Step-by-step Workflow for Low-Level Analysis of Single-Cell RNA-Seq Data with Bioconductor. *F1000Res* (2016) 5:2122. doi:10.12688/f1000research.9501.2

59. Bacher R, Chu L-F, Leng N, Gasch AP, Thomson JA, Stewart RM, et al. SCnorm: Robust Normalization of Single-Cell RNA-Seq Data. *Nat Methods* (2017) 14(6):584–6. doi:10.1038/nmeth.4263

60. Jia C, Hu Y, Kelly D, Kim J, Li M, Zhang NR. Accounting for Technical Noise in Differential Expression Analysis of Single-Cell RNA Sequencing Data. *Nucleic Acids Res* (2017) 45(19):10978–88. doi:10.1093/nar/gkx754

61. Kharchenko PV, Silberstein L, Scadden DT. Bayesian Approach to Single-Cell Differential Expression Analysis. *Nat Methods* (2014) 11(7):740–2. doi:10.1038/nmeth.2967

62. Cole MB, Risso D, Wagner A, DeTomaso D, Ngai J, Purdom E, et al. Performance Assessment and Selection of Normalization Procedures for Single-Cell RNA-Seq. *Cel Syst* (2019) 8(4):315–28. doi:10.1016/j.cels.2019.03.010

63. Wang T, Li B, Nelson CE, Nabavi S. Comparative Analysis of Differential Gene Expression Analysis Tools for Single-Cell RNA Sequencing Data. *BMC Bioinform* (2019) 20(1):40. doi:10.1186/s12859-019-2599-6

64. Yu C, Yu J, Yao X, Wu WK, Lu Y, Tang S, et al. Discovery of Biclonal Origin and a Novel Oncogene SLC12A5 in colon Cancer by Single-Cell Sequencing. *Cell Res* (2014) 24(6):701–12. doi:10.1038/cr.2014.43

65. Wu H, Zhang X-Y, Hu Z, Hou Q, Zhang H, Li Y, et al. Evolution and Heterogeneity of Non-hereditary Colorectal Cancer Revealed by Single-Cell Exome Sequencing. *Oncogene* (2017) 36(20):2857–67. doi:10.1038/onc.2016.438

66. Roerink SF, Sasaki N, Lee-Six H, Young MD, Alexandrov LB, Behjati S, et al. Intra-tumour Diversification in Colorectal Cancer at the Single-Cell Level. *Nature* (2018) 556(7702):457–62. doi:10.1038/s41586-018-0024-3

67. Bian S, Hou Y, Zhou X, Li X, Yong J, Wang Y, et al. Single-cell Multiomics Sequencing and Analyses of Human Colorectal Cancer. *Science* (2018) 362(6418):1060–3. doi:10.1126/science.aao3791

68. Zhou Y, Bian S, Zhou X, Cui Y, Wang W, Wen L, et al. Single-Cell Multiomics Sequencing Reveals Prevalent Genomic Alterations in Tumor Stromal Cells of

Human Colorectal Cancer. *Cancer Cell* (2020) 38(6):818–82. doi:10.1016/j. ccell.2020.09.015

69. Wang Q, Wang Z, Zhang Z, Zhang W, Zhang M, Shen Z, et al. Landscape of Cell Heterogeneity and Evolutionary Trajectory in Ulcerative Colitis-Associated Colon Cancer Revealed by Single-Cell RNA Sequencing. *Chin J Cancer Res* (2021) 33(2):271–88. doi:10.21147/j.issn.1000-9604.2021.02.13

70. Liu Y, Liu X, Xu Q, Gao X, Linghu E. A Prognostic Model of Colon Cancer Based on the Microenvironment Component Score via Single Cell Sequencing. *In Vivo* (2022) 36(2):753–63. doi:10.21873/invivo.12762

71. Arneson N, Hughes S, Houlston R, Done S. Whole-Genome Amplification by Degenerate Oligonucleotide Primed PCR (DOP-PCR). *Cold Spring Harb Protoc* (2008) 2008:pdb.prot4919. doi:10.1101/pdb.prot4919

72. Silander K, Saarela J. Whole Genome Amplification with Phi29 DNA Polymerase to Enable Genetic or Genomic Analysis of Samples of Low DNA Yield. In: M Starkey R Elaswarapu, editors. *Genomics Protocols*, 439. Totowa, NJ: Humana Press (2008). p. 1–18. doi:10.1007/978-1-59745-188-8_1

73. Sasagawa Y, Nikaido I, Hayashi T, Danno H, Uno KD, Imai T, et al. Quartz-Seq: A Highly Reproducible and Sensitive Single-Cell RNA Sequencing Method, Reveals Non-genetic Gene-Expression Heterogeneity. *Genome Biol* (2013) 14(4):R31. doi:10.1186/gb-2013-14-4-r31

74. Ramsköld D, Luo S, Wang Y-C, Li R, Deng Q, Faridani OR, et al. Full-length mRNA-Seq from Single-Cell Levels of RNA and Individual Circulating Tumor Cells. *Nat Biotechnol* (2012) 30(8):777–82. doi:10. 1038/nbt.2282

75. Nygaard V. Options Available for Profiling Small Samples: A Review of Sample Amplification Technology when Combined with Microarray Profiling. *Nucleic Acids Res* (2006) 34(3):996–1014. doi:10.1093/nar/ gkj499

Tumor-Derived Exosomal RNA From Fine-Needle Aspiration Supernatant as a Novel Liquid Biopsy for Molecular Diagnosis of Cancer

Guorong Li[1][*][†], Dongdong Liu[2][*][†], Pascale Flandrin[3], Yang Zhang[4], Claude Lambert[5], Nora Mallouk[6] and Michèle Cottier[7]

[1]Department of Digestive Surgery and Urology, North Hospital, CHU Saint-Etienne, Saint-Etienne, France, [2]Department of Laboratory Science, The Second Affiliated Hospital of Guangzhou University of Chinese Medicine, Guangzhou, China, [3]Laboratory of Molecular Biology, North Hospital, CHU Saint-Etienne, Saint-Etienne, France, [4]Guangzhou HopeTech Biological Technology Co., Ltd., Guangzhou, China, [5]Section of Flow Cytometry, Immunology Laboratory, North Hospital, CHU Saint-Etienne, Saint-Etienne, France, [6]Center of Electronic Microscopy, CMES, Faculty of Medicine, University Jean Monnet, Saint-Etienne, France, [7]Laboratory of Cytopathology, North Hospital, CHU Saint-Etienne, Saint-Etienne, France

Background: We hypothesized that the fine needle aspiration (FNA) supernatant from tumor might contain tumor-derived exosomes. The objective of this pilot study was to test if tumor-derived exosomal RNA could be found in FNA supernatants for molecular diagnosis of cancer.

Methods: 10 FNA samples from pancreatic tumor were included. After the routine recuperation of cellular material by centrifugation, the cell-free Cytolyt liquid was collected instead of being discarded. 10 ml Cytolyt was used to isolate the exosomes. Transmission electronic microscopy (TEM) was used to examine the presence of exosomes. The exosomal marker CD63 was analyzed by flow cytometry. The exosomal RNA was extracted. RT-qPCR was performed to detect the GAPDH and the tumor marker of glypican 1 gene expression.

Results: TEM confirmed the presence of exosomes from FNA supernatants. Flow cytometry showed a strong positive expression of exosome marker CD63. The concentration of exosomal RNA ranged from 18.81 to 354.75 ng/μl with an average of 81.76 ng/μl. The average exosomal RNA quantity was 1390.01 ng (range from 319.77 to 6030.75 ng) with an average 260/280 ratio of 2.12. GAPDH was detectable in all samples. Exosomal glypican 1 was detected in all samples of pancreatic ductal adenorcarcinomas (3/3) and absent from benign cystic samples (3/3). Furthermore, exosomal glypican 1 was positive in one sample with a non-contributive cytology and in one sample in which no malignant cell was found.

Conclusion: This is the first report that the supernatants from FNA biopsy may contain tumor-derived exosomal RNA. These tumor-derived exosomes from FNA may provide a new liquid biopsy for the molecular diagnosis of cancer.

Keywords: exosomes, pancreatic adenocarcinoma, liquid biopsy, FNA supernatant, molecular diagnosis, glypican 1

INTRODUCTION

Pancreatic ductal adenocarcinoma (PDAC) is one of major leading cause of cancer-related deaths in the United States and in Europe. Most of patients have an unresectable tumor at the time of diagnosis due to locoregional invasion or distant metastasis [1–3]. The diagnosis by tissue biopsy is needed in the clinical circumstances. The diagnosis of a benign tumor can lead to initiate a conservative treatment or an imaging follow-up. A preoperative tissue diagnosis is performed by using image-guided fine needle aspiration (FNA) or needle biopsies. Percutaneous pancreatic FNA cytologic sampling has been described since 1975 [4]. The sensitivity of percutaneous imaging-guided FNA biopsy in the diagnosis of pancreatic masse ranges from 62% to 100% [5]. Nowadays, EUS-guided FNA (EUS-FNA) has been performed frequently to make a preoperative diagnosis and to stage pancreatic carcinoma. Although some studies suggest an improved sensitivity, experts agree that interpreting pancreatic EUS-FNA samples can be inherently difficult. The interpretation is challenging especially when cellular materials are scant and/or bloody, as often observed on EUS-FNA samples. Non-diagnostic samples (inadequate or equivocal diagnoses) from pancreas and other organs for EUS-FNA samples range from 11% to 30%. A molecular marker that can help in differentiating the malignant cells of pancreatic adenocarcinoma from the benign cells of reactive ductal epithelium would be very utile [6].

Liquid biopsy is a recent topic [7]. Liquid biopsy is based on the detection of tumor markers in body fluid, mostly in the blood, urine, saliva, or another fluid. Liquid biopsy is considered to be preferable to tissue biopsy because it is less invasive. Exosomes are membrane-bound vesicles secreted by all types of cells into the extracellular space. It has been found that exosomes play an important role in physiological and pathological processes. Many studies have shown that exosomes participate in cancer development and cancer progression. Exosomal research has become a hot subjet in the research area of biomarkers because exosomes carry specific proteins, lipids and nucleic acids of their cellular origins [8]. More importantly, exosomes provide a convenient source of potential disease biomarkers because they are ample in accessible body fluids. In fact, exosome has rapidly become as a major source of liquid biopsy.

In clinical routine, FNA supernatants are discarded. FNA supernatant contains the liquid from tumor, making it an attractive source of liquid biopsy. Tumor DNA has been found in FNA supernatant which can be used for mutation analysis in solid pancreatic tumor [9–11]. In this pilot study, we hypothesize that FNA supernatant may contain tumor-derived exosomes. We established a technique to isolate tumor-derived exosomes from FNA supernatant and tested if tumor-derived exosomes from FNA could be used as a molecular tool to diagnose cancer.

MATERIALS AND METHODS

Patients

The pancreatic FNA samples were randomly included. The indication for a pancreatic FNA biopsy was that patient had either a cystic or a solid pancreatic mass. Four patients had a solid tumor, two patients had a mixed cystic and solid tumor and four patients had a cystic tumor. The tumor size ranged from 2.0 to 6.1 cm. There were three males and seven females. Their age ranged from 49 to 84 years old. An experienced clinician performed the EUS-FNA of pancreatic lesion as a clinical routine. As a routine practice, the cellular materials of FNA biopsy were put in 30 Cytolyt solution, which was sent to cytology laboratory. As a laboratory routine, the Cytolyt solution was centrifuged at 1500 rmp for 5 min to obtain the cells. The cellular material was used for cytological diagnosis. The supernatant was collected instead of being discarded. The supernatant was stocked in −20°C until the isolation of exosome. The standard technique of ThinPrep with the Papapicolau coloration was carried out by laboratory technicians. The cytological diagnosis was performed as a laboratory routine examination. The cellularity was routinely classed as satisfactory cellular material, scant cellular material and non-cellular material according to our previous publication [12]. The collection of cytoponction samples for analysis was performed in the framework of cytology biobank which was reviewed and approved by the local IRB (protocol code: DC20121659).

Isolation of Exosomes From Fine Needle Aspiration Supernatant

10 ml FNA supernatant was utilized to isolate the exosomes by using a commercial exosome isolation solution (Hope Tech Biotechnology Co. Ltd., Guangzhou). Briefly, 2 ml of isolation solution was put into the supernatant. The mixture of solution was vortexed and placed in a refrigerator overnight. The mixture was then centrifuged at 3000 g for 30 min at 4°C to collect the exosomes.

Transmission Electronic Microscopy of Exosomes From Fine Needle Aspiration Supernatant

Transmission electron microscopy was used to examine the exosomes resuspended in 50 μl PBS. 10 μl of exosome solution was put on grids and left to adhere for 20 min. The grids were washed three times by using distilled water. The exosomes were negatively stained with uranyl acetate. Then exosomes were observed using a Hatachi electron microscopy.

Flow Cytometry of Exosomal Marker CD63

FCM was utilized to check the exosomal marker CD63. We added 1 μl of Aldehyde/sulphate latex beads (A37304, ThermoFisher) to 200 μl of exosome suspension. The solution was well mixed. Then we added 800 μl of PBS into the solution, and the mixture was left to incubate for 2 h at room temperature on a rotary wheel. The beads were collected by centrifugation at 4000 g for 5 min, and the supernatant was discarded. The beads were washed by the addition of 1 ml PBS and then were centrifuged at 4000 g for 5 min. Finally, the beads were suspended in PBS. The antibody of anti-human CD63-FITC (IM1165U, Beckman

TABLE 1 | Cytological characteristics.

Patient no.	Sex	Age	Tumor type	Cellularity	Cytological Diagnosis
1	Female	72	Solid	Satisfactory	PDAC
2	Female	70	Solid	Satisfactory	PDAC
3	Female	51	Solid	Satisfactory	PDAC
4	Female	84	Solid	Non-cellular	Not contributive
5	Male	75	Heterogene	Satisfactory	No malignant cells
6	Male	64	Heterogene	Satisfactory	No malignant cells
7	Female	49	Cystic	Scant	Cyst
8	Female	71	Cystic	Satisfactory	Cyst
9	Female	69	Cystic	Scant	Cyst
10	male	57	Cystic	Non-cellular	Not contributive

Coulter) or the antibody of an isotype control (A07795, Beckman Coulter) was added according to the standard protocol for FCM. The antibody was incubated for 30 min at dark. After twice washing with PBS, the staining was analyzed by using a conventional FCM.

Extraction of Exosomal RNA

We performed the total RNA extraction by using miRNeasy Micro Kit according to the manufacture instructions with some modifications (Qiagen S.A.). Briefly, 500 μl Qiazol solution (GITC-containing buffer) was added to dissolve the exosomes. Then 100 μl chloroform was added. The mixture was vortexed and centrifuged at 14,000 rmp at 4°C for 15 min. The supernatant was secured and 1.5 volume of 100% ethanol was added. The extraction column (Qiagen S.A.) was used to extract the total RNA from the mixture. The column was washed, respectively by RWT buffer and by REP buffer. Finally, the toal RNA was eluted in 17 μl RNase free water. The RNA was then quantified by using Nanodrop. The size distribution of exosomal RNA was analyzed by using a 2100 Bioanalyzer (Agilent Technologies). The RNA specimens were kept in −80°C until use.

RT-qPCR of Tumor Markers in Exosomes

We performed one-step RT-qPCR by using Taqman Reverse Transcription Kit (Invitrogen). We performed PCR in 25 μl reaction mixture containing 3 μl RNA, 0.5 μl of primers/probe and 12.5 μl PCR mix. After a denaturing temperature at 95°C for 10 min, 40 cycles were carried out with denaturing temperature at 95°C for 15 s, annealing temperature at 60°C for 20 s and extension at 72°C for 34 s. A positive control of universal carcinoma RNA standard and a negative control (PCR mix without RNA) were performed in each round of PCR. To examine the quality of extracted RNA, we checked the GAPDH gene expression. The primers and probes for GAPDH and glypican 1 were the commercial products of Life Technologies (TaqMan® Gene Expression Assay, Invitrogen-Life Technologies). The cycle threshold (Ct) value was set up by using the detection software SDS v2.0.1 (Applied Biosystem). GAPDH was utilized as the housekeeping gene. A Ct value less than 35 was considered as positive.

RESULTS

Cytological Diagnosis

There were four solid tumors, two heterogene tumors and four cystic tumors. **Table 1** shows the cellularity and cytological diagnosis. There were six samples with satisfactory cellularity, two samples with scant cellularity and two samples with non-cellular material. Pancreatic adenocarcinoma was found in three samples. Two samples were diagnosed with no cancer cells. Three samples were marked with a cyst. Finally, two samples were non-contributive.

Transmission Electronic Microscopy and Flow Cytometry of Exosomes From Fine Needle Aspiration Supernatant

Figure 1 shows the exosomes under electronic microscopy. TEM analyses indicated that the isolated exosomes from FNA supernatant were within the expected size range and with typical exosome morphology (**Figure 1**). The cup-shaped vesicles were observed together with aggregated vesicles. The abundant supernatant exosomes in cancer patients were observed. The size of exosomes was about 100–150 nm. Two experiments were performed with similar results. FCM demonstrated that the exosomes had a strong positive for exosomal marker CD63 (**Figure 2**).
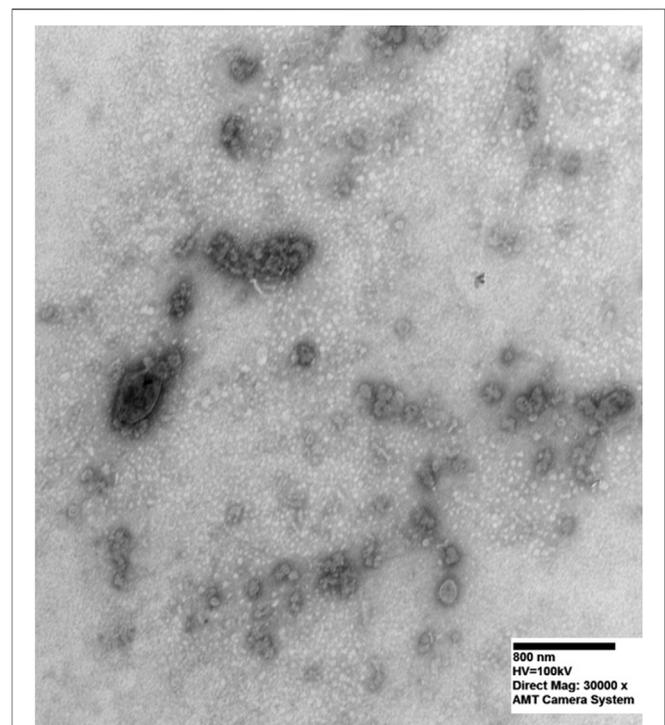
FIGURE 1 | Transmission electron microscopy of exosomes in FNA supernatant. Typical exosome morphology of cup-shaped vesicles was observed along with aggregated vesicles. Image was taken under 30,000 magnification.

FIGURE 2 | Flow cytometry analysis of exosome marker CD63. The exosomes showed a strong positive expression for exosome marker CD63.
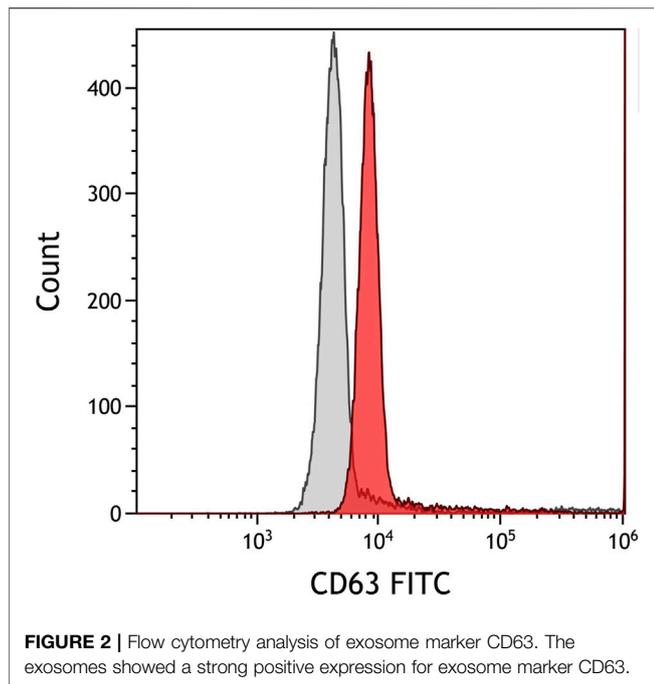
Exosomal RNA Quantity and Quality

Table 2 shows the RNA quantity and quality. The concentration of RNA ranged from 18.81 to 354.75 ng/µl with an average of 81.76 ng/µl. The RNA quantity ranged from 319.77 to 6030.75 ng with an average of 1390.01 ng. The 260/280 ratio ranged from 1.76 to 2.75 with an average of 2.12. The quantity and quality of RNA in supernatant exosomes were excellent. We found that RNA quantity in scant and non-cellular samples was abundant. An example of RNA size distribution is shown in **Figure 3**. The size distribution of the exosomal RNA varied greatly among the samples. The electrophoretic analysis showed that the value of DV200 (the percentage of RNA fragments >200 nucleotides) was less than 50% in the majority of samples.

Tumor Marker Glypican 1 Expression From Exosomes

All samples had a positive GAPDH expression. **Table 2** shows the RT-qPCR result of glypican 1. Tumor marker glypican 1 was detected in all samples of pancreatic adenorcarcinomas and absent from benign samples. Furthermore, exosomal glypican 1 was positive in one sample of scant cellularity with a non-contributive cytology and in one sample in which no malignant cell was found.

DISCUSSION

Exosomes are recently utilized as a novel and important source of liquid biopsy. Exosomes carry the same RNA markers as the cells of their origin. Tumoral RNA markers may be enriched in tumor-derived exosomes. In this pilot study, we found that FNA supernatant contained abundant tumor-derived exosomal RNA with an excellent quantity. More importantly, we found that exosomal RNA quantity in scant and non-cellular samples was abundant.

Clinically, FNA is a pratical tool of obtaining tissue material. With the increasing use of molecular markers, the tissue material is not only used for routine diagnosis but also for molecular tests. It is recommended to utilize optimally the tissue material [13–16]. However, it may be difficult to fulfill this task since the tissue materials can be limited while the demand is increasing. Several researchers have found that FNA supernatants contain tumor DNA, which can be used for molecular testing in pancreatic cancer [7–9]. The purpose is to find the tumor DNA mutations before the targeted therapy. Tumor DNA is also found in FNA supernatant of FNA samples from thyroid and lung tumors [17, 18]. Ye et al found that discarded supernatants from thyroid FNA needle rinses could provide large amounts of DNA for the detection of BRAF mutations even when the corresponding FNA smear was sparsely cellular [18]. However, no tumor-derived exosome from FNA biopsy has been studied so far for the diagnostic purpose. We decided to seek for the exosomes in FNA supernatant as a novel liquid biopsy for cancer diagnosis.

Cytological analyses are often confounded by sampling failure and interobserver variability. As other FNA samples, there are two major problems for pancreatic FNA biopsy. One problem is for the lack of tissue material and another is the difficulty in interpretation of morphology. The traditional tumor markers in the biopsy samples are used for the purpose of diagnosis. In this study, we confirmed the presence of exosomes in pancreatic FNA supernatant. Glypican 1 is a heparan sulphate proteoglycan in cell

TABLE 2 | Exosomal RNA quantity and quality.

Patient no.	Concentration RNA (ng/µl)	Ratio 260/280	Quantity RNA (ng)	Glypican 1 expression
1	77.80	2.07	1322.60	Positive
2	85.91	2.04	1460.47	Positive
3	46.10	2.05	783.70	Positive
4	43.36	2.07	737.12	Positive
5	96.27	2.09	1636.59	Positive
6	22.44	2.75	381.48	Negative
7	41.17	1.80	699.89	Negative
8	18.81	2.05	319.77	Negative
9	31.04	1.76	527.68	Negative
10	354.75	1.92	6030.75	Negative
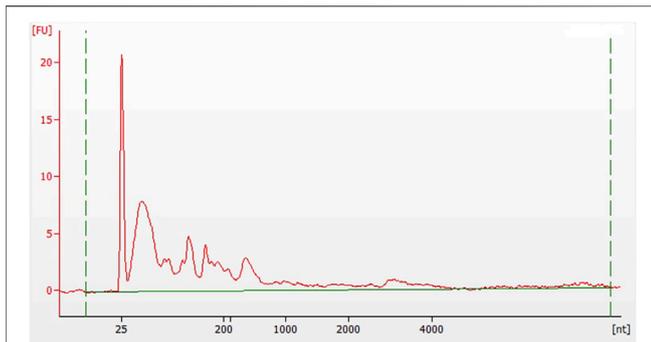
FIGURE 3 | Fragment analysis of exosomal RNA. Electrophoretic analysis of a sample demonstrated that the value of DV200 (the percentage of RNA fragments >200 nucleotides) was less than 50%. FU stands for the fluorescence unit, and nt for the nucleotide.

surface. It is overexpressed in many solid tumors. Its role is to regulate tumor development, progression and metastasis [19]. Many reports support that glypican 1 is a new marker for pancreatic adenorcarcinoma. Recently, Melo et al found that exosomes positive for glypican 1 could detect all stages of pancreatic adenocarcinomas with a high sensitivity and specificity [20]. Frampton et al found that glypican 1 was highly expressed on circulating exosomes in early and late stages of pancreatic cancers, when compared to normal controls and those with benign pancreatic diseases [21]. However, it may be difficult to detect the exosomal glypican 1 in blood for the purpose of diagnosis because of the composition heterogeneity of blood exosomes. In this pilot study, we found that exosomal glypican 1 could be detected in FNA supernatants. All pancreatic adenocarcinomas had positive exosomal glypican 1 while benign tumors were negative. Furthermore, we got some evidence that the exosome glypican 1 could help cytological diagnosis. In patient n°4, the cytology was non-contributive because of non-cellularity, but its exosome RNA was abundant and its exosme glypican 1 was positive. This result may suggest a pancreatic adenocarcinoma. In patient n°5, no cancer cell was found although its cellularity was satisfactory. But the exosomal glypican 1 was positive in this sample, which may suggest a pancreatic adenocarcinoma. We agree that it would be interesting to look for the final pathological diagnosis of these two patients if they were operated on. But our goal was to prove the existence of tumor-derived exosomal RNA in FNA supernatants. We believe that exosomal glypican 1 in pancreartic FNA supernatant will become a powerful molecular adjunct to cytological diagnosis of pancreatic adenocarcima.

The pancreatic FNA Cytolyt supernatants are routinely discarded. It is very easy to make a suggestion of using them for molecular tests. Our results indicate that FNA supernatants provide tumor-derived exosomes that can be utilized directly for nucleic acid extraction. Theoretically, RNA is protected from the degradation by exosome membrane. To our knowledge, it is the first report that a FNA supernatant contains abundantly the exosomal RNA. A FNA biopsy is not only useful for a tissue diagnosis, but it is also an excellent tool for a liquid biopsy. It means an immediate translation of exosome technique into clinical use of cytological diagnosis. However, this is a pilot study. The major limitation is that the number in this study was limited. Large studies are needed to confirm our results and its diagnostic value. Another limitation is that only one tumor marker of glypican 1 was tested. We think that other molecular tests are also possible by using the exosomes from FNA supernatant, i.e., DNA-based molecular tests.

CONCLUSION

This is the first report that the supernatants from FNA biopsy may contain tumor-derived exosomes. These tumor-derived exosomes may provide a new source of liquid biopsy for the molecular diagnosis of cancer.

DATA AVAILABILITY STATEMENT

The original contributions presented in the study are included in the article/supplementary material, further inquiries can be directed to the corresponding authors.

ETHICS STATEMENT

The protocol involving human participants was reviewed and approved by the local ethics committee of CHU Saint Etienne. The written informed consent for pancreatic EUS-FNA as well as for cytoponction sampling was obtained from each patient.

AUTHOR CONTRIBUTIONS

Conceptualization, GL, DL, and MC; methodology, GL, DL, PF, YZ, CL, and NM; formal analysis, GL, DL, PF, YZ, CL, NM, and MC; writing—original draft preparation, GL and DL; writing—review and editing, GL, DL, and MC.

CONFLICT OF INTEREST

YZ was employed by Guangzhou HopeTech Biological Technology Co., Ltd.

The remaining authors declare that the research was conducted in the absence of any commercial or financial relationships that could be construed as a potential conflict of interest.

REFERENCES

1. McGuigan A, Kelly P, Turkington RC, Jones C, Coleman HG, McCain RS, et al. Pancreatic Cancer: A Review of Clinical Diagnosis, Epidemiology, Treatment and Outcomes. *World J Gastroenterol* (2018) 24(43):4846–61. doi:10.3748/wjg.v24.i43.4846

2. Siegel RL, Miller KD, Jemal A. Cancer Statistics, 2020. *CA Cancer J Clin* (2020) 70(1):7–30. doi:10.3322/caac.21590

3. Groot VP, Gemenetzis G, Blair AB, Rivero-Soto RJ, Yu J, Javed AA, et al. Defining and Predicting Early Recurrence in 957 Patients with Resected Pancreatic Ductal Adenocarcinoma. *Ann Surg* (2019) 269(6):1154–62. doi:10.1097/SLA.0000000000002734

4. Smith EH, Bartrum RJ, Chang YC, D'Orsi CJ, Lokich J, Abbruzzese A, et al. Percutaneous Aspiration Biopsy of the Pancreas under Ultrasonic Guidance. *N Engl J Med* (1975) 292(16):825–8. doi:10.1056/nejm197504172921603

5. Zamboni GA, D'Onofrio M, Idili A, Malagò R, Iozzia R, Manfrin E, et al. Ultrasound-guided Percutaneous fine-needle Aspiration of 545 Focal Pancreatic Lesions. *Am J Roentgenol* (2009) 193(6):1691–5. doi:10.2214/AJR.09.2958

6. Jhala N, Jhala D, Vickers SM, Eltoum I, Batra SK, Manne U, et al. Biomarkers in Diagnosis of Pancreatic Carcinoma in Fine-Needle Aspirates. *Am J Clin Pathol* (2006) 126(4):572–9. doi:10.1309/cev30be088cbdqd9

7. Palmirotta R, Lovero D, Cafforio P, Felici C, Mannavola F, Pellè E, et al. Liquid Biopsy of Cancer: A Multimodal Diagnostic Tool in Clinical Oncology. *Ther Adv Med Oncol* (2018) 10:1758835918794630. doi:10.1177/1758835918794630

8. Keller S, Ridinger J, Rupp AK, Janssen JW, Altevogt P. Body Fluid Derived Exosomes as a Novel Template for Clinical Diagnostics. *J Transl Med* (2011) 9:86. doi:10.1186/1479-5876-9-86

9. Finkelstein SD, Bibbo M, Kowalski TE, Loren DE, Siddiqui AA, Solomides C, et al. Mutational Analysis of Cytocentrifugation Supernatant Fluid from Pancreatic Solid Mass Lesions. *Diagn Cytopathol* (2014) 42(8):719–25. doi:10.1002/dc.23048

10. Deftereos G, Finkelstein SD, Jackson SA, Ellsworth EM, Krishnamurti U, Liu Y, et al. The Value of Mutational Profiling of the Cytocentrifugation Supernatant Fluid from fine-needle Aspiration of Pancreatic Solid Mass Lesions. *Mod Pathol* (2014) 27(4):594–601. doi:10.1038/modpathol.2013.147

11. Roy-Chowdhuri S, Mehrotra M, Bolivar AM, Kanagal-Shamanna R, Barkoh BA, Hannigan B, et al. Salvaging the Supernatant: Next Generation Cytopathology for Solid Tumor Mutation Profiling. *Mod Pathol* (2018) 31(7):1036–45. doi:10.1038/s41379-018-0006-x

12. Wen J, Li G, Berremila SA, Klein JP, Péoc'h M, Cottier M, et al. Assessment of Cellular Adequacy of fine Needle Aspiration Biopsy for Small Solid Renal Tumors. *Cytopathology* (2018) 29(5):444–8. doi:10.1111/cyt.12579

13. VanderLaan PA. Molecular Markers: Implications for Cytopathology and Specimen Collection. *Cancer Cytopathol* (2015) 123(8):454–60. doi:10.1002/cncy.21560

14. Coley SM, Crapanzano JP, Saqi A. FNA, Core Biopsy, or Both for the Diagnosis of Lung Carcinoma: Obtaining Sufficient Tissue for a Specific Diagnosis and Molecular Testing. *Cancer Cytopathol* (2015) 123(5):318–26. doi:10.1002/cncy.21527

15. Schneider F, Smith MA, Lane MC, Pantanowitz L, Dacic S, Ohori NP, et al. Adequacy of Core Needle Biopsy Specimens and fine-needle Aspirates for Molecular Testing of Lung Adenocarcinomas. *Am J Clin Pathol* (2015) 143(2):193–200. doi:10.1309/AJCPMY8UI7WSFSYY

16. Fetzer R, Duey M, Pena V, Wanzer D, Kirkpatrick J, Chau D, et al. Role of Cytotechnologists in Rapid Onsite Adequacy Assessment of Cytology Materials for Diagnostic Workup and Specimen Allocation for Ancillary Testing Using a Standardized Protocol. *J Am Soc Cytopathol* (2020) 9(2):67–75. doi:10.1016/j.jasc.2019.08.005

17. Hannigan B, Ye W, Mehrotra M, Lam V, Bolivar A, Zalles S, et al. Liquid Biopsy Assay for Lung Carcinoma Using Centrifuged Supernatants from fine-needle Aspiration Specimens. *Ann Oncol* (2019) 30(6):963–9. doi:10.1093/annonc/mdz102

18. Ye W, Hannigan B, Zalles S, Mehrotra M, Barkoh BA, Williams MD, et al. Centrifuged Supernatants from FNA Provide a Liquid Biopsy Option for Clinical Next-Generation Sequencing of Thyroid Nodules. *Cancer Cytopathol* (2019) 127(3):146–60. doi:10.1002/cncy.22098

19. Lund ME, Campbell DH, Walsh BJ. The Role of Glypican-1 in the Tumour Microenvironment. *Adv Exp Med Biol* (2020) 1245:163–76. doi:10.1007/978-3-030-40146-7_8

20. Melo SA, Luecke LB, Kahlert C, Fernandez AF, Gammon ST, Kaye J, et al. Glypican-1 Identifies Cancer Exosomes and Detects Early Pancreatic Cancer. *Nature* (2015) 523(7559):177–82. doi:10.1038/nature14581

21. Frampton AE, Prado MM, López-Jiménez E, Fajardo-Puerta AB, Jawad ZAR, Lawton P, et al. Glypican-1 Is Enriched in Circulating-Exosomes in Pancreatic Cancer and Correlates with Tumor burden. *Oncotarget* (2018) 9(27):19006–13. doi:10.18632/oncotarget.24873

Mid-Infrared Imaging Characterization to Differentiate Lung Cancer Subtypes

E. Kontsek[1]*, A. Pesti[1], J. Slezsák[2], P. Gordon[3], T. Tornóczki[4], G. Smuk[4], S. Gergely[2] and A. Kiss[1]*

[1]2nd Department of Pathology, Semmelweis University, Budapest, Hungary, [2]Department of Applied Biotechnology and Food Science, Budapest University of Technology and Economics, Budapest, Hungary, [3]Department of Electronics Technology, Budapest University of Technology and Economics, Budapest, Hungary, [4]Department of Pathology, Medical School and Clinical Center, University of Pécs, Pécs, Hungary

Introduction: Lung cancer is the most common malignancy worldwide. Squamous cell carcinoma (SQ) and adenocarcinoma (LUAD) are the two most frequent histological subtypes. Small cell carcinoma (SCLC) subtype has the worst prognosis. Differential diagnosis is essential for proper oncological treatment. Life science associated mid- and near-infrared based microscopic techniques have been developed exponentially, especially in the past decade. Vibrational spectroscopy is a potential non-destructive approach to investigate malignancies.

Aims: Our goal was to differentiate lung cancer subtypes by their label-free mid-infrared spectra using supervised multivariate analyses.

Material and Methods: Formalin-fixed paraffin-embedded (FFPE) samples were selected from the archives. Three subtypes were selected for each group: 10-10 cases SQ, LUAD and SCLC. 2 μm thick sections were cut and laid on aluminium coated glass slides. Transflection optical setup was applied on Perkin-Elmer infrared microscope. 250×600 μm areas were imaged and the so-called mid-infrared fingerprint region (1800-648cm^{-1}) was further analysed with linear discriminant analysis (LDA) and support vector machine (SVM) methods.

Results: Both "patient-based" and "pixel-based" approaches were examined. Patient-based analysis by using 3 LDA models and 2 SVM models resulted in different separations. The higher the cut-off value the lower is the accuracy. The linear C-support vector classification (C-SVC) SVM resulted in the best (100%) accuracy for the three subtypes using a 50% cut-off value. The pixel-based analysis gave, similarly, the linear C-SVC SVM model to be the most efficient in the statistical indicators (SQ sensitivity 81.65%, LUAD sensitivity 82.89% and SCLC sensitivity 88.89%). The spectra cut-off, the kernel function and the algorithm function influence the accuracy.

Conclusion: Mid-Infrared imaging could be used to differentiate FFPE lung cancer subtypes. Supervised multivariate tools are promising to accurately separate lung tumor subtypes. The long-term perspective is to develop a spectroscopy-based diagnostic tool, revolutionizing medical differential diagnostics, especially cancer identification.

Keywords: lung cancer, fingerprint region, transflectance, SVM, LDA, FTIR, infrared

INTRODUCTION

Lung Tumors

In 2018 lung cancer was the most commonly diagnosed tumor and the leading cause of death in both sexes worldwide [1]. Preoperative biopsy materials have particular importance and the volume of biopsy material is limited. The clinical sampling also determines the feasible pathological methods. Brush cytology is often performed, however, diagnostic methods on cells or cell groups are more limited than histological analysis on FFPE samples collected by bronchoscopic tissue sampling. There is a need for ancillary diagnostics to determine histological subtypes to save material for the upcoming molecular diagnostics. Infrared spectroscopy might be one of these tools [2]. Optical fibre-based techniques combined with bronchoscopes or transthoracic needles may also disrupt and improve the current diagnostic pathways [3].

For a long time, the differential diagnosis between small cell versus non-small cell lung cancer was the most important clinicopathological aspect. Squamous cell carcinoma (SQ) and adenocarcinoma (LUAD) are the two most frequent histological subtypes. Small cell carcinoma (SCLC) subtype has the worst prognosis. There are rare tumor types or mixed entities such as mesothelioma or adenosquamous carcinoma. The development of targeted therapies and their spread in the routine oncological treatment required subtype-specific differentiation and definition of the tissue of origin even in dedifferentiated tumors and cytological specimens. This can be achieved by immunohistochemical typing [4, 5]. The most targeted therapies are available for the adenocarcinoma subtype.

The routine histological subtypization is based on Hematoxylin and Eosin (H&E) staining and five to six immunohistochemical reactions. Despite the low number of thin sections, the feasibility of high-quality nucleic acid isolation is endangered due to the size and consistency of the tissue core.

The above-mentioned aspect explains the need for new methods that can determine the origin of a single cell or group of cells without requiring immunohistochemical reactions, therefore, leaving more material for DNA or RNA isolation and consequent molecular pathological analysis. Infrared spectroscopy could do this and we aimed to build up classification models. We focused on the differential diagnostic application of FT-IR in the most frequent tumor types [6]. There are molecular, immunohistochemical markers to distinguish histological subtypes [7], however, these altogether small differences would not be detected by FT-IR since it is expected to reveal rather a spectral fingerprint characteristic of subtypes than a different quantitative compositional alteration on the level of specific proteins (e.g., p63, TTF1).

Infrared Spectroscopy

The spectral range over 780 nm is called infrared, which is conventionally divided into near-, mid- and far-infrared (NIR, MIR, FIR, respectively). The wavelength range of NIR is defined from 780 to 2500 nm (12,820-4000 cm^{-1}—since due to the dispersed Fourier-transform (FT) spectrophotometers the

wavenumber is typically measured in units of cm^{-1}), the wavelengths of MIR are between 2500 and 25,000 nm (4000-400 cm^{-1}) and the FIR range is between 25 and 1000 μm (400-10 cm^{-1}). The higher the wavenumber, the higher the energy of the light. NIR and MIR photons elevate the chemical bonds to higher energy levels, causing deformation motions (e.g., angular changes). The FIR light has lower energy so it can excite the rotation of the atoms in the bonds. The quick and non-destructive NIR and MIR spectroscopy techniques are mostly used for investigating biological systems, while FIR is less relevant from this point of view and is not applied because of the shallow energy level. The mid-infrared area includes the so-called fingerprint region (1800-400 cm^{-1}) where lipids, protein, amide I/II and nucleic acid peaks are highly representative [8].

One of the earliest MIR spectroscopic applications was to determine the cis/trans conformation of lipids [9]. MIR techniques were developed to analyse ingredients in milk [10, 11] and wine [12, 13]. Both NIR and MIR techniques are widespread in the field of biological matrix analysis. The qualitative and quantitative application of NIR in the agro-food sector began in the 1960s. Plants, animal products and processed foods from these are samples of complex biological origin, containing various contents of water, proteins, lipids and carbohydrates. Infrared analytics of grains and cereal-based products became a widespread technology, with the main focus being on the changes in protein content [14] and quality during ripening [15], and the monitoring of milling [16]. Additionally, in the field of pharmacology chemical structure of drug compounds [17] and polymers such as hydrogels [18] are proved by MIR spectroscopy as well.

MIR photons have less energy, therefore, the spatial penetration is shorter whereas the signal-to-noise ratio of the MIR spectra is about two orders of magnitude higher than in the case of NIR. There are fewer medical applications of MIR methods than that of NIR applications. MIR optical fibre, however, have been commercially available since 2016, whereas earlier only laboratory tools existed [19–22]. In a study, the breast cancer imaging of 15 patients was carried out using mid- and long-wave infrared cameras [23]. In another study, urine samples from a small cohort of healthy women as well as female patients with gynaecological malignancies were investigated with MIR resulting in diagnoses with high accuracy [24]. The basic tissue processing of pathological specimens and an imaging protocol were created by Zahdi et al. [25]. A further study has highlighted the pitfalls and best practices of tissue preparation methods for FT-IR spectroscopic analysis [26]. The most common method is to use fluorescent dyes, however, there is also another approach which chooses marker-free FT-IR imaging as a tool with promising results on lung tumour subtyping [27]. Großerueschkamp et al. analysed fresh frozen samples using random forest algorithms. They set up a 3-level decision-making scheme and even at a more detailed level they were able to successfully recognize adenocarcinoma subtypes as well [27]. Gayoud et al. focused on squamous cell FFPE sample preneoplastic and neoplastic separations on 34 samples with PCA and PLS-DA tools [28]. Akalin et al. choose spectral pretreatment as first step using Mie scattering and extended multiplicative
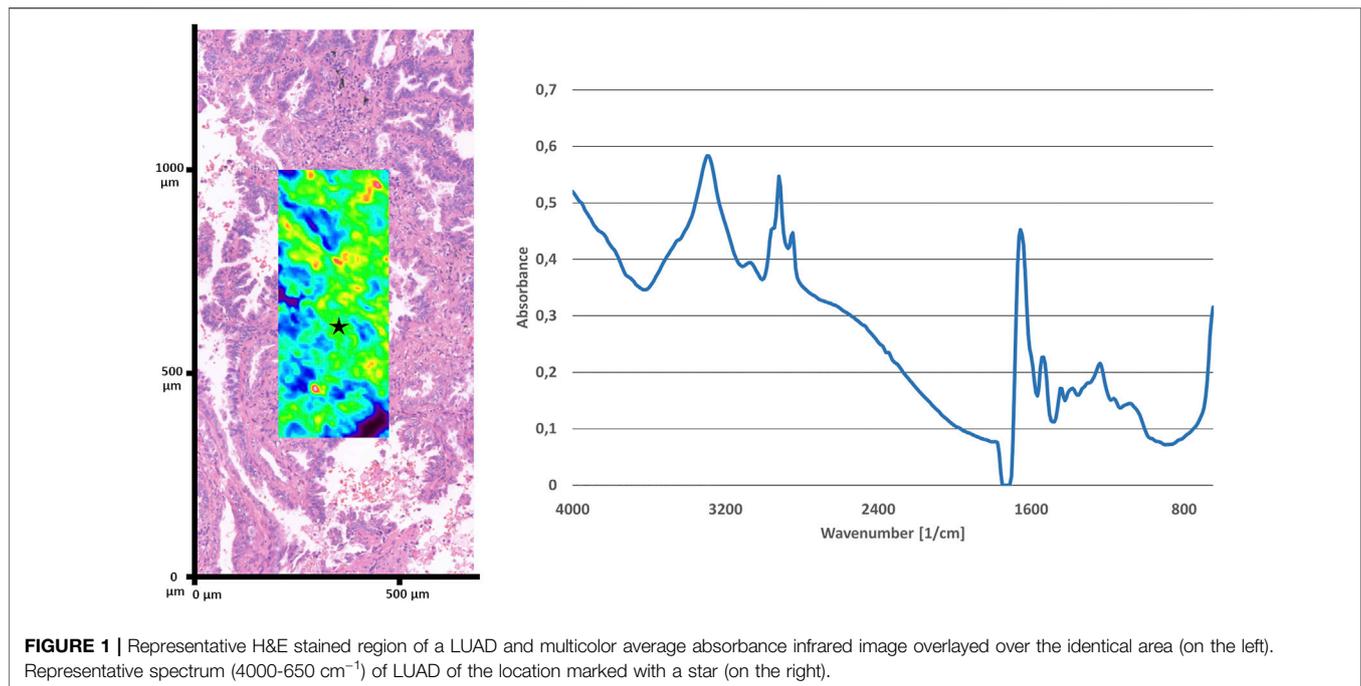
FIGURE 1 | Representative H&E stained region of a LUAD and multicolor average absorbance infrared image overlayed over the identical area (on the left). Representative spectrum (4000-650 cm^{-1}) of LUAD of the location marked with a star (on the right).

signal correction (EMSC) algorithms. They get rid of the low signal quality spectra gained from tissue microarrays (TMA) and then processed via hierarchic clustering and SVM [29]. Molecular expression patterns resulting also from mutated genes and proteins represent such a complexity that can not be expected to be precisely reflected by MIR spectra. MIR rather detects a fingerprint representative of the above-mentioned molecular complexity of a tumor. Mass spectrometry might focus either on specific molecular changes in the molecular composition or similarly detect a complex pattern. Spectral bands that can be assigned to chemical functions or to macromolecules are collected in a table published by Le Naour et al. [30]. The purpose of the present study was to differentiate lung tumor subtypes using label-free mid-infrared imaging.

MATERIALS AND METHODS

Aluminium Coated Slides
Thin-film metal layers were deposited onto glass slides by vacuum evaporation to gain mid-infrared capable reflective surface. An electron-beam evaporation source was applied in a high-vacuum chamber, in which the glass slides were fastened onto the rotary sample holder. Aluminium was evaporated at 10^{-4} Pa for 20 min at an accelerating voltage of 7 kV and beam current of 200 mA, resulting in a layer thickness of *ca.* 150 nm.

Lung Cancer Samples
A total of 30 FFPE lung cancer biopsies were selected from the archive of 2nd Department of Pathology Semmelweis University and Department of Pathology University of Pécs 10 for each subtype. 2 μm slides were cut from paraffin-embedded blocks and

were deparaffinized two times 10 min xylene. The use of human FFPE samples was approved by the Hungarian Medical Research Council, Budapest, Hungary (no. 61303-2/2018/EKU). In the routine workflow the sample preparation takes 1 day after grossing.

Infrared Imaging
Fourier transform mid-infrared imaging was used for collecting spectra with transflection optical setup. The feasibility of this approach has been tested on the separation of ethanol fixed cell lines, this has been reported previously [31]. Spotlight 400 microscope (Perkin Elmer Inc., Waltham, MA, United States) was connected to Spectrum 400 spectrophotometer used for scanning images. The Mercury Cadmium Tellurite (MCT) detector collected spectra with 32 scans with a resolution of 16 cm^{-1} and data interval of 8 cm^{-1} were recorded for each spectrum in the mid-infrared wavelength range between 4000 and 648 nm. The 250 μm × 600 μm images were scanned (**Figure 1**) by pixel size 6.25 μm × 6.25 μm. A single image contained 40 × 96 pixels and resulted in 3,840 spectra on a 0.15 mm^2 area. The acquisition time for each selected area was 46 min.

Data Processing
Atmospheric Correction and Noise Reduction
The acquired images were treated with two built-in algorithms of the SpectrumIMAGE R1.6.5.0396 software (Perkin Elmer Inc., Waltham, Massachusetts, United States) for atmospheric correction and noise reduction. The atmospheric CO_2/H_2O suppression by the least square fitting of the algorithm affected the atmospheric correction of the spectra. (Patent No.: US 6,518,753 B1) The noise reduction was based on a 20-factor

TABLE 1 | Clinicopathological features of the patients.

Case	Subtype	Age	Sex	Specimen type	Stage
1	SQ	54	Male	Resection	T2bNxMx
2	LUAD	48	Male	Resection	T2aNxMx
3	SQ	59	Male	Biopsy	Not applicable
4	SQ	67	Male	Biopsy	Not applicable
5	LUAD	57	Male	Resection	Not applicable
6	LUAD	48	Male	Resection	T3NxMx
7	SCLC	59	Male	Biopsy	T2N2M1
8	SQ	66	Female	Biopsy	T3N1M0
9	SCLC	51	Male	Resection	T2aN0Mx
10	SCLC	65	Male	Biopsy	T4N1M1
11	SQ	68	Male	Resection	T2aN0M0
12	SCLC	71	Male	Biopsy	T4N2M1
13	SQ	75	Male	Resection	T2bN0M0
14	SCLC	59	Female	Biopsy	T4N2M1b
15	LUAD	65	Female	Biopsy	T4N3Mx
16	SCLC	72	Female	Biopsy	T3N1Mx
17	LUAD	79	Female	Resection	T1aNxMx
18	SQ	65	Male	Biopsy	T3N0M0
19	SQ	60	Male	Resection	T1bNxMx
20	LUAD	78	Female	Resection	T2aNxMx
21	LUAD	63	Male	Resection	T1cN0Mx
22	LUAD	63	Female	Resection	T2aN2Mx
23	SCLC	57	Female	Resection	T2aN0Mx
24	LUAD	65	Female	Biopsy	TaN3M1c
25	SCLC	52	Male	Biopsy	T4N3M0
26	SCLC	64	Female	Biopsy	Not applicable
27	SCLC	69	Female	Biopsy	Not applicable
28	SQ	67	Male	Resection	T2bN0Mx
29	SQ	71	Male	Resection	T2aN0Mx
30	LUAD	58	Male	Resection	T2aNxMx

principal component analysis. Since the noise has lower weights, the 20-factor-based reconstructed spectrum is noise reduced. This method does not lead to the broadening of the spectrum peaks, unlike smoothing.

From the whole spectrum the so-called fingerprint subregion was analysed. In case of the fingerprint range of measured IR spectra there are 145 wavenumbers (1800-648 cm^{-1} wavenumber range) considered as variables. According to a large amount of data, it is difficult to interpret the data cube, therefore some information may partly stay hidden.

Support Vector Machine

Classification by SVM is a method based on statistical learning. The essence of SVM is to determine the hyperplane with the maximum margin for linearly separable data. The reason for the maximum margin is that decision boundaries with a large margin tend to have better generalization error than those with a small margin. The method has a wide range of applications in statistical analysis in almost all disciplines. The main advantage of the method is that it can be extended to non-linear data sets using kernel functions. In order to perform the analysis, the algorithm must be trained on a part of the data set, which contains a category variable, and then validated on the other part of the data. Once these operations have been performed, the accuracy of the method can be deduced from the results. Another advantage of the support vector machine is that it has good generalisation capabilities and can be easily applied to multidimensional data.

The confusion matrix summarizes the prediction results on the classification problem. Unscrambler X 10.4 (CAMO Software AS, Oslo, Norway) software was applied to perform the SVMs.

Linear Discriminant Analysis

LDA is a method for separating two or more classes by considering several quantitative variables simultaneously. A prerequisite for its application is that objects are already divided into classes. We must, therefore, be familiar with the classes that are identified by this classifying variable.

LDA is a classification method in which n-dimensional patterns are transformed into an m-dimensional space (m < n) by linear transformation. Consequently, samples from the same class will be located close to each other, while samples from different classes will be located far in space. The method is a supervised classification method, unlike the unsupervised, e.g., Cluster and Principal component analyses. The purpose of LDA is to determine the best fitting parameters for grouping the samples in the constructed model. The already constructed model can be used to project unknown samples. LDA is an uncomplicated method to use and is approximated on Bayes' formula [32]. The projected results can be also put in a confusion matrix as described earlier.

Unscrambler X 10.4 (CAMO Software AS, Oslo, Norway) software was applied to perform the classifications.

RESULTS

10-10 specimens were selected from each of the three histological subtypes (**Table 1**). Cases 2 and 6 are resected tumours from the same patient operated on two different locations at different timepoints. After identifying the tumorous region on the H&E slides, the consecutive slides' parallel area was imaged on the aluminium coated slides using the infrared microscope. The scheme of technology is visualized by a graphical workflow (**Figure 2**). The acquired spectra were collected and treated with atmospheric correction and noise reduction.

The spectra of the acquired images were put into a table, from which every second spectra were selected and used as a training set. A total of 5 analyses were performed using three LDA (using linear, quadratic and Mahalanobis distances) and two SVM (linear nu-SVC SVM and linear C-SVC SVM settings) models. We ran the other part of the datasets on these models and the methods predicted the histological subtype.

Two approaches were used to examine the data. We examined both "patient-based" and "pixel-based" analyses. The "patient-based" classifications are shown first. This approach is based on majority projection, therefore, the lowest recommended cut-off value is 50%. Each spectrum was classified individually by the five above-mentioned mathematical models. We have sorted the results by sample into bias matrices. The proportion of correctly classified spectra from each patient sample (3,840 spectra per sample) was considered as the decisive factor for the correct classification. The different cut-off values were compared in order to rank the accuracy of the models (**Table 2**).

FIGURE 2 | The scheme of experimental setup.
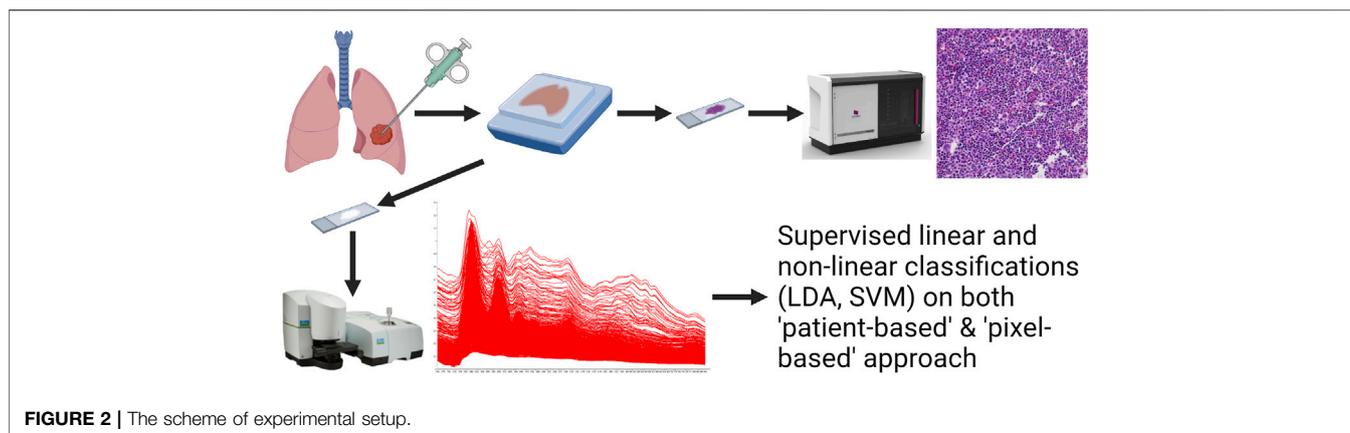
TABLE 2 | Accuracy of the prediction models using different cut-off values.

Models cut-off	Linear nu-SVC SVM	Linear C-SVC SVM	Linear LDA	Quadratic LDA	Mahalanobis LDA
50%					
SQ	90% (9/10)	100% (10/10)	70% (7/10)	100% (10/10)	0% (0/10)
SCLC	90% (9/10)	100% (10/10)	50% (5/10)	80% (8/10)	0% (0/10)
LUAD	10% (1/10)	100% (10/10)	20% (2/10)	20% (2/10)	100% (10/10)
60%					
SQ	80% (8/10)	80% (8/10)	60% (6/10)	100% (10/10)	0% (0/10)
SCLC	90% (9/10)	90% (9/10)	40% (4/10)	70% (7/10)	0% (0/10)
LUAD	0% (0/10)	80% (8/10)	20% (1/10)	20% (2/10)	100% (10/10)
70%					
SQ	50% (5/10)	80% (8/10)	50% (5/10)	90% (9/10)	0% (0/10)
SCLC	90% (9/10)	90% (9/10)	40% (4/10)	60% (6/10)	0% (0/10)
LUAD	0% (0/10)	70% (7/10)	20% (2/10)	20% (2/10)	100% (10/10)
80%					
SQ	20% (2/10)	70% (7/10)	50% (5/10)	90% (9/10)	0% (0/10)
SCLC	80% (8/10)	80% (8/10)	40% (4/10)	50% (5/10)	0% (0/10)
LUAD	0% (0/10)	60% (6/10)	20% (2/10)	20% (2/10)	100% (10/10)
90%					
SQ	10% (1/10)	20% (2/10)	40% (4/10)	70% (7/10)	0% (0/10)
SCLC	40% (4/10)	70% (7/10)	40% (4/10)	30% (3/10)	0% (0/10)
LUAD	0% (0/10)	60% (6/10)	20% (2/10)	20% (2/10)	100% (10/10)
95%					
SQ	0% (0/10)	20% (2/10)	40% (4/10)	30% (3/10)	0% (0/10)
SCLC	40% (4/10)	60% (6/10)	10% (1/10)	20% (2/10)	0% (0/10)
LUAD	0% (0/10)	40% (4/10)	20% (2/10)	20% (2/10)	100% (10/10)

Linear C-SVC SVM model with a 50% cut-off was the most successful regarding the separation of the subtypes. For interpretation of the table selecting e.g., 70% cut-off value and linear C-SVC SVM one could see that the cut-off value was not achieved in only 6 out of 30 cases: 2 samples in SQ, 1 SCLC and 3 samples in LUAD. However, these cases were also correctly predicted if we classify the samples based on the 50% cut-off value. Of course, the fine-tuning of the above-described method could improve the other models as well. It might be worthy of testing lower than 50% cut-off values, however, this approach would certainly require bigger cohorts and further testing of mixed differentiation such as adenosquamous carcinomas which feature both adenocarcinoma and squamous cell carcinoma subtypes.

By examining these five models on a pixel basis, we can obtain cumulative data for each subtype based on the prediction of each spectrum. The performance of the five models can be compared in terms of sensitivity, specificity, positive predictive value (ppv) and negative predictive value (npv) characteristics. Overall, consistent with the patient-based approach, the linear C-SVC SVM model proved to be the best again with sensitivity ranging from 81.645% to 88.885% and specificity from 90.484% to 94.784% regarding histological subtypes (**Table 3**). Quadratic LDA model achieved higher sensitivity for determining SQ predictions compared to linear C-SVC SVM but with lower specificity. Similarly, for spectra of LUAD samples, quadratic LDA gave 99% specificity but lagged behind SVM in sensitivity.

TABLE 3 | The performance of the five models.

	SQ	LUAD	SCLC
Linear nu-SVC SVM			
Sensitivity	71.290%	8.261%	84.192%
Specificity	51.706%	92.294%	87.872%
Ppv	42.465%	34.895%	77.633%
Npv	78.270%	66.800%	91.747%
Linear C-SVC SVM			
Sensitivity	81.645%	82.890%	88.885%
Specificity	90.484%	91.442%	94.784%
Ppv	81.096%	82.885%	89.495%
Npv	90.791%	91.445%	94.461%
Linear LDA			
Sensitivity	70.900%	20.001%	50.878%
Specificity	50.469%	100.000%	70.420%
Ppv	41.715%	100.000%	46.237%
Npv	77.622%	71.429%	74.141%
Quadratic LDA			
Sensitivity	91.562%	23.387%	68.405%
Specificity	58.896%	99.398%	83.382%
Ppv	52.692%	95.107%	67.300%
Npv	93.315%	72.182%	84.072%
Mahalanobis LDA			
Sensitivity	0.005%	100.000%	0.010%
Specificity	100.000%	0.008%	100.000%
Ppv	100.000%	33.335%	100.000%
Npv	66.668%	100.000%	66.669%

The quadratic LDA has a 95.107% ppv for LUAD which is better than the 82.885% of the C-SVC SVM performance.

The classification by Mahalanobis LDA was completely wrong. The model considered virtually all spectra as adenocarcinomas. That is why a 100% sensitivity was obtained for the spectra of the LUAD samples, but the specificity is 0.008%. The SQ and SCLC specificities gave a vain value of 100% since the sensitivity values are close to zero.

DISCUSSION

In this paper, we present a marker-free and automated diagnostic FT-IR imaging-based tool for pathological decision support. Classification of histologically significant lung tumor subtypes was achieved. We also highlighted the differences between five multivariate data analysis models.

The accuracy of these models was calculated using several cut-off parameters. The higher the accuracy the lower the cut-off in general. A strong bias was observed regarding the Mahalanobis model because every sample was predicted into one class. The best separation was reached by Linear C-SVC SVM model combined with 50% cut-off value according to our findings. Further optimization of the cut-off value would require a larger cohort. The pixel-based predictions also proved to be successful. Overall the C-SVC SVM performed better than the other 4 models.

The discriminative power of Linear C-SVC SVM method outperformed the others, however, certain individual statistical metrics of the other methods—such as sensitivity, specificity, ppv, npv—were better regarding the histological subtypes. Experienced pathologists in their routine activity combine the

advantages of several approaches, therefore, the above-mentioned parameters are excellent [33]. The Linear C-SVC SVM sensitivity and specificity values are in a comparable range with pathology-associated image analysis tools such as the PAPNET for cervical smear [34]. The infrared spectral analysis has a promising perspective to develop this method to assist intraoperative decision-making similar to mass spectrometry-assisted tools. The correct tissue classification by mass spectrometry was characterized by high accuracy with a sensitivity of 90.5% and specificity of 89.7% which is comparable with our method [35].

These approaches promise reproducibility, objectivity, and higher accuracy compared to current methodologies for lung tumor diagnostics. There is a growing need for personalization in medicine which requires a fast and accurate way of differential diagnosis. The approach has yet to be validated on a larger scale.

Altogether, the overall training time using half of the spectra for different models took between 2 and 12 h. However, the prediction time using these models was tremendously shortened: 5–10 min. The major delay in the current routine workflow of pathology is the sample preparation which needs 1 day after grossing. Based on the H&E image the infrared acquisition time of the selected area takes only 46 min. Analysis of native surgical specimens would reduce diagnostic intervals and enable on-site measurements. An intraoperative approach could also be executed with different detection e.g., Raman spectroscopy works better in an aqueous medium like unfixed, on-site specimens.

These *in vitro* approaches might serve as the basis to develop a dye-free intraoperative technique to facilitate surgical decision-making [27, 36]. Altogether, our *in vitro* results project the feasibility of infrared imaging to identify different cancer subtypes. Optional other ancillary methods would be the detection of tumor type specific tumor-associated DNA, however, there are no clinically reliable markers available so far.

The infrared technique would have an advantage as non-destructive and even on-site. We developed our method on histologically verified tissue sections. Long-standing problem is the adequacy of the sampling for the diagnostic needs. The oncoteam decision-making requires steadily increasing tissue-related diagnostic information. Certain genetic data need next generation sequencing, the other histological, immunohistochemical or fluorescent *in situ* hybridization information. Infrared spectroscopy might provide necessary data from less or minimal amounts of tissue. That means that biopsy material will be saved for other necessary methods, therefore, less or minimal invasive sampling would be enough [37].

The selection of the proper cut-off value secures the specificity of the analysis. Therefore, tumors featuring areas of different histological subtypes such as adenosquamous carcinomas of the lung could be used to test the feasibility of possibly lower cut-off values of the methods. This could improve the power of separation. Adenosquamous carcinomas are a rare mixed differentiation subtype of non–small cell carcinoma of the lung, constituting 0.4%–4% of cases. p63 IHC reaction is the tool to identify the squamous component. The lowest cut-off value could be determined on a large number of mixed entities.

Infrared imaging might be suitable to identify the lung cancer subtypes, therefore, fewer slides would be necessary for IHC and

more tissue would be preserved for molecular pathology to select potential novel therapies. Larger datasets must be analyzed to further support our results.

In our study, label-free mid-infrared imaging was used to acquire spectra from three lung cancer subtypes. LDAs and SVMs were performed on all the investigated subgroups in the fingerprint mid-infrared region. Based on our results SVM models performed better although spectral pretreatments might further increase the accuracy, therefore, it could be an additional option. We successfully demonstrated the feasibility of our infrared method to separate cancer subtypes types by their label-free mid-infrared spectra with highlighted range. In conclusion, our data suggest the usage of transflective optical set and 1800-648 cm^{-1} spectral range to gain spectra.

DATA AVAILABILITY STATEMENT

The raw data supporting the conclusion of this article will be made available by the authors, without undue reservation.

ETHICS STATEMENT

The studies involving human participants were reviewed and approved by the Medical Research Council (ETT TUKEB) 7-8 Széchenyi István tér, Budapest, H-1051, Hungary. Written informed consent for participation was not required for this study in accordance with the national legislation and the institutional requirements. Written informed consent was not obtained from the individual(s) for the publication of any potentially identifiable images or data included in this article.

AUTHOR CONTRIBUTIONS

FUNDING

CONFLICT OF INTEREST

The authors declare that the research was conducted in the absence of any commercial or financial relationships that could be construed as a potential conflict of interest.

REFERENCES

1. Bray F, Ferlay J, Soerjomataram I, Siegel RL, Torre LA, Jemal A. Global Cancer Statistics 2018: GLOBOCAN Estimates of Incidence and Mortality Worldwide for 36 Cancers in 185 Countries. *CA Cancer J Clin* (2018) 68(6):394–424. doi:10.3322/caac.21492
2. Finlayson D, Rinaldi C, Baker MJ. Is Infrared Spectroscopy Ready for the Clinic? *Anal Chem* (2019) 91(19):12117–28. doi:10.1021/acs.analchem.9b02280
3. Fernandes S, Williams G, Williams E, Ehrlich K, Stone J, Finlayson N, et al. Solitary Pulmonary Nodule Imaging Approaches and the Role of Optical Fibre-Based Technologies. *Eur Respir J* (2021) 57(3):2002537. doi:10.1183/13993003.02537-2020
4. Loo PS, Thomas SC, Nicolson MC, Fyfe MN, Kerr KM. Subtyping of Undifferentiated Non-small Cell Carcinomas in Bronchial Biopsy Specimens. *J Thorac Oncol* (2010) 5(4):442–7. doi:10.1097/JTO.0b013e3181d40fac
5. Rossi G, Pelosi G, Graziano P, Barbareschi M, Papotti M. A Reevaluation of the Clinical Significance of Histological Subtyping of Non-small-cell Lung Carcinoma: Diagnostic Algorithms in the Era of Personalized Treatments. *Int J Surg Pathol* (2009) 17(3):206–18. doi:10.1177/1066896909336178
6. Su KY, Lee WL. Fourier Transform Infrared Spectroscopy as a Cancer Screening and Diagnostic Tool: A Review and Prospects. *Cancers* (2020) 12(1):E115. doi:10.3390/cancers12010115
7. Yatabe Y, Dacic S, Borczuk AC, Warth A, Russell PA, Lantuejoul S, et al. Best Practices Recommendations for Diagnostic Immunohistochemistry in Lung Cancer. *J Thorac Oncol* (2019) 14(3):377–407. doi:10.1016/j.jtho.2018.12.005

8. Balan V, Mihai CT, Cojocaru FD, Uritu CM, Dodi G, Botezat D, et al. Vibrational Spectroscopy Fingerprinting in Medicine: From Molecular to Clinical Practice. *Materials* (2019) 12(18):E2884. doi:10.3390/ma12182884
9. Baumann WJ, Madson TH, Weseman BJ. "Plasmalogen-type" Cyclic Acetals: Formation and Conformation of the 1, 3-dioxanes and 1, 3-dioxolanes from 1-O-Cis-Alk-1′-Enyl-Sn-Glycerols. *J Lipid Res* (1972) 13(5):640–50. doi:10.1016/s0022-2275(20)39369-x
10. O'Sullivan A, O'Connor B, Kelly A, McGrath MJ. The Use of Chemical and Infrared Methods for Analysis of Milk and Dairy Products. *Int J Dairy Technol* (1999) 52(4):139–48. doi:10.1111/j.1471-0307.1999.tb02856.x
11. Goulden JDS. Analysis of Milk by Infra-red Absorption. *J Dairy Res* (1964) 31(03):273–84. doi:10.1017/s0022029900018203
12. GarciaJares CM, Medina B. Application of Multivariate Calibration to the Simultaneous Routine Determination of Ethanol, Glycerol, Fructose, Glucose and Total Residual Sugars in Botrytized-Grape Sweet Wines by Means of Near-Infrared Reflectance Spectroscopy. *Fresenius' J Anal Chem* (1997) 357(1):86–91. doi:10.1007/s002160050117
13. Nieuwoudt HH, Prior BA, Pretorius IS, Manley M, Bauer FF. Principal Component Analysis Applied to Fourier Transform Infrared Spectroscopy for the Design of Calibration Sets for Glycerol Prediction Models in Wine and for the Detection and Classification of Outlier Samples. *J Agric Food Chem* (2004) 52(12):3726–35. doi:10.1021/jf035431q
14. Kays SE, Barton FE, Windham WR. Predicting Protein Content by Near Infrared Reflectance Spectroscopy in Diverse Cereal Food Products. *J Near Infrared Spectrosc* (2000) 8(1):35–43. doi:10.1255/jnirs.262
15. Gergely S, Salgo A. Changes in Carbohydrate Content during Wheat Maturation - what Is Measured by Near Infrared Spectroscopy? *J Near Infrared Spectrosc* (2005) 13(1):9–17. doi:10.1255/jnirs.452

16. Huang H, Yu H, Xu H, Ying Y. Near Infrared Spectroscopy for On/in-Line Monitoring of Quality in Foods and Beverages: A Review. *J Food Eng* (2008) 87(3):303–13. doi:10.1016/j.jfoodeng.2007.12.022

17. Juriga D, Laszlo I, Ludanyi K, Klebovich I, Chae CH, Zrinyi M. Kinetics of Dopamine Release from Poly(aspartamide)-Based Prodrugs. *Acta Biomater* (2018) 76:225–38. doi:10.1016/j.actbio.2018.06.030

18. Juriga D, Kalman EE, Toth K, Barczikai D, Szollosi D, Foldes A, et al. Analysis of Three-Dimensional Cell Migration in Dopamine-Modified Poly(aspartic Acid)-Based Hydrogels. *Gels* (2022) 8(2):65. doi:10.3390/gels8020065

19. Bogomolov A, Belikova V, Zabarylo UJ, Bibikova O, Usenov I, Sakharova T, et al. Synergy Effect of Combining Fluorescence and Mid Infrared Fiber Spectroscopy for Kidney Tumor Diagnostics. *Sensors (Basel)* (2017) 17(11): E2548. doi:10.3390/s17112548

20. Sojka L, Tang Z, Furniss D, Sakr H, Fang Y, Beres-Pawlik E, et al. Mid-infrared Emission in Tb^{3+}-Doped Selenide Glass Fiber. *J Opt Soc Am B* (2017) 34(3): A70–A79. doi:10.1364/josab.34.000a70

21. Nallala J, Lloyd GR, Hermes M, Shepherd N, Stone N. Enhanced Spectral Histology in the colon Using High-Magnification Benchtop FTIR Imaging. *Vibrational Spectrosc* (2017) 91:83–91. doi:10.1016/j.vibspec.2016.08.013

22. Seddon AB, Benson TM, Sujecki S, Abdel-Moneim N, Tang ZQ, Furniss D, et al. Towards the Mid-infrared Optical Biopsy. In: Optical Biopsy Xiv: Toward Real-Time Spectroscopic Imaging and Diagnosis; 2016 7 Mar; San Francisco, CA (2016). p. 9703.

23. Joro R, Laaperi AL, Dastidar P, Soimakallio S, Kuukasjarvi T, Toivonen T, et al. Imaging of Breast Cancer with Mid- and Long-Wave Infrared Camera. *J Med Eng Technol* (2008) 32(3):189–97. doi:10.1080/03091900701234358

24. Paraskevaidi M, Morais CLM, Lima KMG, Ashton KM, Stringfellow HF, Martin-Hirsch PL, et al. Potential of Mid-infrared Spectroscopy as a Non-invasive Diagnostic Test in Urine for Endometrial or Ovarian Cancer. *Analyst* (2018) 143(13):3156–63. doi:10.1039/c8an00027a

25. Sreedhar H, Varma VK, Nguyen PL, Davidson B, Akkina S, Guzman G, et al. High-definition Fourier Transform Infrared (FT-IR) Spectroscopic Imaging of Human Tissue Sections towards Improving Pathology. *J Vis Exp* (2015)(95) 52332. doi:10.3791/52332

26. Zohdi V, Whelan DR, Wood BR, Pearson JT, Bambery KR, Black MJ. Importance of Tissue Preparation Methods in FTIR Micro-spectroscopical Analysis of Biological Tissues: 'Traps for New Users. *PLoS One* (2015) 10(2): e0116491. doi:10.1371/journal.pone.0116491

27. Grosserueschkamp F, Kallenbach-Thieltges A, Behrens T, Bruning T, Altmayer M, Stamatis G, et al. Marker-free Automated Histopathological Annotation of Lung Tumour Subtypes by FTIR Imaging. *Analyst* (2015) 140(7):2114–20. doi:10.1039/c4an01978d

28. Gaydou V, Polette M, Gobinet C, Kileztky C, Angiboust JF, Birembaut P, et al. New Insights into Spectral Histopathology: Infrared-Based Scoring of Tumour Aggressiveness of Squamous Cell Lung Carcinomas. *Chem Sci* (2019) 10(15): 4246–58. doi:10.1039/c8sc04320e

29. Akalin A, Mu X, Kon MA, Ergin A, Remiszewski SH, Thompson CM, et al. Classification of Malignant and Benign Tumors of the Lung by Infrared Spectral Histopathology (SHP). *Lab Invest* (2015) 95(4):697–21. doi:10.1038/labinvest.2015.55

30. Le Naour F, Bralet MP, Debois D, Sandt C, Guettier C, Dumas P, et al. Chemical Imaging on Liver Steatosis Using Synchrotron Infrared and ToF-SIMS Microspectroscopies. *Plos One* (2009) 4(10):e7408. doi:10.1371/journal.pone.0007408

31. Kontsek E, Pesti A, Bjornstedt M, Uveges T, Szabo E, Garay T, et al. Mid-Infrared Imaging is Able to Characterize and Separate Cancer Cell Lines. *Pathol Oncol Res* (2020) 26(4):2401–7. doi:10.1007/s12253-020-00825-z

32. James G, Witten D, Hastie T, Tibshirani R. Classification. In: *An Introduction to Statistical Learning: With Applications in R*. New York, NY: Springer US (2021). p. 129–95.

33. Paech DC, Weston AR, Pavlakis N, Gill A, Rajan N, Barraclough H, et al. A Systematic Review of the Interobserver Variability for Histology in the Differentiation between Squamous and Nonsquamous Non-small Cell Lung Cancer. *J Thorac Oncol* (2011) 6(1):55–63. doi:10.1097/JTO.0b013e3181bc0878

34. Irwig L, Macaskill P, Farnsworth A, Wright RG, McCool J, Barratt A, et al. A Randomized Crossover Trial of PAPNET for Primary Cervical Screening. *J Clin Epidemiol* (2004) 57(1):75–81. doi:10.1016/S0895-4356(03)00259-2

35. Phelps DL, Balog J, Gildea LF, Bodai Z, Savage A, El-Bahrawy MA, et al. The Surgical Intelligent Knife Distinguishes normal, Borderline and Malignant Gynaecological Tissues Using Rapid Evaporative Ionisation Mass Spectrometry (REIMS). *Br J Cancer* (2018) 118(10):1349–58. doi:10.1038/s41416-018-0048-3

36. Petersen D, Mavarani L, Niedieker D, Freier E, Tannapfel A, Kotting C, et al. Virtual Staining of colon Cancer Tissue by Label-free Raman Micro-spectroscopy. *Analyst* (2017) 142(8):1207–15. doi:10.1039/c6an02072k

37. Tian P, Wang Y, Li L, Zhou Y, Luo W, Li W. CT-Guided Transthoracic Core Needle Biopsy for Small Pulmonary Lesions: Diagnostic Performance and Adequacy for Molecular Testing. *J Thorac Dis* (2017) 9(2):333–43. doi:10.21037/jtd.2017.02.16

Check for
updates

The Activation of PDGFRβ on Mononuclear Stromal/Tumor Cells in Giant Cell Tumor of Bone After Denosumab Treatment. An Immunohistochemical Study of Five Cases

Imre Antal[1], Zsuzsanna Pápai[2], Miklós Szendrői[1], Tamás Perlaky[1], Katalin Dezső[3], Zoltán Lippai[3] and Zoltán Sápi[3]*

[1]Department of Orthopaedics, Semmelweis University, Budapest, Hungary, [2]Department of Oncology, Hungarian Defence Forces Medical Center, Budapest, Hungary, [3]Department of Pathology and Experimental Cancer Research, Semmelweis University, Budapest, Hungary

Due to the relatively high recurrence rate and the destructive nature of the tumor, the treatment of giant cell tumor is still a challenge. Denosumab appeared to be a promising candidate as a therapeutic drug. However, several studies have reported that tumors can recur during/after treatment with denosumab. Based on activated receptor tyrosine kinase signaling pattern of the stromal/tumor cells, a combination treatment with denosumab and sunitinib has recently been proposed to inhibit recurrences. This prompted us to investigate the PDGFRβ expression of five denosumab treated cases using both primary and recurrent tumors during and after denosumab treatment. In addition, to recognise morphological changes, immunohistochemical analysis of H3F3A and PDGFRβ was also performed. As an effect of denosumab treatment, the permanent absence of giant cells associated with severe to mild fibrosis was the most consistent morphological change, but H3F3A positive stromal/tumor cells were observed in all cases. Furthermore, an increased immunopositivity of PDGFRβ in stromal/tumor cells was evident in all recurrent cases during denosumab treatment. Upon tumor recurrence (after the discontinuation of denosumab treatment) the intensity of PDGFRβ immunostaining in stromal/tumor cells was restored/decreased. Our results confirm (for the first time) the activation of PDGFRβ on mononuclear stromal/tumor cells at protein level as an effect of denosumab treatment, which has so far only been demonstrated by phosphoprotein array analysis (protein lysates). The decreased PDGFRβ activity after the discontinuation of denosumab treatmeant and the increased PDGFRβ activity during denosumab treatment underlines the need for denosumab and sunitinib combination therapy.

Keywords: giant cell tumor of bone, denosumab, PDGFRβ, combination therapy, sunitinib

INTRODUCTION

According to the latest WHO definition, Giant cell tumor of bone (GCTB) is a locally aggressive and rarely metastasizing neoplasm (1). It most frequently occurs in the epiphysis of the long bones of young adults. Histologically, a mononuclear cellular component and osteoclast-like giant cells can be distinguished. The Mononuclear cellular component can be further subdivided into round histiocytic cells (without cytogenetic alterations) and more elongated (oval or spindle-shaped) cells called as neoplastic cells, harboring both numerical chromosomal alterations and H3.3 G34W mutations (2, 3). The gold standard of treatment is surgical: curettage and high-speed burring of the defect with or without the use of adjuvants such as phenol, liquid nitrogen and bone cement (4). Depending on the size and location of the tumor and the type of surgery, the rate of local recurrence is still high (10%–31%). Still, about 95% of cases can be cured with repeated surgery. According to larger series, due to the large destruction of the bone, articular cartilage surface and massive soft tissue component, resection, as primary procedure, might be necessary in about 13%–20% (5, 6). This means however, to sacrifice the adjacent joint and to replace the defect by endoprosthesis in young patients. Furthermore, the rare axial location, the destruction of the sacrum and vertebral body can pose an unsalvageable problem with limited surgical treatment options. In such cases, to avoid mutilating surgery with substantial morbidity, denosumab treatment was launched by Thomas et al (2010) which appeared to be very promising (7). However, several studies have reported that GCTB can recur during/after treatment with denosumab (8-11) which may pose additional challenges. Based on activated receptor tyrosine kinase signaling pattern of stromal/tumor cells, a combination treatment with denosumab and sunitinib has recently been proposed to inhibit recurrences (12). This prompted us to investigate the PDGFRβ expression of five denosumab treated cases using both primary and recurrent tumors during and after denosumab treatment.

Patients and Methods

Patients

Five patients with histologically proven GCTB were selected between 01. 2007 and 12. 2019 from the file of Semmelweis University. Except one case (malignant transformation of GCTB), the original biopsies, as well as the biopsies of the recurrent tumors during denosumab treatment/or immediately after treatment and biopsies of recurrent tumors after at least 6 months of denosumab treatment were available. In the case of the malignant transformation, the original biopsy and the biopsy from malignant GCTB/osteosarcoma (during denosumab treatment) were examined. Clinical data are summarized in **Table 1**. All five patients had a "high risk tumor" presented with extensive bone loss, pathologic fracture, or destruction of the cortical/subchondral bone, so conservative surgery (curettage and bone grafting) and joint salvage were not possible at presentation. Resection of the GCTB would have been associated with potentially poor function and significant morbidity. At least two recurrences were observed in all cases except the GCTB with malignant transformation (with only one recurrence). None of them had a history of malignancy or radiotherapy of the affected bone. The denosumab treatment did not affect dental and jaw conditions, and the patients were not previously treated with bisphosphonate.

All patient gave a written informed consent for denosumab treatment and their consent to the scientific use of the results. The protocol was approved by the Research Ethics Board of the Semmelweis University (TUKEB 155/2012). CT and MRI of the affected area were performed every 3 months in all patients. The images taken before and after the denosumab treatment were compared by expert radiologists.

Histology and Immunohistochemistry

H&E slides were evaluated for diagnostic purpose in the initial biopsy, and H3F3A immunohistochemistry was used to confirm the diagnosis of GCTB. Changes in the histology caused by denosumab treatment were noted and followed during treatment and after discontinuation of denosumab treatment.

Immunohistochemistry was performed on deparaffinized, rehydrated sections obtained from a representative formalin-

TABLE 1 | Clinical data of denosumab treated patients.

Case number	1	2	3	4	5
Gender	Female	Male	Female	Male	Male
Age (at presentation; years)	20	40	41	39	28
Location	os ischii	dist. femur	dist. tibia	dist. radius	prox. femur
Recurrence	3x	4x	3x	2x	1x*
Pathological fracture	No	yes	no	yes	No
Pain/swelling	Yes	yes	yes	yes	Yes
Enneking classification	aggr.	aggr.	aggr.	aggr.	aggr.
Denosumab treatment time (months)	15	12	24	7	6
Type of reoperation	curettage+ resection	curettage+	curettage+	resection+	resection++
Follow up after denosumab treatment (months)	10	13	24	8	6
Present status	NED	stable disease	stable disease	NED	Died

*Abbreviations: dist., distalis; prox., proximalis; *, malignant transformation in recurrence, malignant giant cell tumor of bone/osteosarcoma; aggr., agressive; curettage+, curettage + adjuvant treatment; resection+, resection + fibula autograft; resection++, resection + endoprothesis; NED, no evidence of disease.*

TABLE 2 | Immunohistochemistry results of primary and denosumab treated GCTB samples (whole-slide evaluation).

Case number	PDGFRβ	H3F3A (% of mononuclear cells)
1 primary	+, diffuse	80
1 recurrence den.	++/+++, diffuse	50
1 recurrence after den	+, focal	60
2 primary	+, focal	90
2 recurrence den.	+++, diffuse	50
2 recurrence after den.	+/++, diffuse	60
3 primary	+, diffuse	70
3 recurrence den.	++, diffuse	40
3 recurrence after den.	+, focal	50
4 primary	+, focal	80
4 recurrence den.	++, diffuse	50
4 recurrence after den.	+, focal	50
5 primary	+, diffuse	70
5 recurrence den.	+++, focal	20

Abbreviations: recurrence den., recurrence during denosumab treatment; recurrence after den., recurrence after denosumab treatment.

fixed, paraffin-embedded block from each case using antibody-specific epitope retrieval techniques with the Bond-Max (Leica Biosystems, Wetzlar, Germany) automated system for the detection of the following antigens: PDGFRβ (Cell Signaling Technology, rabbit monoclonal IgG, 28E1, 1:100), H3F3A (RevMAb Biosciences, rabbit monoclonal IgG, RM263, 1:300). The immunohistochemical results were scored according to staining intensity and distribution in case of PDGFRβ, and in case of H3F3A the percentage of nuclear positivity was taken into account. Recurrences during denosumab treatment or very shortly after denosumab treatment (less than 1 month) were termed as "recurrence during denosumab treatment" and recurrences after more than 6 months of discontinuation of denosumab treatment were called as "recurrence after denosumab treatment" (**Table 2**).

RESULTS

Clinical Response

Four patients experienced significant pain relief by the end of the third month after starting the denosumab treatment. The swelling of soft tissues decreased and the movement of the adjacent joint improved.

Comparing CT and MR images before and after denosumab treatment, four patients showed stabilisation (no progression) but only two patients showed a reduction in defect size. The thickness of the cortical bone was increased, the pathologic fractures were healed. Inside of the cystic defect new bone formation, mineralization was detected in every case however, residual cysts varying in size and number remained detectable. In two patients, the indication for surgery was residual cysts filled by solid tissue in another one local recurrence 1 year after finishing the treatment occurred wich needed a resection. One patient had a complex deformity following the healing of his pathological fracture
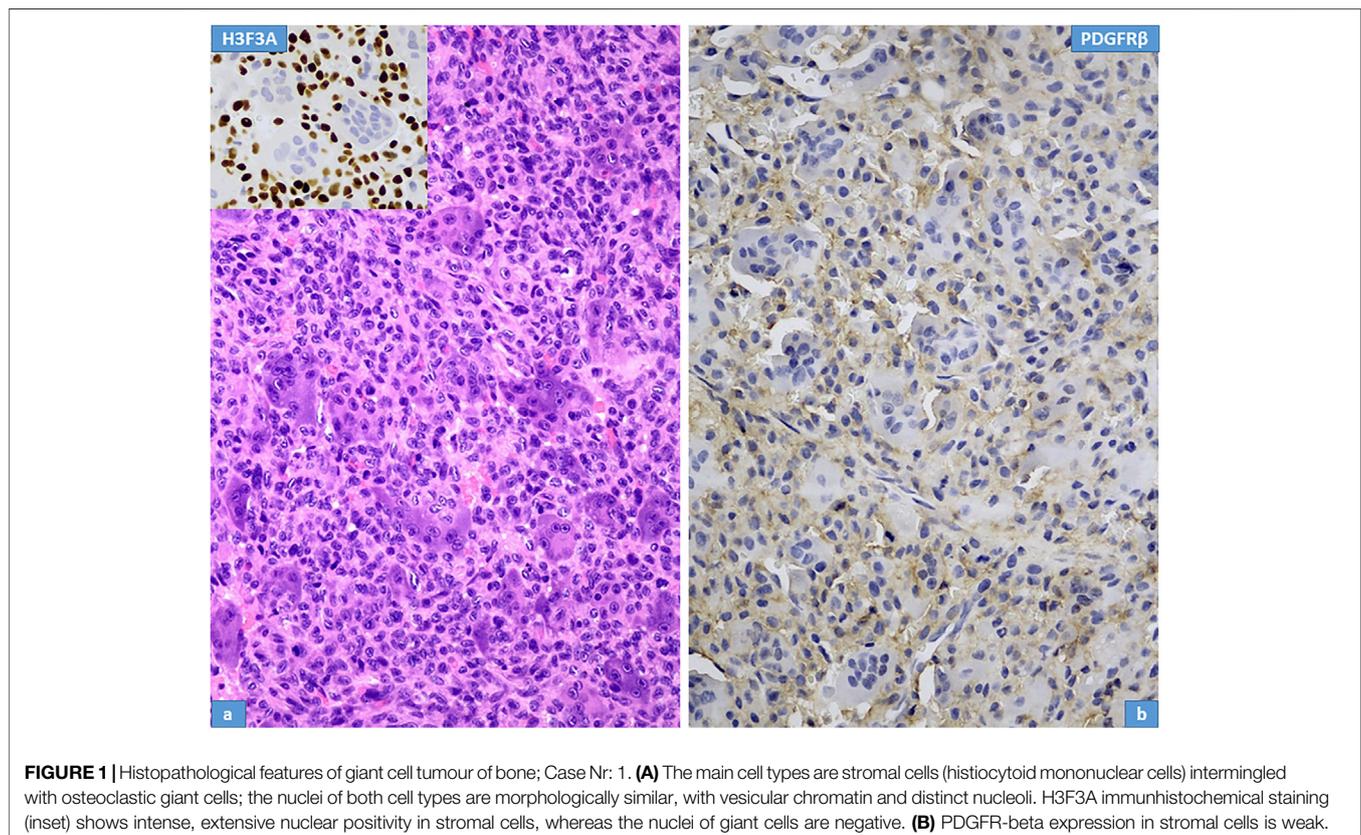
FIGURE 1 | Histopathological features of giant cell tumour of bone; Case Nr: 1. **(A)** The main cell types are stromal cells (histiocytoid mononuclear cells) intermingled with osteoclastic giant cells; the nuclei of both cell types are morphologically similar, with vesicular chromatin and distinct nucleoli. H3F3A immunhistochemical staining (inset) shows intense, extensive nuclear positivity in stromal cells, whereas the nuclei of giant cells are negative. **(B)** PDGFR-beta expression in stromal cells is weak.
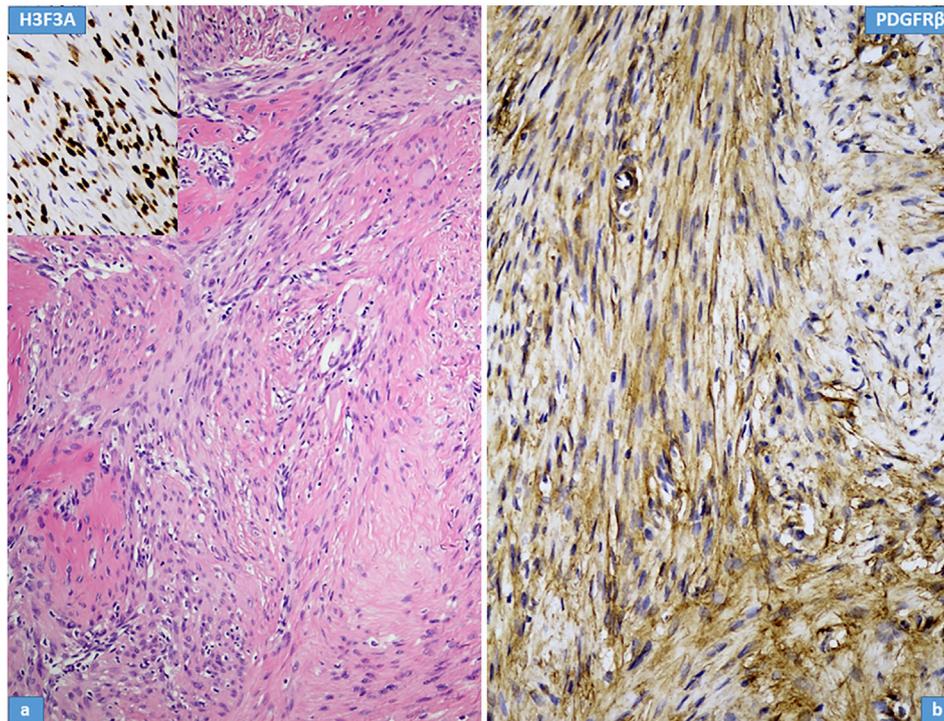
FIGURE 2 | Histological features of recurrent giant cell tumour of bone during denosumab treatment; Case Nr: 1. **(A)** The most important histological features include a reduction in giant cells, a decrease in neoplastic stromal cells, an increase in fibrotic tissue and bone formation. Immunohistochemical staining for H3F3A (inset) is preserved in stromal cells. **(B)** Intense PDGFR-beta expression is observed in stromal cells.

of the distal radius, which led to loss of function of the wrist. The defects of the former two patients were curetted rinsed by phenol as adjuvant treatment and filled up by morzelised bone. The distal part of the radius was resected in one patient and autologous fibula was used to replace the defect. As a result of follow up, two patients have no evidence of disease, another two have a stable disease with residual cysts, and one patient died (malignant transformation of GCTB). The patient who died was a 28-year-old male with a large lytic lesion in his proximal femur. To avoid the resection of the proximal femur and scarification of the hip joint, he had denosumab treatment for 6 months. His hip pain ceased after the first month. Seven months after the onset of the treatment, his lower extremities became paretic. MRI revealed metastatic tumorous foci in the third, fourth lumbar vertebral bodies and in the first sacral segment. Decompression and stabilization of these segments were performed and tumor tissue was sent for histological examination. This revealed a malignant transformation, malignant GCTB/osteosarcoma. The patient's general condition improved, he was able to walk again, but his pain in the left hip joint increased again. Radiography revealed a progression of the defect, tumorous bone production and a pathological fracture. A palliative surgery, conventional hip endoprosthesis was implanted and adjuvant chemotherapy according COSS protocol was started. He died with his disease before his chemotherapy could have been finished.

Histology, Immunohistochemistry

Microscopically, the primary biopsy/curettage (in all case) displayed a characteristic admixture of rounded mononuclear histiocytic, spindle-shaped mononuclear neoplastic stromal cells and large reactive multinucleated osteoclast like giant cells, resulting in the diagnosis of GCTB (**Figures 1A**, **4A**,E, **5A**,E). In all cases the diagnosis was confirmed by H3F3A immunohistochemistry and the percentage of nuclear positivity of the mononuclear cells were counted. The range was between 70%–90% (**Table 2**) (**Figure 1A** inset). Recurrent cases during denosumab treatment showed various histologic picture, but the most consistent alteration was the permanent absence of giant cells. Bone formation, ossification, severe to mild fibrosis, bundles of loose fibrous tissue, thin-walled vessels and a proliferation of mononuclear cells with bland, spindle nuclei were observed in different proportion as a typical response to denosumab treatment (13) (**Figures 2A**, **4C**,G, **5C**). In case 5, the recurrent tumor showed a malignant transformation with highly cellular, atypical spindle cell proliferation. Unequivocal tumorous osteoid formation and high mitotic rate (8%–10/HPF) was obvious (**Figure 5G**). H3F3A immunohistochemistry still was positive in all cases, but in a much lower percentage compared to the primary biopsy/curettage (range: 40%–50%), especially in case of malignant transformation (20%) (**Table 2**) (**Figure 2A** inset, 5g inset). The histology of recurrent cases after denosumab treatment was more similar to the histology of primary biopsies than to recurrent tumors during denosumab treatment, but more or less fibrosis and bone formation could be observed in each case (**Figure 3A**). The

FIGURE 3 | Histological features of recurrent giant cell tumour of bone after denosumab treatment; Case Nr: 1. **(A)** Similar to the primary tumor, giant cells and admixed stromal cells are observed in a mild fibrotic background. Immunohistochemical staining for H3F3A (inset) is preserved in stromal cells. **(B)** Weak PDGFR-beta expression is observed in stromal cells.

percentage of H3F3A positivity was in between of the primary and recurrent (during denosumab treatment) cases, namely 50%–60% (**Table 2**) (**Figure 3A** inset). Generally, PDGFRβ immunohistochemistry was positive in each cases including primary and recurrent tumors (both during and after denosumab treatment), but with different intensity and distribution. Primary biopsies displayed only weak positivity with either diffuse or focal distribution (**Table 2**) (**Figures 1B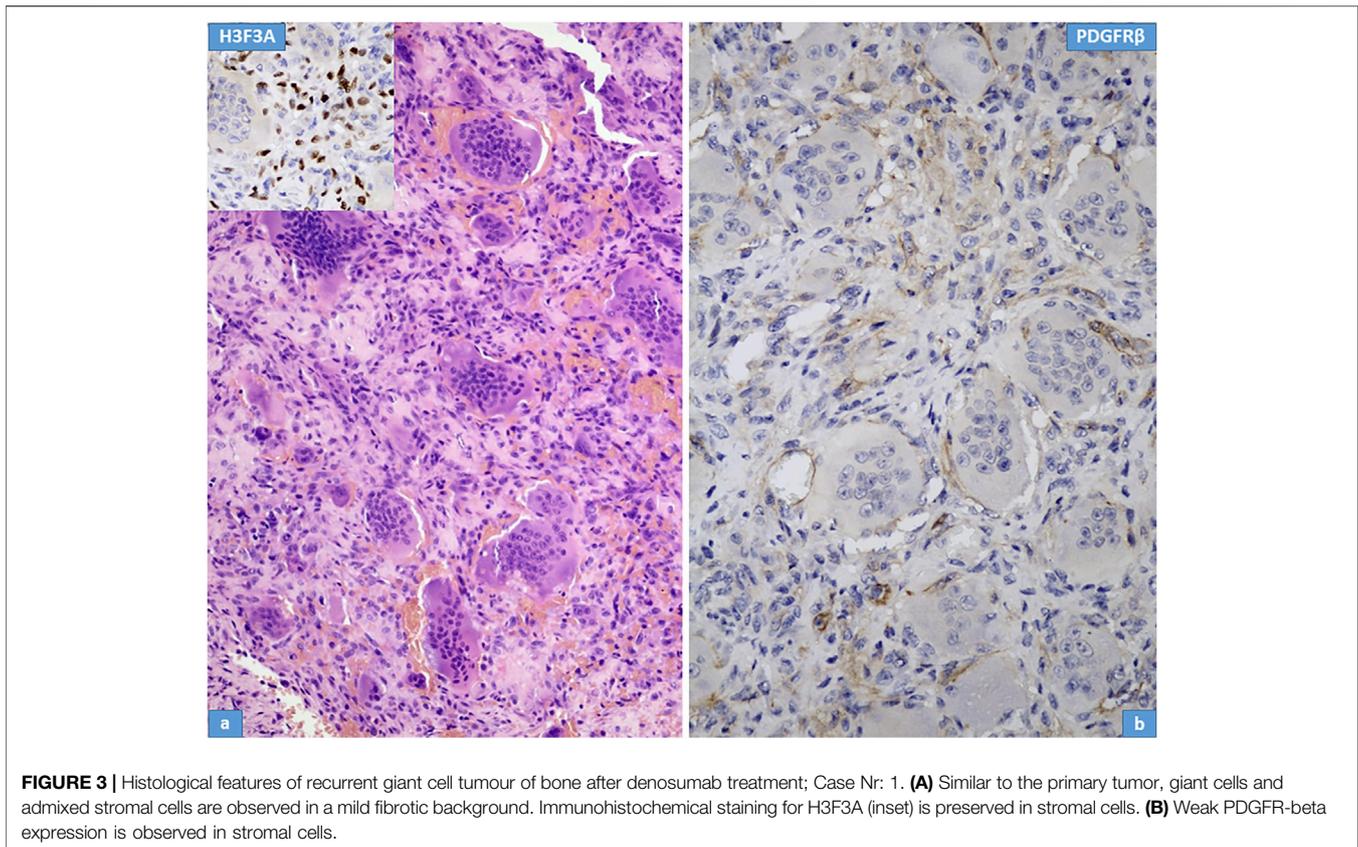**, **4B**,F, **5B**,F). In contrast, recurrent tumors during denosumab treatment showed moderate to strong PDGFRβ positivity in a diffuse way (**Figures 2B**, **4D**,H, **5D**), except the case with malignant transformation, which pointed strong but focal positivity (**Figure 5H**). Recurrent tumors after denosumab treatment displayed a similar intensity of PDGFRβ immunostaining as it could be observed in the primary biopsies which means, the intensity of PDGFRβ immunostaining in stroma/tumor cells was restored/decreased (**Table 2**) (**Figure 3B**). We investigated two cases of reccurent GCTB without denosumab treatment, but we found the same weak PDGFRB positivity in both cases; very similar to the five primary cases demonstrated in **Figures 1**, **4B**,F, **5B**, F (**Supplementary Figure S1**).

DISCUSSION

GCTB is a locally aggressive and rarely metastasizing neoplasm histologically composed of a mononuclear cellular component (round histiocytes and elongated neoplastic cells) and osteoclast-like giant cells (14). It is still difficult to understand the cell biology of GCTB, that is the interaction of the different cell types, but a generally accepted concept has been described by Forsyth et al (15) recently: there is a crosstalk between m/wt nucleosome H3.3, telomeres and osteoclastogenesis. Extensive studies (16-18) revealed the mechanism of interaction between the macrophage and osteoclast-like cell populations, which express nuclear factor kappa B (RANK) and the stromal cells, which produce RANK ligand (RANKL). Another landmark discovery was the H3.3 G34W mutation, which proved to be characteristic of GCTB by Behjati et al (19). This mutation can be demonstrated by H3F3A immunohistochemistry and proved highly specific and sensitive to both GCTB and malignant GCTB (3). Behjati et al thought that it was possible that histone 3.3 mutations directly led to osteoclast recruitment, for example through alteration of expression of essential osteoclast signals such as RANK ligand or colony stimulating factor 1 (19). However, recently L. Cottone et al (20) found that H3.3 G34W had no impact on the expression of RANKL and osteoprotegerin, as previously was proposed by Behjati et al. Instead, the Signal Peptide CUB Domain And EGF Like Domain Containing 3 (SCUBE3), a secreted member of the transforming growth factor beta (TGFβ) family, was the most significantly downregulated gene in H3.3 G34W compared to H3.3 WT cells. In this way, SCUBE3 is a valid candidate for regulating osteoclast recruitment (20).

FIGURE 4 | Histological characteristics of Cases Nr: 2 and 3. **(A,E)** Primary tumours, mixed giant cells and stromal cells are observed in a mild fibrotic background. **(B, F)** Weak focal PDGFR beta staining is observed in stromal cells. **(C,G)** During denosumab treatment a decrease in giant cells, surviving neoplastic stromal cells in fibrotic background and bone formation are observed with intense PDGFR-beta expression **(D,H)** in neoplastic stromal cells.

Due to the high rate of local recurrence (10%–31%) and the frequently mutilating surgical intervention (about 5%–10%, especially in unresectable cases), new treatment approaches are vital. Denosumab, a pure humanized monoclonal antibody against RANK-L, has been has been the most promising treatment choice. It reduces the number of osteoclast-like giant cells and the mitotic activity in its precursor cells, leading to the reduction of the aggressive osteolytic activity and also facilitates optimal bone remodeling, described by Thomas et al (7). Thomas et al found a positive histological response in 100% and positive radiological response (stable disease) in 66% of the patients, whereas bone repair occurred in 29% of the cases. Unfortunately, recent studies reported frequent recurrences following the denosumab treatment (13, 21, 22). Traub et al (22) in all their 20 patients observed recurrences during/following denosumab treatment despite reduction in pain intensity and positive histologic and radiological response. Matcuk et al (21) described rapid recurrence of GCTB after cessation of long-term denosumab therapy. Although fortunately very rare, malignant transformation of denosumab treated GCTB is now well-established, as recently reported by Palmerini et al (23). Last year (2021), Mahdal et al (12) described sunitinib as a new target for precision medicine treatment of GCTB; found effective in the treatment of neoplastic stromal cells with activated PDGFRβ signaling. They used fresh-frozen tumor samples and tumor-derived cell lines and an increase in PDGFRβ phosphorylation was found in fresh frozen tumour samples, but it was not statistically significant. However, using tyrosine kinase inhibitor sunitinib *in vitro*, a direct inhibition of the stromal cell proliferation and the differentiation of stromal cells into fibroblast-like cells in the tumor tissue samples was also observed. Furthermore, they performed an off-label treatment with sunitinib (combined with denosumab) in a GCTB-diagnosed patient with aggressive course and gained complete remission/healing. These findings (12) prompted us to investigate the PDGFRβ expression of five denosumab treated cases using both primary and recurrent tumors during and after denosumab treatment. Although the number of cases is not high, it is still enough and unique, because we had four cases where the primary tumor, recurrent tumor during denosumab treatment and recurrent tumor after denosumab treatment were available to examine the possible change in the intensity and distribution of PDGFRβ immunostaining. The fifth case demonstrated a malignant transformation in the recurrence as a rare event and because the patient died on his disease, we could examine only the primary and recurrent tumors. The main question was the effect of denosumab treatment on mononuclear tumor cells (characterized by H3F3A immunopositivity), concerning PDGFRβ expression. It was obvious that denosumab treatment facilitated the increase of PDGFRβ expression, both in intensity and distribution of each
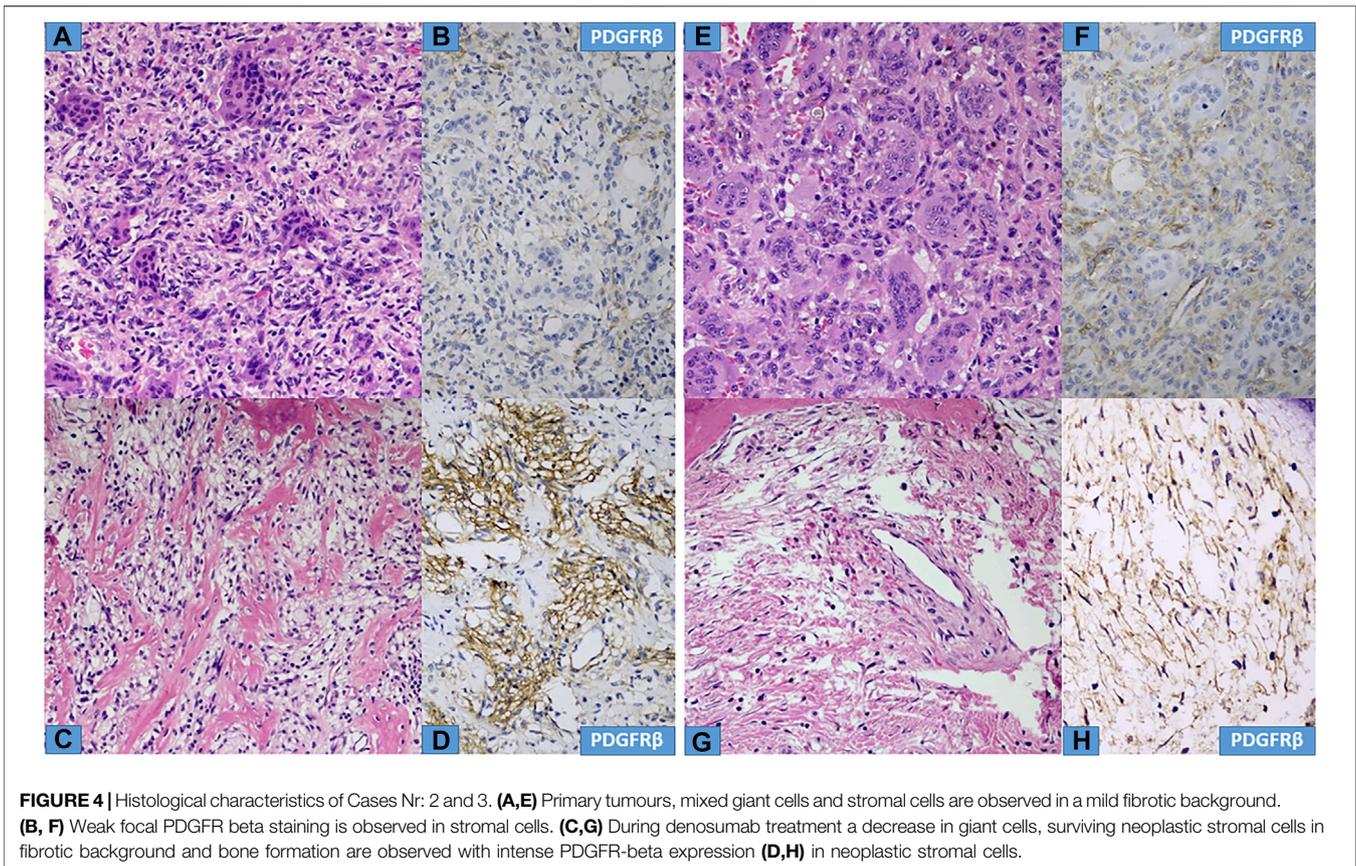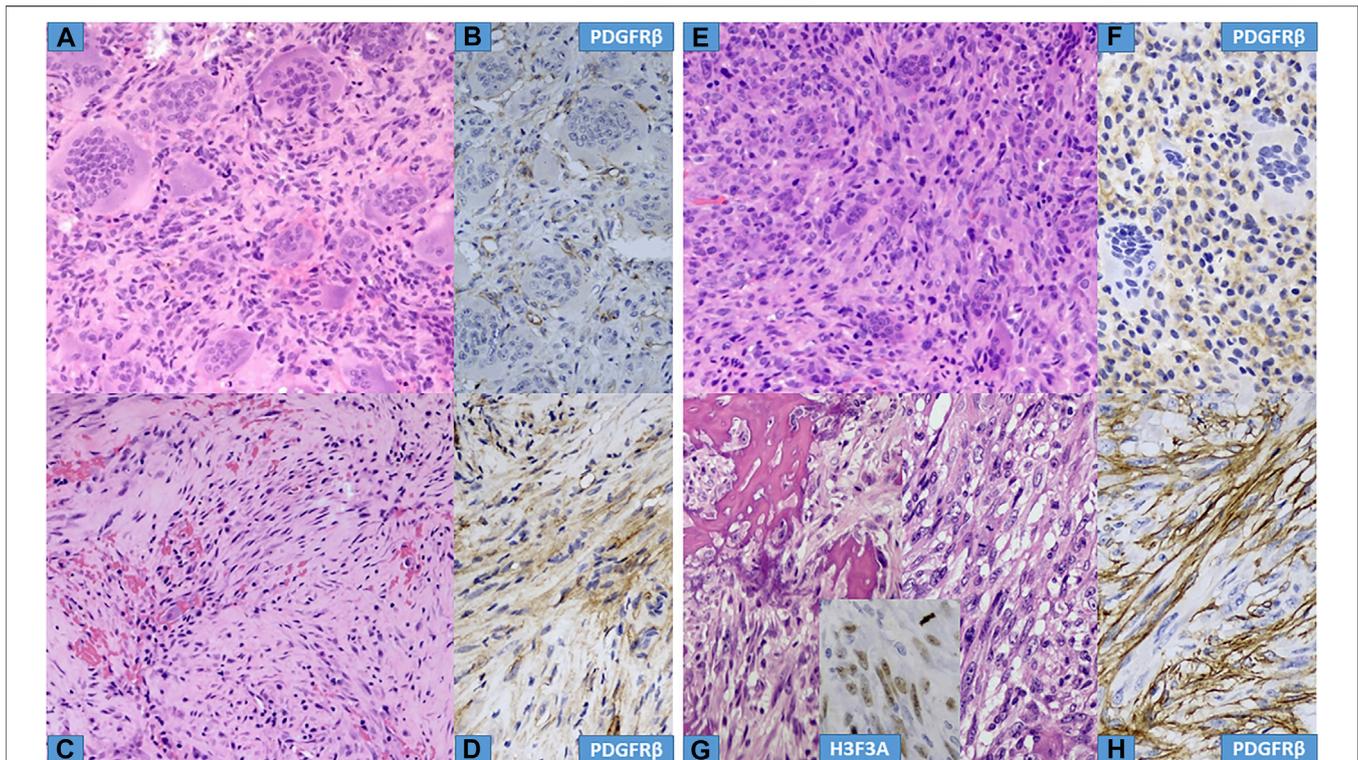
FIGURE 5 | Histological characteristics of Cases Nr: 4 and 5. **(A,E)** Primary tumours, mixed giant cells and stromal cells are observed in a mild fibrotic background. **(B,F)** Weak focal PDGFR-beta staining is observed in stromal cells. **(C,D)** (case Nr: 4) During denosumab treatment a decrease in giant cells, surviving neoplastic stromal cells in fibrotic background are observed with intense PDGFR-beta expression. **(G,H)**. (case Nr: 5) Recurrent tumor during Denosumab treatment showed significant cellular atypia, with increased mitotic figures (malignant GCTB), and intense PDGFR-beta expression in stromal cells. Inset shows focal H3F3A positivity in malignant stromal cells.

cases (**Table 2**) (**Figures 1**, **2**, **4**, **5**). The fact, that the intensity of PDGFRβ immunostaining in tumor cells was decreased in recurrences after denosumab treatment (**Table 2**; **Figure 3**) confirms the causing role of denosumab regarding PDGFRβ overexpression however, the precise mechanism is not known. There is a small debate in the literature regarding the diagnostic role of H3F3A, but we agree (and experienced) with others that practically all GCTBs are H3F3A positive including malignant GCTBs. In our study, we found variable percentage of H3F3A nuclear positivity among mononuclear cells (20–90%), but the tendency was clear: the percentage was lower in denosumab treated cases (**Table 2**). Explanation of the former finding can be the relative high number of reactive histiocytes, fibroblasts and bone forming osteoblasts as reactive non-neoplastic cells. The H3F3A positive malignant tumor cells in our malignant GCTB with increased PDGFRβ expression further brace the theory that in rare instances H3.3 G34W mutations combined with PDGFRβ overexpression may cause malignant transformation.

CONCLUSION

Summing up our findings, we certified the activation/overexpression of PDGFRβ on mononuclear stromal/tumor cells at protein level (paraffin sections) as an effect of denosumab treatment. Our results also support the need to treat the PDGFRβ activated GCTB cases with denosumab and sunatinib as a combination therapy to prevent further recurrences and to prevent an accidental malignant transformation. The decreased PDGFRβ activity after discontinuation of denosumab treatmeant and the increased PDGFRβ activity during denosumab treatment underlines the need for denosumab and sunitinib combination therapy. However, the low case number is certainly a limitation of the study and further confirmation with higher case number could be necessary.

DATA AVAILABILITY STATEMENT

The raw data supporting the conclusion of this article will be made available by the authors, without undue reservation.

ETHICS STATEMENT

The studies involving human participants were reviewed and approved by the Research Ethics Board of the Semmelweis University (TUKEB 155/2012). The patients/participants provided their written informed consent to participate in this study.

AUTHOR CONTRIBUTIONS

Study concept and design: IA and ZS. Data acquisition: IA, MS, and TP. Data analysis and interpretation: IA and ZS. Manuscript preparation: IA, KD, and ZS. Manuscript editing: ZL and ZS. Manuscript revising: ZP, MS, TP, and ZS. Final approval of the manuscript: IA, ZP, MS, TP, KD, ZL, and ZS.

FUNDING

REFERENCES

1. WHO. *Soft Tissue and Bone Tumours*. Argonay: Naturaprint (2020).

2. Moskovszky L, Szuhai K, Krenacs T, Hogendoorn PC, Szendroi M, Benassi MS, et al. Genomic Instability in Giant Cell Tumor of Bone. A Study of 52 Cases Using DNA Ploidy, Relocalization FISH, and Array-CGH Analysis. *Genes Chromosomes Cancer* (2009) 48(6):468–79. doi:10.1002/gcc.20656

3. Amary F, Berisha F, Ye H, Gupta M, Gutteridge A, Baumhoer D, et al. H3F3A (Histone 3.3) G34W Immunohistochemistry: A Reliable Marker Defining Benign and Malignant Giant Cell Tumor of Bone. *Am J Surg Pathol* (2017) 41(8):1059–68. doi:10.1097/PAS.0000000000000859

4. van der Heijden L, Dijkstra PDS, Blay JY, Gelderblom H. Giant Cell Tumour of Bone in the Denosumab Era. *Eur J Cancer* (2017) 77:75–83. doi:10.1016/j.ejca.2017.02.021

5. Balke M, Schremper L, Gebert C, Ahrens H, Streitbuerger A, Koehler G, et al. Giant Cell Tumor of Bone: Treatment and Outcome of 214 Cases. *J Cancer Res Clin Oncol* (2008) 134(9):969–78. doi:10.1007/s00432-008-0370-x

6. Arbeitsgemeinschaft K, Becker WT, Dohle J, Bernd L, Braun A, Cserhati M, et al. Local Recurrence of Giant Cell Tumor of Bone after Intralesional Treatment with and without Adjuvant Therapy. *J Bone Jt Surg Am* (2008) 90(5):1060–7. doi:10.2106/JBJS.D.02771

7. Thomas D, Henshaw R, Skubitz K, Chawla S, Staddon A, Blay JY, et al. Denosumab in Patients with Giant-Cell Tumour of Bone: an Open-Label, Phase 2 Study. *Lancet Oncol* (2010) 11(3):275–80. doi:10.1016/S1470-2045(10)70010-3

8. Jamshidi K, Gharehdaghi M, Hajialiloo SS, Mirkazemi M, Ghaffarzadehgan K, Izanloo A. Denosumab in Patients with Giant Cell Tumor and its Recurrence: A Systematic Review. *Arch Bone Jt Surg* (2018) 6(4):260–8.

9. Chen X, Li H, Zhu S, Wang Y, Qian W. Pre-operative Denosumab Is Associated with Higher Risk of Local Recurrence in Giant Cell Tumor of Bone: a Systematic Review and Meta-Analysis. *BMC Musculoskelet Disord* (2020) 21(1):256. doi:10.1186/s12891-020-03294-2

10. Lipplaa A, Dijkstra S, Gelderblom H. Challenges of Denosumab in Giant Cell Tumor of Bone, and Other Giant Cell-Rich Tumors of Bone. *Curr Opin Oncol* (2019) 31(4):329–35. doi:10.1097/CCO.0000000000000529

11. Hasenfratz M, Mellert K, Marienfeld R, von Baer A, Schultheiss M, Roitman PD, et al. Profiling of Three H3F3A-Mutated and Denosumab-Treated Giant Cell Tumors of Bone Points to Diverging Pathways during Progression and Malignant Transformation. *Sci Rep* (2021) 11(1):5709. doi:10.1038/s41598-021-85319-x

12. Mahdal M, Neradil J, Mudry P, Paukovcekova S, Staniczkova Zambo I, Urban J, et al. New Target for Precision Medicine Treatment of Giant-Cell Tumor of Bone: Sunitinib Is Effective in the Treatment of Neoplastic Stromal Cells with Activated PDGFRβ Signaling.. *Cancers (Basel)* (2021) 13(14):3543. doi:10.3390/cancers13143543

13. Roitman PD, Jauk F, Farfalli GL, Albergo JI, Aponte-Tinao LA. Denosumab-treated Giant Cell Tumor of Bone. Its Histologic Spectrum and Potential Diagnostic Pitfalls. *Hum Pathol* (2017) 63:89–97. doi:10.1016/j.humpath.2017.02.008

14. Szendroi M. Giant-cell Tumour of Bone. *The J Bone Jt Surg Br volume* (2004) 86(1):5–12. doi:10.1302/0301-620x.86b1.14053

15. Forsyth RG, Krenacs T, Athanasou N, Hogendoorn PCW. Cell Biology of Giant Cell Tumour of Bone: Crosstalk between M/wt Nucleosome H3.3, Telomeres and Osteoclastogenesis. *Cancers (Basel)* (2021) 13(20):5119. doi:10.3390/cancers13205119

16. Athanasou NABM, Forsyth R, Reid RP, Sapi Z. Giant Cell Tumor of Bone. In: Fletcher CDBJ, Hogendoorn PC, editors. *WHO Classification of Tumours of Soft Tissue and Bone*. 4th ed.. Lyon: IARC Press (2013). p. 321–4.

17. Roux S, Amazit L, Meduri G, Guiochon-Mantel A, Milgrom E, Mariette X. RANK (Receptor Activator of Nuclear Factor Kappa B) and RANK Ligand Are Expressed in Giant Cell Tumors of Bone. *Am J Clin Pathol* (2002) 117(2):210–6. doi:10.1309/BPET-F2PE-P2BD-J3P3

18. Atkins GJ, Kostakis P, Vincent C, Farrugia AN, Houchins JP, Findlay DM, et al. RANK Expression as a Cell Surface Marker of Human Osteoclast Precursors in Peripheral Blood, Bone Marrow, and Giant Cell Tumors of Bone. *J Bone Miner Res* (2006) 21(9):1339–49. doi:10.1359/jbmr.060604

19. Behjati S, Tarpey PS, Presneau N, Scheipl S, Pillay N, Van Loo P, et al. Distinct H3F3A and H3F3B Driver Mutations Define Chondroblastoma and Giant Cell Tumor of Bone. *Nat Genet* (2013) 45(12):1479–82. doi:10.1038/ng.2814

20. Cottone L, Ligammari L, Knowles HJ, Lee HM, Henderson S, Bianco S, et al. Aberrant Paracrine Signalling Underlies the Mutant Histone-Driven Giant Cell Tumour of Bone. *J Pathol* (2021) 255:S16.

21. Matcuk GR, Jr, Patel DB, Schein AJ, White EA, Menendez LR. Giant Cell Tumor: Rapid Recurrence after Cessation of Long-Term Denosumab Therapy. *Skeletal Radiol* (2015) 44(7):1027–31. doi:10.1007/s00256-015-2117-5

22. Traub F, Singh J, Dickson BC, Leung S, Mohankumar R, Blackstein ME, et al. Efficacy of Denosumab in Joint Preservation for Patients with Giant Cell Tumour of the Bone. *Eur J Cancer* (2016) 59:1–12. doi:10.1016/j.ejca.2016.01.006

23. Palmerini E, Seeger LL, Gambarotti M, Righi A, Reichardt P, Bukata S, et al. Malignancy in Giant Cell Tumor of Bone: Analysis of an Open-Label Phase 2 Study of Denosumab. *BMC Cancer* (2021) 21(1):89. doi:10.1186/s12885-020-07739-8

CONFLICT OF INTEREST

The authors declare that the research was conducted in the absence of any commercial or financial relationships that could be construed as a potential conflict of interest.

SUPPLEMENTARY MATERIAL

The Supplementary Material for this article can be found online at: https://www.por-journal.com/articles/10.3389/pore.2022.1610633/full#supplementary-material

Supplementary Figure 1 | (A,B) Immunohistochemical reaction of PDGFRB of two recurrent GCTB cases without denosumab treatment. Note the same weak positivity as in **Figures 1**, **4B,F**, **5B,F**.

Check for
updates

Gene Expression Patterns of Osteopontin Isoforms and Integrins in Malignant Melanoma

Krisztina Jámbor[1,2], Viktória Koroknai[2,3], Tímea Kiss[2], István Szász[2,3], Péter Pikó[2,3] and Margit Balázs[2,3]*

[1]Doctoral School of Health Sciences, University of Debrecen, Debrecen, Hungary, [2]Department of Public Health and Epidemiology, Faculty of Medicine, University of Debrecen, Debrecen, Hungary, [3]ELKH-DE Public Health Research Group, University of Debrecen, Debrecen, Hungary

Osteopontin (OPN) is a multifunctional glycoprotein that physiologically interacts with different types of integrins. It is considered to be a possible prognostic biomarker in certain tumor types; however, various splicing isoforms exist, which have not been investigated in melanoma. We aimed to define the relative expression pattern of five *OPN* isoforms and clarify the prognostic significance of the splice variants in melanoma. We also aimed to investigate the expression pattern of eight integrins in the same tumors. Gene expression analyses revealed that the relative expression of *OPNa, OPNb*, and *OPNc* is significantly higher in metastatic tumors compared to primary lesions ($p < 0.01$), whereas the expression of *OPN4* and *OPN5* was low in both. The more aggressive nodular melanomas had higher expression levels compared to the superficial spreading subtype ($p \leq 0.05$). The relative expression of the eight tested integrins was low, with only the expression of *ITGB3* being detectable in nodular melanoma (Median$_{log2}$ = 1.274). A positive correlation was found between Breslow thickness and the expression of *OPNc* variant, whereby thicker tumors (>4 mm) had significantly higher expression ($p \leq 0.05$). The Breslow thickness was negatively correlated with the expression of *OPN4*, and similarly with *ITGA2*. *OPNc* also exhibited significant positive correlation with the presence of metastasis. Our data show that high expression of *OPNa*, *OPNb*, and especially *OPNc* and low expression of *OPN4* and *ITGA2* are associated with an advanced stage of tumor progression and poor prognosis in melanoma.

Keywords: gene expression, melanoma progression, osteopontin, osteopontin splice variants, integrins

INTRODUCTION

Osteopontin (OPN or SPP1) is a multifunctional glycoprotein that physiologically interacts with different types of integrins. OPN is considered to be a possible prognostic biomarker in certain tumor types including malignant melanoma (1, 2). Depending on the intracellular or extracellular localization, the expression of OPN is closely related to tumor proliferation, invasion, metastasis, and tumor microenvironment formation (3). These multifunctional biological roles are probably associated with the capacity for OPN to interact with different molecules, including cell surface receptors such as integrin and cluster of differentiation (CD44), intracellular signaling molecules, calcium, and heparin (4). OPN possesses three critical integrin binding sequences: the well conserved RGD domain (arginine–glycine–aspartic acid) that facilitated the interaction of OPN with αv

integrins (especially αvβ1, αvβ3, and αvβ5); the SVVYGLR (serine–valine–valine–tyrosine–glutamate–leucine–arginine) domain, which may bind to α4β1, α4β7, and α9β1 integrins; and the ELVTDFP sequence on the N-terminal, which can bind α4β1 (5). The OPN protein is a member of the SIBLING (small integrin-binding ligand N-linked glycoprotein) family, whose members interact with CD44 and integrins through the characteristic domain. OPN is a secreted protein; however, the existence of a nonsecreted intracellular form (iOPN) has also been reported, which can be localized in the cytoplasm and nucleus and has a slightly different function than secreted OPN (sOPN) (6–8). OPN takes part in several normal physiological processes (vascularization, immune responses, inflammation, tissue remodeling, and cell adhesion) but also influences numerous aspects of tumorigenesis and metastasis (cell survival, proliferation, adhesion, migration, and invasion) (9, 10). Through the connection with integrins and CD44, OPN influences the PI3K/AKT signaling pathway, resulting in NF-κB-mediated cell proliferation and survival. Moreover, the interaction of OPN with αvβ3 integrin, in particular, affects the Ras/Raf/MEK/ERK signaling pathway and enhances the metastatic phenotype of several cancer cell types (11).

The primary transcript of the *OPN* gene is subject to alternative splicing, generating five splice isoforms: *OPNa, OPNb, OPNc, OPN4* and *OPN5* (3). The splicing variants differ in their gene structure: *OPNa* can be considered as the full-length isoform containing seven exons, *OPNb* lacks exon 5, and *OPNc* lacks exon 4. Both exon 4 and exon 5 are missing from *OPN* transcript variant 4, and, interestingly *OPN5*, has all seven exons supplemented with an extra exon derived from the retention of a portion from the intron 3 in the canonical isoform (12). Their translation results proteins called OPNa (314 amino acids), OPNb (300 amino acids), and OPNc (284 amino acids), which are widely studied and functionally well characterized, whereas OPN4 (273 amino acids) and OPN5 (327 amino acids) have only been recently identified (12–14). The splice variants are abnormally expressed in different types of tumors (3, 12). The high expression level of OPNc is indicative of adverse outcomes (nodal involvement, metastasis, and recurrence) in breast cancer, whereas the overexpression of the OPNa splice variant was observed in connection with the tumor growth of lung cancer cells, and OPNa was found to have a key role in thyroid cancer tumor progression (15, 16).

Recently, OPN has received increasing attention, with several studies investigating its role as a potential biomarker in different cancers, including melanoma (17–19). We previously observed, in our high-throughput microarray-based gene expression study, that ulcerated melanomas exhibit 6-fold higher expression of the *SPP1/OPN* gene compared to non-ulcerated melanomas (20). These results were also validated by qRT-PCR showing that elevated *OPN* mRNA expression is significantly associated with unfavorable prognostic parameters such as late stages (Clark stages IV–V), elevated Breslow thickness (≥4.00 mm), and ulcerated tumor surface (21). However, the expression patterns and the role of the *OPN* variants have not yet been described in human malignant melanoma. The expression of *OPN* splice variants in nonmelanoma skin cancers has only recently been investigated (22).

TABLE 1 | Clinicopathological parameters of melanoma tissue samples.

Variables	n
Primary melanoma samples (*n* = 31)	
SSM[a]	21
NM[b]	10
Gender	
Male	16
Female	15
Age (years)	
20–50	7
>50	24
Breslow thickness (mm)[c]	
<2.00	8
2.01-4.00	14
>4.00	9
Clark's level	
II–III	13
IV–V	17
n.d.	1
Ulceration	
Absent	18
Present	13
Localisation	
Trunk	15
Extremities	13
Head	3
Metastasis formation[d]	
Non-metastatic	13
Metastatic	18
Melanoma metastases (*n* = 10)	
Male	7
Female	3
Age (years)	
20–50	2
>50	8
Localization	
Regional lymph node	4
Regional (sub)cutaneous	3
Distant	3

[a]SSM, superficial spreading melanoma.
[b]NM, nodular melanoma.
[c]Thickness categories based on the current melanoma staging system.
[d]Patients with follow-up periods of 5 years were included into the study.

The aim of our study was to characterize the relative gene expression levels of *OPN* isoforms and clarify the prognostic significance of the five splice variants in primary and metastatic malignant melanoma. We also aimed to investigate the expression patterns of different integrins (*ITGA2, ITGA3, ITGA5, ITGA6, ITGA9, ITGAV, ITGB1,* and *ITGB3*) and assess their potential correlation with the clinicopathological parameters and osteopontin in the same tumors.

MATERIALS AND METHODS

Melanoma Tissue Samples

Melanoma tissues were obtained from the Department of Dermatology at the University of Debrecen, Hungary. This study was approved by the Regional and Institutional Ethics Committee of the University of Debrecen Clinical Center [ETT TUKEB 26364-1/2012/EKU (449/PI/12)] and was carried out according to all relevant

TABLE 2 | Primer sequences of OPN splice variants, reference gene and integrins used for qRT-PCR.

Gene	Nucleotide sequence	T annealing (°C)
OPNa F	ATCTCCTAGCCCCACAGAAT	55
OPNa R	CATCAGACTGGTGAGAATCATC	
OPNb F	ATCTCCTAGCCCCAGAGAC	55
OPNb R	AAAATCAGTGACCAGTTCATCAG	
OPNc F	TGAGGAAAAGCAGAATGCTG	57
OPNc R	GTCAATGGAGTCCTGGCTGT	
OPN4 F	GGAAAAGCAGACCCTTCC	55
OPN4 R	CATATGTGTCTACTGTGGGG	
OPN5 F	AACAAATGGGCATTGTCCCC	59
OPN5 R	GCAGTCTAATTGCAGTGACCC	
CYPA F	CTCGAATAAGTTTGACTTG	60
CYPA R	CTAGGCATGGGAGGGAACA	
ITGA2 F	CACAAAGACACAGGTGGGGT	62
ITGA2 R	TGGGATGTCTGGGATGTTGC	
ITGA3 F	GCCCACAAGGATGACTGTG	60
ITGA3 R	GCTGGTCTTCTGACCCTGA	
ITGA5 F	GAGCAAGAGCCGGATAGAGG	55
ITGA5 R	CTGCTCCCCAAACACTTCCA	
ITGA6 F	AAACTGCGTCCCATTCCCA	60
ITGA6 R	TGTCGTCTCCACATCCCTC	
ITGA9 F	CGGTACACCTACCTGGGCTA	58
ITGA9 R	AAACCTTGCCGATGCCTTTG	
ITGAV F	AATGTTGTGCCGGATGTTTCTT	58
ITGAV R	CGGGTAGAAGACCAGTCACAT	
ITGB1 F	CCAAATGGGACACGGGTGAA	58
ITGB1 R	GTGTTGTGGGATTTGCACGG	
ITGB3 F	CCTCATCACCATCCACGACC	62
ITGB3 R	GTTGTTGGCTGTGTCCCATT	

regulations. Written informed consent was obtained from the patients. Lesions were diagnosed on the basis of formalin-fixed paraffin-embedded tissue sections stained with hematoxylin–eosin. A total of 31 primary and 10 metastatic melanoma samples were analyzed. The metastatic samples were derived from different patients other than the primary tumors. The follow up period of patients was 5 years. The clinical–pathological parameters of the melanoma tissue samples are summarized in **Table 1**.

Before RNA isolation all melanoma tissue samples were examined for the content of tumor cells and the adjacent normal tissues were removed to ensure that normal cell contamination will not influence the results. The tumor cell content of tissues analysed were ≥80% for each sample. The total RNA was isolated from frozen melanoma tissues using the RNeasy Plus Mini Kit (Qiagen GmbH, Hilden, Germany) according to the manufacturer's protocol. The concentration and the quality of the RNA was determined using NanoDrop ND-1000 UV–vis Spectrophotometer V3.3.0 (NanoDrop Technologies, Wilmington, DE, United States). The absorbance ratios of 260 nm/280 nm of all RNA samples were 1.8 or above and the 260 nm/230 nm ratios were 2.0 or above. cDNA synthesis of 600 ng total RNA was performed using a High Capacity cDNA Reverse Transcription Kit (Applied Biosystems, Foster City, CA, United States) according to the manufacturer's protocol.

qRT-PCR

Gene expression levels of OPN splice variants (*OPNa*, *OPNb*, *OPNc*, *OPN4*, and *OPN5*) and integrins (*ITGA2*, *ITGA3*, *ITGA5*,

ITGA6, *ITGA9*, *ITGAV*, *ITGB1*, and *ITGB3*) were determined by real-time PCR using Xceed qPCR Probe 2x Mix Hi-ROX (Institute of Applied Biotechnologies, Prague, Czech Republic) and a LightCycler® 480 Instrument II (Roche Diagnostics Nederland BV, Almere, Netherlands). Each reaction contained 15 ng cDNA and was run on the LightCycler® 480 instrument. Conditions for real-time PCR included the following steps: preactivation: 95°C 1 min; followed by 45 cycles of the following program: 95°C 5 s (denaturation), annealing 55–62°C for 10 s (specific annealing temperature and the sequence of each primer can be found in **Table 2**), extension 72°C 15 s, cooling at 40°C for 30 s; finished by melting curve analysis. Primers were obtained from Life Technologies. To analyze qRT-PCR data, cyclophilin A (CYPA) was used as a reference gene and the Livak method ($2^{-\Delta\Delta CT}$ equation) was applied [23]. Pooled nevi ($n = 8$) was used as a normalization control for the melanoma tissue samples. Statistical analysis was performed using IBM SPSS (Statistical Package for Social Sciences) Statistics for Windows, version 25.0 (IBM Corp., Armonk, NY, United States).

Statistical Analysis

The expression data were analyzed in the melanoma tissue samples classified by histological tissue subtype, Breslow thickness of the primary tumors, and Clark staging. The following Breslow thickness groups were applied based on the current melanoma staging system: tissues from tumors with less than 2 mm thickness ($n = 8$), between 2 and 4 mm ($n = 14$), and tumors with more than 4 mm thickness ($n = 9$) [24]. The Kruskal–Wallis H test was used to determine the significant differences of expression data between more than two groups. A two-sided Mann–Whitney U test was applied to reveal significant differences between the expression data of two certain tissue sample groups. Stepwise regression analysis was applied to select those OPN variants and integrins whose expression demonstrate a relationship with the Breslow thickness (as a continuous variant) independently of each other and without collinearity. Linear regression (adjusted for age and sex) was carried out to determine which of these variants were significantly associated with Breslow thickness. Primary melanomas were also grouped according to whether the patient was diagnosed with metastasis or did not develop metastasis during the follow-up (5 years) period. The expression data were analyzed by logistic regression. $p < 0.05$ was considered to indicate statistically significant differences in each case.

RESULTS

Relative Gene Expression of OPN Splicing Isoforms and Their Comparison in Melanoma Tissue Subtypes

The median gene expression values determined for *OPN* splicing isoforms in SSM, NM, and melanoma metastasis tissue samples are summarized in **Supplementary Table S1**. In **Figure 1**, boxplots show the relative expression of the five splice variants (*OPNa*, *OPNb*, *OPNc*, *OPN4*, and *OPN5*) in superficial spreading melanomas, nodular melanomas, and melanoma metastasis. The
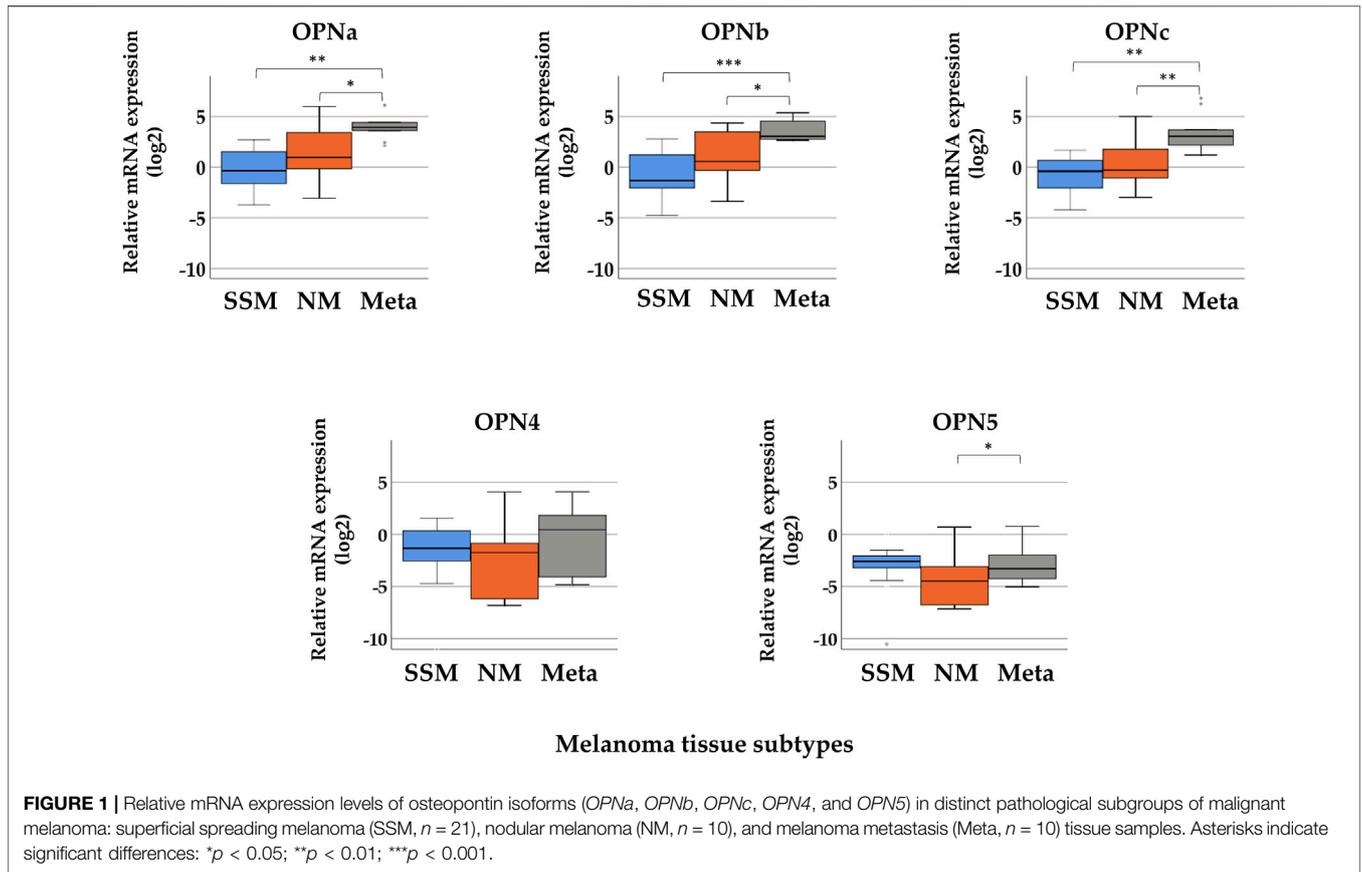
FIGURE 1 | Relative mRNA expression levels of osteopontin isoforms (*OPNa*, *OPNb*, *OPNc*, *OPN4*, and *OPN5*) in distinct pathological subgroups of malignant melanoma: superficial spreading melanoma (SSM, *n* = 21), nodular melanoma (NM, *n* = 10), and melanoma metastasis (Meta, *n* = 10) tissue samples. Asterisks indicate significant differences: *$p < 0.05$; **$p < 0.01$; ***$p < 0.001$.

highest expression of *OPNa* (median = 3.925), *OPNb* (median = 3.043), and *OPNc* (median = 3.060) was detected in melanoma metastasis, which significantly differed when compared to the nodular and superficial tissue samples ($p \leq 0.05$). The relative expression levels of *OPN4* and *OPN5* were very low in all pathological subtypes, and they were downregulated relative to nevi (except in the case of *OPN4* in metastasis). A significant difference in the expression of *OPN5* was observed only between nodular and melanoma metastasis tissues ($p \leq 0.05$).

Comparison of the Relative Gene Expression of OPN Splice Variants in Tissues Classified by Breslow Thickness and Clark Stages in Primary Tumor Samples

Investigating the relative gene expression of the OPN isoforms in the three thickness groups, the Kruskal–Wallis H test showed significant differences in the relative expression of *OPNc* between the groups (<2 mm (median = −1.24), 2–4 mm (median = −0.57), and >4 mm (median = 1.40); $p = 0.008$). When comparing two groups with each other, tissues samples with >4 mm Breslow thickness showed significantly higher relative expression of *OPNc* than samples with 2–4 mm thickness (Mann–Whitney U test $p = 0.023$), and tissues with less than 2 mm exhibited the lowest expression (**Figure 2**). This trend of elevation can also be observed in the expression of *OPNa* and *OPNb* variants as the thickness increases; however, these differences were not

considered significant. The mRNA expression of *OPN4* and *OPN5* did not show significant association with Breslow thickness. **Supplementary Table S2** summarizes the median values of each group. We did not find significant association between the relative gene expression levels of the different OPN splice variants and Clark stages.

Relative Gene Expression of Integrins and Their Comparison in Pathological Subgroups of Melanoma Tissues

Boxplots of the expression levels of the eight integrin genes in subgroups of melanoma tissue samples are presented in **Figure 3**. Excluding *ITGA2*, seven integrins exhibited no significant differences in gene expression between different tissue subtypes. A significant difference in the gene expression level of *ITGA2* was found in SSM tissue samples (median = −1.622) compared with NM (median = −3.630) and melanoma metastasis (median = −4.807) tissue samples. (Kruskal–Wallis H test, $p = 0.001$; Mann–Whitney U test, $p = 0.002$). However, the expression of the eight tested integrin genes was, overall, extremely low (with negative values for medians indicating downregulation) except *ITGB3*, which showed measurable values without significant differences in expression (median values: $M_{SSM} = 0.168$, $M_{NM} = 1.274$, and $M_{Metastasis} = −0.863$). **Supplementary Table S3** summarizes the median values of relative gene expression data in each melanoma tissue subgroup.

FIGURE 2 | Comparison of the relative mRNA expression of osteopontin isoforms (*OPNa*, *OPNb*, *OPNc*, *OPN4*, and *OPN5*) in malignant melanoma tissue samples from tumors with different Breslow thicknesses: < 2 mm (*n* = 8), 2–4 mm (*n* = 14), and >4 mm (*n* = 9). Significant differences (*$*p ≤ 0.05$; **$p ≤ 0.01$; ***$p ≤ 0.001$ Mann–Whitney test, Kruskal–Wallis test) are indicated by asterisks.
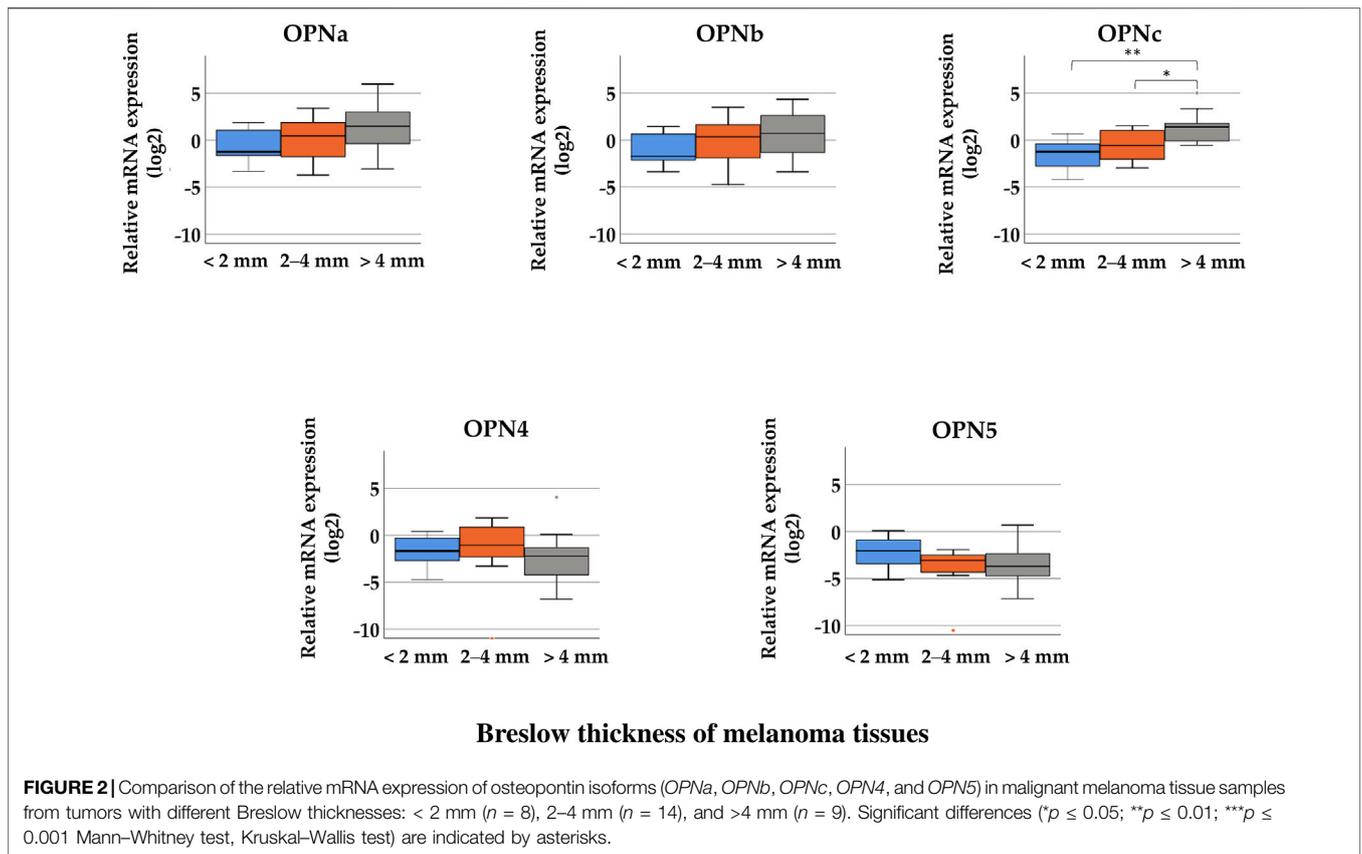
Relationship Between the Relative Gene Expression of Integrins and the Clinicopathological Data (Breslow Thickness and Clark Staging) of Primary Melanoma Tissues

In the cases of *ITGA2*, *ITGA6*, *ITGA9*, *ITGAV*, *ITGB1*, and *ITGB3*, significant differences were observed between the three Breslow thickness groups (**Figure 4**, Kruskal–Wallis test, $p < 0.05$). Tumor samples with more than 4 mm thickness exhibited significantly lower relative expression levels of *ITGA3, ITGA6, ITGA9, ITGAV,* and *ITGB1* than samples belonging to the 2–4 mm Breslow thickness category (Mann–Whitney test, $p < 0.05$). *ITGB3* exhibited significantly higher relative expression in tissues with 2–4 mm and >4 mm Breslow thickness, and was the highest in the group with 2–4 mm thickness. Median values can be found in **Supplementary Table S4**.

Tissue samples of primary tumors were also differentiated according to Clark stages: earlier stages (II–III, $n = 13$), and later stages (IV–V, $n = 17$) **Supplementary Figure S1** shows that a significant difference was observed only in the case of *ITGA2*: tissues with a later Clark stage (IV–V) exhibited lower mRNA expression (mean = −1.35) than samples with earlier stage (II–III) (mean = −3.57) (Mann–Whitney *U* test, $p < 0.005$).

Correlation of the Relative Expression of Osteopontin Variants and Integrins

The gene expression data of OPN variants and integrins analyzed with Spearman's correlation revealed positive correlations of expression between *OPN4* and most of the integrins: *ITGB3* ($r = 0.604$), *ITGA5* ($r = 0.530$), *ITGA9* ($r = 0.530$), *ITGAV* ($r = 0.520$), *ITGB1* ($r = 0.590$), *ITGA3* ($r = 0.585$), and *ITGA6* ($r = 0.500$) ($p < 0.01$). Positive correlations of expression were also observed between *OPN5* and *ITGA2* ($r = 0.447$), *ITGAV* ($r = 0.504$) ($p < 0.01$), *ITGB1* ($r = 0.348$), *ITGA3* ($r = 0.361$), and *ITGA6* ($r = 0.406$) ($p < 0.05$). Negative correlations of expression were observed between *ITGA2* and *OPNa* ($r = −0.480$), *OPNb* ($r = −0.416$), and *OPNc* ($r = −0.540$) ($p < 0.01$) and between *ITGA6* and *OPNc* ($r = −0.392$) ($p < 0.05$). A table with the results of the Spearman's rho correlation can be found in **Supplementary Table S5** and graphs of significantly correlating variables in **Supplementary Figures S2–S5**.

Correlation of OPN Variants and ITGs With Breslow Thickness (As a Continuous Outcome in mm) Based on the Results of Stepwise and Linear Regression Analysis

As a result of stepwise regression analysis, the expression of two osteopontin variants, *OPNc* and *OPN4*, and two integrins,

FIGURE 3 | Relative mRNA expression levels of integrin (*ITGA2*, *ITGA3*, *ITGA5*, *ITGA6*, *ITGA9*, *ITGAV*, *ITGB1*, and *ITGB3*) genes in distinct pathological subgroups of malignant melanoma: superficial spreading melanoma (SSM, $n = 20$), nodular melanoma (NM, $n = 9$), and melanoma metastasis (Meta, $n = 10$) tissue samples. Asterisks indicate significant differences (*$p < 0.05$; **$p < 0.01$; ***$p < 0.001$).
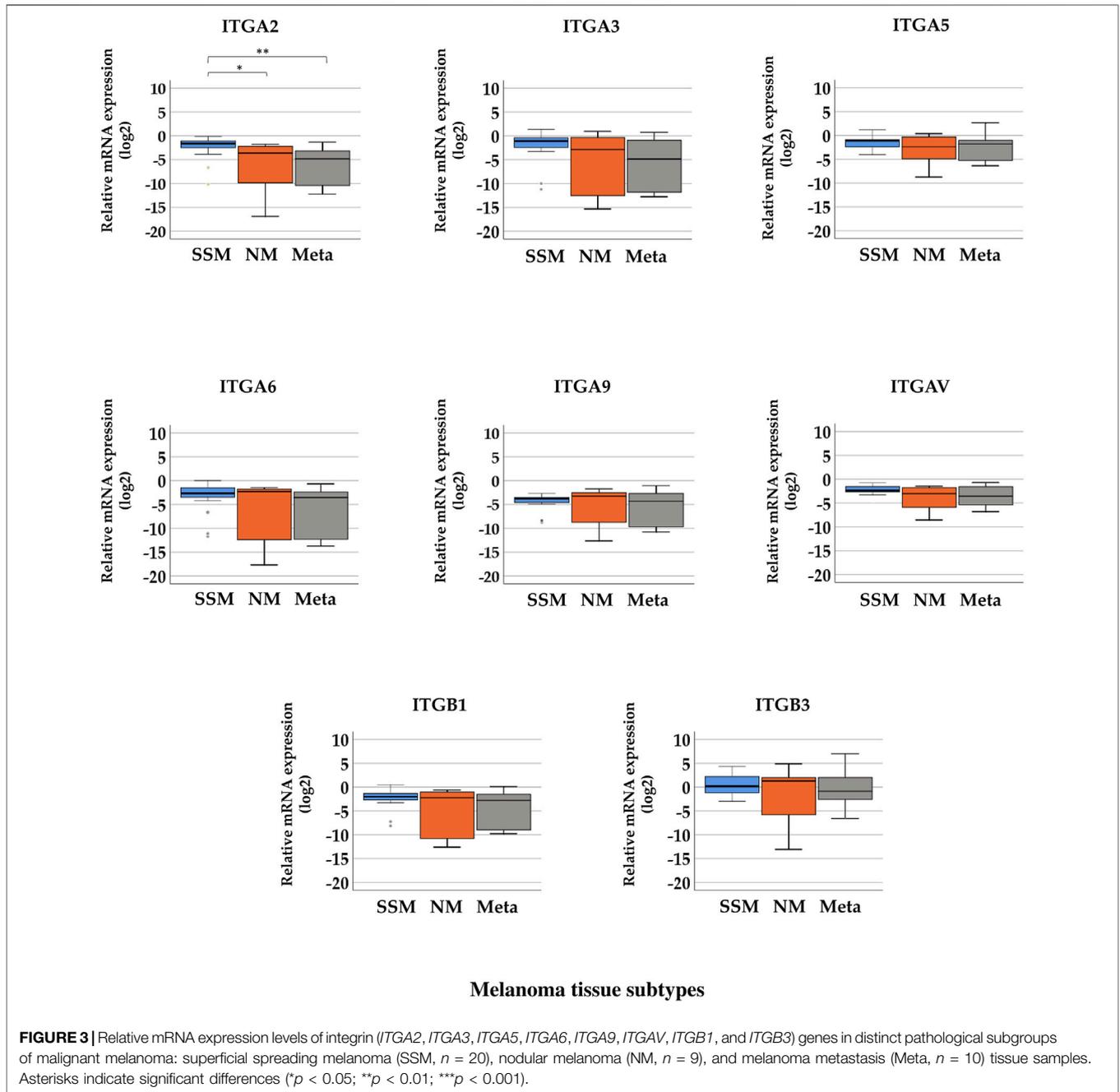
ITGA5 and *ITGA2*, was determined to be linked with Breslow thickness independently. The linear regression analysis of these variants revealed that their relationship with Breslow thickness was significant; however, while the beta value of *OPNc* was 0.217, indicating a positive correlation, the negative beta value of *OPN4*, −0.762, indicates a negative correlation with Breslow thickness. In the case of integrins, *ITGA2* had a significant negative correlation (β value = −23.061), but *ITGA5* showed a significant positive correlation (β value = 2.697) with Breslow thickness. A 0.1 unit ($2^{-\Delta\Delta Ct}$) decrease in *ITGA2*

expression is associated with 2.3 mm increase of Breslow thickness. See **Table 3** for more details.

Logistic Regression: Relative Expression of OPN Variants and Presence of Metastasis

The results of logistic regression show that *OPNc* expression (log2 transformed data) is significantly positively correlated with the presence of metastasis (OR = 1.931, $p = 0.044$) (**Table 4**), whereas *OPN4* was not significantly correlated (OR = 0.962,
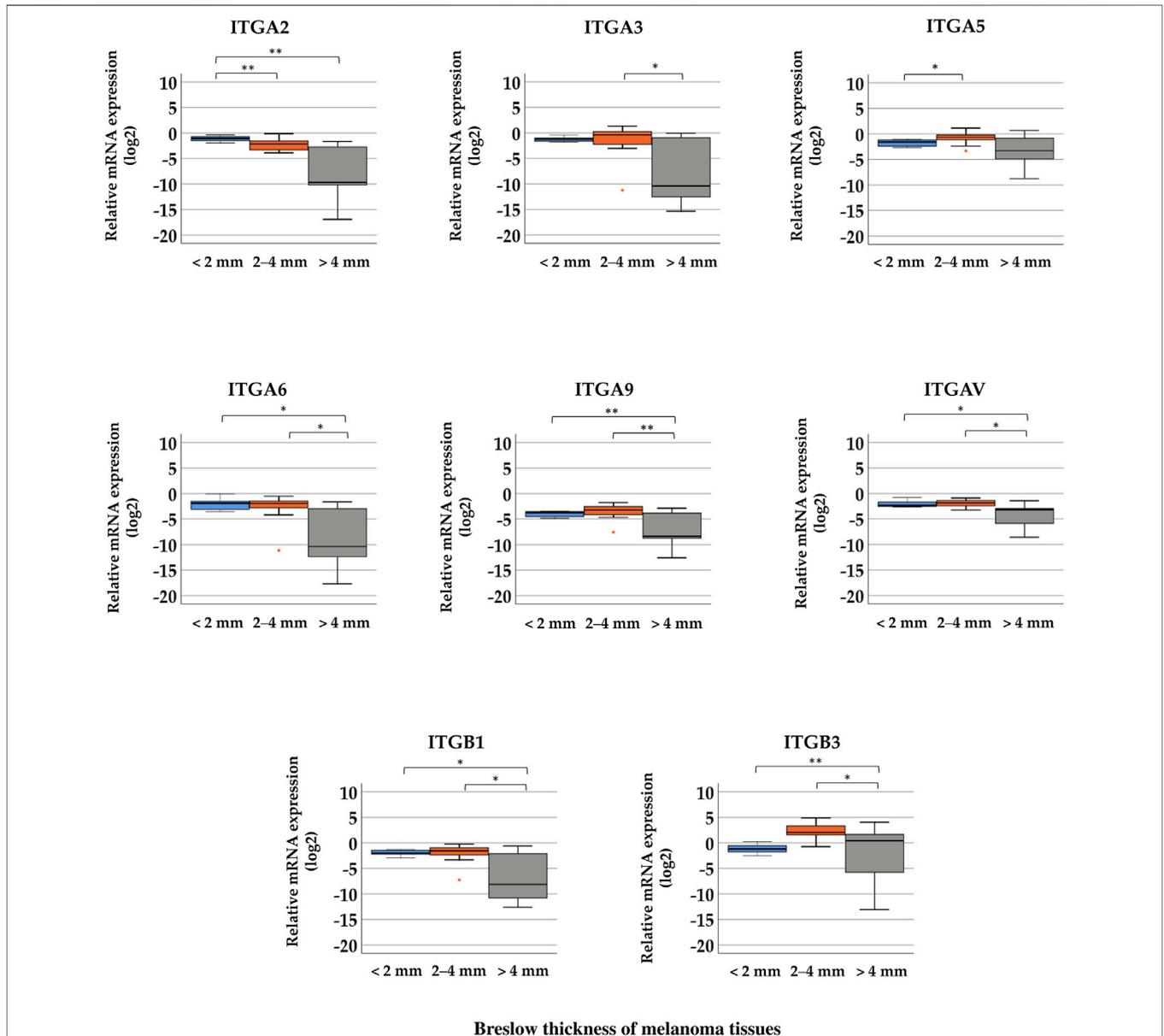
FIGURE 4 | Comparison of relative mRNA expression levels of integrin (*ITGA2*, *ITGA3*, *ITGA5*, *ITGA6*, *ITGA9*, *ITGAV*, *ITGB1*, and *ITGB3*) genes in melanoma tissue samples grouped by distinct Breslow thickness: <2 mm (*n* = 8), 2–4 mm (*n* = 12), and >4 mm (*n* = 9). Significant differences (*$*p \le 0.05$; **$p \le 0.01$; ***$p \le$ 0.001 Mann–Whitney test, Kruskal–Wallis test) are indicated by asterisks.

p = 0.773) with the presence of metastasis. Integrins did not show significant correlation with the presence of metastasis.

DISCUSSION

Osteopontin (OPN), a multifunctional protein, has been widely studied as a promising biomarker in various types of tumors for monitoring tumor progression, invasion, metastasis formation and drug resistance (13, 25). The association between the aberrant expression of osteopontin and melanoma invasion, metastasis formation, and radio/drug resistance has been recently described (1, 3, 25–27). The biological functions of tumor-associated gene products are extensively regulated via pre- and posttranscriptional modifications, resulting in alternative splicing of OPN. Alternative splicing of various mRNA products of a single gene is a critical mechanism for generating proteomic diversity. OPNa, OPNb, and OPNc variants were first described in glioma, and the two additional splice variants (OPN4 and OPN5) were found in esophageal adenocarcinomas and glioblastomas (28). Because the different splice variants of OPN are associated with different types of cancers, it is assumed that the isotypes may have different functions. Osteopontin isoforms display functional

TABLE 3 | Linear regression analyses of the gene expression of OPN splice variants and integrins with the Breslow thickness of primary melanomas.

Osteopontin isoforms	β	95% CI	p-value
OPNa	0.115	−0.011–0.242	0.071
OPNb	0.172	−0.069–0.414	0.155
OPNc	**0.217**	**0.112–0.322**	**<0.001**
OPN4	**−0.762**	**−1.343–(−0.181)**	**0.012**
OPN5	−3.030	−8.237–2,176	0.242
Integrins	**β**	**95% CI**	**p-value**
ITGA2	**−23.061**	**−30.158–(−15.964)**	**<0.001**
ITGA3	−2.338	−6.861–2.185	0.296
ITGA5	**2.697**	**0.956–4.438**	**0.004**
ITGA6	−9.079	−20.317–2.158	0.108
ITGA9	−14.345	−41.876–13.185	0.292
ITGAV	−15.465	−30.958–0.046	0.051
ITGB1	−5.086	−13.612–3.440	0.229
ITGB3	0.023	−0.099–0.146	0.7

β is a regression coefficients which indicates the direction and size of effect between variables. CI: confidence interval. Bold values indicates significant associations.

TABLE 4 | Logistic regression analyses of the gene expressions OPN splice variants and integrins in relation of metastasis formation of malignant melanoma.

Osteopontin isoforms	OR	95% CI	p-value
OPNa	1.223	0.855–1.749	0.270
OPNb	1.070	0.759–1.507	0.699
OPNc	**1.931**	**1.018–3.661**	**0.044**
OPN4	0.962	0.743–1.248	0.773
OPN5	1.144	0.867–1.509	0.341
Integrins	**OR**	**95% CI**	**p-value**
ITGA2	0.685	0.348–1.349	0.274
ITGA3	0.411	0.135–1.250	0.117
ITGA5	0.889	0.396–1.996	0.776
ITGA6	0.560	0.234–1.337	0.191
ITGA9	0.675	0.407–1.120	0.129
ITGAV	0.280	0.065–1.207	0.088
ITGB1	0.333	0.085–1.305	0.115
ITGB3	0.836	0.642–1.088	0.182

OR, odds ratio; CI, confidence interval. Bold values indicates significant associations.

heterogeneity and cell and tissue specificity, which still poses challenges while providing opportunities for novel diagnostic, prognostic, and therapeutic strategies (13).

Most of the studies investigating the role of OPN splice variants have focused on the expression of *OPNa*, *OPNb*, and *OPNc*; however, the data in distinct tumor types are conflicting, and the functional heterogeneity of the variants serves as motivation for researchers to define the role of OPN splice variants in each type of cancer. In addition, at present, no data on the isoform expression patterns in malignant melanoma are available. Therefore, in this study, our primary aim was to study the expression profile of five *OPN* splice variants (*OPNa*, *OPNb*, *OPNc*, *OPN4*, and *OPN5*) in different types of malignant melanoma tissues and investigate the association with the clinicopathological features of tumor tissues. In addition, because OPN signaling occurs through different integrin receptors, we also aimed to examine the relative mRNA expression profile of eight integrins (*ITGA2*, *ITGA3*, *ITGA5*, *ITGA6*, *ITGA9*, *ITGAV*, *ITGB1*, and *ITGB3*) and analyze the correlation of the relative expression of osteopontin variants and integrins in the same melanoma samples.

We found elevated relative mRNA expression of *OPN* variants (*OPNa*, *OPNb*, and *OPNc*) in nodular melanomas and melanoma metastasis compared to samples of superficial spreading melanoma. The significant increase of these isoforms in the more advanced stages indicates that they may contribute to tumor progression and worse outcome, since lower survival rates were observed in NM and metastatic melanoma patients (29). The significant elevation of *OPNc* expression in thicker melanoma tissue samples suggests that it is associated with increasing Breslow thickness. The elevating tendencies of the expression levels of the other variants were similar; however, none were found to be significant in the comparison. Our further statistical analysis also confirmed the significant positive association

of *OPNc* with Breslow thickness: a one-unit increase in *OPNc* expression is associated with a 0.217 increase in Breslow thickness. Based on our observations, it is possible that *OPNc* expression has a crucial role in melanoma tumor progression, and that elevated levels of this variant can contribute to progression toward advanced stages of disease and even the induction of metastasis formation, and it can thus serve as an indicator of an aggressive phenotype.

The expression of *OPN* splice variants has already been investigated in hematological malignancies, thyroid tumors, and gastric cancers (18, 30). Wide variations were observed in the expression patterns and the predominantly expressed variant(s) depending on the tumor type; therefore, it is difficult to establish a possible universal nature or profile. It could be convenient to establish the expression profile of each splice variant in each distinct cancer type. To date, it has been observed that the OPNa mRNA levels were significantly associated with high TNM staging and unfavorable clinical outcomes in gastric cancer; moreover, *OPNa* and *OPNb* are correlated with short overall and disease-free survival of patients (30). It was pointed out that *OPNc* expression is also associated with advanced stage, tumor recurrence, and metastasis formation; thus, *OPNc* is considered to be a promising prognostic factor in breast cancer (15). In our results, the elevated expression of the *OPNc* variant in an advanced stage of primary melanoma and melanoma metastasis samples in addition to its significant correlation with the presence of metastasis indicates the importance of *OPNc* in melanoma progression, metastasis formation, and the relationship with the aggressive phenotype, which justifies its further investigation at multiple levels as a promising prognostic biomarker in malignant melanoma. Since no specific antibodies against these splice variants are currently available (except for *OPNc* from Gallus Immunotech Inc. which is a polyclonal antibody), the future development of the OPN isotype antibodies could also be an important step forward in the characterization of these variants. Moreover, investigating the specific role of each splice variant in

melanoma progression could bring us closer to developing potential targetable molecules in melanoma therapy.

While the exact role of *OPNc* overexpression on tumor progression is unknown, there are several possible explanations for its association with metastasis. Since *OPNc* variant lacks exon 4, which contains the target sequence for transglutaminase, it lacks an important domain for calcium induced aggregation and transglutamination (31). *OPNc*, unlike the other isoforms, cannot form polymeric complexes. This might be the essential reason for the pathological role of *OPNc* and it may not be cross-linked with extracellular matrix and thus it results cell migration. The full length OPN aggregates and enhances cell adhesion and therefore reduces dissemination of tumor cells, whereas *OPNc* promotes tumor invasion and metastasis formation because of its lack of aggregation (32). The non-aggregative nature of *OPNc* is in concert with the relative resistance to polymerization (33). On the other hand, *OPNc* can stimulate cell proliferation rates independently of growth factors, a feature of proteins typically involved in tumor progression (34). While numerous studies suggest that OPN plays a key role in mediating tumor progression and metastasis by regulating various pathways, very few data are available for the role of different OPN splice variants, the expression patterns of the OPN isoforms in malignant melanoma was first described in the present study. In order to discover the detailed functional role of *OPNc*, the 3D structure of the variant might be useful. It is an important step that the tertiary structure of *OPNc* was successfully predicted by Sivakumar and this predicted structure might be used for computational drug design of *OPNc* with respect to cancer prevention (31).

Aside from the three most frequently studied OPN variants, we also investigated the expression of *OPN4* and *OPN5* isoforms that were recently described (4, 35). Surprisingly, relative expression of *OPN4* and *OPN5* was low in primary as well as metastatic tissues. Though statistical analysis showed a significant difference in *OPN5* expression between nodular melanoma and melanoma metastasis histological subtypes, *OPN4* and *OPN5* were downregulated, and the median expression values did not exceed zero on the logarithmic scale (except in the case of *OPN4* in melanoma metastasis). Although significant differences were not found when comparing their expression between the sample groups for different Breslow thicknesses, logistic regression demonstrated a significant negative correlation between *OPN4* and Breslow thickness and conversely in the case of *OPNc*, which was positive correlated. Moreover, the analysis of the Spearman's correlation between osteopontin splice variants and integrins in expression data revealed the positive correlation of *OPN4* expression with that of most of the integrins and the negative correlation of *ITGA2* expression with that of most of the osteopontins, suggesting that *OPN4* may have an expression profile more similar to that of the integrins than that of the osteopontins.

The expression of the *OPN4* and *OPN5* variants was previously investigated in esophageal adenocarcinoma tissue samples (4), where, unlike in our study, it was found that the expression of *OPN4* and *OPN5* was elevated in primary tumors

when compared to normal and Barrett's samples, and the isoforms were co-overexpressed. In another study, the expression of these two isoforms was found to be variable in most of the tested 7 cell lines (prostate tumor, ovarian cancer, B-cell precursor acute lymphoid leukemia, breast cancer, colorectal cancer, and thyroid and lung tumors) (31). Except for in the two breast cancer cell lines, *OPN4* and *OPN5* were found to be co-expressed in the other 5 cell lines, but the expression patterns differed from those of the previously characterized *OPNa, OPNb,* and *OPNc* variants (31). According to the study of Chou et al., besides the predominant expression of *OPNa* variant, *OPN4* was found to be minimally expressed in normal skin and nonmelanoma skin cancer, but *OPN5* exhibited higher expression in normal skin than *OPNb* and *OPNc*, and *OPN5* was more highly expressed in nonmelanoma skin cancer than *OPNc* (22). Taken together, the expression of *OPN4* and *OPN5* splice variants appears to vary widely in distinct tumor types, but in melanoma, they slightly have a different expression profile than the three predominant splice variants.

In connection with the expression profile of integrins, our results show that the relative mRNA expression levels of the investigated integrin genes are extremely low except in one case. Median values of the integrin expression levels in SSM, NM, and melanoma metastasis were equally below zero, which means they are downregulated compared to the nevus control. As the exception, *ITGB3* appeared to be upregulated in SSM and NM tissue samples. Moreover, when comparing integrin gene expression in melanoma tissues with distinct Breslow thickness, a significantly higher *ITGB3* expression was observed in thicker tissue samples (2–4 mm and > 4 mm) compared to tissues with lower Breslow thickness (<2 mm) (p = 0.004). This result is in accordance with the relevant literature: in malignant melanoma, upregulated expression of subunit β3 was found in the vertical growth phase, which was linked with disease progression and correlated with poor survival and lymph node and lung metastasis formation (36, 37).

Other previous *in vivo* and *in vitro* studies have also investigated altered integrin expression, summarized in detail by Arias-Mejias et al. (38). It was found that elevated expression of integrin β3 protein (the dimerized form is αvβ3 or αIIbβ3) in human melanoma cells and tissues was associated with tumor progression, organ-specific metastasis formation, disease recurrence, and decreased long-term survival (39, 40). In our earlier study we identified metastasis correlated genes, including many genes involved in signaling in the immune system (HLA antigens), cell adhesion and cell motility networks (40, 41). These networks involve genes such as that of integrins (*ITGA2, ITGA3, ITGA4, ITGA9, ITGB5* or *ITGB8*). Investigating the expression of these genes in metastatic primary melanomas and metastases, we found that *ITGA3* was downregulated in both regional and distant organ metastases compared to the metastatic primary lesions. In the present study, even the direction of the mRNA expression was similar for *ITGA3*, we observed significant decrease only for the *ITGA2* gene in the metastatic tumors. The inconsistency between the two investigations can be

explained by the fact that the composition of primary tumor groups was different between the two studies.

In our case, interestingly, a significant difference between the histological subtypes was observed only in the expression of *ITGA2*; however, it displays a decreasing tendency in NM and metastasis samples compared to SSM. Relative expression of integrins in melanoma tissue samples with distinct Breslow thicknesses varies, six integrins (*ITGA3*, *ITGA6*, *ITGA9*, *ITGAV*, *ITGB1*, and *ITGB3*) out of the eight showed a significant difference between the 2–4 mm and the > 4 mm group (lowest expression in the thickest group), and again, expression of *ITGA2* showed a significant decrease as the thickness increased. Linear regression analysis indicated that while *ITGA5* had positive correlation with Breslow thickness (as a continuous variant) *ITGA2* was in strong significant inverse correlation with the Breslow thickness of the tumor. These results suggest that downregulation of *ITGA2* may be linked with tumor progression in malignant melanoma. This hypothesis seems to be supported by the results of *in vitro* studies with breast cancer mouse models, which suggest that integrin α2 might function as a metastasis suppressor (42). Moreover, decreased expression of the α2 subunit was found to be associated with more advanced status, such as higher tumor nodal status or presence of metastasis (41). Madamanchi et al. describe that certain other cancer types (prostate, colon, and lung cancer) also seem to be associated with reduced integrin α2β1, which is associated with tumor progression and metastasis. However, they also note that other cancer types were associated with high α2β1 integrin expression levels; hence, the exact biological role of this integrin is being heavily debated (43). Indeed, the relevance of the α2β1 integrin as a main regulator of metastasis in tumor cells was discovered only in recent years, and these findings appear to be controversial compared with the results of the previously mentioned studies. The crucial role of the α2β1 integrin has been determined in cancer types including melanoma, as it is responsible for regulating cell migration, survival, proliferation, and metastasis formation in the lung and liver (44, 45). Upregulation of α2β1 was found in highly metastatic melanoma compared to nonmetastatic or poorly metastatic cell lines, where it was associated with enhanced cell migration (38). Increased expression of α2β1 in malignant melanoma compared to benign tumors was found to stimulate angiogenesis and facilitate tumor growth (46).

Though acquiring a comprehensive understanding of integrin signaling is challenging, some possible reasons may explain the differences in the expression of the various integrins and their role in tumor progression. Single nucleotide polymorphisms may change the affinity of *ITGA2* for transcription factors, which can alter the transcription rate (47). Enhancing transcription–coactivator complex binding can increase *ITGA2* transcription. In addition, different posttranslational modifications, such as sialylation and glycosylation, can modify the role of integrins in tumor progression (48, 49).

The data of the current study are the first to describe the relative mRNA expression of five osteopontin splice variants in primary and metastatic melanoma tissue samples. We found that the expression levels of *OPNa, OPNb*, and *OPNc* were significantly higher in the metastatic lesions compared to the primary tumors, and *OPNc* was significantly positively correlated with increasing Breslow thickness in the primary tumors. The expression of the recently described *OPN4* and *OPN5* isoforms was shown to be downregulated in the evaluated melanoma subtypes, and *OPN4* exhibited a significant negative correlation with Breslow thickness. The relative expression of eight integrins was very low; only *ITGB3* showed detectable expression in metastatic tumors compared to the primary lesions; moreover, *ITGA2* showed significant negative correlation with the Breslow thickness of the primary tumors. Our data show that high expression of *OPNa, OPNb*, and *OPNc* is associated with poor prognosis, and *OPN4* and *ITGA2* may have an opposite role in melanoma progression. Nevertheless, further studies are needed to more specifically characterize the involvement of osteopontin splice variants in malignant melanoma progression and their interaction with integrins in cancer.

DATA AVAILABILITY STATEMENT

The original data presented in this study are included in the article as well as in the **Supplementary Material**, further inquiries can be directed to the corresponding author.

ETHICS STATEMENT

The study was conducted according to the guidelines of the Declaration of Helsinki and approved by the Regional and Institutional Ethics Committee of the University of Debrecen [Document No.: 25364-1/2012/EKU (449/PI/12. and DE RKEB/IKEB: 4820-2017)] and by the Ethics Committee of the Hungarian Scientific Council on Health (Reference No.: 6674/2014 EKU and 17876/218). Informed consent was obtained from all subjects involved in the study. The patients/participants provided their written informed consent to participate in this study.

AUTHOR CONTRIBUTIONS

MB, KJ, and TK conceived and designed the study. KJ and TK performed the experiments. KJ, TK, and PP analyzed the data. KJ, IS, PP, and VK performed statistical analyses and designed the figures and tables. KJ wrote the first draft of the manuscript. VK, IS, and KJ were involved to write the final version of the manuscript. PP, TK, KJ, VK, and IS approved the manuscript. MB finalized the manuscript. MB were responsible for supervision and funding acquisition.

FUNDING

CONFLICT OF INTEREST

The authors declare that the research was conducted in the absence of any commercial or financial relationships that could be construed as a potential conflict of interest.

SUPPLEMENTARY MATERIAL

The Supplementary Material for this article can be found online at: https://www.por-journal.com/articles/10.3389/pore.2022.1610608/full#supplementary-material

Supplementary Figure S1 | Relative mRNA expression of ITGA2 gene in malignant melanoma tissue samples from tumors with different Clark stages: earlier stages (II–III. n = 13) and later stages (IV–V. n = 17).

Supplementary Figure S2 | Graphs illustrating the significant positive correlations (Spearman's rho) between expression of OPN4 and integrin genes (*ITGB3*, *ITGA5*, *ITGA9*, *ITGAV*, *ITGB1*, *ITGA3*, and *ITGA6*).

Supplementary Figure S3 | Graphs illustrating the significant positive correlations (Spearman's rho) between the expression of *OPN5* and integrin genes (*ITGA2*, *ITGAV*, *ITGB1*, *ITGA3*, and *ITGA6*).

Supplementary Figure S4 | Graphs illustrating the significant negative correlations (Spearman's rho) between the gene expression of *ITGA2* and osteopontin splice variants (*OPNa*, *OPNb*, *OPNc*).

Supplementary Figure S5 | Graphs illustrating the significant negative correlation (Spearman's rho) between the expression of ITGA6 and OPNc.

REFERENCES

1. Zhao Y, Huang C. The Role of Osteopontin in the Development and Metastasis of Melanoma. *Melanoma Res* (2021) 31(4):283–9. doi:10.1097/CMR.0000000000000753

2. Rangel J, Nosrati M, Torabian S, Shaikh L, Leong SP, Haqq C, et al. Osteopontin as a Molecular Prognostic Marker for Melanoma. *Cancer* (2008) 112(1):144–50. doi:10.1002/cncr.23147

3. Gimba ERP, Brum MCM, De Moraes GN. Full-length Osteopontin and its Splice Variants as Modulators of Chemoresistance and Radioresistance (Review). *Int J Oncol* (2019) 54(2):420–30. doi:10.3892/ijo.2018.4656

4. Lin J, Myers AL, Wang Z, Nancarrow DJ, Ferrer-Torres D, Handlogten A, et al. Osteopontin (OPN/SPP1) Isoforms Collectively Enhance Tumor Cell Invasion and Dissemination in Esophageal Adenocarcinoma. *Oncotarget* (2015) 6(26):22239–57. doi:10.18632/oncotarget.4161

5. Yokosaki Y, Tanaka K, Higashikawa F, Yamashita K, Eboshida A. Distinct Structural Requirements for Binding of the Integrins αvβ6, αvβ3, αvβ5, α5β1 and α9β1 to Osteopontin. *Matrix Biol* (2005) 24(6):418–27. doi:10.1016/j.matbio.2005.05.005

6. Inoue M, Shinohara ML. Intracellular Osteopontin (iOPN) and Immunity. *Immunol Res* (2011) 49(1-3):160–72. doi:10.1007/s12026-010-8179-5

7. Del Prete A, Scutera S, Sozzani S, Musso T. Role of Osteopontin in Dendritic Cell Shaping of Immune Responses. *Cytokine Growth Factor Rev* (2019) 50:19–28. doi:10.1016/j.cytogfr.2019.05.004

8. Leavenworth JW, Verbinnen B, Wang Q, Shen E, Cantor H. Intracellular Osteopontin Regulates Homeostasis and Function of Natural Killer Cells. *Proc Natl Acad Sci U S A* (2015) 112(2):494–9. doi:10.1073/pnas.1423011112

9. Anborgh PH, Mutrie JC, Tuck AB, Chambers AF. Role of the Metastasis-Promoting Protein Osteopontin in the Tumour Microenvironment. *J Cel Mol Med* (2010) 14(8):2037–44. doi:10.1111/j.1582-4934.2010.01115.x

10. Cho HJ, Cho HJ, Kim HS. Osteopontin: A Multifunctional Protein at the Crossroads of Inflammation, Atherosclerosis, and Vascular Calcification. *Curr Atheroscler Rep* (2009) 11(3):206–13. doi:10.1007/s11883-009-0032-8

11. Pang X, Gong K, Zhang X, Wu S, Cui Y, Qian BZ, et al. Osteopontin as a Multifaceted Driver of Bone Metastasis and Drug Resistance. *Pharmacol Res* (2019) 144:235–44. doi:10.1016/j.phrs.2019.04.030

12. Briones-Orta MA, Avendano-Vazquez SE, Aparicio-Bautista DI, Coombes JD, Weber GF, Syn WK, et al. Osteopontin Splice Variants and Polymorphisms in Cancer Progression and Prognosis. *Biochim Biophys Acta Rev Cancer* (2017) 1868(1):93–108. doi:10.1016/j.bbcan.2017.02.005

13. Hao C, Cui Y, Owen S, Li W, Cheng S, Jiang WG, et al. Human Osteopontin: Potential Clinical Applications in Cancer (Review). *Int J Mol Med* (2017) 39(6):1327–37. doi:10.3892/ijmm.2017.2964

14. Lamort AS, Giopanou I, Psallidas I, Stathopoulos GT. Osteopontin as a Link between Inflammation and Cancer: The Thorax in the Spotlight. *Cells* (2019) 8(8):E815. doi:10.3390/cells8080815

15. Pang H, Lu H, Song H, Meng Q, Zhao Y, Liu N, et al. Prognostic Values of Osteopontin-C, E-Cadherin and Beta-Catenin in Breast Cancer. *Cancer Epidemiol* (2013) 37(6):985–92. doi:10.1016/j.canep.2013.08.005

16. Sun SJ, Wu CC, Sheu GT, Chang HY, Chen MY, Lin YY, et al. Integrin β3 and CD44 Levels Determine the Effects of the OPN-A Splicing Variant on Lung Cancer Cell Growth. *Oncotarget* (2016) 7(34):55572–84. doi:10.18632/oncotarget.10865

17. Han X, Wang W, He J, Jiang L, Li X. Osteopontin as a Biomarker for Osteosarcoma Therapy and Prognosis. *Oncol Lett* (2019) 17(3):2592–8. doi:10.3892/ol.2019.9905

18. Viana B, Gomes AVP, Gimba ERP, Ferreira LB. Osteopontin Expression in Thyroid Cancer: Deciphering EMT-Related Molecular Mechanisms. *Biomedicines* (2021) 9(10):1372. doi:10.3390/biomedicines9101372

19. Amilca-Seba K, Sabbah M, Larsen AK, Denis JA. Osteopontin as a Regulator of Colorectal Cancer Progression and its Clinical Applications. *Cancers (Basel)* (2021) 13(15):3793. doi:10.3390/cancers13153793

20. Rakosy Z, Ecsedi S, Toth R, Vizkeleti L, Hernandez-Vargas H, Lazar V, et al. Integrative Genomics Identifies Gene Signature Associated with Melanoma Ulceration. *PLoS One* (2013) 8(1):e54958. doi:10.1371/journal.pone.0054958

21. Kiss T, Ecsedi S, Vizkeleti L, Koroknai V, Emri G, Kovacs N, et al. The Role of Osteopontin Expression in Melanoma Progression. *Tumour Biol* (2015) 36(10):7841–7. doi:10.1007/s13277-015-3495-y

22. Chou CF, Huang CC, Bin Dabil N, Chang PL. Assessing SPP1/Osteopontin (OPN) Splice Variants and Their Association to Nonmelanoma Skin Cancer by Absolute Quantification: Identification of OPN-5 Subvariants and Their Protein Coding Potential. *Cancer Invest* (2021) 39(6-7):559–70. doi:10.1080/07357907.2021.1933015

23. Livak KJ, Schmittgen TD. Analysis of Relative Gene Expression Data Using Real-Time Quantitative PCR and the 2(-Delta Delta C(T)) Method. *Methods* (2001) 25(4):402–8. doi:10.1006/meth.2001.1262

24. Scolyer RA, Rawson RV, Gershenwald JE, Ferguson PM, Prieto VG. Melanoma Pathology Reporting and Staging. *Mod Pathol* (2020) 33(1):15–24. doi:10.1038/s41379-019-0402-x

25. Patel V, Szasz I, Koroknai V, Kiss T, Balazs M. Molecular Alterations Associated with Acquired Drug Resistance during Combined Treatment with Encorafenib and Binimetinib in Melanoma Cell Lines. *Cancers* (2021) 13(23):6058. doi:10.3390/cancers13236058

26. Kiss T, Jambor K, Koroknai V, Szasz I, Bardos H, Mokanszki A, et al. Silencing Osteopontin Expression Inhibits Proliferation, Invasion and Induce Altered Protein Expression in Melanoma Cells. *Pathol Oncol Res* (2021) 27:581395. doi:10.3389/pore.2021.581395

27. Szasz I, Koroknai V, Kiss T, Vizkeleti L, Adany R, Balazs M, et al. Molecular Alterations Associated with Acquired Resistance to BRAFV600E Targeted Therapy in Melanoma Cells. *Melanoma Res* (2019) 29(4):390–400. doi:10.1097/CMR.0000000000000588

28. Kijewska M, Kocyk M, Kloss M, Stepniak K, Korwek Z, Polakowska R, et al. The Embryonic Type of SPP1 Transcriptional Regulation is Re-activated in Glioblastoma. *Oncotarget* (2017) 8(10):16340–55. doi:10.18632/oncotarget.14092

29. El Sharouni MA, van Diest PJ, Witkamp AJ, Sigurdsson V, van Gils CH. Subtyping Cutaneous Melanoma Matters. *JNCI Cancer Spectr* (2020) 4(6):pkaa097. doi:10.1093/jncics/pkaa097

30. Hao CC, Cui YX, Lane J, Jia SQ, Ji JF, Jiang WG, et al. Distinctive Prognostic Value and Cellular Functions of Osteopontin Splice Variants in Human Gastric Cancer. *Cells* (2021) 10(7):1820. doi:10.3390/cells10071820

31. Sivakumar S, Niranjali Devaraj S. Tertiary Structure Prediction and Identification of Druggable Pocket in the Cancer Biomarker - Osteopontin-C. *J Diabetes Metab Disord* (2014) 13(1):13. doi:10.1186/2251-6581-13-13

32. He B, Mirza M, Weber GF. An Osteopontin Splice Variant Induces Anchorage Independence in Human Breast Cancer Cells. *Oncogene* (2006) 25(15):2192–202. doi:10.1038/sj.onc.1209248

33. Nishimichi N, Hayashita-Kinoh H, Chen C, Matsuda H, Sheppard D, Yokosaki Y, et al. Osteopontin Undergoes Polymerization *In Vivo* and Gains Chemotactic Activity for Neutrophils Mediated by Integrin Alpha9beta1. *J Biol Chem* (2011) 286(13):11170–8. doi:10.1074/jbc.M110.189258

34. Tilli TM, Franco VF, Robbs BK, Wanderley JL, da Silva FR, de Mello KD, et al. Osteopontin-c Splicing Isoform Contributes to Ovarian Cancer Progression. *Mol Cancer Res* (2011) 9(3):280–93. doi:10.1158/1541-7786.MCR-10-0463

35. Silva GR, Mattos DS, Bastos ACF, Viana B, Brum MCM, Ferreira LB, et al. Osteopontin-4 and Osteopontin-5 Splice Variants are Expressed in Several Tumor Cell Lines. *Mol Biol Rep* (2020) 47(10):8339–45. doi:10.1007/s11033-020-05867-9

36. Danen EH, Ten Berge PJ, Van Muijen GN, Van 't Hof-Grootenboer AE, Brocker EB, Ruiter DJ, et al. Emergence of α5β1 Fibronectin- and αvβ3 Vitronectin-Receptor Expression in Melanocytic Tumour Progression. *Histopathology* (1994) 24(3):249–56. doi:10.1111/j.1365-2559.1994.tb00517.x

37. Hieken TJ, Ronan SG, Farolan M, Shilkaitis AL, Das Gupta TK. Molecular Prognostic Markers in Intermediate-Thickness Cutaneous Malignant Melanoma. *Cancer* (1999) 85(2):375–82. doi:10.1002/(sici)1097-0142(19990115)85:2<375::aid-cncr15>3.0.co;2-1

38. Arias-Mejias SM, Warda KY, Quattrocchi E, Alonso-Quinones H, Sominidi-Damodaran S, Meves A, et al. The Role of Integrins in Melanoma: A Review. *Int J Dermatol* (2020) 59(5):525–34. doi:10.1111/ijd.14850

39. Huang R, Rofstad EK. Integrins as Therapeutic Targets in the Organ-specific Metastasis of Human Malignant Melanoma. *J Exp Clin Cancer Res* (2018) 37(1):92. doi:10.1186/s13046-018-0763-x

40. Vizkeleti L, Kiss T, Koroknai V, Ecsedi S, Papp O, Szasz I, et al. Altered Integrin Expression Patterns Shown by Microarray in Human Cutaneous Melanoma. *Melanoma Res* (2017) 27(3):180–8. doi:10.1097/Cmr.0000000000000322

41. Martin TA, Jiang WG. Evaluation of the Expression of Stem Cell Markers in Human Breast Cancer Reveals a Correlation with Clinical Progression and Metastatic Disease in Ductal Carcinoma. *Oncol Rep* (2014) 31(1):262–72. doi:10.3892/or.2013.2813

42. Ramirez NE, Zhang Z, Madamanchi A, Boyd KL, O'Rear LD, Nashabi A, et al. The αβ Integrin is a Metastasis Suppressor in Mouse Models and Human Cancer. *J Clin Invest* (2011) 121(1):226–37. doi:10.1172/JCI42328

43. Madamanchi A, Santoro SA, Zutter MM. α2β1 Integrin. *Adv Exp Med Biol* (2014) 819:41–60. doi:10.1007/978-94-017-9153-3_3

44. Bartolome RA, Torres S, Isern de Val S, Escudero-Paniagua B, Calvino E, Teixido J, et al. VE-Cadherin RGD Motifs Promote Metastasis and Constitute a Potential Therapeutic Target in Melanoma and Breast Cancers. *Oncotarget* (2017) 8(1):215–27. doi:10.18632/oncotarget.13832

45. Yoshimura K, Meckel KF, Laird LS, Chia CY, Park JJ, Olino KL, et al. Integrin Alpha2 Mediates Selective Metastasis to the Liver. *Cancer Res* (2009) 69(18):7320–8. doi:10.1158/0008-5472.CAN-09-0315

46. Naci D, Vuori K, Aoudjit F. Alpha2beta1 Integrin in Cancer Development and Chemoresistance. *Semin Cancer Biol* (2015) 35:145–53. doi:10.1016/j.semcancer.2015.08.004

47. Di Paola J, Jugessur A, Goldman T, Reiland J, Tallman D, Sayago C, et al. Platelet Glycoprotein I(b)alpha and Integrin Alpha2 Beta1 Polymorphisms: Gene Frequencies and Linkage Disequilibrium in a Population Diversity Panel. *J Thromb Haemost* (2005) 3(7):1511–21. doi:10.1111/j.1538-7836.2005.01273.x

48. Cheli Y, Williams SA, Ballotti R, Nugent DJ, Kunicki TJ. Enhanced Binding of poly(ADP-Ribose)polymerase-1 and Ku80/70 to the ITGA2 Promoter via an Extended Cytosine-Adenosine Repeat. *PLoS One* (2010) 5(1):e8743. doi:10.1371/journal.pone.0008743

49. Adorno-Cruz V, Liu H. Regulation and Functions of Integrin α2 in Cell Adhesion and Disease. *Genes Dis* (2019) 6(1):16–24. doi:10.1016/j.gendis.2018.12.003

Check for updates

Relationships of Cuproptosis-Related Genes With Clinical Outcomes and the Tumour Immune Microenvironment in Hepatocellular Carcinoma

Xi Chen[1][†], Gang Hu[2][†], Li Xiong[3][†] and Qingqing Xu[4]*

[1]Department of Thoracic Oncology, Huangshi Central Hospital, Affiliated Hospital of Hubei Polytechnic University, Edong Healthcare Group, Huangshi, China, [2]Department of Breast Surgery, Thyroid Surgery, Huangshi Central Hospital, Affiliated Hospital of Hubei Polytechnic University, Edong Healthcare Group, Huangshi, China, [3]Department of Radiology, Huangshi Central Hospital, Affiliated Hospital of Hubei Polytechnic University, Edong Healthcare Group, Huangshi, China, [4]Department of Pathology, Huangshi Central Hospital, Affiliated Hospital of Hubei Polytechnic University, Edong Healthcare Group, Huangshi, China

Background: Cuproptosis is a recently identified form of regulated cell death that plays a critical role in the onset and progression of various cancers. However, the effects of cuproptosis-related genes (CRGs) on hepatocellular carcinoma (HCC) are poorly understood. This study aimed to identify the cuproptosis subtypes and established a novel prognostic signature of HCC.

Methods: We collected gene expression data and clinical outcomes from the TCGA, ICGC, and GEO datasets, analysed and identified 16 CRGs and the different subtypes of cuproptosis related to overall survival (OS), and further examined the differences in prognosis and immune infiltration among the subtypes. Subtypes-related differentially expressed genes (DEGs) were employed to build a prognostic signature. The relationship of the signature with the immune landscape as well as the sensitivity to different therapies was explored. Moreover, a nomogram was constructed to predict the outcome based on different clinicopathological characteristics.

Results: Three cuproptosis subtypes were identified on the basis of 16 CRGs, and subtype B had an advanced clinical stage and worse OS. The immune response and function in subtype B were significantly suppressed, which may be an important reason for its poor prognosis. Based on the DEGs among the three subtypes, a prognostic model of five CRGs was constructed in the training set, and its predictive ability was validated in two external validation sets. HCC patients were classified into high and low-risk subgroups according to the risk score, and found that patients in the low-risk group showed significantly higher survival possibilities than those in the high-risk group ($p < 0.001$). The independent predictive performance of the risk score was assessed and verified by multivariate Cox regression analysis ($p < 0.001$). We further created an accurate

Abbreviations: CRGs, Cuproptosis-related genes; DCA, Decision curve analysis; DEGs, Differentially expressed genes; ICIs, Immune checkpoint inhibitors; OS, Overall survival; PCA, Principal component analysis; RCD, Regulated cell death; TCGA, The Cancer Genome Atlas; TIICs, Tumour immune infiltration cells; TME, Tumour microenvironment.

nomogram to improve the clinical applicability of the risk score, showing good predictive ability and calibration. Low- and high-risk patients exhibit distinct immune cell infiltration and immune checkpoint changes. By further analyzing the risk score, patients in the high-risk group were found to be resistant to immunotherapy and a variety of chemotherapy drugs.

Conclusion: Our study identified three cuproptosis subtypes and established a novel prognostic model that provides new insights into HCC subtype prognostic assessment and guides more effective treatment regimens.

Keywords: immunotherapy, hepatocellular carcinoma, immune infiltration, prognostic model, cuproptosis

INTRODUCTION

Hepatocellular carcinoma (HCC) comprises approximately 90% of primary liver cancers in the world. It is the fifth most prevalent cancer and ranks fourth among cancer-related deaths worldwide [1]. HCC causes approximately 800,000 deaths each year and seems to have a heavy disease burden [2]. In the past 2 or 3 years, there have been some notable advances in the treatment of HCC, such as resection and transplantation [3, 4]. Recently, immunotherapy and molecular targeted therapy for HCC have also been developed and are expected to become new treatment approaches [5,6,7]. However, the survival rate of HCC is still far from satisfactory due to a low rate of early detection, a tendency for recurrence, and chemotherapy resistance [8]. Therefore, it is of great significance for us to identify accurate biomarkers in the diagnosis stage of patients with HCC to evaluate the prognosis of HCC.

Regulated cell death (RCD) is the primary mechanism for eliminating damaged, infected, or redundant cells [9, 10]. Apoptosis was originally thought to be the only RCD mechanism. Nevertheless, as the understanding of the cellular mechanisms that mediate RCD continues to grow, many new forms of non-apoptotic RCD have been discovered, including ferroptosis, pyroptosis, necroptosis, and autophagic cell death [9, 11, 10]. In 2012, Dixon et al. [12] defined the term ferroptosis to describe the form of cell death induced by the small molecule Erastin, which is iron ion-catalyzed necrotic cell death by inhibiting cystine import, resulting in glutathione depletion and phospholipid peroxidase glutathione peroxidase inactivation 4 (GPX4). Ferroptosis was related to the pathophysiological changes of many cancers [13, 14]. Triggering ferroptosis as a novel approach to cancer treatment is highly anticipated and an active area of research. Pyroptosis is an inflammatory RCD that is mainly triggered by inflammatory caspases and gasdermin family proteins and is manifested by the continuous swelling of cells until cell membrane rupture and death [15].

Interestingly, a recent study by Tsvetkov and others revealed that intracellular copper induces a new form of RCD distinct from oxidative stress-related cell death, known as "cuproptosis" [16]. It occurs through the direct binding of copper to fatty acylated components of the tricarboxylic acid cycle, resulting in fatty acylated protein aggregation and iron-sulphur cluster protein loss, leading to proteotoxic stress and ultimately cell death [16]. Studies have shown that an imbalance in copper homeostasis affects tumour growth, causing irreversible damage. Copper can induce multiple forms of cell death through various mechanisms, including reactive oxygen species accumulation, proteasome inhibition, and anti-angiogenesis [17]. For example, blocking SLC31A1-dependent copper uptake increases autophagy in pancreatic cancer cells against cell death [18]. At present, several genes and proteins have been shown to regulate cuproptosis, including FDX1, LIAS, LIPT1, PDHA1, and PDHB [16]. However, the expression patterns and clinical value of cuproptosis-related genes (CRGs) in HCC remain unclear.

In this study, we firstly built a predictive signature based on CRGs as a prognostic biomarker. Next, we created an accurate nomogram to improve the clinical applicability of the risk score. In addition, we analyzed the correlation of CRGs with the prognosis, the TME, immune checkpoint genes, chemotherapy sensitivity, and immunotherapy.

MATERIALS AND METHODS

Data Source

The RNA-seq data and clinical traits for HCC patients were obtained and extracted from the TCGA, ICGC, and GEO (GSE14520) datasets. Among them, TCGA contained 371 samples, GSE14520 contained 242 samples, and ICGC contained 260 samples. The "sva" and "limma" R packages were implemented to integrate and normalize the RNA-seq data and microarrays separately. The data of 265 HCC patients with complete clinical information and follow-up time in TCGA were used as the training set to build a prognostic model related to cuproptosis, and the GSE14520 dataset (221 patients) and ICGC dataset (232 patients) were used as two external validation sets. Additionally, 16 CRGs (PDHA1, DLD, DLAT, PDHB, GLS, MTF1, SLC31A1, CDKN2A, LIPT1, FDX1, LIAS, ATP7A, ATP7B, BAD, CCS, MTOR, and NRF2) used in this study were obtained from previous publications [16,18–24].

Unsupervised Consensus Clustering of the HCC Molecular Subtypes

With the "ConsensusClusterPlus" R package, a consensus clustering method was applied to categorize patients into different molecular

subtypes on the basis of the CRG expression levels. The optimal number of subtypes k was identified by considering where the magnitude of the cophenetic correlation coefficient decreased. Subsequently, the relationship between molecular subtypes and clinicopathological features and prognosis were compared.

Immune Landscape of the Molecular Subtypes

We explored the difference of each subtype in the TME score using the ESTIMATE algorithm. In addition, the CIBERSORT algorithm was used to predict HCC samples' immune-infiltrating cells. Upon entering the samples' expression data, we obtained the sample's proportion of 22 immune-infiltrating cells.

Construction and Validation of the Cuproptosis-Related Gene Predictive Signature

The "limma" R package was employed to screen the differentially expressed genes (DEGs) between different subtypes according to the following criteria: |fold change| > 1.5 and $p < 0.05$. We used a univariate Cox analysis based on DEGs to assess the prognostic significance of candidate DEGs in HCC. After further adjustment, multivariate Cox regression (stepwise model) was performed to identify the pivotal genes, which were employed to build prognostic signature. The coefficients obtained from the regression algorithm were used to obtain the risk scores based on the following formula:

$$\text{Risk score} = ExpGene1*\beta1 + ExpGene2*\beta2 + ... + ExpGenen*\beta n$$

Furthermore, the patients were classified into two risk groups (high and low) using the median as the cut-off value. Kaplan-Meier survival curves were generated to assess differences between the two risk groups. A ROC curve was employed to evaluate the performance of the model. Principal component analysis (PCA) was conducted using the "prcomp" function of the "stats" R package to explore the distribution of different groups.

We chose two datasets, GSE14520 and ICGC, as the external verification set to verify the predictive accuracy of the signature. Patients were stratified into high- and low-risk groups based on the cut-off point of the risk score of the TCGA set. Kaplan–Meier survival curves were generated to assess the differences between the two risk groups. ROC curves and PCA were employed to evaluate the validity of the prognostic signature.

Prognostic Value of the Risk Model

We analysed the association of the risk scores with clinicopathological traits, including age, sex, grade, pathologic stage, and surgical procedure. To determine whether the signature was an independent prognostic indicator, we performed univariate and multivariate Cox analyses.

Nomogram Construction and Assessment

The multivariate Cox regression analysis of clinical parameters and risk score were utilized to build a prognostic nomogram using the "rms" package. The ROC curve was ploted to assess the predictive accuracy of the nomogram. Decision curve analysis (DCA) was used to assess the clinical benefits and utility of the nomogram. Afterward, calibration plots were developed to evaluate the correlation between the actual and predicted survival.

Tumour Immune Microenvironment Analysis

To clarify the potential regulatory role of the signature in immune cell infiltration, we explored the infiltration of 22 immune cells in the low- and high-risk groups. Considering the importance of immune checkpoint-related gene expression levels for immune checkpoint inhibitor therapy, we assessed the relationship between the risk score and immune checkpoint expression in HCC patients. Meanwhile, the potential response of HCC samples to immunotherapy was inferred by the TIDE algorithm [25].

Investigation of Differences in the Chemotherapeutic Efficacy

To assess the significance of the predictive signature in predicting the sensitivity to chemotherapy in HCC, the "pRRophetic" package was used to calculate the IC50 of the main chemotherapeutic medications used in the treatment of HCC patients.

Functional Enrichment Analysis

To explore the signalling pathways in which the cuproptosis-related signature may be involved in regulation, DEGs between the two risk score subgroups were retrieved ($|\log_2 FC| \geq 2$ and adjusted $p < 0.01$) for GO and Kyoto Encyclopedia of Genes and Genomes (KEGG) analyses with "cluster Profiler" in R.

RESULTS

Unsupervised Consensus Clustering of the HCC Molecular Subtypes

Based on the expression of 16 CRGs, a consensus clustering method was carried out in the TCGA cohort. At a clustering variable (k) of 3, the intragroup and intergroup correlations were high and low, respectively, suggesting that the 371 HCC patients clustered into three groups (**Figure 1A**). PCA demonstrated that the individuals were distributed into three delineated clusters (**Figure 1B**). Kaplan-Meier survival curves revealed that patients in subtype B had a markedly shorter OS than those in subtypes A and C ($p < 0.001$; **Figure 1C**). The heatmap displayed the distribution of the clinicopathological traits and CRG expression among the three subtypes (**Figure 1D**). Most CRGs had lower expression levels in subtype B than in the other subtypes (**Figure 1D**). Patients in subtype B were elderly, had a higher grade, and had an advanced pathologic stage (**Figure 1D**).

FIGURE 1 | HCC subtypes according to cuproptosis-related genes. **(A)** The consensus score matrix of all samples in the TCGA set at k = 3. **(B)** The PCA distribution plot distinguished three subtypes. **(C)** Kaplan–Meier curve of the three subtypes. **(D)** Heatmap of clinical traits and cuproptosis-related gene expression in the three subtypes. **(E)** The enrichment scores of 22 immune cells in the three subtypes.
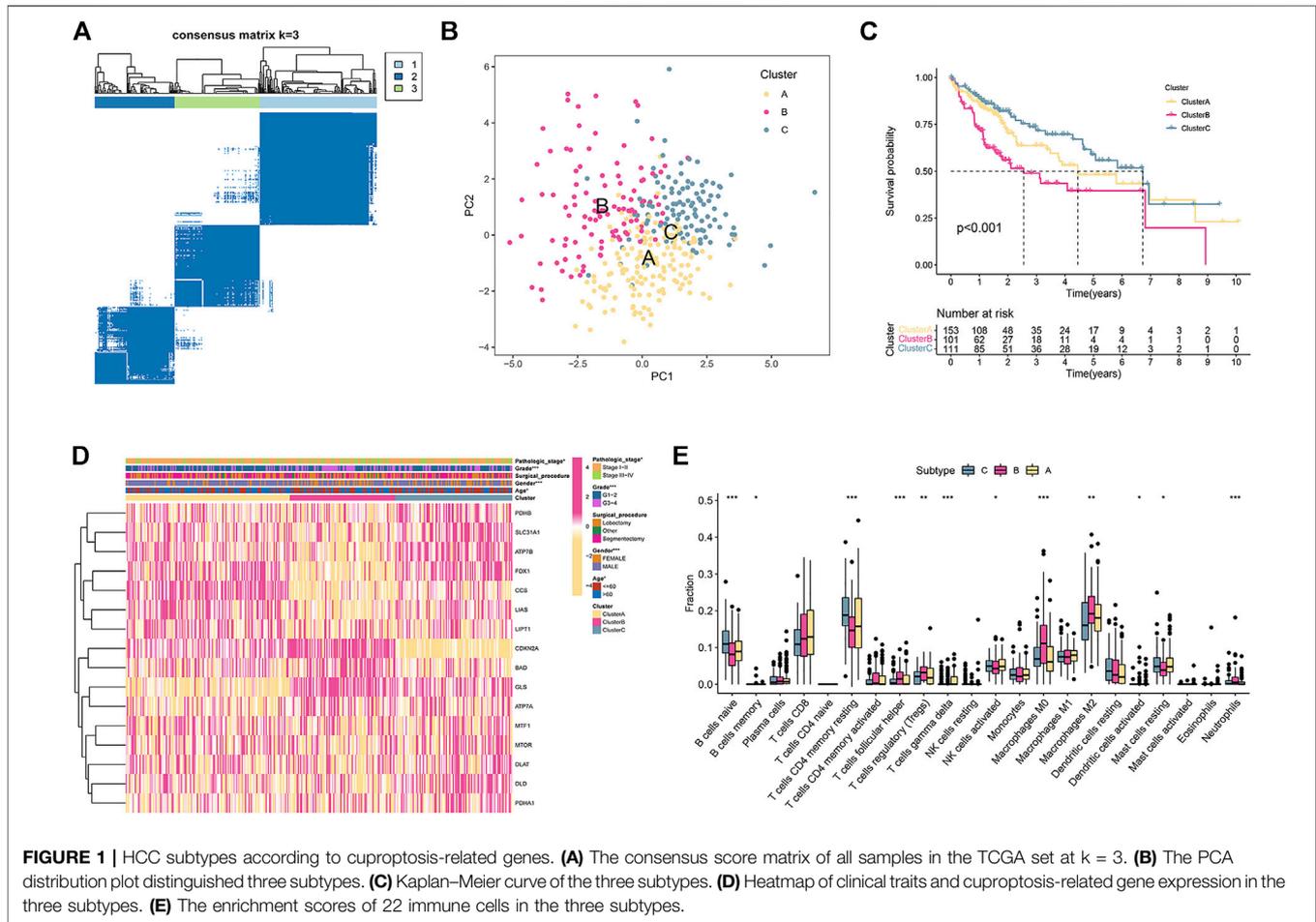
Immune Landscape of the Molecular Subtypes

We further examined whether any differences were observed regarding TIICs to investigate the immunological characteristics of HCC. The CIBERSORT algorithms were used to explore the associations among TIICs and the three subtypes. The fraction of memory and resting memory CD4 T cells, resting mast cells, naive B cells, activated dendritic cells, and activated NK cells were significantly downregulated in subtype B ($p < 0.05$; **Figure 1E**). In contrast, helper follicular cells, Tregs, neutrophils, and M0 and M2 macrophages were markedly upregulated in subtype B ($p < 0.05$).

Construction and Validation of the Cuproptosis-Related Gene Predictive Signature

Based on the criteria of $p < 0.05$ and |FC| > 1.5, and 81 subtype-related DEGs were identified (**Figure 2A**). Then, 21 prognosis-related DEGs were found significantly correlated with the OS of HCC patients according to univariate Cox regression analysis ($p < 0.05$; **Figure 2B**). Furthermore, we conducted multivariant Cox regression analysis on these 21 genes. According to the

Akaike information criterion (AIC) value, we finally obtained five genes to construct risk models, including HPR, LAMB1, PFKFB3, CLEC3B, and CFH (**Figure 2C**). Afterward, we computed the risk score as follows:

$$\text{Risk score} = 0.1273 \times \text{expression}(\text{HPR}) + 0.2161 \times \text{expression}(\text{LAMB1})$$
$$+ 0.2006 \times \text{expression}(\text{PFKFB3}) - 0.2951 \times \text{expression}(\text{CLEC3B})$$
$$- 0.1589 \times \text{expression}(\text{CFH}).$$

The median risk score was used as the cut-off to categorize the HCC patients into two groups: low-risk ($n = 183$) and high-risk ($n = 182$). **Figure 2D** represents the status of survival and the distribution of the risk scores, whereas **Figure 2E** shows the relative expression of the 5 genes for each patient in the two groups. According to the Kaplan-Meier plot, patients with high risk showed a considerably lower OS (**Figure 2F**). The distribution of cuproptosis subtypes, risk score, and survival status are shown in **Figure 2G**. PCA could divide patients with different risks into two groups (**Figure 2H**). ROC evaluated the prediction performance of the signature. The AUC showed that the 3- and 5-year OS were 0.827 and 0.780, respectively (**Figure 2I**).

The reliability of the signature related to cuproptosis was verified by two external validation cohorts (GSE14520 and ICGC). The risk score was established by using the previous

FIGURE 2 | Establishment and validation of the prognostic signature in the training cohort. **(A)** Venn diagram to identify differentially expressed genes (DEGs) among the different subtypes. **(B)** Univariate Cox regression analysis of 21 DEGs. **(C)** The presentation of five independent prognostic genes in multivariate Cox regression analysis. **(D)** Risk score distribution and survival status of patients. **(E)** The relative expression of the five genes in different risk groups. **(F)** Kaplan-Meier curves of OS in different risk groups. **(G)** The distribution of cuproptosis subtypes, risk score, and survival status. **(H)** PCA displays an obvious difference in transcriptomes between the two risk groups. **(I)** ROC curve of survival rate for the signature.

formula. The status of survival and the distribution of the risk scores, and the relative expression of the five genes for each patient in each of the two groups are shown in **Figures 3A,B**. PCA could divide patients with different risks into two clusters (**Figures 3C,D**). Low-risk patients had favorable OS compared with their high-risk counterparts (**Figures 3E,F**). The ROC curve demonstrated that the signature had a favorable predictive performance (**Figures 3G,H**).

Prognostic Value of the Risk Model

The correlation between the risk score and clinicopathological traits was further analyzed. As shown in **Figures 4A,B**, the risk score was correlated with grade ($p = 0.01$) and pathologic stage ($p = 0.011$). To further confirm the independence of the model, we performed univariate and multivariate Cox analyses. As shown in **Figures 4C,D**, the risk score, surgical procedure, and pathologic stage were independent prognostic factors.

FIGURE 3 | Validation of the cuproptosis-related signature in the GSE14520 and ICGC cohorts. **(A,B)** The distribution of risk scores and survival status of patients in the GSE14520 **(A)** and ICGC cohorts **(B)**. **(C,D)** PCA plot for two subgroups in the GSE14520 **(C)** and ICGC cohorts **(D)** **(E,F)** Kaplan-Meier curves of OS in the GSE14520 **(E)** and ICGC cohorts **(F)**. **(G,H)** ROC curve for assessing the prognostic value of the signature in the GSE14520 **(G)** and ICGC cohorts **(H)**.

FIGURE 4 | Prognostic value of the signature. **(A)** The relationship between the risk score and tumor grade. **(B)** The relationship between the risk score and pathologic stage. **(C,D)** Univariate and multivariate analyses indicated the prognostic value of the risk score.

FIGURE 5 | Development and assessment of the prognostic nomogram. **(A)** The nomogram that integrated the risk score, stage, and surgery predicted the probability of the 3- and 5-year OS. **(B)** The 3- and 5-year time-dependent ROC curves. **(C,D)** The calibration curves for 3- **(C)** and 5-year OS **(D)**. **(E)** Decision curve analysis of the nomogram, risk score, age, sex, grade, surgical procedure, and pathologic stage.

Nomogram Construction and Assessment

Based on the above results, a nomogram was built to forecast the survival risk in HCC patients. The nomogram, which is based on risk score, surgical procedure, and pathologic stage, can predict the three- and five-year OS (**Figure 5A**). In order to assess the sensitivity and specificity of the nomogram on the prognosis, the ROC was performed. The nomogram displayed AUC values of 0.721 and 0.707 at 3- and 5-year in the ROC analysis, respectively (**Figure 5B**). We also used the 3- and 5-year calibration plots to prove that the proposed nomogram had a similar performance compared to an ideal model (**Figures 5C,D**). Furthermore, the DCA showed better clinical benefit and utility of nomogram for predicting OS (**Figure 5E**).

Tumour Immune Microenvironment Analysis

We performed CIBERSORT algorithms for different immune cell subsets, to further study the relationship between risk score and immune status in the two subgroups. As shown in **Figure 6A**, the high-risk group had lower levels of infiltration in a variety of immune cells, including resting memory CD4 T cells, CD8 T cells, resting NK cells, activated NK cells, and resting mast cells. In contrast, the high-risk group had higher infiltration of M0 and M2 macrophages. We further investigated the potential role of the signature in assessing the immunotherapy efficacy of ICIs in HCC patients by analyzing the

association between the signature and prevalent ICI targets. Patients in the low-risk group had higher expression of these genes (e.g., CD274, CTLA4, HAVCR2, and PDCD-1) in comparison to the high-risk group (**Figure 6B**). In terms of immunotherapy, we explored the responses of HCC samples to immunotherapy. Compared with HCC patients with high-risk score, patients with low-risk score were more sensitive to immunotherapy (**Figure 6C**).

Investigation of Differences in Chemotherapeutic Efficacy

Distinct HCC subgroups should be used to guide clinical treatment. Correlation between the risk score and the sensitivity to chemotherapy was investigated. The results indicated that the IC_{50} values of sorafenib, lapatinib, metformin, temsirolimus, palbociclib (PD-0332991), and erlotinib were significantly lower in samples of the low-risk group, while the IC_{50} values of bleomycin, dasatinib, veliparib (ABT-888), ABT-263, and FTI-277 were significantly lower in samples of the high-risk group (**Figures 6D–N**).

Functional Enrichment Analysis

According to the criteria for FDR < 0.01 and |FC| > 1.5, we identified 334 DEGs in HCC samples (**Figure 7A**). According to GO analysis, the biological processes of DEGs were primarily enriched in response to a toxic substance, detoxification of copper

FIGURE 6 | Immune landscape and drug sensitivity analyses between the low- and high-risk groups. **(A)** The proportion of 22 immune infiltrating cells in the low- and high-risk groups. **(B)** The expression levels of the immune checkpoints in different risk subgroups. **(C)** Comparison of the TIDE scores between the different risk groups. **(D–N)** Chemotherapeutic sensitivity of patients in the different risk subgroups.

ion, and stress response to copper ion (**Figure 7B**). The cellular components of the DEGs were mainly enriched in blood microparticles, high-density lipoprotein particles, and

endocytic vesicle lumen (**Figure 7B**). The molecular functions of DEGs were mainly enriched in oxygen binding, haem binding, and tetrapyrrole binding (**Figure 7B**). KEGG pathway analyses

FIGURE 7 | Functional enrichment analysis between the low- and high-risk groups. **(A)** Volcano plot of 334 DEGs between the different risk groups. **(B,C)** GO and KEGG enrichment analyses of DEGs among the two risk groups.
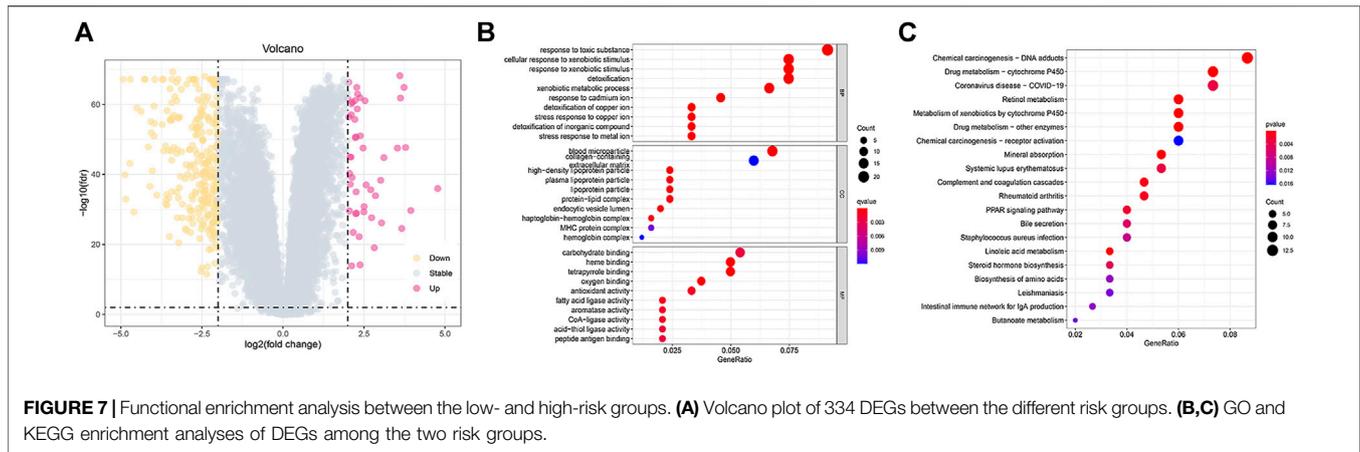
revealed that these genes were primarily enriched in chemical carcinogenesis-DNA adducts, drug metabolism-cytochrome P450, linoleic acid metabolism, and drug metabolism-other enzymes (**Figure 7C**).

DISCUSSION

After developing chronic fibrotic liver disease caused by viral or metabolic aetiologies, patients tend to progress to HCC [26]. Nevertheless, the key issue at present is that there is no robust estimation system that can reliably estimate the HCC risk or diagnose HCC during its early stages [27]. As a result, identifying biomarkers is critical for early detection, prognostic analysis, and individualized therapy of HCC.

RCD, or, more specifically, cell suicide, is not only essential in embryonic development but also plays a critical role in the occurrence and development of diseases, especially malignancies [11]. Apoptosis is one of the most classic forms of programmed cell death and is considered the most promising target for tumor therapy [28]. In addition to classical apoptosis, several other forms of RCD have been identified [11]. Copper ionophore-induced cell death is a novel cell death pathway that is distinctly different from traditional death methods [16]. Cuproptosis plays an important role in tumorigenesis and cancer therapy [18, 16, 29]. Dysregulation of CRGs has been shown to be involved in the pathogenesis and development of multiple types of cancer. Li et al. [30] showed that copper chaperone for superoxide dismutase (CCS) promotes breast cancer cell growth and migration by regulating ROS-mediated ERK1/2 activity. Vyas et al. [31] reveal that copper-dependent ATP7B upregulation drives resistance to platinum toxicity in a TMEM16A-overexpressing head and neck cancer model.

Physiologically, enterocytes take up bioavailable copper ions from the diet in a Ctr1-dependent manner, and upon incorporation, cuprous ions are transported to ATP7A, which pumps Cu^+ from enterocytes into the blood. Copper ions reach the liver through the portal vein and enter hepatocytes through Ctr1 to form membrane pores. Then, Cu^+ can be secreted into bile or blood through the Atox1/ATP7B/ceruloplasmin pathway. In the blood, this

micronutrient can reach peripheral tissues and be reabsorbed by Ctr1 [32]. Wilson's disease (WD) is an autosomal recessive disorder caused by mutations in the ATP7B gene, which encodes the copper-transporting ATPase, resulting in impaired hepatic copper excretion [33]. Copper metabolism must be tightly controlled in order to achieve homeostasis and avoid disorders. A hereditary or acquired copper unbalance may cause or aggravate many diseases, including cardiovascular diseases, neurodegenerative diseases, Genetic disorders, metabolic diseases, and cancer [34, 35].

The main risk factors for HCC are hepatotropic viruses (HBV and HCV) [36]. In addition, nonalcoholic fatty liver disease (NAFLD) is already the fastest growing cause of HCC in the USA [37]. Evidence reports that inadequate copper intake serum concentration is involved in the pathogenesis of NAFLD. Intrahepatic and serum copper concentrations were lower in subjects with NAFLD compared with other liver diseases [38]. NAFLD-cirrhotic patients were characterized by a statistical significant enhancement of serum copper levels, even more evident in HCC patients [39, 38]. Patients with hepatolenticular degeneration due to impaired copper metabolism have a high incidence of HCC [40], so we hypothesize that cuproptosis has a correlation with the development of HCC. However, the mechanism of action of cuproptosis affecting HCC is not clear.

RCD-based HCC subtype and/or prognostic models are becoming a research hotspot for predicting HCC prognosis. Growing evidence suggests that prognostic models based on next-generation sequencing and public databases provide more comprehensive clinical-genetic prognostic value [41,42,43]. The role including clinical relevance and prognostic significance of CRGs in HCC is unknown. In the present study, TCGA and two external databases (GEO and ICGC) were employed to collect gene expression and clinicopathological information as the training and validation cohorts, respectively. According to an unsupervised consensus clustering analysis of 16 CRGs, HCC patients were categorized into three subtypes. Compared with patients with other subtypes, patients with subtype B had worse OS. The level of immune cell infiltration also differed greatly among the subtypes. The contents of infiltrated immune cells in subtype A and C were significantly higher than those in subtype B, which seemed to contradict its worse survival outcome.

To better evaluate each HCC patient's prognosis and therapeutic response, it is essential to construct a cuproptosis signature, which could generate a cuproptosis model for individual prediction. Therefore, we identified 81 cuproptosis subtype-related DEGs and developed and tested a novel prognostic signature in HCC patients by using the identified DEGs. The signature contained five cuproptosis-associated genes: PFKFB3, CLEC3B, CFH, HPR, and LAMB1. PFKFB3, a key molecule in glucose metabolism in the cytoplasm, obviously accelerates the rate of glycolysis and is expressed in rapidly proliferating cells and multiple cancers [44]. PFKFB3 can promote cell cycle progression and inhibit apoptosis through Cdk1-mediated phosphorylation of p27, while MAPK increases PFKFB3 transcripts to accelerate cell proliferation [44]. PFKFB3 has been shown to affect the tumorigenesis and progression of HCC through various mechanisms and is a potential target for the treatment of HCC [44–47]. Li et al. [44] found markedly increased OS in individuals with PFKFB3-overexpressing tumors in comparison with the low-expression group. Knockdown of PFKFB3 reduces glucose consumption and disrupts DNA repair function, resulting in G2/M phase arrest and apoptosis in HCC cells. Mechanistically, blockade of PFKFB3 inhibits hepatocellular carcinoma growth by impairing DNA repair via AKT. Matsumoto et al. [46] revealed that inhibition of PFKFB3 suppressed tumor growth and induced tumor vascular normalization in HCC. CLEC3B, a member of the C-type lectin superfamily, has been reported to be downregulated in serum and tumor tissues of HCC [48, 49]. Dai et al. [48] found that downregulation of exosomal CLEC3B in HCC promoted metastasis and angiogenesis through AMPK and VEGF signaling. CFH is a critical regulatory protein of the alternative complement pathway. Mao et al. [50] showed that CFH is enriched in extracellular vesicles (EVs) of metastatic HCC cells and it protects HCC cells by evading complement attack, thereby promoting HCC progression. Therefore, the expression of CRGs was strongly associated with the tumorigenesis, invasion, and outcomes of hepatocellular cancer, corroborating our findings.

The HCC patients were then divided into two risk subgroups based on the calculated cut-off point. Kaplan-Meier curves indicated that the OS rate was markedly higher in the low-risk group than in the high-risk group. The time-dependent ROC curve showed that the risk score presented a good performance for survival prediction. External validation confirmed the value of the predictive signature. Furthermore, multivariate Cox regression analysis confirmed that the risk score was a prognostic factor independent of clinical characteristics. We then developed a nomogram for predicting 3- and 5-year OS in HCC patients, and we also verified the accuracy of the nomogram by calibration. Taken together, the signature may be effective in predicting patient outcomes, thereby facilitating the implementation and evaluation of the model in future clinical practice.

The tumor immune microenvironment is crucial in the initiation and progression of HCC [51]. We calculated 22 TIICs in the two risk subgroups according to the CIBERSORT algorithm. We observed that risk scores were negatively correlated with resting memory CD4 T cells, CD8 T cells, resting and activated NK cells, whereas risk scores were positively correlated M0 and M2 macrophages, indicating that the signature may significantly contribute to modulating immune cell infiltration. Emerging experiments and clinical studies have found that immunotherapy does have advantages that traditional anti-tumor treatments cannot match, which can improve the prognosis of HCC patients [6, 5]. ICI therapy targeting anti-PD-1 or PD-L1 is a crucial step in a combination regimen to improve the prognosis of HCC patients [52]. The combination of anti-CTLA4 and anti-PD-L1 increased tumor-infiltrating lymphocyte function and restored HCC-derived T cell responses to tumor antigens [53]. In the present study, a novel cuproptosis-based signature was built to investigate the relationship between ICIs and the risk score as a predictor of immunotherapy response. The expression of PD-1, PD-L1, and CTLA4 was significantly lower in the high-risk group, suggesting that the signature might be potentially useful for predicting responses to ICI-targeted therapy. We observed lower TIDE scores in low-risk patients compared with high-risk HCC patients. This suggests that low-risk patients are less likely to have tumor immune evasion and are more likely to benefit from immunotherapy, which further explains their better prognosis. We next investigated the correlation between risk score and chemotherapeutic drug sensitivity. And the results indicated patients with high-risk scores seemed to be more responsive to bleomycin, dasatinib, and veliparib, while low-risk patients were more sensitive to sorafenib, lapatinib, metformin, temsirolimus, and palbociclib. The combination of immunotherapy and chemotherapy may provide precise and individualized treatment with different risk scores.

CONCLUSION

We successfully identified three distinct subtypes of cuproptosis and established a novel prognostic model, providing new insights into the prediction of the outcome of HCC and its response to chemotherapy and immunotherapy.

DATA AVAILABILITY STATEMENT

Publicly available datasets were analyzed in this study. This data can be found here: The public datasets were obtained from TCGA (https://portal.gdc.cancer.gov/) and GEO (https://www.ncbi.nlm.nih.gov/geo/).

AUTHOR CONTRIBUTIONS

XC and QQX: Design of the study. XC: Data acquisition and analysis. GH and LX: Data visualization. XC, GH, and LX: Manuscript drafting, and QQX: Revised the final manuscript. All authors contributed to the article and approved the submitted version.

CONFLICT OF INTEREST

The authors declare that the research was conducted in the absence of any commercial or financial relationships that could be construed as a potential conflict of interest.

REFERENCES

1. Kanwal F, Singal AG. Surveillance for Hepatocellular Carcinoma: Current Best Practice and Future Direction. *Gastroenterology* (2019) 157:54–64. doi:10.1053/j.gastro.2019.02.049

2. Cadoux M, Caruso S, Pham S, Gougelet A, Pophillat C, Riou R, et al. Expression of NKG2D Ligands Is Downregulated by β-catenin Signalling and Associates with HCC Aggressiveness. *J Hepatol* (2021) 74:1386–97. doi:10.1016/j.jhep.2021.01.017

3. Heller M, Parikh ND, Fidelman N, Owen D. Frontiers of Therapy for Hepatocellular Carcinoma. *Abdom Radiol (Ny)* (2021) 46:3648–59. doi:10.1007/s00261-021-03065-0

4. Jiří T, Igor K, Mba. Hepatocellular Carcinoma Future Treatment Options. *Klin Onkol* (2020) 33:26–9. doi:10.14735/amko20203S26

5. Sangro B, Sarobe P, Hervás-Stubbs S, Melero I. Advances in Immunotherapy for Hepatocellular Carcinoma. *Nat Rev Gastroenterol Hepatol* (2021) 18:525–43. doi:10.1038/s41575-021-00438-0

6. Zongyi Y, Xiaowu L. Immunotherapy for Hepatocellular Carcinoma. *Cancer Lett* (2020) 470:8–17. doi:10.1016/j.canlet.2019.12.002

7. Huang A, Yang XR, Chung WY, Dennison AR, Zhou J. Targeted Therapy for Hepatocellular Carcinoma. *Signal Transduct Target Ther* (2020) 5:146. doi:10.1038/s41392-020-00264-x

8. Gordan JD, Kennedy EB, Abou-Alfa GK, Beg MS, Brower ST, Gade TP, et al. Systemic Therapy for Advanced Hepatocellular Carcinoma: ASCO Guideline. *J Clin Oncol* (2020) 38:4317–45. doi:10.1200/jco.20.02672

9. Sauler M, Bazan IS, Lee PJ. Cell Death in the Lung: The Apoptosis-Necroptosis Axis. *Annu Rev Physiol* (2019) 81:375–402. doi:10.1146/annurev-physiol-020518-114320

10. Tang D, Kang R, Berghe TV, Vandenabeele P, Kroemer G. The Molecular Machinery of Regulated Cell Death. *Cell Res* (2019) 29:347–64. doi:10.1038/s41422-019-0164-5

11. Koren E, Fuchs Y. Modes of Regulated Cell Death in Cancer. *Cancer Discov* (2021) 11:245–65. doi:10.1158/2159-8290.Cd-20-0789

12. Dixon SJ, Lemberg KM, Lamprecht MR, Skouta R, Zaitsev EM, Gleason CE, et al. Ferroptosis: an Iron-dependent Form of Nonapoptotic Cell Death. *Cell* (2012) 149:1060–72. doi:10.1016/j.cell.2012.03.042

13. Mou Y, Wang J, Wu J, He D, Zhang C, Duan C, et al. Ferroptosis, a New Form of Cell Death: Opportunities and Challenges in Cancer. *J Hematol Oncol* (2019) 12:34. doi:10.1186/s13045-019-0720-y

14. Liang C, Zhang X, Yang M, Dong X. Recent Progress in Ferroptosis Inducers for Cancer Therapy. *Adv Mater* (2019) 31:e1904197. doi:10.1002/adma.201904197

15. Tan Y, Chen Q, Li X, Zeng Z, Xiong W, Li G, et al. Pyroptosis: a New Paradigm of Cell Death for Fighting against Cancer. *J Exp Clin Cancer Res* (2021) 40:153. doi:10.1186/s13046-021-01959-x

16. Tsvetkov P, Coy S, Petrova B, Dreishpoon M, Verma A, Abdusamad M, et al. Copper Induces Cell Death by Targeting Lipoylated TCA Cycle Proteins. *Science* (2022) 375:1254–61. doi:10.1126/science.abf0529

17. Jiang Y, Huo Z, Qi X, Zuo T, Wu Z. Copper-induced Tumor Cell Death Mechanisms and Antitumor Theragnostic Applications of Copper Complexes. *Nanomedicine (London, England)* (2022) 17:303–24. doi:10.2217/nnm-2021-0374

18. Yu Z, Zhou R, Zhao Y, Pan Y, Liang H, Zhang JS, et al. Blockage of SLC31A1-dependent Copper Absorption Increases Pancreatic Cancer Cell Autophagy to Resist Cell Death. *Cell Prolif* (2019) 52:e12568. doi:10.1111/cpr.12568

19. Gao W, Huang Z, Duan J, Nice EC, Lin J, Huang C. Elesclomol Induces Copper-dependent Ferroptosis in Colorectal Cancer Cells via Degradation of ATP7A. *Mol Oncol* (2021) 15:3527–44. doi:10.1002/1878-0261.13079

20. Polishchuk EV, Merolla A, Lichtmannegger J, Romano A, Indrieri A, Ilyechova EY, et al. Activation of Autophagy, Observed in Liver Tissues from Patients with Wilson Disease and from ATP7B-Deficient Animals, Protects Hepatocytes from Copper-Induced Apoptosis. *Gastroenterology* (2019) 156:1173–89. e5. doi:10.1053/j.gastro.2018.11.032

21. Saito A, Hayashi T, Okuno S, Ferrand-Drake M, Chan PH. Overexpression of Copper/zinc Superoxide Dismutase in Transgenic Mice Protects against Neuronal Cell Death after Transient Focal Ischemia by Blocking Activation of the Bad Cell Death Signaling Pathway. *J Neurosci* (2003) 23:1710–8. doi:10.1523/jneurosci.23-05-01710.2003

22. Grasso M, Bond GJ, Kim YJ, Boyd S, Matson Dzebo M, Valenzuela S, et al. The Copper Chaperone CCS Facilitates Copper Binding to MEK1/2 to Promote Kinase Activation. *J Biol Chem* (2021) 297:101314. doi:10.1016/j.jbc.2021.101314

23. Luo Q, Song Y, Kang J, Wu Y, Wu F, Li Y, et al. mtROS-mediated Akt/AMPK/mTOR Pathway Was Involved in Copper-Induced Autophagy and it Attenuates Copper-Induced Apoptosis in RAW264.7 Mouse Monocytes. *Redox Biol* (2021) 41:101912. doi:10.1016/j.redox.2021.101912

24. Ren X, Li Y, Zhou Y, Hu W, Yang C, Jing Q, et al. Overcoming the Compensatory Elevation of NRF2 Renders Hepatocellular Carcinoma Cells More Vulnerable to Disulfiram/copper-Induced Ferroptosis. *Redox Biol* (2021) 46:102122. doi:10.1016/j.redox.2021.102122

25. Jiang P, Gu S, Pan D, Fu J, Sahu A, Hu X, et al. Signatures of T Cell Dysfunction and Exclusion Predict Cancer Immunotherapy Response. *Nat Med* (2018) 24:1550–8. doi:10.1038/s41591-018-0136-1

26. Kulik L, El-Serag HB. Epidemiology and Management of Hepatocellular Carcinoma. *Gastroenterology* (2019) 156:477–91. doi:10.1053/j.gastro.2018.08.065

27. Ioannou GN. HCC Surveillance after SVR in Patients with F3/F4 Fibrosis. *J Hepatol* (2021) 74:458–65. doi:10.1016/j.jhep.2020.10.016

28. Carneiro BA, El-Deiry WS. Targeting Apoptosis in Cancer Therapy. *Nat Rev Clin Oncol* (2020) 17:395–417. doi:10.1038/s41571-020-0341-y

29. Kaur P, Johnson A, Northcote-Smith J, Lu C, Suntharalingam K. Immunogenic Cell Death of Breast Cancer Stem Cells Induced by an Endoplasmic Reticulum-Targeting Copper(II) Complex. *Chembiochem* (2020) 21:3618–24. doi:10.1002/cbic.202000553

30. Li Y, Liang R, Zhang X, Wang J, Shan C, Liu S, et al. Copper Chaperone for Superoxide Dismutase Promotes Breast Cancer Cell Proliferation and Migration via ROS-Mediated MAPK/ERK Signaling. *Front Pharmacol* (2019) 10:356. doi:10.3389/fphar.2019.00356

31. Vyas A, Duvvuri U, Kiselyov K. Copper-dependent ATP7B Up-Regulation Drives the Resistance of TMEM16A-Overexpressing Head-And-Neck Cancer Models to Platinum Toxicity. *Biochem J* (2019) 476:3705–19. doi:10.1042/bcj20190591

32. Gupta S. Cell Therapy to Remove Excess Copper in Wilson's Disease. *Ann N Y Acad Sci* (2014) 1315:70–80. doi:10.1111/nyas.12450

33. Lorincz MT. Wilson Disease and Related Copper Disorders. *Handb Clin Neurol* (2018) 147:279–92. doi:10.1016/b978-0-444-63233-3.00018-x

34. Chen J, Jiang Y, Shi H, Peng Y, Fan X, Li C. The Molecular Mechanisms of Copper Metabolism and its Roles in Human Diseases. *Pflugers Arch* (2020) 472:1415–29. doi:10.1007/s00424-020-02412-2

35. Li Y. Copper Homeostasis: Emerging Target for Cancer Treatment. *IUBMB Life* (2020) 72:1900–8. doi:10.1002/iub.2341

36. Singal AG, Lampertico P, Nahon P. Epidemiology and Surveillance for Hepatocellular Carcinoma: New Trends. *J Hepatol* (2020) 72:250–61. doi:10.1016/j.jhep.2019.08.025

37. Huang DQ, El-Serag HB, Loomba R. Global Epidemiology of NAFLD-Related HCC: Trends, Predictions, Risk Factors and Prevention. *Nat Rev Gastroenterol Hepatol* (2021) 18:223–38. doi:10.1038/s41575-020-00381-6

38. Antonucci L, Porcu C, Iannucci G, Balsano C, Barbaro B. Non-Alcoholic Fatty Liver Disease and Nutritional Implications: Special Focus on Copper. *Nutrients* (2017) 9:E1137. doi:10.3390/nu9101137

39. Porcu C, Antonucci L, Barbaro B, Illi B, Nasi S, Martini M, et al. Copper/MYC/CTR1 Interplay: a Dangerous Relationship in Hepatocellular Carcinoma. *Oncotarget* (2018) 9:9325–43. doi:10.18632/oncotarget.24282

40. Gunjan D, Shalimar, Nadda N, Kedia S, Nayak B, Paul SB, et al. Hepatocellular Carcinoma: An Unusual Complication of Longstanding Wilson Disease. *J Clin Exp Hepatol* (2017) 7:152–4. doi:10.1016/j.jceh.2016.09.012

41. Huo J, Cai J, Guan G, Liu H, Wu L. A Ferroptosis and Pyroptosis Molecular Subtype-Related Signature Applicable for Prognosis and Immune Microenvironment Estimation in Hepatocellular Carcinoma. *Front Cel Dev Biol* (2021) 9:761839. doi:10.3389/fcell.2021.761839

42. Liu Z, Wang L, Liu L, Lu T, Jiao D, Sun Y, et al. The Identification and Validation of Two Heterogenous Subtypes and a Risk Signature Based on Ferroptosis in Hepatocellular Carcinoma. *Front Oncol* (2021) 11:619242. doi:10.3389/fonc.2021.619242

43. Yang H, Jiang Q. A Multi-Omics-Based Investigation of the Immunological and Prognostic Impact of Necroptosis-Related Genes in Patients with Hepatocellular Carcinoma. *J Clin Lab Anal* (2022) 36:e24346. doi:10.1002/jcla.24346

44. Shi WK, Zhu XD, Wang CH, Zhang YY, Cai H, Li XL, et al. PFKFB3 Blockade Inhibits Hepatocellular Carcinoma Growth by Impairing DNA Repair through AKT. *Cell Death Dis* (2018) 9:428. doi:10.1038/s41419-018-0435-y

45. Chen DP, Ning WR, Jiang ZZ, Peng ZP, Zhu LY, Zhuang SM, et al. Glycolytic Activation of Peritumoral Monocytes Fosters Immune Privilege via the PFKFB3-PD-L1 axis in Human Hepatocellular Carcinoma. *J Hepatol* (2019) 71:333–43. doi:10.1016/j.jhep.2019.04.007

46. Matsumoto K, Noda T, Kobayashi S, Sakano Y, Yokota Y, Iwagami Y, et al. Inhibition of Glycolytic Activator PFKFB3 Suppresses Tumor Growth and Induces Tumor Vessel Normalization in Hepatocellular Carcinoma. *Cancer Lett* (2021) 500:29–40. doi:10.1016/j.canlet.2020.12.011

47. Long Q, Zou X, Song Y, Duan Z, Liu L. PFKFB3/HIF-1α Feedback Loop Modulates Sorafenib Resistance in Hepatocellular Carcinoma Cells. *Biochem Biophys Res Commun* (2019) 513:642–50. doi:10.1016/j.bbrc.2019.03.109

48. Dai W, Wang Y, Yang T, Wang J, Wu W, Gu J. Downregulation of Exosomal CLEC3B in Hepatocellular Carcinoma Promotes Metastasis and Angiogenesis via AMPK and VEGF Signals. *Cell Commun Signal* (2019) 17:113. doi:10.1186/s12964-019-0423-6

49. Xie XW, Jiang SS, Li X. CLEC3B as a Potential Prognostic Biomarker in Hepatocellular Carcinoma. *Front Mol Biosci* (2020) 7:614034. doi:10.3389/fmolb.2020.614034

50. Mao X, Zhou L, Tey SK, Ma APY, Yeung CLS, Ng TH, et al. Tumour Extracellular Vesicle-Derived Complement Factor H Promotes Tumorigenesis and Metastasis by Inhibiting Complement-dependent Cytotoxicity of Tumour Cells. *J Extracell Vesicles* (2020) 10:e12031. doi:10.1002/jev2.12031

51. Fu Y, Liu S, Zeng S, Shen H. From Bench to Bed: the Tumor Immune Microenvironment and Current Immunotherapeutic Strategies for Hepatocellular Carcinoma. *J Exp Clin Cancer Res* (2019) 38:396. doi:10.1186/s13046-019-1396-4

52. Cheng AL, Hsu C, Chan SL, Choo SP, Kudo M. Challenges of Combination Therapy with Immune Checkpoint Inhibitors for Hepatocellular Carcinoma. *J Hepatol* (2020) 72:307–19. doi:10.1016/j.jhep.2019.09.025

53. Zhou G, Sprengers D, Boor PPC, Doukas M, Schutz H, Mancham S, et al. Antibodies against Immune Checkpoint Molecules Restore Functions of Tumor-Infiltrating T Cells in Hepatocellular Carcinomas. *Gastroenterology* (2017) 153:1107–19. e10. doi:10.1053/j.gastro.2017.06.017

On-Target Side Effects of Targeted Therapeutics of Cancer

József Tímár[1]* and Andrea Uhlyarik[2]

[1]Departments of Pathology, Forensic and Insurance Medicine, Semmelweis University, Budapest, Hungary, [2]Internal Medicine and Oncology, Semmelweis University, Budapest, Hungary

The concept of precision medicine is based on the identification of hallmarks of cancer to exploit them as drug targets. The basic idea was that in this way the therapeutic modalities will be more effective and the side effects will be less. Since the majority of these novel modalities are not specific for a cancer-related biological process or a cancer-specific (mutant) target protein, it is not a surprise that we had to learn new type of side effects, because these therapeutics also affect physiological or pathological processes. Even more, in cases of some of these novel therapies we were able to discover new molecular mechanisms of physiological and pathological processes. Identification of the on-target side effects of targeted drugs can help to prevent the development of them or better manage the patients when emerge during cancer therapy.

Keywords: immunotherapy, target therapy, bone therapy, angiogenesis inhibitor, side effect, pathomechanism

INTRODUCTION

Precision medicine emerged on the basis of genetic characterization of various cancers, establishing molecular classifications paving the way for the development of various target therapies. Major aim was to design more tumor-specific therapies to spare normal tissues. Today the majority of precision medicine drugs are not specific for mutant targets of the cancer cells since they are active on wild type targets as well, opening the way for the development of the so-called on-target side effects. Although, some of the novel targeted drugs are selective for mutant targets, they can affect wild type ones as well. This is especially true for angiogenesis inhibitors, bone metastasis inhibitors or the new immune checkpoint inhibitors. Herein we summarize the on-target side effects of the target therapies and the underlying pathological or molecular mechanisms behind them, since recognition of those mechanisms can prevent side effect development or can help to manage of them.

ANGIOGENESIS INHIBITORS

It is one of the hallmark of cancer that it can provide its own vascularization beyond the growth of one mm^3 (1). Cancer tissue vascularization mechanism has various forms but most frequently involves neoangiogenesis. Major trigger and regulator of this process is the cancer hypoxia (either true or mimicked) directed by HIF transcription factors activities leading to production of angiogenic cytokines, mainly VEGFA (1). When the basic pathomechanism was revealed new therapeutic approaches have been developed to neutralize VEGF or inhibit the tyrosine kinase activity of its receptors VEGFR1/2. Interestingly, while these novel anti-angiogenic agents were able to fulfill the expectations by inhibiting tumor induced neoangiogenesis in preclinical models, but they were not able to do it in cancer patients, rather their effect was mainly the "normalization" of the tumor's aberrant vasculature (2) Meanwhile, novel unforeseen side effects emerged upon such therapies:

FIGURE 1 | Capillary proliferation in chronic inflammation. **(A)** Proliferating fibroblasts and capillaries in granulation tissue. HE staining. Bar: 100 μm. **(B)** Immunohistochemical labeling of endothelial cells in granulation tissue. Note that beside small capillaries, individual endothelial cells are also present. CD34 immunolabeling. Bar: 200 μm. With permission of Hungarian Society of Clinical Oncology (5).

FIGURE 2 | Histology of bone metastasis of breast cancer. **(A)** HE staining. **(B)** Osteoclast labeling of bone metastasis. Tartarate-resistant acid phosphatase reaction. Bars: 200 μm. With permission of Hungarian Society of Clinical Oncology (5).

bleeding, wound healing disturbances, hypertension and the question immediately raised if those side effects are on-target ones?

Bleeding and Thromboembolic Event

Production and the physiological distribution of VEGF was not known before. When the biodistribution of anti-VEGF antibodies was analysed in human, it was noted that it stays in the circulation for hours and it was found to be incorporated into platelets. These studies identified platelets as the largest VEGF depo in the body, which fact explains why anti-VEGF antibody therapies disturb platelet functions and cause bleeding and thrombotic events (3).

Other characteristic side effect of the anti-angiogenic agents is arterial thrombotic events, the pathomechanism of which is different form the above mentioned one. These agents has a strong effect on normal microcapillary systems and have an endothelial- and a pericyte-dependent component leading to the loss of vasodilatation potential. Furthermore, angiogenesis inhibitors, especially the so called multikinase ones, are characterized by depletion of pericytes in microcapillaries, most probably due to the inhibition of PDGFR activities.
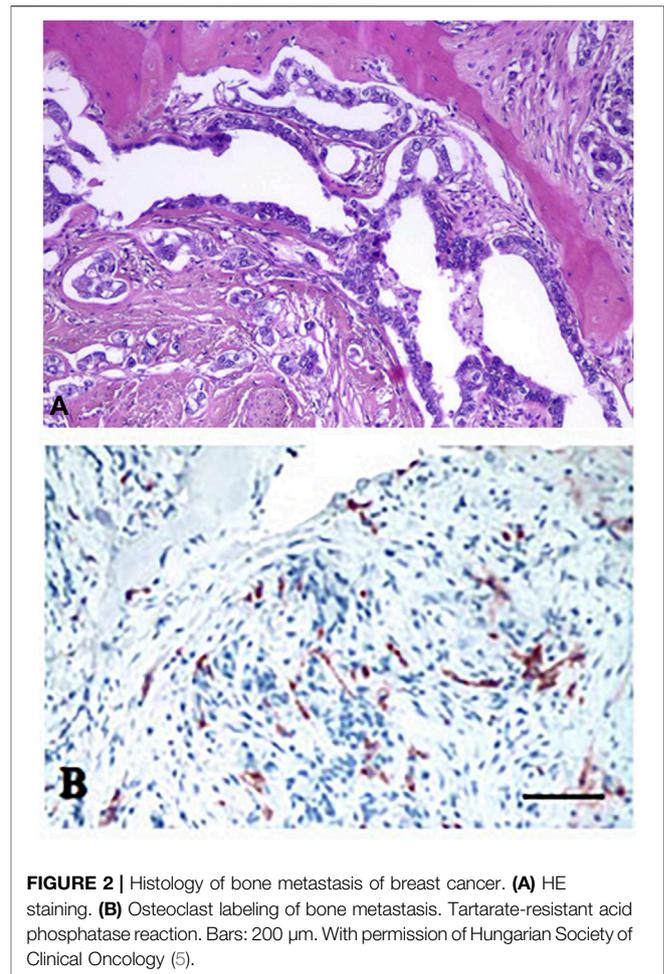
These combined effects on endothelial cells and pericytes, increase the risk of rupture of atherosclerotic plaques leading to thrombotic complications upon therapies (4).

Wound Healing Disturbances

Mechanical injuries to various tissues, especially surgical wounds are healed by formation of granulation tissues. Which is composed of proliferating capillaries, fibroblasts and chronic inflammatory cells (**Figure 1**.) and the wound is replaced by novel vascularized connective tissue. Although angiogenesis inhibitors are unable to inhibit tumor-induced neoangiogenesis, they are effective inhibitors of the sprouting type capillarogenesis, which will lead to wound healing disturbances in cancer patients (1).

Hypertension

Hypertension is a classical side effect of angiogenesis inhibitors, but the anti-VEGF agents are better from this aspect than the VEGFR inhibitors. In experimental models it was shown that anti-VEGF agents induce acute hypotension which can be treated by NOS inhibitors. On the other hand, studies revealed that the developing hypertension in treated cancer patients is due to the decreased capillary densitiy of the
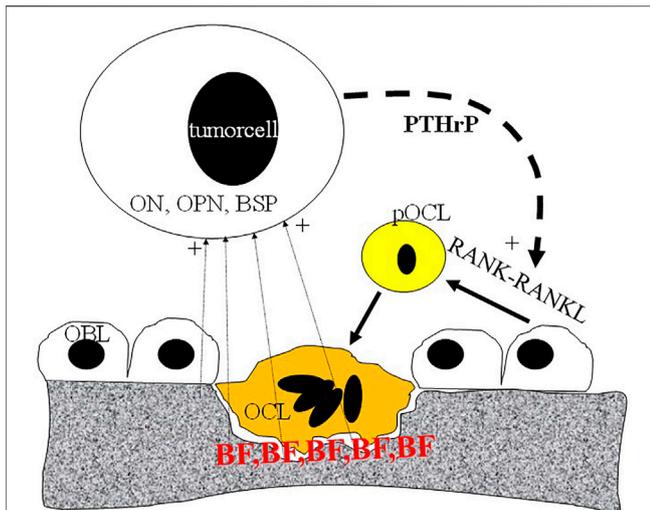
FIGURE 3 | Schematic representation of metastatic tumor cell-bone tissue interaction. Tumor cells produce PTHrP (parathromone-like protein) as well as bone-specific matrix components osteopontin (OPN), osteonectin (ON) and bone sialoprotein (BSP). PTHrP stimulate osteoblasts (OBL) to differentiate into pre-osteoclast (pOCL) mediated by the RANKL/RANK receptor system. Ultimately activated osteoclasts degrade the mineralized bone tissue which process is blocked by bisphosphonates (BP) deposited into the bone tissue.

renal medulla, again providing evidence for the characteristic effects on microcapillaries (6).

HIF2a Inhibitor: Anemia

Recently a novel class of anti-angiogenic agents entered into clinical practice: the HIF2a inhibitor, belzutifan. This novel drug is designed to block HIF2a activity and prevents the induction of specific HIF-regulated genes such as VEGFA, EPO, GLUT1 but leaves unaffected CA9 or LDHA (regulated by HIF1a) (7). This drug obtained FDA approval in VHL-syndrome patients with cRCC, CNS-hemangioblastoma or pancreatic NET (8). Belzutifan is efficiently inhibits VHL-mutated tumor growth, but blocking of EPO expression by belzutifan results in treated patients decreased RBC count, HgB levels and consequent systemic hypoxia (9). Due to the mechanism of action of this drug, the use of erythropoetin stimulating agents is contraindicated to treat these side effects.

BONE METASTASIS INHIBITORS: BISPHOSPHONATES AND ANTI-RANKL ANTIBODIES

Development of bone metastasis of various cancers has a common pathomechanism: cooperative interaction of cancer cells with the bone microenvironment as well as with osteoblasts and more importantly osteoclasts (**Figure 2**). Cancer cells which are capable for bone metastassis formation are producing PTHrP, which promotes osteoclast differentiation and activity through the RANK/RANKL receptor system (**Figure 3**). Based on this mechanism, two types of therapies

have been developed, and both are targeting osteoclasts: anti-RANKL antibodies and bisphosphonates (BF). The latest drug types have been designed to target osteoclasts, since they accumulate preferentially in mineralized bones. Bisphosphonates form ATP-conjugates and this way they block activation of osteoclast in bone resorption and induce their apoptosis. The second generation bisphosphonates (amino-BF) have another mechanism of action, they are effective prenylation inhibitors by this secondary activity they activate macrophages and T cells resulting in the increased TNFa and IL-6 levels (10). These differences in mechanism of action are important to understand the development of side effects upon their application (11).

Both bisphosphonates and anti-RANKL antibodies induce therapy resistant osteonecrosis (12, 13). The cause of that particular side effect is the inhibition of osteoclast activities necessary for bone remodeling and regeneration. Such processes are very active in case of acute periodontitis which can turn into massive osteonecrosis upon bone metastasis inhibitor treatment (14).

Use of aminobisphosphonates can result in the development of another type of side-effect: fever and acute phase reaction. Caused by activation of macrophages and release of inflammatory cytokines. On the other hand, in case of anti-RANKL antibody therapies infections may emerge due to the fact that these antibodies accumulate in lymph nodes as well, where their inhibitory effect on macrophages may result in the inhibition of acute inflammatory responses (9, 10). Today, bone metastasis therapies can be combined with anti-angiogenic therapeutics which further increase the risk of development of osteonecrosis, since bone remodeling and regeneration in case of periodontitis requires also formation of novel capillaries (12, 13, 14).

IMMUNE CHECKPOINT INHIBITORS

Discovery of immune checkpoints revolutionized the way we think about immune regulation. In case of adaptive immunity the regulatory phase seems to be equally important as compared to stimulatory phase, since that ensures the development of immune tolerance. This process is regulated by immune checkpoints, PD1, TIGIT, TIM-3, CD-200R1, BTLA, VISTA, LAG-3 and CTLA-4 expressed by activated T cells while their ligands are expressed mostly by dendritic cells and T cells, but some of them can be expressed by peripheral non-immune cells as well (PDL1/2, CD-200 or PSGL1). The role of CTLA-4 is to block antigen presentation by inhibiting the activation of CD28 and preventing IL-2 production. CTLA-4 is also expressed by Treg cells maintaining long lasting immunotolerance. Expression of PD1 is relatively broader, since beside T cells, it is expressed by B cells, NK cells and macrophages (15). Knocking out PD1 in animal models results in the development of lupus-like systemic autoimmune diseases, On the other hand, knocking out CTLA-4 in animals, leads to more fatal autoimmune diseases as compared to PD-1 knockouts (16, 17). Since immune checkpoints play a crucial role in anti-tumoral immune responses, the introduction

TABLE 1 | Autoimmune side effects of the immuncheckpoint inhibitors. (see refs. (17-27)).

	Anti-PD1/anti-PDL1 antibodies	Anti-CTLA4 antibody	Combination
Dermatitis	+	+	+
Colitis	+	+	+
Pneumonitis	+		+
Endocrinopathy	+ (thyreoiditis)	++ (hypophysitis)	++
Hepatitis	+	+	++
Myocarditis			+
Autoimmune events of the nervous system		+	+
Arthritis	+		+

of immune checkpoint inhibitors revolutionized cancer management, but resulted in the emergence of a new class of side effects, autoimmune diseases.

Anti-CTLA4 Antibody Therapy

Administration of Ipilimumab (anti-CTLA-4 antibody) to cancer patients induces dose dependently immune-related adverse events (irAE), at higher doses the frequency of grade >3 events is 37% while at lower doses 18%, developing after 2–3 months of therapy. The most frequent irAE is colitis, but dermatitis, hepatitis, endocrinopathies (thyreoiditis, hypophysitis) are also prevalent. Interestingly, at lower rate myasthenia gravis, uveitis, ganglionopathies or even autoimmune thrombocytopenia can also occur (18).

Anti-PD-1 Antibody Therapies

The serious irAE incidence of anti-PD1 therapies is lower as compared to anti-CTLA-4 (grade >3irAE <10%), but unfortunately they can occur later, can be long lasting, and more difficult to treat. Forms of these autoimmune diseases are similar to anti-CTLA-4 therapy, except arthritis and pneumonitis (19, 20).

Anti-PDL1 Antibody Therapies

The irAE incidence of these therapies is lower as compared to anti-PD1, since this type of treatment does not affect the PDL2/PD1 axis and for example the incidence of pneumonitis is half as compared to anti-PD1 therapies (21, 22, 23).

Anti-CTLA4 and anti-PD1 Combination Therapies

Although the anti-tumor efficacy of this combination immunotherapy is much higher, it also increase the incidence rate of irAE which are also more serious as compared to monotherapies. The most frequent forms are colitis, dermatitis, endocrinopathies and hepatitis (24, 25). In NSCLC patients in the combination arm myocarditis, pneumonitis and renal insufficiency predominated (26, 27, 28). A summary of irAEs of immune checkpoint inhibitors is presented on **Table 1**.

Dermatitis

This is one of the most frequent irAE in case of checkpoint inhibitor therapies and occurs as lichenoid or spongiotic form. Extreme forms are involve more than 30% of the body surface.
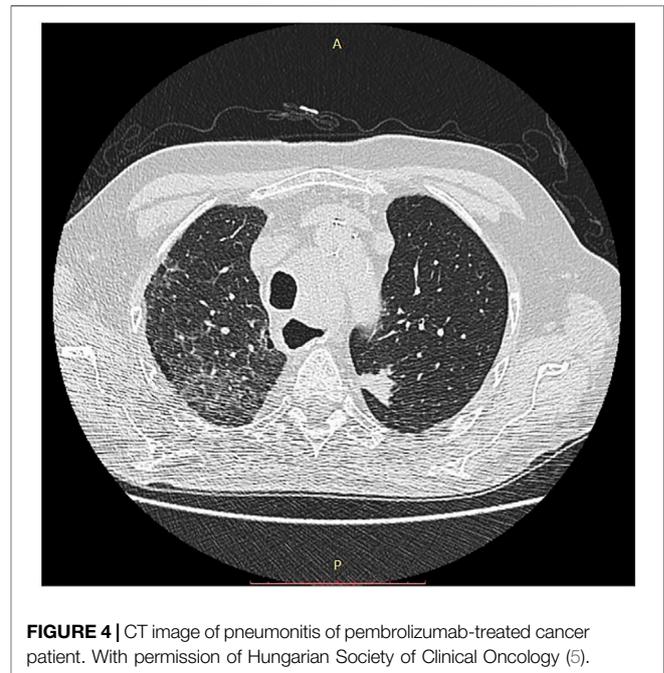
FIGURE 4 | CT image of pneumonitis of pembrolizumab-treated cancer patient. With permission of Hungarian Society of Clinical Oncology (5).

The autoimmune inflammation takes place at the interface of the epidermis-dermis and involves the accessory organs of the dermis (hair bulb and sweat glands). The incidence of cutaneous inflammations in psoriatic patients is more frequent but the treatment also activate the original disease. Frequently the autoimmune inflammation also involves mucosal surfaces as well (18, 19, 20, 21, 22, 23, 24, 25, 26, 27, 28).

Colitis

This inflammation type is also very frequent in immune checkpoint inhibitor therapies, especially in case of anti-CTLA-4 antibody administration. It appears as ulcerative colitis with epithelial damage and crypt abscess infiltrated by mixed immune cells (leukocytes and lymphocytes). The severity of the inflammation must be determined from colonic biopsy specimen. In case of the predominant ulcerations, massive anti-inflammatory treatment can be necessary. The key factor behind this induced autoimmune disease is the depletion of the mucosal Treg cells, which is more prevalent in patients with CTLA-4 polymorphism (Y60C). Interestingly, the pathomechanism of the

anti-PD1/PDL1 antibody treatment induced enteritis is different, since all inflammatory cells overexpress PD1. Furthermore, the composition of the patient's microbiome is also an important factor, since the incidence of colitis is higher in those patients where their microbiome is lacking bacteria which are poliamine transport- or B vitamin biosynthesis negatives (18, 19, 20, 21, 22, 23, 24, 25, 26, 27, 28).

Pneumonitis

Autoimmune disease of the lung as irAE is the characteristics of the anti-PD1/PDL1 therapies and is more frequent in the COPD patients. The pathological spectrum is broad from ARDS and interstitial pneumonitis to sarcoidosis-like forms. Among fatal irAE pneumonitis is the leading cause, therefore early diagnosis is very important. Beside COPD other predisposing factors are smoking, and previous chemo- or radiotherapy. The bronchioalveolar lavage used to be lymphocyte-rich where the physiological ratio of CD4/CD8 is changed significantly (18, 19, 20, 21, 22, 23, 24, 25, 26, 27, 28) (**Figure 4**).

Endocrinopathies

Hypophysitis is a novel autoimmune disease specific for immune checkpoint inhibitor therapies, especially of the anti-CTLA-4 one. This is an acute inflammation of the anterior lobe of the hypophysis which may lead to compression of the chiasma opticum. Peripheral consequences of the hypophysitis can be adrenal gland insufficiency, thyroid dysfunction or gonadal insufficiencies. In this autoimmune complication one can detect circulating autoantibodies against TSH-, FSH- or ACTH-producing cells. It is also important that the TSH- and prolactin-producing cells spontaneously express CTLA-4. It is also important, that the inflammation takes place in form of type-II hypersensitivity reaction. It is also interesting that in case of anti-PD1/PDL1 therapies there is another target organ which the thyroid. These therapies initially inducing hyperfunction which later turn into hypothyreosis (18, 19, 20, 21, 22, 23, 24, 25, 26, 27, 28).

Hepatitis

Administration of immuncheckpoint inhibitors, especially in combination, frequently results in hepatitis diagnosed by increased (>3x) transaminase levels, when biopsy is indicated. Histopathologically it is characterized by panlobular inflammation which is accompanied by focal or confluent hepatocyte necrosis. It can appear as lobular granulomatous inflammation, when histiocytes accumulate around lipid vacuoles and fibrin (18, 19, 20, 21, 22, 23, 24, 25, 26, 27, 28).

Myocarditis, Myositis

This is a rare form of irAE in case of immunecheckpoint inhibitor therapies but among fatal cases it is relatively more frequent. Histologically myocarditis is characterized by an inflammatory exudate rich in T cells, but lacking immuncomplex deposition. In a small proportion of treated patients myositis may also occur, which can lead to myasthenia gravis and necrosis of muscles. Histologically, there is a peri- and endomysial mixed inflammatory exudate of T-, B-cells and macrophages,

however, anti-AchR or myositis-autoantibodies are missing (18, 19, 20, 21, 22, 23, 24, 25, 26, 27, 28).

Neurological Autoimmune Diseases

Administration of checkpoint inhibitors may induce autoimmune reactions in the CNS in form of aseptic meningitis or encephalitis. Since the symptoms can be indispensable from CNS metastasis the diagnosis is very important based on the examination of the liquor or serum since in this irAE autoantibodies can be detected against NMDA receptor, contactin-associated protein-2 or Hu protein. Autoimmune inflammation can also be induced in the peripheral nerves affecting the neuromuscular junction or the nerves itself leading to demyelinization (18, 19, 20, 21, 22, 23, 24, 25, 26, 27, 28).

Autoimmune Adverse Events as Predictive Markers of the Efficacy of Checkpoint Inhibitor Therapies

Since immuncheckpoint inhibitors are not cancer-specific or selective treatments, they enhance the activity of the entire adaptive immune system resulting in the above mentioned autoimmune adverse events. That was the reason, why it was proposed that the autoimmune adverse events can be used as positive predictive marker for anti-cancer efficacies of these therapies. Such studies mostly done in case of melanoma, which demonstrated that emergence of early immunological adverse events (after 12 weeks) significantly associated with overall survival and it has an independent predictive power (29, 30). A meta-analysis of ICI-treated cancer patients indicated that the OS and PFS of those patients who has irAE is significantly longer (31). It is of note, that not all type of irAE has such a predictive value, but dermatitis, endocrinopathy and colitis, exclusively. In case of melanoma patients it was an early observation that upon ICI treatment vitiligo may appear in the dermis and this clinical feature may be used also as a positive predictive marker (32). This side effect is based on the fact that melanocytes and melanoma cells share several common protein markers, mostly melanosome-associated ones, therefore the antitumoral immune response can be also anti-melanocyte one.

ONCOGENE TARGETED THERAPIES

Anti-HER-2 Antibodies and HER-2 Inhibitors

Identification of the molecular subclass of breast cancer, the HER-2 amplified form, initiated a revolutionary change in the treatment of this cancer, originally using anti-HER-2 antibodies, later complementing it with small molecular TK inhibitors (33). However, it was early discovered that the administration of these therapies has a unique side effect, the cardiotoxicity due to decreased left ventricle ejection fraction. Furthermore, it was clear that the risk of cardiotoxicity dramatically increases when this type of target therapy is combined with the commonly used chemotherapy, antracyclins. Studies revealed that HER-2 and EGFR4 receptors play a crucial role in
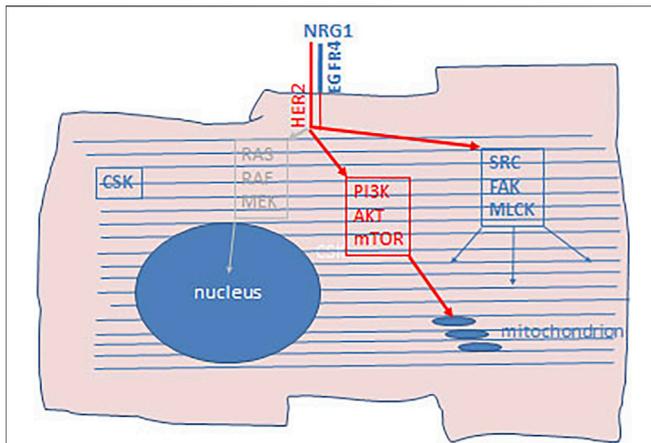
FIGURE 5 | Schematic presentation of cardiotixicity pathway of HER-2 inhibitors. Cardiomyocytes express HER-2/EGFR4 aspecially in hypoxic condition as well as neuregulin-1 (NRG1). In adult differentiated cardiocytes the RAS-RAF-MEK mitotic arm of this signaling pathway does not operational. Upon HER-2 inhibition PI3K/AKT/mTOR arm of the signaling pathway is blocked which activate mitochondrial apoptotic pathway. Furthermore, since the SRC/FAK/MLCK arm of this signaling pathway is also blocked, regeneration of the actomyosin complex is also inhibited. CSK, cytoskeleton.

FIGURE 6 | Demonstration of the presence of epirubicin (red autofluorescence) in SCID mice after 5 min of i.v. administration using fluorescence microscopy of frozen sections. **(A)** Subcutaneously growing human breast cancer tumor tissue. Note the red fluorescence of the tumor cell nuclei. Bar: 200 µm. **(B)** Cardiac muscle tissue. Note the red fluorescence in the nuclei of the cardiomyocytes. Bar: 400 µm. With permission of Hungarian Society of Clinical Oncology (5).

cardiomyocytes (34). HER-2 receptor is a ligand-less kinase receptor, whereas EGFR4 has ligand which is NRG1 in case of myocardium. The NRG1-EGFR-4/HER-2 receptor complex and the associated signaling pathway plays a key role during embryonal development of the heart. In adults, this receptor complex is involved in the everyday function of the heart muscle, in the accomodative hypertrophy and muscle cell survival upon various form of stress. In other cell types activation of HER-2 results in the activation of the mitotic signaling pathway (RAS-MEK-ERK), but not in cardiomyocytes. In differentiated cardiomyocytes the HER-2/EGFR4 signaling pathway activates the lipidkinase (PI3K/AKT) and the SRC/FAK arm of that pathway. The target of the lipidkinase pathway activation is the NOS-system, to decrease the production of free radicals, stimulate the β-adrenergic activity and block apoptotic pathways. Stimulation of the SRC/FAK pathway is responsible for actomyosin function by the activation of MLCK (**Figure 5**). Blocking of HER-2 decreases the NOS activity thereby increasing ROS levels leading to disturbed mitochondrial function in cardiomyocytes. Furthermore, HER-2 blocking and the inhibited PI3K/AKT activity induces the intrinsic mitochondrion-related apoptotic pathway by increasing BCL2 and decreasing BCL-XL levels. Histologically, swelling of the mitochondria in cardiomycytes is a hallmark of this effect. On the other hand, decreased MLCK activity promote disintegration of the actomyosin complex, also recognizable by histology (33, 34).

As mentioned before, the risk of cardial side effects is higher when anti-HER-2 therapies are combined with antracyclin chemotherapy of breast cancer. One of the main cause of the cardiotoxicity of antracyclins is the fact that this drug rapidly accumulate in the nuclei of cardiomyocytes (since this is a DNA-binding molecule) of the well-perfused heart after i.v. administration (**Figure 6**). Antracyclins induce vacuolar degeneration and cell necrosis, irreversible damages in the heart muscle, while the effects of the anti-HER2 therapies is reversible in heart muscle, therefore after suspension of the administration of the targeted drugs cardiac functions usually improve. The antracyclin-induced cardiotoxicity (cell stress) activates the NRG1/EGFR4/HER2 receptor complex, which improves the survival of the cardiomyocytes. However, when the two drugs are combined, the adaptive potential of the heart muscle decreases leading to irreversible myocyte damages (apoptosis and necrosis) (35).

EGFR Inhibitors

EGF is the most important regeneratory ligand of the skin epithelia, but it is also involved in maintenance of the integrity of the epidermis and the function of the accessory glands. EGF acts through the EGFR1 receptor, which is therefore constitutively expressed by the epithelial cells (**Figure 7**). Anti-EGFR antibody- and EGFR-TK inhibitor therapies are all characterized by inducing dry skin, acneiform rashes, and

FIGURE 7 | Demonstration of skin rash induced by anti-EGFR treatment (Cetuximab) of colorectal cancer patient. **(A)** EGFR1 protein in dermal epithelium of frozen section of the human skin using anti-EGFR antibody (cytoplasmic domain) and FITC labelled secondary anti-mouse antibody. Note the intense labeling of the epithelial cells (green fluorescence). Bar: 100 µm. **(B)** Macrosopic picure of skin rash. With permission of Hungarian Society of Clinical Oncology (5).

FIGURE 8 | Histology of skin tumors induced by BRAF inhibitor therapy of melanoma patients. **(A)** Keratoacantoma. Bar: 400 µm. **(B)** Squamous carcinoma. HE staining. Bar: 200 µm. With permission of Hungarian Society of Clinical Oncology (5).

decrease in the defense function leading to infections (36). One of the consequence of this is the bacterial folliculitis. Since the growth of nails is also governed by EGF/EGFR1, it is not much a surprise that these therapies induce paronychia, inflammation of the periungual tissues. Hair growth is also regulated by EGF/EGFR1, accordingly, the anti-EGFR therapies has significant side effects. Since EGFR1 is the initiator of the growth phase (anagen) of hair, significant disturbances occur upon therapeutic inhibition leading to folliculitis and follicular necrosis as well as alopecia. Although these side effects used to be low grade, but can lead to the dose-decrease of these drugs. The first generation EGFR TK inhibitors are not mutation selective unlike the second and third generation ones, where the incidence of these skin toxicities is much lower (37).

BRAF Inhibitors

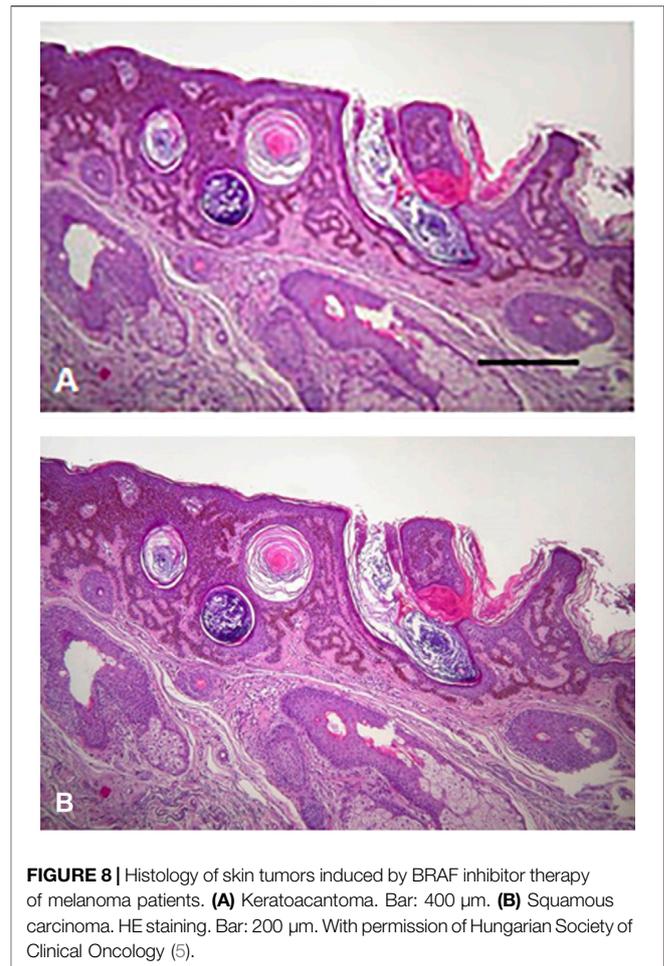BRAF mutant tumors (melanoma, lung adenocarcinoma anaplastic thyroid- or colon cancer) can be treated by BRAF inhibitors (38). Although these tumors used to respond well to such a target therapy, this type of drugs were the first where upon administration of a target therapy for one cancer type induced the development of another(39, 40). In melanoma patients treated with BRAF inhibitors a characteristic side effect can be observed with high frequency, development of benign epithelial tumors (keratoacantoma, papilloma) or malignant ones (squamous cancer) (**Figure 8**) as well as new nevi or induced novel melanomas. However, these tumors can easily be detected and treated appropriately. Unfortunately, BRAF inhibitors can induce other cancer types as well, such as head and neck-, colorectal cancer or glioblastoma.

BRAF inhibitors designed as mutant-selective small molecular inhibitors but they have an inhibitory effect on the wild type protein as well. In normal cells BRAF inhibitors induce the activation of the MAPK pathway, due to the induced homo-or heterodimer formation of wild type C-RAF or BRAF. Today BRAF inhibitors are used frequently in combination with MEK inhibitors, in that case of this paradoxical MAPK activation is less frequent. It is interesting, that in RAS mutant premalignant lesions this MAPK activation finalizes the carcinogenic process (**Figure 9**). As a result, HRAS mutant squamous- and head and neck cancers, NRAS mutant novel melanomas or
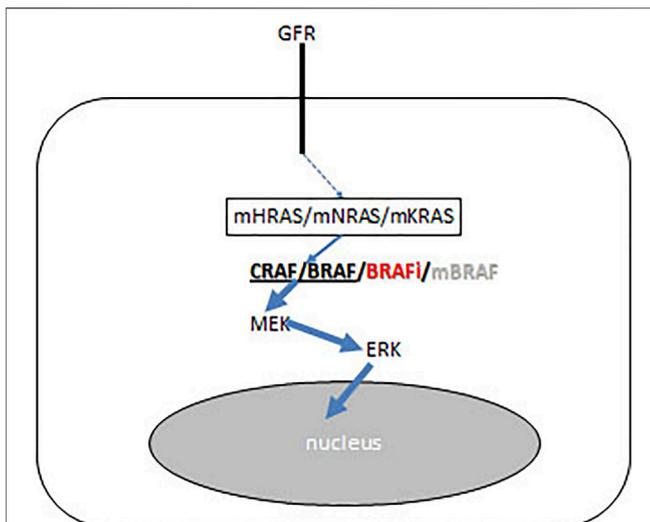
FIGURE 9 | Schematic presentation of BRAF inhibitor effect on the growth factor receptor (GFR) signaling pathways of precursor cancer cells where carcinogenesis iniciated by RAS mutation (KRAS/NRAS/HRAS). BRAF inhibitor induces CRAF/BRAF homo- and heterodimerisation and activates the RAF-MEK ERK mitogenic signaling pathway. Arrow thickness represents signal intensities.
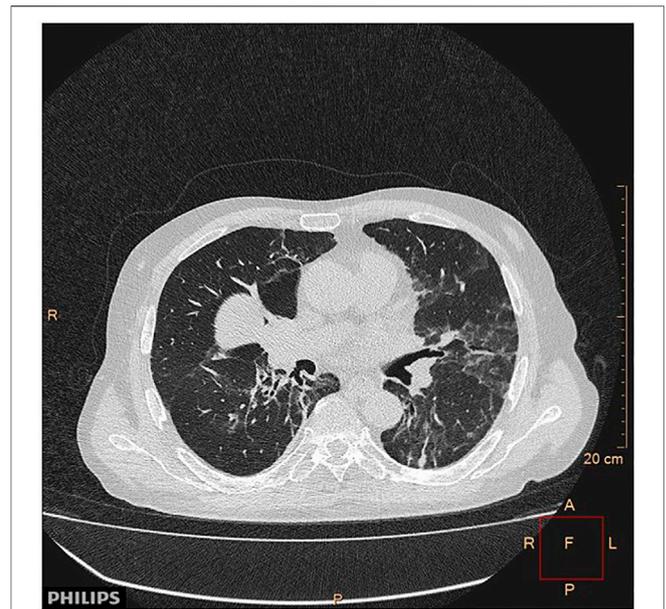

FIGURE 10 | CT image of the pneumonitis caused by everolimus treatment of cancer patient. With permission of Hungarian Society of Clinical Oncology (5).

myelomonocytic leukemia and KRAS mutant colorectal cancers could be developed upon BRAF inhibitor therapies (38, 39, 40).

Multikinase Inhibitors

Advent of target therapy started with the development of ABL inhibitors for BCR-ABL fusion positive CML. The original first generation but even the later generation ABL inhibitors are still "dirty" drugs in a sense that they inhibit other kinases especially KIT. Since KIT is the master regulator of the bone marrow progenitor cells, the administration of these non-specific ABL inhibitors results in myelosupression (41, 42). Furthermore, this type of side effect characterizes also any type of KIT inhibitor. Furthermore, KIT is the master regulator of melanocyte differentiation, accordingly KIT inhibitors induce vitiligo and hair color changes (40).

Multikinase inhibitors are now widely used in several cancer types and most of them has VEGFR2 and or PDGFR inhibitory activity. Accordingly, the typical side effects of the angiogenesis inhibitors, such as bleeding and thromboembolism can be considered on-target side effects.

It is a novel class of multikinase inhibitors, the ALK inhibitors which are most effective in ALK-fusion positive lung adenocarcinoma. ALK inhibitors also have significant side effects such as pneumonitis, neurological-, cardiological-, gastrointestinal-, and urogenital toxicities but none of them was shown to be considered as on-target ones (43).

However, this cannot be applied to the new TRK inhibitors which are registered in TRK-fusion positive malignancies. TRK inhibitors have three targets, TRK-A, TRK-B and TRK-C which differ in ligands and functions. NGF is the ligand of TRK-A, BDNF and neurtrophin-4 are ligands for

TRK-B while neurotrophin-3 is the ligand of TRK-C. These receptors are key regulators of the development of the nervous system. Since TRK-inhibitors are registered as tumor-agnostic therapies, it is important to consider that the development of the nervous system is ongoing in children till age two, therefore in case of TRK-fusion positive pediatric tumors the unique side effect profiles of those inhibitors must be considered. On the other hand, TRK inhibitor administration in adults can also lead to neurological toxicities and uniquely pain after cessation of therapy (44). This side effect is a typical "on-target" side effect since sensory nerves express TRK-A and NGF is an important modulator of pain. Furthermore, TRK receptors are important in various functions of ganglion cells of CNS as well, accordingly dizziness, cognitive dysfunctions or ataxia all have to be considered "on-target" side effects.

PI3K/AKT/mTOR Inhibitors

The PI3K/AKT/mammalian target of rapamycin (PI3K/AKT/mTOR) signaling pathway plays a key role in many cellular function. The inhibitors of this signaling pathway could be divided into five subgroups, as follows: panPI3K inhibitors, dual PI3K/mTOR inhibitors, PI3K isoform-specific inhibitors, AKT inhibitors, and mTOR inhibitors. The pathomechanism of the side effects are not completely clear in all instances, but as mTOR inhibitors are immunosuppressors, such an effect must always be considered in cancer patients. Inhibition of the different PI3K isoforms could cause different side effects, but some of them should be considered as class-effect of these drugs (45). Most of the adverse events are dose dependent, but sometimes they are idiosyncratic and unpredictable (46).

Hyperglycemia

The PI3K/AKT/mTOR signaling pathway is one of the key effector of the insulin receptor (IR) and insulin receptor substrate proteins (IRS), and therefore it is an important regulator of the effect of insulin. The PI3K/AKT/mTOR axis regulate many targets, such as glycogen synthase kinase 3β (GSK3β) and the forkhead box protein O1 (FoxO1). These effectors increase the glycogen synthesis, and inhibit the gluconeogenesis, therefore lower the blood glucose level. It is not a surprise accordingly, that hyperglycemia is one of the more frequent adverse effect of PI3K/AKT/mTOR inhibitor treatment. The hyperglycemia, induced by PI3K inhibitors is isoform specific, mainly experienced during a PI3Kα specific treatment (45). Hyperglycemia is a major problem with PI3K inhibitors, which stimulated development of guidelines (47).

Hyperlipidemia

Hyperlipidemia is also a frequent side effect of mTOR inhibition therapy. The mTOR pathway is an important regulator of the lipid metabolism. The mTOR kinases form large protein complexes, the mTOR complex 1 (mTORC1) and mTOR complex 2 (mTORC2). The activated complexes enhance the accumulation of triglycerides, promote adipogenesis and lipogenesis, and inhibit catabolic processes, such as lipolysis and β-oxidation (45, 46, 47, 48).

Pneumonitis

Most mTOR inhibitor treatment induce pneumonitis (**Figure 10**). The pathomechanism of this side effect is not yet fully clarified. Taken the role of mTOR pathway in the regulation of the innate and adaptive immune systems into consideration, immune mediated processes probably plays a role in the development of pneumonitis, similarly to the immune checkpoint inhibitors. Interestingly, de frequency of the incidence of pneumonitis varies in different clinical trials, despite it is considered as an "on target" side effect(45). For example, in breast cancer clinical trials the incidence of pneumonitis was found to be 7.6% compared to pancreatic neuroendocrine clinical trials in which the frequency of pneumonitis was much higher, 17% (48, 49). There are also available reports on a much higher incidence, reaching 49% (31). Pneumonitis is a dose dependent adverse event, the severity of pneumonitis regress with dose reduction, and usually ends after discontinuation of mTOR inhibition (45). MTOR inhibitor treatment-induced pneumonitis, similarly to the case of immunotherapy, is associated with treatment outcomes (50).

Overall survival (OS) and progression-free survival (PFS) were significantly longer in those individuals, who developed pneumonitis, as compared to those, who did not. Also, stable disease (SD) was more frequent in patients who developed pneumonitis, than in those who did not (45).

Dermatological Side Effects, Stomatitis

The mTOR targeted treatments frequently cause a wide range of dermatological and mucosal side effects, such as rash, acne-like lesions and mucositis. The pathomechanism of the dermatological side effects of mTOR targeted therapy is related to the inhibition of EGFR, similarly to EGFR target therapies (45, 46).

Hepatotoxicity

The PI3K plays a key role in the survival of hepatocytes, therefore the inhibition of PI3K induces apoptosis and liver injury. Hepatotoxicity is frequently associated with PI3K inhibitor treatment, especially with pan-PI3K and PI3Kδ inhibitor therapy. The hepatotoxicity associated with pan-PI3K inhibitors is usually mild, while the hepatotoxicity induced by the PI3Kδ inhibitor idelalisib, is frequent and severe. Autoimmunity is the possible underlying patomechanism, since the liver biopsy of patient suffering idelalisib induced hepatitis shows activated T cell infiltration and treatment with steroids is usually effective (46).

AUTHOR CONTRIBUTIONS

UA: Concept generation, corrections, figures JT: Concept generation, figures, writing, finalization.

FUNDING

CONFLICT OF INTEREST

JT is the editor-in-chief of Pathology and Oncology Research.

The remaining author declares that the research was conducted in the absence of any commercial or financial relationships that could be construed as a potential conflict of interest.

REFERENCES

1. Sebestyén A, Kopper L, Danko T, Tímár J. Hypoxia Signaling in Cancer: from Basics to Clinical Practice. *Pathol Oncol Res* (2021) 27:1609802. doi:10.3389/pore.2021.1609802

2. Cheng K, Liu C-F, Rao G-W. Anti-angiogenic Agents: A Review on Vascular Endothelial Growth Factor Receptor-2 (VEGFR-2) Inhibitors. *Curr Med Chem* (2021) 28:2540–64. doi:10.2174/0929867327666200514082425

3. Salgado R, Benoy I, Bogers R, Wejtien R, Vermeulen P, Dirix L, et al. Platelets and Vascular Endothelial Growth Factor (VEGF): a Morphological and Functional Study. *Angiogenesis* (2001) 4:37–43. doi:10.1023/a:1016611230747

4. Touyz RM, Herrmann SMS, Herrmann J. Vascular Toxicities with VEGF Inhibitor Therapies-Focus on Hypertension and Arterial Thrombotic Events. *J Am Soc Hypertens* (2018) 12:409–25. doi:10.1016/j.jash.2018.03.008

5. Tímár J, Uhlyarik A. A Célzott Kezelések Célzott Mellékhatásai. *KLINIKAI ONKOLÓGIA* (2022) 9:157–68. (in Hungarian).

6. Versmissen J, Mirabito Colafella KM, Koolen SLW, Danser AHJ. Vascular Cardio-Oncology: Vascular Endothelial Growth Factor Inhibitors and Hypertension. *Cardiovasc Res* (2019) 113:904–14. doi:10.1093/cvr/cvz022

7. Chen W, Hill H, Christie A, Kim MS, Pavia-Jimenez A, Homayoun F, et al. Targeting Renal Cell Carcinoma with a HIF-2 Antagonist. *Nature* (2016) 539: 112–7. doi:10.1038/nature19796

8. Food and Drug Administration. *US Food and Drug Administration* (2022). Available from: www.fda.gov/resources-information-approved-drugs.

9. Jonasch E, Donskov F, Iliopoulos O, Rathmell WK, Narayan VK, Maughan B, et al. Belzutifan for renal cell carcinoma in von Hippel-Lindau disease. *N Engl J Med* (2022) 385:2036–46. doi:10.1056/nejmoa2103425

10. Shapiro CL. Bone-modifying Agents (BMAs) in Breast Cancer. *Clin Breast Cancer* (2021) 25:e618–e630. doi:10.1016/j.clbc.2021.04.009

11. Casimiro S, Vilhais G, Gomes I, Costa L. The Roadmap of RANKL/RANK Pathway in Cancer. *Cells* (1978) 10:1978. doi:10.3390/cells10081978

12. Jara MA, Varghese J, Hu MI. Adverse Events Associated with Bone-Directed Therapies in Patients with Cancer. *Bone* (2022) 158:115901. doi:10.1016/j.bone.2021.115901

13. Jackson C, Freeman ALJ, Szlamka Z, Spiegelhalter DJ. The Adverse Effects of Bisphosphonates in Breast Cancer: A Systematic Review and Network Meta-Analysis. *PLoS ONE* (2021) 16:e0246441. doi:10.1371/journal.pone.0246441

14. Lorusso L, Pieruzzi L, Gabriele M, Morinaro E. Osteonecrosis of the Jaw. *J Endocrinol Invest* (2021) 44:2537–66.

15. Zarour HM. Reversing T-Cell Dysfunction and Exhaustion in Cancer. *Clin Cancer Res* (2016) 22:1856–64. doi:10.1158/1078-0432.CCR-15-1849

16. Joller N, Peters A, Anderson AC, Kuchroo VK. Immune Checkpoints in central Nervous System Autoimmunity. *Immunol Rev* (2012) 248:122–39. doi:10.1111/j.1600-065X.2012.01136.x

17. Zhai Y, moosavi R, chen M. Immune Checkpoints a Novel Class of Therapeutic Targets for Autoimmune Diseases. *Front Immunol* (2021) 12: 645699. doi:10.3389/fimmu.2021.645699

18. Eggermont AM, Chiarion-Sileni V, Grobb J, Dummer R, Wolchok JD, Schmidt H, et al. Prolonged Survival in stageIII Melanoma with Ipilimumab Adjuvant Therapy. *N Engl J Med* (2016) 375:1845–55. doi:10.1056/NEJMoa1611299

19. Robert C, Long GV, brady B, Dutriaux C, Maio M, Mortier L, et al. Nivolumab in Previously Untreated Melanoma without BRAF Mutation. *N Engl J Med* (2015) 372:320–30. doi:10.1056/NEJMoa1412082

20. Herbst RS, Baas P, Kim DW, Felip E, Perez-Gracia JL, Han JY, et al. Pembrolizumab versus Docetaxel for Previously Treated, PD-L1-Positive, Advanced Non-small-cell Lung Cancer (KEYNOTE-010): a Randomised Controlled Trial. *Lancet* (2016) 387:1540–50. doi:10.1016/S0140-6736(15)01281-7

21. Gulley JL, Rajan A, Spigel TR, Iannotti N, Chandler J, Wong DJL, et al. Avelumab for Patients with Previously Treated Metastatic or Recurrent Non-small-cell Lung Cancer (JAVELIN Solid Tumor): Dose-Expansion Cohort of a Multicentre, Open-Label, Phase 1b Trial. *Lancet Oncol* (2017) 18:599–610. doi:10.1016/S1470-2045(17)30240-1

22. Rittmayer A, Barlesi A, Waterkamp D, Park K, Ciadiello F, Hida T, et al. Atezolizumab versus Docetaxel in Pati4nts with Previously Treated NSCLC (OAK): a Phase III Open Label Multicenter Randomized Controlled Trial. *Lancet* (2017) 389:255–65.

23. Garassino MC, Cho BC, Kim JH, Mazieres J, Vansteenkiste J, Lena H, et al. Durvalumab as Third-Line or Later Treatment for Advanced Non-small-cell Lung Cancer (ATLANTIC): an Open-Label, Single-Arm, Phase 2 Study. *Lancet Oncol* (2018) 19:521–36. doi:10.1016/S1470-2045(18)30144-X

24. Martins F, Sofyia L, Sykiotis GP, Lamine F, Maillard M, Fraga M, et al. Adverse Effects of Immune-Checkpoint Inhibitors: Epidemiology, Management and Surveillance. *Nat Rev Clin Oncol* (2019) 16:563–80. doi:10.1038/s41571-019-0218-0

25. Ralli M, Boticelli A, Visconti IC, Angelletti D, Fiore M, Marchetti P, et al. Immunotherapy in the Treatment of Metastatic Melanoma: Current Knowledge and Future Directions. *J Immunol Res* (2020) 2020:9235638. doi:10.1155/2020/9235638

26. Hellmann MD, Rizvi NA, Goldman JW, Gettinger SN, Borghaei H, Brahmer JR, et al. Nivolumab Plus Ipilimumab as First-Line Treatment for Advanced Non-small-cell Lung Cancer (CheckMate 012): Results of an Open Label, Phase 1, Multicohort Study. *Lancet Oncol* (2017) 18:31–41. doi:10.1016/S1470-2045(16)30624-6

27. Motzer RJ, Tannir NM, McDermott DF, Frontera OA, Melichar B, Choueiri TK, et al. Nivolumab Plus Ipilimumab versus Sunitinib in Advanced Renal-Cell Carcinoma. *N Engl J Med* (2018) 378:1277–90. doi:10.1056/NEJMoa1712126

28. Hellmann MD, Ciuleanu T-E, Plizansky A, Lee JS, Otterson GA, Audigier-Valette C, et al. Nivolumab Plus Ipilimumab in Lung Cancer with a High Tumor Mutational burden. *N Engl J Med* (2018) 378:2093–104. doi:10.1056/NEJMoa1801946

29. Bouwhuis MG, tenHagen TLM, Suciu S, Eggermont AMM. Autoimmunity and Treatment Outcome in Melanoma. *Curr Opin Oncol* (2011) 23:170–6. doi:10.1097/CCO.0b013e328341edff

30. Ye W, Olsson-Brown A, Watson RA, Cheung VTF, Morgan RD, Nassiri I, et al. Checkpoint Blocker Induced Autoimmunity Is Associated with Favourable Outcome in Metastatic Melanoma and Distinct T-Cell Expression Profiles. *Br J Cancer* (2021) 124:1661–9. doi:10.1038/s41416-021-01310-3

31. Zhong L, Wu Q, Chen F, Liu J, Xie X. Immune-related Adverse Events: Promising Predictors for Efficacy of Immune Checkpoint Inhibitors. *Cancer Immunol Immunother* (2021) 70:2559–76. doi:10.1007/s00262-020-02803-5

32. Guida M, Strippoli S, Maule M, Quaglino P, Ramondetta A, Queirolo P, et al. Immune Checkpoint Inhibitor Associated Vitiligo and its Impact on Survival in Patients with Metastatic Melanoma. *ESMO Open* (2021) 6:100064. doi:10.1016/j.esmoop.2021.100064

33. Wu Q, Bai B, Tian C, Li D, Yu H, Song B, et al. The Molecular Mechaisms of Cardiotoxicity Induced by HER2, VEGF, and Tyrosine Kinase Inhibitors. *Cardiovasc Drugs Ther* (2021) 36:511–24. doi:10.1007/s10557-021-07181-3

34. D'Uva G, Tzahor E. The Key Roles of ERBB2 in Cardiac Regeneration. *Cell Cycle* (2015) 14:2383–4. doi:10.1080/15384101.2015.1063292

35. Anjos M, Fontes-Oliveira M, Costa VM, Santos M, Ferreira R. An Update of the Molecular Mechanisms Undelying Doxorubicin Plus Trastuzumab Induced Cardiotoxicity. *Life Sci* (2021) 280:119760. doi:10.1016/j.lfs.2021.119760

36. Hampton T. New Insight on Preventing EGFR Inhibitor-Induced Adverse Effects. *JAMA* (2020) 323:814–5. doi:10.1001/jama.2020.0812

37. Galimont-Collen AFS, Vos LE, Lavrijsen APM, Ouwerkerk J, Gelderblom H. Classification and Management of Skin, Hair, Nail and Mucosal Side-Effects of Epidermal Growth Factor Receptor (EGFR) Inhibitors. *Eur J Cancer* (2007) 43: 845–51. doi:10.1016/j.ejca.2006.11.016

38. Subbiah V, Baik C, Kirkwood JM. Clinical Development of BRAF Plus MEK Inhibitor Combinations. *Trends Cancer* (2020) 6:797–810. doi:10.1016/j.trecan.2020.05.009

39. Moreira A, Lebbé C, Heinzerling L. MAPK Blockade, Toxicities, Pathogenesis and Management. *Curr Opin Oncol* (2021) 33:139–45. doi:10.1097/CCO.0000000000000710

40. Livingstone E, Zimmer L, Vaubel J, Schadendorf D. BRAF, MEK and KIT Inhibitors for Melanoma: Adverse Events and Their Management. *Chi Clin Oncol* (2014) 29.

41. Galanis A, Levis M. Inhibition of C-Kit by Tyrosine Kinase Inhibitors. *Haematologica* (2015) 100:e77–9. doi:10.3324/haematol.2014.117028

42. Fachi MM, Tonin FS, Leonart L, Rotta I, Fernandez-Llimos F, Pontarolo R. Haematological Adverse Events Associated with Tyrosine Kinase Inhibitors in Chronic Myeloid Leukaemia: A Network Meta-Analysis. *Br J Clin Pharmacol* (2019) 85:2280–91. doi:10.1111/bcp.13933

43. Hou H, Sun D, Jiang M, Liu D, Zhou N, Zhu J, et al. The Safety and Serious Adverse Events of Approved ALK Inhibitors in Malignancies. A Meta-Analysis. *Cancer Manag Res* (2019) 11:4109–18. doi:10.2147/CMAR.S190098

44. Liu D, Lin FA, Offin M, Falcon CJ, Marciano-Goroff YR, Lin A, et al. Characterization of On-Target Adverse Events Caused by TRK Inhibitor Therapy. *Ann Oncol* (2020) 31:1207–15. doi:10.1016/j.annonc.2020.05.006

45. Zhang Y, Yan H, Xu Z, Yang B, Luo P, He Q. Molecular Basis for Class Side Effects Associated with PI3K/AKT/mTOR Pathway Inhibitors. *Expert Opin Drug Metab Toxicol* (2019) 15:767–74. doi:10.1080/17425255.2019.1663169

46. Pallet N, Legendre C. Adverse Events Associated with mTOR Inhibitors. *Expert Opin Drug Saf* (2013) 12:177–86. doi:10.1517/14740338.2013.752814

47. Tankova T, Senkus E, Beloyartseva M, Bortsnar S, Catrinoiu D, Frolova MS, et al. Management Strategies for Hyprglycemia Associated with the A-Selectgive PI3K Inhibitor Alpelisib for the Treatment of Breast Cancer. *Cancers* (2022) 14:1598. doi:10.3390/cancers14071598

48. Caron A, Richard D, Laplante M. The Roles of mTOR Complexes in Lipid Metabolism. *Annu Rev Nutr* (2015) 35:321–48. doi:10.1146/annurev-nutr-071714-034355

49. Generali D, Montemurro F, Bordonaro R, Mafodda A, Romito S, Michelotti A, et al. Everolimus Plus Exemestane in Advanced Breast Cancer: Safety Results of the BALLET Study on Patients Previously Treated without and with

Chemotherapy in the Metastatic Setting. *Oncologist* (2017) 22:648–54. doi:10.1634/theoncologist.2016-0461

50. Yao JC, Shah MH, Ito T, Bohas CL, Wolin EM, Van Cutsem E, et al. Everolimus for Advanced Pancreatic Neuroendocrine Tumors. *N Engl J Med* (2011) 364:514–23. doi:10.1056/NEJMoa1009290

GLOSSARY

ARDS adult respiratory distress syndrome

BF bisphosphonate

BSP bone sialoprotein

CML chronic myelocytic leukemia

CNS central nervous system

COPD chronic obstructive pulmonary disease

CSK cytoskeleton

GFR growth factor receptor

HgB hemoglobin

HIF hypoxia inducible factor

ICI immune checkpoint inhibitor

IR insulin receptor

irAE immune related adverse event

IRS insulin receptor substrate protein

MLCK myosin light chain kinase

NET neuroendocrine tumor

NK natiral killer

NOS nitricoxid synthase

NSCLC non-small cell lung cancer

OBL osteoblast

OCL osteoclast

ON osteonectin

OPN osteopontin

OS overall survival

PDGFR PDGF receptor

PFS progression-free survival

PTHrP parathyroid hormon-related protein

RBC red blood cell

RCC renal cell cancer

ROS reactive oxigen species

TK tirozine kinase

VEGFR VEGF receptor

Check for updates

Plasma Extracellular Vesicles-Derived miR-99a-5p: A Potential Biomarker to Predict Early Head and Neck Squamous Cell Carcinoma

Qiang Huang[1,2†], Yu-Jie Shen[1,2†], Chi-Yao Hsueh[1,2†], Yi-Fan Zhang[1,2], Xiao-Hui Yuan[1,2], Yu-Juan Zhou[1,2], Jiao-Yu Li[3], Lan Lin[4†*], Chun-Ping Wu[1,2*] and Chun-Yan Hu[4*]

[1]Department of Otorhinolaryngology, Eye & ENT Hospital, Fudan University, Shanghai, China, [2]Shanghai Key Clinical Disciplines of Otorhinolaryngology, Shanghai, China, [3]Department of Pediatric, Xinhua Hospital, Shanghai Jiaotong University School of Medicine, Shanghai, China, [4]Department of Pathology, Eye & ENT Hospital, Fudan University, Shanghai, China

Purpose: This study aimed to investigate the applicability of plasma extracellular vesicles (EVs) miR-99a-5p as a potential head and neck squamous cell carcinoma (HNSCC) diagnostic biomarker.

Methods: The miRNA expression of HNSCC tissue and plasma EVs were profiled by small RNA sequencing. qRT-PCR was performed to detect miR-99a-5p expression in HNSCC ($n = 93$) and benign disease ($n = 39$) plasma EVs and formalin-fixed and paraffin-embedded (FFPE) tissue ($n = 110$). We constructed receiver-operating characteristic curves to investigate the diagnostic efficiency of plasma EVs miR-99a-5p.

Results: Tumor tissue exhibited lower miR-99a-5p than para-tumor tissue. Patients with high miR-99a-5p expression exhibited significantly more p16 positive status. In contrast, HNSCC plasma EVs harbored more miR-99a-5p than the benign disease group. Plasma EVs miR-99a-5p distinguished HNSCC with area under the curve (AUC) of 0.7494 (95% CI: 0.6692–0.8296; $p < 0.0001$), with 61.54% sensitivity and 75.27% specificity, respectively. Furthermore, plasma EVs miR-99a-5p also distinguished early HNSCC with AUC of 0.7394 (95% CI: 0.6284–0.8504; $p = 0.0002$), with 79.07% sensitivity and 61.54% specificity, respectively.

Conclusion: Plasma EVs miR-99a-5p is a potential biomarker for predicting early HNSCC.

Keywords: biomarker, HNSCC, HPV, plasma extracellular vesicles, miR-99a-5p

INTRODUCTION

Head and neck squamous cell carcinoma (HNSCC), a heterogeneous collection of malignancies, accounts for approximately 90% of all head and neck cancers and is closely associated with human papilloma virus (HPV) infection [1]. The epidemiology, pathophysiology, and response to treatment of HPV+ HNSCC differ sharply from that of HPV− disease. Overall, HPV positive is associated with more favorable clinical outcomes [2]. Notably, HNSCC patients are at a high risk of cervical lymph node metastases. Cervical lymph node involvement is a well-known prognostic marker for HNSCC [3], and the presence of positive lymph nodes is thought to be a

predictor of poor patient outcomes [4]. This highlights the importance of the early diagnosis of HNSCC. However, no screening strategy has yet proven to be effective for the detection of early HNSCC.

Plasma extracellular vesicles (EVs) are increasingly being promoted as potential disease detection biomarkers [5]. The cargo carried by EVs mimics the content of the parental cells and could be secreted into the peripheral circulation where they could be detected [6]. Shortly after Valida et al. [7] reported that EVs, especially exosomes, contained RNA components in 2007, Taylor et al. reported the possibility of using the miRNA components of EVs to identify diagnostic markers for ovarian cancer [8]. Guo et al. discovered and validated plasma EVs miR-95-3p/miR-26b-5p and its combination with CA19-9 serum levels for distinguishing pancreatic ductal adenocarcinoma from chronic pancreatitis [9]. These findings suggest the potential of plasma EVs miRNAs as differential diagnostic biomarkers in tumor patients [10].

MiR-99a-5p acts as a tumor suppressor by inhibiting proliferation, migration, and invasion and has been found to be dysregulated in several tumors, including bladder cancer [11], esophageal cancer [12] and HNSCC [13]. Furthermore, miR-99a-5p can be detected in plasma EVs during the identification and evaluation of biomarkers in cancer patients [14, 15]. However, little is known about the diagnostic potential of plasma EVs miR-99a-5p in HNSCC patients.

Hence, we sought to investigate the applicability of plasma EVs miR-99a-5p expression levels as a minimally invasive HNSCC diagnostic biomarker.

METHODS AND MATERIALS

Patient Tissue and Ethics Approval

HNSCC tumor and para-tumor fresh tissue (n = 3 pairs) and formalin-fixed and paraffin-embedded (FFPE) HNSCC tissue (n = 110) were obtained from patients diagnosed with HNSCC (mainly hypopharyngeal and laryngeal squamous cell carcinoma) pathologically after surgery from October 2019 to October 2021. Plasma samples were obtained from HNSCC patients (n = 93) and benign disease patients (n = 39) from October 2019 to October 2021. All patient samples were obtained from the Department of Otorhinolaryngology, Eye & ENT Hospital of Fudan University. All participants provided written informed consent forms. This study was approved by the Ethics Committee of the Eye & ENT Hospital of Fudan University (NO. 2018036).

RNA Isolation and qRT-PCR

Total RNA was isolated from FFPE tissue with an RNeasy FFPE Kit (QIAGEN, Germany) and from fresh tumor tissue and plasma EVs with TRIzol reagent (Invitrogen, Thermo Fisher Scientific) according to the manufacturer's instructions, measured by a microspectrophotometer Nanodrop 2000 (Thermo Fisher Scientific), with the ratio of OD260/OD280 > 1.8, and then reversed-transcribed using an Evo M-MLV Mix Kit with gDNA Clean for qPCR (AG11728,

Accurate Biology, Hunan, China). The housekeeping genes U6 was used as internal references to normalize gene expression for miRNA. The primers were designed and synthesized by Sangon Biotech (Shanghai). The sequences of primers used are as follows: miR-99a-5p: 5′ AACCCGTAGATCCGATCTTGT G 3′; U6: 5′ GTGCTCGCTTCGGCAGCACAT 3′. qRT-PCR was performed using SYBR® Green Premix Pro Taq HS qPCR Kit (AG11718, Accurate Biology, Hunan, China) with the ABI 7500 Real-Time PCR System (Life Technologies, Shanghai, China) using the $2^{-\Delta\Delta Ct}$ method.

Isolation and Purification of EVs

Peripheral blood samples were obtained in an ethylene diamine tetraacetic acid (EDTA)-coated tube (BD Pharmingen, New Jersey, USA) before surgery. Hemocytes were separated by centrifugation at 2,000 g for 15 min at 4°C. The clear top layer was obtained by another centrifugation at 10,000 g for 30 min at 4°C. The EVs derived from the plasma samples were isolated with Total Exosome Precipitation Reagent (Invitrogen, Thermo Fisher Scientific) according to the manufacturer's instructions.

Confirmation and Characterization of Plasma EVs

The morphological characteristics, size distributions, and marker detection of EVs pellets were examined by transmission electron microscopy (TEM), nanoparticle tracking analysis (NTA), and immunoblotting analysis, according to the methods described in our previous studies [16, 17].

Small RNA Sequencing and Data Analysis

Small RNA library preparation and sample sequencing were performed with the assistance of Beijing Novogene Co., Ltd., using an Illumina HiSeq™ 2500 device. Total RNA from fresh HNSCC and para-tumor tissue (n = 3 pairs) and plasma EVs (n = 6 for HNSCC patients, n = 3 for benign disease patients) were concatenated with 5′ and 3′ adaptors. The quantity and integrity of RNA yield was assessed by using the Qubit®2.0 (Invitvogen, USA) and Agilent 2200 TapeStation (Agilent Technologies, USA) separately. After cDNA synthesis and PCR amplification, the cDNA library (18–40 nt) was obtained using an acrylamide gel purification method, and single-end sequencing was then performed. The raw data (Raw reads) obtained by sequencing were filtered first: the joints at both ends of the reads were removed, and the reads with fragment length <17 nt and low-quality reads were removed to complete the preliminary filtering of data and obtain high-quality data (Clean reads). The distribution map of genome-wide reads was obtained by comparing Clean reads with the reference genome, and the Clean reads were annotated by ncRNA classification. The miRNA expression were calculated by RPM (Reads Per Million) values (RPM=(number of reads mapping to miRNA/number of reads in Clean data)×10^6). Differential expression between two sets of samples was calculated by edgeR algorithm according to the criteria of |$\log_2$(Fold Change)|≥1 and p-value < 0.05.

FIGURE 1 | miR-99a-5p is downregulated in HNSCC tissue and is associated with HPV infection status. **(A)** Heatmap demonstrating the differentially expressed miRNAs (FDR <1%); those with difference of expression (more than 2-fold change) are shown (n = 3 pairs of tumor and corresponding para-tumor tissue). On the heatmap vertical axis are reported the names of the most significant miRNAs differentially expressed between the two groups, and on the heatmap horizontal axis are the sample identification numbers. **(B)** Volcano plots of miRNA-seq data demonstrating upregulated and downregulated genes in HNSCC tumor tissue compared to para-tumor tissue; red, upregulated; blue, downregulated. **(C)** The expression of miR-99a-5p in normal tissue (n = 44) and HNSCC tissue (n = 497) as downloaded from TCGA project *via* Genomic Data Commons Data Portal. The expression values of genes from miRNA-seq data were scaled with log2(RPM +0.01). **(D)** Overall survival of HNSCC patients in groups of high/low expression of miR-99a-5p (Log-rank test p = 0.0004, Gehan-Breslow-Wilcoxon test p = 0.003).

Bioinformatics Analysis

The expression of miR-99a-5p was downloaded from the latest TCGA project (Data Release 32.0) *via* the Genomic Data Commons Data Portal [18] (https://portal.gdc.cancer.gov/). The expression values of genes from miRNA-seq data were scaled with $\log_2$(RPM +0.01). A Kaplan–Meier plot was used to assess the correlation between the expression of miR-99a-5p in HNSCC.

Statistical Analysis

Statistical analysis was performed using the Mann–Whitney test to evaluate the differences between the two groups. The Chi-square testing was used for the statistical calculation of categorical data. Kaplan-Meier method was used to calculate the survival rate, and Log-rank (Mantel-Cox) test and Gehan-Breslow-Wilcoxon test were used to test the difference in survival rate. GraphPad Prism 8.0 was used for statistical analyses and scientific graphing. The results are expressed as mean ± standard deviation (SD). Receiver-operating characteristic (ROC) curves were performed by plotting the true positive (sensitivity) against the false-positive (1-specificity) rate, and the area under the curve (AUC) was calculated. Optimal cut-off values were established based on the highest value obtained in the ROC curve analysis according to the likelihood ratio. Differences were considered significant if the p value was <0.05 (*), <0.01(**), <0.001(***), or <0.0001 (****), as indicated in each figure legend.

TABLE 1 | Correlation between miR-99a-5p and clinicopathologic characteristics in 110 HNSCC FFPE tissue.

Parameter	All patients		High expression		Low expression		p value
	n = 110	%	n = 22	%	n = 88	%	
Age							0.1510
≤60	60	54.5	15	68.2	45	51.1	
> 60	50	45.5	7	31.8	43	48.9	
Gender							>0.9999
Female	1	0.9	0	0	1	1.1	
Male	109	99.1	22	100	87	98.9	
Smoking history							0.3940
No	25	22.7	3	13.6	22	25	
Yes	85	77.3	19	86.4	66	75	
Drinking history							0.1247
No	35	31.8	10	45.5	25	28.4	
Yes	75	68.2	12	54.5	63	71.6	
Hypertension							0.6971
No	66	60	14	63.6	52	59.1	
Yes	44	40	8	36.4	36	40.9	
Diabetes							0.2253
No	99	90	18	81.8	81	92	
Yes	11	10	4	18.2	7	8	
p16							*<0.0001**
Negative	92	83.6	7	31.8	85	96.6	
Positive	18	16.4	15	68.2	3	3.4	
T stage							0.8485
T1+T2	52	47.3	10	45.5	42	47.7	
T3+T4	58	52.7	12	54.5	46	52.3	
Lymph node metastasis							>0.9999
Negative	20	18.2	4	18.2	16	18.2	
Positive	90	81.8	18	81.8	72	81.8	
Clinical stage							>0.9999
I + II	7	6.4	1	4.5	6	6.8	
III + IV	103	93.6	21	95.5	82	93.2	
Maximum tumor diameter (MTD)							0.5010
<3 cm	62	56.4	11	50	51	58	
≥3 cm	48	43.6	11	50	37	42	
Differentiation							0.3670
High+ High-moderate	92	83.6	17	77.3	75	85.2	
Moderate+ moderate-low	18	16.4	5	22.7	13	14.8	
Recurrence							0.3880
No	61	55.5	14	63.6	47	53.4	
Yes	49	44.5	8	36.4	41	46.6	
Death							0.3811
No	66	60	15	68.2	51	58	
Yes	44	40	7	31.8	37	42	

*p value was tested from Fisher's exact test.

RESULTS

miR-99a-5p Is Downregulated in HNSCC Tissue and Is Associated With HPV Infection Status

To depict the comprehensive miRNA profile with abnormal expression, miRNA sequencing was performed in three paired HNSCC tumors and para-tumor tissue. Differentially expressed miRNAs are listed in **Figure 1A**. miRNA-99a-5p was consequently selected for further study due to its high expression in para-tumors but low expression in HNSCC tumors (**Figure 1B**). Moreover, we verified the expression of miR-99a-5p in the Cancer Genome Atlas (TCGA) cohort. Data

from 44 normal tissues and 497 HNSCC tumors confirmed that miR-99a-5p expression was higher in normal tissues than in tumor tissues, which was consistent with the sequencing results (**Figure 1C**). Furthermore, the Kaplan–Meier plot showed that low expression of miR-99a-5p in HNSCC tissues negatively affected the prognosis of HNSCC patients ($p < 0.05$) (**Figure 1D**).

We further determined miR-99a-5p expression in 110 HNSCC FFPE tissue using qRT-PCR. Detailed clinical and pathological data are depicted in **Table 1**. Overall, patients with high miR-99a-5p expression exhibited significantly more p16 positive status in pathological samples than did patients with low miR-99a-5p expression ($p < 0.0001$). No further significant associations were found

FIGURE 2 | miR-99a-5p is upregulated in HNSCC plasma EVs. **(A)** The morphological characteristics of EVs derived from the plasma of HNSCC patients and benign disease patients (Scale bar: 0.5 μm). Partially amplified images are shown in the frame. **(B)** Immunoblotting analysis of the EVs markers of CD63 and CD9, and the negative marker Calnexin in plasma EVs derived from two cases of HNSCC patients and two cases of benign disease patients. **(C)** Size distribution and concentration of plasma EVs detected by NTA. **(D)** Heatmap demonstrating the differentially expressed miRNAs in plasma EVs (FDR <1%); those with difference of expression (more than 2-fold change) are shown (n = 3 benign disease patients; n = 6 HNSCC patients). On the heatmap vertical axis are reported the names of the most significant miRNAs differentially expressed between the two groups, and on the heatmap horizontal axis are the sample identification numbers.

between miR-99a-5p levels in HNSCC tissue and clinicopathological features (T stage, lymph node metastasis, clinical stage, tumor diameter, or pathological differentiation). We also found no difference in tissue miR-99a-5p levels in terms of prognosis ($p = 0.3880$) or recurrence ($p = 0.3881$) in HNSCC patients.

Collectively, these findings suggest that miR-99a-5p may play an important role in inhibiting the progression of HNSCC and is associated with HPV infection status.

miR-99a-5p is Upregulated in HNSCC Plasma EVs

Considering the promising results obtained in tissue samples and the significant anti-tumor properties of miR-99a-5p previously described in HNSCC [19], we hypothesized that the tumor excreted cancer-suppressing miR-99a-5p into the peripheral circulation in the form of EVs to maintain survival [20]. To confirm this hypothesis and further describe the miRNA expression profile in plasma EVs of HNSCC patients, we isolated EVs from the plasma of six HNSCC

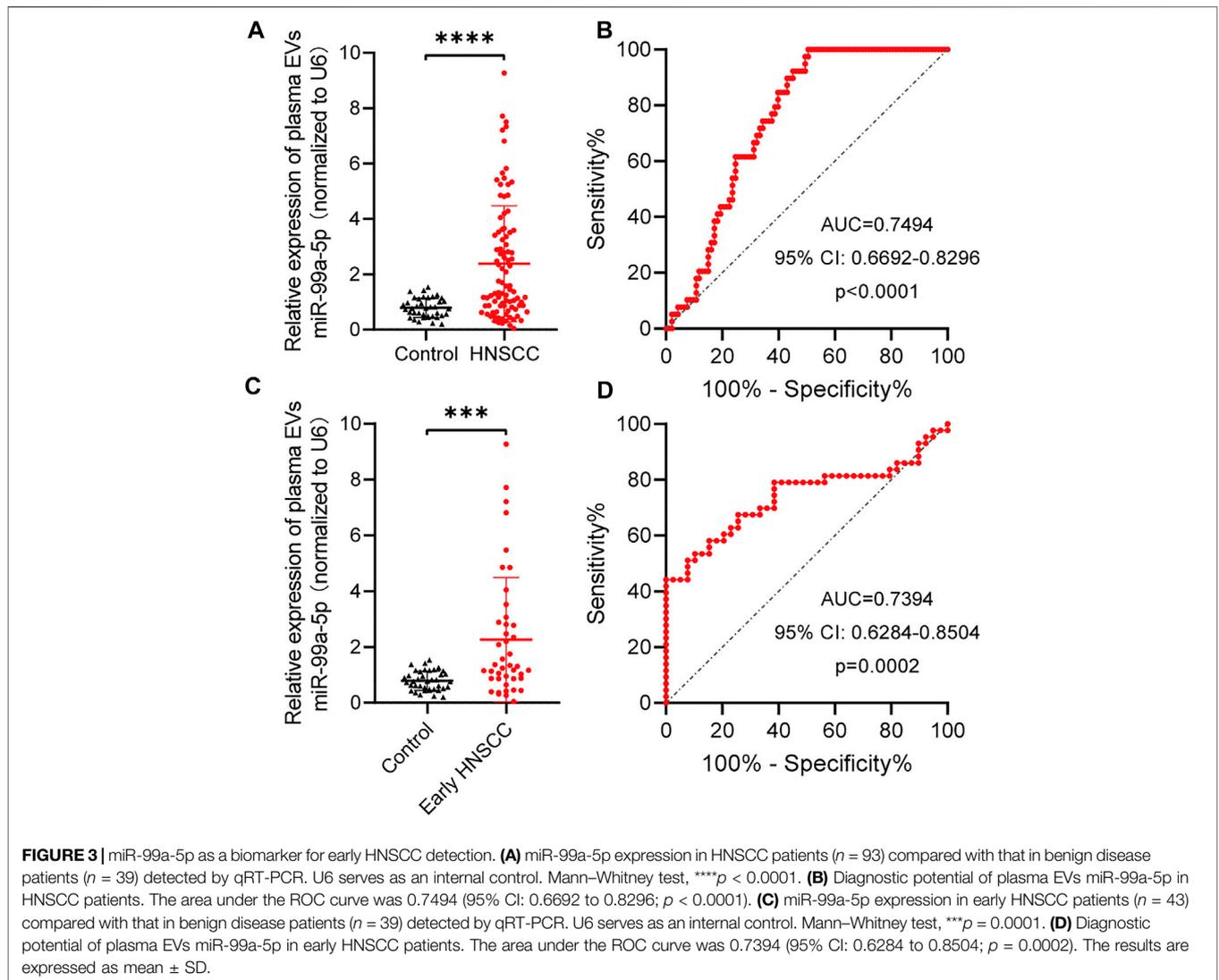patients and three benign disease patients, and then performed miRNA sequencing.

We found that the EVs we isolated had a representative saucer-shaped vesicle structure with a double-layer membrane, according to the TEM analysis (**Figure 2A**). We further verified the expression of EVs surface markers CD63 and CD9, together with the negative marker Calnexin. Furthermore, plasma EVs did not express platelet and immune cell marker genes CD41 and CD11b (**Figure 2B**). The NTA results showed that the average size of the EVs was 157.6 ± 68.7 nm for EVs derived from patients with benign disease and 161.6 ± 58.6 nm for HNSCC patients-derived EVs (**Figure 2C**). These results confirmed that the EVs we isolated had representative morphology, appropriate size distribution, and precise surface markers typical of EVs.

Further, we identified several miRNAs, including miR-1228-5p and miR-4466, that were highly expressed in the plasma EVs of HNSCC patients through miRNA sequencing. Clinicopathological features of HNSCC patients undergoing plasma EVs miRNA sequencing are summarized in **Table 2**. Surprisingly, we found that, contrary to the miR-99a-5p level in

TABLE 2 | Clinicopathological features of HNSCC patients undergoing plasma EVs miRNA sequencing.

No.	Gender	Age	Tumor type	T stage	N stage	Clinical stage	Pathological differentiation	p16 status
1	Male	73	LSCC	3	1	III	Well-moderately	Positive
2	Male	74	LSCC	3	1	III	Well-moderately	Positive
3	Male	64	HPSCC	4	2	IV	Poor	Positive
4	Male	68	HPSCC	4	1	IV	Well-moderately	Negative
5	Male	65	HPSCC	3	1	III	Poor	Negative
6	Male	69	HPSCC	3	2	IV	Poor	Positive

LSCC, laryngeal squamous cell carcinoma; HPSCC, hypopharyngeal squamous cell carcinoma.

FIGURE 3 | miR-99a-5p as a biomarker for early HNSCC detection. **(A)** miR-99a-5p expression in HNSCC patients (*n* = 93) compared with that in benign disease patients (*n* = 39) detected by qRT-PCR. U6 serves as an internal control. Mann–Whitney test, ****p < 0.0001. **(B)** Diagnostic potential of plasma EVs miR-99a-5p in HNSCC patients. The area under the ROC curve was 0.7494 (95% CI: 0.6692 to 0.8296; p < 0.0001). **(C)** miR-99a-5p expression in early HNSCC patients (*n* = 43) compared with that in benign disease patients (*n* = 39) detected by qRT-PCR. U6 serves as an internal control. Mann–Whitney test, ***p = 0.0001. **(D)** Diagnostic potential of plasma EVs miR-99a-5p in early HNSCC patients. The area under the ROC curve was 0.7394 (95% CI: 0.6284 to 0.8504; p = 0.0002). The results are expressed as mean ± SD.

tissue, miR-99a-5p expression levels in circulating plasma EVs were significantly higher in HNSCC patients than in benign disease controls (**Figure 2D**).

The unexpected opposite trend in tissue and plasma EVs suggests that circulating plasma EVs miR-99a-5p may be a potential biomarker for the detection of HNSCC.

TABLE 3 | Correlation between plasma EVs miR-99a-5p and clinicopathologic characteristics in 93 HNSCC patients.

Parameter	All patients		High expression		Low expression		p value
	$n = 93$	%	$n = 38$	%	$n = 55$	%	
Age							**0.0129***
≤60	22	23.7	14	36.8	8	14.5	
>60	71	76.3	24	63.2	47	85.5	
Gender							0.0650
Female	3	3.2	3	7.9	0	0	
Male	90	96.8	35	92.1	55	100	
Smoking history							0.9185
No	25	26.9	10	26.3	15	27.3	
Yes	68	73.1	28	73.7	40	72.7	
Drinking history							0.4071
No	34	36.6	12	31.6	22	40	
Yes	59	63.4	26	68.4	33	60	
Hypertension							0.5451
No	50	53.8	19	50	31	56.4	
Yes	43	46.2	19	50	24	43.6	
Diabetes							0.1906
No	83	89.2	36	94.7	47	85.5	
Yes	10	10.8	2	5.3	8	14.5	
p16							**0.0134**[†]
Negative	70	75.3	34	89.5	36	65.5	
Positive	23	24.7	4	10.5	19	34.5	
T stage							0.2769
T1+T2	43	46.2	15	39.5	28	50.9	
T3+T4	50	53.8	23	60.5	27	49.1	
Lymph node metastasis							0.6989
Negative	29	31.2	11	28.9	18	32.7	
Positive	64	68.8	27	71.1	37	67.3	
Clinical stage							0.7305
I + II	18	19.4	8	21.1	10	18.2	
III + IV	75	80.6	30	78.9	45	81.8	
Maximum tumor diameter (MTD)							0.8957
<3 cm	35	37.6	14	36.8	21	38.2	
≥3 cm	58	62.4	24	63.2	34	61.8	
Differentiation							0.3476
High + High-moderate	81	87.1	35	92.1	46	83.6	
Moderate + moderate-low	12	12.9	3	7.9	9	16.4	

*p value was tested from Chi-square test.
†p value was tested from Fisher's exact test.

miR-99a-5p as a Biomarker for Early HNSCC Detection

To further confirm the hypothesis previously proposed, we explored the diagnostic value of plasma EVs miR-99a-5p as a minimally invasive HNSCC diagnostic biomarker. We isolated plasma EVs from HNSCC patients (n = 93) and benign disease patients ($n = 39$) and assessed the miR-99a-5p expression level by qRT-PCR. We found that miR-99a-5p expression levels were significantly higher in plasma EVs from HNSCC patients (median: 1.445) than in those from benign disease patients (median: 0.7687) ($p < 0.0001$) (**Figure 3A**). Detailed clinical and pathological data on 93 HNSCC patients are presented in **Table 3**. Overall, patients with high plasma EVs miR-99a-5p expression were significantly younger ($p = 0.0129$) and had a lower p16 positive status in pathological samples ($p = 0.0134$) than those with low expression. No further significant associations were found between miR-99a-5p levels in HNSCC plasma EVs and clinicopathological features (T stage, lymph node

metastasis, clinical stage, tumor diameter, or pathological differentiation).

To assess the potential value of plasma EVs miR-99a-5p for the diagnosis of HNSCC, ROC curves were constructed to distinguish HNSCC patients from benign disease patients (**Figure 3B**). The AUC was 0.7494 (95% CI: 0.6692–0.8296; $p < 0.0001$). When the optimal cut-off value was 0.8537, the sensitivity and specificity were 61.54% (0.4590–0.7511) and 75.27% (0.6562–0.8292), respectively.

Given the current lack of effective biomarkers for early HNSCC, we further explored whether plasma EVs miR-99a-5p could be a biomarker for early HNSCC detection. We found that early HNSCC patients ($n = 43$) had higher expression levels of miR-99a-5p in plasma EVs than benign disease patients ($p = 0.0001$) (**Figure 3C**). Plasma EVs miR-99a-5p expression level was able to discriminate early HNSCC from benign disease patients with an AUC of 0.7394 (95% CI: 0.6284–0.8504; $p = 0.0002$). Furthermore, using the cut-off value mentioned above,

the sensitivity and specificity were 79.07% (0.6479–0.8858) and 61.54% (0.4590–0.7511), respectively (**Figure 3D**).

Collectively, plasma EVs miR-99a-5p levels distinguished early HNSCC and were associated with HPV infection status of patients with HNSCC.

DISCUSSION

Plasma EVs present several advantages in carrying cargo from tumor tissue that make them reliable and specific for use as diagnostic tools [5]. These include being stable molecules that can be easily detected in peripheral circulation plasma and the fact that their expression has been correlated with clinicopathological features, thus offering promise as prognostic and predictive biomarkers [21]. We previously demonstrated that plasma EVs TGFβ1 is higher in HNSCC patients than in control patients, and is associated with clinicopathological features of HNSCC patients. More importantly, plasma EVs TGFβ1 expression could clearly distinguish between HNSCC and control patients with higher diagnostic efficiency than total TGFβ1 expression in plasma [16].

Several studies have reported that plasma EVs miRNAs are potential biomarkers for the diagnosis and survival prediction of HNSCC patients [22]. A recent study found that increased plasma EVs miR-491-5p levels were associated with poor overall survival and disease-free survival in HNSCC patients. Plasma EVs miR-491-5p was able to distinguish HNSCC patients with sensitivity and specificity of 46.6% and 100%, respectively [23].

In the current study, we first confirmed the high expression of miR-99a-5p in para-tumor tissue *via* miRNA sequencing and further verified it using TCGA data. The upregulation of miR-99a-5p in para-tumor tissue is also consistent with previous studies [19, 24]. Notably, the expression of miR-1246 was consistent in tumor tissue and plasma EVs in our previous study [17]. However, we found that miR-99a-5p expression in tumor tissue and plasma EVs showed an opposite trend in HNSCC patients. This unexpected opposite trend of miR-99a-5p in tissue and plasma was also reported by Garrido-Cano [21] and Torres [25] in breast cancer and endometrioid endometrial carcinoma. Moreover, other investigators have demonstrated that several other miRNAs have opposite expression patterns in tissues and peripheral blood [26, 27, 28]. These suggests that circulating miR-99a-5p, especially in plasma EVs, may be a potential biomarker for the detection of HNSCC.

MiR-99a-5p has been reported as a tumor suppressor in cancer. Tamai et al. showed that miR-99a-5p induced cellular senescence in gemcitabine-resistant bladder cancer cells by targeting SMARCD1 [11]. Sun et al. found that miRNA-99a-5p suppresses cell proliferation, migration, and invasion by targeting isoprenylcysteine carboxylmethyltransferase (ICMT) in oral squamous cell carcinoma [13]. Based on these findings and our data, we speculated that HNSCC cells might release the tumor suppressor miR-99a-5p into the peripheral circulation through EVs to maintain their

survival. Selective EVs packaging and the release of miRNAs have been reported to occur in cancer cells as a means of eliminating tumor suppressors [29, 30, 31]. However, the processes by which miRNAs are selectively packed in plasma EVs remain poorly understood [32, 33]. Our results reinforce the concept of selective release, which may explain the discrepancy between tissue and plasma EVs.

Further, in this study, we observed a relationship between the miR-99a-5p expression level and HPV infection status. Overall, HPV positive was associated with more favorable clinical outcomes in HNSCC patients [2]. Although the miR-99a-5p expression level was not associated with clinical outcomes, patients with high miR-99a-5p expression in tissue had a significantly more p16 positive status in pathological samples than patients with low miR-99a-5p expression. By contrast, patients with high miR-99a-5p expression in plasma EVs had less p16 positive status in pathological samples than that of patients with low expression, which is consistent with the opposite trend we observed in tissue and plasma EVs. Further research is needed to clarify the relationship between miR-99a-5p and HPV infection status.

There were several limitations to this investigation. First, validating the diagnostic efficiency of plasma EVs miR-99a-5p with multi-centric validation research is required. Our study lacked prognostic data, as all cases were newly diagnosed (from October 2019 to October 2021). Therefore, the prognostic value of plasma EVs miR-99a-5p could not be evaluated in this study. Second, although we ruled out the possibility that plasma EVs are derived from platelets and immune cells, whether they are completely derived from HNSCC remains to be discussed. This is also one of the bottlenecks restricting plasma EVs as an indicator of tumor diagnosis and prognosis, which needs more efforts to solve. Third, the reasons for the opposite trend of miRNA in HNSCC tumor tissues and plasma EVs have not been studied in detail. More studies should focus on the key pathways and provide an explanation for the opposite trend.

To the best of our knowledge, this is the first study to evaluate the clinical application of plasma EVs miR-99a-5p as a diagnostic biomarker in HNSCC patients. Our study demonstrates two important clinical findings. First, we found that miR-99a-5p is downregulated in HNSCC tissue and is associated with HPV infection status. Second, we identified the dynamic change of miR-99a-5p between tissue and plasma EVs, and confirmed that plasma EVs miR-99a-5p is a potential diagnostic biomarker for early HNSCC patients.

Collectively, we primarily evaluated the value and provided evidence of plasma EVs miR-99a-5p as a biomarker for early HNSCC. This may help improve early HNSCC detection.

DATA AVAILABILITY STATEMENT

The datasets generated during and/or analysed during the current study are available from the corresponding authors on reasonable request.

ETHICS STATEMENT

The studies involving human participants were reviewed and approved by Ethics Committee of the Eye & ENT Hospital of Fudan University. The patients/participants provided their written informed consent to participate in this study.

AUTHOR CONTRIBUTIONS

Conceptualization: QH, LL, C-PW, and C-YH; Methodology: QH, Y-JS, and C-YH; Validation and formal analysis: QH, Y-JS, and C-YH; Investigation: QH, Y-JS, and C-YH; Data curation: QH, Y-FZ, X-HY, Y-JZ, and J-YL; Writing—original draft preparation: QH, Y-JS, and C-YH; Writing—review and editing: QH, LL, C-PW, and C-YH; Visualization: QH, Y-JS, and C-YH; Supervision: LL, C-PW, and C-YH; Funding acquisition: CYH. All authors read and approved the final manuscript.

FUNDING

CONFLICT OF INTEREST

The authors declare that the research was conducted in the absence of any commercial or financial relationships that could be construed as a potential conflict of interest.

REFERENCES

1. Cramer JD, Burtness B, Le QT, Ferris RL. The Changing Therapeutic Landscape of Head and Neck Cancer. *Nat Rev Clin Oncol* (2019) 16(11): 669–83. doi:10.1038/s41571-019-0227-z

2. Johnson DE, Burtness B, Leemans CR, Lui VWY, Bauman JE, Grandis JR. Head and Neck Squamous Cell Carcinoma. *Nat Rev Dis Primers* (2020) 6(1): 92. doi:10.1038/s41572-020-00224-3

3. Lin H, Wang T, Heng Y, Zhu X, Zhou L, Zhang M, et al. Risk Stratification of Postoperative Recurrence in Hypopharyngeal Squamous-Cell Carcinoma Patients with Nodal Metastasis. *J Cancer Res Clin Oncol* (2021) 147(3): 803–11. doi:10.1007/s00432-020-03337-0

4. Heng Y, Zhang D, Zhou L, Zhang M, Wu C, Tao L. Assessment and Treatment Strategies for Occult Contralateral Lymph Node Metastasis in Hypopharyngeal Squamous Cell Carcinoma Patients with Ipsilateral Node-Positive Necks. *Oral Oncol* (2021) 114:105183. doi:10.1016/j.oraloncology.2021.105183

5. Möller A, Lobb RJ. The Evolving Translational Potential of Small Extracellular Vesicles in Cancer. *Nat Rev Cancer* (2020) 20(12):697–709. doi:10.1038/s41568-020-00299-w

6. LeBleu VS, Kalluri R. Exosomes as a Multicomponent Biomarker Platform in Cancer. *Trends Cancer* (2020) 6(9):767–74. doi:10.1016/j.trecan.2020.03.007

7. Valadi H, Ekström K, Bossios A, Sjöstrand M, Lee JJ, Lötvall JO. Exosome-mediated Transfer of mRNAs and microRNAs Is a Novel Mechanism of Genetic Exchange between Cells. *Nat Cel Biol* (2007) 9(6):654–9. doi:10.1038/ncb1596

8. Taylor DD, Gercel-Taylor C. MicroRNA Signatures of Tumor-Derived Exosomes as Diagnostic Biomarkers of Ovarian Cancer. *Gynecol Oncol* (2008) 110(1):13–21. doi:10.1016/j.ygyno.2008.04.033

9. Guo S, Qin H, Liu K, Wang H, Bai S, Liu S, et al. Blood Small Extracellular Vesicles Derived miRNAs to Differentiate Pancreatic Ductal Adenocarcinoma from Chronic Pancreatitis. *Clin Transl Med* (2021) 11(9):e520. doi:10.1002/ctm2.520

10. Gao S, Guo W, Liu T, Liang N, Ma Q, Gao Y, et al. Plasma Extracellular Vesicle microRNA Profiling and the Identification of a Diagnostic Signature for Stage I Lung Adenocarcinoma. *Cancer Sci* (2022) 113(2):648–59. doi:10.1111/cas.15222

11. Tamai M, Tatarano S, Okamura S, Fukumoto W, Kawakami I, Osako Y, et al. microRNA-99a-5p Induces Cellular Senescence in Gemcitabine-Resistant Bladder Cancer by Targeting SMARCD1. *Mol Oncol* (2022) 16(6):1329–46. doi:10.1002/1878-0261.13192

12. Liu Z, Wu K, Gu S, Wang W, Xie S, Lu T, et al. A Methyltransferase-like 14/miR-99a-5p/tribble 2 Positive Feedback Circuit Promotes Cancer Stem Cell Persistence and Radioresistance via Histone Deacetylase 2-mediated Epigenetic Modulation in Esophageal Squamous Cell Carcinoma. *Clin Transl Med* (2021) 11(9):e545. doi:10.1002/ctm2.545

13. Sun X, Yan H. MicroRNA-99a-5p Suppresses Cell Proliferation, Migration, and Invasion by Targeting Isoprenylcysteine Carboxylmethyltransferase in Oral Squamous Cell Carcinoma. *J Int Med Res* (2021) 49(5):300060520939031. doi:10.1177/0300060520939031

14. Guo T, Wang Y, Jia J, Mao X, Stankiewicz E, Scandura G, et al. The Identification of Plasma Exosomal miR-423-3p as a Potential Predictive Biomarker for Prostate Cancer Castration-Resistance Development by Plasma Exosomal miRNA Sequencing. *Front Cel Dev Biol* (2020) 8:602493. doi:10.3389/fcell.2020.602493

15. Zheng D, Zhu Y, Zhang J, Zhang W, Wang H, Chen H, et al. Identification and Evaluation of Circulating Small Extracellular Vesicle microRNAs as Diagnostic Biomarkers for Patients with Indeterminate Pulmonary Nodules. *J Nanobiotechnology* (2022) 20(1):172. doi:10.1186/s12951-022-01366-0

16. Huang Q, Hsueh CY, Shen YJ, Guo Y, Huang JM, Zhang YF, et al. Small Extracellular Vesicle-Packaged TGFβ1 Promotes the Reprogramming of normal Fibroblasts into Cancer-Associated Fibroblasts by Regulating Fibronectin in Head and Neck Squamous Cell Carcinoma. *Cancer Lett* (2021) 517:1–13. doi:10.1016/j.canlet.2021.05.017

17. Huang Q, Hsueh C, Guo Y, Wu X, Li J, Zhou L. Lack of miR-1246 in Small Extracellular Vesicle Blunts Tumorigenesis of Laryngeal Carcinoma Cells by Regulating Cyclin G2. *IUBMB Life* (2020) 72(7):1491–503. doi:10.1002/iub.2274

18. Li JH, Liu S, Zhou H, Qu LH, Yang JH. starBase v2.0: Decoding miRNA-ceRNA, miRNA-ncRNA and Protein–RNA Interaction Networks from Large-Scale CLIP-Seq Data. *Nucleic Acids Res* (2014) 42(D1):D92–7. doi:10.1093/nar/gkt1248

19. Chen Y, Yao J, Qin Y, Hu K, Wu F, Fang Y. Biological Role and Clinical Value of miR-99a-5p in Head and Neck Squamous Cell Carcinoma (HNSCC): A Bioinformatics-based Study. *FEBS Open Bio* (2018) 8(8):1280–98. doi:10.1002/2211-5463.12478

20. Kalluri R, LeBleu VS. The Biology, Function, and Biomedical Applications of Exosomes. *Science* (2020) 367(6478):eaau6977. doi:10.1126/science.aau6977

21. Garrido-Cano I, Constâncio V, Adam-Artigues A, Lameirinhas A, Simon S, Ortega B, et al. Circulating miR-99a-5p Expression in Plasma: A Potential Biomarker for Early Diagnosis of Breast Cancer. *Int J Mol Sci* (2020) 21(19): 7427. doi:10.3390/ijms21197427

22. Bigagli E, Locatello LG, Di Stadio A, Maggiore G, Valdarnini F, Bambi F, et al. Extracellular Vesicles miR-210 as a Potential Biomarker for Diagnosis and Survival Prediction of Oral Squamous Cell Carcinoma Patients. *J Oral Pathol Med* (2022) 51(4):350–7. doi:10.1111/jop.13263

23. Panvongsa W, Siripoon T, Worakitchanon W, Arsa L, Trachu N, Jinawath N, et al. Plasma Extracellular Vesicle microRNA-491-5p as Diagnostic and Prognostic Marker for Head and Neck Squamous Cell Carcinoma. *Cancer Sci* (2021) 112(10):4257–69. doi:10.1111/cas.15067

24. Zhang Q, Chen Y, Hu SQ, Pu YM, Zhang K, Wang YX. A HPV16-Related Prognostic Indicator for Head and Neck Squamous Cell Carcinoma. *Ann Transl Med* (2020) 8(22):1492. doi:10.21037/atm-20-6338

25. Torres A, Torres K, Pesci A, Ceccaroni M, Paszkowski T, Cassandrini P, et al. Deregulation of miR-100, miR-99a and miR-199b in Tissues and Plasma Coexists with Increased Expression of mTOR Kinase in Endometrioid Endometrial Carcinoma. *BMC Cancer* (2012) 12:369. doi:10.1186/1471-2407-12-369

26. van Schooneveld E, Wouters MC, Van der Auwera I, Peeters DJ, Wildiers H, Van Dam PA, et al. Expression Profiling of Cancerous and normal Breast Tissues Identifies microRNAs that Are Differentially Expressed in Serum from Patients with (Metastatic) Breast Cancer and Healthy Volunteers. *Breast Cancer Res* (2012) 14(1):R34. doi:10.1186/bcr3127

27. Cuk K, Zucknick M, Heil J, Madhavan D, Schott S, Turchinovich A, et al. Circulating microRNAs in Plasma as Early Detection Markers for Breast Cancer. *Int J Cancer* (2013) 132(7):1602–12. doi:10.1002/ijc.27799

28. Chan M, Liaw CS, Ji SM, Tan HH, Wong CY, Thike AA, et al. Identification of Circulating microRNA Signatures for Breast Cancer Detection. *Clin Cancer Res* (2013) 19(16):4477–87. doi:10.1158/1078-0432.CCR-12-3401

29. Teng Y, Ren Y, Hu X, Mu J, Samykutty A, Zhuang X, et al. MVP-Mediated Exosomal Sorting of miR-193a Promotes colon Cancer Progression. *Nat Commun* (2017) 8:14448. doi:10.1038/ncomms14448

30. Xu X, Liu Y, Li Y, Chen H, Zhang Y, Liu J, et al. Selective Exosome Exclusion of miR-375 by Glioma Cells Promotes Glioma Progression by Activating the CTGF-EGFR Pathway. *J Exp Clin Cancer Res* (2021) 40(1):16. doi:10.1186/s13046-020-01810-9

31. Qi Y, Jin C, Qiu W, Zhao R, Wang S, Li B, et al. The Dual Role of Glioma Exosomal microRNAs: Glioma Eliminates Tumor Suppressor miR-1298-5p via Exosomes to Promote Immunosuppressive Effects of MDSCs. *Cell Death Dis* (2022) 13(5):426. doi:10.1038/s41419-022-04872-z

32. Temoche-Diaz MM, Shurtleff MJ, Nottingham RM, Yao J, Fadadu RP, Lambowitz AM, et al. Distinct Mechanisms of microRNA Sorting into Cancer Cell-Derived Extracellular Vesicle Subtypes. *eLife* (2019) 8:e47544. doi:10.7554/eLife.47544

33. Shurtleff MJ, Temoche-Diaz MM, Karfilis KV, Ri S, Schekman R. Y-Box Protein 1 Is Required to Sort microRNAs into Exosomes in Cells and in a Cell-free Reaction. *eLife* (2019) 5:e19276. doi:10.7554/eLife.19276

Check for
updates

Improved Accuracy of Lymph Node Staging and Long-Term Survival Benefit in Colorectal Cancer With *Ex Vivo* Arterial Methylene Blue Infiltration

Nóra Suszták[1,2]*[†], István Besznyák[3†], Kálmán Almási[4†], Attila Bursics[3], Dóra Kelemen[5], David W. Borowski[6†] and Balázs Bánky[7†]

[1]Faculty of Medicine, Semmelweis University, Budapest, Hungary, [2]Department of Surgery, St. Imre University Teaching Hospital, Budapest, Hungary, [3]Department of Surgery, Uzsoki Street Hospital, Budapest, Hungary, [4]Department of Pathology, Aladar Petz County Teaching Hospital, Győr, Hungary, [5]Department of Pathology, Uzsoki Street Hospital, Budapest, Hungary, [6]Department of Surgery, Welwitschia Hospital, Walvis Bay, Namibia, [7]Department of Surgery, Transplantation and Gastroenterology, Semmelweis University, Budapest, Hungary

Introduction: *Ex vivo* methylene blue (MB) injection into the main supplying arteries of the colorectal specimen after surgical removal is an uncomplicated technique to support lymph node harvest during pathological evaluation. The primary aim of this randomized, interventional, bicentric trial was to evaluate the impact of MB injection on lymph node yield, with secondary aims assessing the accuracy of lymph node staging and the effect on 5-year overall survival for patients undergoing resection of colorectal cancer.

Methods: In the study period between December 2013 and August 2015, 200 colorectal resections were performed at two independent onco-surgery centers of Hungary. Following surgical resection, each specimen was randomly assigned either to the control (standard pathological work-up) or to the MB staining group before formaldehyde fixation. Patient-level surgical and clinical data were retrieved from routinely collected clinical datasets. Survival status data were obtained from the National Health Insurance Fund of Hungary.

Results: A total of 162 specimens, 82 in the control and 80 in the MB groups, were included for analysis. Baseline characteristics were equally distributed among study groups, except for specimen length. Both the median of total number of lymph nodes retrieved (control 11 ± 8 [0–33] nodes vs. MB 14 ± 6 [0–42] nodes; $p < 0.01$), and the ratio of cases with at least 12 removed lymph nodes (36/82, 43.9% vs. 53/80, 66.3%; $p < 0.01$) were higher in the MB group. The rate of accurate lymph node staging was non-significantly improved. As for rectal cancer, nodal staging accuracy (16/31, 51.6% vs. 23/30, 76.7%; $p = 0.04$) and the proportion with minimum 12 lymph node retrieval (7/31, 22.6%, vs. 18/30, 60%; $p < 0.01$) was improved by MB injection. In Mantel–Cox

---

Abbreviations: CME, complete mesocolic excision; CRC, colorectal cancer; LN, lymph node; MB, methylene blue; NAT, neoadjuvant treatment; TME, total mesorectal excision; UICC, Union for International Cancer Control.

regression, a statistically significant survival benefit with methylene blue injection at 5 years post-surgery was proven (51.2% vs. 68.8%; *p* = 0.04).

Conclusion: In our experience, postoperative *ex vivo* arterial methylene blue injection appears to be an uncomplicated technique, improving lymph node yield and decreasing the chance of insufficient nodal staging. The technique might also associate with a 5-year overall survival benefit.

Keywords: colorectal cancer, overall survival, methylene blue, nodal staging accuracy, lymph node staging

INTRODUCTION

Colorectal cancer (CRC) is the second most common cause of cancer death worldwide [1]. Currently, the cornerstone of treatment is surgery with curative intent, and as such, *en bloc* removal of the local lymph node (LN) field is a key aspect of the operation [2]. Operative perfection of lymph node clearance, called complete mesocolic excision (CME) in the case of colon lesions, and total mesorectal excision (TME) in the case of rectal tumors, is associated with survival benefit and local recurrence reduction [3, 4]. Accurate lymph node staging based on histopathologic examination of each available lymph node (or as many nodes as possible) is recommended both as a prognostic tool and decision basis of adjuvant chemotherapy [2, 5, 6]. In 2009, the *Union for International Cancer Control* (UICC) recommended at least 12 lymph nodes to be harvested and reported, in order to adequately exclude node-positive disease [7]. Differentiating between stage II and stage III colorectal cancer is paramount, as most stage II CRC requires no adjuvant treatment, while surgical removal of stage III cancers with at least one metastatic lymph node or presence of extranodal tumor deposits should usually be followed by chemotherapy [2]. In the case of insufficient lymph node retrieval from the surgical specimen, node-negative tumors leave some uncertainty regarding the reliability of a pN0 stage. Incorrect classification may lead to inadequate postoperative management either way, which might contribute to a worse prognosis [8]. The estimated understaging rates may be as high as 6% in some studies [9, 10]. In particular, the subset of patients who undergo pre-operative chemo-irradiation may have fewer lymph nodes due to the effect of neoadjuvant treatment (NAT), but may also have better outcomes despite suboptimal lymph node harvest and examination [11]. Other studies have previously demonstrated that an increased number of histopathologically examined lymph nodes seems to be associated with better long-term survival [8, 12, 13].

The obvious need for accurate lymph node staging has led to the development of several techniques to improve the lymph node yield. The traditional visualization and manual palpation of the mesocolon for lymph nodes is performed first by the pathologist. However, 80% of mesorectal lymph nodes are smaller than 3 mm, and at least half of metastatic lymph nodes are smaller than 5 mm [14, 15]. Additional methods employed by the pathologist include fat clearance techniques with xylene, alcohol or acetone, which can improve visualization of lymph nodes within the mesocolic or mesorectal fat. Although these methods have been demonstrated to increase lymph node

harvest, they can be time-consuming, expensive and harmful for personnel due to toxic components [16, 17]. In some countries, pathologist assistants are employed to enhance the number of dissected lymph nodes, but due to increased costs, this strategy may be unaffordable in some healthcare systems [18].

Methylene blue (MB) injection into the main supplying artery of the removed colorectal specimen is a low-cost, simple and non-hazardous maneuver [19–21]. It results in accumulation of the blue dye in the vessels, lymphatic channels and lymph nodes, providing the pathologist with a good color contrast between nodes and surrounding fat tissue. This *ex vivo* method was first introduced by Märkl et al. in 2007, and multiple groups have adopted this approach considering its feasibility and affordability [9, 20–33]. Our study aimed to examine the method of MB injection in a randomized setting within an Eastern European healthcare system. The primary outcome of the study included the overall LN harvest, and the proportion of accurately staged patients. The secondary aim was to analyze the effect of lymph node staging on 5-year overall survival of recruited patients.

MATERIALS AND METHODS

Study Sites

A randomized, interventional trial was conducted at two independent onco-surgery centers (St. Borbala Hospital in Tatabánya and Uzsoki Street Hospital in Budapest, Hungary). Both high-volume colorectal centers ran more than 150 elective colorectal surgical cases *per annum* during the study period of 20 months between December 2013 and August 2015. Both sites shared the same enrollment, randomization and specimen processing protocols.

Power Calculation

An *a priori* power calculation was performed for primary outcome measures (total lymph node count and nodal staging accuracy), based on published data and our unpublished local pilot [20]. At least 85 cases on each arm were required to detect a 20% improvement of lymph node yield between study arms, with a 5% level of statistical significance and 80% statistical power. We calculated with a 10% case dropout, therefore we planned 200 cases to recruit with a 1:1 randomization ratio at both sites.

Randomisation of Specimens

At each site, colorectal cancer cases with prior histopathological verification from colonoscopic biopsy specimens, or without

FIGURE 1 | *Ex vivo* methylene blue solution injection into the supplying artery of the colorectal specimen after surgical removal.

prior histopathological verification but with high clinical suspicion by colonoscopic presentation and computed tomographic imaging, undergoing segmental colon or rectum resection were enrolled in the study. Surgically removed specimens were randomly allocated to either MB or conventional specimen processing as controls in the operating room promptly after resection, by choosing one of 100 pre-prepared, sealed envelopes at each site.

Specimen Processing

Native, freshly removed colorectal specimens from the control group were directly placed in routine 10% buffered neutral formaldehyde solution for 48–72 h. Specimens of the MB group were laid out, and the main supplying artery or arteries were cannulated with a 20 G cannula, according to the standard central vascular ligation technique. Then, 50 mg of MB was diluted with 30 ml saline, and the solution was injected into the main arterial trunk(s) until the dye appeared on the cut surfaces of the specimen (**Figure 1**). The dyeing process was executed in the operating room on a back table. Finally, specimens were placed in 10% buffered neutral formaldehyde solution for 48–72 h. All specimens were then processed according to pathological routine following standard practice.

Pathological Evaluation

After visual inspection and palpation, pathologists harvested as many lymph nodes from each specimen as possible. MB staining, the number of extracted lymph nodes, and the number of metastasis-positive lymph nodes were documented in the pathological report. Accurate lymph node staging was defined as any case with at least one positive lymph node, report of extranodal tumor deposit, or pN0 stage based on at least 12 examined lymph nodes. As a quality indicator of work-up, a ratio of cases with at least 12 lymph nodes retrieved was also evaluated retrospectively.

Data Processing

A separate, anonymized database was built for data collection. Demographic data, tumor localization, surgical access,

concomitant neoadjuvant therapy, operating surgeons, evaluating pathologists, details of the pathological report (TNM stage, histology grade, CME/TME surgical grade, specimen length, total number of dissected lymph nodes and metastatic lymph nodes) were collected. Both the results of randomization and pathological results were collected from the hospital documentation systems. Additional pre-planned appointments of patients, besides the routine surgical and oncological follow-ups were not arranged. Further follow-up data of included patients were extracted from the hospital documentation systems, and after 5 years of study completion, the survival status and time to death within 60 months post-surgery were collected electronically from the database of the National Health Insurance Fund of Hungary.

Statistical Analysis

Continuous variables with normal distribution were analyzed with their mean ± standard deviation, while skewed distributed variables were reported as median with interquartile range (IQR) and minimum-maximum ranges. Categorical variables were reported as absolute numbers (n) with relative percentages (%) of the given group. Normal distribution of continuous variables was determined by the Shapiro–Wilk test. Continuous variables were compared using Student's t-test or the Mann–Whitney U-test. Categorical variables were compared using chi-squared tests. For correlation analysis, Pearson and Spearman Rho tests were used. The effect of intervention on survival was studied using a Mantel–Cox regression analysis, based on Kaplan–Meier curves and log-rank test. Level of statistical significance was set at a two-tailed p value of <0.05. All statistical analyses were done using SPSS version 24.0 (SPSS Inc., Chicago, IL, United States).

Primary and Secondary Outcomes

Primary endpoints of the study included 1) the total number of harvested lymph nodes, and 2) the rate of accurate lymph node staging. Secondary outcome was overall survival at 5 years post-operatively for each group.
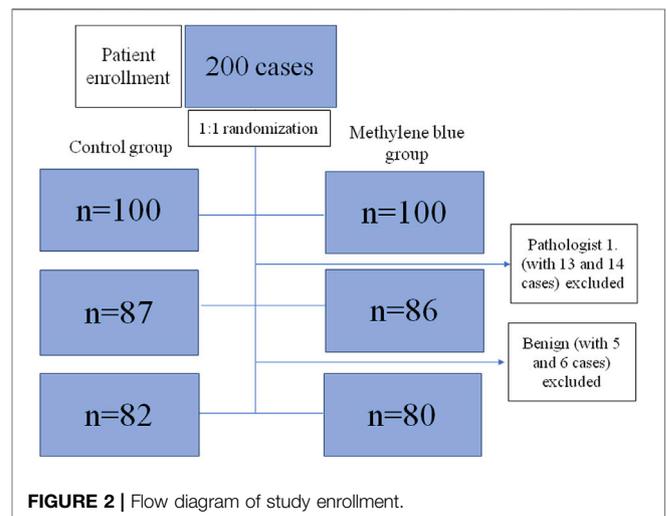

FIGURE 2 | Flow diagram of study enrollment.

TABLE 1 | Distribution of baseline clinical and oncological parameters among included patients, grouped by study intervention.

Parameter	Control group (n = 82)	MB group (n = 80)	p value
Age (years, median ± IQR, min–max)	73 ± 15 (32–88)	73 ± 16 (40–92)	0.81[a]
Sex (n, %)			
Female	40 (48.8%)	40 (50%)	0.88[b]
Male	42 (51.2%)	40 (50%)	
Tumor site (n, %)			
Cecum	11 (13.4%)	9 (11.3%)	0.91[b]
Ascending colon	11 (13.4%)	7 (8.8%)	
Hepatic flexure	3 (3.7%)	3 (3.8%)	
Transverse colon	3 (3.7%)	5 (6.3%)	
Splenic flexure	1 (1.2%)	1 (1.3%)	
Descending colon	0 (0%)	1 (1.3%)	
Sigmoid colon	22 (26.8%)	24 (30.0%)	
Rectum	31 (37.8%)	30 (37.5%)	
Operation type (n, %)			
Right colectomy	26 (31.7%)	20 (25%)	0.23[b]
Extended right colectomy	0 (0%)	4 (5%)	
Transverse colectomy	2 (2.4%)	0 (0%)	
Left colectomy	2 (2.4%)	1 (1.3%)	
Sigmoid colectomy	2 (2.4%)	3 (3.8%)	
Anterior rectum resection	44 (53.7%)	43 (53.8%)	
Abdomino-perineal excision of the rectum	6 (7.3%)	9 (11.3%)	
Surgical access (n, %)			
Open	36 (43.9%)	37 (46.3%)	0.11[b]
Laparoscopic	45 (54.9%)	37 (46.3%)	
Converted	1 (1.2%)	6 (7.5%)	
T stage (n, %)			
Tis	1 (1.2%)	1 (1.3%)	0.48[b]
T1	6 (7.3%)	5 (6.3%)	
T2	10 (12.2%)	10 (12.5%)	
T3	57 (69.5%)	61 (76.3%)	
T4	8 (9.8%)	3 (3.8%)	
N stage (n, %)			
N0	47 (57.3%)	43 (53.8%)	0.89[b]
N1	24 (29.3%)	26 (32.5%)	
N2	11 (13.4%)	11 (13.8%)	
M stage (n, %)			
M0	71 (86.6%)	76 (95%)	0.06[b]
M1	11 (13.4%)	4 (5%)	
AJCC Stage			
0	1 (1.2%)	1 (1.3%)	0.37[b]
I	11 (13.4%)	15 (18.8%)	
II	30 (36.6%)	27 (33.8%)	
III	29 (35.4%)	33 (41.3%)	
IV	11 (13.4%)	4 (5%)	
Pathologists participating in the study (n, %)			
P1	15 (18.3%)	13 (16.3%)	0.98[b]
P2	5 (6.1%)	5 (6.3%)	
P3	18 (22%)	20 (25%)	
P4	4 (4.9%)	7 (8.8%)	
P5	3 (3.6%)	3 (3.8%)	
P6	5 (6.1%)	4 (5%)	
P7	3 (3.6%)	3 (3.8%)	
P8	9 (11%)	9 (11.3%)	
P9	7 (8.5%)	4 (5%)	
P10	13 (15.8%)	11 (13.8%)	
P11	0 (0%)	1 (1.3%)	

(Continued on following page)

TABLE 1 | (*Continued*) Distribution of baseline clinical and oncological parameters among included patients, grouped by study intervention.

Parameter	Control group (*n* = 82)	MB group (*n* = 80)	*p* value
Surgeons participating in the study (n, %)			
S1	4 (4.9%)	6 (7.5%)	0.46[b]
S2	17 (20.7%)	17 (21.3%)	
S3	11(13.4%)	4 (5%)	
S4	4 (4.9%)	7 (8.7%)	
S5	0 (0%)	2 (2.5%)	
S6	2 (2.4%)	3 (3.8%)	
S7	2 (2.4%)	3 (3.8%)	
S8	0 (0%)	1 (1.3%)	
S9	13 (15.8%)	10 (12.5%)	
S10	1 (1.2%)	1 (1.3%)	
S11	1 (1.2%)	0 (0%)	
S12	1 (1.2%)	0 (0%)	
S13	2 (2.4%)	4 (5%)	
S14	5 (6.1%)	6 (7.5%)	
S15	1 (1.2%)	4 (5%)	
S16	1 (1.2%)	0 (0%)	
S17	0 (0%)	1 (1.3%)	
S18	5 (6.1%)	5 (6.3%)	
S19	3 (3.6%)	1 (1.3%)	
S20	7 (8.5%)	2 (2.5%)	
S21	0 (0%)	2 (2.5%)	
S22	2 (2.4%)	1 (1.3%)	
Included patients at each site (n, %)			
H1	35 (42.7%)	35 (43.8%)	0.87[b]
H2	47 (57.3%)	45 (56.3%)	
Neoadjuvant therapy received (n, %)	16 (19.5%)	14 (17.5%)	0.74[b]
Specimen length (centimeters, median ± IQR, min–max)	22 ± 11 (5–52)	25 ± 10 (9–83)	**0.03**[a]

The bold values mean that those vales has reached a level of significance.
H1: St. Borbala Hospital, Tatabánya, H2: Uzsoki Street Hospital, Budapest.
[a]Mann-Whitney U test.
[b]Chi-square test.

RESULTS

Patient Enrollment

The Patient enrollment flow diagram is reported in **Figure 2**. Over the period of 20 months, one hundred cases of elective colon or rectal resections were included at each of the two hospitals. One of the pathologists decided not to participate in the study, thus his cases were excluded (13 cases and 14 cases in the control and MB groups, respectively.) Likewise, a further 11 cases with benign histopathology were also excluded, five from the control and six from the MB group. A total of 162 specimens, 82 in the control and 80 in the MB groups, were included.

Baseline Demographic and Clinical Characteristics of the Two Groups

MB and control groups were found to be statistically comparable regarding patient age, sex, tumor site, type of operation, laparoscopic or open access surgery, TNM staging, CME/TME surgical grade, variability of operating surgeons and pathologists, as well as hospital site (**Table 1**). Although the median specimen length was significantly higher in the MB group (25 ± 10 cm vs. 22 ± 11 cm; *p* = 0.03), specimen length and total number of retrieved lymph nodes were proved to be independent in

Pearson's correlation test (*p* = 0.58) and Spearman's Rho correlation test (*p* = 0.55).

Lymph Node Count and Nodal Staging Accuracy

Parameters of lymph node count and nodal staging accuracy are described in **Table 2**. The total number of lymph nodes retrieved from specimens was higher in the MB group, compared to the control group. Separate analysis of colon and rectal cancer subgroups showed that improvement of the lymph node yield is mainly focused to the rectal subgroup, while in the colon subgroup, this improvement did not reach statistical significance. The ratio of cases with at least 12 retrieved lymph nodes was significantly higher in the MB group compared to the control group. There was a tendency for a higher rate of accurate lymph node staging, as an improvement was noted in the MB group (81.3%), compared to the control group (69.5%). Lymph node staging accuracy was significantly higher among rectal cases in the MB group, while no statistical difference was found among colonic cases between groups. During analysis, 30 cases of rectal cancers were operated on after neoadjuvant chemo-irradiation. Although the mean of the positive lymph node count was unchanged by the intervention, nodal staging accuracy showed

TABLE 2 | Lymph node count and nodal staging accuracy, grouped by experimental arms and tumor site.

Lymph node counts	Control group (n = 82)	MB group (n = 80)	p value
Total lymph node count (nodes, median ± IQR, min–max)			
Total (rectum + colon)	11 ± 8 (0–33)	14 ± 6 (0–42)	**<0.01**[a]
Colon	12 ± 7 (4–33)	14 ± 8 (2–42)	0.13[a]
Rectum (total)	8 ± 8 (0–23)	12.5 ± 8 (2–28)	**0.01**[a]
Rectum (neoadjuvant)	6.5 ± 6 (0–23)	12 ± 9 (2–19)	**0.04**[a]
Rectum (without neoadjuvant)	10 ± 11(2–20)	13.5 ± 6 (6–28)	0.15[a]
Positive lymph node count (nodes, mean ± SD, min-max)			
Total (rectum + colon)	1.6 ± 3.6 (0–20)	1.5 ± 2.4 (0–12)	0.35[a]
Colon	2 ± 4.4 (0–20)	1.5 ± 2.6 (0–12)	0.69[a]
Rectum (total)	0.8 ± 1.64 (0–6)	1.3 ± 2.1 (0–9)	0.31[a]
Rectum (neoadjuvant)	0.8 ± 1.6 (0–6)	1 ± 2.4 (0–9)	0.98[a]
Rectum (without neoadjuvant)	0.9 ± 1 (0–5)	1.6 ± 3 (0–5)	0.28[a]
Proportion with ≥12 nodes examined, per total number of lymph nodes (n, %)			
Total (rectum + colon)	36/82 (43.9%)	53/80 (66.3%)	**<0.01**[b]
Colon	29/51 (56.9%)	35/50 (70%)	0.17[b]
Rectum (total)	7/31 (22.6%)	18/30 (60%)	**<0.01**[b]
Rectum (neoadjuvant)	2/16 (12.5%)	8/14 (57.1%)	**0.01**[b]
Rectum (without neoadjuvant)	5/15 (33.3%)	10/16 (62.5%)	0.10[b]
Accurate nodal staging, per total (n, %)			
Total (rectum + colon)	57/82 (69.5%)	65/80 (81.3%)	0.08[b]
Colon	41/51 (80.4%)	42/50 (84%)	0.64[b]
Rectum (total)	16/31 (51.6%)	23/30 (76.7%)	**0.04**[b]
Rectum (neoadjuvant)	7/16 (43.8%)	9/14 (64.3%)	0.26[b]
Rectum (without neoadjuvant)	9/15 (60%)	14/16 (87.5%)	0.08[b]

The bold values mean that those values have reached a level of significance.
[a]Mann-Whitney U test.
[b]Chi-square test.

a statistically non-significant tendency for improvement, while the total lymph node counts and the proportion of ≥12 lymph node retrieval reached statistically significant improvement by MB injection.

Survival Analysis

Each case was censored at 60 months of follow-up. Non-stratified Kaplan-Meier curves of overall survival were undivided until ~24 months, and clearly split afterwards (**Figure 3**). In Mantel-Cox regression, methylene blue injection showed a statistically significant survival benefit at 5 years after operation (51.2% vs. 68.8%; $p = 0.04$). In the stratified analysis, patients from the control group of early CRC stages (AJCC Stages 0, I and II) had a significantly lower overall survival, in contrast to the MB subgroup (64.3% vs. 86.0%; $p = 0.02$), while in advanced CRC stages (AJCC Stages III and IV), no statistically significant survival benefit could be observed (37.5% vs. 48.6%; $p = 0.57$) (**Figures 4**, **5**).
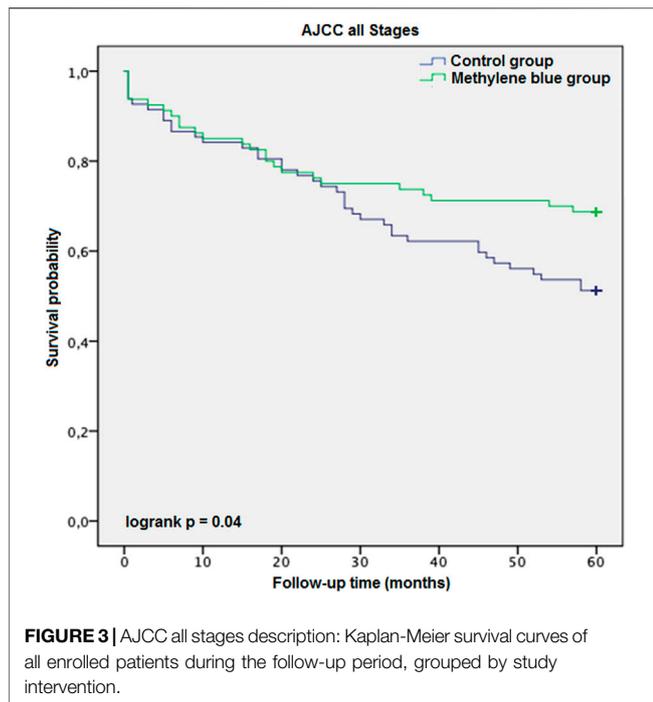
DISCUSSION

There has been a controversial discussion in the literature about the necessary number of dissected lymph nodes during colorectal cancer pathological evaluation. The cut-off threshold varied from 6 to 20 extracted lymph nodes in different studies [34]. Conventionally, the UICC, the *American Joint Committee on Cancer*, the *National Quality Forum*, *National Comprehensive Cancer Network* and the *College of American Pathologists* recommend a minimum number of 12 lymph nodes for accurate staging, as the quality measure of both surgical lymph node clearance and pathological workup [34]. On the other hand, a recently published high volume study proposed a minimal cut-off value above 21 lymph nodes [8]. Regardless of the recommendations, the majority of dissected colorectal specimens does not reach the minimum recommended lymph node count, especially in cases of rectal cancer after neoadjuvant chemo-irradiation [12, 35, 36].

Our results are largely consistent with those found in the literature. Application of this method might result in an increase of lymph node yield [9, 19–33]. Although a tendency for increment could be observed in each subgroup, a statistically significant improvement was documented among rectum cancer cases but not for colonic cases.

Furthermore, methylene blue staining provided a significant increase in the rate of sufficient (≥12) lymph node detection in our study, as a quality measure for pathological work-up. In the control group, lymph node harvest reached the minimal number in less than half of all cases, while with MB staining, two-thirds of the cases were sufficiently reported. This effect was again more pronounced in the rectal cancer subgroup. Reviewing the related articles from the literature, the rate of insufficient lymph node harvest could possibly be diminished, even close to zero, with the help of MB staining [9, 20–24, 27].

FIGURE 3 | AJCC all stages description: Kaplan-Meier survival curves of all enrolled patients during the follow-up period, grouped by study intervention.

Lymph node staging accuracy is a complex term, covering the minimal number (≥12) of dissected lymph nodes, and N1c (with extranodal tumor deposit) stages and others with at least one positive lymph node (N1–2). In our experience, the rate of accurate lymph node staging by methylene blue injection was markedly improved, but this tendency did not reach the level of statistical significance. In further subgroup analysis, lymph node staging accuracy significantly improved among rectal cancer cases without neoadjuvant therapy, while no statistical difference was found in the colon cancer subgroup. Similar findings have been reported by other scientific groups [20, 21, 24, 27]. Regarding the small lymph nodes of the colorectal mesentery, there is great deal of inconsistency. Some authors, like Märkl et al. reported that most of the metastatic lymph nodes are simply noticeable by pathological examination [21]. Similarly, in the analysis of Reima et al., only 8% of the patients had metastasis in small-diameter (≤4 mm) lymph nodes, meaning that small lymph nodes may not be subject of major clinical interest [27]. On the other hand, other authors state that the majority (or at least half) of metastatic lymph nodes are located in lymph nodes smaller than 5 mm [37–39]. In these cases, methylene blue staining might help in the detection of these otherwise difficult-to-retrieve small metastatic lymph nodes.

Recently, a few trials have reported a significant increment of the metastatic lymph node count during the methylene blue technique, compared to the conventional lymph node dissection, leading to stage migration or upstaging [9, 30, 31]. For example, Jepsen et al. observed a significant increase in the rate of positive lymph nodes, resulting in an upstaging from UICC stage I or II to stage III, however in advanced cancer (T3/4), no upstaging was detected [31]. In addition, Liu et al. published a

significantly raised rate of node positive lymph nodes resulting in an upstaging in 4 cases out of 66 [9]. In our study, in spite of the improved number of examined lymph nodes, this was not observable. Our experimental setting however was not designed to point out nodal stage migration.

It is well established that neoadjuvant chemo-irradiation negatively affects lymph node yield in rectal cancer cases, as preoperative treatment leads to fibrosis and lymph node size decrease in the affected area, causing a lack of properly dissectible lymph nodes [9,40–42]. However, this phenomenon may not negatively influence oncological outcomes, if we consider the decreased number and size of mesorectal lymph nodes as a favorable marker of neoadjuvant treatment effectivity [29]. This might be in line with the observation reported by Gurawaila et al., as fewer retrieved mesorectal lymph nodes correlated with effectiveness of oncotherapy after NAT [11].

Methylene blue injection has been successfully applied in the pathological investigation of rectal cancers in a few recent studies [20, 24, 29, 32]. Borowski et al., Klepšytė et al. and Münster et al. found that the use of MB injection led to a higher lymph node yield among patients who have received NAT, and the number of cases with insufficient lymph node detection was reduced, while no increase of the lymph node recovery in the subgroup of rectal cancer without preoperative radio-chemotherapy was observed [20, 29, 32]. Similar results were obtained in our research. In our experience, the use of MB injection showed a clinically relevant impact on the total lymph node count, the rate of sufficient (≥12) lymph node extraction, and lymph node staging accuracy in patient subgroups with rectal cancer.

Lymph node yield has a significant association with long term survival [43]. This is probably due to accurate nodal staging and the appropriate indication of adjuvant chemotherapy. Even one positive lymph node can cause a staging shift from stage II to stage III CRC, leading to different postoperative treatment [44, 45]. While stage II CRCs do not always require adjuvant treatment, stage III cancers are followed by adjuvant chemotherapy, as long as the patient is fit enough to complete it [44, 45]. Therefore, an insufficient lymph node extraction might contribute to a worse prognosis [8]. Although several methods have been introduced to increase the number of the dissected lymph node yield, most of them lack information on direct survival benefit [16–22, 24, 26, 27, 29–32]. We found that MB injection might be associated with improved 5-year overall survival among patients with colorectal cancer, undergoing colorectal resection. Similarly, Liu et al. have also investigated the overall survival after methylene blue injection in rectal cancer. However, their study showed no long-term benefit [9]. We observed no difference between the control and the MB arms until 24 months. After a period of a 2-year follow-up, Kaplan-Meier survival curves split up, and at 5 years postoperatively, the difference reached the level of statistical significance. Furthermore, in our stratified subgroup analysis, data suggested that cases with early CRC could profit the most from the MB staining method. The difference between the findings of Liu et al. and our group might be explainable by the alternation of adjuvant oncotherapy strategies among insufficiently staged cases. While Liu et al. reported that their
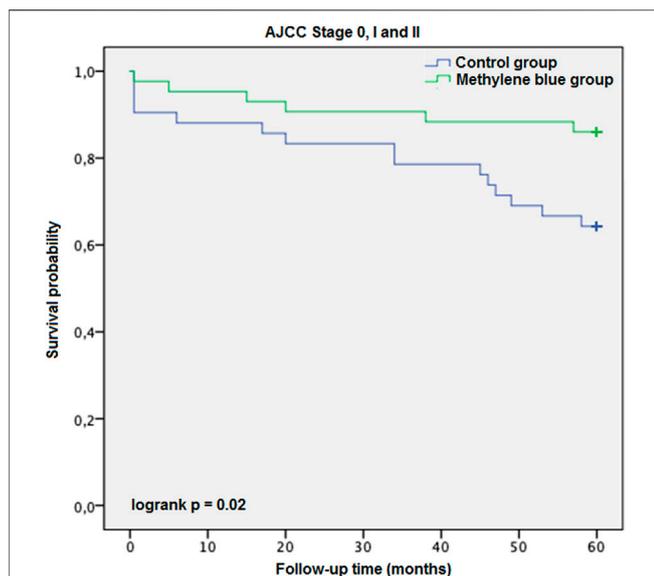
FIGURE 4 | AJCC Stage 0, I and II description: Kaplan-Meier survival curves of enrolled patients with early stage colorectal cancer (AJCC Stages 0, I and II) during the follow-up period, grouped by study intervention.
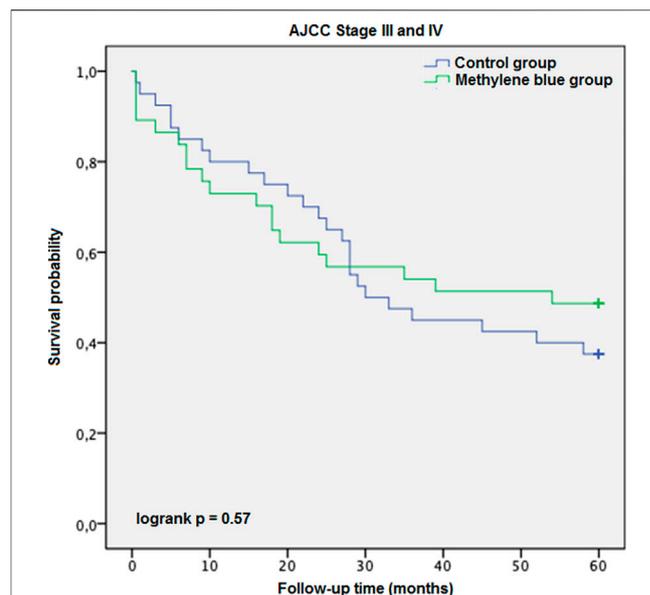

FIGURE 5 | AJCC Stage III and IV description: Kaplan-Meier survival curves of enrolled patients with advanced colorectal cancer (AJCC Stages III and IV) during the follow-up period, grouped by study intervention.

colorectal multidisciplinary team rostered these patients for adjuvant chemotherapy, in our practice, we prefer not to treat patients with less than 12 negative lymph nodes. The necessity of adjuvant chemotherapy in stage II with insufficient (≤12) lymph node removal has a controversial interpretation in the literature. Current colorectal cancer guidelines recommend that early CRCs with less than 12 examined lymph nodes should be considered high-risk for recurrence, and are associated with increased mortality, and therefore, adjuvant chemotherapy should be administered among these cases [44, 45]. Despite this recommendation, the majority of patients could not be given adjuvant chemotherapy due to advanced age and associated comorbidities, which would limit the overall tolerance during chemotherapy [46]. Considering these features, methylene blue injection could play a major role in the appropriate lymph node detection, reducing uncertainty of staging resulting in under- or overtreatment.

Limitations

Our study has limitations. One of our experienced pathologists refused to participate in the trial, and regardless of the methylene blue injection, he performed a fat-dissolving internal step to improve lymph node recognition. His cases had to be excluded from the study. Methylene blue dyeing may not be optimal for every pathologist, particularly if other methods of enhanced lymph node detection are used routinely already. Other techniques of lymph node harvesting (for example alcoholic fixation and fat-dissolving techniques) might have been used as controls. Additionally, the exact sizes of lymph nodes, especially positive lymph nodes, were not recorded in the pathological documentation. Therefore, we cannot comment on the

efficacy of methylene blue injection on identification of smaller mesenteric lymph nodes. Furthermore, a detailed analysis of distinct clinical subgroups to assess effectivity of MB injection would have required an *a priori* power calculation for this purpose, and as such, statistically non-significant results in our subgroups may have stemmed from a type II statistical error.

CONCLUSION

In our study, application of the methylene blue staining technique resulted in an increment of examined lymph node yield, and an improvement of lymph node staging with a 5-year overall survival benefit of patients with colorectal cancer undergoing colorectal resection. In conclusion, methylene blue staining technique seems a reasonable approach to be adapted for routine use in healthcare systems with limited staff and expenditure.

DATA AVAILABILITY STATEMENT

The raw data supporting the conclusion of this article will be made available by the authors, without undue reservation.

ETHICS STATEMENT

Ethics approval: Ethics approval was obtained from the Institutional Ethics Committee for Research and Development

and the Medical Research Council of Hungary. Clinical Trial Registration Number: IV/3228/2021-EKU (Medical Research Council, Hungary) Clinicaltrials.gov Identifier: NCT04842968. Written informed consent for participation was not required for this study in accordance with the national legislation and the institutional requirements.

AUTHOR CONTRIBUTIONS

NS: texting of the manuscript, statistical analysis, literature review, data collection at St. Borbala Hospital site. IB: data collection at Uzsoki Street Hospital. KA: study design, supervision of pathological work-up at St. Borbala Hospital site. AB: supervision of study at Uzsoki Street Hospital site. DK: supervision of pathological work-up at Uzsoki Street Hospital site. DWB: interpretation of statistics and English formulation of the manuscript. BB: study design, ethical

approval gaining, statistical analysis, correction of the manuscript, supervision of study at St. Borbala Hospital site.

CONFLICT OF INTEREST

The authors declare that the research was conducted in the absence of any commercial or financial relationships that could be construed as a potential conflict of interest.
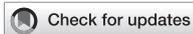
ACKNOWLEDGMENTS

REFERENCES

1. Observatory WGC. Estimated Number of Deaths Worldwide, Both Sexes, All Ages (Graph) (2021). Available at: https://gco.iarc.fr/ (Accessed 04 2021, 01).

2. Wright FC, Law CH, Berry S, Smith AJ. Clinically Important Aspects of Lymph Node Assessment in colon Cancer. J Surg Oncol (2009) 99(4):248–55. doi:10.1002/jso.21226

3. Hohenberger W, Weber K, Matzel K, Papadopoulos T, Merkel S. Standardized Surgery for Colonic Cancer: Complete Mesocolic Excision and central Ligation-Ttechnical Notes and Outcome. Colorectal Dis (2009) 11(4):354–64. discussion 64-5. doi:10.1111/j.1463-1318.2008.01735.x

4. Havenga K, Enker WE, Norstein J, Moriya Y, Heald RJ, van Houwelingen HC, et al. Improved Survival and Local Control after Total Mesorectal Excision or D3 Lymphadenectomy in the Treatment of Primary Rectal Cancer: an International Analysis of 1411 Patients. Eur J Surg Oncol (1999) 25(4):368–74. doi:10.1053/ejso.1999.0659

5. Kulendran M, Stebbing JF, Marks CG, Rockall TA. Predictive and Prognostic Factors in Colorectal Cancer: a Personalized Approach. Cancers (Basel) (2011) 3(2):1622–38. doi:10.3390/cancers3021622

6. Le Voyer TE, Sigurdson ER, Hanlon AL, Mayer RJ, Macdonald JS, Catalano PJ, et al. Colon Cancer Survival Is Associated with Increasing Number of Lymph Nodes Analyzed: a Secondary Survey of Intergroup Trial INT-0089. J Clin Oncol (2003) 21(15):2912–9. doi:10.1200/JCO.2003.05.062

7. Sobin LH, Gospodarowicz MK, Wittekind C. 7th Ed. UICC International Union against Cancer. Wiley-Blackwell (2009). TNM Classification of Malignant Tumours

8. Lei P, Ruan Y, Liu J, Zhang Q, Tang X, Wu J. Prognostic Impact of the Number of Examined Lymph Nodes in Stage II Colorectal Adenocarcinoma: A Retrospective Study. Gastroenterol Res Pract (2020) 2020:8065972. doi:10.1155/2020/8065972

9. Liu J, Huang P, Zheng Z, Chen T, Wei H. Modified Methylene Blue Injection Improves Lymph Node Harvest in Rectal Cancer. ANZ J Surg (2017) 87(4):247–51. doi:10.1111/ans.12889

10. Hamza A, Sakhi R, Khawar S, Alrajjal A, Edens J, Khurram MS, et al. Role of "Second Look" Lymph Node Search in Harvesting Optimal Number of Lymph Nodes for Staging of Colorectal Carcinoma. Gastroenterol Res Pract (2018) 2018:1985031. doi:10.1155/2018/1985031

11. Gurawalia J, Dev K, Nayak SP, Kurpad V, Pandey A. Less Than 12 Lymph Nodes in the Surgical Specimen after Neoadjuvant Chemo-Radiotherapy: an Indicator of Tumor Regression in Locally Advanced Rectal Cancer? J Gastrointest Oncol (2016) 7(6):946–57. doi:10.21037/jgo.2016.09.03

12. Trepanier M, Erkan A, Kouyoumdjian A, Nassif G, Albert M, Monson J, et al. Examining the Relationship between Lymph Node Harvest and Survival in Patients Undergoing Colectomy for colon Adenocarcinoma. Surgery (2019) 166(4):639–47. doi:10.1016/j.surg.2019.03.027

13. Tsai HL, Lu CY, Hsieh JS, Wu DC, Jan CM, Chai CY, et al. The Prognostic Significance of Total Lymph Node Harvest in Patients with T2-4N0M0 Colorectal Cancer. J Gastrointest Surg (2007) 11(5):660–5. doi:10.1007/s11605-007-0119-x

14. Topor B, Acland R, Kolodko V, Galandiuk S. Mesorectal Lymph Nodes: Their Location and Distribution within the Mesorectum. Dis Colon Rectum (2003) 46(6):779–85. doi:10.1007/s10350-004-6656-4

15. Markl B, Rossle J, Arnholdt HM, Schaller T, Krammer I, Cacchi C, et al. The Clinical Significance of Lymph Node Size in colon Cancer. Mod Pathol (2012) 25(10):1413–22. doi:10.1038/modpathol.2012.92

16. Cawthorn SJ, Gibbs NM, Marks CG. Clearance Technique for the Detection of Lymph Nodes in Colorectal Cancer. Br J Surg (1986) 73(1):58–60. doi:10.1002/bjs.1800730124

17. Basten O, Bandorski D, Bismarck C, Neumann K, Fisseler-Eckhoff A. Acetone Compression. A Fast, Standardized Method to Investigate Gastrointestinal Lymph Nodes. Pathologe (2010) 31(3):218–24. doi:10.1007/s00292-009-1256-7

18. Reese JA, Hall C, Bowles K, Moesinger RC. Colorectal Surgical Specimen Lymph Node Harvest: Improvement of Lymph Node Yield with a Pathology Assistant. J Gastrointest Surg (2009) 13(8):1459–63. doi:10.1007/s11605-009-0820-z

19. Markl B, Kerwel TG, Wagner T, Anthuber M, Arnholdt HM. Methylene Blue Injection into the Rectal Artery as a Simple Method to Improve Lymph Node Harvest in Rectal Cancer. Mod Pathol (2007) 20(7):797–801. doi:10.1038/modpathol.3800824

20. Borowski DW, Banky B, Banerjee AK, Agarwal AK, Tabaqchali MA, Garg DK, et al. Intra-arterial Methylene Blue Injection into Ex Vivo Colorectal Cancer Specimens Improves Lymph Node Staging Accuracy: a Randomized Controlled Trial. Colorectal Dis (2014) 16(9):681–9. doi:10.1111/codi.12681

21. Markl B, Schaller T, Krammer I, Cacchi C, Arnholdt HM, Schenkirsch G, et al. Methylene Blue-Assisted Lymph Node Dissection Technique Is Not Associated with an Increased Detection of Lymph Node Metastases in Colorectal Cancer. Mod Pathol (2013) 26(9):1246–54. doi:10.1038/modpathol.2013.61

22. Cai HK, He HF, Tian W, Zhou MQ, Hu Y, Deng YC. Colorectal Cancer Lymph Node Staining by Activated Carbon Nanoparticles Suspension In Vivo or Methylene Blue In Vitro. World J Gastroenterol (2012) 18(42):6148–54. doi:10.3748/wjg.v18.i42.6148

23. Tornroos A, Shabo I, Druvefors B, Arbman G, Olsson H. Postoperative Intra-arterial Methylene Blue Injection of Colorectal Cancer Specimens Increases the Number of Lymph Nodes Recovered. Histopathology (2011) 58(3):408–13. doi:10.1111/j.1365-2559.2011.03755.x

24. Kerwel TG, Spatz J, Anthuber M, Wunsch K, Arnholdt H, Markl B. Injecting Methylene Blue into the Inferior Mesenteric Artery Assures an Adequate Lymph Node Harvest and Eliminates Pathologist Variability in Nodal Staging for Rectal Cancer. Dis Colon Rectum (2009) 52(5):935–41. doi:10.1007/DCR.0b013e31819f28c9

25. Markl B, Kerwel T, Jahnig H, Anthuber M, Arnholdt H. Lymph Node Preparation in Colorectal Cancer. *Ex Vivo* Methylene Blue Injection as a Novel Technique to Improve Lymph Node Visualization. *Pathologe* (2008) 29(4):274–9. doi:10.1007/s00292-007-0950-6

26. Markl B, Olbrich G, Schenkirsch G, Kretsinger H, Kriening B, Anthuber M. Clinical Significance of International Union against Cancer pN Staging and Lymph Node Ratio in Node-Positive Colorectal Cancer after Advanced Lymph Node Dissection. *Dis Colon Rectum* (2016) 59(5):386–95. doi:10.1097/DCR.0000000000000569

27. Reima H, Saar H, Innos K, Soplepmann J. Methylene Blue Intra-arterial Staining of Resected Colorectal Cancer Specimens Improves Accuracy of Nodal Staging: A Randomized Controlled Trial. *Eur J Surg Oncol* (2016) 42(11):1642–6. doi:10.1016/j.ejso.2016.06.001

28. Vasala A, Nair HG, Rao ST, Tagore KR, Murthy SS, Fonseca D. Impact of Methylene Blue Staining in the Retrieval of Lymph Nodes in Resected Colorectal Cancer Specimens. *Indian J Pathol Microbiol* (2016) 59(4):504–6. doi:10.4103/0377-4929.191804

29. Munster M, Hanisch U, Tuffaha M, Kube R, Ptok H. *Ex Vivo* Intra-arterial Methylene Blue Injection in Rectal Cancer Specimens Increases the Lymph-Node Harvest, Especially after Preoperative Radiation. *World J Surg* (2016) 40(2):463–70. doi:10.1007/s00268-015-3230-2

30. Kir G, Alimoglu O, Sarbay BC, Bas G. *Ex Vivo* intra-arterial Methylene Blue Injection in the Operation Theater May Improve the Detection of Lymph Node Metastases in Colorectal Cancer. *Pathol Res Pract* (2014) 210(12):818–21. doi:10.1016/j.prp.2014.09.003

31. Jepsen RK, Ingeholm P, Lund EL. Upstaging of Early Colorectal Cancers Following Improved Lymph Node Yield after Methylene Blue Injection. *Histopathology* (2012) 61(5):788–94. doi:10.1111/j.1365-2559.2012.04287.x

32. Klepsyte E, Samalavicius NE. Injection of Methylene Blue Solution into the Inferior Mesenteric Artery of Resected Rectal Specimens for Rectal Cancer as a Method for Increasing the Lymph Node Harvest. *Tech Coloproctol* (2012) 16(3):207–11. doi:10.1007/s10151-012-0816-7

33. Markl B, Kerwel TG, Jahnig HG, Oruzio D, Arnholdt HM, Scholer C, et al. Methylene Blue-Assisted Lymph Node Dissection in colon Specimens: a Prospective, Randomized Study. *Am J Clin Pathol* (2008) 130(6):913–9. doi:10.1309/AJCPVAPB5APABJNX

34. Chapman B, Paquette C, Tooke C, Schwartz M, Osler T, Weaver D, et al. Impact of Schwartz Enhanced Visualization Solution on Staging Colorectal Cancer and Clinicopathological Features Associated with Lymph Node Count. *Dis Colon Rectum* (2013) 56(9):1028–35. doi:10.1097/DCR.0b013e31829c41ba

35. Johnson PM, Malatjalian D, Porter GA. Adequacy of Nodal Harvest in Colorectal Cancer: a Consecutive Cohort Study. *J Gastrointest Surg* (2002) 6(6):883–8. discussion 9–90. doi:10.1016/s1091-255x(02)00131-2

36. Marks JH, Valsdottir EB, Rather AA, Nweze IC, Newman DA, Chernick MR. Fewer Than 12 Lymph Nodes Can Be Expected in a Surgical Specimen after High-Dose Chemoradiation Therapy for Rectal Cancer. *Dis Colon Rectum* (2010) 53(7):1023–9. doi:10.1007/DCR.0b013e3181dadeb4

37. Vather R, Sammour T, Kahokehr A, Connolly A, Hill A. Quantitative Lymph Node Evaluation as an Independent Marker of Long-Term Prognosis in Stage III Rectal Cancer. *ANZ J Surg* (2011) 81(12):883–8. doi:10.1111/j.1445-2197.2010.05595.x

38. Resch A, Langner C. Lymph Node Staging in Colorectal Cancer: Old Controversies and Recent Advances. *World J Gastroenterol* (2013) 19(46):8515–26. doi:10.3748/wjg.v19.i46.8515

39. Haboubi NY, Abdalla SA, Amini S, Clark P, Dougal M, Dube A, et al. The Novel Combination of Fat Clearance and Immunohistochemistry Improves Prediction of the Outcome of Patients with Colorectal Carcinomas: a Preliminary Study. *Int J Colorectal Dis* (1998) 13(2):99–102. doi:10.1007/s003840050143

40. Wijesuriya RE, Deen KI, Hewavisenthi J, Balawardana J, Perera M. Neoadjuvant Therapy for Rectal Cancer Down-Stages the Tumor but Reduces Lymph Node Harvest Significantly. *Surg Today* (2005) 35(6):442–5. doi:10.1007/s00595-004-2956-5

41. Baxter NN, Morris AM, Rothenberger DA, Tepper JE. Impact of Preoperative Radiation for Rectal Cancer on Subsequent Lymph Node Evaluation: a Population-Based Analysis. *Int J Radiat Oncol Biol Phys* (2005) 61(2):426–31. doi:10.1016/j.ijrobp.2004.06.259

42. Mekenkamp LJ, van Krieken JH, Marijnen CA, van de Velde CJ, Nagtegaal ID, Pathology Review C, et al. Lymph Node Retrieval in Rectal Cancer Is Dependent on many Factors-Tthe Role of the Tumor, the Patient, the Surgeon, the Radiotherapist, and the Pathologist. *Am J Surg Pathol* (2009) 33(10):1547–53. doi:10.1097/PAS.0b013e3181b2e01f

43. Foo CC, Ku C, Wei R, Yip J, Tsang J, Chan TY, et al. How Does Lymph Node Yield Affect Survival Outcomes of Stage I and II colon Cancer? *World J Surg Oncol* (2020) 18(1):22. doi:10.1186/s12957-020-1802-6

44. Argiles G, Tabernero J, Labianca R, Hochhauser D, Salazar R, Iveson T, et al. Localised colon Cancer: ESMO Clinical Practice Guidelines for Diagnosis, Treatment and Follow-Up. *Ann Oncol* (2020) 31(10):1291–305. doi:10.1016/j.annonc.2020.06.022

45. Benson AB, Venook AP, Al-Hawary MM, Arain MA, Chen YJ, Ciombor KK, et al. Colon Cancer, Version 2.2021, NCCN Clinical Practice Guidelines in Oncology. *J Natl Compr Canc Netw* (2021) 19(3):329–59. doi:10.6004/jnccn.2021.0012

46. Wells KO, Hawkins AT, Krishnamurthy DM, Dharmarajan S, Glasgow SC, Hunt SR, et al. Omission of Adjuvant Chemotherapy Is Associated with Increased Mortality in Patients with T3N0 Colon Cancer with Inadequate Lymph Node Harvest. *Dis Colon Rectum* (2017) 60(1):15–21. doi:10.1097/DCR.0000000000000729

Check for updates

MET gene alterations predict poor survival following chemotherapy in patients with advanced cancer

Jihoon Ko[1†], Jaeyun Jung[1†], Seung Tae Kim[1], Jung Yong Hong[1],
Sehhoon Park[1], Joon Oh Park[1], Young Suk Park[1], Ho Yeong Lim[1],
Soomin Ahn[2], Kyoung-Mee Kim[2], Won Ki Kang[1] and Jeeyun Lee[1*]

[1]Division of Hematology-Oncology, Department of Medicine, Samsung Medical Center, School of
Medicine, Sungkyunkwan University, Seoul, South Korea, [2]Department of Pathology and Translational
Genomics, Samsung Medical Center, School of Medicine, Sungkyunkwan University, Seoul, South Korea

Background: To aid in oncology drug development, we investigated MET proto-oncogene receptor tyrosine kinase gene aberrations in 2,239 oncology patients who underwent next-generation sequencing (NGS) in clinical practice.

Materials and methods: From November 2019 to January 2021, 2,239 patients with advanced solid tumors who visited oncology clinics underwent NGS. The NGS panel included >500 comprehensive NGS tests using archival tissue specimens. Programmed death-ligand 1(PD-L1) 22C3 assay results and clinical records regarding initial chemotherapy were available for 1,137 (50.8%) and 1,761 (78.7%) patients, respectively for overall survival (OS) analysis.

Results: The 2,239 patients represented 37 types of cancer. The NGS panel included >500 genes, microsatellite instability status, tumor mutational burden, and fusions. The most common cancer types were colorectal ($N = 702$), gastric ($N = 481$), and sarcoma ($N = 180$). MET aberrations were detected in 212 patients. All MET-amplified tumors had microsatellite stable status, and 8 had a high tumor mutational burden. Of 46 patients with MET-amplified cancers, 8 had MET-positive protein expression by immunohistochemistry (2+ and 3+). MET fusion was detected in 10 patients. Partner genes of MET fusion included ST7, TFEC, LRRD1, CFTR, CAV1, PCM1, HLA-DRB1, and CAPZA2. In survival analysis, patients with amplification of MET gene fusion had shorter OS and progression-free survival (PFS) than those without. Thus, MET aberration was determined to be a factor of response to chemotherapy.

Conclusion: Approximately 2.1% and 0.4% of patients with advanced solid tumors demonstrated MET gene amplification and fusion, respectively, and displayed a worse response to chemotherapy and significantly shorter OS and PFS than those without MET gene amplification or fusion.

KEYWORDS

next-generation sequencing, oncogene, overall survival analysis, MET, MET alterations, chemotherapy, cancer

Introduction

MET proto-oncogene receptor tyrosine kinase plays a pivotal role in multiple cellular processes such as carcinogenesis and tumor progression in several solid tumor types [1,2,3]. Studies have shown that dysregulation of MET signaling pathway including gene amplification, overexpression of the ligand and/or receptor, autocrine signaling, and paracrine signaling has been indicated as a cancer-associated mechanism [4,5,6,7]. Because MET plays a critical role in cancer progression, its inhibition could have a substantial impact on the treatment outcome of patients with solid tumors with an aberrant MET pathway. For instance, approximately 5% of patients with gastric cancer (GC) have increased copy numbers (no. of gene copies >4) of the MET gene [8,9,10,11,12]. Moreover, the MET Gastric trial, in which patients with GC with MET overexpression (immunohistochemistry [IHC], 2+/3+) received onartuzumab, an anti-MET monoclonal antibody, plus FOLFOX did not demonstrate significantly improved survival [13]. Additionally, the VIKTORY basket trial observed a promising overall response rate of 50% among 20 patients with MET-amplified GC [14] using savolitinib, a MET tyrosine kinase inhibitor (TKI). Several trials of MET-targeted agents are ongoing, specifically for patients with GC [10, 11].

MET amplification has been reported in 5%–26% of cases to be implicated in the acquired resistance to epithelial growth factor receptor TKIs [15]. Moreover, MET alterations have been identified in primary tumors and metastatic lesions of several types of cancer, including head and neck, papillary renal cell carcinoma, liver, ovarian, and non-small cell lung cancer [16]. Elevated levels of the HGF receptor ligand or overexpression of MET is often associated with resistance to chemotherapy and radiotherapy [17]. Overall, MET dysregulation is recognized as a negative prognostic factor in many solid cancers. However, few studies have provided real-world data of MET dysregulation across many types of cancer. Additionally, more countries including the United States, Korea, and Japan, are adopting the use of next generation sequencing (NGS) in clinical practice for patients with metastatic cancer [14, 18, 19]. Therefore, understanding the prevalence of MET-aberrant solid tumor types is vital to optimize clinical trial design.

This study aimed to investigate the incidence of MET aberrations, including copy number variations (CNVs), especially gene amplification, and/or fusions using a 500-gene NGS panel as real-world, pan-cancer data. Furthermore, we analyzed the impact of MET alterations on response to chemotherapy and survival.

Materials and methods

Ethical approval

This retrospective study was approved by the Institutional Review Board of Samsung Medical Center (IRB File No. 2021-09-052). All patients who participated in this study provided written informed consent prior to NGS, and additional informed consent was waived by the IRB. This study was performed in accordance with the principles of the Declaration of Helsinki and Korean Good Clinical Practice guidelines.

DNA extraction

Tumor regions were micro-dissected for most tumor tissues, except for the samples used in genomic DNA extraction. Genomic DNA was isolated from formalin-fixed paraffin-embedded (FFPE) tissue fragments and purified using AllPrep DNA/RNA FFPE Kit (Qiagen, Venlo, Netherlands). DNA concentration was measured using a Qubit dsDNA HS assay kit (Thermo Fisher Scientific, Waltham, MA, United States), and 40 ng DNA was used as the input for library preparation. The DNA integrity number, a measure of DNA fragment size and quality, was determined using the Genomic DNA ScreenTape assay on an Agilent 2,200 TapeStation system (Agilent Technologies, Santa Clara, CA, United States).

Library preparation and data analysis

The DNA library was prepared using a hybrid capture-based TruSight Oncology 500 (TSO 500) DNA/RNA NextSeq Kit according to the manufacturer's protocol. During library preparation, enrichment chemistry was optimized to capture nucleic acid targets from FFPE tissues. Unique molecular identifiers were used in TSO 500 analysis to determine the unique coverage at each position and reduce any background noise caused by sequencing and deamination artifacts in the samples. This technique enables thxe detection of variants at low variant allele frequencies while simultaneously suppressing errors, thereby providing high specificity.

Sequence data were analyzed for clinically relevant classes of genomic alterations, including single nucleotide variants (SNVs), small insertions and deletions (indels), CNVs, and rearrangements/fusions. Results of SNVs and small indels with a variant allele frequency of <2% were excluded. Average CNVs of more than four were considered as gain and those less than one were considered as loss. Only gain (gene amplification) was analyzed in the TSO 500-CNV analysis, and RNA translocation-supporting reads of >4–12 were considered as translocation, which was dependent on the quality of the sample. Data outputs exported from the TSO 500 pipeline (Illumina, San Diego, CA, United States) were annotated using the Ensembl Variant Effect Predictor Annotation Engine with information from databases, such as dbSNP, gnomAD genome and exome, 1,000 genomes, ClinVar, COSMIC, RefSeq, and Ensembl [20]. The processed genomic changes were categorized according to a four-tier system proposed by

TABLE 1 Clinicopathologic features of study patient.

Sex	
Male	1,342 (60.0%)
Female	894 (40.0%)
TMB	
Low	1,905 (85.2%)
High	332 (14.8%)
MSI	
Low	13 (0.6%)
High	38 (1.7%)
MSS	2,187 (97.7%)
CNV	2,515
Tier I/II	841 (33.4%)
Tier III	1,674 (66.6%)
Fusion	383
Tier I/II	149 (38.9%)
Tier III	234 (61.1%)
SNV	44,534
Tier I/II	1,663 (3.7%)
Tier III	42,871 (96.3%)

TABLE 2 Tumor types in the cohort.

Tumor type	#Patient
Adrenocortical carcinoma	1 (0.04%)
AOV cancer (Ampulla of Vater)	24 (1.07%)
Bladder cancer	73 (3.26%)
Brain tumor	1 (0.04%)
Breast cancer	29 (1.30%)
CCC (Cholangiocellular carcinoma)	157 (7.01%)
Cervical cancer	1 (0.04%)
Colorectal cancer	702 (31.35%)
Duodenal cancer	6 (0.27%)
EAC cancer (Esophageal adenocarcinoma)	1 (0.04%)
Esophageal cancer	1 (0.04%)
Fallopian tube cancer	1 (0.04%)
Gallbladder cancer	49 (2.19%)
Gastric cancer	481 (21.48%)
GIST (Gastrointestinal stromal tumor)	17 (0.76%)
HCC (Hepatocellular carcinoma)	46 (2.05%)
Head and Neck cancer	18 (0.80%)
Kidney cancer	9 (0.40%)
Malignant solitary fibrous tumor	5 (0.22%)
Malignant thymoma	1 (0.04%)
Melanoma	111 (4.96%)
Merkel cell carcinoma	1 (0.04%)
MUO (Metastasis of unknown origin)	25 (1.12%)
NET (Neuroendocrine tumors)	24 (1.07%)
Neurofibromatosis	1 (0.04%)
NSCLC (Non-small cell lung cancer)	119 (5.31%)
Ovarian cancer	9 (0.40%)
Paget's disease	2 (0.09%)
Pancreatic cancer	123 (5.49%)
Prostate cancer	5 (0.22%)
Sarcoma	180 (8.04%)
SCLC (Small cell lung cancer)	1 (0.04%)
Skin cancer	4 (0.18%)
Small bowel cancer	4 (0.18%)
Thymic carcinoma	2 (0.09%)
Thyroid cancer	3 (0.13%)
Tracheobronchial adenoid cystic carcinoma	1 (0.04%)
Uterine cancer	1 (0.04%)
	2,239

the American Society of Clinical Oncology/College of American Pathologists and annotated with proper Ref. [21]. The TSO 500 pipeline (Illumina) was used to evaluate tumor mutational burden (TMB) and microsatellite instability (MSI) statuses [20]. TMB was calculated by excluding any variant with an observed allele count ≥ 10 in any of the GnomAD exome, genome, and 1,000 genomes databases, and including variants in the coding region (RefSeq Cds), variant frequency $\geq 5\%$, coverage $\geq 50\times$, SNVs, and indels, as well as including and excluding nonsynonymous and synonymous variants. The effective panel size for TMB was the total coding region with coverage $>50\times$. MSI was calculated from the microsatellite sites to evaluate instability relative to a set of normal baseline samples based on entropy metrics. The percentage of unstable MSI sites out of the total assessed MSI sites was reported as a sample-level microsatellite score.
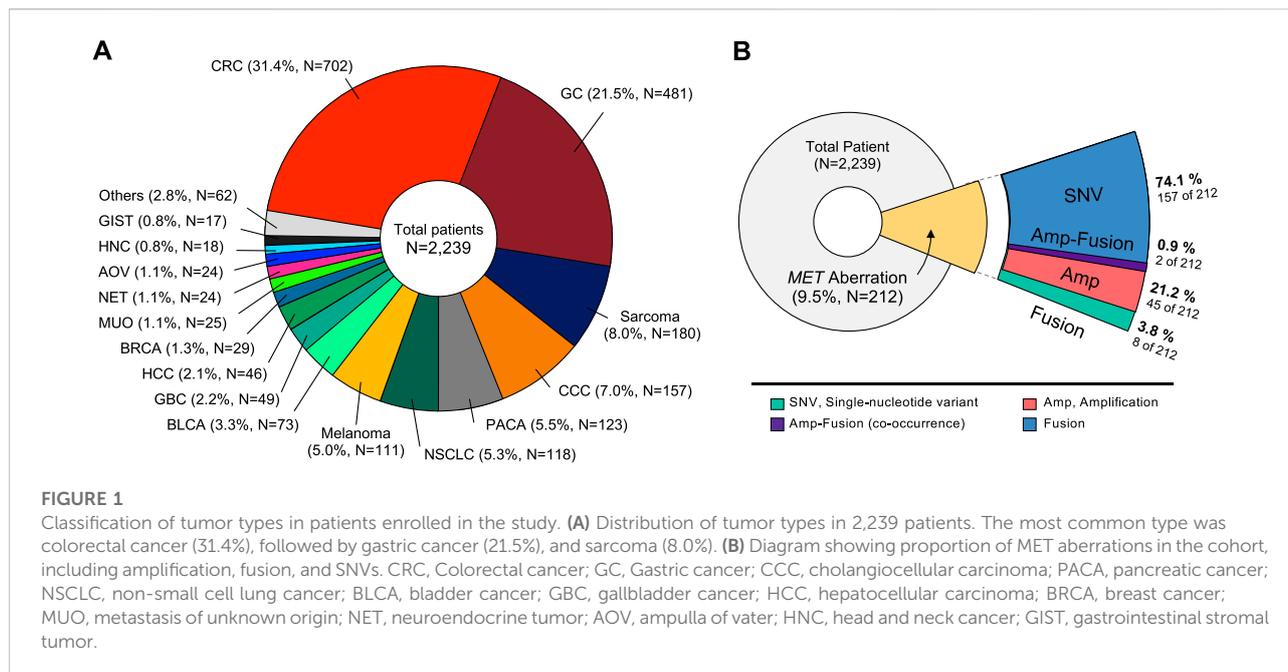
Statistical analysis

Data are presented as the mean $\pm$ SD. All statistical analyses were performed using GraphPad Prism 8.0 (GraphPad Software, San Diego, CA, United States; http://www.graphpad.com/). Statistical significance was set at $p < 0.05$. All statistical tests were two-sided. Correlations between clinicopathologic features were analyzed using a t-test, Fisher exact test, or one-way analysis of variance, as appropriate. Overall survival (OS) was defined as the time from the first treatment to the date of death. Progression-free survival (PFS) was defined as the time from the first treatment to the date of disease progression or death from any cause. The Kaplan-Meier method was used to analyze all survival events, and the 95% confidence interval for the median time to each event was computed. All statistical analyses were performed using Prism 8 (GraphPad Software, San Diego, CA, United States; http://www.graphpad.com/) or R for windows (version 4.1.2, https://cran.r-project.org/bin/windows/base/). RStudio desktop 1.4 was used for drawing all graphics (RStudio Team, Boston, MA, United States; https://www.rstudio.com/products/rstudio/download/).

FIGURE 1
Classification of tumor types in patients enrolled in the study. **(A)** Distribution of tumor types in 2,239 patients. The most common type was colorectal cancer (31.4%), followed by gastric cancer (21.5%), and sarcoma (8.0%). **(B)** Diagram showing proportion of MET aberrations in the cohort, including amplification, fusion, and SNVs. CRC, Colorectal cancer; GC, Gastric cancer; CCC, cholangiocellular carcinoma; PACA, pancreatic cancer; NSCLC, non-small cell lung cancer; BLCA, bladder cancer; GBC, gallbladder cancer; HCC, hepatocellular carcinoma; BRCA, breast cancer; MUO, metastasis of unknown origin; NET, neuroendocrine tumor; AOV, ampulla of vater; HNC, head and neck cancer; GIST, gastrointestinal stromal tumor.

Results

Patient cohort

We conducted a study of aberrant genes utilizing NGS with a panel targeting more than 500 oncogenes (TSO500, Illumina) in a total of 2,239 patients with advanced cancer (Table 1). By gender, there were 1,342 males (60.0%) and 894 females (40.0%). And as for TMB, 332 cases (14.8%) of High-TMB (≥13 mut/Mb) and 1,905 cases (85.2%) of Low-TMB were found. In the case of MSI, 13 cases (0.6%) with low-MSI, 38 cases (1.7%) with high-MSI, and most of the rest were MSS (microsatellite stability). In this cohort, 38 types of cancer were identified (Table 2). The most common cancers were colorectal cancer (702 cases, 31.4%), gastric cancer (481 cases, 21.5%), and sarcoma (180 cases, 8.0%) in that order (Figure 1A). MET aberrations, known to be strongly correlated with tumorigenesis and metastasis, were found in a total of 212 patients. The incidence of alterations were: MET gene amplification (21.2%), MET fusion (3.8%), co-occurrence of amplification and fusion (0.9%), and SNV (74.1%) (Figure 1B).

MET gene amplification

We specifically investigated MET gene amplification in MET aberration involving copy number and structural changes as well as nucleotide variants. In this case, we collected the cases more than 4 copies of MET gene. The patients' age ranged from 30 to 82 years with a median of 58 years, and no gender bias was observed. Of the 47 patients with MET amplification, 14 had GC

(2.9% of total GC patients), 10 (1.4%) had colorectal cancer, 7 (6.3%) had melanoma, 6 (3.8%) had cholangiocellular carcinoma (CCC), 2 each had sarcoma (1.1%); hepatocellular carcinoma (HCC) (4.3%); pancreatic cancer (1.6%); and non-small cell lung cancer (1.7%), and gallbladder cancer (4.1%). In addition, we investigated tumors with a high incidence of MET amplification. The incidence of MET amplification among melanoma patients was 6.3%, which showed a high expression rate within the group. Furthermore, 4.3% of HCC patients, 3.8% of CCC patients, and 3.1% of GC patients showed a high incidence of MET amplification (Figure 2A). We analyzed the range of number of amplified MET copies in the patient group. MET copy numbers ranged from 3.1 to 52.2 with a median of 7.2. The highest level of MET copy number is 52.2 identified in a GC patient (Figure 2B). Moreover, all MET-amplified tumors had MSS status and 4.3% ($N = 2$) of cases had a high TMB status (≥13 mut/Mb) (TMB ranged from 0.8 to 15.7 with median of 7.0). In the pan-tumor analysis of patients with PD-L1 IHC data available, no correlation between PD-L1 expression and MET amplification was observed. The overall genomic landscape including known oncogenes in the MET-amplified patient cohort is provided in Figure 2C. Briefly, most MET-amplified patients had concurrent mutations in TP53, APC, and ARID1A across all cancer types surveyed in this study (Figure 2C).

MET gene fusion

MET fusion occurs due to gene rearrangement and has been observed in various types of cancer. As mentioned above,
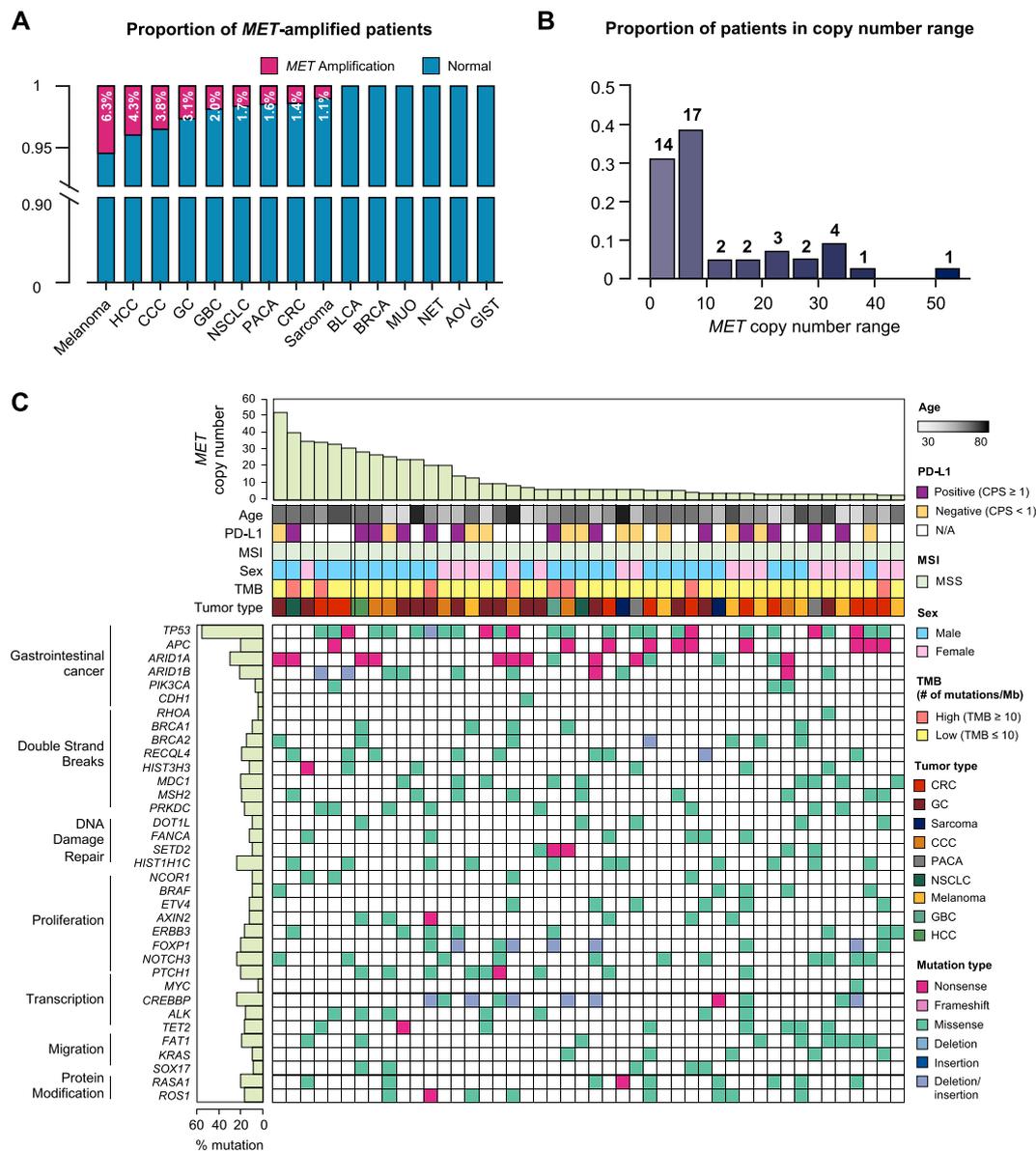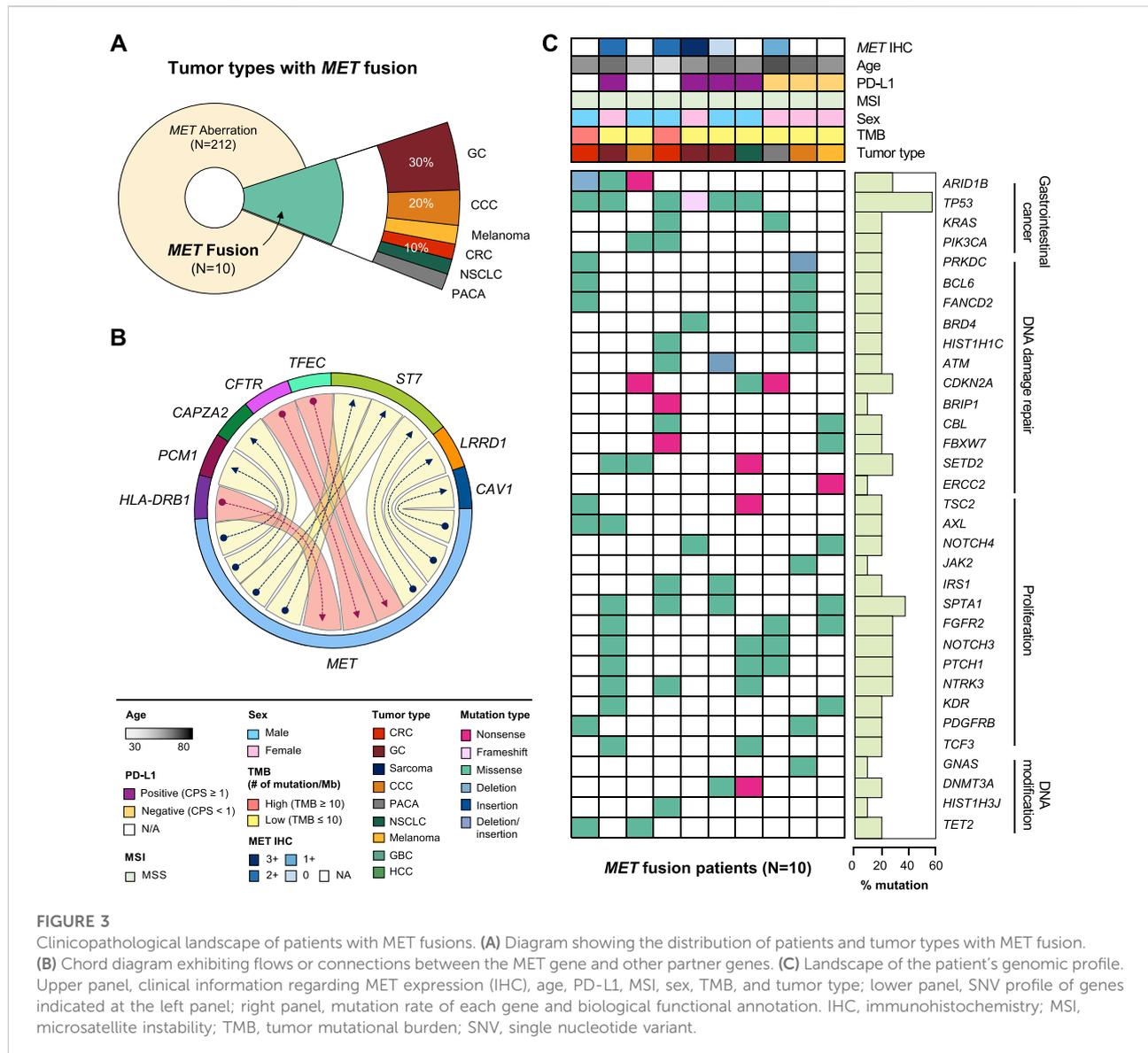
FIGURE 2
Genomic landscape of cancer patients with MET copy number variations. **(A)** Bar graph showing the incidence of MET amplification by tumor type. **(B)** The distribution of MET-amplified patients according to copy number. **(C)** The landscape of patients' genomic profiles. Top panel, copy number of each patient; middle panel, clinical information including age, PD-L1 expression (IHC), MSI, sex, TMB, and cancer type; bottom panel, oncoprint showing SNV type of genes listed at the left. Left panel, the alterations rate of each gene in total samples (N = 46) with biological function annotation. IHC, immunohistochemistry; MSI, microsatellite instability; TMB, tumor mutational burden; SNV, single nucleotide variant.

approximately 0.4% (10 of 2,239) of the patients in this study had MET fusion including cooccurrence of amplification and fusion cases (Figure 3A). The partner genes of MET fusion included ST7, TFEC, LRRD1, CFTR, CAV1, PCM1, CAPZA2, and HAL-DRB1 (Figure 3B). The most frequent gene fusion occurred between MET and ST7. Excluding fusion with PCM1 and CAPZA2, all breaking began in the middle of the MET gene whose front part

was fused to the back part of the partner gene. Regarding mutation type, missense MET alterations was dominant across all tumor types. Moreover, several cases of frameshift deletion, in-frame deletion, and nonsense mutations were observed. The most frequent MET SNVs were MET L211T (N = 24) and A1381T (N = 19). Finally, most patients had concurrent mutations in TP53, KRAS, and ARID1B (Figure 3C).
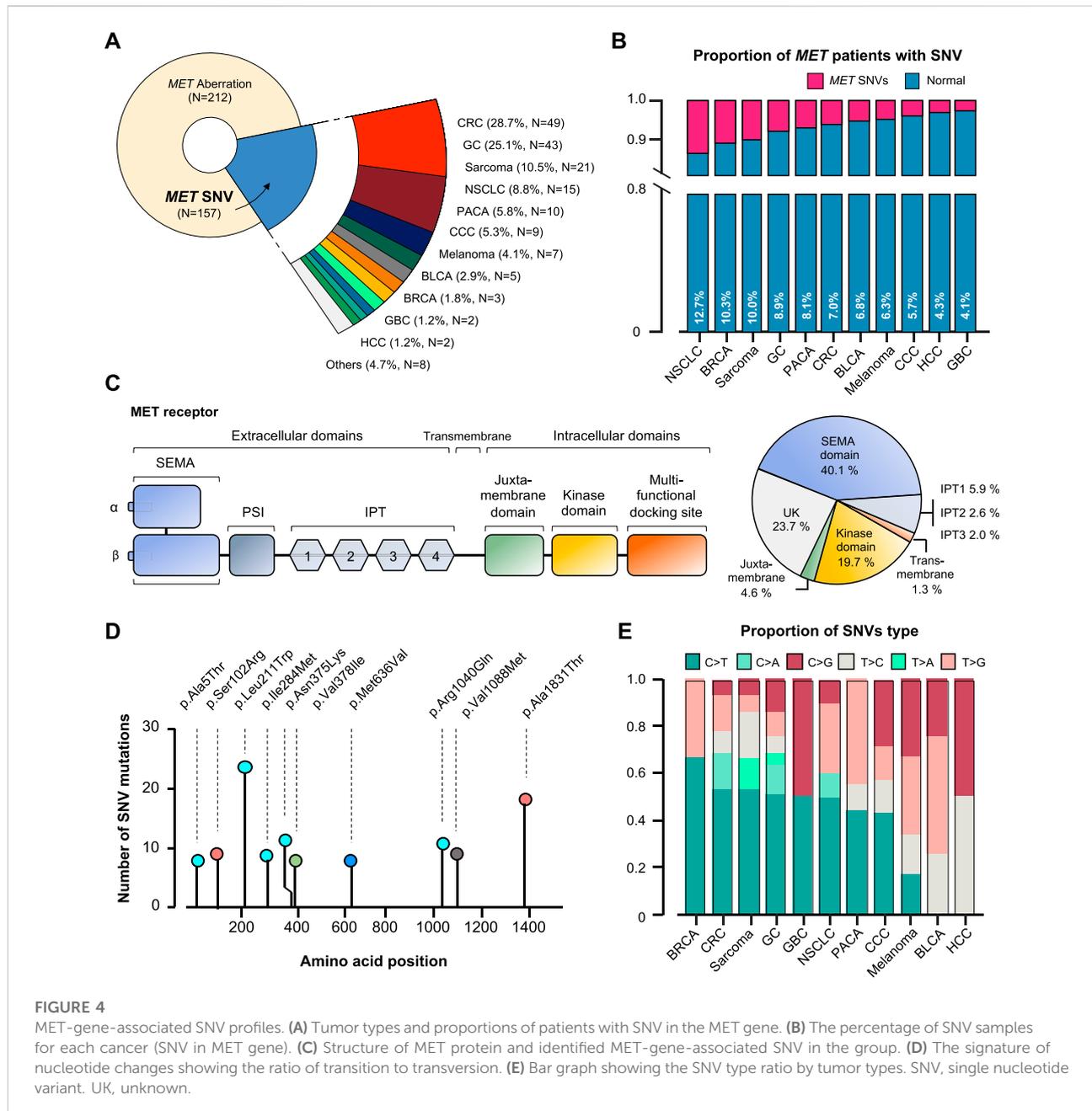
FIGURE 3
Clinicopathological landscape of patients with MET fusions. **(A)** Diagram showing the distribution of patients and tumor types with MET fusion. **(B)** Chord diagram exhibiting flows or connections between the MET gene and other partner genes. **(C)** Landscape of the patient's genomic profile. Upper panel, clinical information regarding MET expression (IHC), age, PD-L1, MSI, sex, TMB, and tumor type; lower panel, SNV profile of genes indicated at the left panel; right panel, mutation rate of each gene and biological functional annotation. IHC, immunohistochemistry; MSI, microsatellite instability; TMB, tumor mutational burden; SNV, single nucleotide variant.

MET Single-Nucleotide variations

Of the 157 MET SNV patients, 28.7% had CRC ($N = 49$), 25.1% had GC ($N = 43$), 10.5% had sarcoma ($N = 21$), 8.8% had NSCLC ($N = 15$), and other tumors (Figure 4A). It was analyzed that the incidence of cancer caused by MET SNV was high in the order of NSCLC (12.7%), breast cancer (BRCA; 10.3%), sarcoma (10.0%), and GC (8.9%) (Figure 4B). We performed single nucleotide variant analysis of MET protein. Of 157, 40.1% ($n = 61$) were detected mainly in the semaphorin (Sema) domain (E168D) ($N = 56$ for exon 2; $n = 5$ for exon 1). And, MET exon 14 juxtamembrane splicing mutations ($N = 7$) were detected (GC 3; Sarcoma 2; CRC 1; and CCC 1). SNV alterations were identified in the MET IPT/TIG (Ig-like, plexins, transcription factors) domain (exon 5-9). In addition,

mutations were detected in the intracellular tyrosine kinase domain of MET (exon 16,18-21) in 19.7% (Figure 4C). We conducted an investigation into sequence variations of amino acids. The p. L211W variant located in coding exon 1 of the MET gene (also known as c.632T>G) was found to have the most T to G substitution at nucleotide position 632 (Figure 4D). We plotted incidence by SNV type relative to tumor type (Figure 4E).

Patients with MET gene aberration showed poor survival

We established the genomic landscape of patients with MET aberrations (Figure 5A). In an alluvial diagram, patients with MET amplification or fusion showed a correlation with disease

FIGURE 4
MET-gene-associated SNV profiles. **(A)** Tumor types and proportions of patients with SNV in the MET gene. **(B)** The percentage of SNV samples for each cancer (SNV in MET gene). **(C)** Structure of MET protein and identified MET-gene-associated SNV in the group. **(D)** The signature of nucleotide changes showing the ratio of transition to transversion. **(E)** Bar graph showing the SNV type ratio by tumor types. SNV, single nucleotide variant. UK, unknown.

progression after first-line chemotherapy (29/41 patients with MET amplification had progressive disease (PD); 4/6 patients with MET fusion had PD) (Figure 5B). Moreover, in the survival curve, patients with MET CNV amplification or fusion showed significantly shorter OS ($p = 0.026$) and PFS ($p = 0.007$). Finally, we compared patients with CNV amplification in the MET gene to those with amplification in any gene. In this comparison, MET-CNV patients showed significantly shorter OS ($p = 0.0039$) and PFS ($p = 0.016$) than patients with amplification in any gene, suggesting that MET amplification is an influential factor for survival following first-line chemotherapy (Figure 5C).

Discussion

In this study, we comprehensively investigated the incidence of MET alterations (gene amplification, SNV, and fusion) in a consecutive series of 2,239 patients with cancer who were candidates for palliative chemotherapy. Our cohort represented 37 different types of cancer. We found the incidence of MET amplification to be 2.1% ($N = 46$) and that of MET fusion to be 0.4% ($N = 10$), while 0.1% of patients ($N = 3$) had both MET amplification and fusion, simultaneously. Additionally, MET amplification was found in nine types of
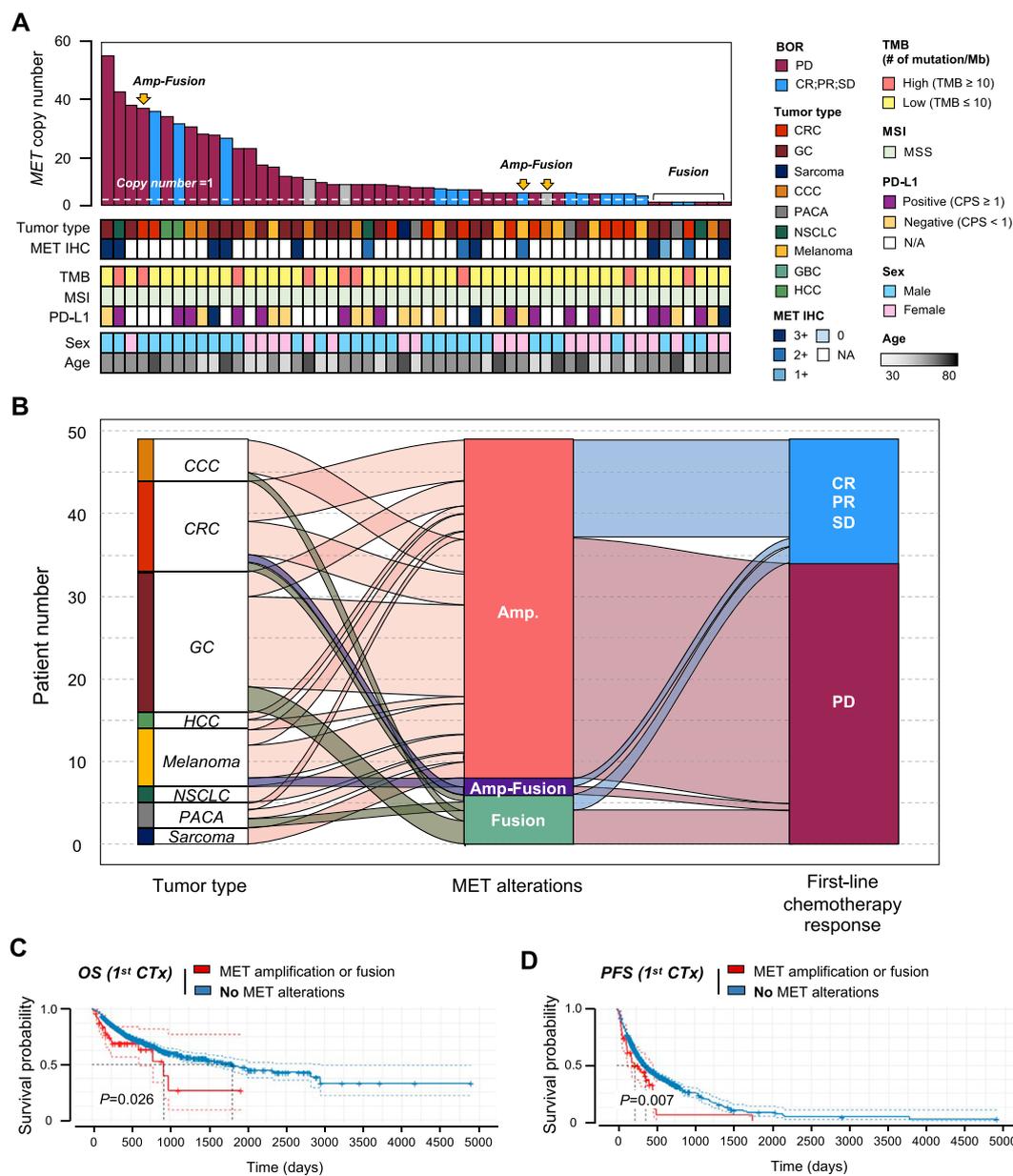
FIGURE 5
Correlation between MET gene alterations and response to first-line chemotherapy. **(A)** Cancer genomic landscape refers to the distribution pattern of MET gene alterations across the genome in tumor types. **(B)** Alluvial diagram showing the distribution of MET aberration in tumor types and the best response to first-line chemotherapy. Kaplan-Meier curves showing **(C)** overall survival (OS) and **(D)** progression-free survival (PFS) with (amplification of fusion) or without MET gene alterations.

cancer. The range of copy numbers varied from 3.1 to 52.2. While most samples demonstrated <10, many samples displayed ≥10 copy numbers. Additionally, we observed a correlation between high copy number and probability of progressive disease. Furthermore, patients with MET aberrations demonstrated a shorter OS and PFS compared to those without. Finally, because patients with MET amplification showed a worse response to chemotherapy and no improved

response to immuno-oncology therapy, a new targeted therapy was warranted for such patients.

Until recently, MET fusion, such as KIF5B-MET, MET-ATXN7L1, and HLA-DRB1-MET had mainly been reported in lung cancer. In our study, MET was most commonly fused with ST7 followed by CFTR, PCM1, LRRD1, CAV1, CAPZA2, and TEFC. Whether patients with MET fusion (according to NGS) or MET-negativity (according to IHC)

respond to MET inhibitors warrants further investigation in future trials [22].

MET-amplified cases (*N* = 11) were confirmed by IHC, and approximately one-third of the patients with MET fusion had MET overexpression at the protein level (Supplementary Figure S1). We employed one of the most commonly used NGS panels in the clinic, namely, TSO 500 (Illumina). Although MET IHC and NGS results showed a strong correlation, more clinics are adopting NGS as a screening platform for oncology patients.

Conclusion

We identified MET gene aberrations in a cohort of Korean patients at the Samsung Medical Center Precision Oncology Clinic. NGS screening identified 46 patients (2.1%) with MET amplification, 10 (0.4%) with MET fusion, and 3 (0.1%) with concurrent amplification and fusion. Aberrant MET genes appeared in various cancers in the following order: gastric cancer (N = 17, 32.1%), colorectal cancer (*N* = 11, 20.8%), and CCC (*N* = 7, 13.2%). MET amplification and fusion occurred concurrently in patients with colorectal cancer and CCC. Additionally, patients with MET aberration (amplification or fusion) demonstrated significantly shorter OS and PFS. Based on our data, NGS panels, particularly TSO 500, may be a feasible, real-world practice for identifying MET aberrations in the clinic. Our data can be used as a guideline for the design of future clinical trials of MET inhibitors.

Data availability statement

The data generated in this study are available within the article and its **Supplementary Material**.

Ethics statement

The studies involving human participants were reviewed and approved by the Samsung Seoul Hospital (SMC) Committee for the use of human samples for experimental studies (IRB File No. 2021-09-052). The patients/participants provided their written informed consent to participate in this study.

Author contributions

Funding

Conflict of interest

The authors declare that the research was conducted in the absence of any commercial or financial relationships that could be construed as a potential conflict of interest.

Acknowledgments

We would like thank our patients and their families for their participation.

Supplementary material

The Supplementary Material for this article can be found online at: https://www.por-journal.com/articles/10.3389/pore. 2022.1610697/full#supplementary-material

References

1. Maulik G, Shrikhande A, Kijima T, Ma-P C, Morrison P, Salgia R. Role of the hepatocyte growth factor receptor, c-Met, in oncogenesis and potential for therapeutic inhibition. *Cytokine Growth Factor Rev* (2002) 13(1):41–59. doi:10. 1016/S1359-6101(01)00029-6

2. Lee J, Seo JW, Jun HJ, Ki CS, Park SH, Park YS, et al. Impact of met amplification on gastric cancer: possible roles as a novel prognostic marker and a potential therapeutic target. *Oncol Rep* (2011) 25(6):1517–24. doi:10.3892/or. 2011.1219

3. Lee SJ, Lee J, Park SH, Park JO, Lim HY, Kang WK, et al. c-MET overexpression in colorectal cancer: a poor prognostic factor for survival. *Clin Colorectal Cancer* (2018) 17(3):165–9. doi:10.1016/j.clcc.2018.02.013

4. Janjigian YY, Tang LH, Coit DG, Kelsen DP, Francone TD, Weiser MR, et al. MET expression and amplification in patients with localized gastric cancer. *Cancer Epidemiol Biomarkers Prev* (2011) 20(5):1021–7. doi:10.1158/1055-9965.EPI-10-1080

5. An X, Wang F, Shao Q, Wang F, Wang Z, Chen C, et al. MET amplification is not rare and predicts unfavorable clinical outcomes in patients with recurrent/ metastatic gastric cancer after chemotherapy. *Cancer* (2014) 120(5):675–82. doi:10. 1002/cncr.28454

6. Peruzzi B, Bottaro DP. Targeting the c-Met signaling pathway in cancer. *Clin Cancer Res* (2006) 1212:3657–60. doi:10.1158/1078-0432. CCR-06-0818

7. Moosavi F, Giovannetti E, Peters GJ, Firuzi O. Combination of HGF/MET-targeting agents and other therapeutic strategies in cancer. *Crit Rev Oncol Hematol* (2021) 160:103234. doi:10.1016/j.critrevonc.2021.103234

8. Lee H, Kim M, Lee H, Jung E, Yang H, Lee B, et al. MET in gastric carcinomas: comparison between protein expression and gene copy number and impact on clinical outcome. *Br J Cancer* (2012) 107(2):325–33. doi:10.1038/bjc.2012.237

9. Inokuchi M, Otsuki S, Fujimori Y, Sato Y, Nakagawa M, Kojima K. Clinical significance of MET in gastric cancer. *World J Gastrointest Oncol* (2015) 7(11):317–27. doi:10.4251/wjgo.v7.i11.317

10. Kawakami H, Okamoto I, Arao T, Okamoto W, Matsumoto K, Taniguchi H, et al. MET amplification as a potential therapeutic target in gastric cancer. *Oncotarget* (2013) 4(1):9–17. doi:10.18632/oncotarget.718

11. Chen C-T, Kim H, Liska D, Gao S, Christensen J, Weiser M. MET activation mediates resistance to lapatinib inhibition of HER2-amplified gastric cancer cells. *Mol Cancer Ther* (2012) 11(3):660–9. doi:10.1158/1535-7163.MCT-11-0754

12. Ha SY, Lee J, Kang SY, Do IG, Ahn S, Park JO, et al. MET overexpression assessed by new interpretation method predicts gene amplification and poor survival in advanced gastric carcinomas. *Mod Pathol* (2013) 26(12):1632–41. doi:10.1038/modpathol.2013.108

13. Shah MA, Cho J-Y, Tan IB, Tebbutt NC, Yen CJ, Kang A, et al. A randomized phase II study of folfox with or without the MET inhibitor onartuzumab in advanced adenocarcinoma of the stomach and gastroesophageal junction. *Oncologist* (2016) 21(9):1085–90. doi:10.1634/theoncologist.2016-0038

14. Lee J, Kim ST, Kim K, Lee H, Kozarewa I, Mortimer PGS, et al. Tumor genomic profiling guides patients with metastatic gastric cancer to targeted treatment: the VIKTORY umbrella trial. *Cancer Discov* (2019) 9(10):1388–405. doi:10.1158/2159-8290.CD-19-0442

15. Bang YJ, Su WC, Schuler M, Nam DH, Lim WT, Bauer TM, et al. Phase 1 study of capmatinib in MET-positive solid tumor patients: dose escalation and expansion of selected cohorts. *Cancer Sci* (2020) 111(2):536–47. doi:10.1111/cas.14254

16. Lorenzato A, Olivero M, Patanè S, Rosso E, Oliaro A, Comoglio PM, et al. Novel somatic mutations of the MET oncogene in human carcinoma metastases activating cell motility and invasion. *Cancer Res* (2002) 62(23):7025–30.

17. Raghav KPS, Gonzalez-Angulo AM, Blumenschein GR, Jr. Role of HGF/MET axis in resistance of lung cancer to contemporary management. *Transl Lung Cancer Res* (2012) 1(3):179–93. doi:10.3978/j.issn.2218-6751.2012.09.04

18. Mukai Y, Ueno H. Establishment and implementation of cancer genomic medicine in japan. *Cancer Sci* (2021) 112(3):970–7. doi:10.1111/cas.14754

19. Fujii S, Magliocco AM, Kim J, Okamoto W, Kim JE, Sawada K, et al. International harmonization of provisional diagnostic criteria for ERBB2-amplified metastatic colorectal cancer allowing for screening by next-generation sequencing panel. *JCO Precis Oncol* (2020) 4:6–19. doi:10.1200/PO.19.00154

20. Pestinger V, Smith M, Sillo T, Findlay JM, Laes JF, Martin G, et al. Use of an integrated pan-cancer oncology enrichment next-generation sequencing assay to measure tumour mutational burden and detect clinically actionable variants. *Mol Diagn Ther* (2020) 24(3):339–49. doi:10.1007/s40291-020-00462-x

21. Karasaki T, Nakajima J, Kakimi K. Neoantigens and whole-exome sequencing. *Gan To Kagaku Ryoho* (2016) 43(7):791–7.

22. Comoglio PM, Giordano S, Trusolino L. Drug development of MET inhibitors: targeting oncogene addiction and expedience. *Nat Rev Drug Discov* (2008) 7(6):504–16. doi:10.1038/nrd2530

Check for updates

PARP-1 genetic polymorphism associated with radiation sensitivity of non-small cell lung cancer

Hetong Wang[1,2†], Haitao Xie[3†], Shuying Wang[4], Jiaying Zhao[5], Ya Gao[6], Jun Chen[1], Yuxia Zhao[2] and Genyan Guo[2*]

[1]Department of Radiation Oncology, The Tenth People's Hospital of Shenyang, Shenyang, China,
[2]Department of Radiation Oncology, The Fourth Affiliated Hospital of China Medical University,
Shenyang, China, [3]Department of Radiation Oncology, Liaoning Cancer Hospital, Shenyang, China,
[4]Shandong Polytechnic College, Jining, China, [5]Department of Radiation Oncology, Qingdao United
Family Healthcare, Qingdao, China, [6]Department of Oncology, Kailuan Hospital, Tangshan, Hebei,
China

About 70% of non-small cell lung cancer (NSCLC) patients require radiotherapy. However, due to the difference in radiation sensitivity, the treatment outcome may differ for the same pathology and choice of treatment. Poly (ADP-ribose) polymerase 1 (PARP-1) is a key gene responsible for DNA repair and is involved in base excision repair as well as repair of single strand break induced by ionizing radiation and oxidative damage. In order to investigate the relationship between PARP-1 gene polymorphism and radiation sensitivity in NSCLC, we collected 141 primary NSCLC patients undergoing three-dimensional conformal radiotherapy. For each case, the gross tumor volumes (GTV) before radiation and that after 40 Gy radiation were measured to calculate the tumor regression rate. TaqMan real-time polymerase chain reaction was performed to genotype the single-nucleotide polymorphisms (SNPs). Genotype frequencies for PARP-1 genotypes were 14.2% for C/C, 44.7% for C/G and 41.1% for G/G. The average tumor regression rate after 40 Gy radiation therapy was 35.1% $\pm$ 0.192. Tumor regression rate of mid-term RT of C/C genotype was 44.6% $\pm$ 0.170, which was higher than that of genotype C/G and G/G (32.4% $\pm$ 0.196 and 34.8% $\pm$ 0.188, respectively) with statistical significance (F = 3.169 p = 0.045). The higher tumor regression rate in patients with C/C genotype suggested that G allele was a protective factor against radiation therapy. Using the median tumor regression rate of 34%, we divided the entire cohort into two groups, and found that the frequency distribution of PARP-1 gene rs3219073 had significant difference between these two groups (p < 0.05). These results showed that PARP-1 gene polymorphism may affect patient radiation sensitivity and predict the efficacy of radiotherapy. It therefore presents an opportunity for developing new therapeutic targets to improve radiotherapy outcome.

KEYWORDS

radiotherapy, polymorphism, non-small cell lung cancer (NSCLC), PARP-1, sensitivity

Introduction

Lung cancer has the highest incidence rate and mortality rate among different malignant tumors [1]. It has a 5-year overall survival rate of less than 15% in USA, and even lower in China [2]. The non-small-cell lung cancer (NSCLC) represents 80%–85% of newly diagnosed lung cancers. Within NSCLC patient population, about 75% patients are un-operable advanced lung cancers. Currently, radiation therapy (RT) is a crucial component for treating these patients. About 64.3% of the patients need RT at different phases during the course of treatment[3, 4]. However, the post-RT tumor regression rate and local control rate can be significantly different among patients. This is mainly due to the difference in radiation sensitivity for each patient, which is closely related to a series of factors such as cell cycle, cell hypoxia, proliferative activity, DNA damage repairing, as well as apoptosis of cells [5–9]. Hence, gene polymorphism, gene mutation and epigenetic modification affecting the underlying radiobiological response can also lead to difference in sensitivity, as interrelated genes have different biological responses to radiation.

DNA repairing mechanism within a cancer cell involves more than 150 genes and five main pathways: base excision repair (BER), nucleotide excision repair (NER), mismatch repair (MMR), double strand break repair (DSBR) and homologous recombination repair (HRR). Each pathway is responsible for repairing different types of DNA damages. The repairing of single strand breaks is mainly performed through BER pathway, which involves key genes such as PARP-1, OGG1, APE1, XRCC1. The BER pathway repairs DNA base damages caused by oxidative reagents and alkylating agents, which plays an important role in the maintenance of DNA integrity [10–12]. It is believed that the ability of BER pathway in repairing damaged DNAs is associated with the radiosensitivity of lung cancer cells.

Poly (ADP-ribose) polymerase 1 (PARP-1) is a key DNA repairing gene closely involved in the BER pathway, and is responsible for single strand break repairing induced by ionizing radiation and oxidative damage [13]. Currently, several types of PARP-1 inhibitors have been studied in clinical trials, which have shown that inhibiting the activity of PARP-1 could inhibit DNA repair and therefore improve the damaging effect of radiotherapy and chemotherapy[14, 15]. In our previous study, it was shown that PARP-1 rs3219073 gene polymorphism was closely associated with the occurrence of lung cancer [16]. In this work, we investigate the effect of PARP-1 gene polymorphism on the radiosensitivity of patient with lung cancer, as well as that on the effectiveness of RT. It is hypothesized that the gene repairing capacity can be affected by PARP-1 gene polymorphism, which might affect the efficacy of RT.

Materials and methods

Study population

All the subjects in this work were Han population in the northern region of China without blood ties. This study has been approved by the Ethics Committee of the Fourth Affiliated Hospital of China Medical University (EC-2019-HY-016). With written consent, the peripheral blood samples were collected, and an epidemiological study was then conducted. This study included 141 primary NSCLC patients recruited from our institution between September 2009 and December 2012. All cases were pathologically confirmed and without lung operational resection. Within the patient cohort, 89 were squamous cell carcinoma, and 52 were adenocarcinoma.

Treatment

All the patient cohort underwent three-dimensional conformal radiotherapy (3D-CRT) treatment consisting of 20 treatment fractions with a total of 40 Gy radiation dose. Within the patient cohort, 88 patients received chemotherapy for 2–4 weeks, and were then treated with radiotherapy 2 weeks after the last chemotherapy and after the hemogram returned normal, the others chose radiotherapy directly and actively without chemotherapy. There was no interruption or chemotherapy during the course of radiotherapy. All patients were simulated using computer tomography (Siemens) in supine, immobilized position. The gross tumor volume (GTV) included the primary tumor and the metastasis lymph node within 1 cm radius or that directly fused with the primary tumor. For each case, the tumor volume was measured before and after treatment. The clinical target volume (CTV) and the planning target volume (PTV) were defined by expanding the GTV with a 6–8 mm margin, and by expanding the CTV with a 6–10 mm margin, respectively. Fixed display window width and window level set by Treatment Planning System (TPS) were used for treatment planning (Pulmonary WW: 1600, WL: -300; mediastinal WW: 400, WL: 800).

3D-CRT was performed using a 6 MV linear accelerator (Siemens), with the 95% prescribed dose line covering 95% of PTV. Patients were re-scanned in the same position at the end of the entire 40 Gy treatment. The tumor target was then re-outlined to update the gross tumor volume (renamed as GTVS), clinical target volume (renamed as CTVS) and planning target volume (renamed as PTVS) after treatment. Tumor regression rate was then calculated from GTV (before RT) and GTVS (after 40 Gy RT) using the following expression: R= (GTV before RT - GTVS after 40 Gy RT)/(GTV before RT) × 100%.

TABLE 1 Tumor regression rate and general characteristics of rs3219073 genotype.

		Patients	Tumor regression rate of mid radiation therapy (mean ± SD)	p-value[a]	Genotype			p-value[b]
					C/C	C/G	G/G	
Gender	Male	105	35.0% ± 19.6%	0.886	13	44	48	0.153
	Female	36	35.5% ± 18.2%		7	19	10	
Age	>60	69	36.3% ± 18.3%	0.479	9	32	28	0.895
	≤60	72	34.0% ± 20.1%		11	31	30	
Smoking status	Yes	98	37.3% ± 18.1%	0.047	12	48	38	0.270
	No	43	30.3% ± 20.8%		8	15	20	
Histology	Squamous carcinoma	89	36.8% ± 19.4%	0.192	12	38	39	0.698
	Adenocarcinoma	52	32.4% ± 18.6%		8	25	19	
Pathological stage	I	11	42.6% ± 19.8%	0.507[c]	2	6	3	0.454
	II	20	32.1% ± 18.6%		1	9	10	
	III	84	34.5% ± 19.7%		13	33	38	
	IV	26	36.3% ± 17.7%		4	15	7	
GTV group	Small volume	71	33.0% ± 19.7%	0.177	11	34	26	0.564
	Large volume	70	37.3% ± 18.5%		9	29	32	

[a]p-value was calculated by t test.
[b]p-value was calculated by χ2 test.
[c]p-value was calculated by variance analysis.

Gene extraction and classification

Two milliliters of peripheral blood samples were collected from each participant and stored in sodium citrate tubes. DNA was then extracted using proteinase K (Merck) digestion and phenol–chloroform (Dingguo Biology)extraction method. Taqman real-time polymerase chain reaction (RT-PCD) was performed (SDS software, Applied Biosystems) to genotype the single-nucleotide polymorphisms (SNPs). To test the PCD pollution in each 96-well plate and to ensure the accuracy of the genotype results, standard testing procedure using duplicate samples, negative controls without template DNA and double distilled water were performed. 10% of the samples were randomly selected to repeat blind assays. RT-PCR reactions were run in 5 μl mixture including 2.5 μl of Taqman Master Mix (2X), 0.25 μl of primer + probe (20X), 1.25 μl of H_2O, and 1.00 μl of genomic DNA. Primers, Taqman probes and Master Mix were designed and provided by Applied Biosystems. PCR conditions included initial denaturing step at 95°C for 10 min followed by 47 cycles at 92°C for 30s and then at 60°C for 60s. Allelic Discrimination program of SDS software (Applied Biosystems) was used to detect the fluorescence intensity of FAM and VIC markers by different alleles, as well as to assay genotypes.

Statistical analysis

Student t tests were used (SPSS 13.0 software) to evaluate the relationship between tumor regression rate and gender, age, and histological type, respectively. Variance analysis was used to evaluate the relationship between the tumor regression rate and the stage. If $p < 0.05$, SNK multiple comparison tests were used, as well as the SNPs. χ2 tests were used to compare genotype distribution between those general characteristics.

Results

Tumor regression rate and general characteristics of rs3219073 genotype

The distributions of selected characteristics of 141 lung cancer cases are shown in Table 1. Genotype frequencies for PARP-1 rs3219073 SNP genotypes were 14.2% for C/C, 44.7% for C/G and 41.1% for G/G. No statistically significant correlation was observed between genotypes and gender, age, smoking status, histological type, or clinical stage ($p > 0.05$), as shown in the Table 1 (last column).

The average tumor regression rate after 40 Gy RT was 35.1% ± 19.2%. Three of them presented larger tumor volume than that before treatment (they were −61.1 cm^3, −3.3 cm^3, −2.92 cm^3 respectively). Tumor regression rates of smoking patients were higher than that of non-smoking patients' ($p = 0.047$). There was no statistically correlation observed between tumor regression rate and gender, age, histological type, or clinical stage ($p > 0.05$).

Although larger volume tumors (volume >= 89.97 cm^3, medium GTV) shrank more than small volume tumors

TABLE 2 Relationship between gene polymorphism and tumor regression rate of mid radiotherapy.

Genotype	Patients	Tumor regression rate of mid radiation therapy. (mean ± SD)	F-value	p-value	LSD p-value
C/C	20	44.6% ± 17.0%			—
C/G	63	32.4% ± 19.6%[a]	3.169	0.045	0.013
G/G	58	34.8% ± 18.8%[a]			0.048
C/G + G/G	121	33.6% ± 19.2%[a]			0.017[b]

[a]Compared with group C/C, p-value was calculated by variance analysis.
[b]p-value was calculated by student t test.

TABLE 3 Distribution difference of Gene polymorphisms groups by median value of tumor regression rate.

Genotype	Patients	≤34%	>34%	χ^2 -value	p-value
C/C	20	6 (30.0%)	14 (70.0%)		
C/G	63	38 (60.3%)	25 (39.7%)	6.152	0.045
G/G	58	27 (46.6%)	31 (53.4%)		
C/G + G/G	121	65 (53.7%)	56 (46.3%)	3.863	0.049

p-value was calculated by variance analysis.

(<89.97 cm³), there was no statistical difference in tumor regression rate between them (p = 0.177, Table 1, last row).

Genetic polymorphisms and curative effect of lung cancer radiotherapy

The effect of radiotherapy differs for different genotype carriers, as shown in Figure 1. Tumor regression rate of mid-term RT of C/C genotype was 44.6% ± 0.170, which was significantly higher than that of the other two genotypes (C/G + G/G, modified value, 33%) with statistical differences (F = 5.87, p = 0.017), as shown in Table 2. In addition, there was significant difference in tumor regression rate between C/C genotype and either of the other two genotypes (C/C vs. C/G, p = 0.013; C/C vs. G/G, p = 0.048). No significant difference was observed between C/G vs. G/G (p = 0.485).
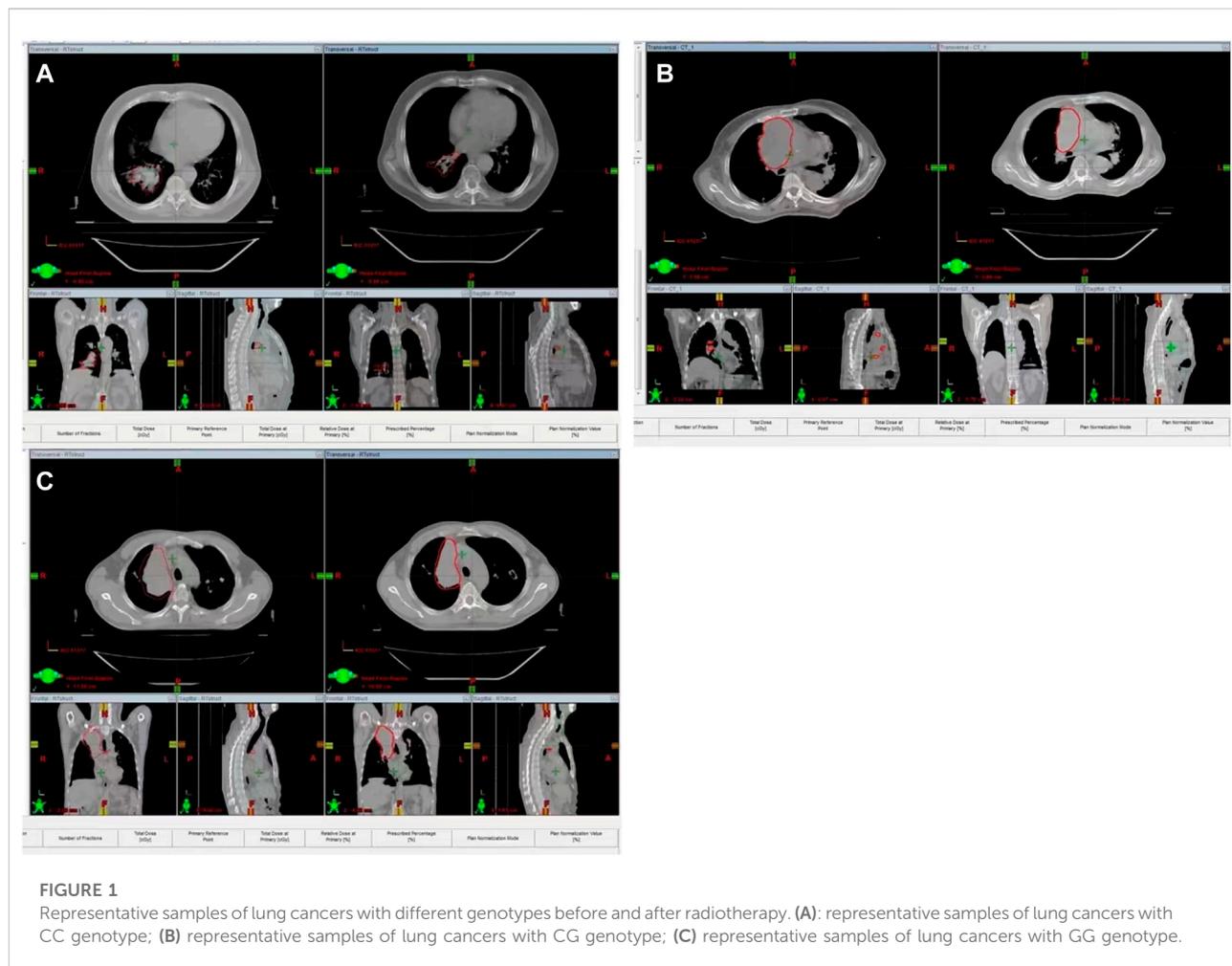
We further divided the entire patient cohort into two groups using the median tumor regression rate of 34.0%, and found that the frequency distribution of PARP-1 gene rs3219073 between the two groups had significant difference (p < 0.05) (Table 3).

Discussion

Studies have demonstrated that radiation therapy can effectively reduce the primary tumor volume, improve local control rate, and may affect the survival time. For example, Fox [17] found that, in the mid-term of RT, the tumor regression rate at 30Gy and 50Gy were 24.7% and 44.3%. Ramsey [18] observed GTV changed every week during the course of RT and found significant decrease of GTV. Although the curative effect of RT is affirmative, tumor shrinkages during RT had been shown to significantly differ among NSCLC patients. Kupelian [19] demonstrated that the tumors with larger original volume had higher tumor regression rate than that with smaller volume. We also had similar observation, despite that no statistical difference was found. Siker [20] and Woodford [21] found that there was no obvious relationship between tumor regression and chemotherapy, pathology, tumor original volume, radiation treatment time, or stages. In this work, we observed that volume changes of primary tumors were not correlated with gender, age, or properties of tumors. Consequently, the possibility that the patient's own gene mutation and epigenetic modifications result in the differences of radiation sensitivity and tumor regression rate should be considered.

In this study, we found a correlation between primary tumor volume change and smoking status (p = 0.047). Studies have shown that cigarette combustion can produce a large amount of oxidation substances and Reactive Oxygen Species (ROS), which might damage cells' genome, biomembrane, macromolecule, as well as DNA structure [10–13,22,23]. The biological effect of

FIGURE 1
Representative samples of lung cancers with different genotypes before and after radiotherapy. **(A)**: representative samples of lung cancers with CC genotype; **(B)** representative samples of lung cancers with CG genotype; **(C)** representative samples of lung cancers with GG genotype.

ionizing radiation is mainly explained by the DNA damage due to direct and indirect interaction with the DNA structure of tumor cells. We observed that DNA oxidative damage caused by smoking might enhance the sensitivity of radiotherapy and contributed to a larger tumor volume reduction in this study.

PARP-1, existing in eukaryotic cells, is the nuclear enzyme that catalyzes poly ADP-ribosylation. PARP-1 can selectively recognize and bind with DNA polymerase in DNA gaps to maintain the integrity of the genome and repair the single strand breaks (SSBs). In addition, PARP-1 can participate in DNA double strand breaks (DSBs) repair along the HR and NHEJ pathway in the DNA replication fork [24]. PARP-1 can also recruit protein MRE11, ATM (ataxiatel angiectasia mutated) to suppress the transcription factors E2F4 and P130 complexes and impact the expression of breast cancer susceptibility genes BRCA1 and RAD5 [25], which transiently protects the DNA gaps and inhibits recombinant. PARP1 could interact with XPA, which enhances the activity of PARP1, the DNA damage-binding protein 2 (DDB2), and transcription factor II H (TFIIH), potentially involved in NER pathway. DNA injuries

caused by oxidizing agents, alkylating agents and ionizing radiation can rapidly activate PARP-1 [15, 26], and complete the DNA damage repair through the mechanisms mentioned above. Therefore, PARP-l plays an important role in maintaining and repairing genomic integrity.

Inhibition of PARP-l may lead to increased susceptibility to tumor by predisposing the body to DNA damage factor caused by ionizing radiation, and increase the therapeutic effect of chemotherapy and radiotherapy on cancer by decreasing DNA repair function [27, 28]. Chalmers AJ et al. observed the radio-sensitization effect of PARP inhibitors *in vitro* and animal models with lung cancer, colorectal cancer, head and neck cancer, glioma, cervical cancer, and prostate cancer[29]. Many PARP-1 inhibitors had been tested in clinical studies [30–34]. Studies have shown that PARP1 inhibitors are involved in cell migration induced by inhibition of erythropoietin. The mechanism is related to the down-regulation of c-fos and expression of Egr-1 [35]. It was also found that mutation of BRCA1 or BRCA2 was a predictor of PARP inhibitors [33, 34]. These studies indicate that PARP-1 is

involved in multiple DNA repair pathways, despite that the mechanism is unclear. In previous studies, we found that the patients carrying G allele had a reduced risk of lung cancer, especially adenocarcinoma. In this study, we excluded the effects of chemotherapy and operation on the curative effects of radiotherapy, and evaluated the radiosensitivity of NSCLC patients using tumor regression rate at mid-RT of 40 Gy/20f. We found that rs3219073 gene polymorphism may affect the radiation sensitivity. Patients with C/C genotype had higher tumor regression rate than that with C/G and G/G genotype ($p = 0.045$). C/C genotype had significant difference from C/G and G/G genotypes in terms of tumor regression rate ($p = 0.013$, $p = 0.048$), respectively. Carrying the G allele is related with reduced tumor regression rate ($p = 0.017$), which suggests that the G allele is a protective factor against RT. On the other hand, patients carrying C allele may be more sensitive to radiation therapy. As far as we know, this is the first study to report the relationship between PARP-1 genetic polymorphisms and radiation sensitivity of NSCLC. DNA is the major target of cell injury caused by ionizing radiation through SSB and DSB. Although part of them could be quickly and fidelity repaired by repair genes, it is the main mechanism of tumor cells killing by ionizing radiation [29, 36]. The rs3219073 C allele gene may suppress the activity of PARP-1 repair gene, which increases lethal cellular damage, inhibits damage repair, and consequently increases the sensitivity and efficacy of RT [37]. Of course, further clinical trials and infra-tests are required to confirm this theory. In summary, PARP-1 gene rs3219073 polymorphism may predict the efficacy of radiotherapy and provide new therapeutic targets to improve the radiotherapy sensitivity of NSCLC patients.

Data availability statement

The data presented in the study are included in the article. Further inquiries can be directed to the corresponding author.

Ethics statement

The studies involving human participants were reviewed and approved by Ethics Committee of the Fourth Affiliated Hospital of China Medical University. The patients/participants provided their written informed consent to participate in this study.

Author contributions

Conception and design: HW, HX, and GG; Administrative support: GG; Provision of study materials or patients: JZ and YG; Collection and assembly of data: HW, SW, and JC; Data analysis and interpretation: HW and SW; Writing-original draft preparation: HW; Writing—review and editing: HW, YZ, and GG; All authors have read and agreed to the published version of the manuscript. All authors listed contributed significantly to the design and implementation of the investigation.

Funding

Conflict of interest

The authors declare that the research was conducted in the absence of any commercial or financial relationships that could be construed as a potential conflict of interest.

References

1. Siegel RL, Miller KD, Fuchs HE, Jemal A. Cancer statistics, 2021. *CA Cancer J Clin* (2021) 71(1):7–33. doi:10.3322/caac.21654

2. Chen W, Zheng R, Baade PD, Zhang S, Zeng H, Bray F, et al. Cancer statistics in China, 2015. *CA Cancer J Clin* (2016) 66(2):115–32. doi:10.3322/caac.21338

3. Rivera MP. Multimodality therapy in the treatment of lung cancer. *Semin Respir Crit Care Med* (2004) 25:3–10. doi:10.1055/s-2004-829639

4. Tyldesley S, Boyd C, Schulze K, Walker H, Mackillop WJ. Estimating the need for radiotherapy for lung cancer: An evidence-based, epidemiologic approach. *Int J Radiat Oncol Biol Phys* (2001) 49(4):973–85. doi:10.1016/s0360-3016(00)01401-2

5. Shimura T, Kakuda S, Ochiai Y, Nakagawa H, Kuwahara Y, Takai Y, et al. Acquired radioresistance of human tumor cells by DNA-pk/akt/gsk3beta-mediated cyclin D1 overexpression. *Oncogene* (2010) 29(34):4826–37. doi:10.1038/onc.2010.238

6. Peltonen JK, Vahakangas KH, Helppi HM, Bloigu R, Paakko P, Turpeenniemi-Hujanen T. Specific Tp53 mutations predict aggressive phenotype in head and neck squamous cell carcinoma: A retrospective archival study. *Head Neck Oncol* (2011) 3: 20. doi:10.1186/1758-3284-3-20

7. Parliament MB, Murray D. Single nucleotide polymorphisms of DNA repair genes as predictors of radioresponse. *Semin Radiat Oncol* (2010) 20(4):232–40. doi:10.1016/j.semradonc.2010.05.003

8. Karar J, Maity A. Modulating the tumor microenvironment to increase radiation responsiveness. *Cancer Biol Ther* (2009) 8(21):1994–2001. doi:10.4161/cbt.8.21.9988

9. Baumann M, Krause M, Hill R. Exploring the role of cancer stem cells in radioresistance. *Nat Rev Cancer* (2008) 8(7):545–54. doi:10.1038/nrc2419

10. Yanbaeva DG, Dentener MA, Creutzberg EC, Wesseling G, Wouters EFM. Systemic effects of smoking. *Chest* (2007) 131(5):1557–66. doi:10.1378/chest.06-2179

11. Lyakhovich VV, Vavilin VA, Zenkov NK, Menshchikova EB. Active defense under oxidative stress. The antioxidant responsive element. *Biochemistry* (2006) 71(9):962–74. doi:10.1134/S0006297906090033

12. Goto M, Ueda K, Hashimoto T, Fujiwara S, Matsuyama K, Kometani T, et al. A formation mechanism for 8-hydroxy-2 '-Deoxyguanosine mediated by peroxidized 2 '-Deoxythymidine. *Free Radic Biol Med* (2008) 45(9):1318–25. doi:10.1016/j.freeradbiomed.2008.08.003

13. van Helden YGJ, Keijer J, Heil SG, Pico C, Palou A, Oliver P, et al. Beta-carotene affects oxidative stress-related DNA damage in lung epithelial cells and in ferret lung. *Carcinogenesis* (2009) 30(12):2070–6. doi:10.1093/carcin/bgp186

14. Morrison C, Smith GC, Stingl L, Jackson SP, Wagner EF, Wang ZQ. Genetic interaction between parp and DNA-pk in V(D)J recombination and tumorigenesis. *Nat Genet* (1997) 17(4):479–82. doi:10.1038/ng1297-479

15. Burkle A. Physiology and pathophysiology of poly(adp-Ribosyl)Ation. *Bioessays* (2001) 23(9):795–806. doi:10.1002/Bies.1115

16. Wang HT, Gao Y, Zhao YX, Yu H, Wang TL, Bai L, et al. Parp-1 Rs3219073 polymorphism may contribute to susceptibility to lung cancer. *Genet Test Mol Biomarkers* (2014) 18(11):736–40. doi:10.1089/gtmb.2014.0106

17. Fox J, Ford E, Redmond K, Zhou J, Wong J, Song DY. Quantification of tumor volume changes during radiotherapy for non-small-cell lung cancer. *Int J Radiat Oncol Biol Phys* (2009) 74(2):341–8. doi:10.1016/j.ijrobp.2008.07.063

18. Ramsey CR, Langen KM, Kupelian PA, Scaperoth DD, Meeks SL, Mahan SL, et al. A technique for adaptive image-guided helical tomotherapy for lung cancer. *Int J Radiat Oncol Biol Phys* (2006) 64(4):1237–44. doi:10.1016/j.ijrobp.2005.11.012

19. Kupelian PA, Ramsey C, Meeks SL, Willoughby TR, Forbes A, Wagner TH, et al. Serial megavoltage ct imaging during external beam radiotherapy for non-small-cell lung cancer: Observations on tumor regression during treatment. *Int J Radiat Oncol Biol Phys* (2005) 63(4):1024–8. doi:10.1016/j.ijrobp.2005.04.046

20. Siker ML, Tome WA, Mehta MP. Tumor volume changes on serial imaging with megavoltage ct for non-small-cell lung cancer during intensity-modulated radiotherapy: How reliable, consistent, and meaningful is the effect? *Int J Radiat Oncol Biol Phys* (2006) 66(1):135–41. doi:10.1016/j.ijrobp.2006.03.064

21. Woodford C, Yartsev S, Dar AR, Bauman G, Van Dyk J. Adaptive radiotherapy planning on decreasing gross tumor volumes as seen on megavoltage computed tomography images. *Int J Radiat Oncol Biol Phys* (2007) 69(4):1316–22. doi:10.1016/j.ijrobp.2007.07.2369

22. Hecht SS. Cigarette smoking and lung cancer: Chemical mechanisms and approaches to prevention. *Lancet Oncol* (2002) 3(8):461–9. doi:10.1016/s1470-2045(02)00815-x

23. Bargagli E, Olivieri C, Bennett D, Prasse A, Muller-Quernheim J, Rottoli P. Oxidative stress in the pathogenesis of diffuse lung diseases: A review. *Respir Med* (2009) 103(9):1245–56. doi:10.1016/j.rmed.2009.04.014

24. Krishnakumar R, Kraus WL. The parp side of the nucleus: Molecular actions, physiological outcomes, and clinical targets. *Mol Cel* (2010) 39(1):8–24. doi:10.1016/j.molcel.2010.06.017

25. Hegan DC, Lu Y, Stachelek GC, Crosby ME, Bindra RS, Glazer PM. Inhibition of poly(adp-ribose) polymerase down-regulates Brca1 and Rad51 in a pathway mediated by E2f4 and P130. *Proc Natl Acad Sci U S A* (2010) 107(5):2201–6. doi:10.1073/pnas.0904783107

26. Masutani M, Nakagama H, Sugimura T. Poly(Adp-Ribose) and carcinogenesis. *Genes Chromosomes Cancer* (2003) 38(4):339–48. doi:10.1002/gcc.10250

27. Rouleau M, Patel A, Hendzel MJ, Kaufmann SH, Poirier GG. Parp inhibition: Parp1 and beyond. *Nat Rev Cancer* (2010) 10(4):293–301. doi:10.1038/nrc2812

28. Camero S, Ceccarelli S, De Felice F, Marampon F, Mannarino O, Camicia L, et al. Parp inhibitors affect growth, survival and radiation susceptibility of human alveolar and embryonal rhabdomyosarcoma cell lines. *J Cancer Res Clin Oncol* (2019) 145(1):137–52. doi:10.1007/s00432-018-2774-6

29. Chalmers AJ, Lakshman M, Chan N, Bristow RG. Poly(Adp-Ribose) polymerase inhibition as a model for synthetic lethality in developing radiation oncology targets. *Semin Radiat Oncol* (2010) 20(4):274–81. doi:10.1016/j.semradonc.2010.06.001

30. Wahner Hendrickson AE, Menefee ME, Hartmann LC, Long HJ, Northfelt DW, Reid JM, et al. A phase I clinical trial of the poly(adp-ribose) polymerase inhibitor veliparib and weekly topotecan in patients with solid tumors. *Clin Cancer Res* (2018) 24(4):744–52. doi:10.1158/1078-0432.CCR-17-1590

31. Kummar S, Kinders R, Gutierrez ME, Rubinstein L, Parchment RE, Phillips LR, et al. Phase 0 clinical trial of the poly (Adp-Ribose) polymerase inhibitor abt-888 in patients with advanced malignancies. *J Clin Oncol* (2009) 27(16):2705–11. doi:10.1200/JCO.2008.19.7681

32. Gadducci A, Cosio S. Randomized clinical trials and real world prospective observational studies on bevacizumab, parp inhibitors, and immune checkpoint inhibitors in the first-line treatment of advanced ovarian carcinoma: A critical review. *Anticancer Res* (2021) 41(10):4673–85. doi:10.21873/anticanres.15281

33. Fong PC, Yap TA, Boss DS, Carden CP, Mergui-Roelvink M, Gourley C, et al. Poly(Adp)-Ribose polymerase inhibition: Frequent durable responses in brca carrier ovarian cancer correlating with platinum-free interval. *J Clin Oncol* (2010) 28(15):2512–9. doi:10.1200/JCO.2009.26.9589

34. Tutt A, Robson M, Garber JE, Domchek SM, Audeh MW, Weitzel JN, et al. Oral poly(adp-ribose) polymerase inhibitor olaparib in patients with Brca1 or Brca2 mutations and advanced breast cancer: A proof-of-concept trial. *Lancet (London, England)* (2010) 376(9737):235–44. doi:10.1016/S0140-6736(10)60892-6

35. Inbar D, Cohen-Armon M, Neumann D. Erythropoietin-driven signalling and cell migration mediated by polyadp-ribosylation. *Br J Cancer* (2012) 107(8):1317–26. doi:10.1038/bjc.2012.395

36. Meyn RE, Munshi A, Haymach JV, Milas L, Ang KK. Receptor signaling as a regulatory mechanism of DNA repair. *Radiother Oncol* (2009) 92(3):316–22. doi:10.1016/j.radonc.2009.06.031

37. Barreto-Andrade JC, Efimova EV, Mauceri HJ, Beckett MA, Sutton HG, Darga TE, et al. Response of human prostate cancer cells and tumors to combining parp inhibition with ionizing radiation. *Mol Cancer Ther* (2011) 10(7):1185–93. doi:10.1158/1535-7163.MCT-11-0061